Technical Report Documentation Page

1. Report No.	2. Government Accession No.	3. Recipient's Catalog No.
FHWA/TX-12/0-5722-1		

4. Title and Subtitle	5. Report Date
PERFORMANCE OF LAP SPLICES IN LARGE-SCALE COLUMN SPECIMENS AFFECTED BY ASR AND/OR DEF	Published: June 2012
	6. Performing Organization Code

7. Author(s)	8. Performing Organization Report No.
Joseph M. Bracci, Paolo Gardoni, M. Kathleen Eck, and David Trejo	Report 0-5722-1

9. Performing Organization Name and Address	10. Work Unit No. (TRAIS)
Texas Transportation Institute The Texas A&M University System College Station, Texas 77843-3135	11. Contract or Grant No. Project 0-5722

12. Sponsoring Agency Name and Address	13. Type of Report and Period Covered
Texas Department of Transportation Research and Technology Implementation Office P.O. Box 5080 Austin, Texas 78763-5080	Technical Report: September 2006–August 2011
	14. Sponsoring Agency Code

15. Supplementary Notes

Project performed in cooperation with the Texas Department of Transportation and the Federal Highway Administration.

Project Title: Lap Splice and Development Length Performance in ASR and/or DEF Damaged Concrete Elements

URL: http://tti.tamu.edu/documents/0-5722-1.pdf

16. Abstract

This research program conducted a large experimental program, which consisted of the design, construction, curing, deterioration, and structural load testing of 16 large-scale column specimens with a critical lap splice region, and then compared and calibrated models developed in the analytical program with the experimental behavior. Specimens were carefully instrumented both internally and externally to monitor the strain behavior of the concrete and reinforcing steel from specimen construction, curing, deterioration, and final structural load testing.

17. Key Words	18. Distribution Statement
Alkali-Silica Reaction, ASR, Delayed Ettringite Formation, DEF, Lap Splice, Reinforced Concrete, Bridge Column	No restrictions. This document is available to the public through NTIS: National Technical Information Service Alexandria, Virginia 22312 http://www.ntis.gov

19. Security Classif. (of this report)	20. Security Classif. (of this page)	21. No. of Pages	22. Price
Unclassified	Unclassified	380	

Form DOT F 1700.7 (8-72) **Reproduction of completed page authorized**

PERFORMANCE OF LAP SPLICES IN LARGE-SCALE COLUMN SPECIMENS AFFECTED BY ASR AND/OR DEF

by

Joseph M. Bracci, Paolo Gardoni, M. Kathleen Eck, and David Trejo

Zachry Department of Civil Engineering and
Texas Transportation Institute

Report 0-5722-1
Project 0-5722
Project Title: Lap Splice and Development Length Performance in ASR and/or DEF Damaged Concrete Elements

Performed in cooperation with the
Texas Department of Transportation
and the
Federal Highway Administration

Published: June 2012

TEXAS TRANSPORTATION INSTITUTE
The Texas A&M University System
College Station, Texas 77843-3135

DISCLAIMER

This research was performed in cooperation with the Texas Department of Transportation (TxDOT) and the Federal Highway Administration (FHWA). The contents of this report reflect the views of the authors, who are responsible for the facts and the accuracy of the data presented herein. The contents do not necessarily reflect the official view or policies of the FHWA or TxDOT. This report does not constitute a standard, specification, or regulation.

This report is not intended for construction, bidding, or permit purposes. The engineer in charge of the project was Joseph M. Bracci, P.E. #79855.

ACKNOWLEDGMENTS

This project was conducted at Texas A&M University and was supported by the Texas Department of Transportation and the Federal Highway Administration through the Texas Transportation Institute. The authors acknowledge the efforts and contributions of the TxDOT project director, Ricardo Gonzalez, and the members of the Project Monitoring Committee, including Keith Ramsay and John Vogel. The authors are grateful and are especially proud of the graduate and undergraduate student researchers involved in the research program including Ryan Alberson, Kathleen Eck, Jason Zidek, Marcus Schniers, and the many other students that contributed during the large-scale specimen construction. The authors also acknowledge Ryan Alberson's significant contribution to the writing of Chapter 2 and sections 5.1 through 5.3. The work of Drs. Young-Hoon Kim and Pillai Radhakrishna are appreciated for their contributions in the Materials Program of the research program. The authors thank Dr. Peter Keating and Mr. Matt Potter of the Civil Engineering High-Bay Structural and Materials Laboratory at Texas A&M University for their technical and logistical assistance during in the construction and structural testing of the large-scale specimens. The authors also acknowledge the donation of the reinforcing steel for the large-scale specimens from CMC Inc., in particular Paul Fredrickson.

TABLE OF CONTENTS

Page

LIST OF FIGURES

Page

LIST OF TABLES

Page

CHAPTER 1:
INTRODUCTION

1.1 PROBLEM STATEMENT

Over the past 25 years or so, the Texas Department of Transportation (TxDOT) has had an aggressive construction program in place to accommodate the expanding population growth within Texas. A significant amount of construction has occurred throughout the state, especially in major metropolitan areas. Because of constrained conditions in metropolitan areas in terms of access space and the raw scale of transportation systems needed to satisfy the increasing traffic demands, the size of transportation structures, both at the member and system levels, have become significantly larger than past construction. Unlike nominal-size concrete placements, large concrete placements can experience elevated temperatures during hydration, which can later lead to cracking and deterioration of these concrete structures. Moreover, contractors have taken aggressive approaches in the construction of such structures to meet the construction demands in these metropolitan areas. In addition to aggressive scheduling and resource allocations, some contractors are believed to have proportioned concrete mixtures with early set cement (Type III) to achieve high early strengths. This way, the forms can be removed more quickly, thus expediting the completion of construction. Although advantageous in minimizing construction costs and build time, this practice may have contributed to the early cracking of many structures (termed premature concrete deterioration).

In addition, the chemical constituents in the cement and aggregates play a key role in the durability of concrete structures. Prof. Folliard's research group at The University of Texas at Austin (Bauer et al. 2006 and Folliard et al. 2006) have documented the fact that high alkali contents in cement, especially in Type III cement, can result in Alkali Silica Reactions (ASR) when used with reactive siliceous aggregates (prominent in Texas) in concrete in the presence of moisture. ASR can lead to the formation of expansive by-products, which in turn can lead to cracking of the concrete. Folliard et al. (2006) and Burgher et al. (2008) also found that concrete

cracking from ASR can lead to other deterioration processes, such as Delayed Ettringite Formation (DEF) and corrosion, which can further reduce the capacity of the structure.

1.2 PREMATURE CONCRETE DETERIORATION MECHANISMS

This section provides an overview of the literature on ASR and DEF as mechanisms of premature concrete deterioration. Prior research has not identified the contribution of either mechanism on the magnitude of deterioration, but the literature has defined certain criteria for the mechanism to be present (Folliard et al. 2006). The section below provides a brief review of ASR and DEF mechanisms, followed by how ASR and DEF influence, or damage, reinforced concrete structures.

1.2.1 Alkali Silica Reaction (ASR)

ASR is the chemical reaction between the alkalis in concrete (generally from high alkali cement contents greater than about 5 lb/cy) and reactive silica found in naturally occurring aggregates from quarries. Conditions required for ASR to develop include reactive silica phases in the aggregate, availability of alkali hydroxides in the pore solution ($[Na^+]$, $[K^+]$, or $[OH^-]$), and sufficient moisture (Folliard et al. 2006). The reaction between the reactive silica in the aggregate and the alkalis in the pore solution produce a by-product, commonly referred to as ASR gel, that expands when exposed to supplemental moisture, causing overall concrete expansion. However, the alkalis and reactive silica are consumed with time and are eventually depleted. As these constituents are consumed, the ASR process will stop unless these constituents are provided from an external source (Folliard et al. 2006).

In addition, Berube et al. (2002) reported that the exposure conditions of concrete will greatly influence the development of surface cracking of concrete members affected by ASR and their expansion. In particular, they reported that wetting and drying cycles greatly promoted surface cracking despite the fact that the surface expansion due to ASR was reduced when the concrete was allowed to dry. This is believed to be a result of the inter-leaching of the alkalis from the surface layer. As the alkali content on the surface layer is reduced, the amount of ASR gel is reduced. This

will lead to differential strains between the interior and surface layers, resulting in cracking of the surface layer. It is also believed that the surface cracking may be exaggerated in members without sufficient confining reinforcement due to the continuing internal ASR expansion.

As the ASR gel forms, Folliard et al. (2006) found that tensile stresses develop internally in the concrete. In general, the hydrated cement paste (HCP) is weaker than the aggregate, and cracking initially occurs in the HCP or along the interface of the aggregate and HCP (Poole 1992, Swamy 1992). Jensen (2003) found that ASR-damaged concrete exhibited both cracking in the HCP and aggregate, and even quantified the amount of cracking in the aggregate. Bazant et al. (2000) modeled the fracture mechanics of ASR using radial cracks propagating from flaws at the aggregate-HCP interface into the HCP using the theories of Poole (1992) and Swamy (1992). The literature indicates that although cracking due to ASR initiates in the HCP, eventual expansion can result in cracking of the aggregates. Aggregate cracking can influence the shear capacity (aggregate interlock) and may be a factor that influences the bond strength of splice reinforcement.

ASR-induced overall concrete expansion can be significant. Fan and Hanson (1998a) measured length changes approaching 0.4 percent (strain of 0.004) in unreinforced concrete specimens subjected to accelerated exposure conditions. In Australia, Carse and Dux (1990) measured even larger expansions, finding up to 0.5 percent expansion on the surface of field structures (high-strength concrete bridges). While these expansions are severe, the presence of reinforcement can substantially reduce the expansion. Fan and Hanson (1998a) measured a 50 percent reduction in the expansion of reacting concrete when 0.54 percent steel reinforcement ratio was added. However, it was also noted that the ASR expansion can still be significant enough to yield the added reinforcement, which occurs at a strain of about 0.002.

1.2.2 Delayed Ettringite Formation (DEF)

In addition to high alkali contents, high cement contents in large volume concrete structures can lead to significant heat generation during the concrete hydration, which potentially can lead to concrete cracking both from thermal stresses and from the later age reformation of ettringite within

the concrete (termed Delayed Ettringite Formation or DEF). Many researchers have developed different hypotheses on how DEF occurs in hardened concrete, including Petrov et al. (2006), Folliard et al. (2006), and Burgher et al. (2008). In general, ettringite forms at early ages in fresh concrete. As the sulfates (typically from the gypsum in the cement) react with the calcium-aluminates in the presence of calcium hydroxide, these sulfates are consumed. Once the sulfate concentration in the pore solution reaches some lower value, the calcium-aluminate react with the already formed ettringite to produce monosulfoaluminate (Folliard et al. 2006). If sulfates are reintroduced to the pore solution, the monosulfoaluminates can revert to ettringite, causing expansive forces and concrete cracking. The sulfates can also be reintroduced from external sources or from internal sources. Ettringite reformation in hardened concrete is likely when the concrete curing temperatures exceed reported values from 148–160°F. When sulfate ions are subjected to high early heat, it is believed that the majority of these ions are physically attached to the calcium silicate hydrate (C-S-H) and are therefore available as a mobile source of sulfate at later ages (Scrivener and Lewis 1997, Odler and Chen 1996). Thus, concretes that experience elevated temperatures during hydration, either from high cement contents or large placements (typical of structures exhibiting cracking in Texas), can potentially be subjected to DEF.

The DEF-induced overall expansion of the concrete can greatly exceed that of ASR. Grattan-Bellew et al. (1998) measured a maximum expansion caused by DEF of greater than 0.4 percent over a period of about 65 days. However, Kelham et al. (1996) found that after several (~5) years of storage, DEF can cause expansions exceeding 2 percent. Unlike ASR where the stresses and cracking initiate at the HCP-aggregate interface, internal stresses from DEF occur in the HCP typically at void locations (Folliard et al., 2006 and Burgher et al., 2008). Although damage initiates in different areas, both mechanisms (ASR and DEF) lead first to cracking of the HCP and depending on the degree of expansion, cracking of the aggregates.

Based on the research of Folliard et al. (2006) and Burgher et al. (2008), TxDOT developed and implemented guidelines for placing concrete (400 Items – Structures, in Standard Specifications for Construction and Maintenance of Highways, Streets, and Bridges) such that certain temperatures are not exceeded during concrete curing. In general, these guidelines have reduced the

likelihood of DEF damage, but structures constructed prior to these guidelines can still be susceptible to DEF and cracking.

In bridge structures in Texas, DEF does not seem to be as prevalent as ASR. In addition, structures for the most part have not been identified as exhibiting only DEF damage, possibly with one exception in San Antonio. In general, it is thought that structures first exhibit cracking due to ASR and then exhibit DEF damage. Although ASR and DEF are different mechanisms of deterioration, in general, both lead to volumetric expansion of the concrete and eventual cracking usually in the tension field of the element from induced loading. This cracking has the potential to reduce the capacity of the structure.

1.2.3 Impact of Internal Expansive Forces on Material Properties and Structural Performance

Engineers design structural members using the mechanical properties of the materials and the principles of engineering mechanics. If concrete deterioration occurs, the material property-structural performance relationships assumed during the initial design may no longer be applicable. It is clear that the expansive products of ASR and DEF lead to internal expansion and potential deterioration of the concrete. Table 1-1 highlights a few studies that have shown the impacts from internal expansion on material properties such as the compressive strength, tensile strength, flexural strength, and the modulus of elasticity on small-scale samples. Table 1-2 shows the results on how expansive forces from ASR and/or DEF impact varying structural performance parameters. With the exception of two studies on the compressive strength, all concrete properties were reduced when internal expansive forces were present. The lack of research done on the effects of internal expansion on the lap length of bars in the concrete, especially at large-scale, is particularly noteworthy for justifying the research program presented here. Also, the data in the tables were primarily obtained from small-scale specimens, which likely do not have the same behavior as large-scale specimens. Field structures are much more complex than small, unstressed, unreinforced, laboratory concrete specimens. These structures have different internal confinement (reinforcement) and loading conditions. Bae et al. (2007) noted that confining reinforcement can limit the expansion of ASR/DEF and reduce the negative impact of ASR/DEF.

Multon et al. (2005) did a study on the structural behavior of concrete beams affected by ASR. The specimens were 9.8 inches × 19.7 inches × 118.1 inches (0.25 m × 0.5 m × 3 m) and included longitudinal reinforcement. It was concluded that the effect of reinforcement on the internal expansion of the concrete is substantial, especially in the longitudinal direction where the largest decrease of strains and deflections took place. However, it was also found that the local offsets of the stirrups had little effect on the transverse deformations. That is, the concrete between the stirrups did not exhibit substantially different expansion than the concrete around the stirrups. Hamada et al. (2003) also found similar results where steel bars reduce the amount of strain in the surface. The closer the bar is to the surface, the higher the strains were in the steel and the smaller the strains were at the concrete surface.

Table 1-2 also shows a lack of research on the effect of internal concrete expansion on the required lap splice length. The present literature on bond strength reductions of lap splice and surrounding concrete due to some form of deterioration pertains mostly to corrosion and studies on the confinement of the surrounding concrete.

Table 1-1. Influence of Internal Expansive Forces on Material Properties.

Author(s)	Material Properties			
	Compressive Strength	Tensile Strength	Flexural Strength	Modulus of Elasticity
Ahmed et al. (1999a and 1999b)	⇩	⇩	⇩	⇩
Monette et al. (2002)	⇧			⇩
Chana and Korobokis (1991)	⇩[1]			
Chana and Korobokis (1991)	⇔	⇩		⇩
Hobbs (1984 and 1986)	⇩[2]	⇩		⇩
Swamy and Al-Asali (1989, 1998)	⇩	⇩	⇩	⇩
Zhang et al. (2002)				⇩[3]

⇩ – reduction; ⇧ – increase; ⇔ – no or minimal change

1. All sample sets (average values) obtained from cores exhibited lower strength values. All sample sets from exposed cylinders except 1 exhibited lower values.
2. Cubes. Results dependent on expansion; larger expansions resulted in reduced compressive strength.
3. Dynamic modulus.

Table 1-2. Influence of Internal Expansive Forces on Structural Performance.

Author(s)	Structural Characteristic					
	Flexure	Bearing	Shear	Bond	Development Length	Fatigue Life
Chana and Korobokis (1991)				⇔[1] & ⇧		
Konoike Constr. Co. Ltd. (unpublished)				⇩		
Chana and Korobokis (1991)	⇔[2]	⇩	⇩			
Chana and Korobokis (1991)			⇧[3]	⇩		
Ahmad et al. (1998)			⇧			
Ahmad et al. (1999a)	⇩			⇩		⇩
Ahmad et al. (1999b)		⇩				
Monette et al. (2002)	⇔		⇧			
Fan and Hanson (1998b)	⇔					
Swamy and Al-Asali (1989)	⇩					

⇩ - reduction; ⇧ - increase; ⇔- no or minimal change

1. Samples with small cover and no stirrups exhibited reduced bond. Samples with adequate cover and stirrups exhibited similar or increased bond when compared with control samples. However, it should be noted that this is likely dependent on the degree of damage.
2. Only an approximate reduction of 4 percent was observed from samples with over 3000 microstrain.
3. Increased shear for samples exhibiting moderate expansion and reduced shear for samples exhibiting severe expansion.

1.2.4 ASR/DEF Effects on Concrete Structures

Since both ASR and DEF can lead to volumetric expansion of the concrete, the initial development of cracking from these mechanisms typically develops in the tension field of the concrete member due to gravity loading. In this research program, the performance of column splice regions with premature concrete deterioration will be investigated. Figure 1-1 and Figure 1-2 show example field structures in Texas where cracks have developed in the column splice regions primarily due to the effects of ASR/DEF. For the column primarily under axial compression load from gravity (Figure 1-1), cracks propagate vertically along the column length in the tension field of the concrete due to Poisson's Effect. For the column of the cantilevered bent (Figure 1-2), cracks develop horizontally due to the applied overturning moment. However, in both cases as ASR/DEF

effects continue, the figures also show cracks that develop in other directions (primarily in the orthogonal direction) from the initial cracks in the tension field. Figure 1-3 shows an example of a bridge bent cap with mapped cracking predominantly influenced by ASR under minor levels of gravity loading (minimum tension field).

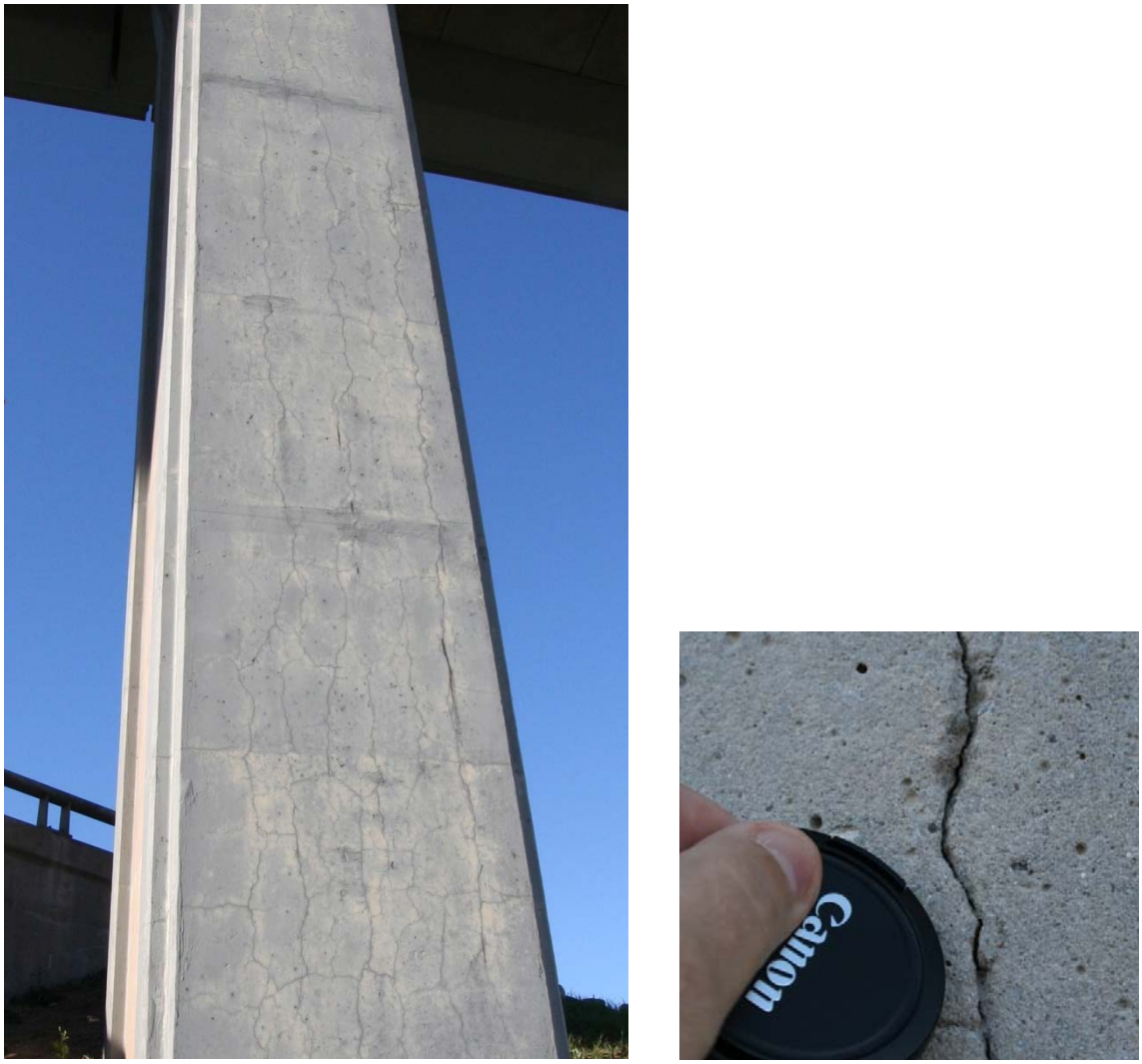

(a) Column Elevation View **(b) Close-up View of a Typical Crack**

Figure 1-1. Cracking in Column under Axial Compression Loads (Houston, TX).

(a) Elevation View and Typical Cracking on Tension Face (Houston, TX)

(b) Elevation View (San Antonio, TX)

Figure 1-2. Cracking in Cantilevered Bents under Axial and Overturning Moments.

Figure 1-3. Cracking in Bent Cap under Minimal External Loading (Houston, TX).

1.3 BOND, DEVELOPMENT LENGTH, AND LAP SPLICE LENGTH

A brief overview of bond and development length of reinforcing steel is next presented, followed by an introduction on how structural codes have been developed and modified over the past 50 years on these issues. Figure 1-4 shows a representation of how bond develops between a deformed reinforcing bar and the surrounding concrete. The developing bond strength results from the following three mechanisms:

- Chemical adhesion between the bar and surrounding concrete.
- The friction force between the reinforcement and concrete.
- The bearing of the ribs against the concrete surface (mechanical anchorage) (MacGregor 1997).

Movement of the reinforcement from applied loads causes the chemical adhesion to be lost and friction forces on the ribs and barrel of the reinforcement to develop. As slip increases, the compressive bearing forces on the ribs become the primary force transfer mechanism. If the concrete cover or the spacing between the reinforcement is sufficiently small, the stresses in the

concrete resisting the bearing forces from the ribs can cause transverse cracks that can lead to splitting of the concrete along the reinforcement and to the loss of bond strength. If the concrete cover and spacing of the longitudinal reinforcement are large or if there is sufficient transverse reinforcement to prevent splitting cracks, the structural member will fail by shearing along a surface around the bar (assuming sufficient stress is provided). The loss of bond through this type of failure is called a "pullout" failure.

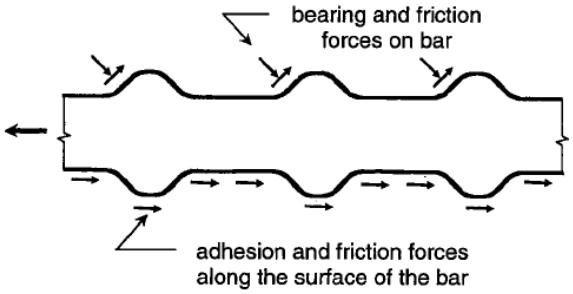

Figure 1-4. Bond Stresses between the Reinforcing Steel and Concrete (Taken from ACI 408 2005).

Section 5 of the AASHTO LRFD Bridge Design Specifications (2004) contains the provisions for the design of bridge and retaining wall components. Subsection 5.11 defines the requirements for the development length and lap splices for reinforcement based on work reported in ACI 318-89 (1989) (as stated in the commentary of AASHTO LRFD 2004).

The 1963 ACI 318 code (ACI 318-63 1963) defined requirements for two different terms called *flexural bond* and *anchorage bond*. *Flexural bond stress* was defined as a function of the rate of change of the moment along the span of the member, i.e., shear. Flexural bond provisions required comparing the peak bond stresses calculated at critical points to a limit stress. However, the complex distribution of bond stresses, especially the existence of extreme variations of bond stresses near flexural cracks, made the flexural bond calculations unrealistic. *Anchorage bond stress* was defined as the average bond stress between a peak stress point of the reinforcement and the end of the reinforcement where the stress is zero. Considering that all bond tests calculate an average bond resistance over a length of embedment, the ACI 318-71 (1971) code dropped the flexural bond concept and defined a development length formula based

on the cross sectional area of the reinforcing bars, yield strength of reinforcing bars (f_y), and the square root of design compressive strength of the concrete (f'_c). Subsequent codes had similar provisions until a new design approach was adopted in ACI 318-95 (1995) that matched observed behavior from many studies more closely.

There are five different sets of descriptive equations for determining development length based on test results of numerous samples and statistical methods discussed below. Orangun et al. (1975 and 1977) established the first set for the development length of reinforcement with and without transverse reinforcement. Darwin et al. (1992) reevaluated the same data that Orangun et al. used, and established an equation for the development length of reinforced samples without transverse reinforcement. Using a larger database, Darwin et al. (1996) established development length equations based on $f_c'^{1/4}$ for reinforcement with and without transverse reinforcement which was different than the established equations that were based on $\sqrt{f_c'}$. Later, Zuo and Darwin (1998 and 2000) further developed the work that Darwin et al. (1996) performed by adding high strength concrete samples into their database. In their equations, Zuo and Darwin (1998) also used $f_c'^{1/4}$ for the effect of compressive strength for reinforcement without transverse reinforcement; however, they found that a power term of ¾ to 1 was better for characterizing the effect of compressive strength on the development length of reinforcement with transverse reinforcement. Lastly, ACI committee 408 (2001) formulated the development length equations by applying minor changes to the equations that Zuo and Darwin (1998 and 2000) developed.

In the ACI 318-08 (2008), the design provisions for the development length of straight reinforcement in tension are based on the following equations that Orangun et al. (1975 and 1977) developed:

$$l_d = \left(\frac{3}{40}\frac{f_y}{\lambda\sqrt{f'_c}}\frac{\Psi_t\Psi_e\Psi_s}{\left(\frac{c_b+K_{tr}}{d_b}\right)}\right)d_b \qquad \text{(Eq. 1-1)}$$

where l_d is the required development length (inches),f_y is yield strength of reinforcement being spliced (psi), f'_c is the 28-day compression strength of the concrete from cylinder testing (psi), Ψ_t is a reinforcement location factor, Ψ_e is a coating factor, Ψ_s is a bar size factor, λ is a factor for the weight of concrete, d_b is reinforcement diameter (inches^2), c_b is the smallest center-to-center cover or spacing dimension (inches), and K_{tr} is the transverse reinforcement index as follows:

$$K_{tr} = \frac{40A_{tr}}{s\,n} \qquad \text{(Eq. 1-2)}$$

where A_{tr} is the area of the transverse reinforcement at the section of the developing longitudinal reinforcement (inches^2), s is the spacing of transverse reinforcement (inches), and n is the number of bars being developed or spliced. To limit the probability of a pullout failure, ACI 318-08 (2008) also requires:

$$\frac{c_b + K_{tr}}{d_b} \leq 2.5 \qquad \text{(Eq. 1-3)}$$

ACI 318-08 (2008) also limits the $\sqrt{f'_c}$ to a maximum value of 100 psi (689.5 kPa). A simpler approach was also mentioned with preselected values of K_{tr}, c_b, and Ψ_s.

ACI 318-08 (2008) defines two types of required lap splices, Class A and Class B. Class A splices can be used when the ratio of provided steel area to required steel area equals to two or more, and 50 percent or less of the steel is spliced within the lap. All other splices are defined as Class B. The lap splice length for Class A splices is equal to the development length of the bar being spliced, where the splice length of Class B splices is 1.3 times the development length of the bar being spliced. Because the AASHTO LRFD (20010) bridge design is based on the 1989 version of the ACI 318-89 (1989) code, it also includes a Class C splice classification that is no longer used in the newer version of the ACI 318-08 (2008) code (removed to encourage splicing bars at points of minimum stress and to stagger the splices). According to AASHTO LRFD (2010), Class C splices required to be 1.7 times the development length of the bar being spliced.

In addition to the ACI 318-08 (2008), there are three additional design provisions that can be followed to calculate development lengths. The first, published by the ACI 408 committee, was adopted as ACI 408.3 (2001) and provides provisions for the development length and splices of deformed reinforcement with high relative rib area. The second is the ACI committee 408 provisions based on the work of Zuo and Darwin (1998 and 2000). The last is the CEB-FIP Model code (1990). In a structural reliability analysis, the ACI 408 committee compared the available design provisions using their database and found that the CEB-FIP code (1990) had more scatter and greater coefficient of variation compared to the other design provisions.

Because AASHTO is widely used to design bridge columns, the AASHTO definitions for development length, l_d, and required splice length were used in this research. The AASHTO LRFD Bridge Design Specification (2004) for l_d is as follows:

$$l_d = \frac{1.25 A_b f_y}{\sqrt{f'_c}} \qquad \text{(Eq. 1-4)}$$

where A_b is the area of the reinforcement being spliced (in in2), f_y is the yield strength of the spliced reinforcement (ksi), and f'_c is the compressive strength of the concrete (ksi). Like ACI 318-08, the AASHTO specifications have different classes of lap splices based on the development length. However, using the ASSHTO specifications (2004), the splice used in this research is classified as a class C splice and is required to be 1.7 l_d, which is further discussed in Section 2.1.

1.4 RESEARCH PROGRAM OBJECTIVES

The major objectives of this research program are to

- Evaluate the experimental behavior of critical column lap splice regions using large-scale specimens under varying levels of premature concrete deterioration due to ASR and/or DEF.
- Develop an analytical model that describes the behavior of a splice region under varying levels of concrete deterioration based on calibration with the experimental behavior.

1.5 RESEARCH METHODOLOGY

The methodology for this research program was to conduct a large experimental program, which consisted of the design, construction, curing, deterioration, and structural load testing of 16 large-scale column specimens with a critical lap splice region, and then compare and calibrate models developed in the analytical program with the experimental behavior. Specimens were carefully instrumented both internally and externally to monitor the strain behavior of the concrete and reinforcing steel from specimen construction, curing, deterioration, and final structural load testing. The analytical program consisted of developing a model of the critical splice region of the specimens that captured the overall force-deformation characteristics of the specimen during structural load testing.

1.6 SCOPE

The scope of this report consists of the following:

- Section 1 (current section) includes the problem statement and background information for the research program.
- Section 2 provides information on the methods and materials used in design, fabrication, and construction of the large-scale specimens with an emphasis on inducing and accelerating ASR and DEF. This section also focuses on the implementation of instrumentation to capture the resulting internal and external surface expansions from ASR and/or DEF and later strains from load testing.
- Section 3 discusses the accelerated environment conditions for the deterioration phase of the large-scale specimens and presents the internal and external surface expansions of the specimens throughout the deterioration phase.
- Section 4 presents a deterministic analytical model that describes the flexural capacity in the splice region of the large-scale specimens (unaffected by ASR/DEF) relative to both three- and four-point load test configurations and proposes an additional factor to account for deterioration of the splice region due to ASR/DEF effects, if necessary.

- Section 5 presents the results of the experimental testing program to date and compares the results with the computations from the analytical model.
- Section 6 presents the summary, conclusion, and future work of this research.

CHAPTER 2:
SPECIMEN DESIGN AND CONSTRUCTION

2.1 DESIGN OF LARGE-SCALE SPECIMENS

This research focuses on the performance of the splice region of a typical reinforced concrete bridge column in Texas subject to ASR and/or DEF. Because in-service bridge columns can vary considerably in size and geometry, a large-scale column (LSC) specimen was designed to utilize a common splice found in the field at the column/foundation connection, which is typical in non-seismic regions.

Figure 2-1 and Figure 2-2 show the reinforcement details for an example bridge column in Houston, TX. The footing has 48 #11 bars (Bars R) that are distributed evenly around the perimeter of the column (see Figure 2-2) and extend 107 inches (2.72 m) into the column. The Bars R overlap with 48 #11 Bars V of the column reinforcing steel to form a lap splice. The hoops in the splice region are #5 reinforcing bars and are spaced at 12 inches (305 mm). The column supports the loads from the bridge deck above, which can be assumed to be primarily an axial compression load. However, during high winds from hurricanes, vehicle collisions, and offset live loadings, large lateral forces can be exerted on the bridge that result in bending moment demands in the column splice region. The tensile strength of the splice is the limiting parameter of the flexural capacity of the column and overall lateral resistance of the bridge. Because the strength of the lap splice is dependent on the bond, the effects of ASR and/or DEF expansion on the bond is of concern. If the bond is decreased enough that the bars slip prior to reaching their yield strength, the capacity of the column may not be high enough to resist the overload structural demands and failure might be possible.

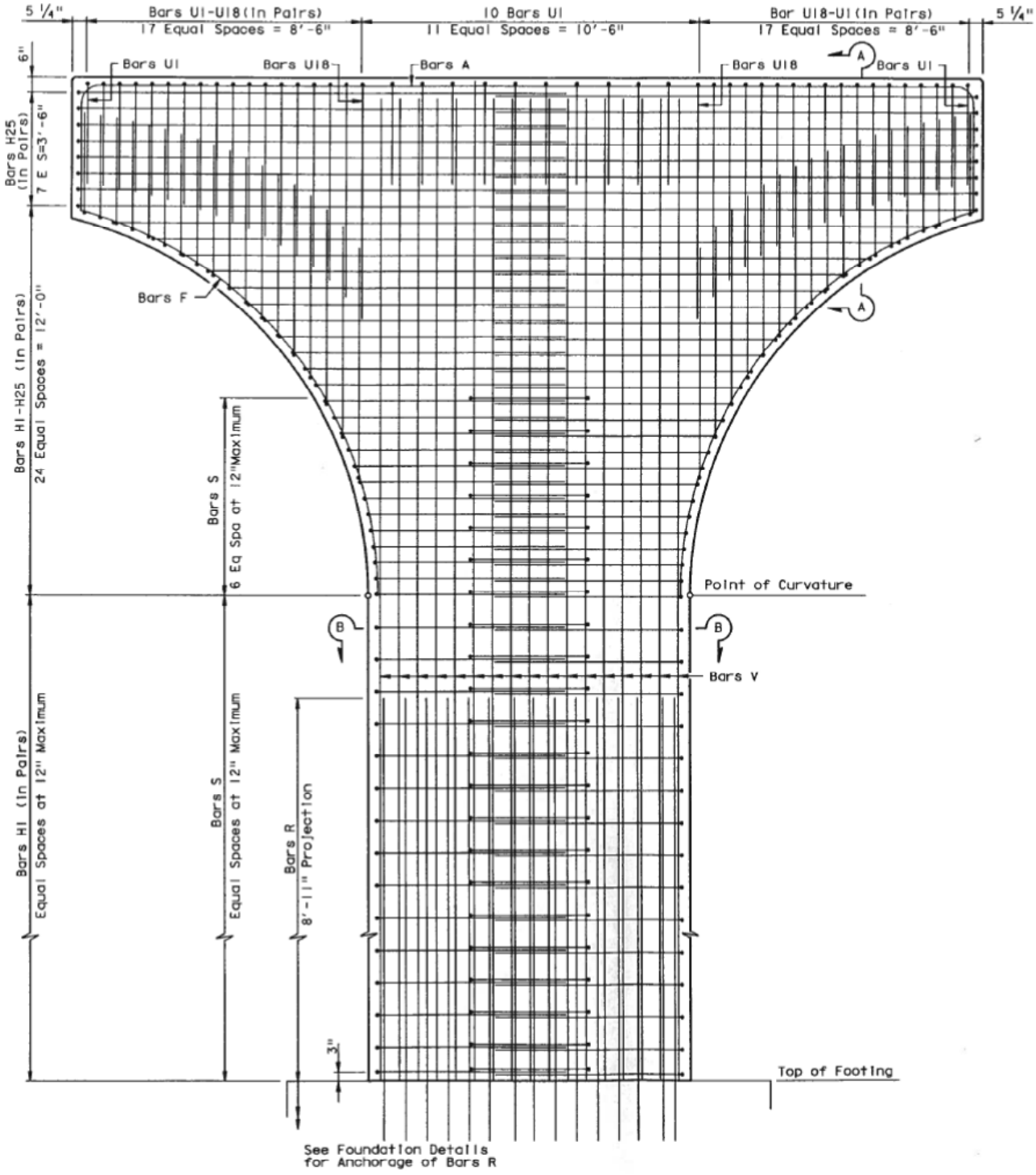

Figure 2-1. Sample TxDOT Column Reinforcement Detail.

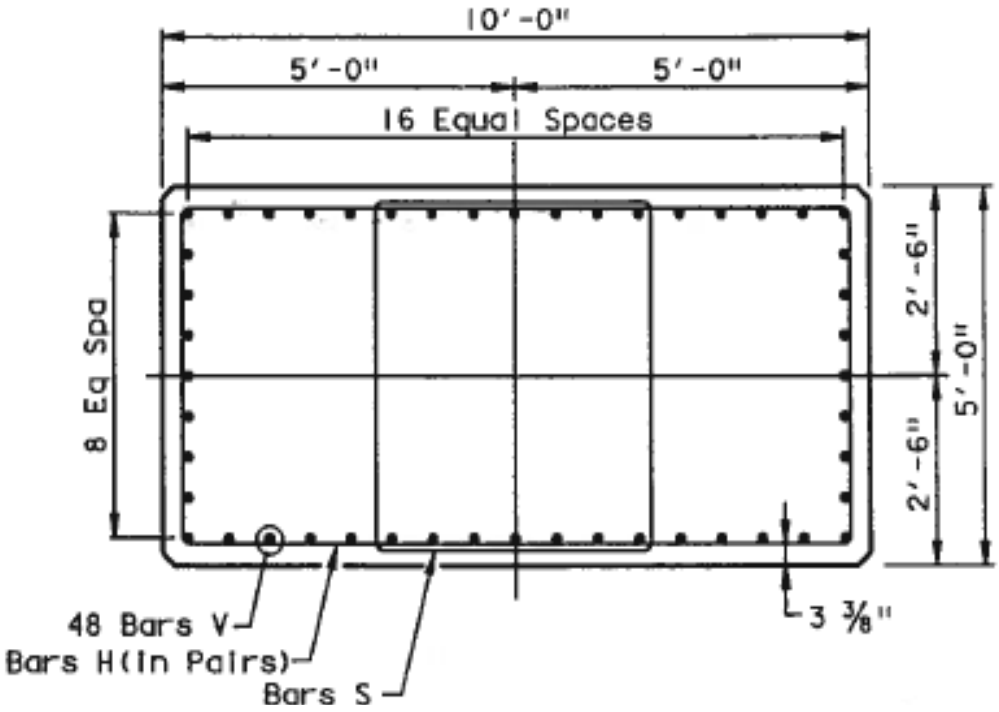

Figure 2-2. Section B-B of the Sample Column.

In an effort to reduce costs and maximize the specimen size based on the constraints of the testing laboratory, 16 LSC specimens were utilized in the experimental research program. Specimens were 2 ft × 4 ft (0.61 m × 1.22 m) in cross section with six #11 bars overlapped in the 9 ft (2.74 m) splice region, which is the typical overlap length for #11 bars used by TxDOT (see Figure 1-1). Figure 2-3 and 2-4 show the dimensions of the rebar layout of the LSC specimens. Additional information about the LSC specimens is presented in Section 2.3.1.

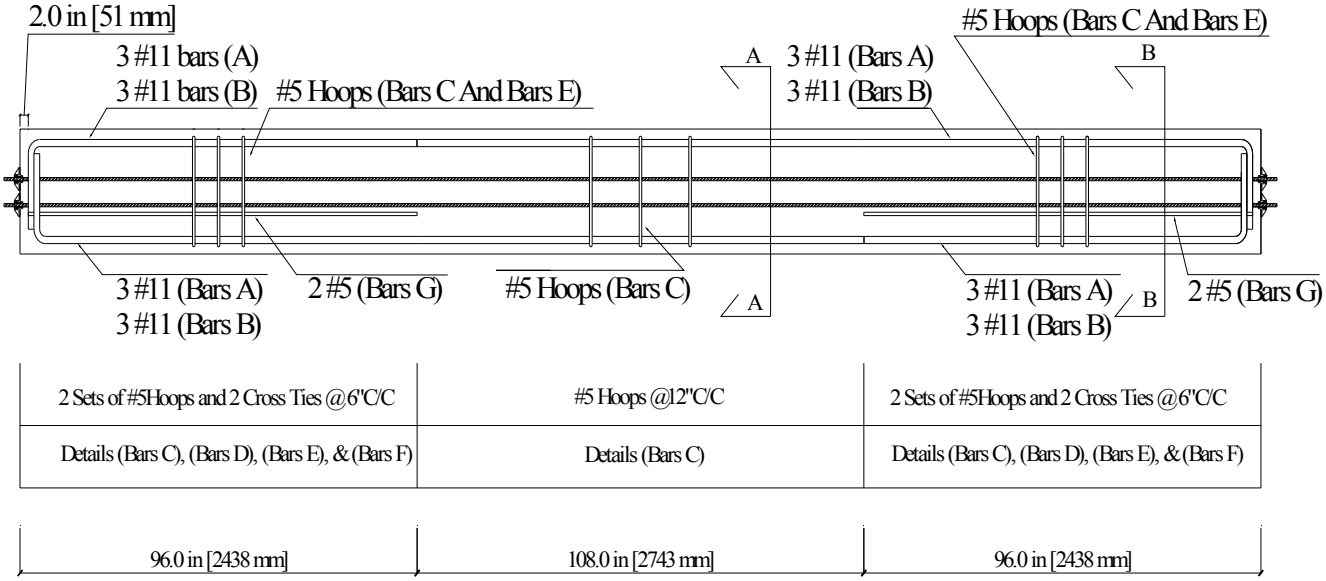

Figure 2-3. Reinforcement Layout.

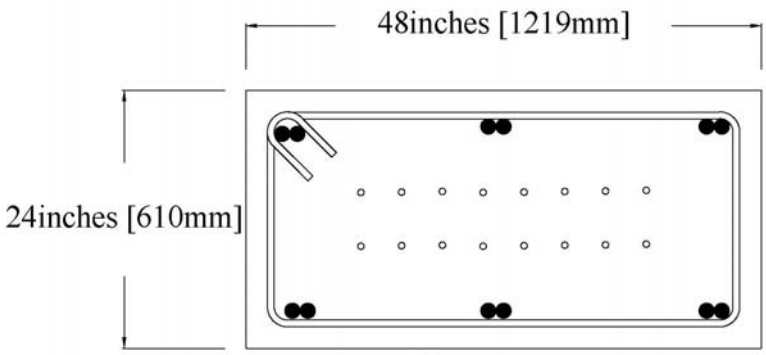

Section A-A Splice Region

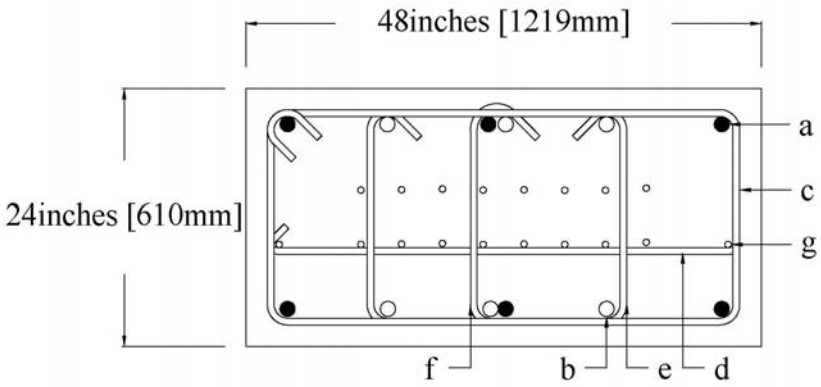

Section B-B End Region

Section B-B Parts	
a	6 #11 Bars A [marked with fill]
b	6 #11 Bars B [marked without fill]
c	#5 Hoops @ 6" C/C (Bars C)
d	#5 Cross Ties @ 6" C/C (Bars D)
e	#5 Hoops @ 6" C/C (Bars E)
f	#5 Cross Ties @ 6" C/C (Bars F)
g	2 #5 Bars (Bars G)

Figure 2-4. Cross Section View of the Reinforcement Layout.

The development length was calculated with ACI 318-08 and AASHTO LRFD Bridge Design Specifications (2010). The required splice length is a function of the development length as presented in Section 1.3. Table 2-1 shows the required splice lengths for the #11 bars for each

code using a concrete compression strength, f'_c, of 5 ksi (34 MPa), and a steel yield strength of 60 ksi, (414 MPa). One requirement for the Class A splice is the area of the reinforcement being spliced should be less than or equal to half the total reinforcement. For the specimens in this research, all of the reinforcement is spliced; therefore, the specimens in this research are considered a Class B splice. The 108-inch (2.74 m) splice length provided is over-designed by 54 percent for ACI 318. For AASHTO, the distinction between Class B and Class C depends on the ratio of area of reinforcement provided to the area required. The provided splice length is $2.1 \times l_d$ which is greater than both the Class B and Class C.

Table 2-1. Splice Lengths for ACI-318 and AASHTO.

	Splice Lengths – inches (m)	
	ACI 318 (2008)	AASHTO (2010)
Class A: 1.0 l_d	54.0 (1.4)	52.4 (1.3)
Class B: 1.3 l_d	70.2 (1.8)	68.1 (1.7)
Class C: 1.7 l_d		89.0 (2.3)

Both ACI 318-08 and the AASHTO LRFD (2004) show the splice length in the specimens are conservatively designed. The question is whether or not the effects of ASR and/or DEF will deteriorate the bond of the reinforcing steel in the splice region of the columns enough to overcome the conservative design. Continuing forward in this work, the AASHTO (2004) version of l_d will be used for all calculations in the specimens of the experimental program.

To evaluate the experimental performance of the splice regions, the LSC specimens will first be load-tested to near-failure using a four-point load test. Figure 2-5 shows that a four-point load test generates a constant moment over the splice region that allows for the weakest section of the region to crack, yield, and ultimately fail. In this test setup, a constant tension force across the entire splice length is created in the bottom longitudinal reinforcement. For an in-service cantilevered bridge column under lateral loading, the bending moment in the column varies linearly from zero at the top to maximum at the column base, which implies that the splice

reinforcement is not loaded uniformly along its length. Therefore, the test setup will yield conservative values in terms of the splice performance.

Following the four-point load test, the LSC specimens will be further tested using a three-point test setup. Figure 2-6 shows that a three-point test creates a uniform shear force throughout the splice region and a linearly increasing moment demand from zero at the support to maximum at the reaction support. Since the peak moment demand for the splice (largest tensile stresses) is at the very center of the splice region and the entire splice region has load-induced shear demands, the overall demands on the splice length region might be somewhat more critical than that in the previous test. The test setups are further discussed in Sections 5.2 and 5.3.

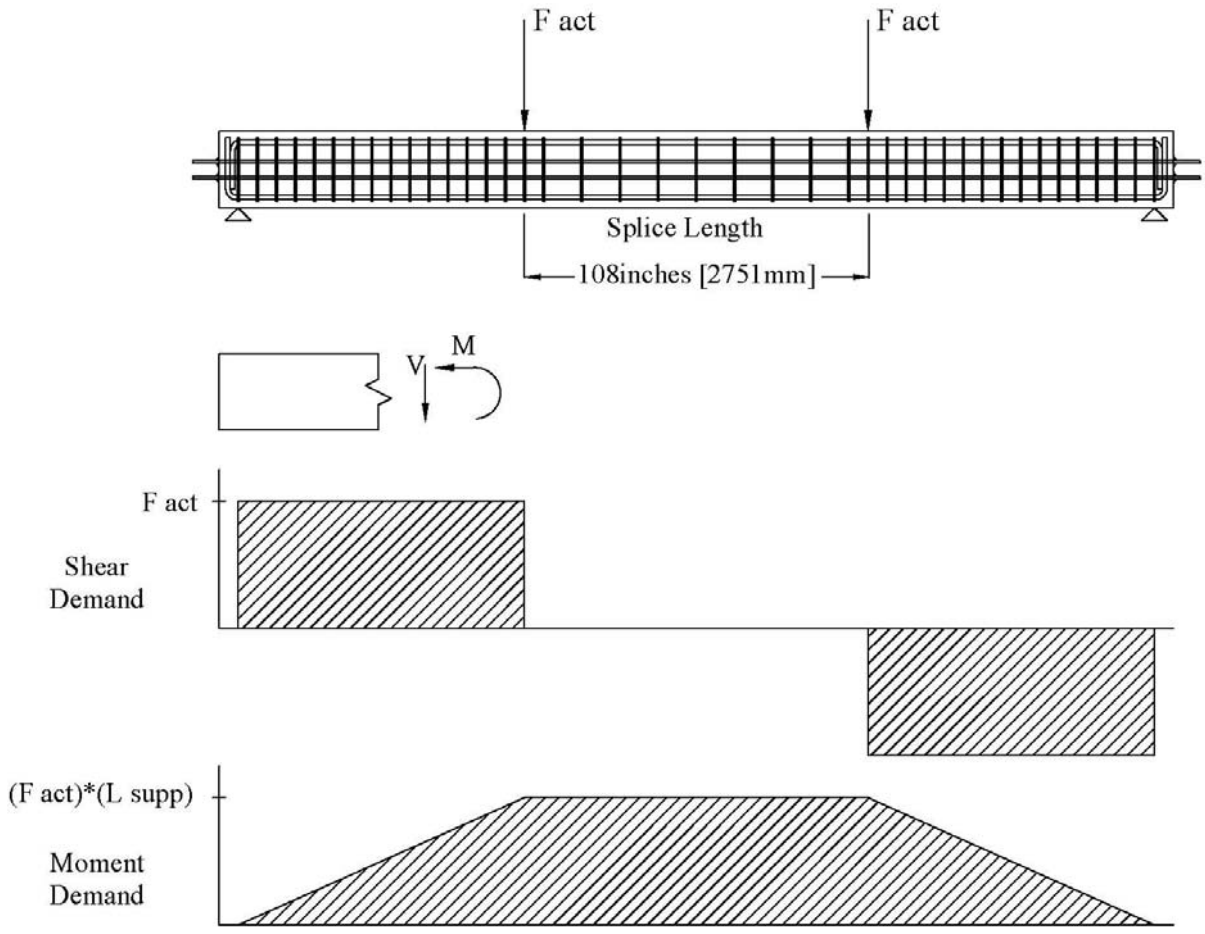

Figure 2-5. Four-Point Load Test.

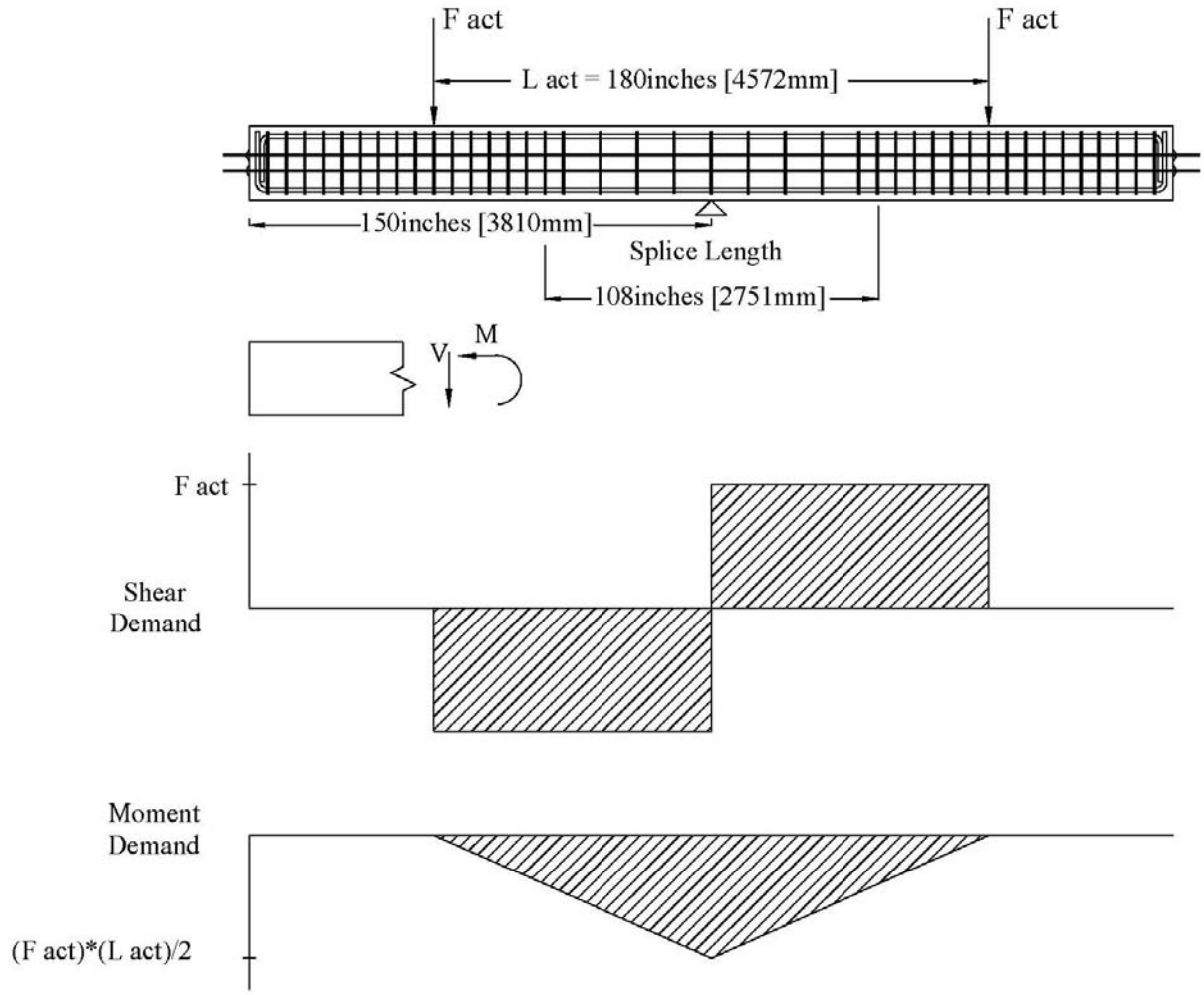

Figure 2-6. Three-Point Load Test.

2.1.1 Simulated Axial Load

To simulate in-service gravity loading on the bridge column, the specimens have 16 0.6 inch (15 mm)-diameter, unbonded, post tensioning (PT) strands. Figure 2-7 shows the PT strands were centered throughout the specimen cross section. The unbonded strands were bound in a plastic sleeve and coated with a lubricating grease to limit friction losses during post tensioning. The strands were terminated through a base plate that sat flush with the concrete on one side and flared out on the other side to accommodate two collets that held the tension in the strand.

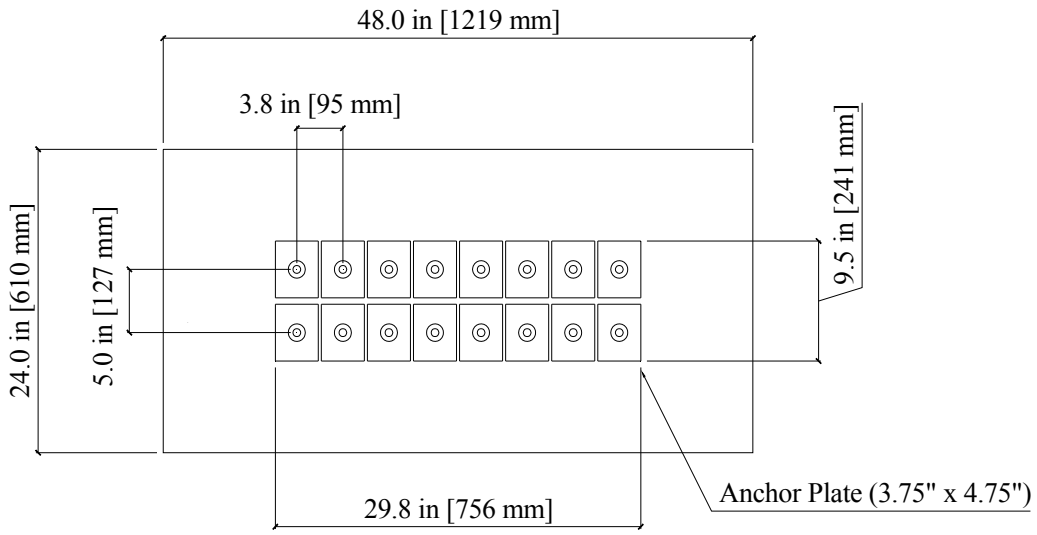

Figure 2-7. Strand Layout (End View).

Figure 2-8 illustrates the strand extending out of the concrete through the base plate and collets. The strands were hydraulically jacked to 0.7 f_{pu}, where f_{pu} is the ultimate tensile stress, as the AASHTO (2007) Specifications required, which results in 36.3 kips (161.47 kN) per strand and a total of 580.5 kips (2582.19 kN) of compression on the column specimen. This level of axial load corresponds to about 10 percent of the axial compression strength of the column, which is commonly found in columns under service loading.

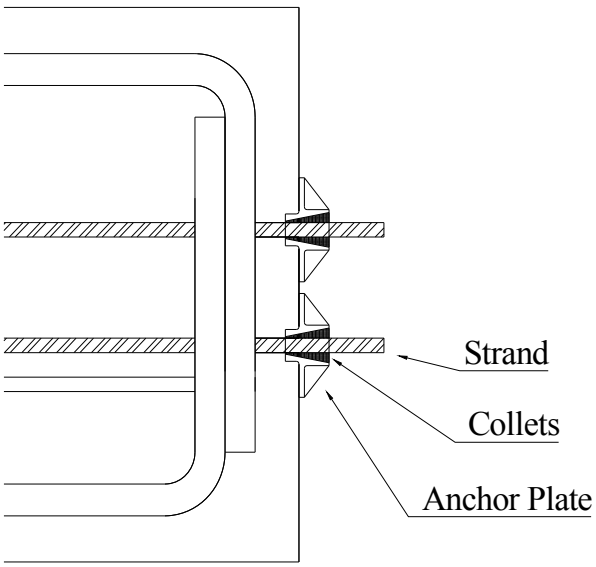

Figure 2-8. Strand End Termination.

2.2 MATERIALS OF CONSTRUCTION

The materials used in this research are briefly discussed in this section. This is not an exhaustive analysis of the materials, but a description of the type of materials used and some of the defining properties. More complete information and specific details on the materials used in this research program, especially regarding the influence of ASR and DEF, are provided in the accompanying materials report of Kim and Trejo (2011).

2.2.1 Coarse and Fine Aggregates

Aggregates were selected based on reactivity to aggressively promote ASR in the concrete and, therefore, not necessarily selected merely on price and location. The coarse aggregates had a maximum size aggregate (MSA) of 1 inch (25.4 mm) and were river gravel from Hanson Aggregates in Garwood, Texas. The load was transported from the quarry to the Texas A&M Riverside campus at the beginning of the project and stored to ensure one source for testing. Figure 2-9 shows the gradation curve of the coarse aggregates used in the concrete that meets ASTM standards.

Fine aggregates were procured from Wright Materials in Robstown, Texas, and stored next to the coarse aggregates at Riverside Campus. Figure 2-10 shows the gradation curve of the fine aggregates used in the concrete that meets ASTM standards.

Table 2-2 shows the measured properties of both coarse and fine aggregates. These properties were measured in accordance with ASTM C136 (Standard Test Method for Sieve Analysis of Fine and Coarse Aggregates), ASTM D 75 (Standard Practice for Sampling Aggregates), ASTM C 127 (Standard Test Method for Density, Relative Density, and Absorption of Coarse Aggregates), and ASTM C 128 (Standard Test Method for Density, Relative Density, and Absorption of Fine Aggregates).

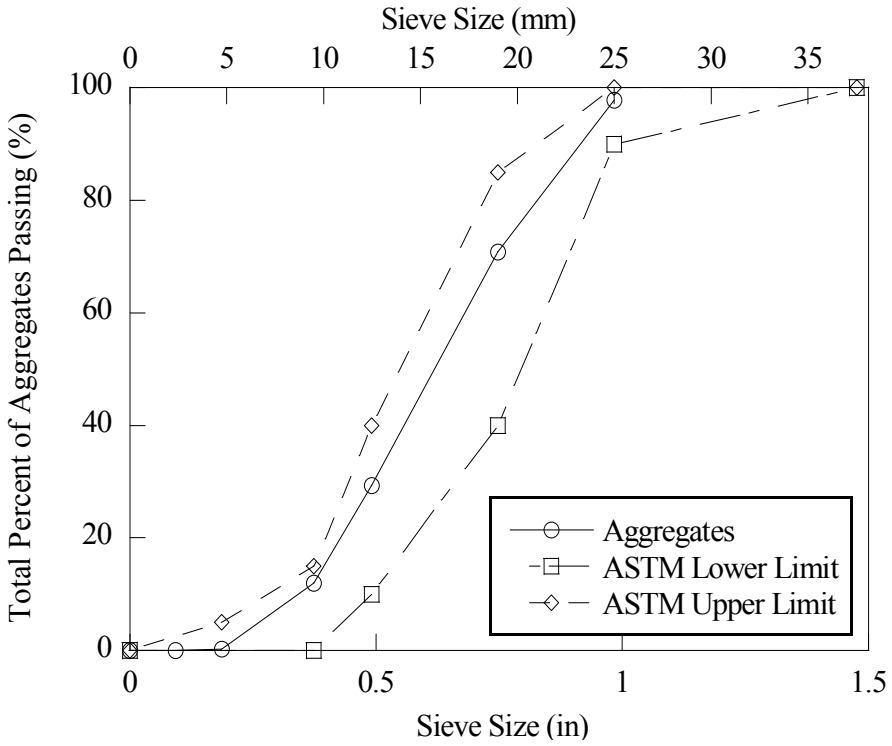

Figure 2-9. Gradation of the Coarse Aggregates.

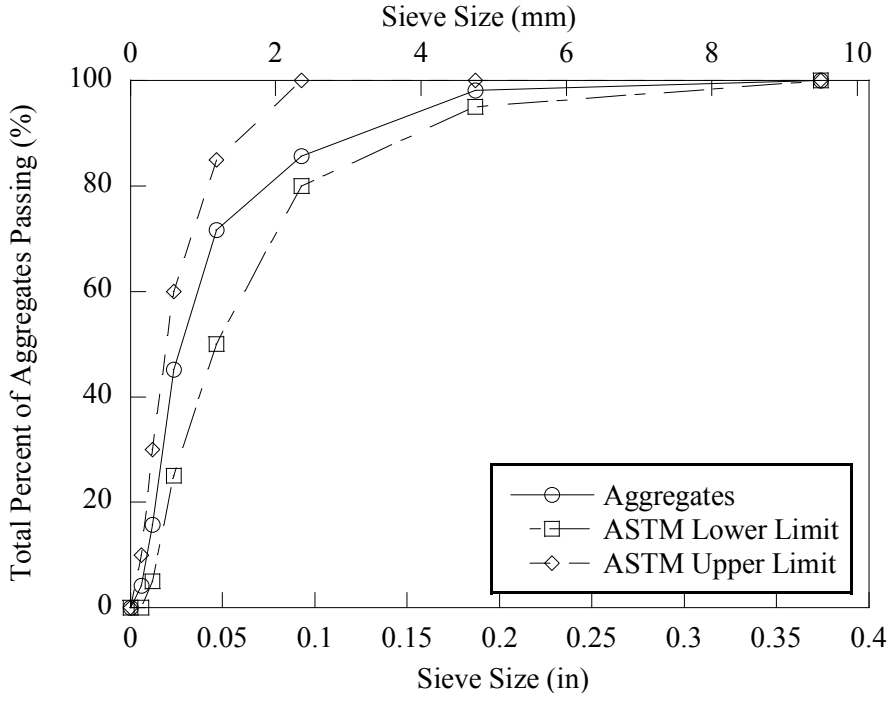

Figure 2-10. Gradation of the Fine Aggregates.

Table 2-2. Measured Aggregate Properties.

	Saturated Surface-Dry Density (g/cm^3)	Dry Density (g/cm^3)	Water Absorption (%)	Fineness Modulus
Coarse Aggregates	2.57	2.55	0.68	3.9
Fine Aggregates	2.58	2.55	1.44	2.79

2.2.2 Cement

Type III cement was used to fabricate all LSC specimens. The cement was procured from Lehigh Cement in Evansville, Pennsylvania, and transported to Texas A&M University in bags on pallets, and stored indoors. This particular cement was used because of the high alkali content to promote ASR in the LSC specimens. Table 2-3 shows the chemical composition of the cement.

2.2.3 Water

Concrete mixing water was taken from a hydrant at the Riverside Campus during the batching process and dispensed directly into the concrete mixing truck. The water source is potable.

2.2.4 Sodium Hydroxide

To further increase the alkalis in the concrete mixture, the researchers mixed 51.3 lb (23.3 kg) of sodium hydroxide (NaOH) tablets into 21.1 gallons (80 L) of water in four containers. This created a supersaturated solution, which was poured into the concrete mixing truck before the NaOH could settle from the solution.

Table 2-3. Lehigh Cement Analysis.

Compound	% Wt.
Na_2O	0.3
MgO	2.8
Al_2O_3	4.8
SiO_2	19.48
P_2O_5	0.16
SO_3	3.66
K_2O	0.88
CaO	61.63
TiO_2	0.2
Fe_2O_3	3.43
Na_2O_e	0.88
Total	99.71
C_3S	55
C_2S	14
C_3A	7
C_4AF	10

2.2.5 Mix Quantities

The target compressive strength of the concrete mixture was 5,000 psi (34.5 MPa). The specific quantities used in each specimen differed slightly due to the moisture content of the coarse and fine aggregates measured during the batching process. Table 2-4 shows the mixture characteristics and Table 2-5 shows the mixture proportions used for the LSC specimens.

Table 2-4. Mixture Characteristics.

	Mix Values
Coarse aggregate (absorption capacity) (%)	0.96
Fine aggregate (absorption capacity) (%)	0.65
NaOH	51.3 lb in 21.14 gallons (23.3kg in 80L)
Anticipated air content (%)	1%
Specific gravity of the cement	3.15
Specific gravity of the coarse aggregates	2.57
Specific gravity of the fine aggregates	2.65

Table 2-5. Mixture Proportions.

Material	SSD (lb/yd^3)
Cement	752
Course Aggregate	1350
Fine Aggregate	1438
Water	361
NaOH	5.7
Water/cement	0.48

2.2.6 Reinforcing Steel

Grade 60 reinforcing steel meeting ASTM A615 specifications was used to fabricate the LSC specimens. From tension coupon testing, the yield strength of the reinforcement exceeded 65 ksi and significant deformability beyond yielding was achieved.

2.3 FABRICATION PROCEDURE

Fabrication of the LSC specimens began in summer 2007. During the trial casting operations, the concrete began to flash-set and honeycombing was observed (see Figure 2-11). The flash-set was due to the Type III cement and the supplemental furnace heating of the aggregates (to very high temperatures) used to promote DEF. Lack of temperature control when heating the aggregates led to boiling and evaporation of the water, which led to accelerated set times and introduced additional voids as shown in Figure 2-11.

Figure 2-11. Voids in the First Trials.

This challenge required a new approach for fabricating and casting the LSC specimens in order to promote the DEF mechanism. Because heating the water required for the mix to attain the 160°F threshold for DEF was not an option due to the large quantity, two other possibilities were considered. The aggregates could be heated using a large aggregate furnace (used to batch asphalt), or electrical heating wires could be used to heat the concrete once it was placed. After investigating the asphalt batching plants and considering the costs and lack of control, the aggregate heater option was deemed unfeasible. In contrast, the electrical heating wires provided many benefits, including the ability to regulate the heat using a feedback closed system with thermocouples. The heating wires were also much more cost-effective, easier to implement, and safer in regard to the risk of fire hazard. This supplemental heating solution is fully described in a concurrent TxDOT research project on the effects of ASR/DEF on D-regions (Mander et al. 2011).

2.3.1 Reinforcement Cage Assembly

The longitudinal reinforcement consisted of 12 #11 bars that lapped over the middle 9 ft (2.74 m) of the LSC specimens. The transverse reinforcement consisted of #5 hoops placed at 12 inches (305 mm) on center in the splice region and two overlapping #5 hoops placed at 6 inches (152 mm) on center outside the splice region to deter failure in these regions. Figure 2-12 shows the individual bar details of the cage and the quantities of each for one specimen.

Starting with Bar A, the top bars were suspended above the ground using a fabricated stand and tied together over the 9 ft (2.74 m) splice length. Careful placement of the instrumented bars with strain gages (full description of the instrumentation is presented later in the report) was ensured such that the gages were untouched during the assembly of the reinforcement. The hoops, Bar C, were then placed over the longitudinal bars and the ends were tied together. Figure 2-3 and Figure 2-4 show overlapping hoops spaced at 6 inches (152.4 mm) on the ends and a single hoop 12 inches (304.8 mm) in the splice region. The top corners of the hoops were then tied to the longitudinal bars.

The pieces labeled Bar B were then slipped underneath the top side of the hoops on both sides of the center longitudinal bars. This allowed for the Bar E pieces to be placed around the center longitudinal bars and the Bar B bars in the end regions. The ends of the Bar E were tied together, centered, and attached to the hoops. Bar E was not used in the splice region of the column. Figure 2-4 shows the reinforcement layout as viewed from the ends of the LSC specimens at Sections A-A and B-B in Figure 2-3.

With the hoops in place, the bottom longitudinal bars, including the two with strain gages, were set in place and tied to the hoops in the corners. This allowed for the final pieces, Bar F and Bar D to be tied into place along the horizontal center and the vertical third point, respectively. Bar G was used to hold Bar D into place and ensure accurate placing.

The last step of the reinforcement cage assembly was to attach chairs to the bottom of the cage to ensure the desired cover of 2 inches (50.8 mm) was attained during the pour. With a spacing of 12 inches (308 mm) in every direction, the chairs were tied to the reinforcement before placing in the form.

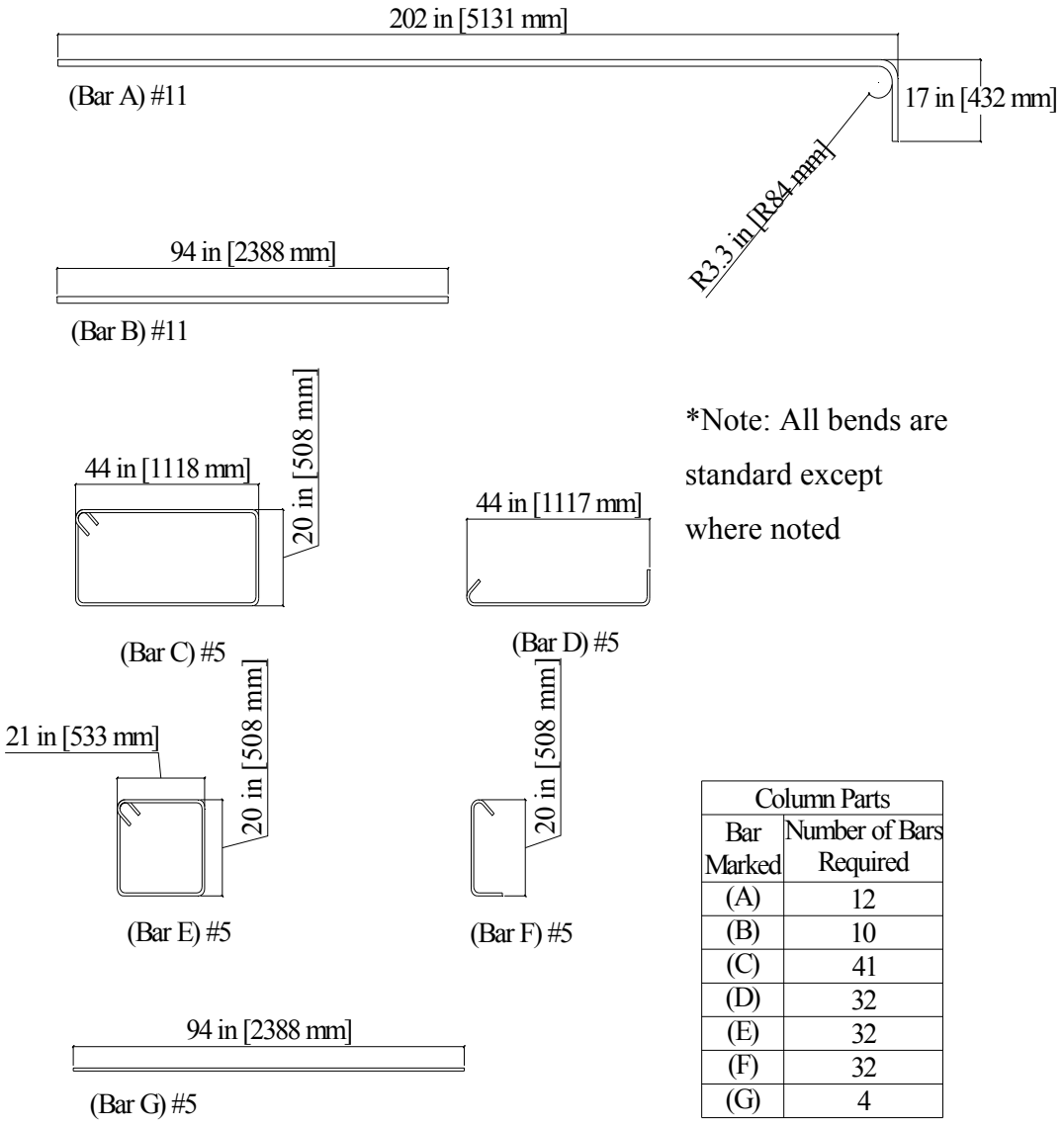

Column Parts	
Bar Marked	Number of Bars Required
(A)	12
(B)	10
(C)	41
(D)	32
(E)	32
(F)	32
(G)	4

Figure 2-12. Reinforcement Types, Quantities, and Dimensions.

2.3.2 Strain Gage Application

Research was performed to ensure that the strain gages (SGs) would be readable and accurate after several months of exposure. Liu (2012) outlines the technique for applying the SGs to the rebar. The ribs on the reinforcing steel were ground flat and then sanded to create a smooth surface for SG application. The SGs were glued to the reinforcing steel and covered with a series of protecting layers to ensure durability of the gages.

2.3.3 Post-Tensioning Strand Installation

Once the reinforcement cage was placed into the formwork, the post-tensioning (PT) strands were put into place through the formwork. The plastic tubing for unbonding the strands was cut off at the ends and the strands were placed through the anchor plates on the ends of the formwork. A hydraulic jack was used to put a slight tension on the strands until any sag was removed from the middle. Ties were also used to suspend the PT strands to avoid excessive sagging. After the concrete gained sufficient strength, each strand was then tensioned to the desired 36.3 kips (161.5 kN) as discussed in Section 2.1.1.

2.3.4 Electrical Resistive Wiring Installation

To promote DEF, Electrical Resistive Wiring (ERW) generated heat that supplemented the LSC specimens to ensure that the concrete temperature was above 160°F (71.1°C) during the curing of the concrete. In the final report of a similar TxDOT project (0-5997), Mander et al. (2011) fully described the design of supplemental heating system for the large-scale specimens. The same supplemental heating system was successfully used in both projects. The ERW was preinstalled in the bottom and top forms, then covered with stainless steel. In addition, ERW was required in the mid-depth of the LSC specimens by one dimensional heat flow analysis. The ERW was pushed through PEX tubing that was strung through the vertical center of the cross section of the LSC specimens at four-points and passed through the end of the form (see Figure 2-13). This protected the ERW and allowed for the wire to be used multiple times. The ERW

solution consisted of three controllable sections to apply heat, which allowed for a more uniform temperature distribution in the concrete throughout the specimen.

In addition to strain gages, 32 thermocouples (TC) were installed throughout the specimen to monitor the heat distribution during curing (see Figure 2-14). The TCs were attached to the reinforcing steel and the wire was routed outside the form for easy access. Figure 2-15 through Figure 2-17 show the typical recorded heat distributions from the TCs embedded in the LSC specimens.

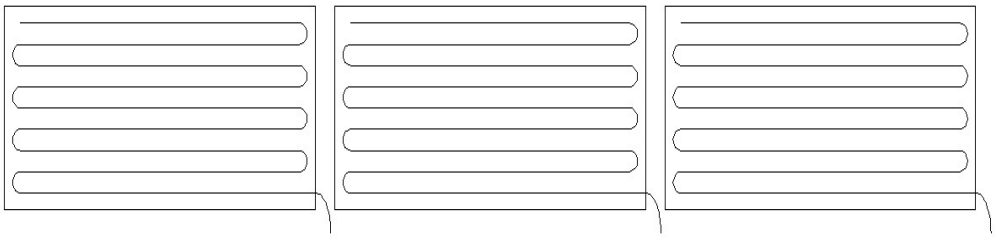

ERW in the Top Panels (Plan View)

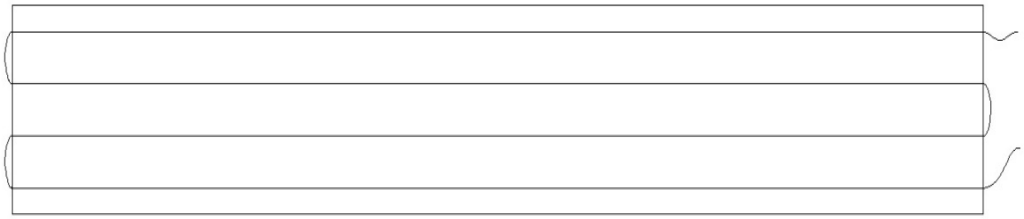

ERW through the middle of the concrete (Plan View)

ERW embedded in the bottom of the form (Plan View)

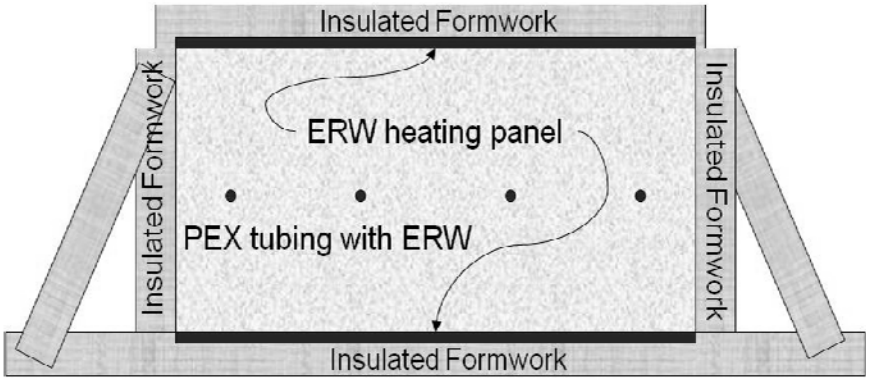

End-View of Heated Formwork

Figure 2-13. ERW Layouts.

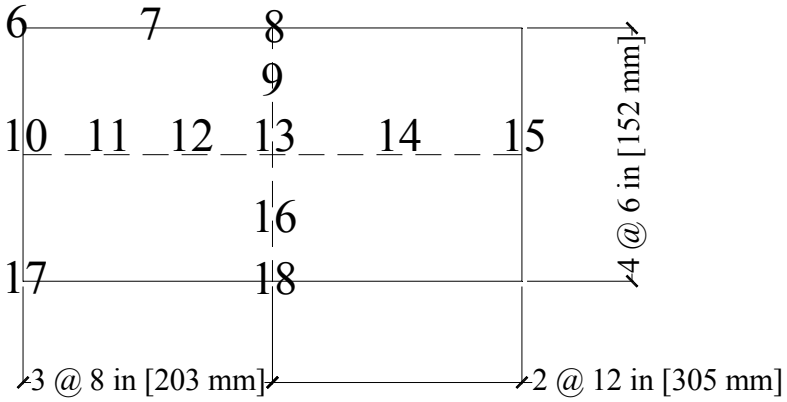

Mid-Span Section

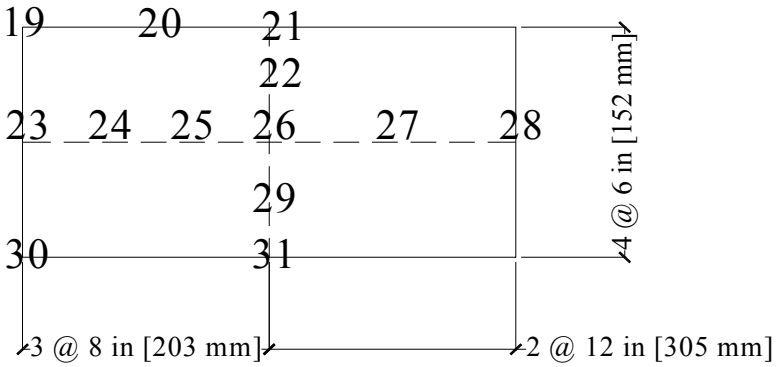

Quarter-Span Section

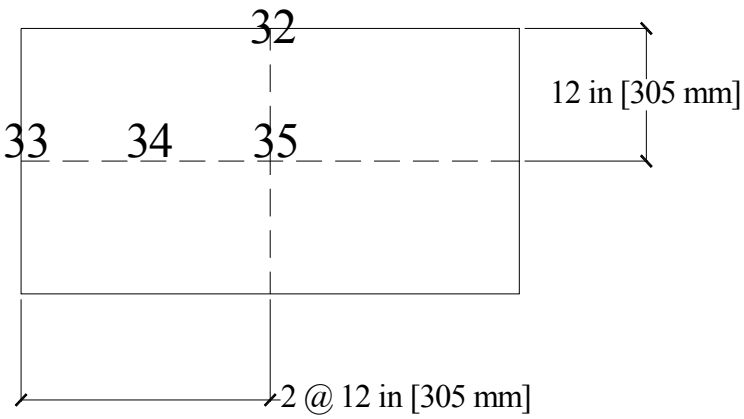

End-Span section

Figure 2-14. Thermocouple Locations.

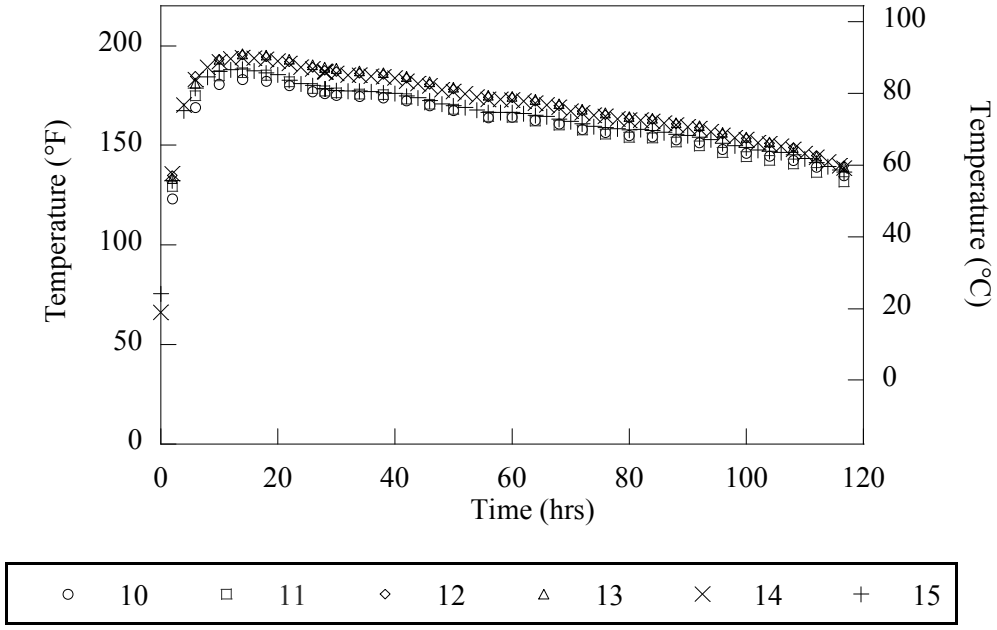

(a) Horizontal Thermocouple Measurements

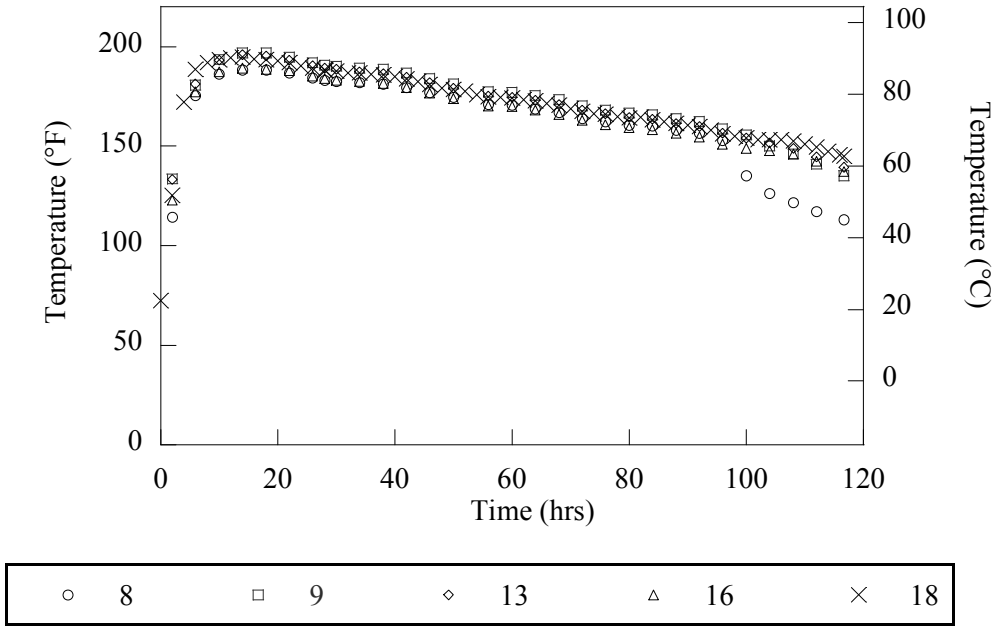

(b) Vertical Thermocouple Measurements

Figure 2-15. Typical Temperature History at Mid-Span Section.

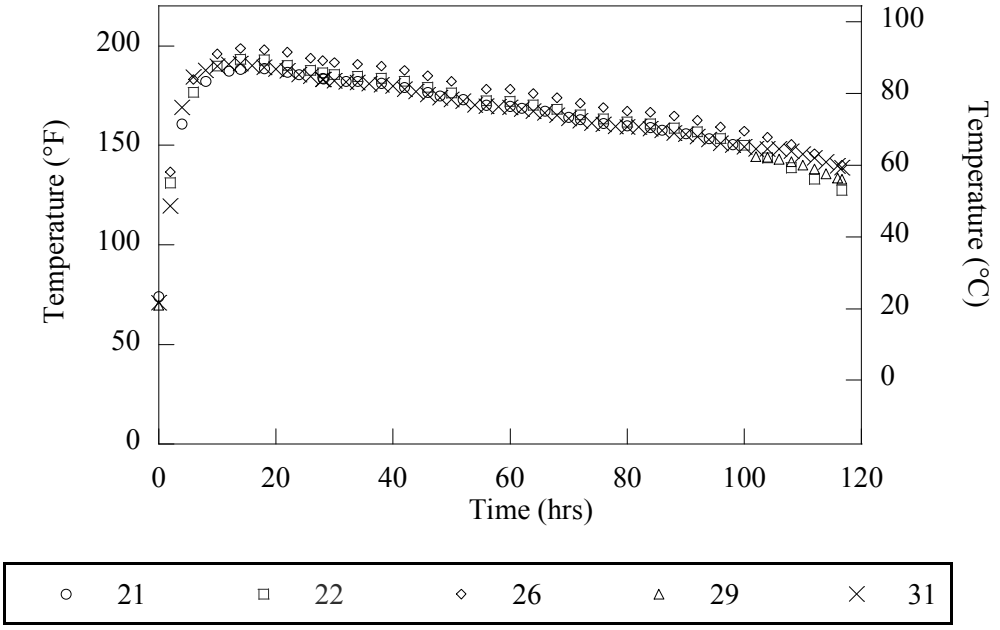

(a) Horizontal Thermocouple Measurements

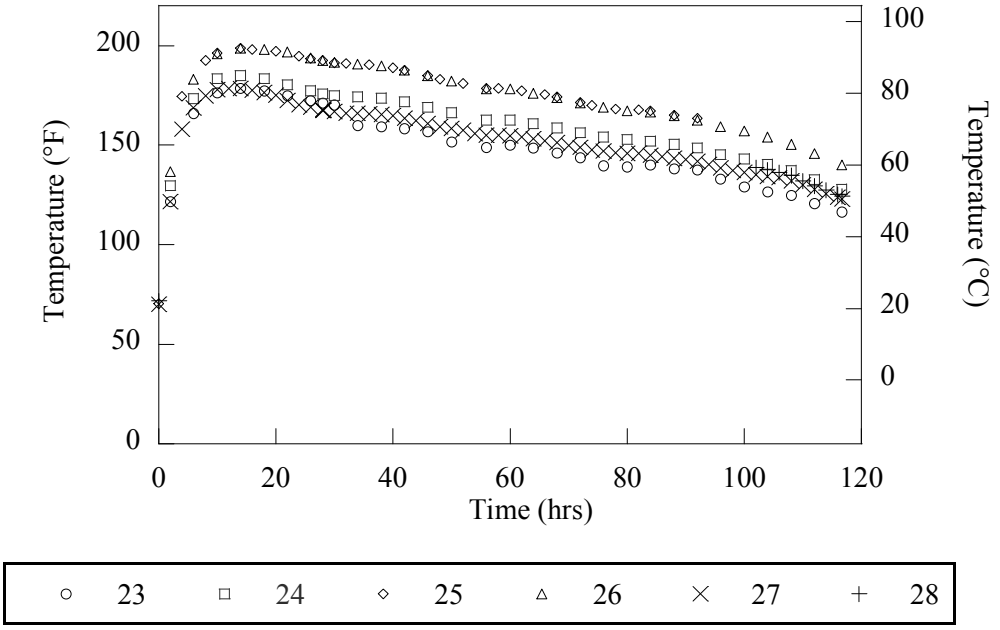

(b) Vertical Thermocouple Measurements

Figure 2-16. Typical Temperature History at Quarter-Span Section.

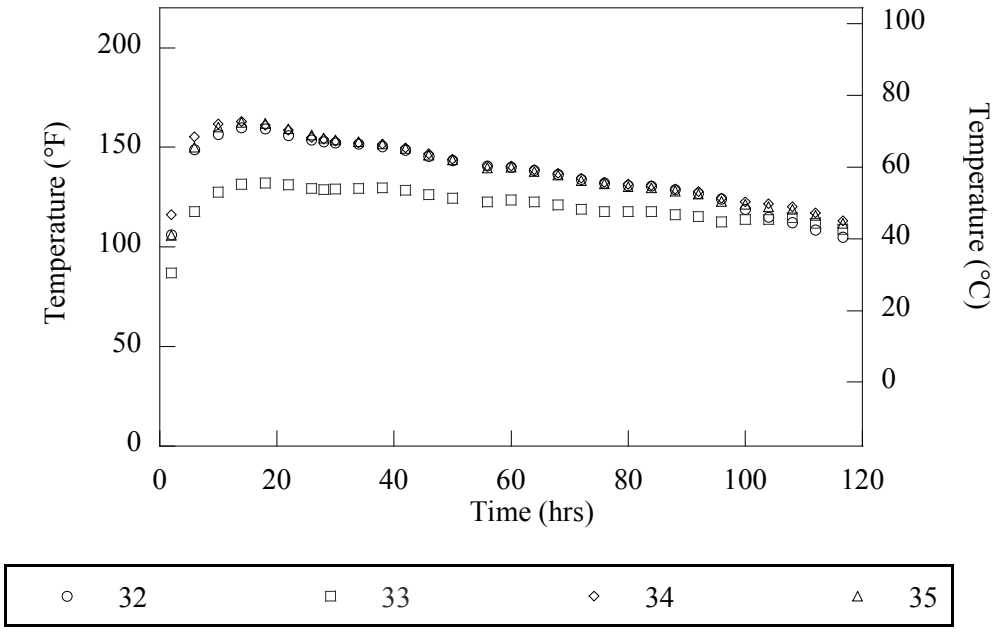

Figure 2-17. Typical Temperature History at End-Span Section.

2.3.5 Batching and Mixing Concrete

Concrete for fabricating the specimens was mixed using a concrete truck. Using a front-end loader and a forklift, the fine and coarse aggregates were first loaded into the truck as shown in Figure 2-18. The front end loader was used to fill a two-yard bucket with up to 4000 lb (17.79 kN) of material. Then the forklift lifted the bucket using straps and a load cell to weigh the aggregates. With the weight recorded, the forklift then set the bucket on the ground. From there, the bucket was picked up using the forks and lifted above the truck. The material was then dumped into the truck and the process was repeated until the required amount of fine and coarse aggregates were added to the truck. Aggregate weights were adjusted for moisture prior to mixing. The truck was then filled with the prescribed amount of water minus 21.14 gallons (80 L), which was added later with the dissolved sodium hydroxide (NaOH) tablets. This completed the batching operation at the Riverside campus.

The concrete truck was then transported to the Structural and Materials Testing Laboratory at the Texas A&M University campus. There in the Laboratory, researchers batched the sodium

hydroxide tablets into four 5 gallon containers and mixed with the water prior to the concrete mixing truck's arrival.

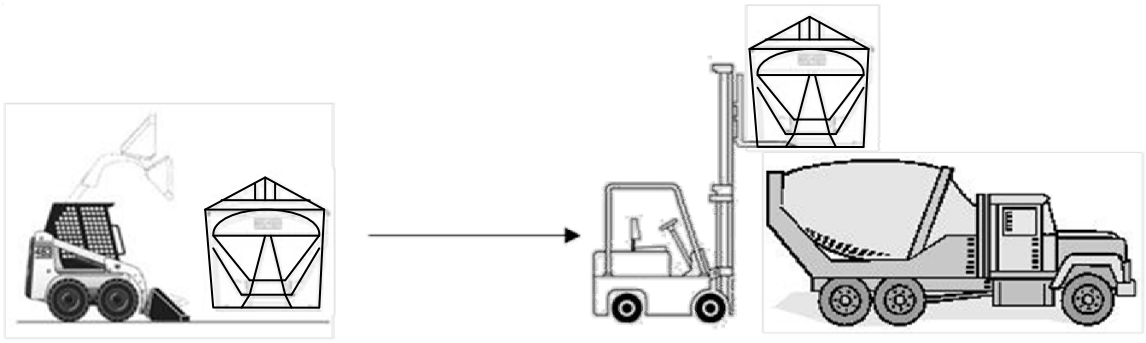

(a) Adding Fine and Coarse Aggregates

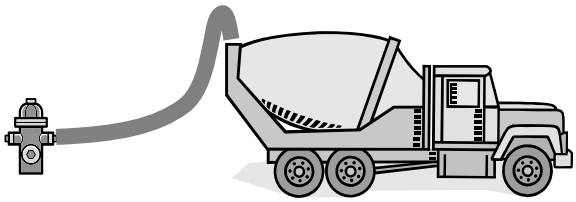

(b) Adding Water

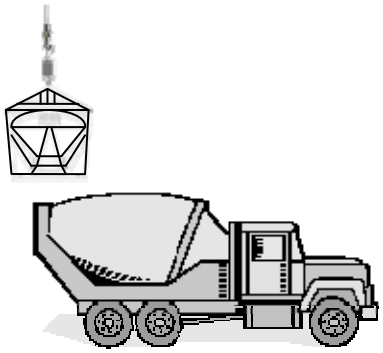

(c) Adding Cement

Figure 2-18. Batching Operations.

After arrival of the truck in the Structures and Materials Testing Laboratory, the cement was added to the truck (see Figure 2-18c and Figure 2-19). After the cement was added, the four containers of sodium hydroxide solution were added into the mixer, which had an added benefit of washing the remaining cement into the mixer as it was poured into the drum. After the

researchers added the sodium hydroxide solution, the concrete mixing truck then mixed the concrete materials for 15 minutes at high speed, which is typical for normal batching operations. Table 2-6 shows the approximate length of time for each operation of the batching process in the laboratory.

Figure 2-19. Dumping Cement into the Mixer.

Table 2-6. Fabrication Procedure in the Structures and Materials Laboratory.

Operation	Approximate Time
Add Cement to the Concrete Truck	30 minutes
Add NaOH solution to the Concrete Truck	5 minutes
Mix Concrete	15 minutes
Perform Slump Test	1 minute
Cast Concrete in LSC specimens Form	15 minutes
Finish Concrete (Screed and Bull Float)	30 minutes
Connect ERW	15 minutes
Cover LSC specimens with Insulating Panels	15 minutes

2.3.6 Casting Specimens

After the concrete materials were mixed for 15 minutes, researchers took a sample from the mixer for a slump test according to ASTM C143 (2000). To assess slump loss over time, the slump was taken every 10 minutes. Figure 2-20 shows that the slump loss for the 16 specimens noticeably varies, most likely due to the varying concrete temperature during batching at different times of the year.

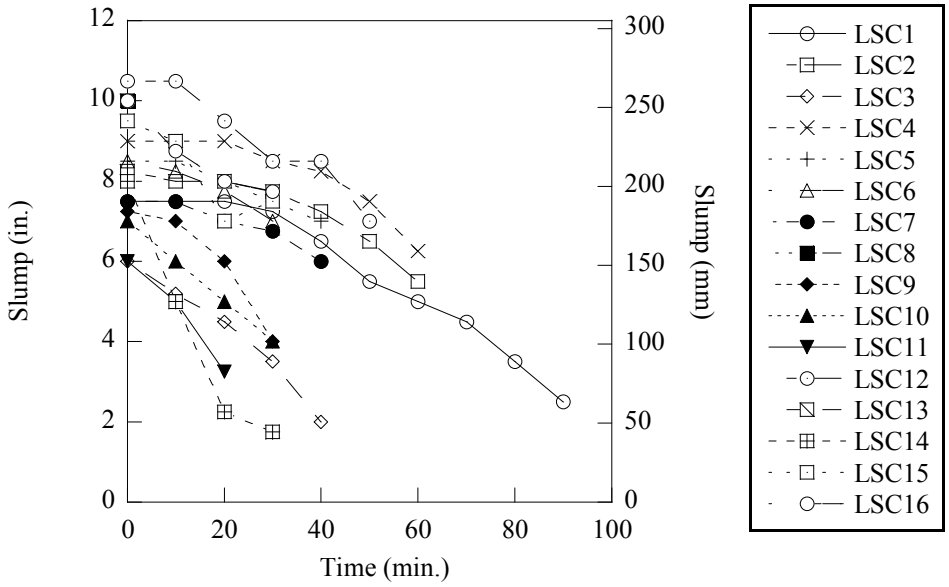

Figure 2-20. Slump versus Time.

The researchers also set aside some concrete to fabricate test samples. Test Samples included 4 inch × 8 inch (102 mm × 204 mm) cylinders for compressive strength testing according to ASTM C39 (2001), and three kinds of prisms:

- Fu prisms for DEF expansion measurements.
- Prisms for ASR/DEF expansion measurement according to ASTM C1293 (2008).
- Prisms for flexural strength tests in ASTM C78 (2007).

Kim and Trejo (2011) further discussed the details of each test sample in a separate materials report for this research.

Figure 2-21 shows the concrete placement. After the form was filled and the concrete consolidated, the concrete was screeded and floated. This process concluded the casting of the concrete.

Figure 2-21. Pouring Concrete in the Form.

2.3.7 Early Age Specimen Conditioning

Shortly after the concrete was floated, the top ERW panels were placed directly on the concrete. Placed end-to-end, the panels covered the top of the specimen except for the last 6 inches (152 mm) on the ends. The wires were routed out the sides of the form for connection to the power supplies. Insulated panels (6 inches [152.4 mm] thick), were then placed on top of the ERW panels to reduce heat loss (see Figure 2-22). These ran the length of the form and completed the insulated form, entombing the specimen. The ERW was connected to the power supplies which controlled the temperature of the concrete to 180°F (82°C) in the bottom, middle and top of the specimen. The ERW was run for two to three days and then switched off to allow the specimen to gradually cool down to reduce the potential for cracking due to thermal variations.

Figure 2-22. Insulated Form with ERW Power Supplies on Top.

During the curing process, the data acquisition system (DAQ) logged data for all sensors in the specimen. The data from the strain gages fluctuated during the placement of the concrete and the heat application period. However, once the heating was switched off and the specimen began to cool down, the strain gages stabilized.

The cooling process consisted of disconnecting the ERW from the power. The top insulation boxes and ERW panels were then removed the next day to allow for further heat loss. After an additional one to three days, the side forms were removed to allow the specimen to reach room temperature. At this point, the strain gages had reached stable values, which were considered as the zero point for testing at a later date.

This concluded the placement procedure. Constructed specimens were stored in the lab until four specimens were completed. Once the fourth specimen was fully completed, the four specimens were transported to the Riverside campus for the deterioration program. The final two specimens constructed remained in the structural testing laboratory, in air-conditioned climate and without supplemental watering, and were used as control specimens without premature concrete deterioration.

2.4 INSTRUMENTATION

The LSC specimens were exposed to environmental conditions to accelerate ASR and DEF. Since DEF likely occurs from high early-age heat, thermocouples (TC) were embedded throughout the concrete specimens to monitor the temperatures during the concrete curing process. Since ASR and DEF cause expansion in the concrete; internal strain gages and concrete embedment gages were installed to monitor this expansion during the deterioration phase and during the structural load tests. Demountable mechanical (DEMEC) points were mounted to the surface of the LSC specimens to measure the external surface strains in the transverse and longitudinal directions along the splice length. Internally, five full-bridge, concrete embedment gages (type KM) were embedded in the concrete to capture the transverse strains of the concrete. Gages were placed 1 inch (25.4 mm) on both sides of the reinforcing hoops. The KM gages were chosen because the KM series of strain gages are designed to be embedded in concrete; the gages are hermetically sealed, bond to surrounding concrete, and have a low elastic modulus that allows for more accuracy. Additionally, two half-bridge strain gages were attached to the hoops for transverse strain measurements. During load testing, the strains in the longitudinal reinforcement in the splice are also monitored to evaluate the tensile behavior of the bar. Ten SGs were installed on bars in the splice region.

2.4.1 External DEMEC Strain Readings

DEMEC points were mounted to the surface of the LSC specimens, allowing a caliper to measure the change in the distance between the points to find the surface expansion throughout the deterioration program. These points were composed of a brass insert and a measurement tip that ELE International manufactured. The DEMECs were placed in holes drilled into the LSC specimens after construction. Figure 2-23 shows the brass insert, measurement tip, and the epoxy holding the DEMEC within the hole, 1 inch (25.4 mm) deep and 7/16 inch (11.11 mm) in diameter. A grid of DEMEC points was installed at 10-inch (254 mm) intervals, which provided distances in the transverse and longitudinal directions for surface strain calculations.

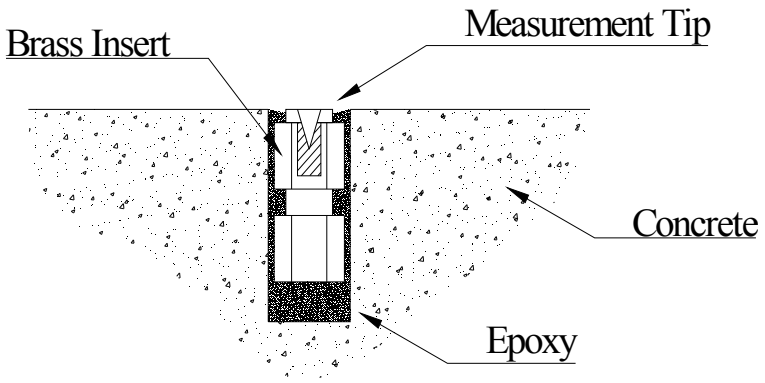

Figure 2-23. Brass Insert with Tip Installed in the Surface of the LSC.

The LSC specimens were initially oriented with the smaller face on top. Each face of the specimen (excluding the ends) was labeled to further explain the instrumentation. Figure 2-24 illustrates the initial orientation and LSC specimen face labels.

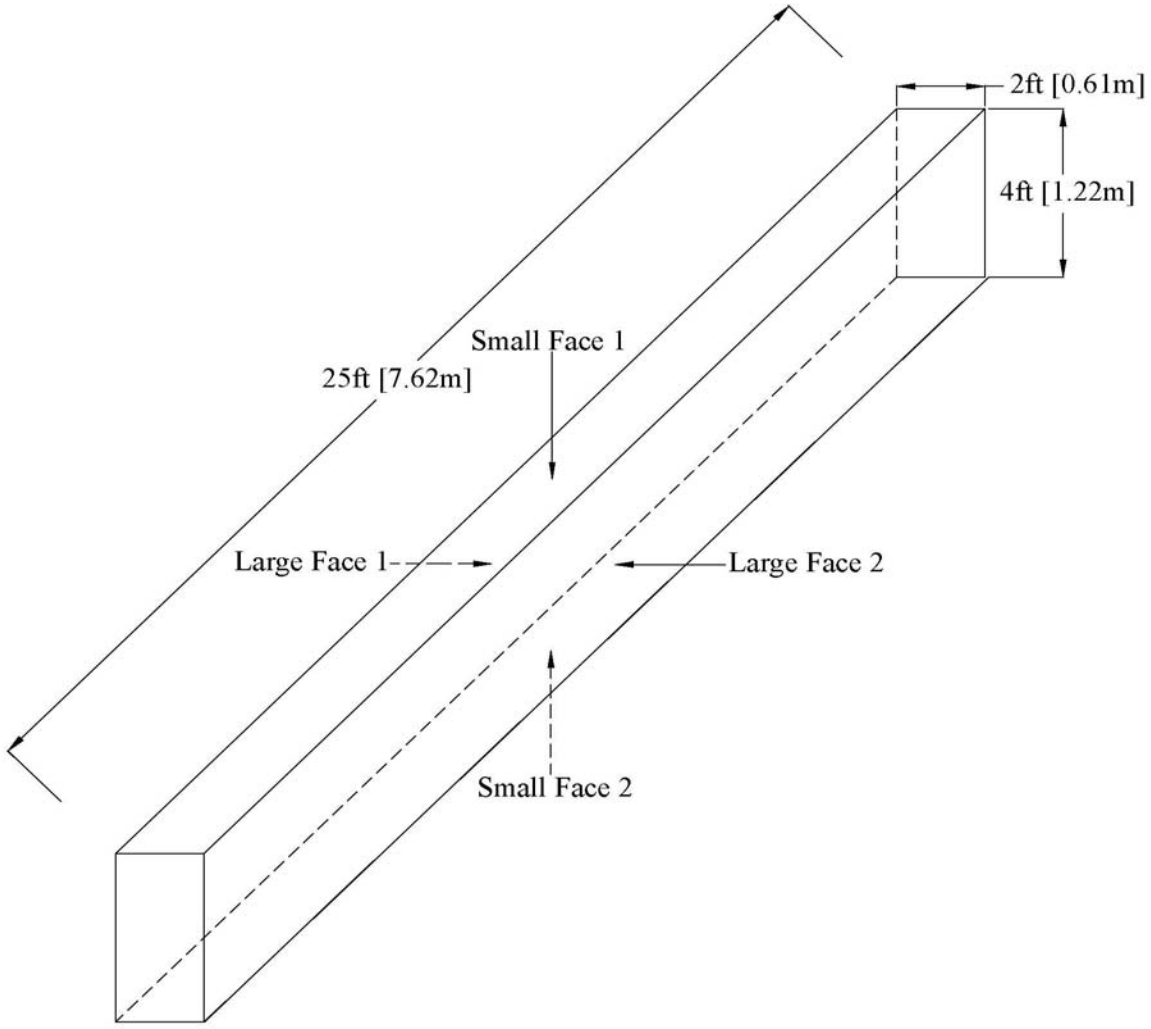

Figure 2-24. Initial LSC Specimen Orientation and Face Labels.

A grid of DEMECs was initially installed on top, Small Face 1, and on one side, Large Face 1, of the LSC specimens along the splice region. On Small Face 1, the 3 × 12 grid consisted of 36 DEMECs spaced at 10 inches (254 mm). A 5 × 12 grid of 60 DEMECs was installed on Large Face 1. Figure 2-25 shows the DEMEC layout on Small Face 1 and Large Face 1. Figure 2-3 shows the 108-inch (2.74 m) long splice region centered longitudinally. The DEMECs completely cover this splice region on Small Face 1 and Large Face 1.

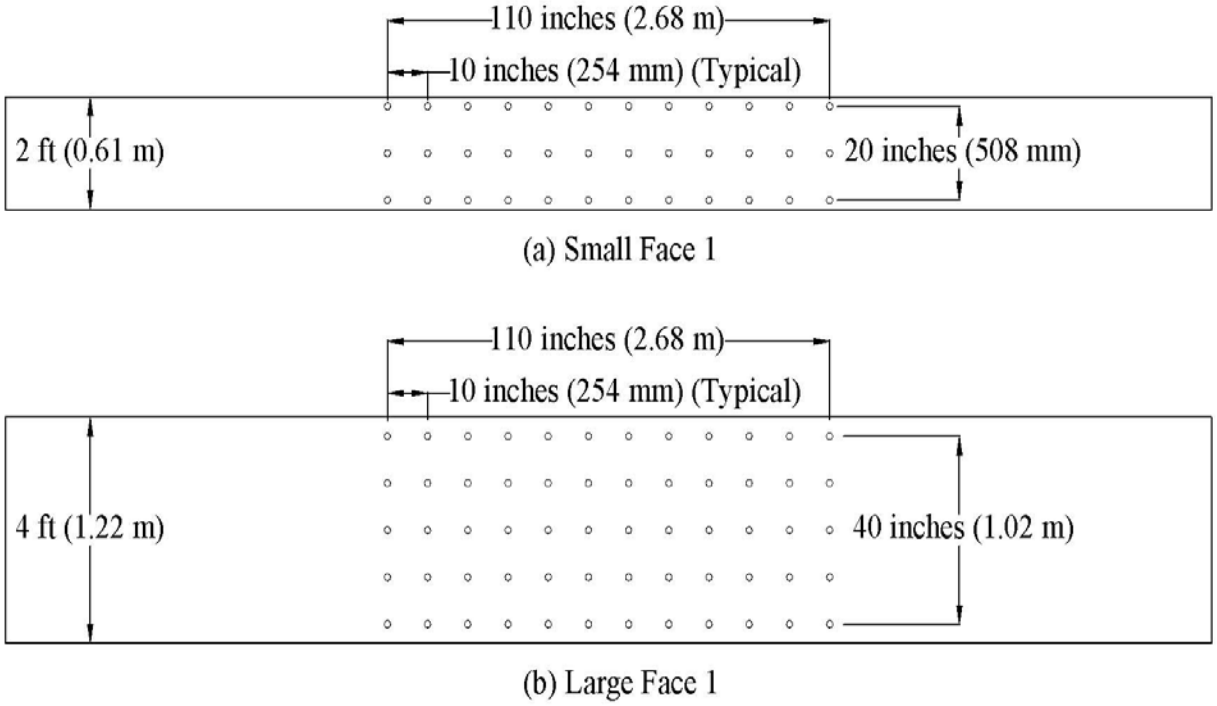

Figure 2-25. DEMEC Layout in the Splice Region.

Figure 2-26 shows the brass inserts attached to aluminum strips, which were used to suspend the brass inserts in the holes and keep them flush with the surface until the epoxy set. A high-modulus epoxy was used to permanently attach the inserts and therefore reduce the error of strain measurements in the future. This was done on the long side first to use gravity in keeping the glue in the holes. The LSC specimens were then rolled onto their sides and the same procedure was used to install the DEMECs on the LSC specimen's Small Face 1.

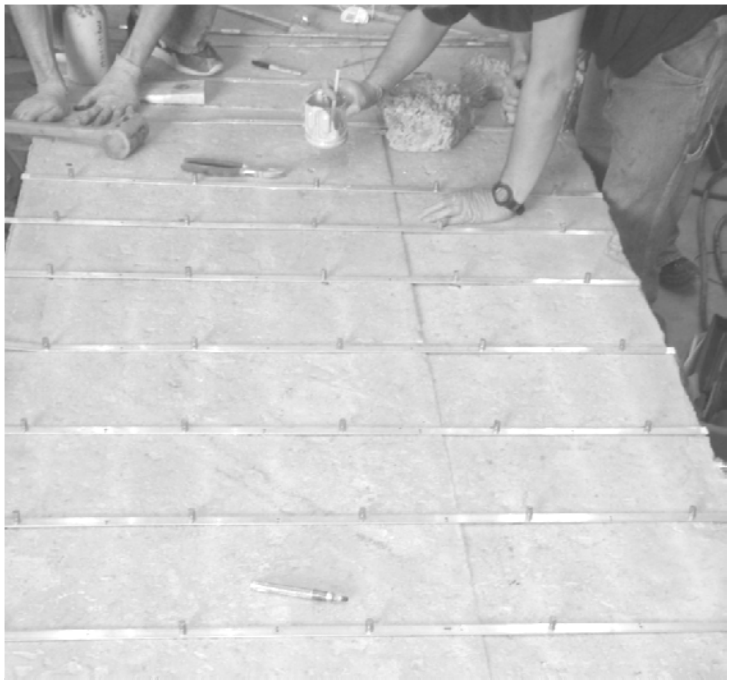

Figure 2-26. DEMEC Installation on the LSC Specimen's Large Face 1.

Once the epoxy hardened, the aluminum strips were unscrewed from the brass inserts and peeled off the concrete. The tips were then inserted into the brass inserts and the grid was measured for initial gage lengths using a caliper with a precision of 0.0005 inches (12.7 μm). This value was later used for strain calculations as the initial length prior to expansions from ASR and DEF.

2.4.2 Electronic Strain Gages

In addition to the DEMECs, several electronic sensors were installed in the specimens to measure the internal strains due to ASR/DEF deterioration and also from load testing. SGs were attached to the reinforcing steel as outlined in Section 2.3.2 and placed for monitoring of ASR/DEF expansive strains and strains from the flexural load testing of the LSC specimens. Figure 2-27 shows eight SGs placed on the longitudinal tension steel in the splice region, four on a center bar, and four on a corner bar. SG 9 and SG 10 were placed on a compression bar in the middle of the splice. Figure 2-28 shows the location of SG11–SG12 placed on the center transverse reinforcement. The strain in the concrete cover and concrete core were measured with KM1–KM4. KM5 measured the radial strain on the Large Face 1 side. SG 11 and SG 12 were used primarily for monitoring expansion in the field, but will pick up strain during load testing if

shear forces are present (three-point load test). The five KM gages were embedded in the concrete at the center of the splice to monitor expansive concrete strains during the deterioration phase. Four of the KM gages were placed such that they were 1 inch (25.4 mm) and 3 inches (76 mm) from each side of the specimen face, and the final KM gage was placed perpendicular to the transverse steel. Note that the KM gages were placed between the column hoops. However, the control specimens were not instrumented with these gages because they were kept in the laboratory (or dry environment), which is not conducive to ASR/DEF deterioration. The embedment gages are used to measure the strain in the cover and the strain inside the hoop. Combined with the strain gages on the reinforcing steel hoop and the DEMECs, this allows for a strain distribution starting from the surface to 3 inches (76.2 mm) below the surface to be generated at 1-inch (25.4 mm) intervals.

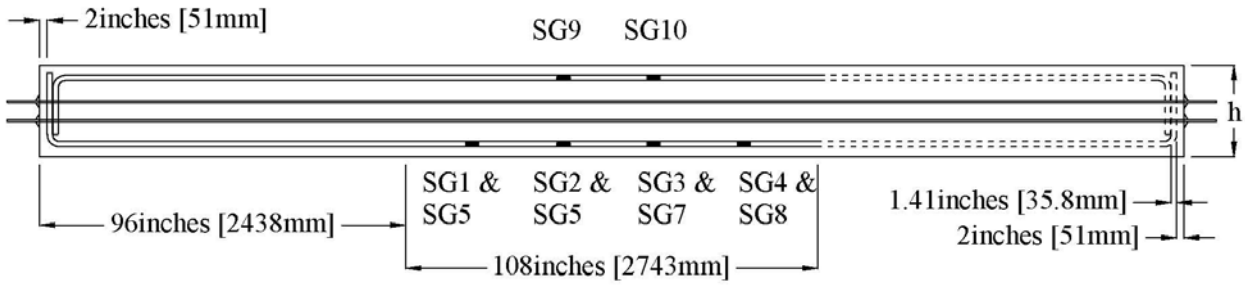

Elevation View

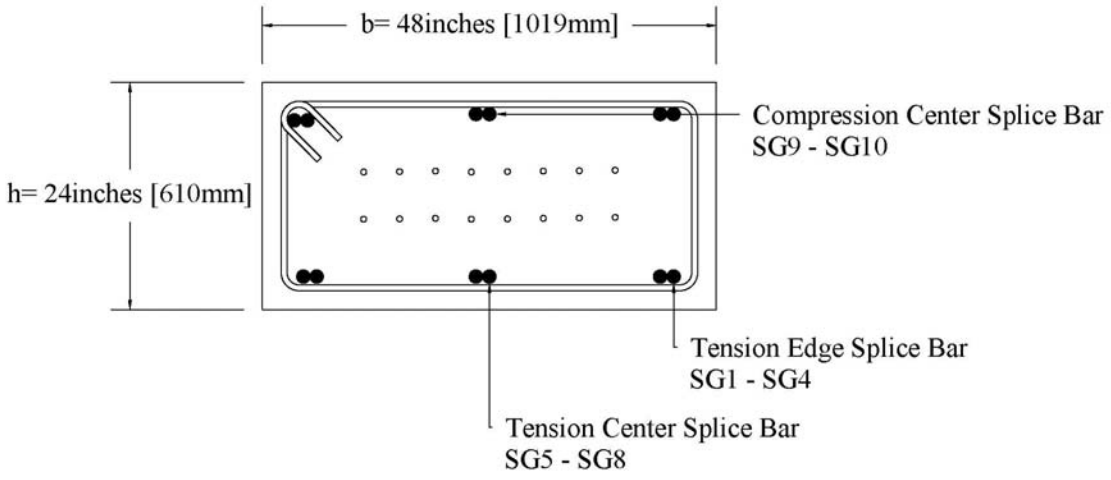

Cross Section

Figure 2-27. Internal Strain Gage Locations on Longitudinal Reinforcement.

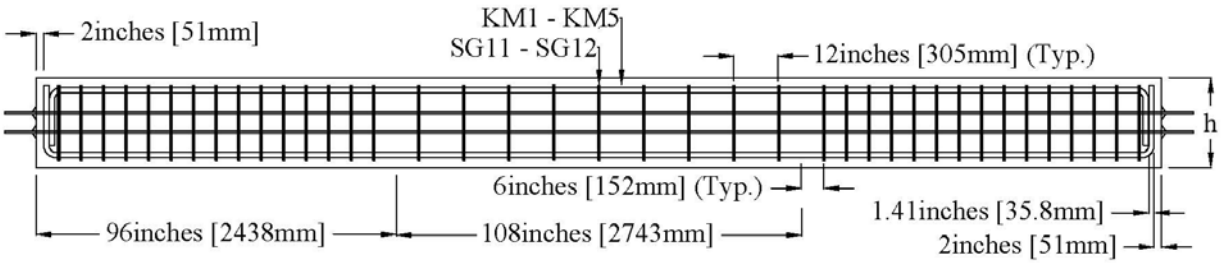

Elevation View

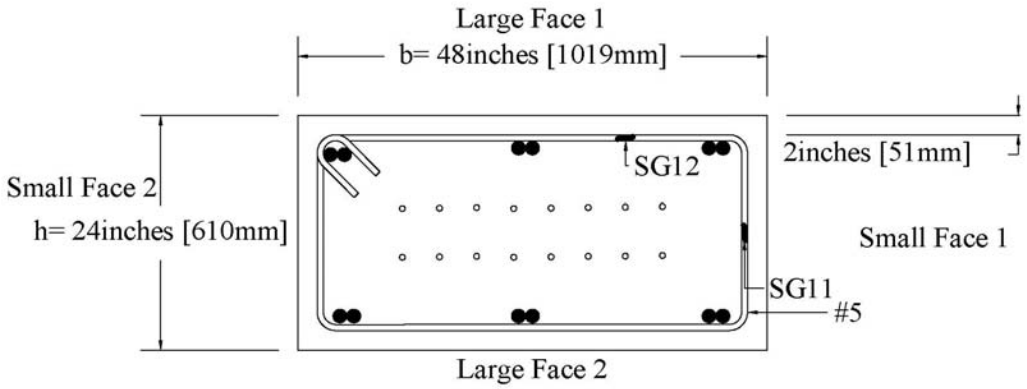

Cross Section with SG11–SG12

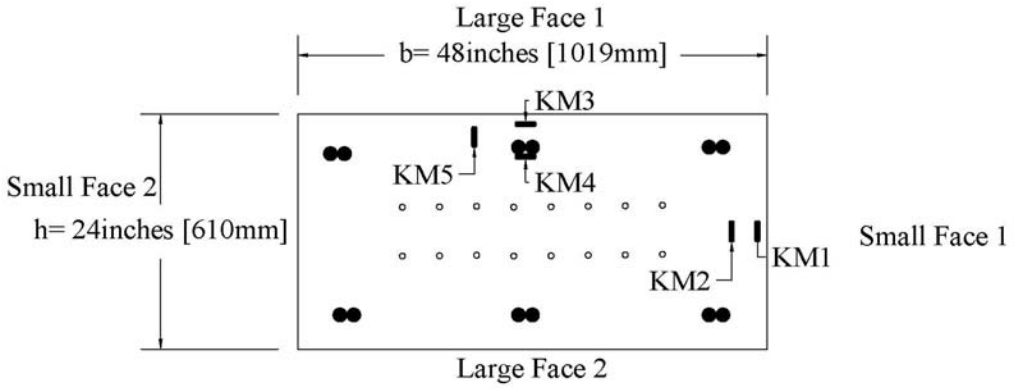

(c) Cross Section with KM1–KM5

Figure 2-28. Internal Strain Gage Locations on Transverse Reinforcement, Concrete Core, and Concrete Cover.

2.5 SUMMARY

Fourteen specimens were constructed and transported to the Riverside campus for the aggressive deterioration program, and two control specimens remained in the climate controlled structural laboratory without supplemental water or moisture required for premature concrete deterioration. The fabrication process for all 16 specimens lasted from January 2008 to September 2008. Due to the research done on the front end of the project, the LSC specimens were successfully constructed and were exposed to the deterioration program in a quick time frame.

CHAPTER 3:
DETERIORATION OF LARGE-SCALE SPECIMENS

3.1 INTRODUCTION

This section describes the process of evaluating the deterioration of the LSC specimens. The exposure conditions, internal and external instrumentation, and specimen behavior due to Alkali Silica Reaction and Delayed Ettringite Formation are included. The monitoring of the specimen expansions during the deterioration process is extremely important since there is only limited capability of measuring the effects of ASR/DEF in field structures. A further assessment of the ASR/DEF deterioration is summarized from the petrographic analysis reports conducted on cores taken from specimens following the structural load test.

3.2 SPECIMEN EXPOSURE CONDITION

Shortly after the construction of LSC specimens and their preloading to replicate service conditions, the specimens were placed outside at the Texas A&M University Riverside Campus in Bryan, TX, where they were exposed to the environmental weather conditions of the area and supplemental water to accelerate the ASR/DEF deterioration mechanisms. A sprinkler system activated four times a day and for 15 minutes each time, supplied the supplemental water. Figure 3-1 and Figure 3-2 show the average temperatures and precipitation in Bryan, TX according to the Weather Channel (2011). The values in the figures are an average of all recorded data, not specific to a year.

The 14 specimens were placed next to each other with the smaller face on top as shown in Figure 3-3. A clear space of about 2–3 ft (0.6–0.9 m) was between each LSC specimen, which allowed the LSC specimens' Small Face 1 to experience direct sunlight. Since Large Face 1 and Large Face 2 were on the sides of the specimen, only the top of each side experienced significant direct sunlight, while the bottom of each side was mostly in the shade of the adjacent LSC specimen. Figure 3-3 shows the LSC specimens at the Riverside Campus with Small Face 1 on top. Figure 3-4 shows the sprinkler system between two specimens. This system wetted the specimens on the three outer faces.

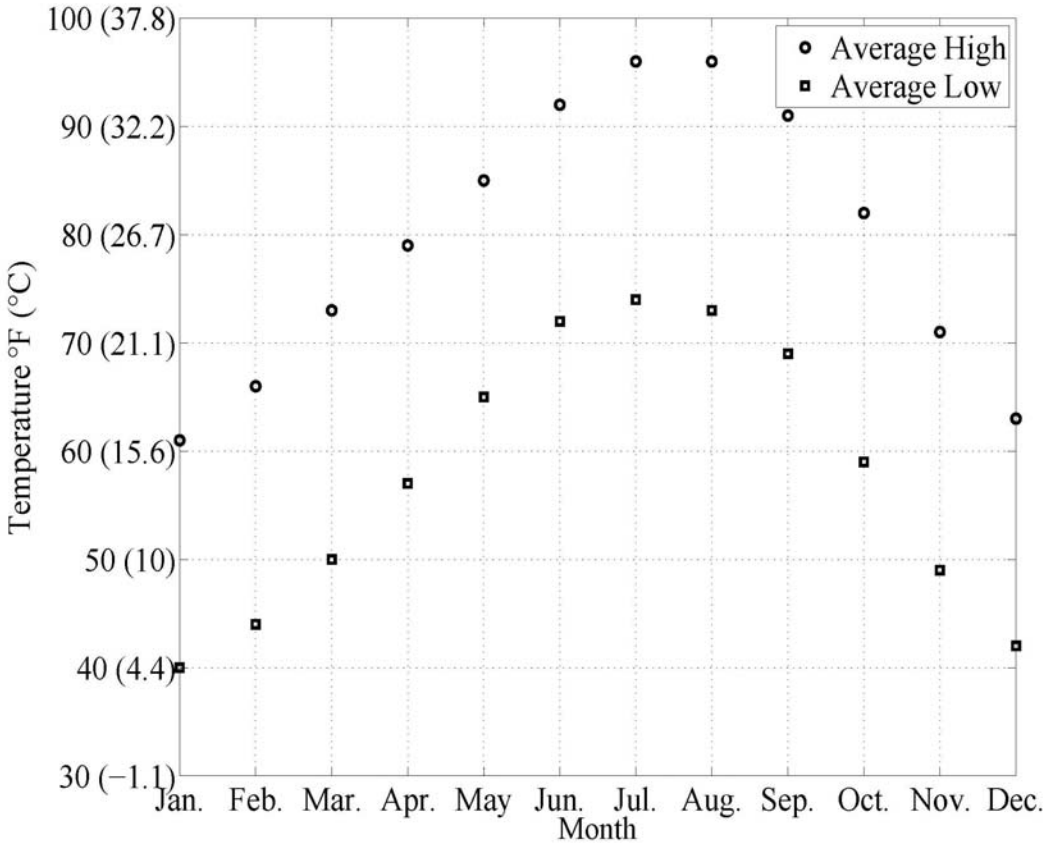

Figure 3-1. Average Temperatures at Riverside Campus in Bryan, TX (Weather Channel 2011).

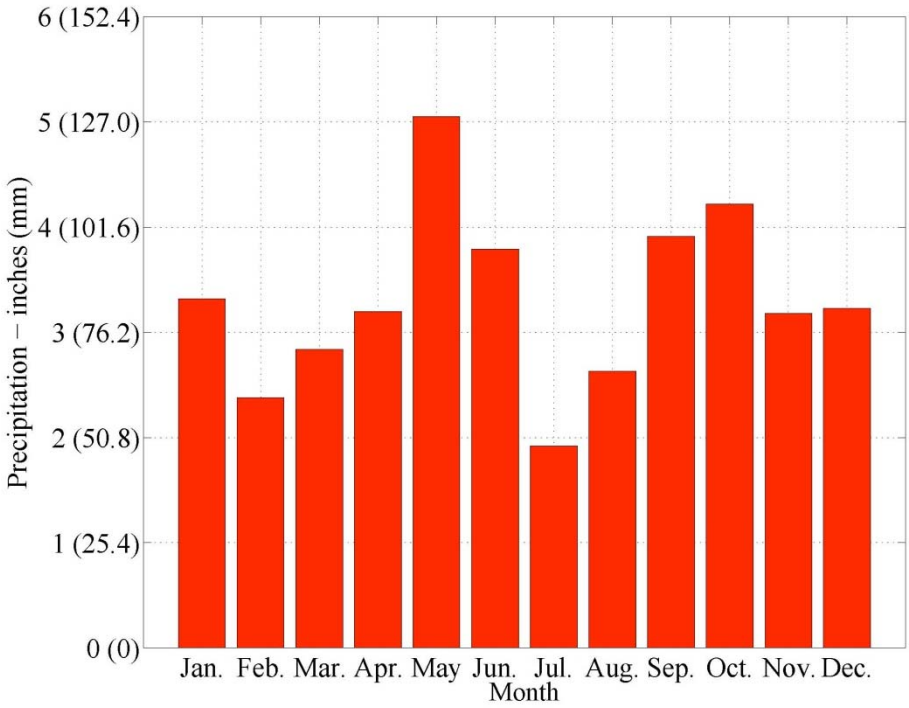

Figure 3-2. Average Precipitation at Riverside Campus in Bryan, TX (Weather Channel 2011).

Figure 3-3. LSC Specimens Exposed to the Environment at the Riverside Campus.

Figure 3-4. Sprinkler System between Two LSC Specimens.

From measured expansion data on the specimens that will be further described later, researchers found that the largest surface expansions resulted on the top or sunny side of the specimen. To provide more uniform expansion throughout the specimens, the LSC specimens were rotated twice during the deterioration program. Figure 3-5 shows the three orientations and the label for each face. The length of the specimens is 25 ft (7.62 m), which is not shown to scale in the figure. Since Small Face 2 had not experienced any direct sunlight or water, the first rotation positioned this face on top. The second rotation was 90°, which positioned Large Face 2 on top, and which was the critical tension side in the subsequent structural load testing. Figure 3-6 shows the specimens during the 3rd orientation.

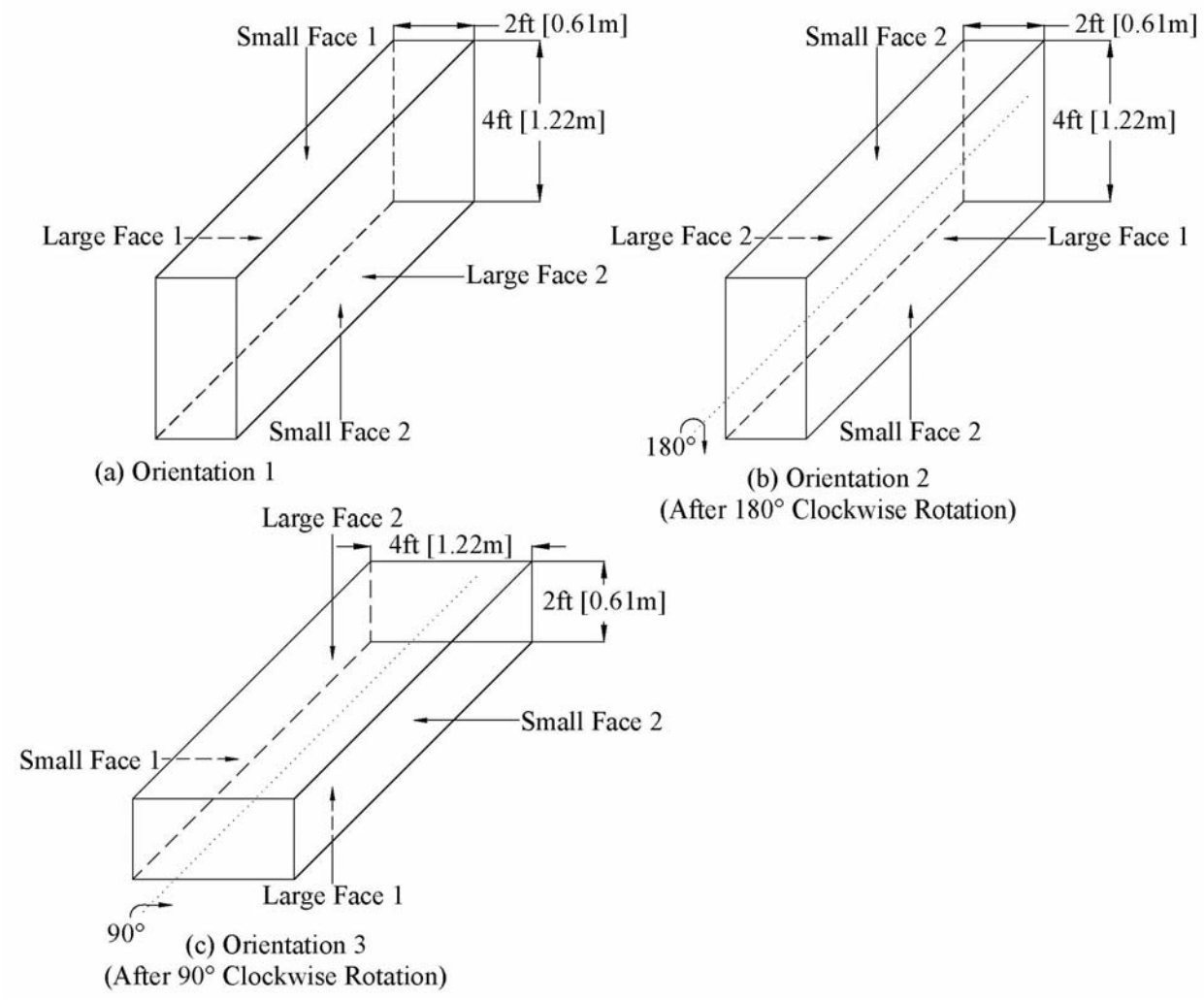

Figure 3-5. Orientations of the LSC Specimens.

Figure 3-6. LSC Specimens at the Riverside Campus during the 3rd Orientation.

Table 3-1 lists the month and year of the specimen casting, first exposure to the environmental conditions with supplemental water, 180° rotation, 90° rotation, and structural load test. LSC1 through LSC4 were transported at the Riverside Campus before May 2008. However, the sprinkler system providing supplemental water was not installed until May. Therefore, these specimens had some time without supplemental water from the sprinkler system. Since water is a necessary component for ASR (Folliard et al. 2006), the researchers defined the initial exposure as the time when the specimens were first exposed to the supplemental water.

Table 3-1. Dates of Exposure, Rotations, and Structural Load Testing.

LSC Specimen #	Date of Casting	Date of Initial Exposure	Date of 180° Clockwise Rotation	Date of 90° Clockwise Rotation	Date of Structural Load Test
1	1/2008	5/2008	7/2009	N/A	8/2010
2	2/2008	5/2008	7/2009	7/2010	TBD
3	2/2008	5/2008	7/2009	N/A	8/2010
4	3/2008	5/2008	7/2009	7/2010	TBD
5	4/2008	5/2008	7/2009	7/2010	7/2011
6	4/2008	5/2008	7/2009	7/2010	TBD
7	4/2008	7/2008	7/2009	7/2010	TBD
8	5/2008	7/2008	7/2009	7/2010	7/2011
9	6/2008	7/2008	7/2009	N/A	2/2010
10	6/2008	7/2008	7/2009	N/A	2/2010
11	6/2008	9/2008	2/2010	7/2010	TBD
12	7/2008	9/2008	2/2010	7/2010	TBD
13	7/2008	9/2008	2/2010	7/2010	TBD
14	8/2008	9/2008	2/2010	7/2010	TBD

3.3 SPECIMEN BEHAVIOR DURING DETERIORATION PHASE

The behavior of the LSC specimens during the environmental exposure conditions was monitored with external surface and internal strain measuring devices. Demountable mechanical (DEMEC) points were mounted on the surface of the specimens and provided a way to measure the external surface expansion during the deterioration process. Electronic strain gages were placed on the reinforcing steel and concrete embedment gages were placed within the concrete specimen to measure the internal deformations during the deterioration process. Chapter 2 describes the placement of the internal instrumentation. The usage and results of the instrumentation is explained below.

3.3.1 Surface Strains between DEMEC Points

Figure 2-25 shows the grid of DEMEC points installed on Small Face 1 and Large Face 1 at the critical splice region. A caliper with a 0.0005-inch (0.0127 mm) precision was used to measure the distance between two DEMEC points in the transverse and longitudinal directions. The surface strain between two points was calculated as follows:

$$\boldsymbol{\varepsilon_d} = \frac{\mathbf{l_d(t) - l_d(0)}}{\mathbf{l_d(0)}} \qquad \text{(Eq. 3-1)}$$

where $l_d(t)$ is the distance between two DEMECs at time, t, and $l_d(0)$ is the initial distance. Transverse and longitudinal distances were measured on Small Face 1 and Large Face 1, then used to calculate a surface strain for each distance meEasured, ε_d. Each distance, d, is numbered 1 through 160. Figure 3-7 shows the grid of DEMECs and numerical labels for the distances used to calculate the strains. Average strains were calculated to give an overall strain along the length of the LSC specimens to help summarize the results. The average strains are labeled by face (Small Face 1 or Large Face 1), strain type (transverse or longitudinal), and strain number. The face name is abbreviated to SF1 and LF1 for Small Face 1 and Large Face 1. The strain type is abbreviated to TS and LS or transverse strain and longitudinal strain. The strain number is given since a few average strains are calculated on each face. The first average transverse strain on Small Face 1 is calculated as follows:

$$\text{SF1 TS1} = \text{average}(\boldsymbol{\varepsilon_{1,\ldots 12}}) \qquad \text{(Eq. 3-2)}$$

where ε_1 through ε_{12} is calculated in Eq. 3-1 for each distance, 1 through 12. The other average strains are calculated in the same way using different ε_d values. For instance, the first longitudinal strain on Large Face 1 (LF1 LS1) is an average of strain values ε_{106} through ε_{116}. The strain values, ε_d, used to calculate the other average strains are shown in Figure 3-7. Note that the length of the face is not shown to scale in Figure 3-7.

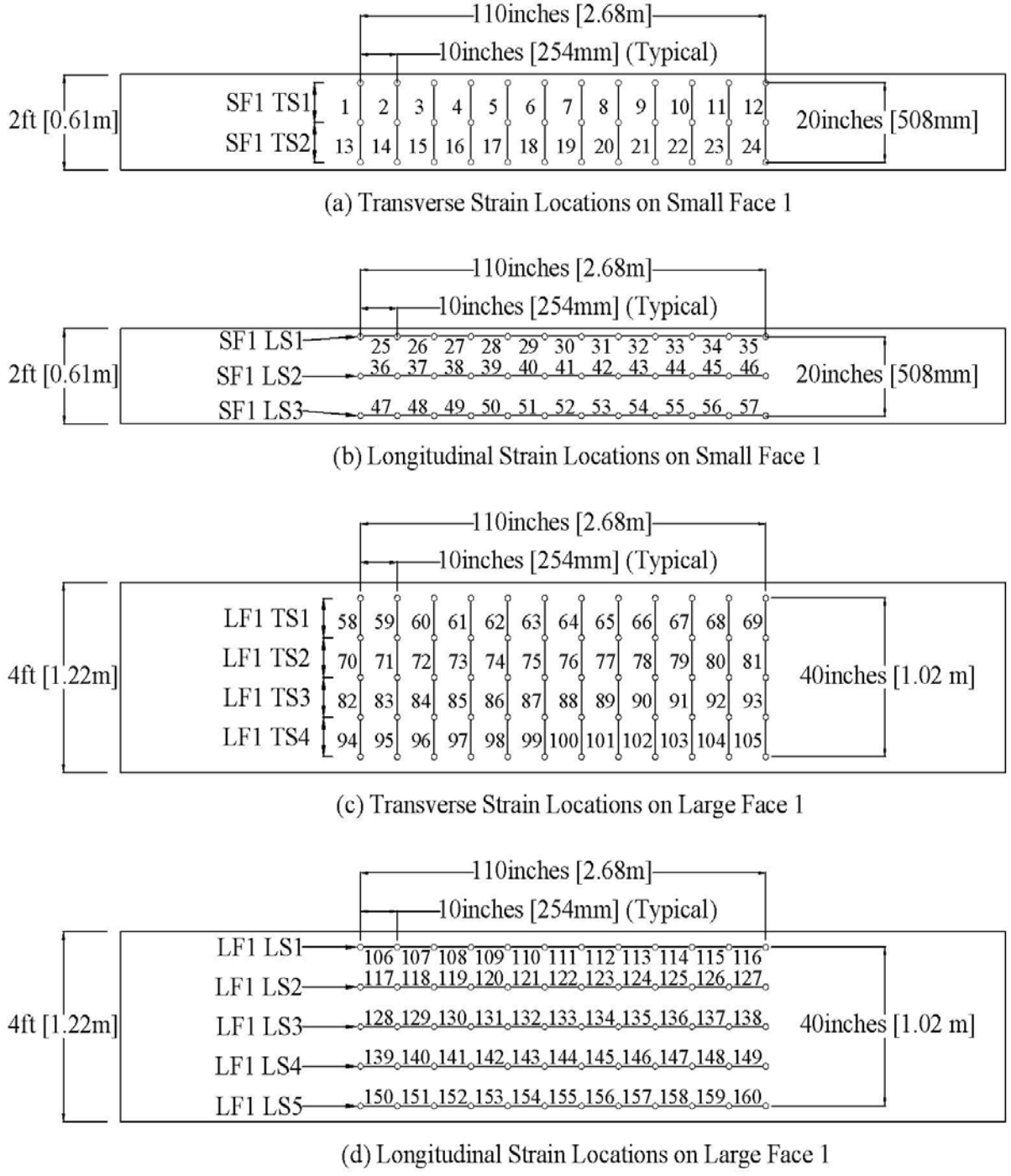

Figure 3-7. Transverse and Longitudinal Strain Locations on the LSC Specimens' Small Face 1 and Large Face 1 during the Initial Orientation.

The averaged strains labeled SF1 TS1, SF1 TS2, LF1 TS1, LF1 TS2, LF1 TS3, and LF1 TS4 from Figure 3-7 were plotted to compare the strains. Figure 3-8 compares the transverse strains on Small Face 1 and Large Face 1. LSC15 and LSC16 were not instrumented with DEMECs since these were the control specimens without ASR/DEF effects. Therefore, no data are shown in the figures for these specimens.

The high temperatures during the summer months resulted in an increase in ASR/DEF expansion for most specimens. The graphs show a grey region behind the strain plots highlighting the expansion during the summer months; the days with a grey background are May 1 through September 30. The slope of the average transverse surface strain on Small Face 1was calculated to show the effect of the summer months (Table 3-2). The specimens exposed to fewer summer months in 2008 had a larger increase in slope during summer 2009. Figure 3-8 shows that the LSC specimens expanded more on Small Face 1 than on the Large Face 1. Also, the strain on the top of Large Face 1 (LF1 TS1) is larger than the strains on the bottom. The top strain on the Large Face, LF1 TS1 reached around 61 percent of the average Small Face 1 transverse strain (SF2 TS Avg.), at the last measurement. An average of the other strains on the Large Face, LF1 TS2 through LF1 TS4, only reached an average of 22 percent of the strain on the Small Face. The LSC specimens did not expand uniformly because the direct sunlight and water caused more expansion on the top of the specimens. Because of this occurrence, the researchers rotated the specimens to provide a more uniform expansion. The last data point in Figure 3-8 is the last measurement before the specimen was rotated for the first time. This rotation inhibited the ability to continue gathering data for Small Face 1 since it shifted its position from top to the bottom.

Table 3-2. Strain Rates during Summer and Non-Summer Months.

	Average Slope (Strain/Month) of SF1 TS Avg.		**Rate of Increase**
	Non-Summer	**Summer**	
Specimens 1–6	0.00045	0.00074	1.7
Specimens 7–10	0.00046	0.00126	2.7
Specimens 11–14	0.00019	0.00119	6.5

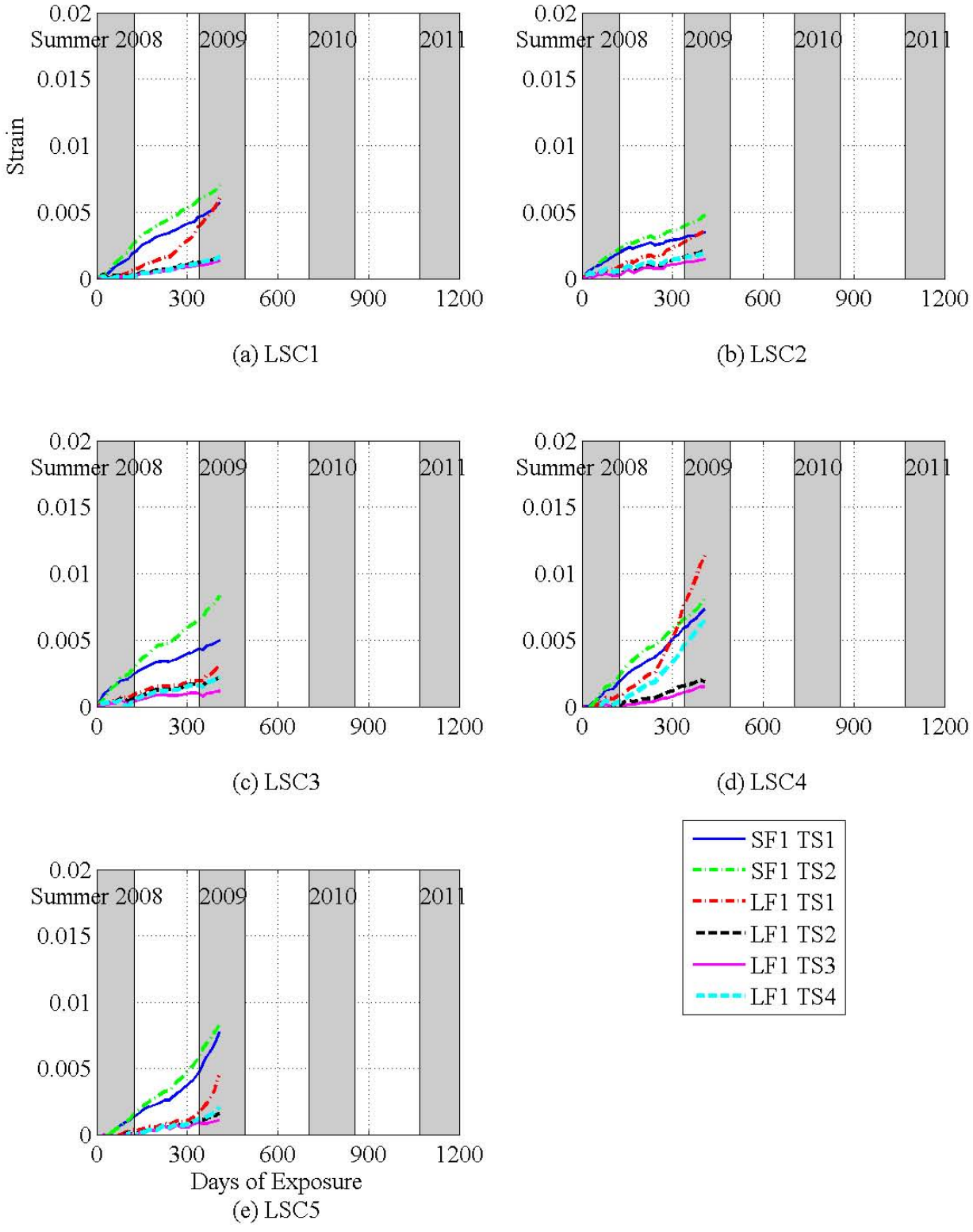

Figure 3-8. Transverse Surface Strains on the LSC Specimens' Small Face 1 and Large Face 1.

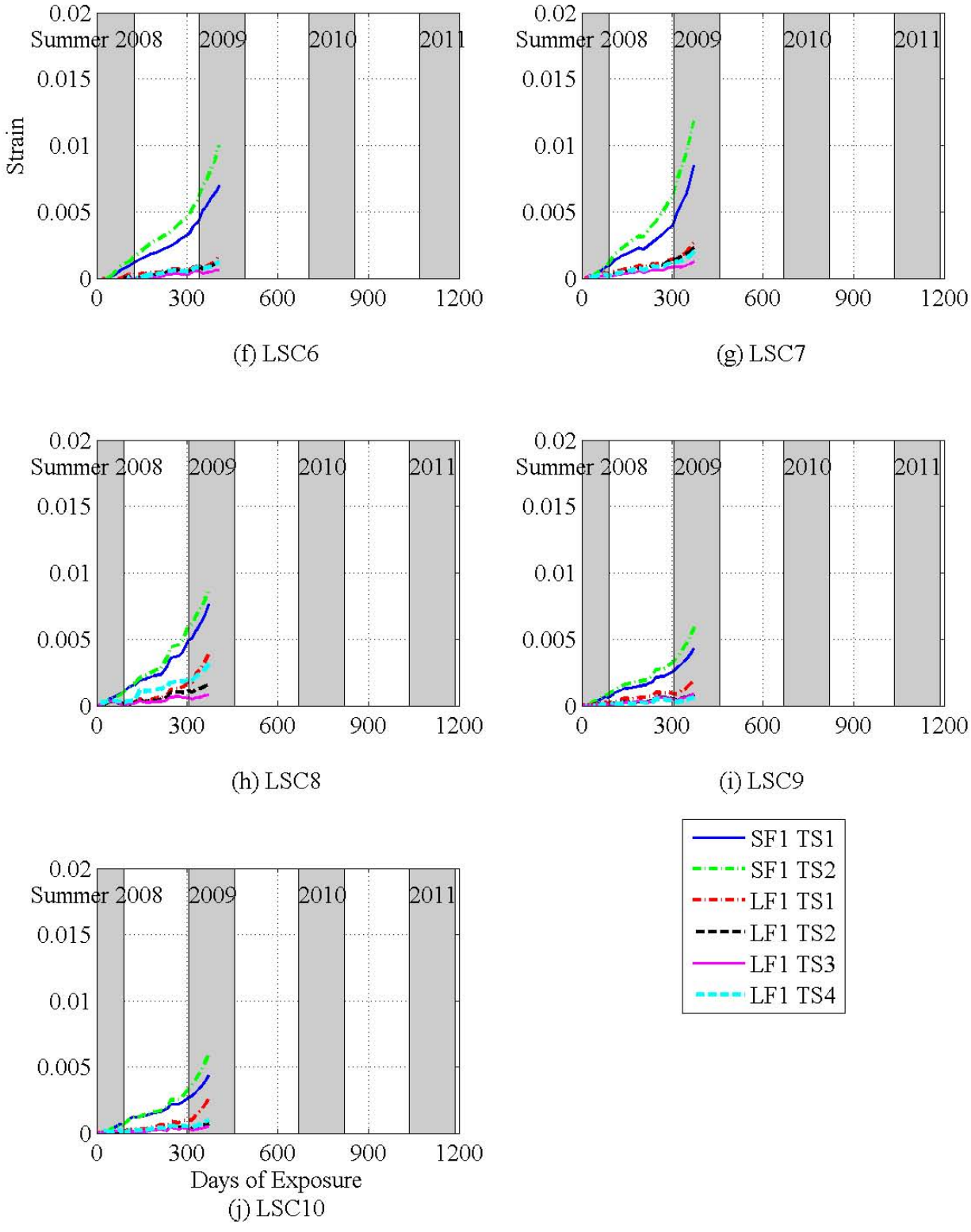

Figure 3-8. Transverse Surface Strains on the LSC Specimens' Small Face 1 and Large Face 1. (Continued)

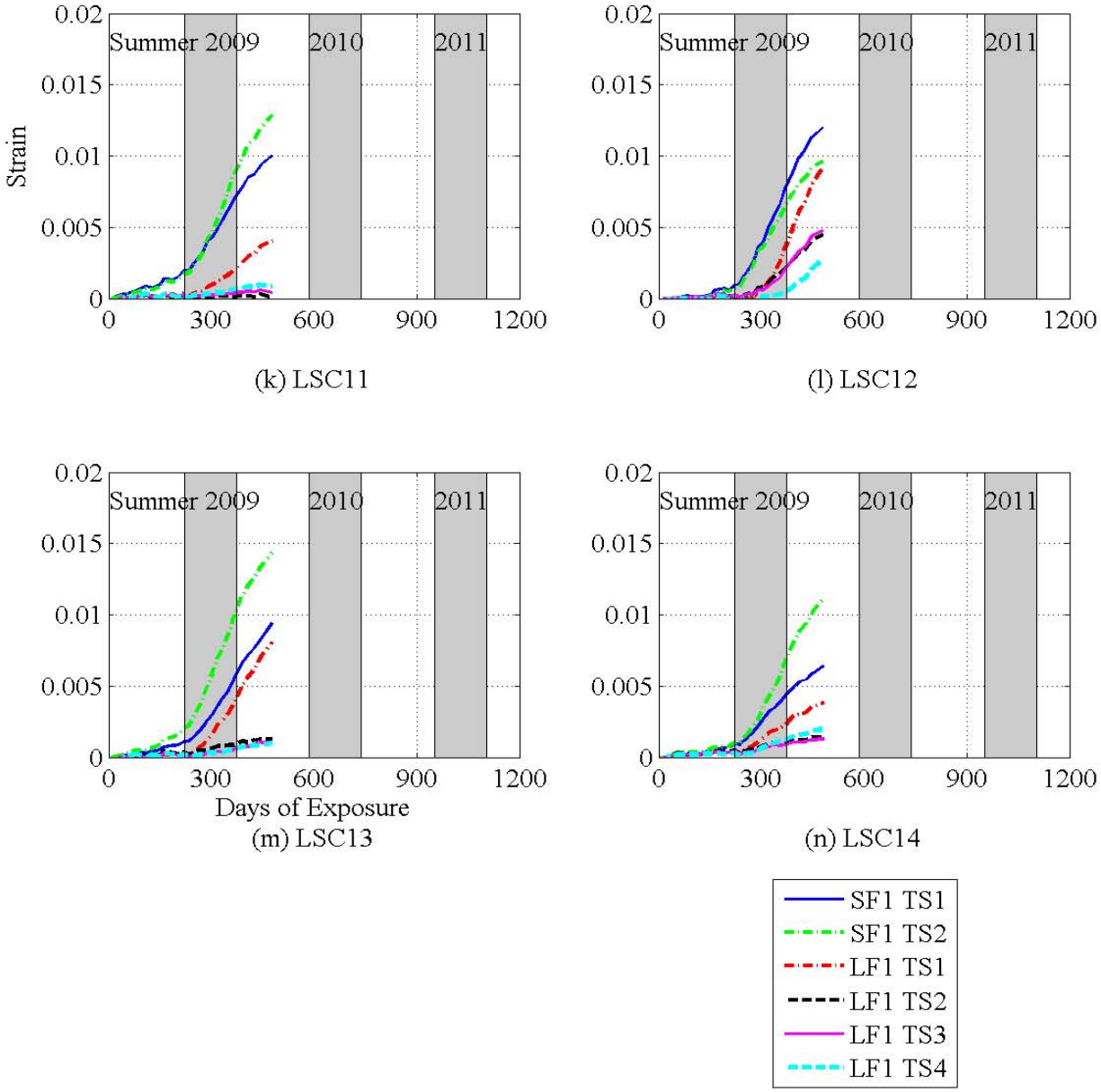

Figure 3-8. Transverse Surface Strains on the LSC Specimens' Small Face 1 and Large Face 1. (Continued)

After the first rotation, Small Face 2 was now on top, available for more surface expansion data. Therefore, additional DEMEC points were mounted on the Small Face 2 to continue the surface strain measurements after the rotation, as discussed in the instrumentation process in Chapter 2. Figure 3-8 shows the two transverse strains on Small Face 1 (SF1 TS1 and SF1 TS2) were similar. Therefore, DEMECs on Small Face 2 were placed in a 2 × 6 grid instead of a 3 × 12 grid on Small Face 1 to reduce measurement collection. The DEMECs were spaced at 10 inches (254 mm) on both faces in the transverse and longitudinal directions. Figure 3-9 shows the DEMEC points in the transverse and longitudinal directions on the Small Face 2. The smaller DEMEC grid pattern provided fewer transverse and longitudinal strains used to calculate average strains along the length of the LSC specimens. The fewer DEMECs provided only one transverse strain (SF2 TS1) and two longitudinal strains (SF2 LS1 and SF2 LS2). Small Face 1 had two transverse strains and three longitudinal strains.

On Large Face 1, the transverse and longitudinal strains (LF1 TS1 and LF1 LS1) were on top of the face during the initial LSC specimen orientation. However, after the 180° rotation in the 2nd orientation, these faces were now on bottom (see Figure 3-9). Note that the length of the LSC specimens is 25 ft (7.62 m), which is not shown to scale in this figure.

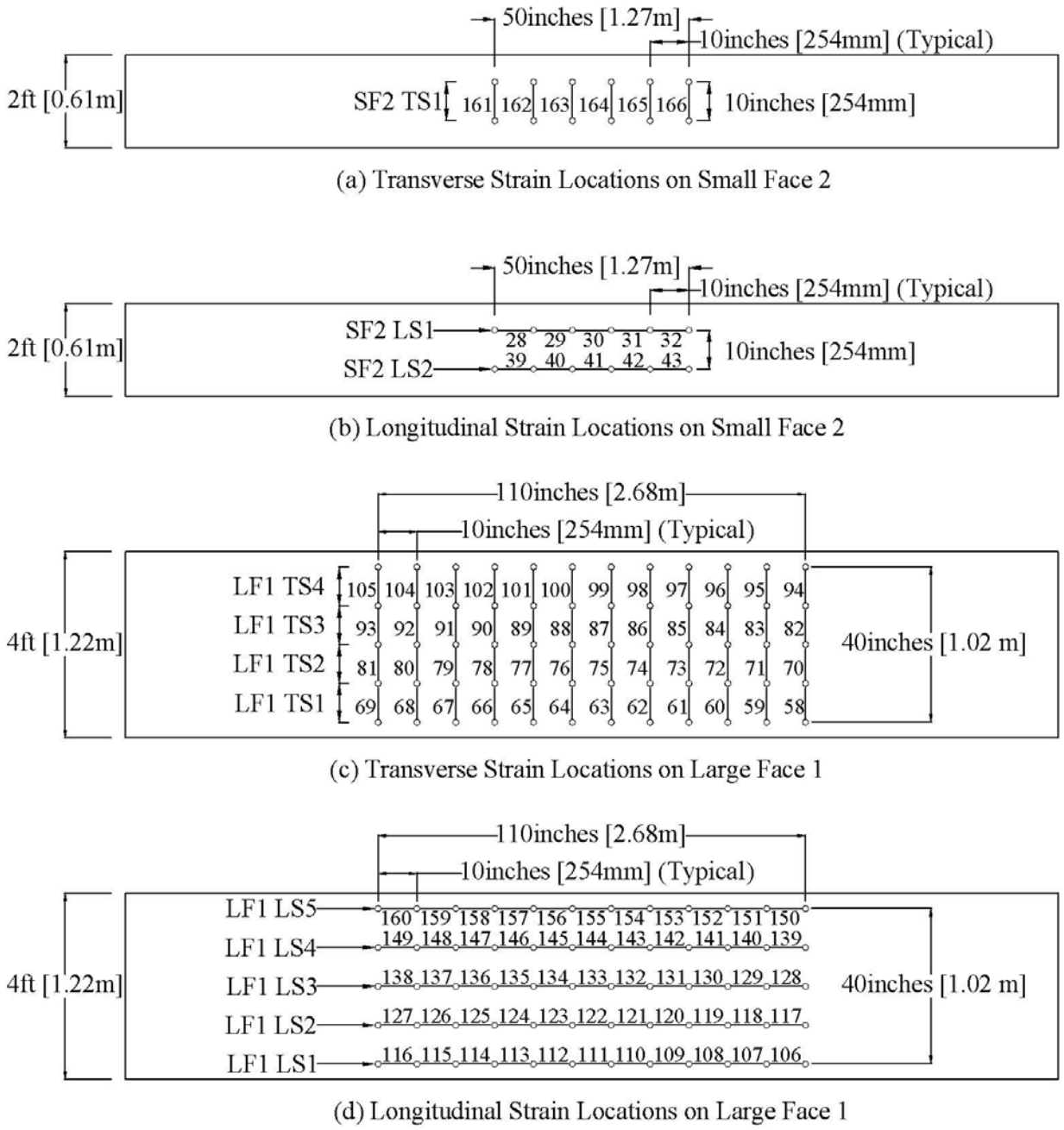

Figure 3-9. Transverse and Longitudinal Strain Locations on the LSC Specimens' Small Face 2 and Large Face 2 during the 2nd Orientation.

After the LSC specimens were rotated 90° for the 3rd orientation, Large Face 1 was placed on the bottom (Figure 3-5). Figure 3-6 shows the LSC specimens during the 3rd orientation with Large Face 2 on top. The distance between each specimen in this orientation was approximately 1 ft. Since Small Face 1 and Small Face 2 significantly expanded while exposed to direct sunlight and

water and now these sides were mostly shaded, no surface data was measured on these faces during the 3rd orientation. New DEMECs were mounted on Large Face 2 following the installation process in Chapter 2. Figure 3-10 shows the DEMECs on Large Face 2 in a 5 × 5 grid compared to the 5 × 12 grid on Large Face 1. The smaller grid provided fewer transverse and longitudinal strains to average; however, there were still four transverse and five longitudinal averaged strains measured along the splice length of the LSC specimens.

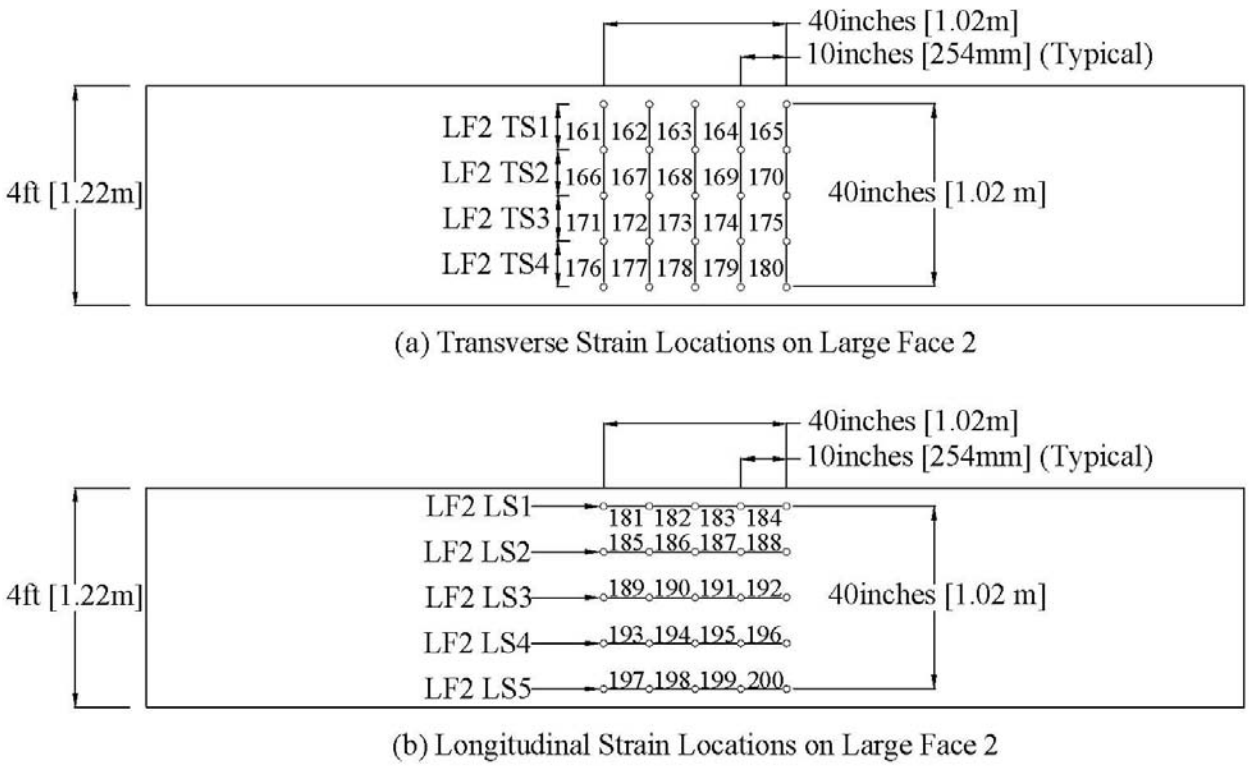

Figure 3-10. Transverse and Longitudinal Strain Locations on the LSC Specimens' Large Face 2 during the 3rd Orientation.

Figure 3-11 and Figure 3-12 show the transverse and longitudinal strains on Small Face 1 and Small Face 2 during the exposure period. These figures also show the surface strains on Small Face 2 with an initial value of zero after the first rotation, since this face was on the bottom and not exposed to direct sunlight. The surface strain measurements discontinued on Small Face 2 after the 2nd rotation. The strain measurements on Large Face 1 continued after the 180° rotation; however, since the top and bottom strains switched, notice the increase of LF1 TS5. After the 90° rotation, surface strain measurements on Large Face 1 discontinued since this face

was no longer accessible. The last values of the four transverse strains and five longitudinal strains on Large Face 1 were used as the initial value for the strains on Large Face 2. This was appropriate since both faces were exposed to the same environment.

Figure 3-11 illustrates the small difference between the two transverse strains on Small Face 1. The two transverse strains were both on top and exposed to direct sunlight, causing similar results. Figure 3-13 and Figure 3-14 show the transverse and longitudinal strains on Large Face 1 and Large Face 2. Since there was a small difference between the two transverse strains on Small Face 1, the average value of the transverse strains on Small Face 1and the transverse strain on Small Face 2 are plotted in Figure 3-13 to compare the strains at different locations.

The "+" symbol depicts the day of 180° rotation of the LSC Specimen. The 90° rotation occurrence is shown on the graph by an "o" symbol. LSC specimens 1, 3, 9, and 10 were tested before the 2nd rotation. These specimens have an "x" on the graph showing when the structural load test occurred. The results from the load tests will be discussed in 0. Once more, the grey region highlighted the summer months (May through September). The legend lists the strain names corresponding to the labels in Figure 3-7, Figure 3-9, and Figure 3-10.

In the following figures, the transverse surface strains are approximately 10 times as large as the longitudinal surface strains. The axial post tensioning strands along the LSC specimens' length simulating a bridge column axial load discussed in Section 2.1.1 and the column longitudinal reinforcement most likely provided the restraint for the expansion in the longitudinal direction. By day 500, the transverse strains exceeded 0.002. Figure 3-14 shows that the longitudinal strains did not reach 0.002. The longitudinal strains were not affected by location as much as the transverse strains since the biggest difference between longitudinal strains at a certain time was 0.0005, whereas the transverse strains had differences of 0.015 on Large Face 1.

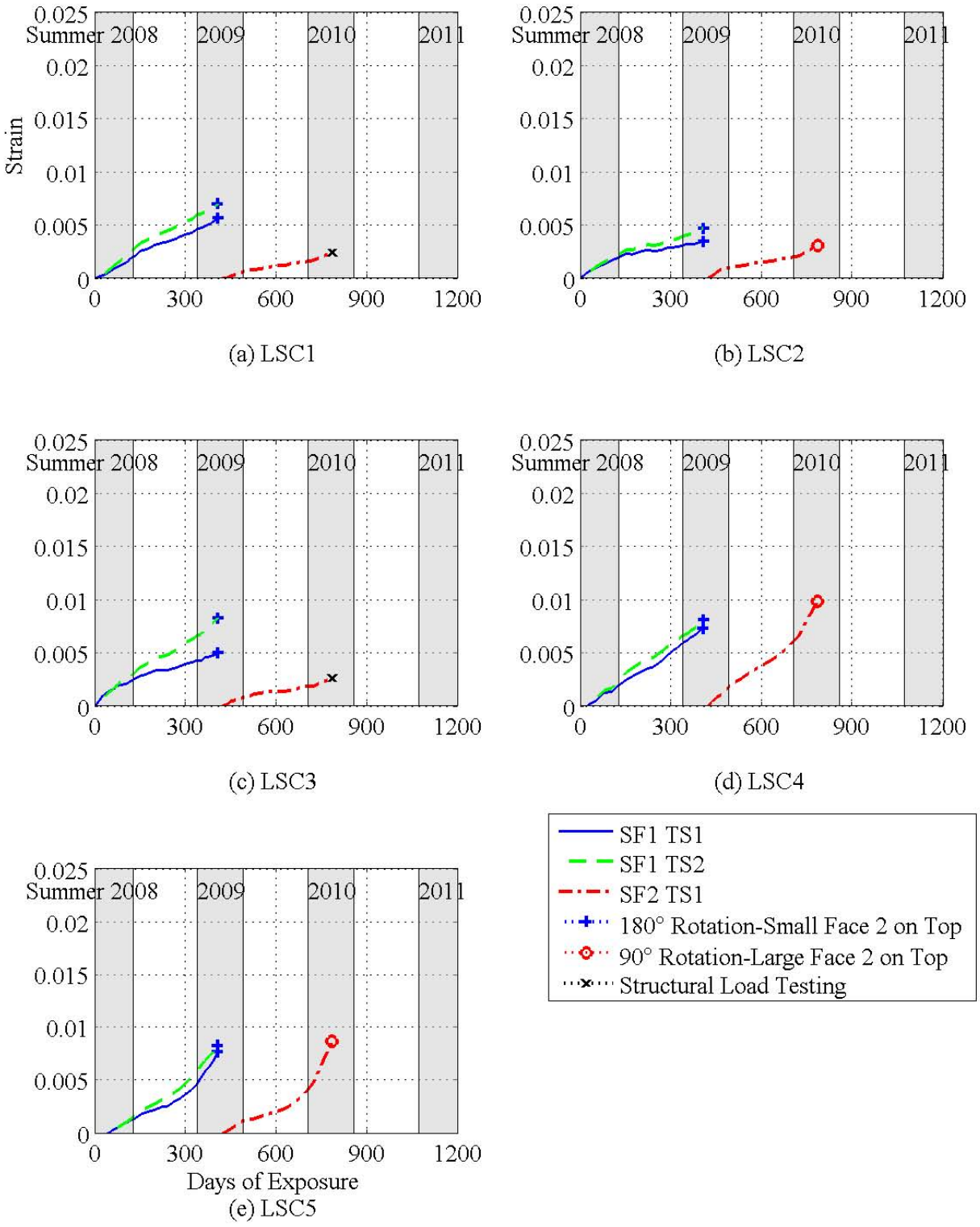

Figure 3-11. Transverse Surface Strains on the LSC Specimens' Small Face 1 and Small Face 2.

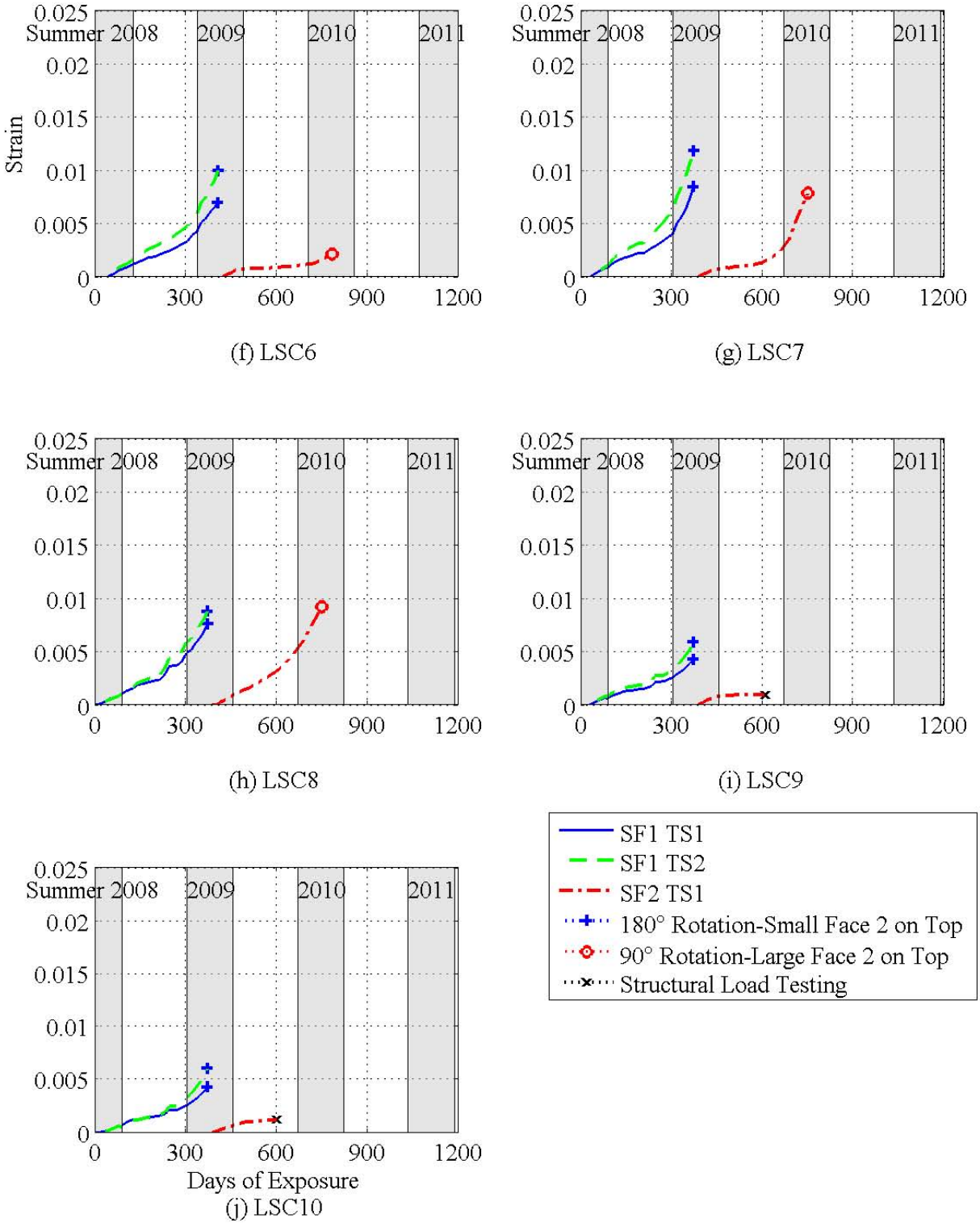

Figure 3-11. Transverse Surface Strains on the LSC Specimens' Small Face 1 and Small Face 2. (Continued)

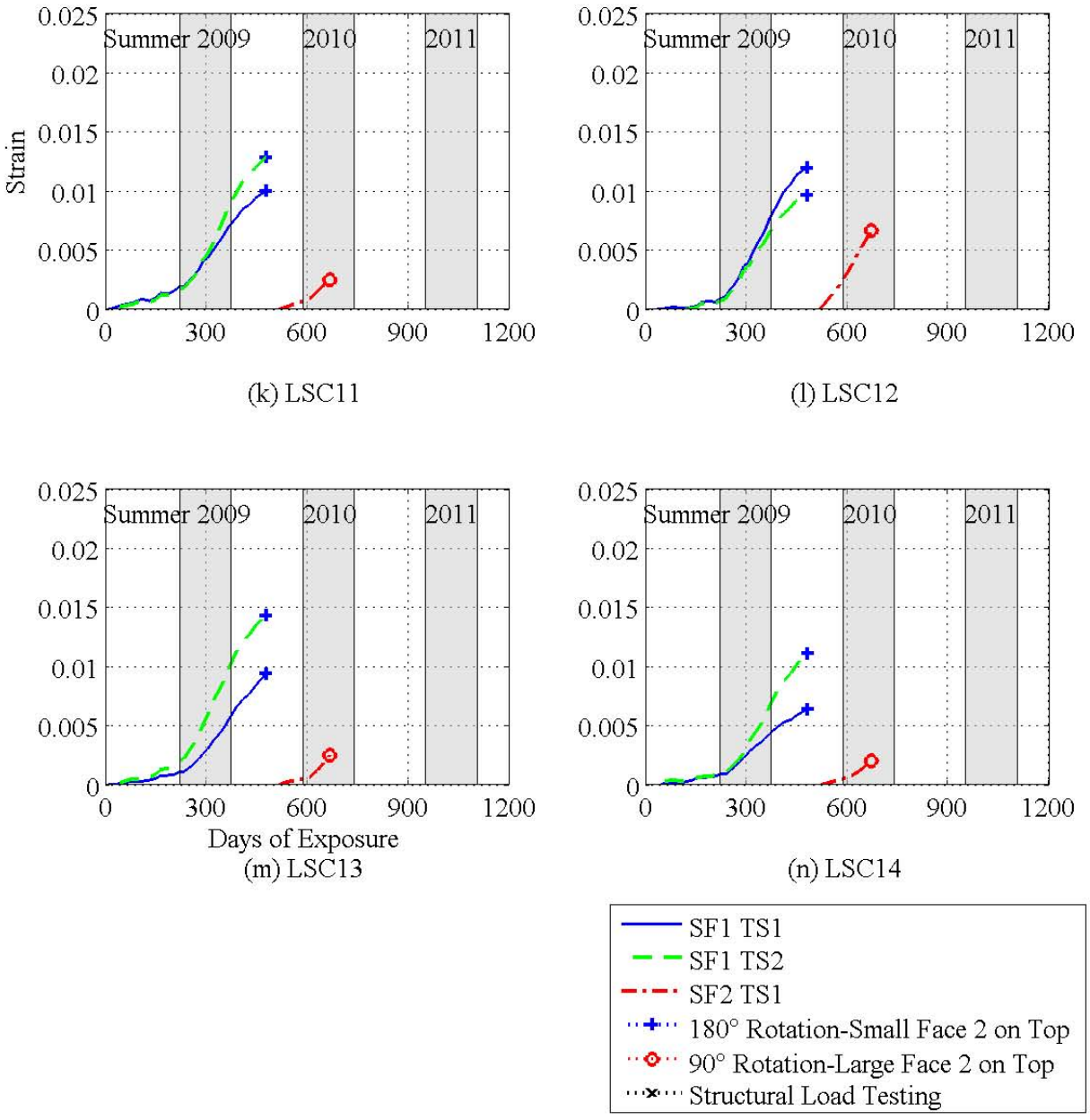

Figure 3-11. Transverse Surface Strains on the LSC Specimens' Small Face 1 and Small Face 2. (Continued)

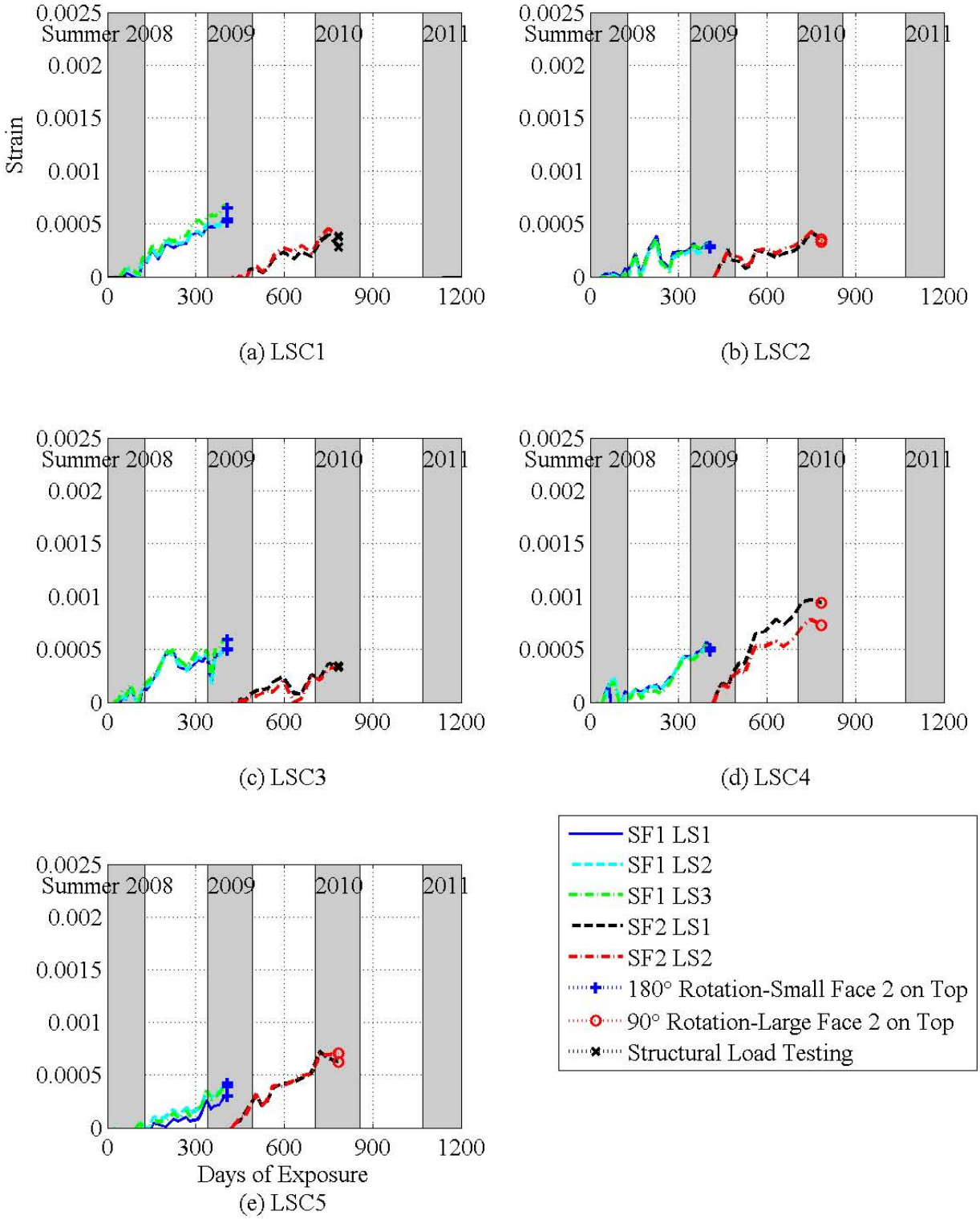

Figure 3-12. Longitudinal Surface Strains on the LSC Specimens' Small Face 1 and Small Face 2.

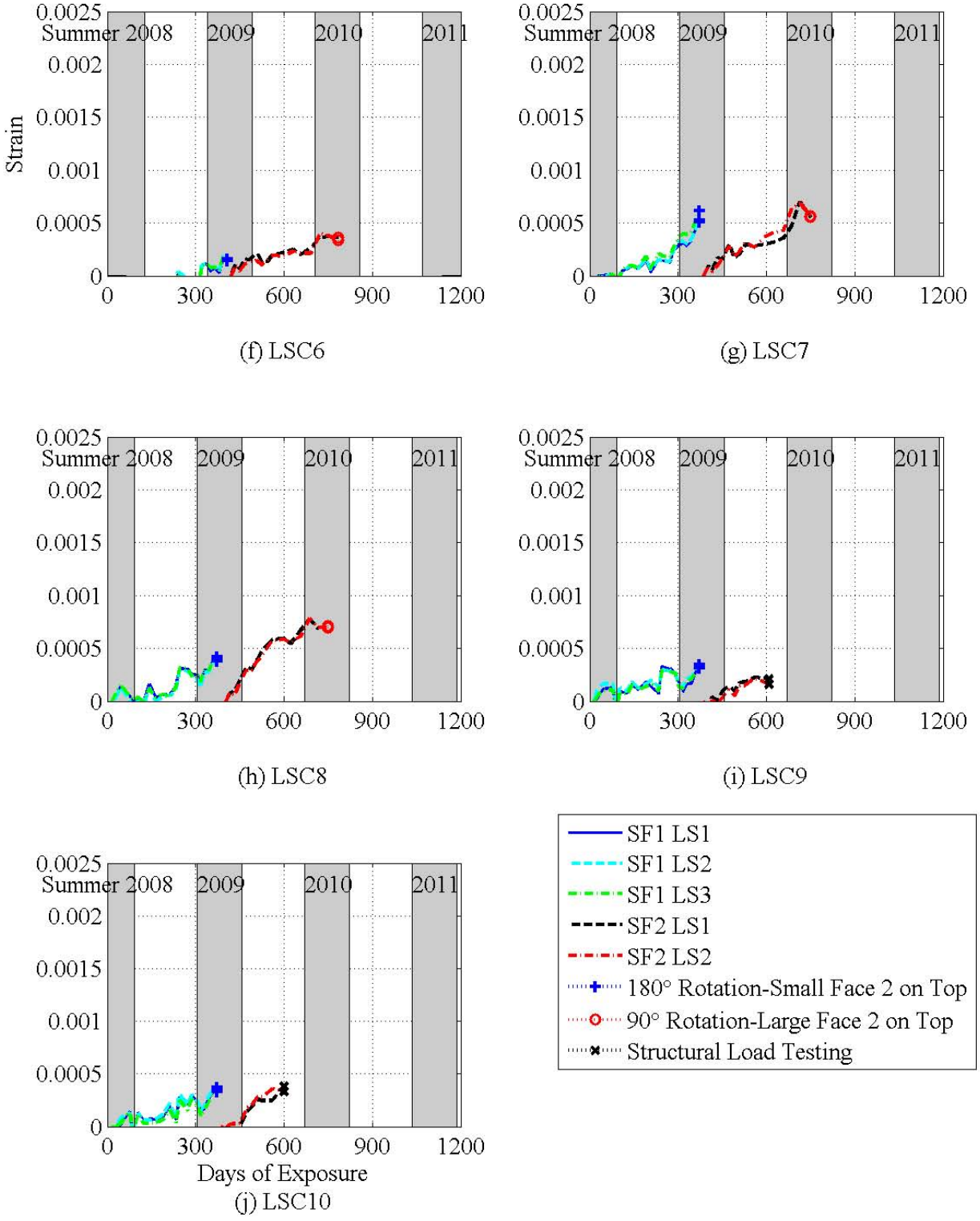

Figure 3-12. Longitudinal Surface Strains on the LSC Specimens' Small Face 1 and Small Face 2. (Continued)

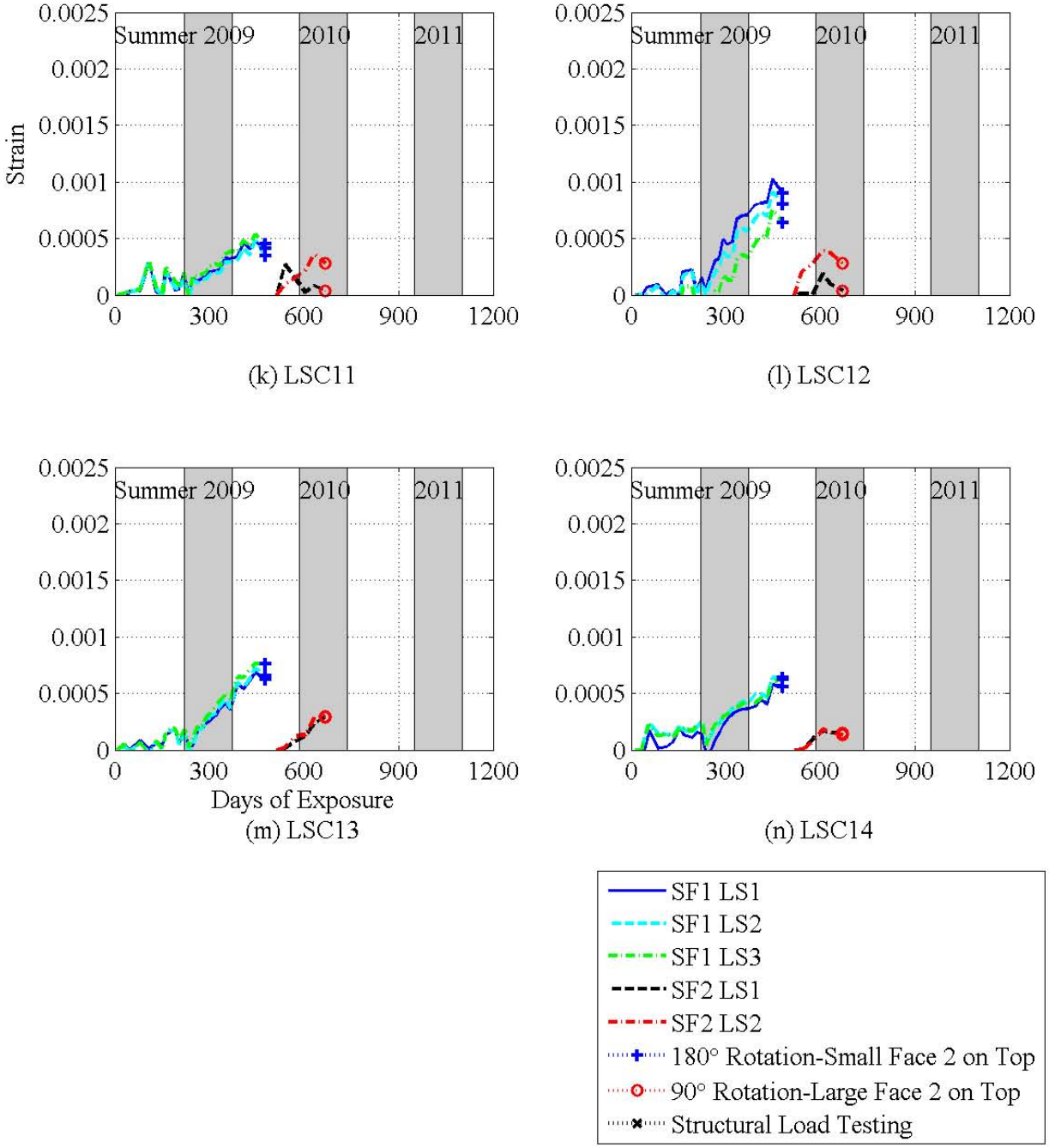

Figure 3-12. Longitudinal Surface Strains on the LSC Specimens' Small Face 1 and Small Face 2. (Continued)

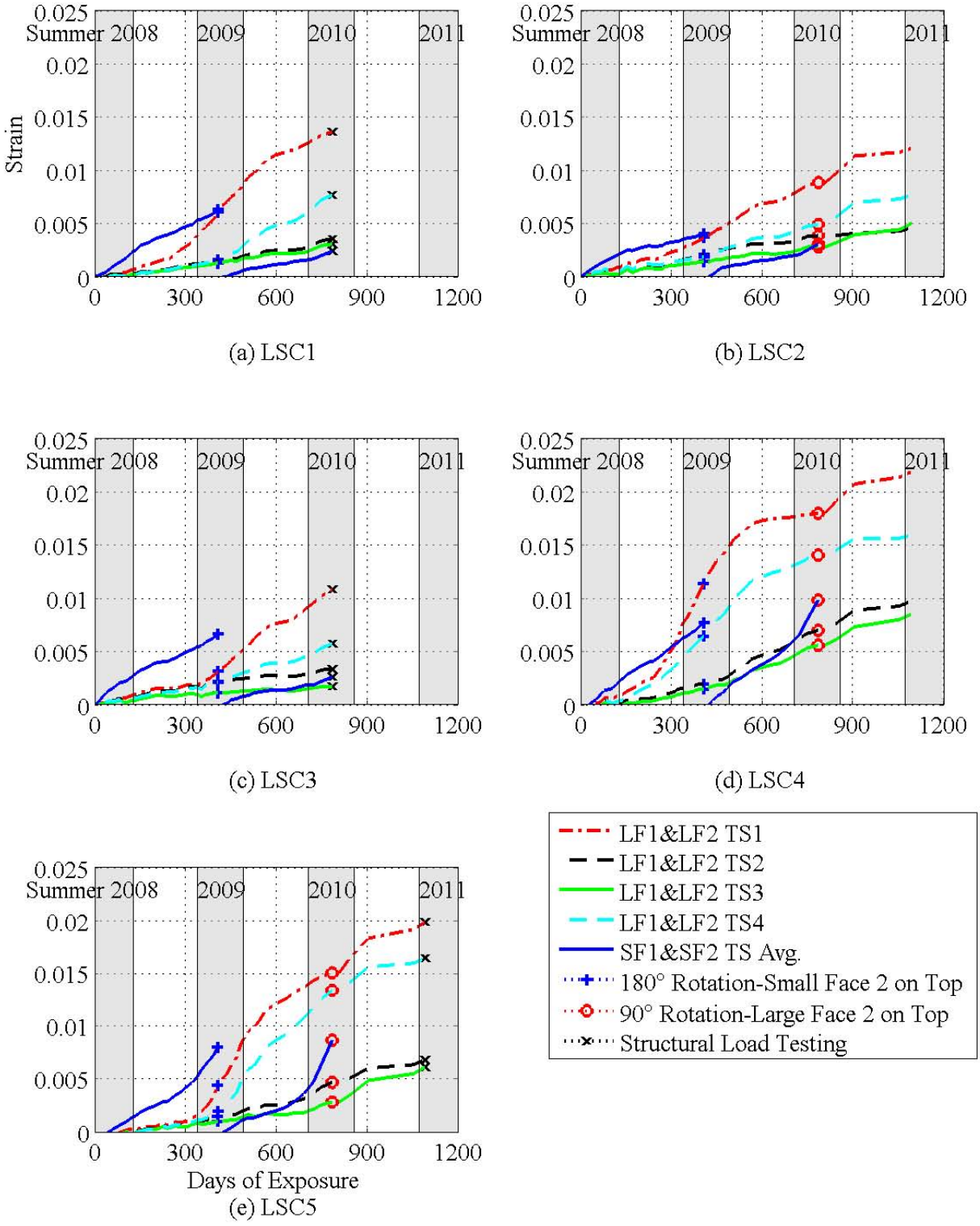

Figure 3-13. Transverse Surface Strains on the LSC Specimens' Large Face 1, Large Face 2, Small Face 1, and Small Face 2.

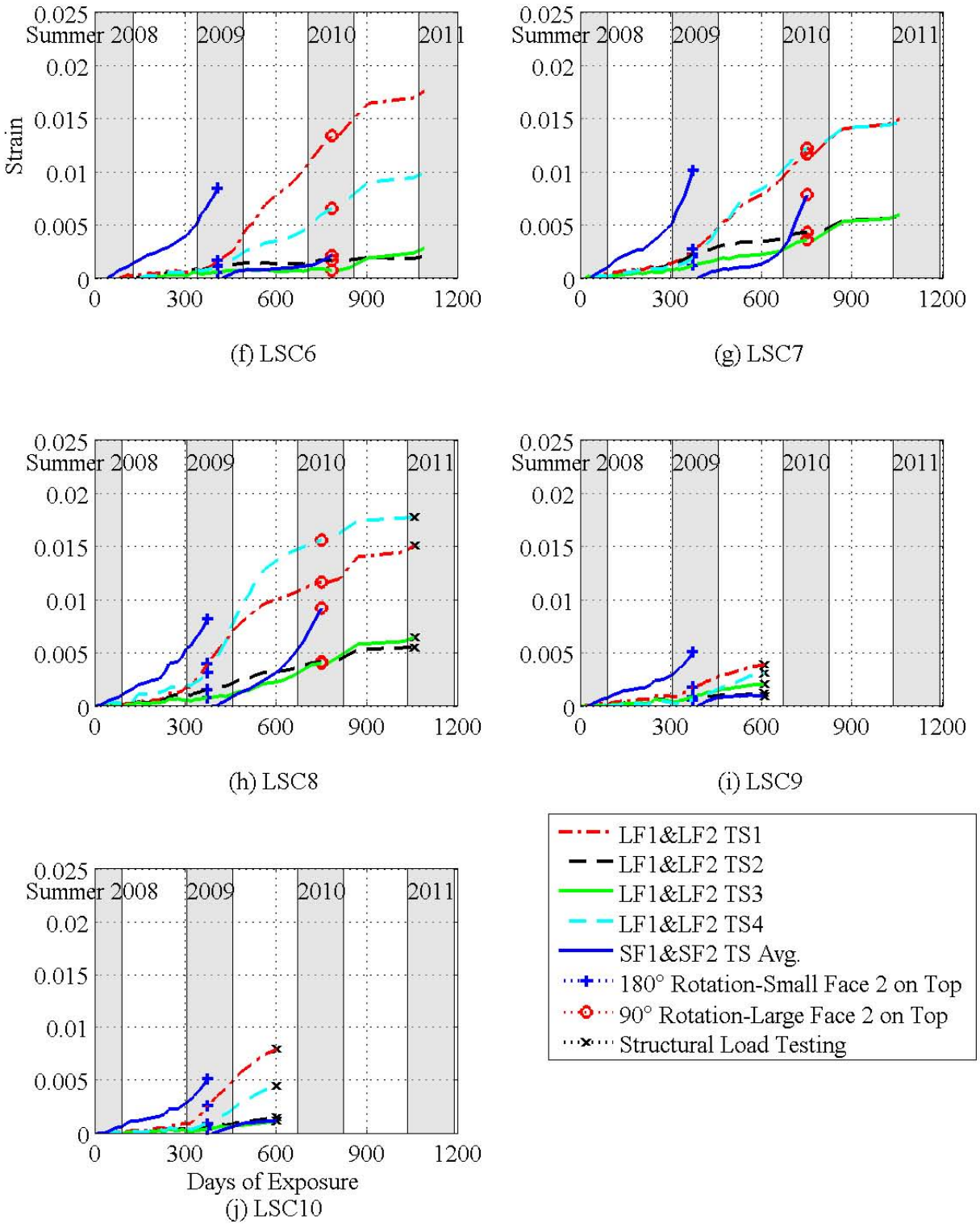

Figure 3-13. Transverse Surface Strains on the LSC Specimens' Large Face 1, Large Face 2, Small Face 1, and Small Face 2. (Continued)

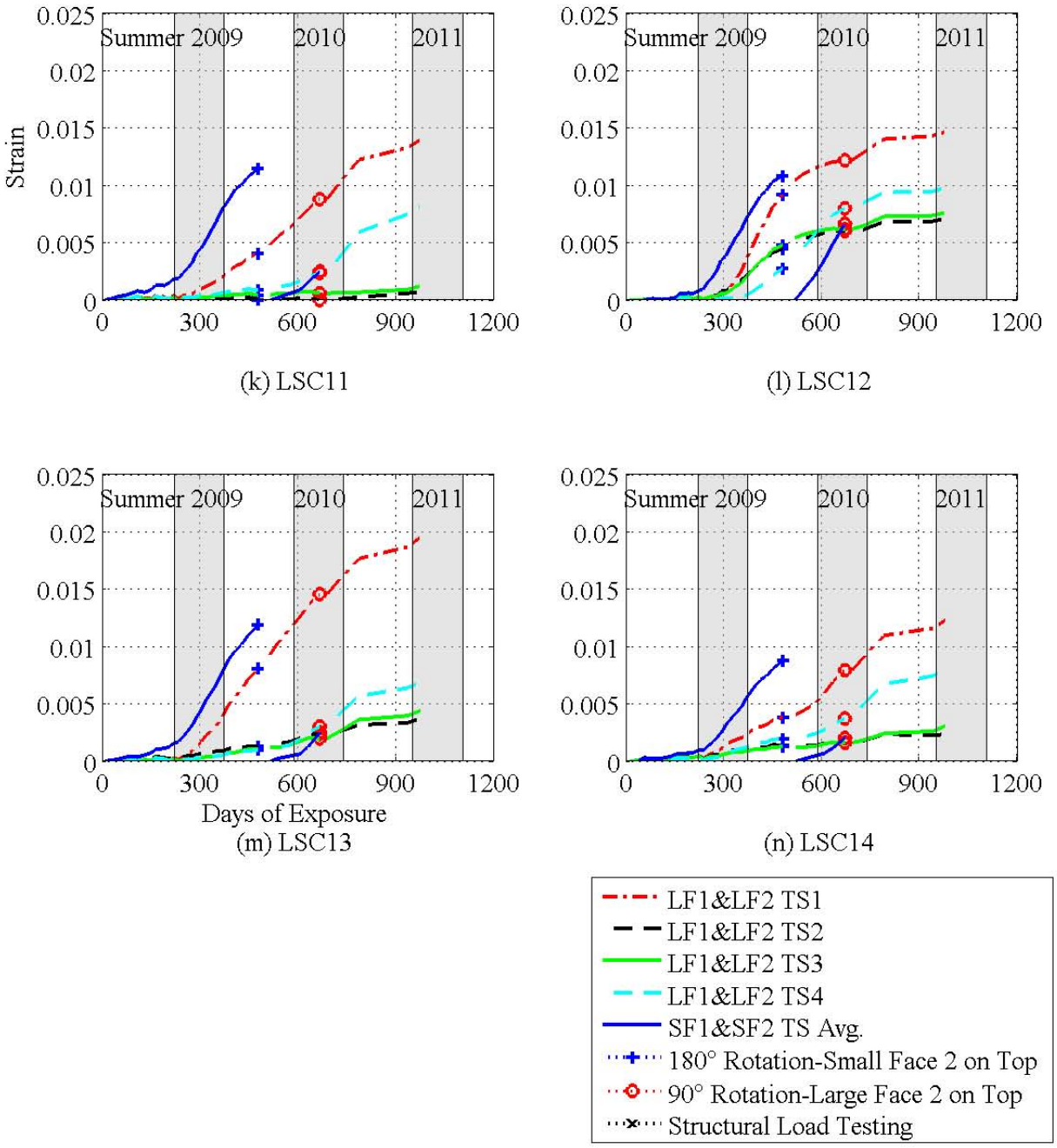

Figure 3-13. Transverse Surface Strains on the LSC Specimens' Large Face 1, Large Face 2, Small Face 1, and Small Face 2. (Continued)

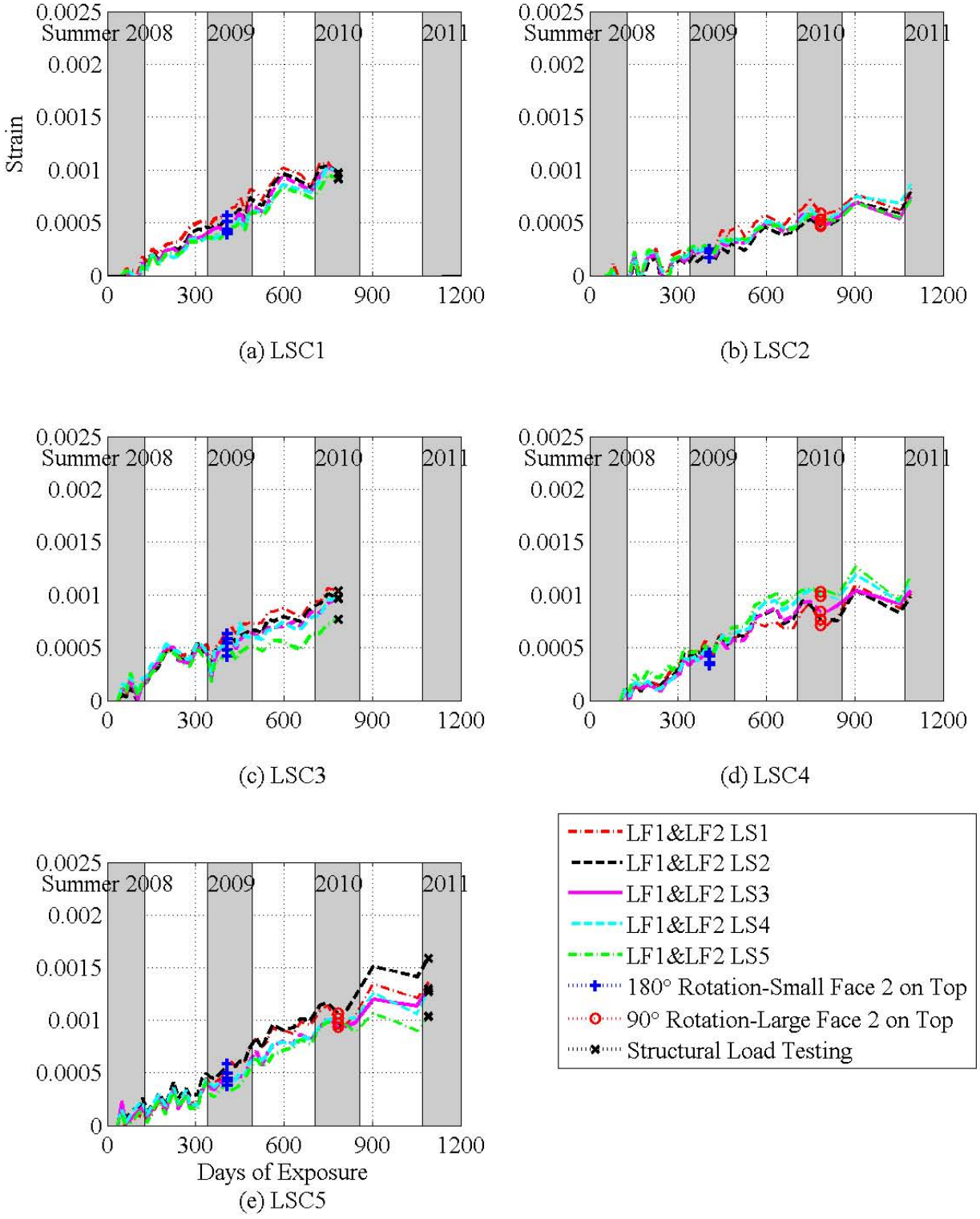

Figure 3-14. Longitudinal Surface Strains on the LSC Specimens' Large Face 1 and Large Face 2.

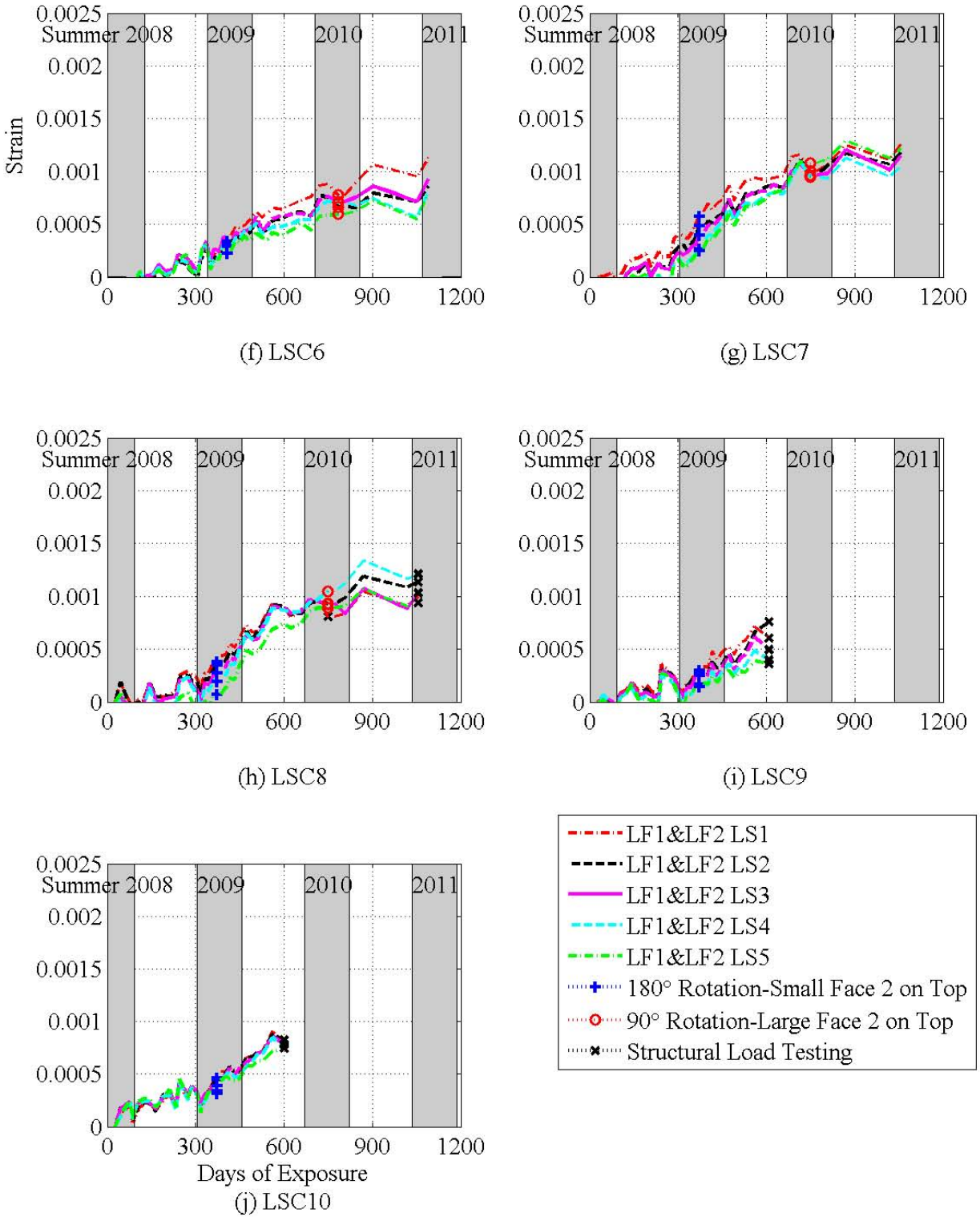

Figure 3-14. Longitudinal Surface Strains on the LSC Specimens' Large Face 1 and Large Face 2. (Continued)

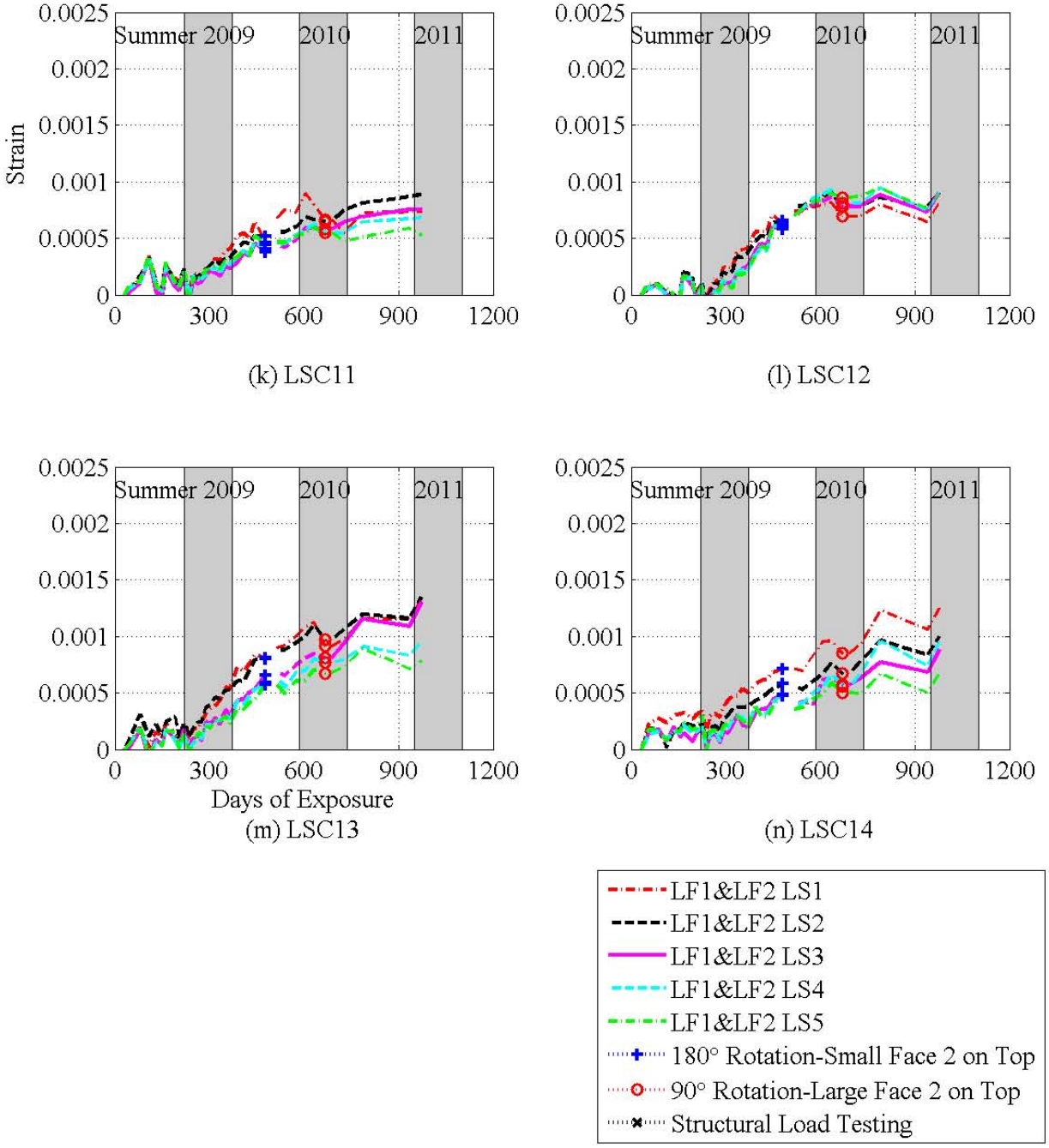

Figure 3-14. Longitudinal Surface Strains on the LSC Specimens' Large Face 1 and Large Face 2. (Continued)

The transverse surface strain on Small Face 2 on LSC specimens 1, 3, 9, and 10 did not reach the transverse surface strains on Small Face 1 before the specimens were tested. Table 3-3 shows the transverse strain on Small Face 2 reached around a third of the values of the transverse strains on Small Face 1 at the time of the structural load test of LSC specimens 1, 3, 9, and 10. The table illustrates that these specimens did not uniformly expand before the structural load test. However, LSC specimens 5 and 8 did have a more uniform expansion before the structural load testing.

Table 3-3. Percent of Transverse Surface Strain on Small Face 2 to Small Face 1 at the Time of the Structural Load Test.

	Last Data Point				
LSC	SF1 TS1	SF1 TS2	SF1 TS Avg.	SF2 TS1	SF2 % of SF1
1	0.0057	0.0070	0.0064	0.0024	38
3	0.0050	0.0083	0.0067	0.0026	39
5	0.0077	0.0083	0.0080	0.0087	109
8	0.0076	0.0088	0.0082	0.0092	112
9	0.0043	0.0059	0.0051	0.0009	18
10	0.0043	0.0061	0.0052	0.0013	25

3.3.2 Crack Width Measurements

In existing bridge columns, cracks can be measured quite easily, while other strain data are more difficult to obtain since instrumentation was not installed prior to bridge construction. However, the surface strains calculated with the DEMECs more accurately represent the total surface expansion since there is micro cracking not visible to the naked eye and also concrete expansion between the cracks due to ASR/DEF. Therefore, the strains from crack width measurements in the large scale specimens were compared to the strain computed using the DEMECs to compare surface strains easily measured in the field to more accurate research data. Figure 3-15 shows the longitudinal cracks on an LSC specimen. To give you an idea of the scale of this figure, the DEMECs are approximately 10 inches (254 mm) apart. There are no visible transverse cracks; therefore, only longitudinal cracks were measured with a crack comparator card. This tool measured crack widths as small as 0.005 inch (0.13 mm) (see Figure 3-16).

Figure 3-15. Longitudinal Cracks from ASR Expansion.

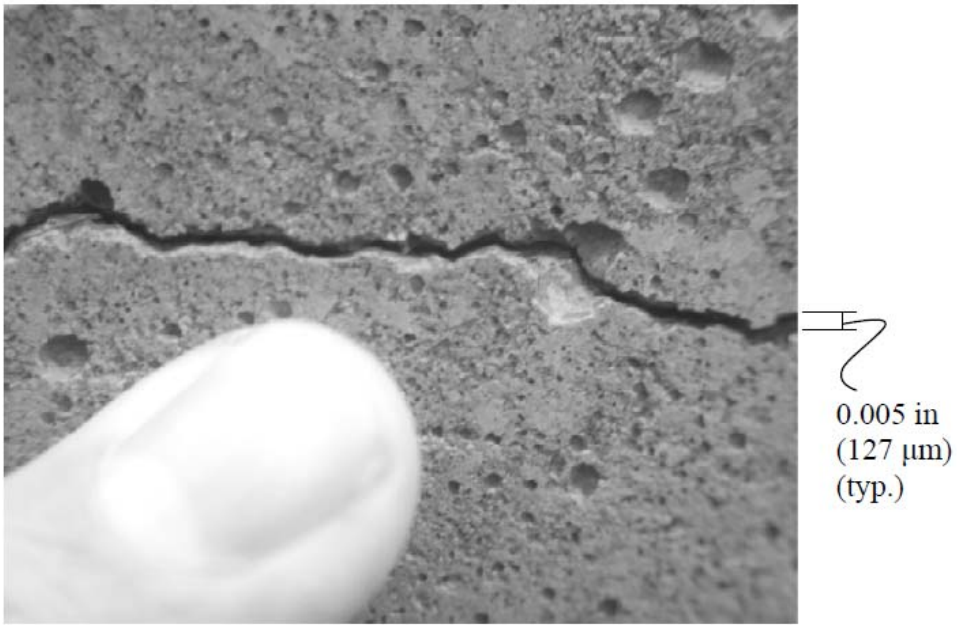

Figure 3-16. Longitudinal Crack Width.

To estimate the expansive strains, the width of the cracks along the transverse direction between DEMECs were added and then divided by the original distance between DEMECs, $l_d(0)$ to give a strain value shown below.

$$\boldsymbol{\varepsilon_{crack}} = \frac{\sum \textbf{crack width}}{\mathbf{l_d(0)}} \qquad \text{(Eq. 3-3)}$$

The longitudinal crack widths were measured along the two center DEMEC lines in the transverse direction for all faces. Figure 3-17 shows the two lines of DEMECs where the cracks were measured. No line is shown between DEMECs on the bottom row of Large Face 1 because the cracks were not measured in this location. After the 180° rotation, the cracks were not measured on the top row between DEMECs so that the crack width measurements would continue in the same location before and after the 180° rotation. The crack widths were measured along all four rows on Large Face 2 after the 90° rotation.

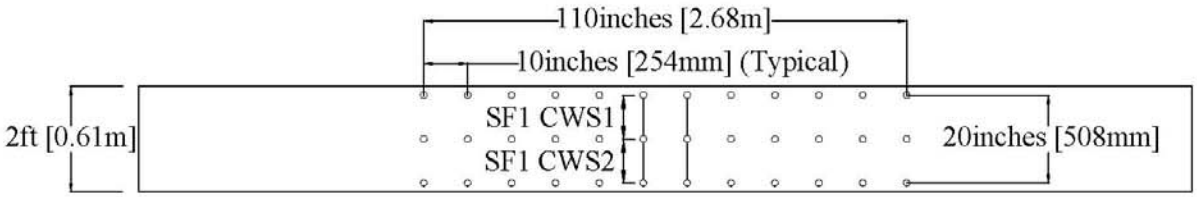

(a) Longitudinal Crack Measurement Locations on Small Face 1during Orientation 1

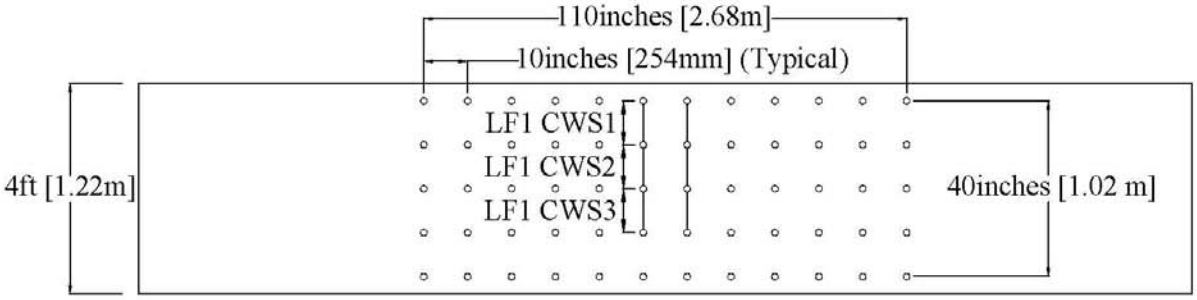

(b) Longitudinal Crack Measurement Locations on Large Face 1 during Orientation 1

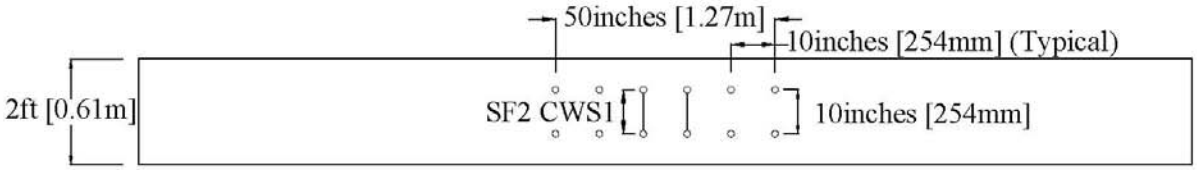

(c) Longitudinal Crack Measurement Locations on Small Face 2 during Orientation 2

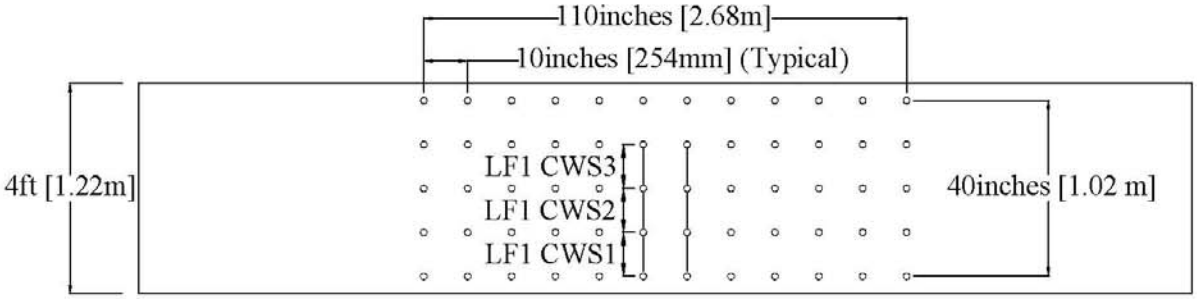

(d) Longitudinal Crack Measurement Locations on Large Face 1 during Orientation 2

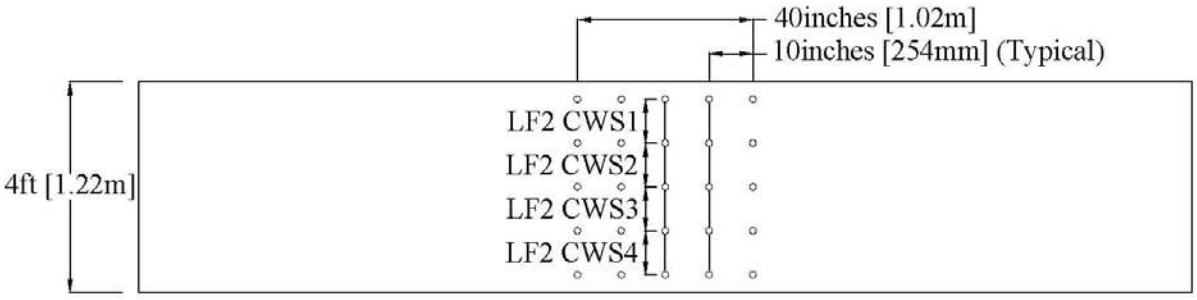

(e) Longitudinal Crack Measurement Locations on Large Face 2 during Orientation 3

Figure 3-17. Crack Width Measurement Locations and Labels on All Faces in Relation to the DEMEC Grid.

The transverse surface strains calculated from measuring the distance between the DEMECs and from summing the longitudinal crack widths between the DEMECs are compared in Figure 3-18 for Small Face 1, Small Face 2, Large Face 1, and Large Face 2. The crack width strains are abbreviated as CWS. The strains are numbered in the same way as the strains calculated with the DEMEC measurements. The surface strains calculated from measuring the distance between the DEMECs plotted in Figure 3-18 are an average of the two lines of DEMECs where cracks were measured and shown in Figure 3-17. These strain values are different from the transverse surface strains in Figure 3-11 and Figure 3-13 that include more strains in the average as explained in Section 3.3.1. No crack width data was taken at the bottom of Large Face 1; however, data was taken in this location on Large Face 1. Therefore, there is only data on Figure 3-17 for LF2 CWS4 during the 3rd orientation. Figure 3-19 shows the crack width strain as a percentage of the DEMEC surface strain measurements.

Figure 3-18 shows the sum of the crack width strains are usually smaller than the surface strains, which are calculated from the measured distance between DEMECS. The crack width strain percentage is highly scattered, but generally converges to about 50 percent of the surface strain. This reduced strain from the sum of the crack widths can be explained by the expansion of the concrete between cracks that was not accounted for and other cracks that were too small to measure. When the DEMECs were first installed on Small Face 2 after the first rotation, the distance between the DEMECs was used as a zero baseline, thus showing no strain. However, cracks had already formed and were measured. Therefore, the high percentage on some of the LSC specimens after the 180° rotation show there was expansion on that face even though there was no sunlight. The strains from the initial crack widths formed while Small Face 2 was on the bottom are less than 0.001, which is very small.

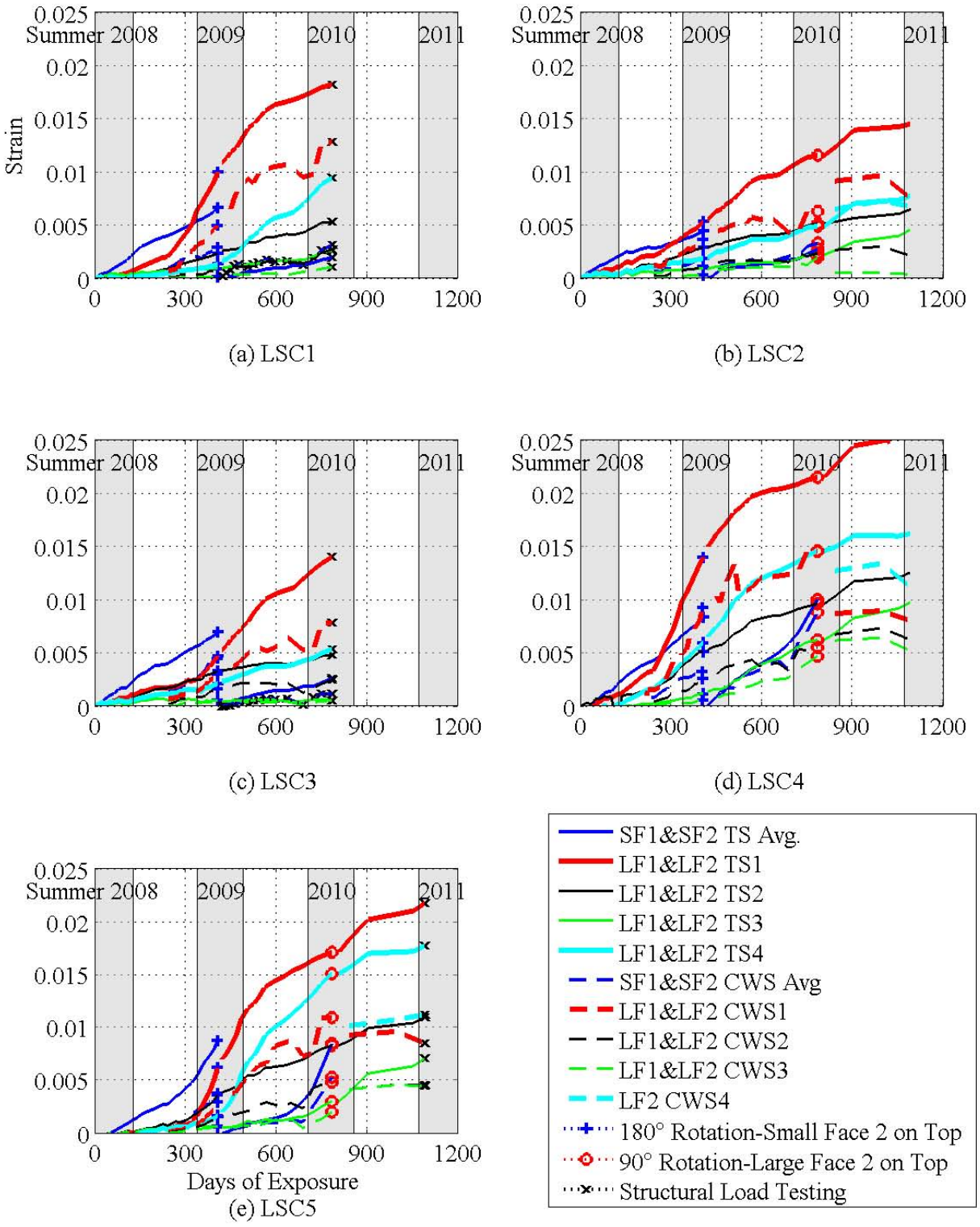

Figure 3-18. Transverse Surface Strains from DEMECs and Crack Width Measurements on All Faces.

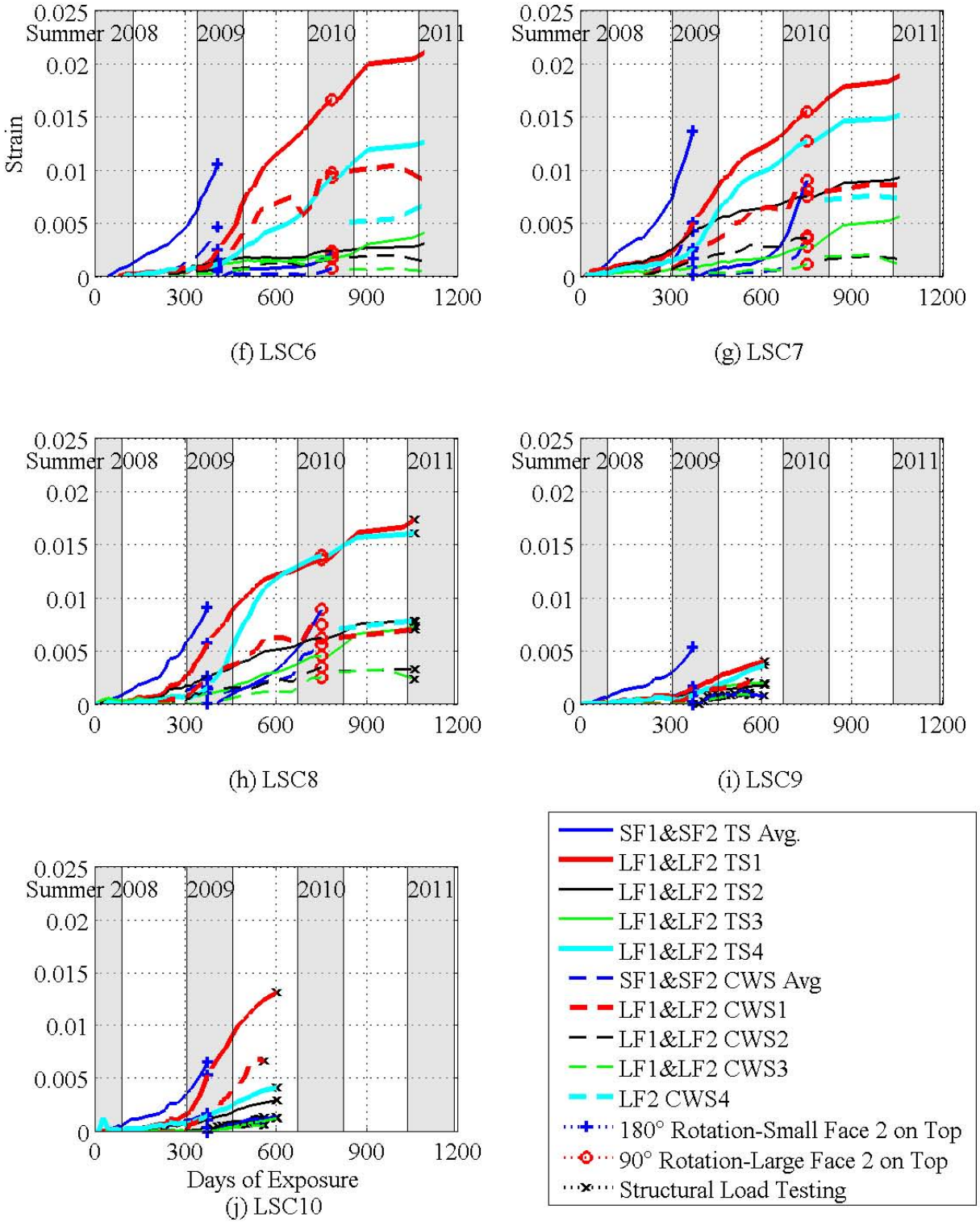

Figure 3-18. Transverse Surface Strains from DEMECs and Crack Width Measurements on All Faces. (Continued)

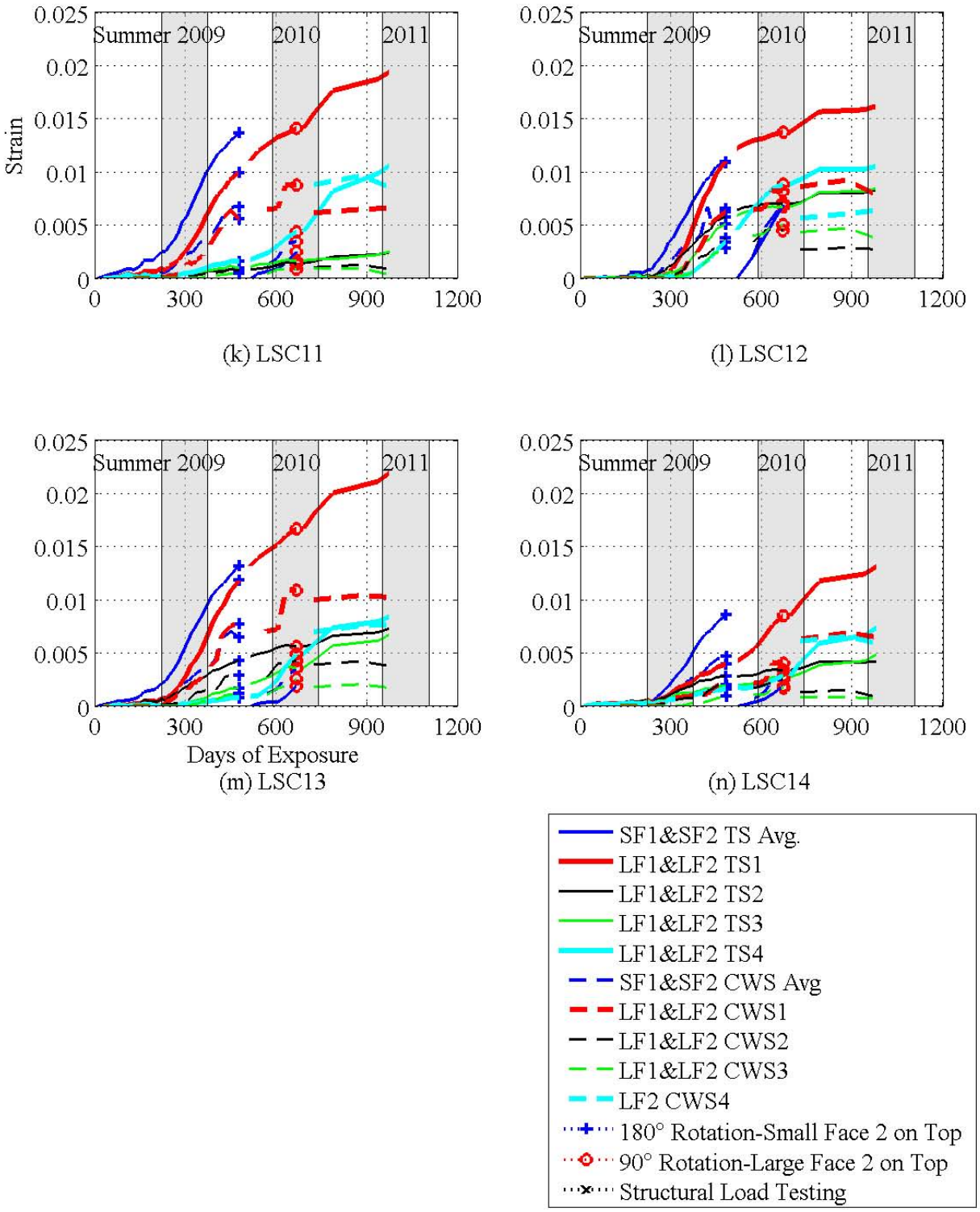

Figure 3-18. Transverse Surface Strains from DEMECs and Crack Width Measurements on All Faces. (Continued)

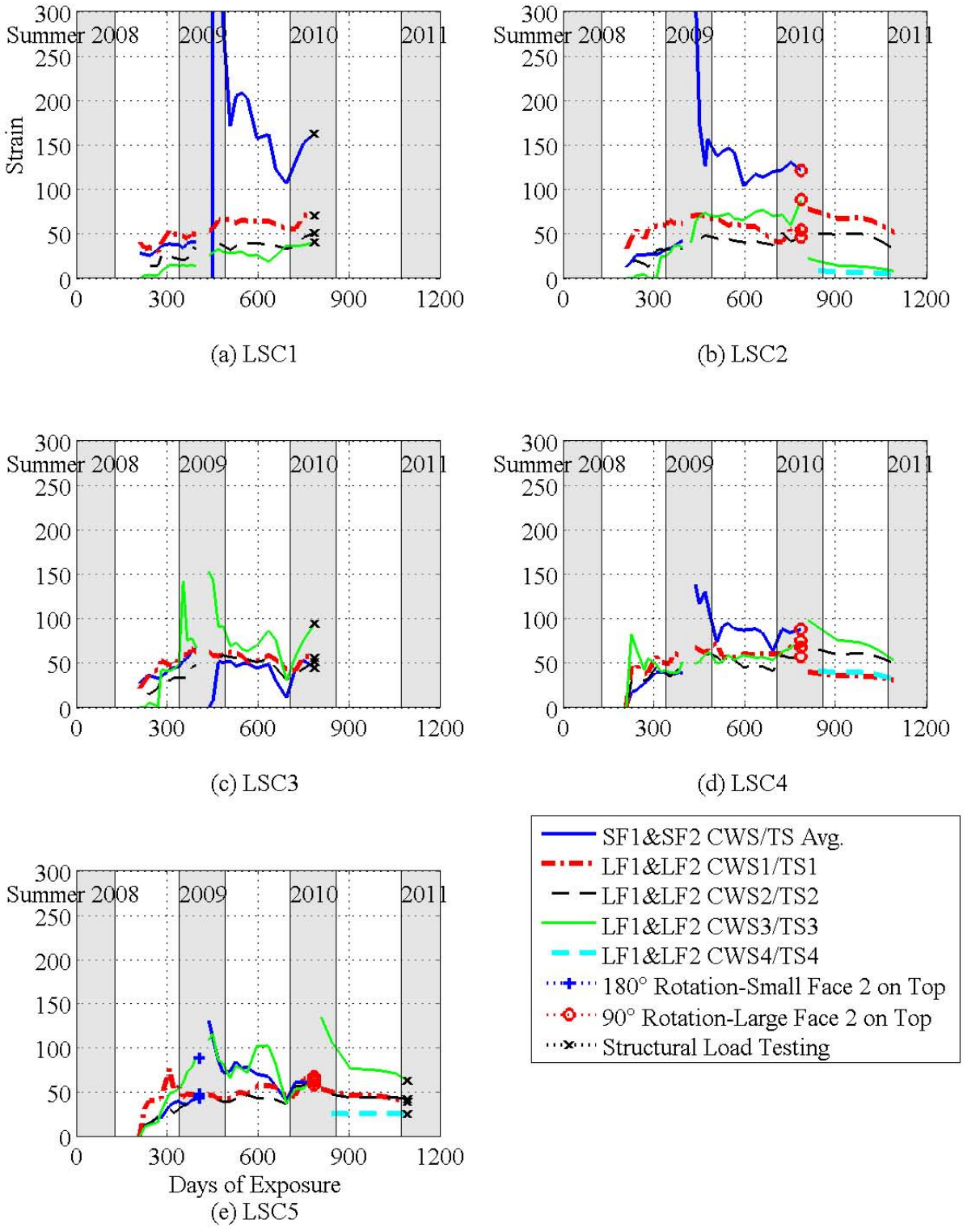

Figure 3-19. Crack Width Strain Percentages of Surface Strains on All Faces.

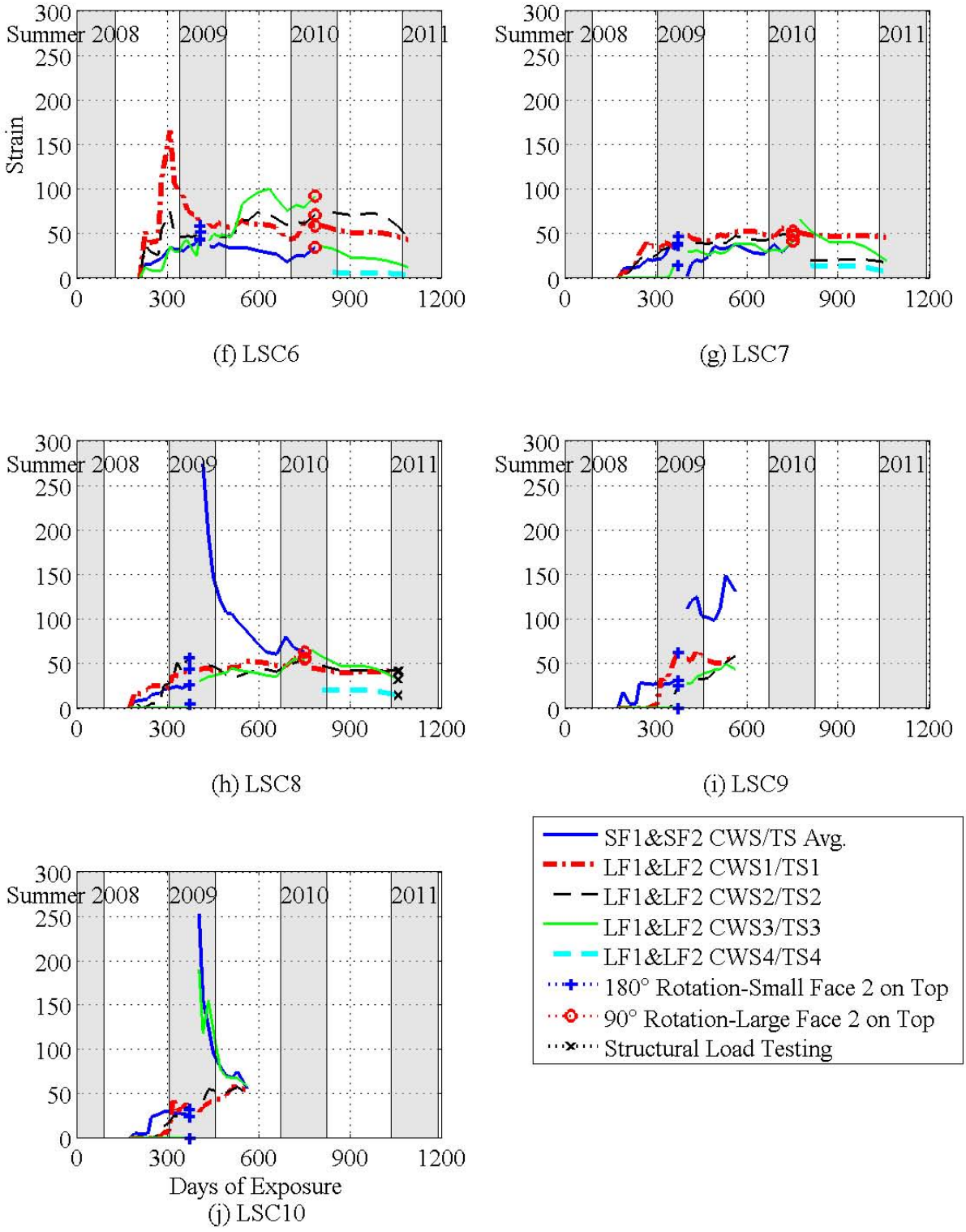

Figure 3-19. Crack Width Strain Percentages of Surface Strains on All Faces. (Continued)

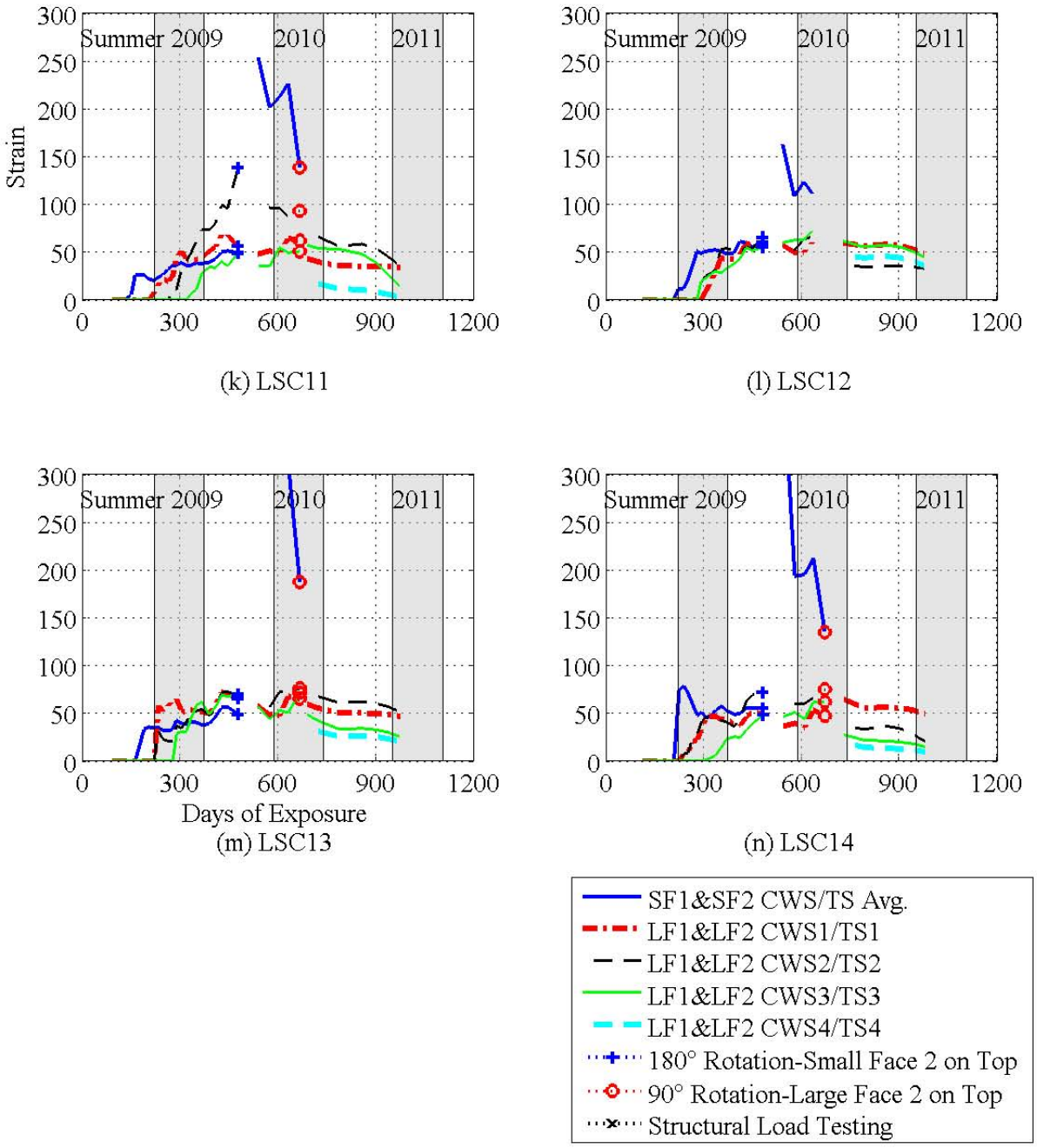

Figure 3-19. Crack Width Strain Percentages of Surface Strains on All Faces. (Continued)

3.3.3 Internal Specimen Strains

The strains in the reinforcing steel were measured with 12 strain gages (SG) as shown in Chapter 2. Eight gages (SG1–SG8) were mounted on the tension bars in the splice region, and two gages (SG9–SG10) were placed on the compression bars (Figure 2-27). The transverse reinforcement was instrumented with SG11 and SG12 (Figure 2-28). The data from the 10 gages on the longitudinal reinforcement were primarily used during the experimental testing; however, the following figures show the strains that occurred during deterioration process before the specimens were tested. Figure 3-20 shows the strains in the edge tension bars with gages: SG1–SG4. Figure 3-21, shows the strains in the center tension bars with gages: SG5–SG8. Figure 3-22 shows the strains in the center compression bars with gages: SG9–SG10. The tension and compression refer to the orientation of the bars during the structural load tests (Figure 2-27).

One strain gage, SG11, was applied to the transverse hoop on the Small Face 1. Another gage, SG12, was placed on the Large Face 1 of the hoop. The internal concrete strains in the LSC specimens were measured using embedded concrete gages (KM). KM1 and KM3 measured the strain in the concrete cover region and were placed in the center of the cover, 1 inch (25.4 mm) from the surface and the steel hoop. Inside the hoop, KM2 and KM4 were placed in the concrete core 1 inch (25.4 mm) from the transverse steel. KM1 and KM2 were installed at the center of Small Face 1. KM3 and KM4 were placed at the center of the Large Face 1. Perpendicular to KM3 and KM4, KM5 was placed to measure the radial strain in the concrete core. The KM gages were placed 6 inches (152 mm) from the instrumented hoop (Figure 2-28).

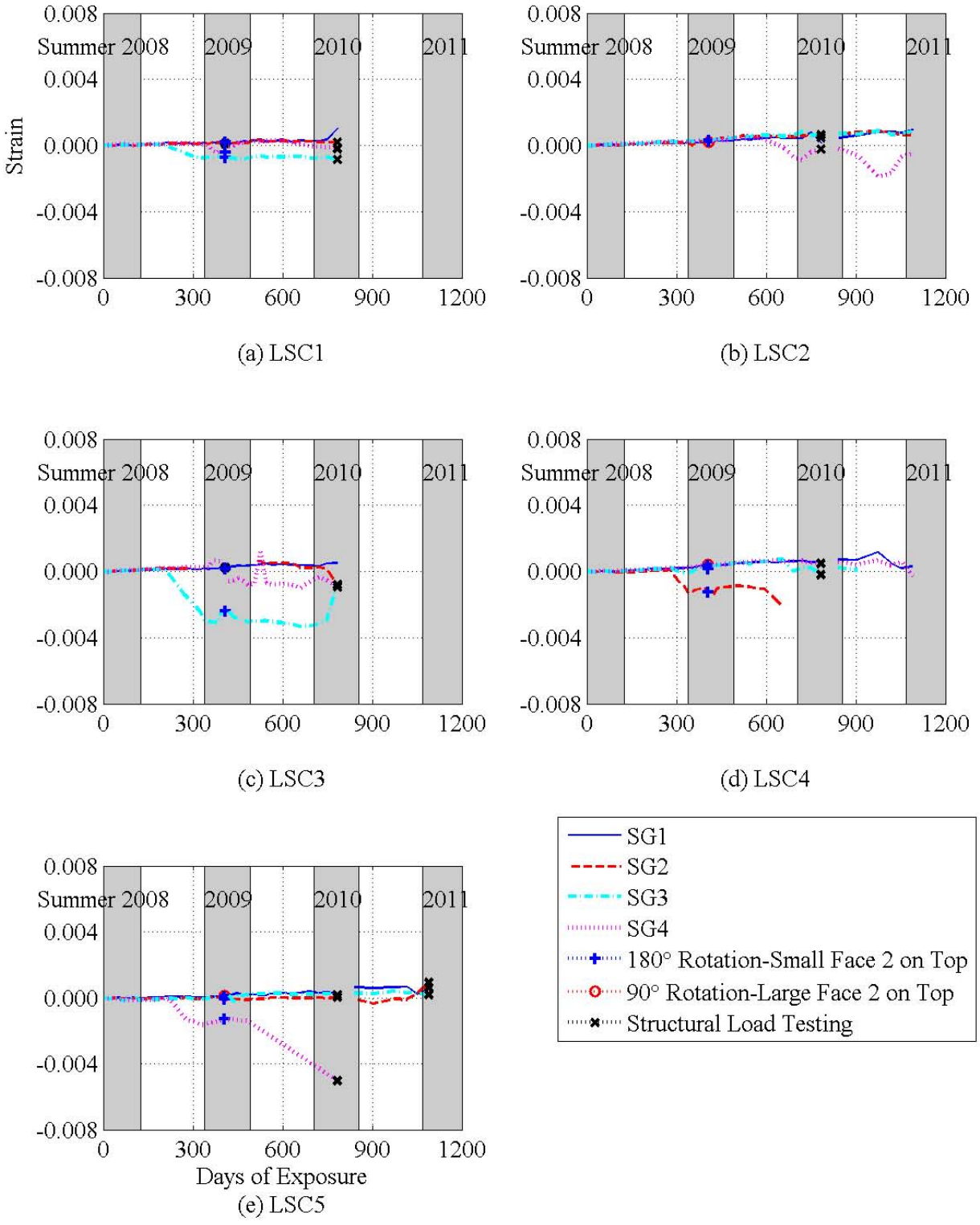

Figure 3-20. Internal Strain Gages (SG1-SG4) along Large Face 1 Tension Steel of the Splice Region.

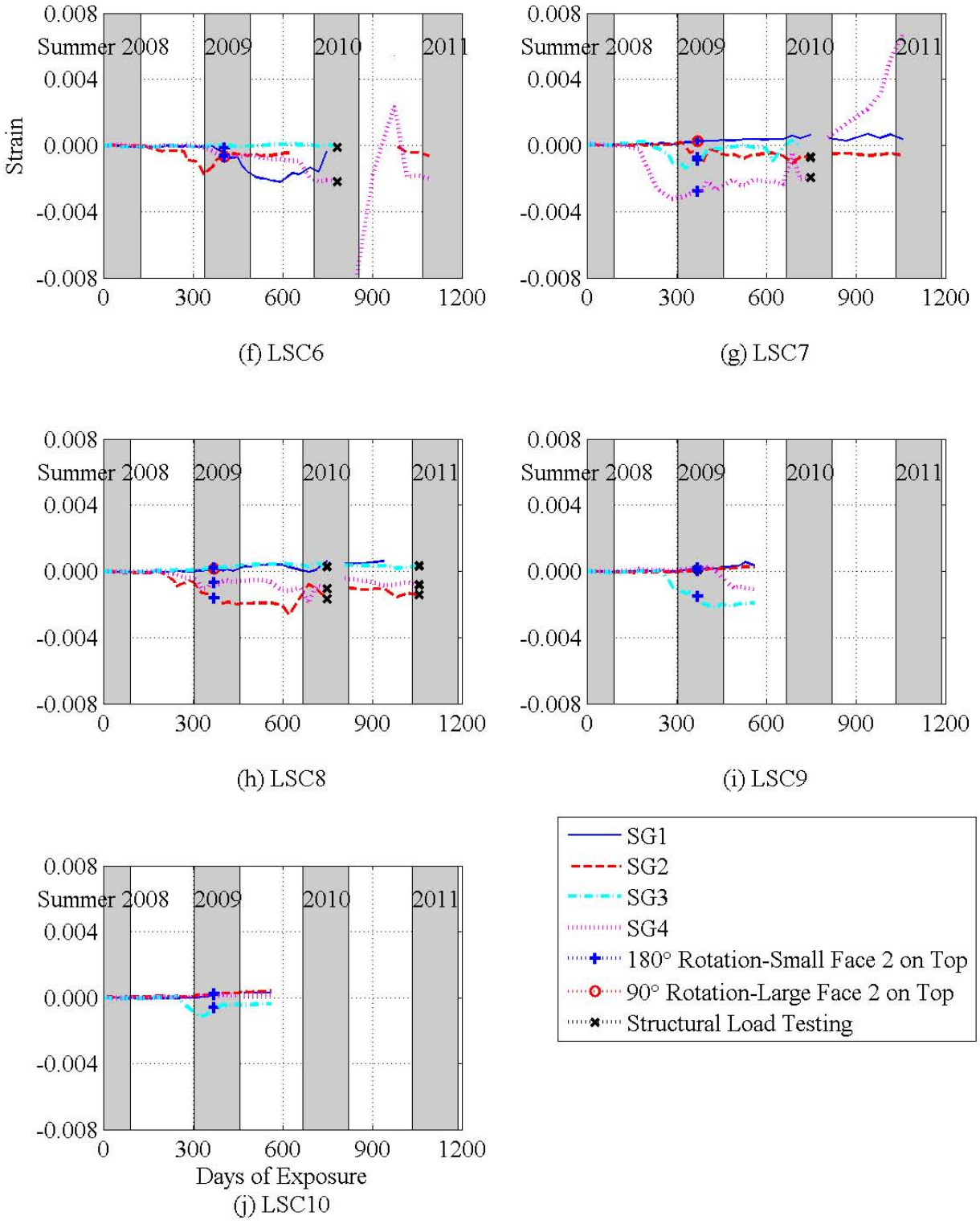

Figure 3-20. Internal Strain Gages (SG1-SG4) along Large Face 1 Tension Steel of the Splice Region. (Continued)

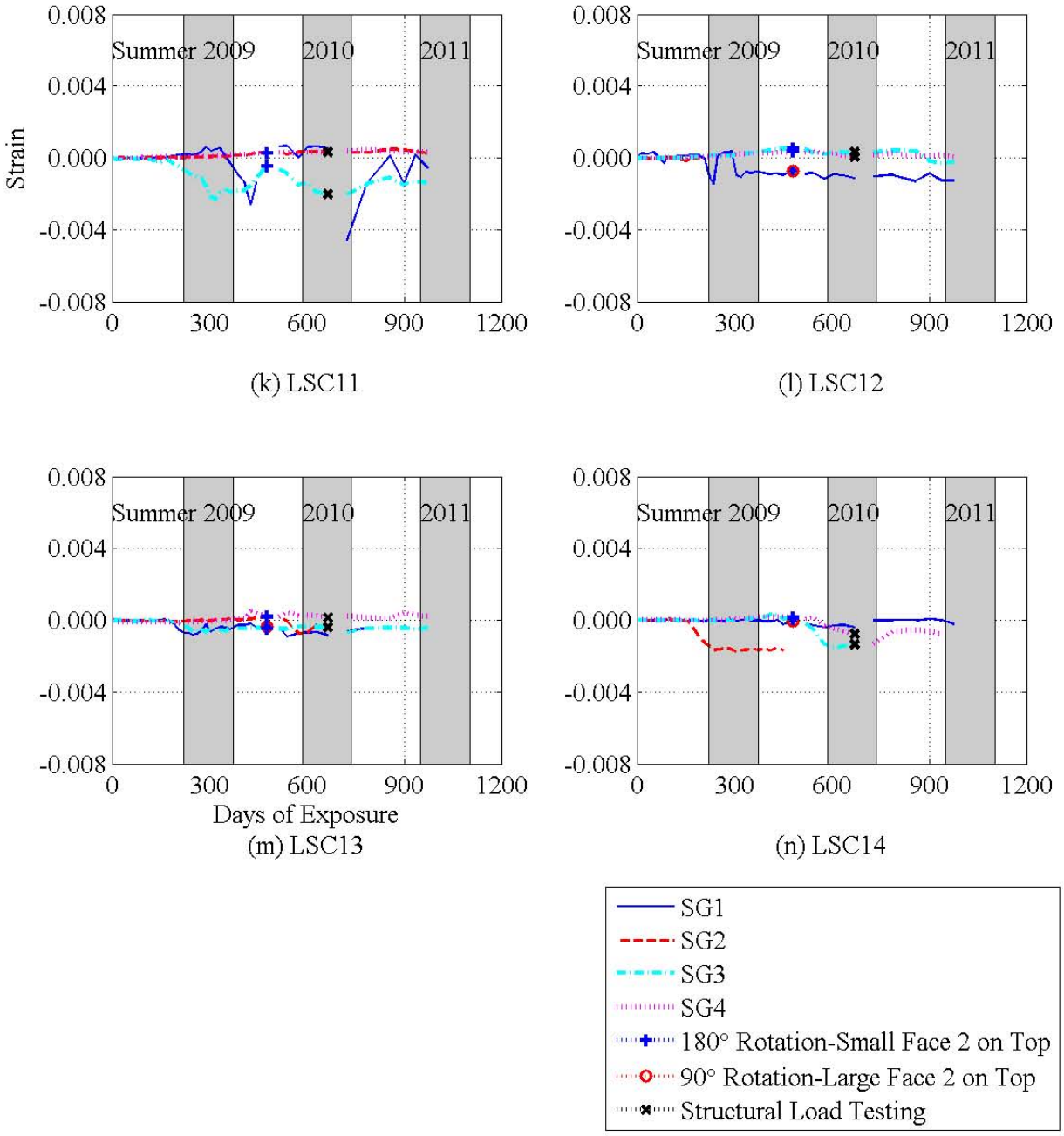

Figure 3-20. Internal Strain Gages (SG1-SG4) along Large Face 1 Tension Steel of the Splice Region. (Continued)

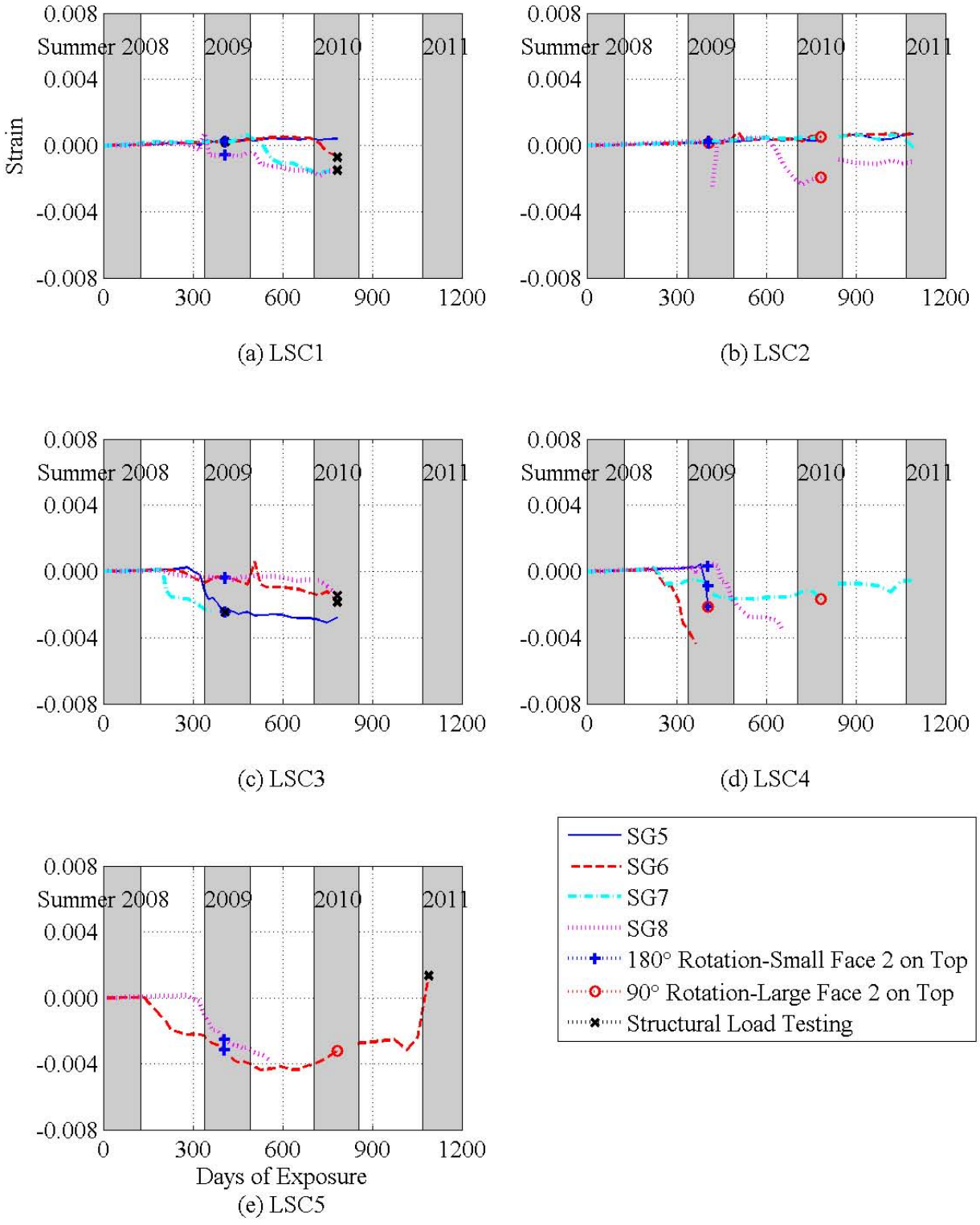

Figure 3-21. Internal Strain Gages (SG5-SG8) along Large Face 1 Tension Steel of the Splice Region.

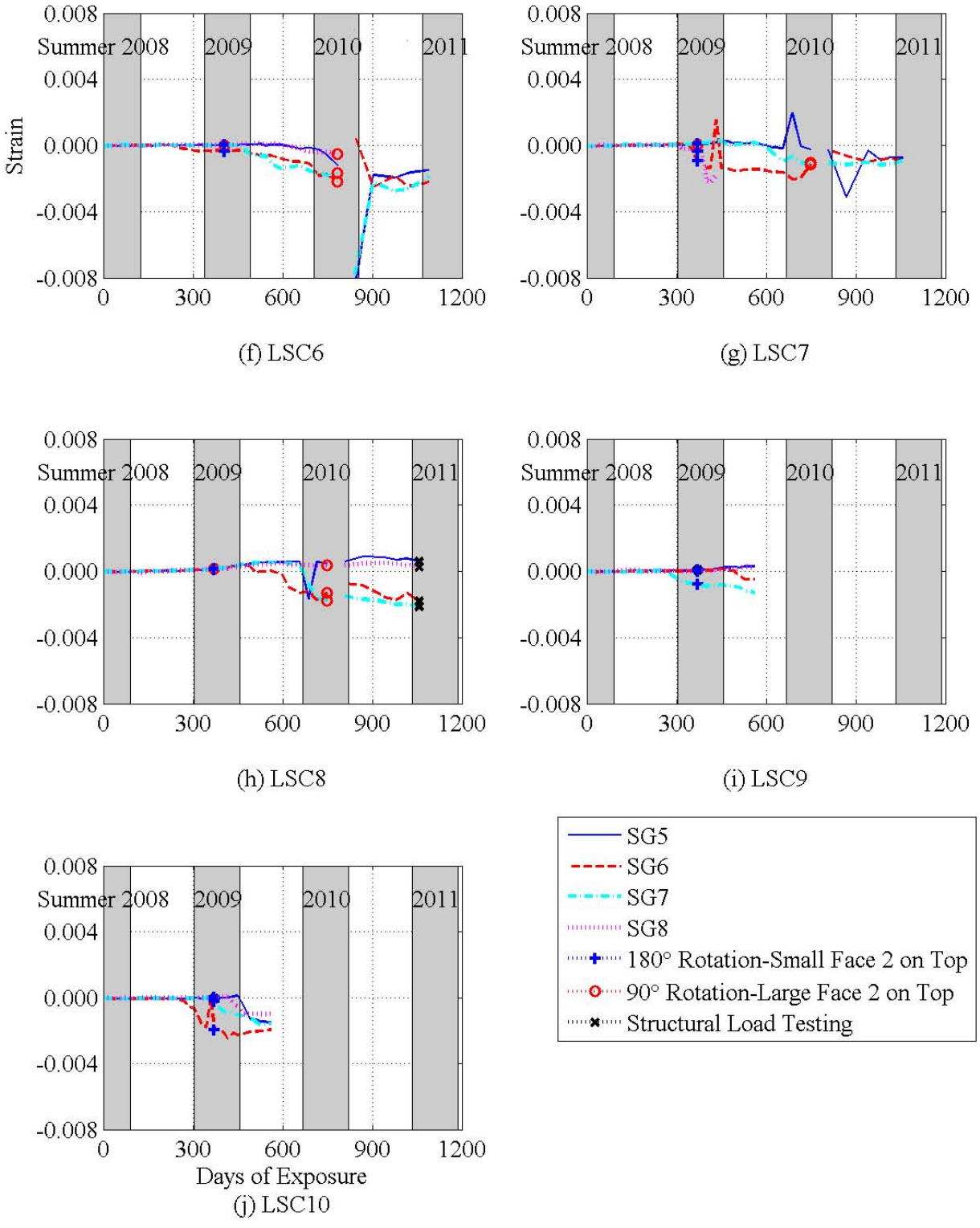

Figure 3-21. Internal Strain Gages (SG5-SG8) along Large Face 1 Tension Steel of the Splice Region. (Continued)

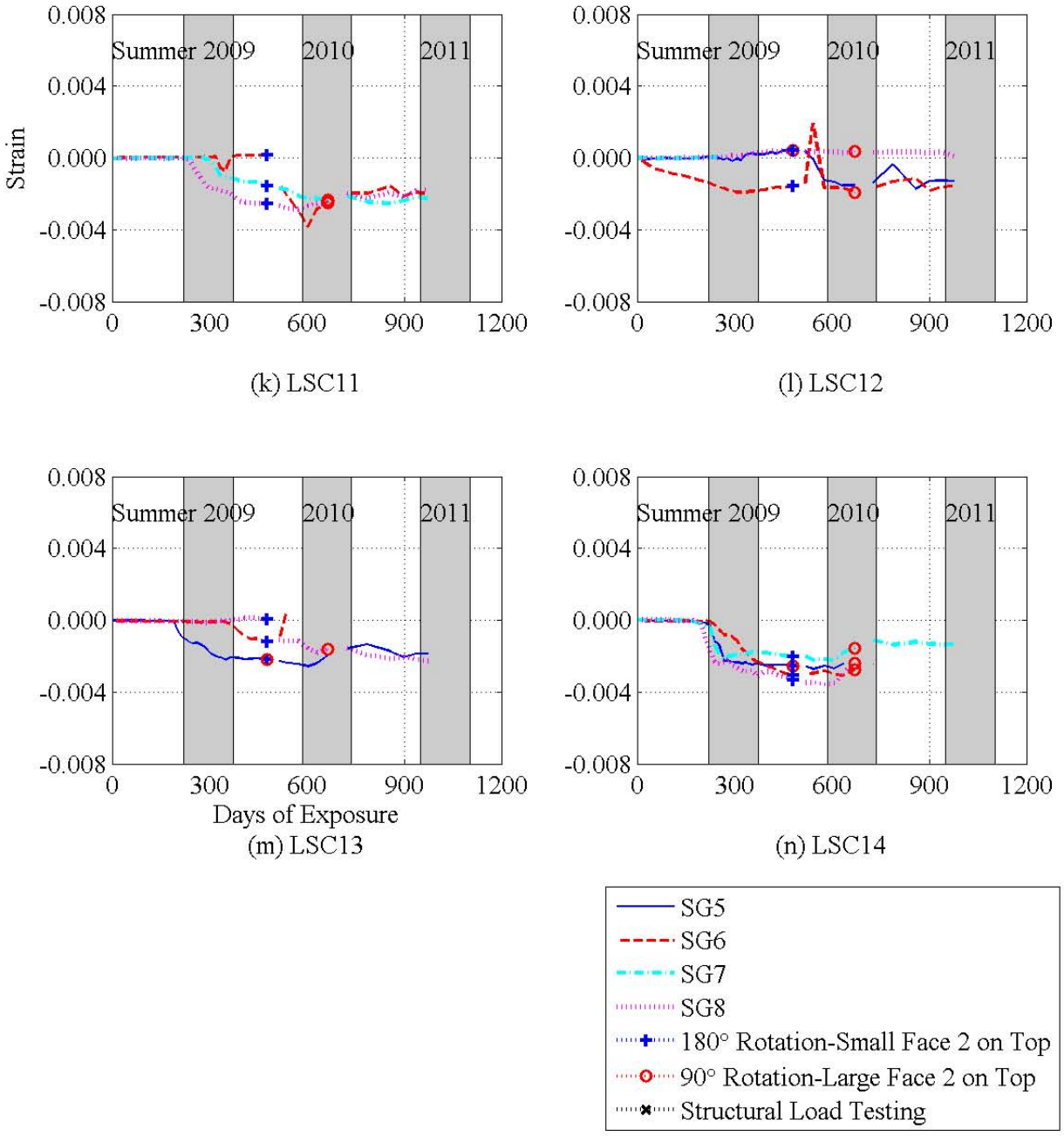

Figure 3-21. Internal Strain Gages (SG5-SG8) along Large Face 1 Tension Steel of the Splice Region. (Continued)

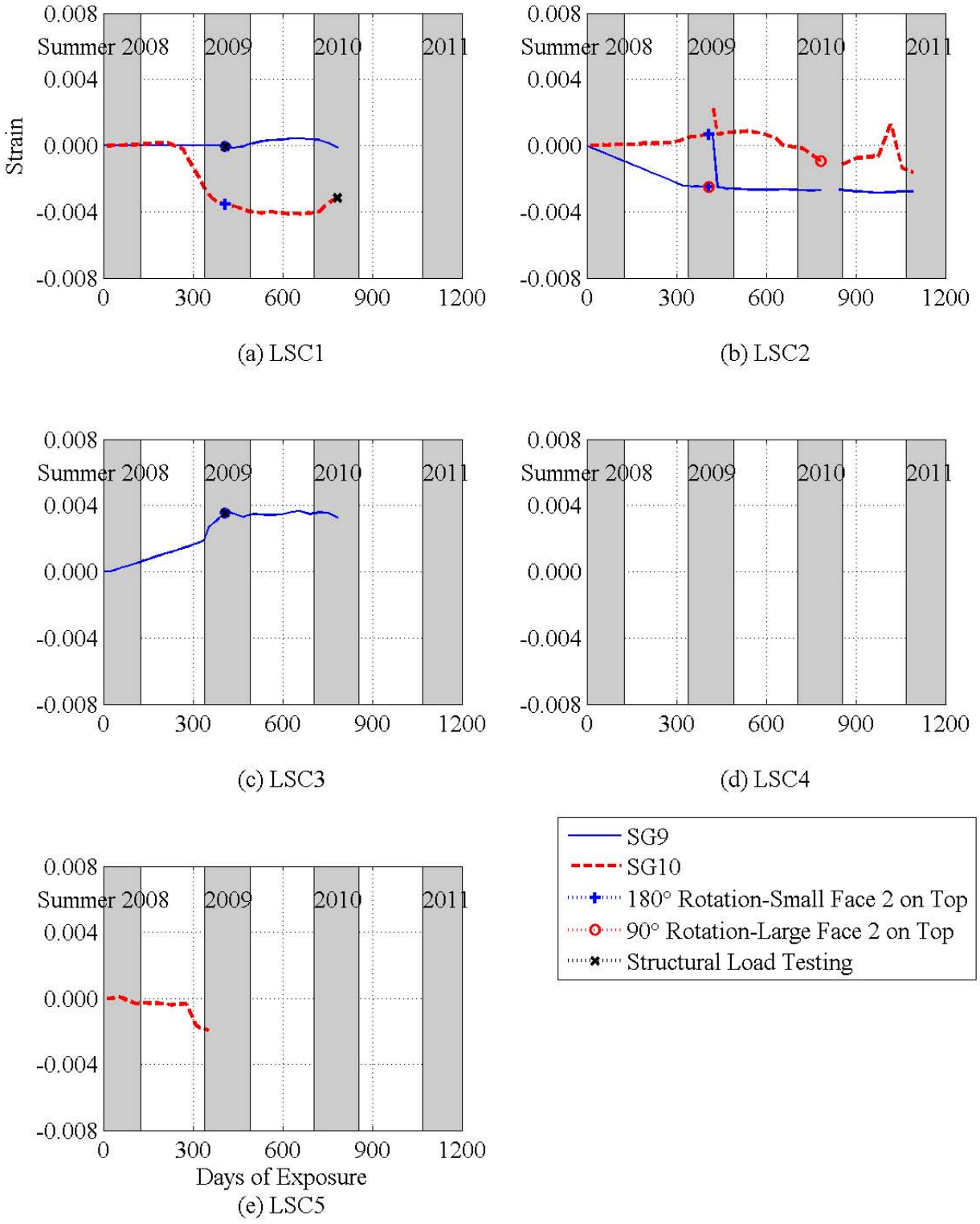

Figure 3-22. Internal Strain Gages (SG9-SG10) along Large Face 2 Compression Steel of the Splice Region.

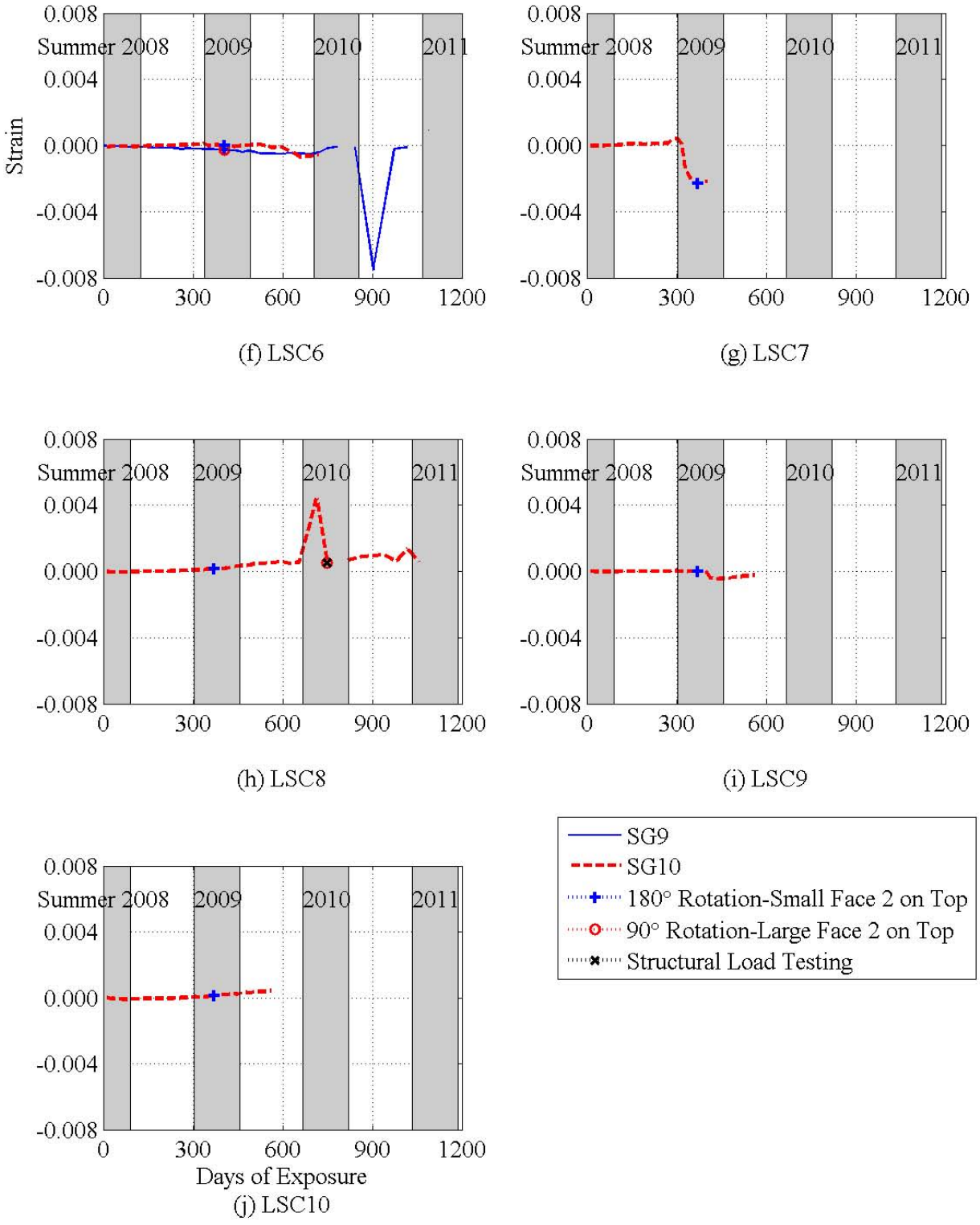

Figure 3-22. Internal Strain Gages (SG9-SG10) along Large Face 2 Compression Steel of the Splice Region. (Continued)

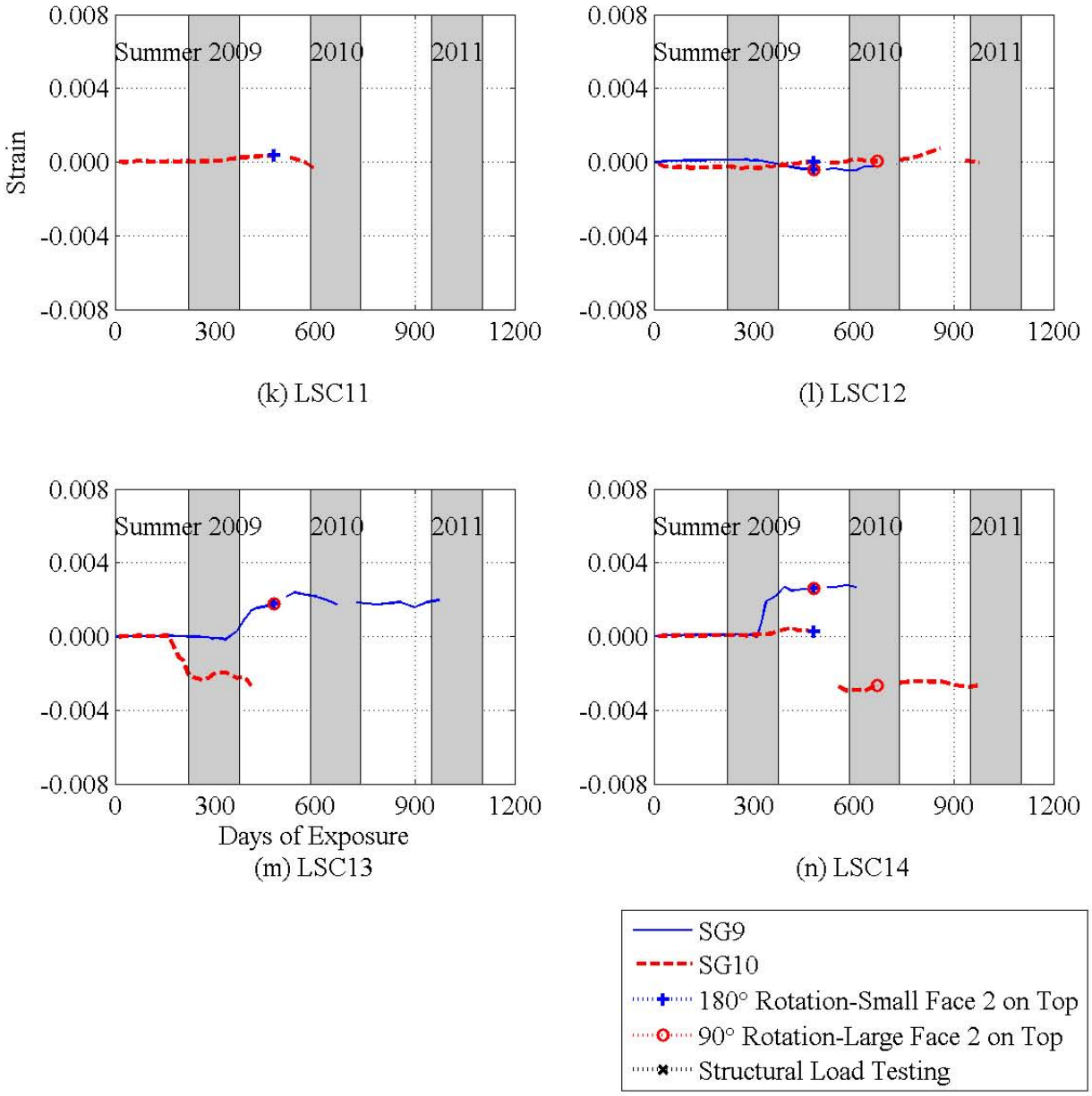

Figure 3-22. Internal Strain Gages (SG9-SG10) along Large Face 2 Compression Steel of the Splice Region. (Continued)

3.3.4 Comparison of Surface and Internal Strains

Figure 3-23 and Figure 3-25 have comparisons of the strains on the surface, inside the concrete cover, on the steel hoop, and the core concrete on the small and large faces, respectively. As the researchers have expected, the cover concrete expanded more than the core concrete (see Figure 3-23 with data measured with KM1 and KM2). Figure 3-24 shows percentages of the surface strains calculated from the measured distance between DEMECs. Since the internal gages were on Small Face 1, the percentages are only calculated for the time than the surface strain was calculated on Small Face 1 which is before the first rotation. At the time of the 180° rotation, the average percentage of the surface strain in the concrete cover, concrete core and steel rebar was 61 percent, 51 percent, and 40 percent on Small Face 1. This shows hoop strains were smaller than the concrete that was on either side of it (both in the concrete cover and core).

Figure 3-25 shows the strains in the concrete and steel hoop on the Large Faces. Similar to the Small Faces, the cover concrete expanded more than the core concrete which is evident through the KM3 and KM4 gages. The average strain in the cover and core concrete at the time of the 180° rotation was 0.0020 and 0.0018. At the time of the 90° rotation, the average strains from the KM3 and KM4 gages were 0.0039 and 0.0036. Figure 3-26 shows the percentages of the surface strain on Large Face 1. The KM3 and KM4 average percentages of the surface strains on Large Face 1 was 63 percent and 55 percent, at the time of the 180° rotation., The percentages at the time of 90° rotation were 53 percent and 48 percent. The percentages lowered since the surface strain values increased at a faster rate than the cover and core concrete strains. The strain in the steel hoop differed on the Large Face 1 than Small Face 1 in that the strains were larger than the concrete on either side. The SG12 average percentages of the surface strain were 83 percent and 78 percent at the first two rotations. The steel on all faces started to yield around Day 300 of exposure with strains above 0.002. Some of internal gages gave bad readings for various possible reasons; therefore, there are a few gaps in the information on the graphs.

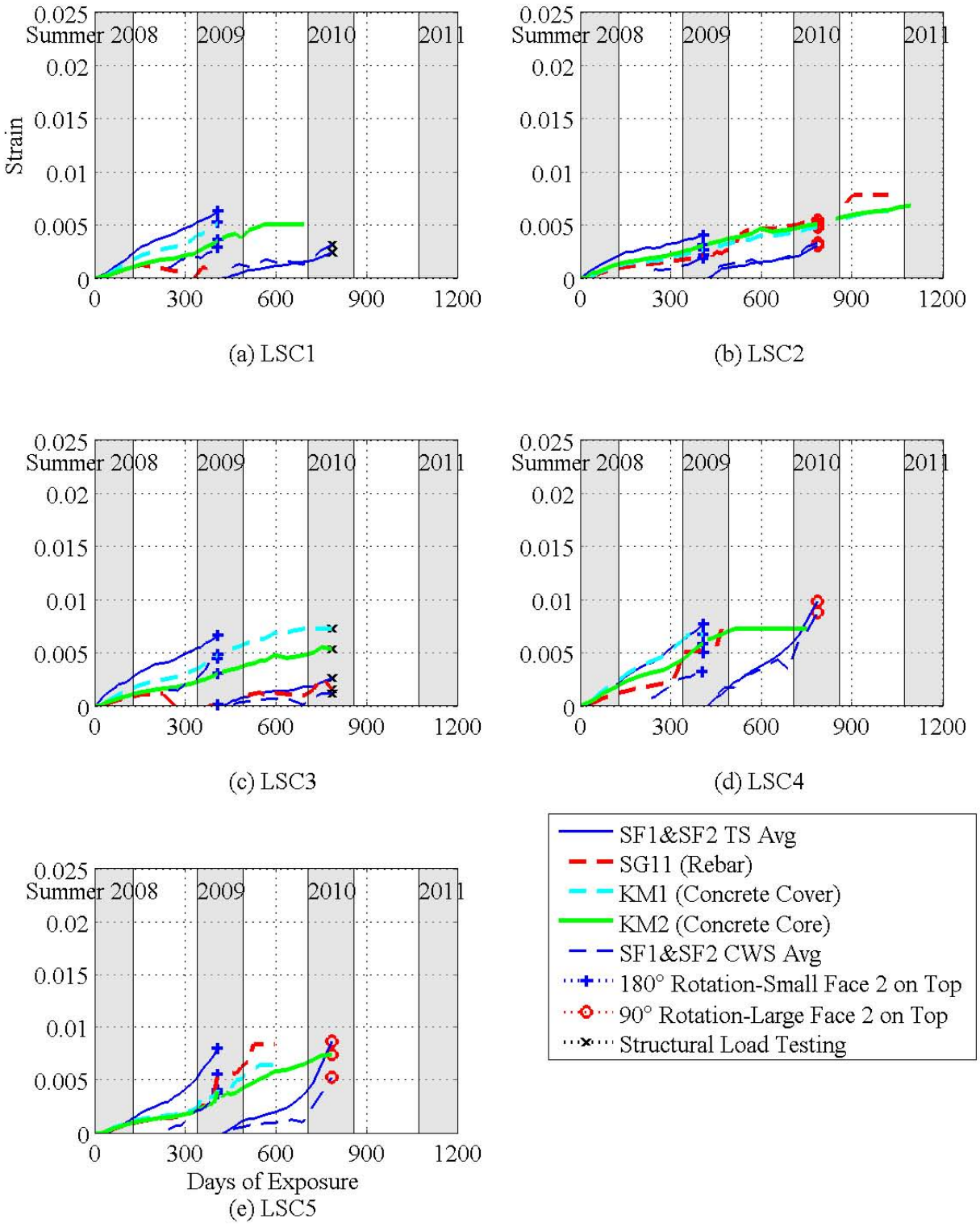

Figure 3-23. Internal and External Strain Measurements on and near the LSC Specimens' Small Face 1 and Small Face 2.

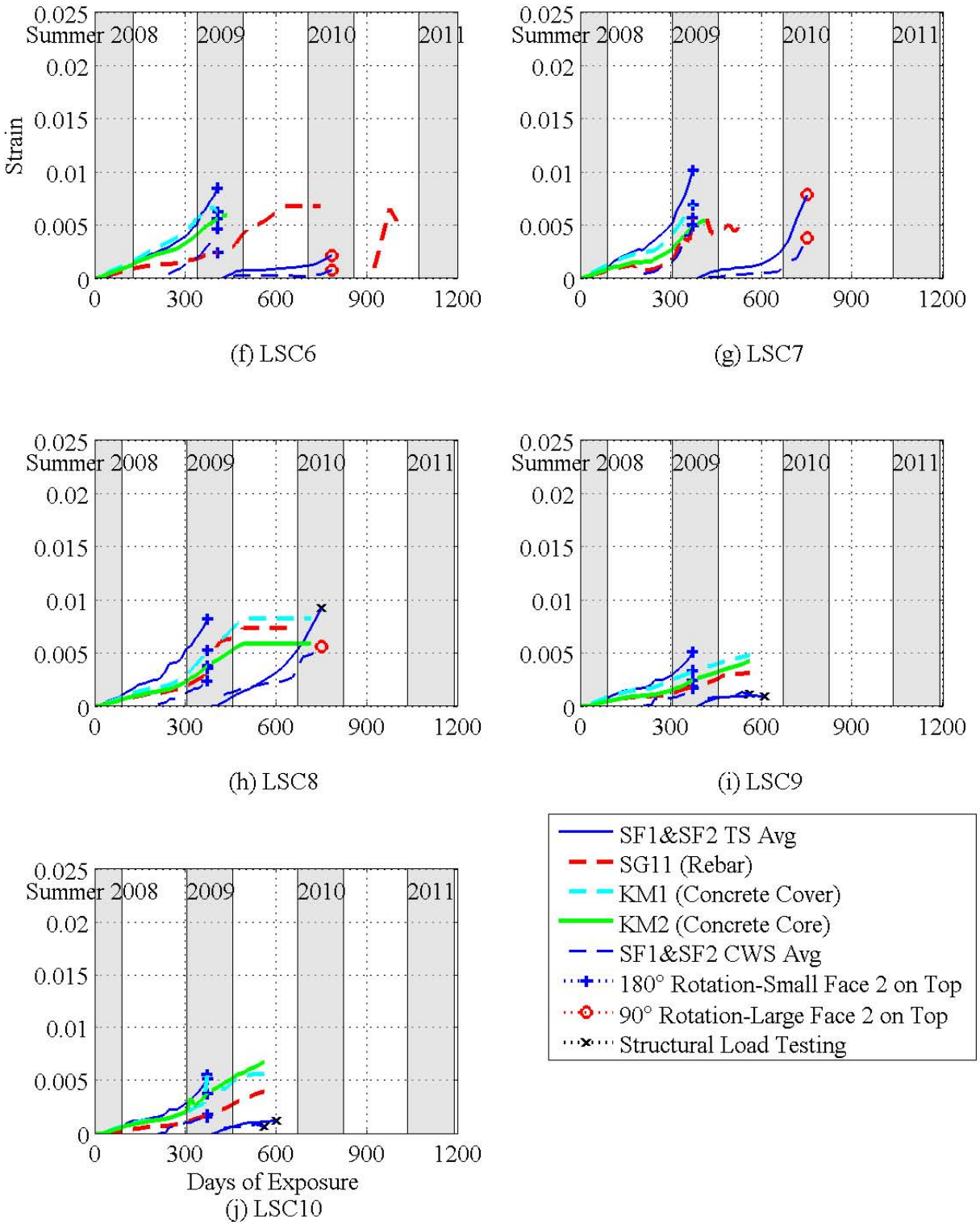

Figure 3-23. Internal and External Strain Measurements on and near the LSC Specimens' Small Face 1 and Small Face 2. (Continued)

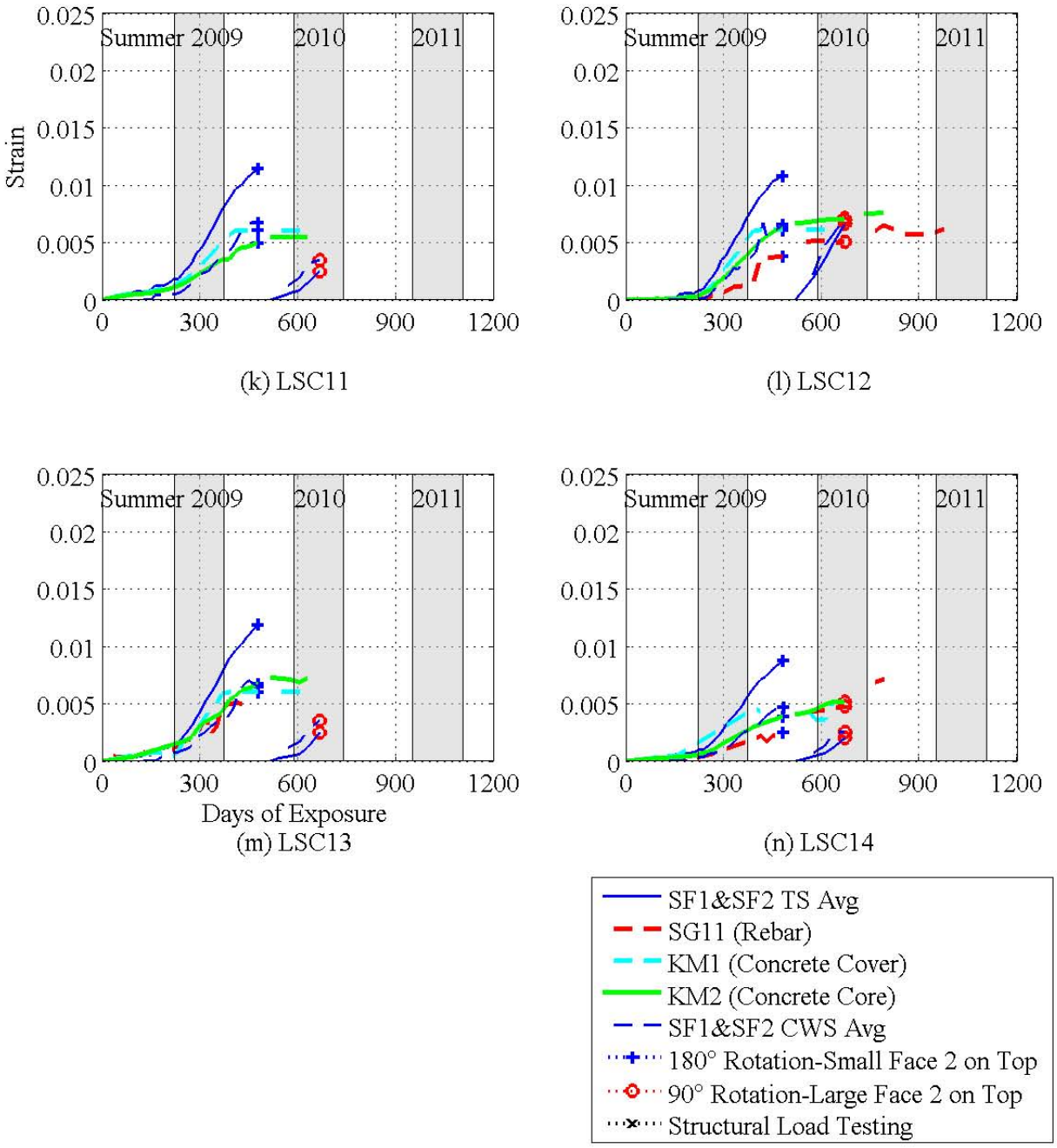

Figure 3-23. Internal and External Strain Measurements on and near the LSC Specimens' Small Face 1 and Small Face 2. (Continued)

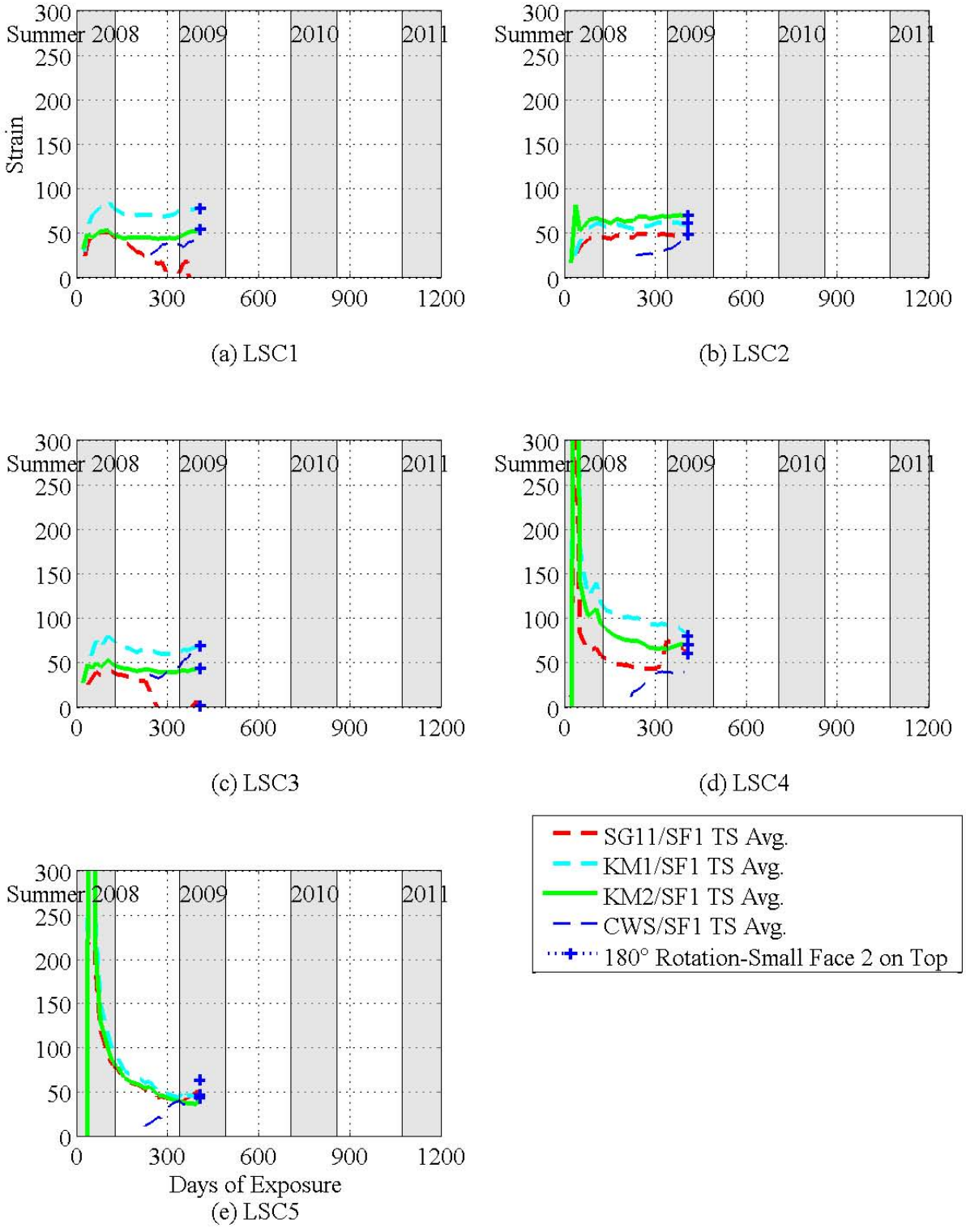

Figure 3-24. Percentages of Surface Strains on LSC Specimens' Small Face 1.

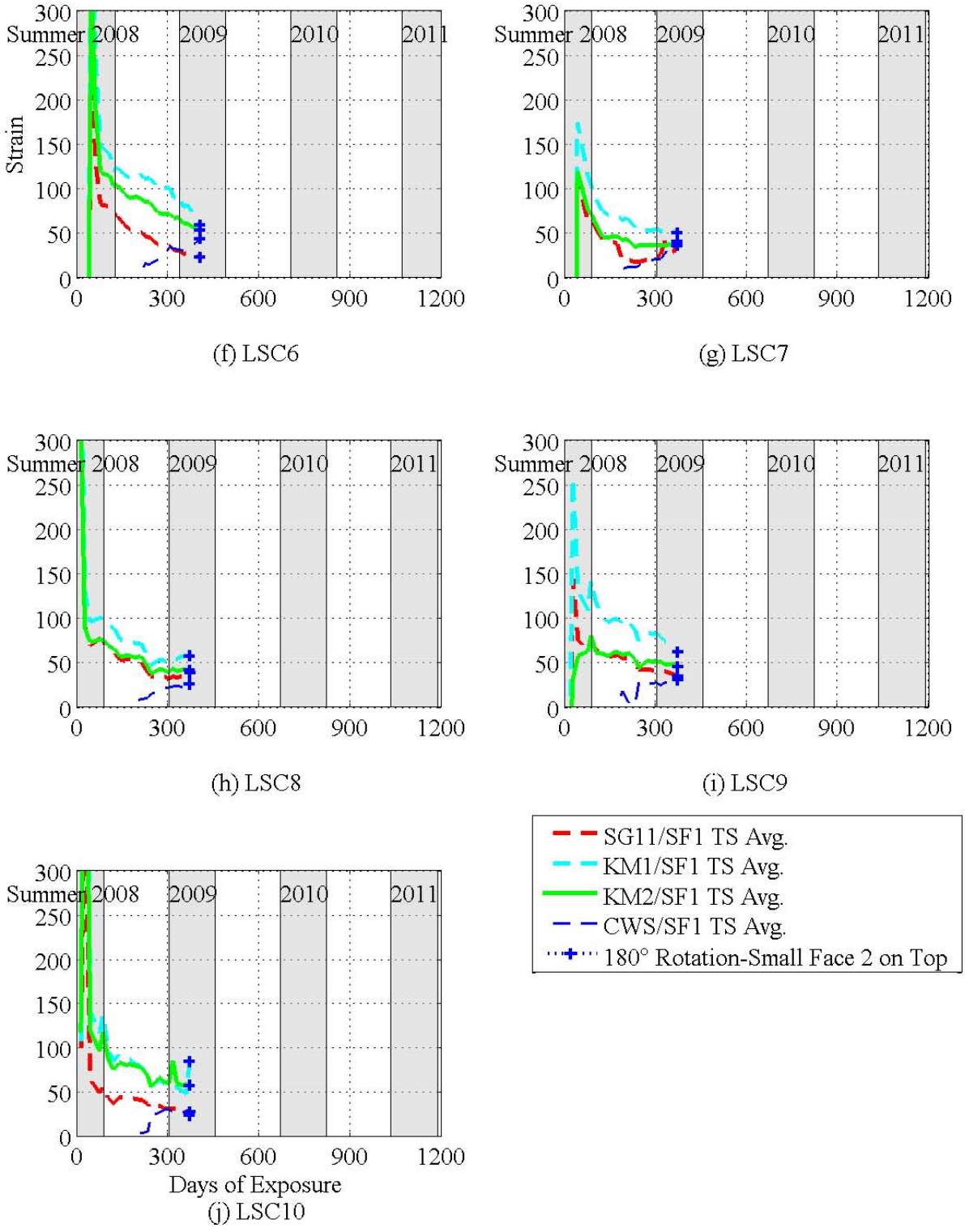

Figure 3-24. Percentages of Surface Strains on LSC Specimens' Small Face 1. (Continued)

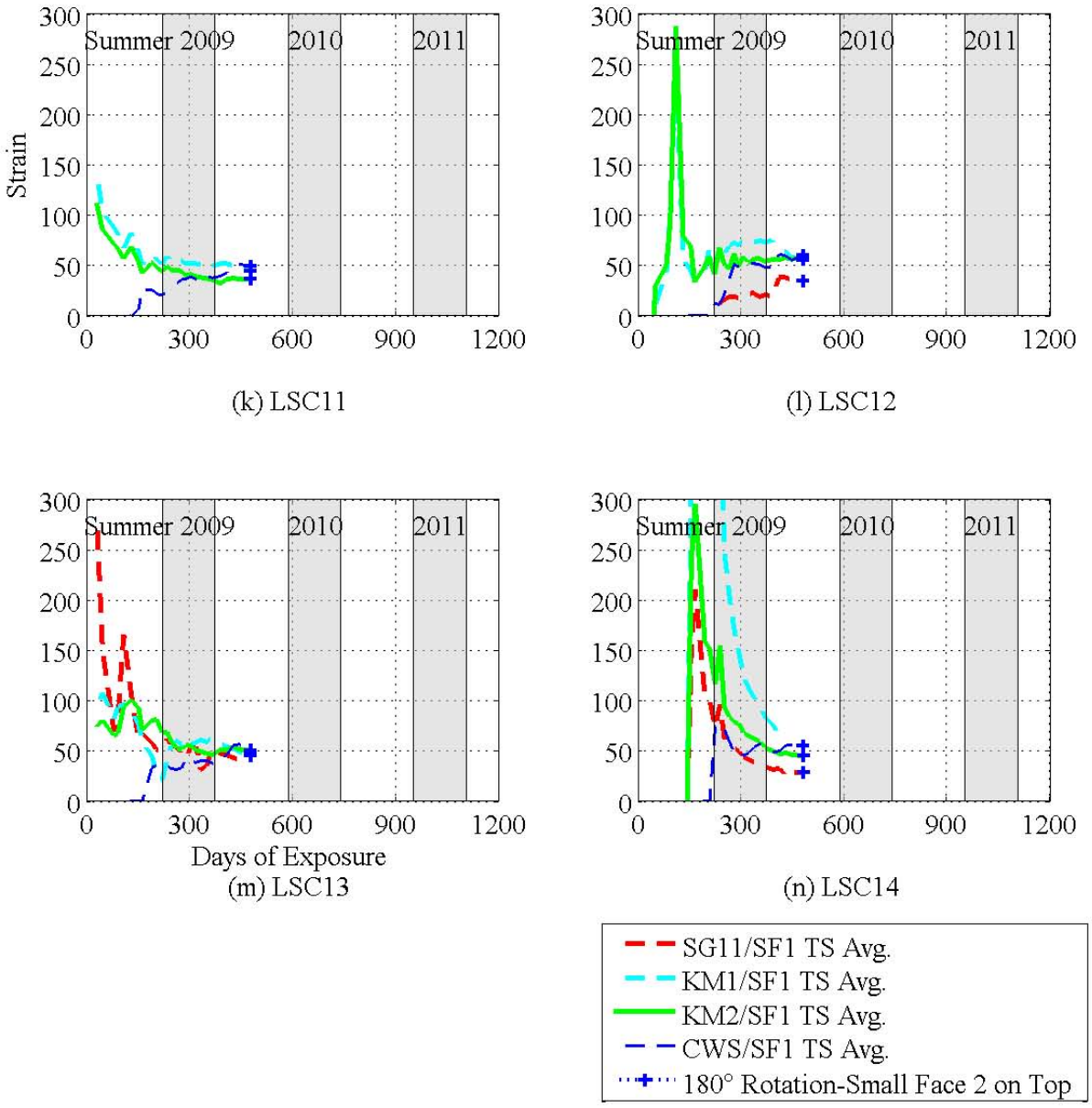

Figure 3-24. Percentages of Surface Strains on LSC Specimens' Small Face 1. (Continued)

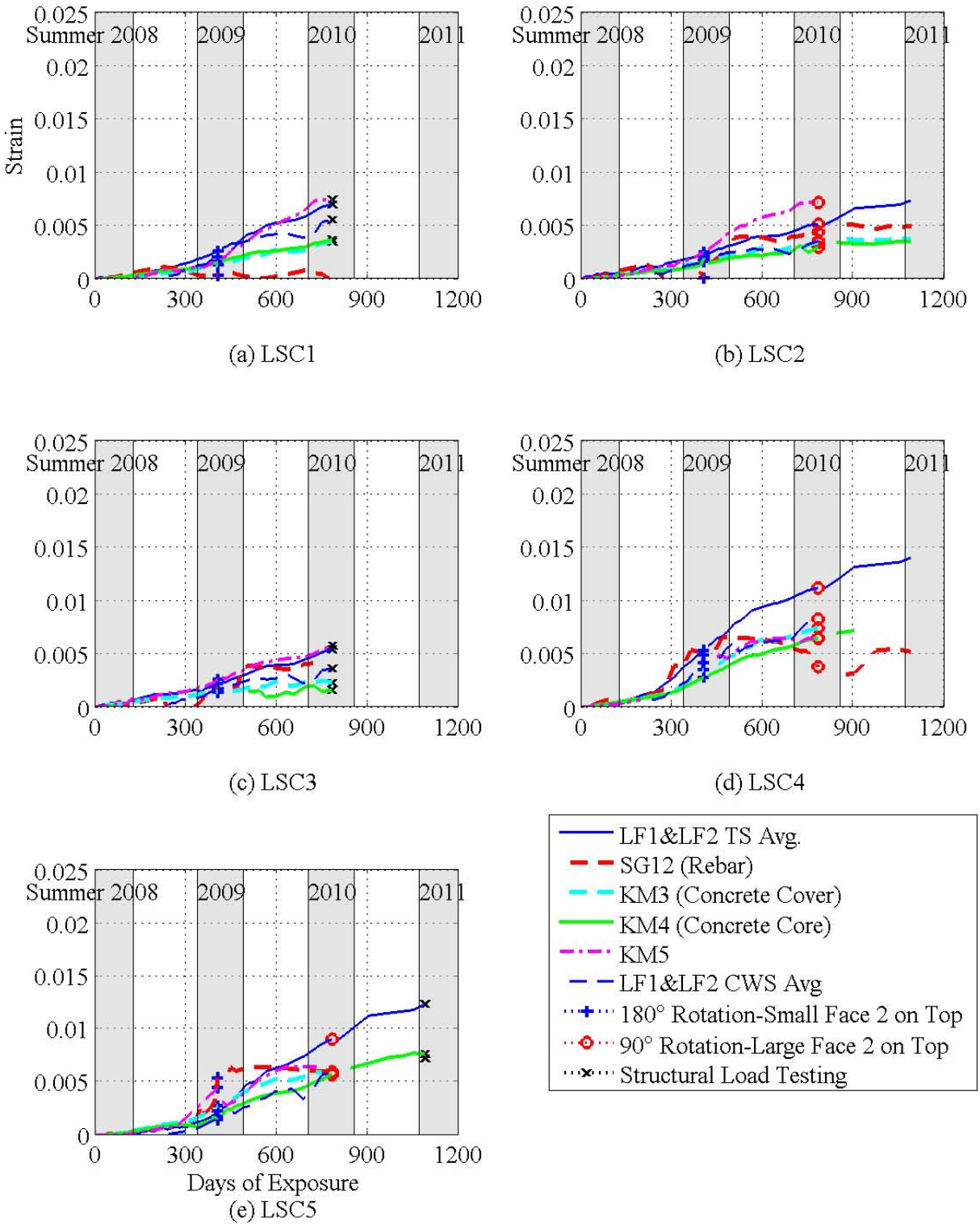

Figure 3-25. Internal and External Strain Measurements on and near the LSC Specimens' Large Face 1 and Large Face 2.

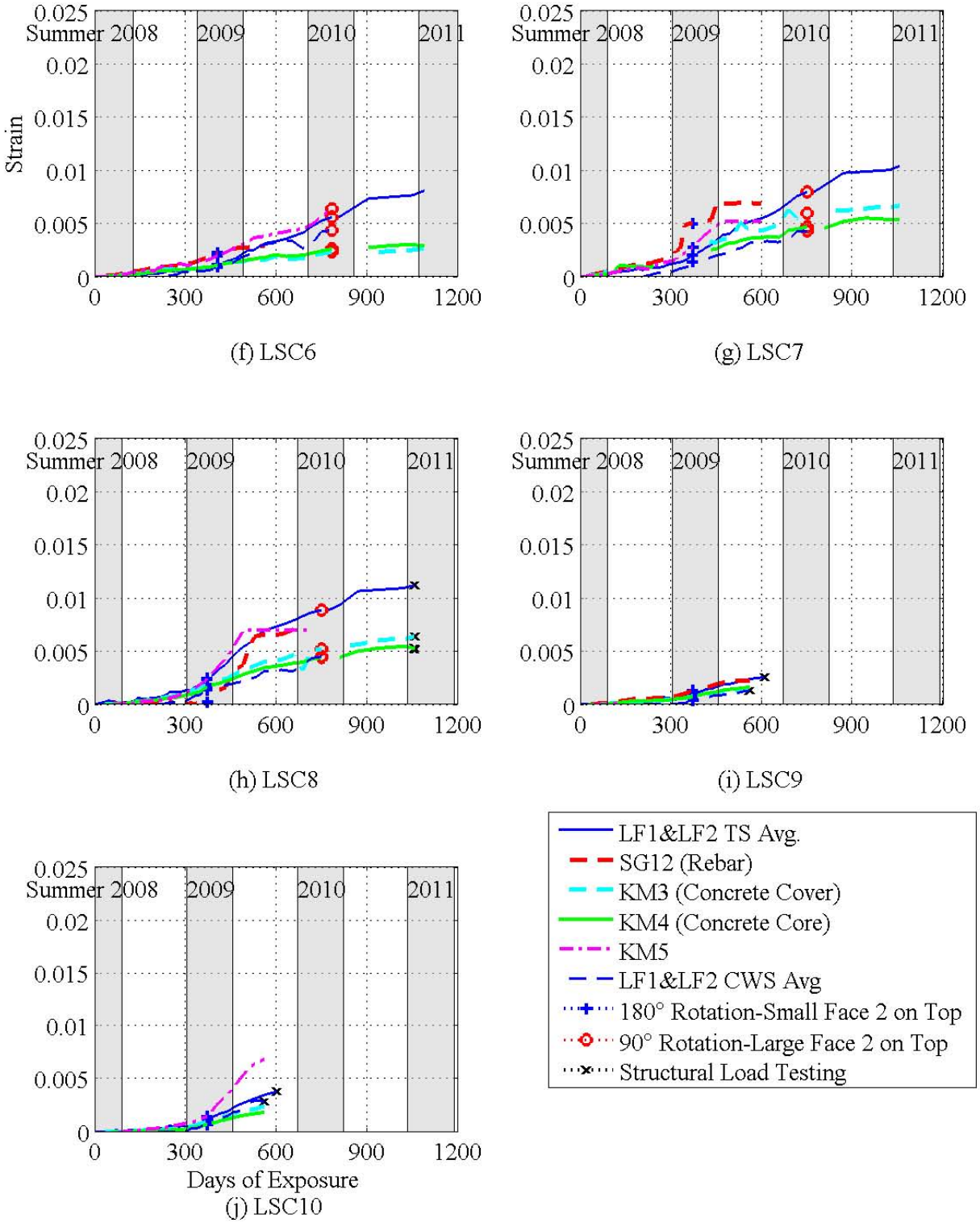

Figure 3-25. Internal and External Strain Measurements on and near the LSC Specimens' Large Face 1 and Large Face 2. (Continued)

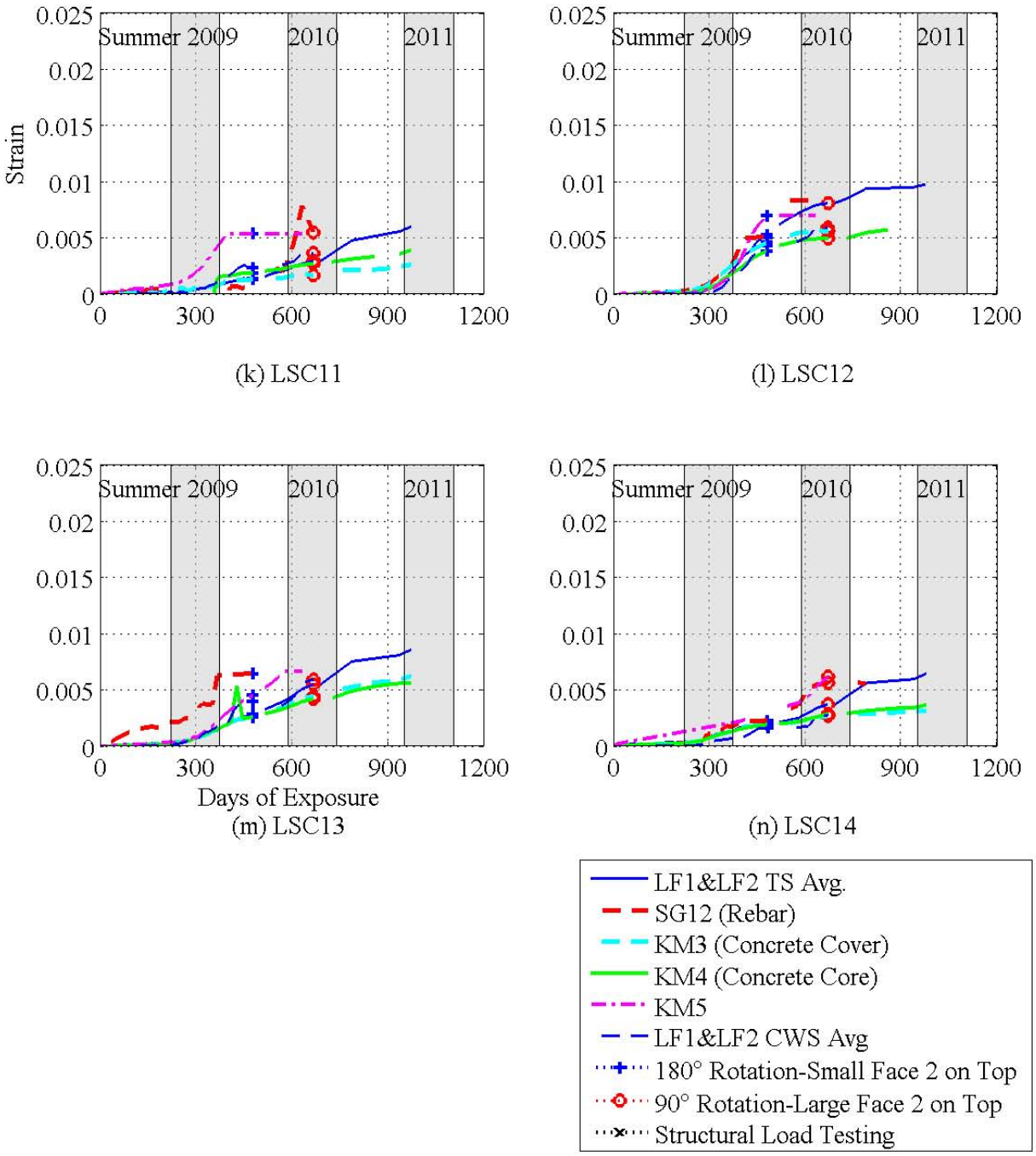

Figure 3-25. Internal and External Strain Measurements on and near the LSC Specimens' Large Face 1 and Large Face 2. (Continued)

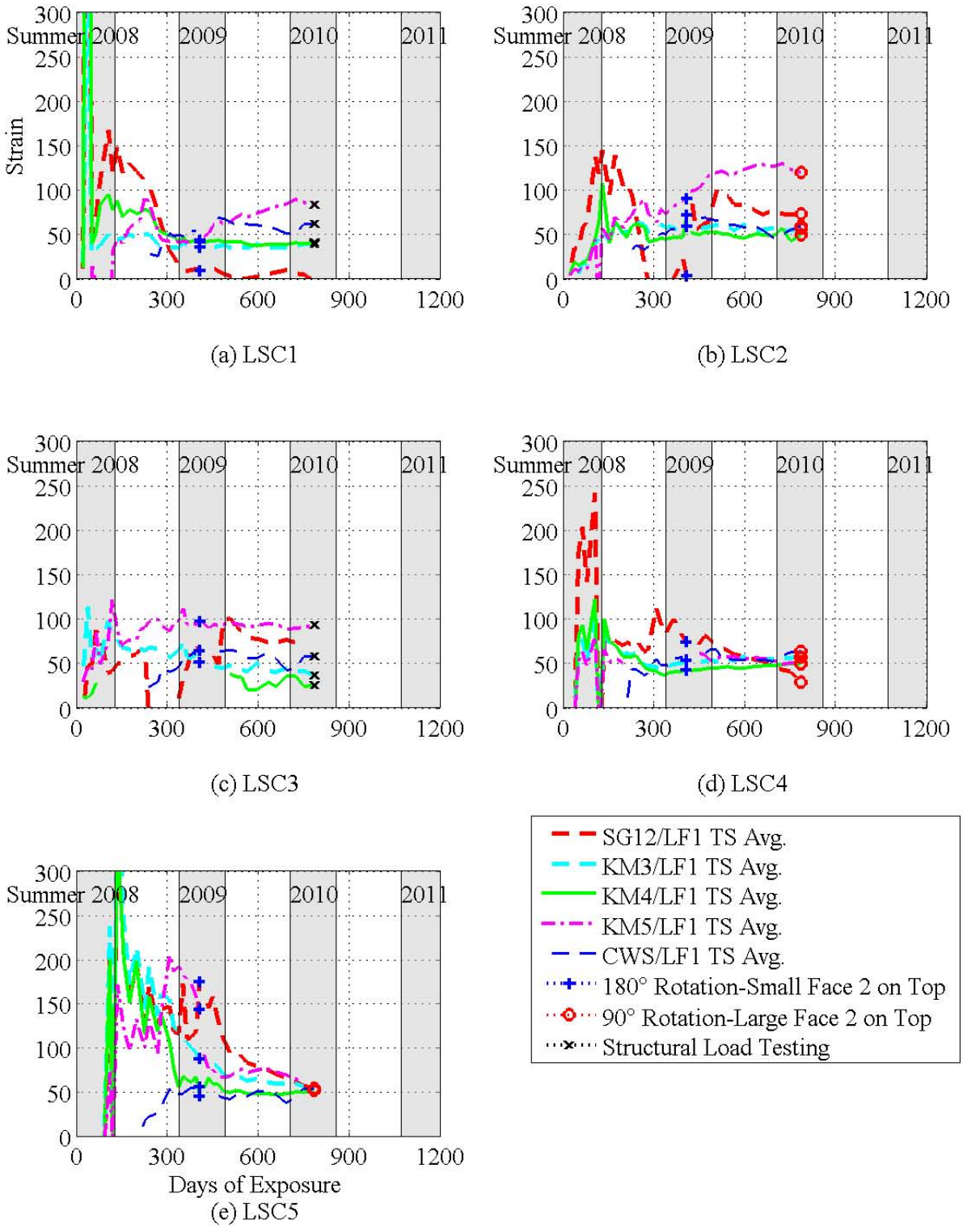

Figure 3-26. Percentages of Surface Strains on LSC Specimens' Large Face 1.

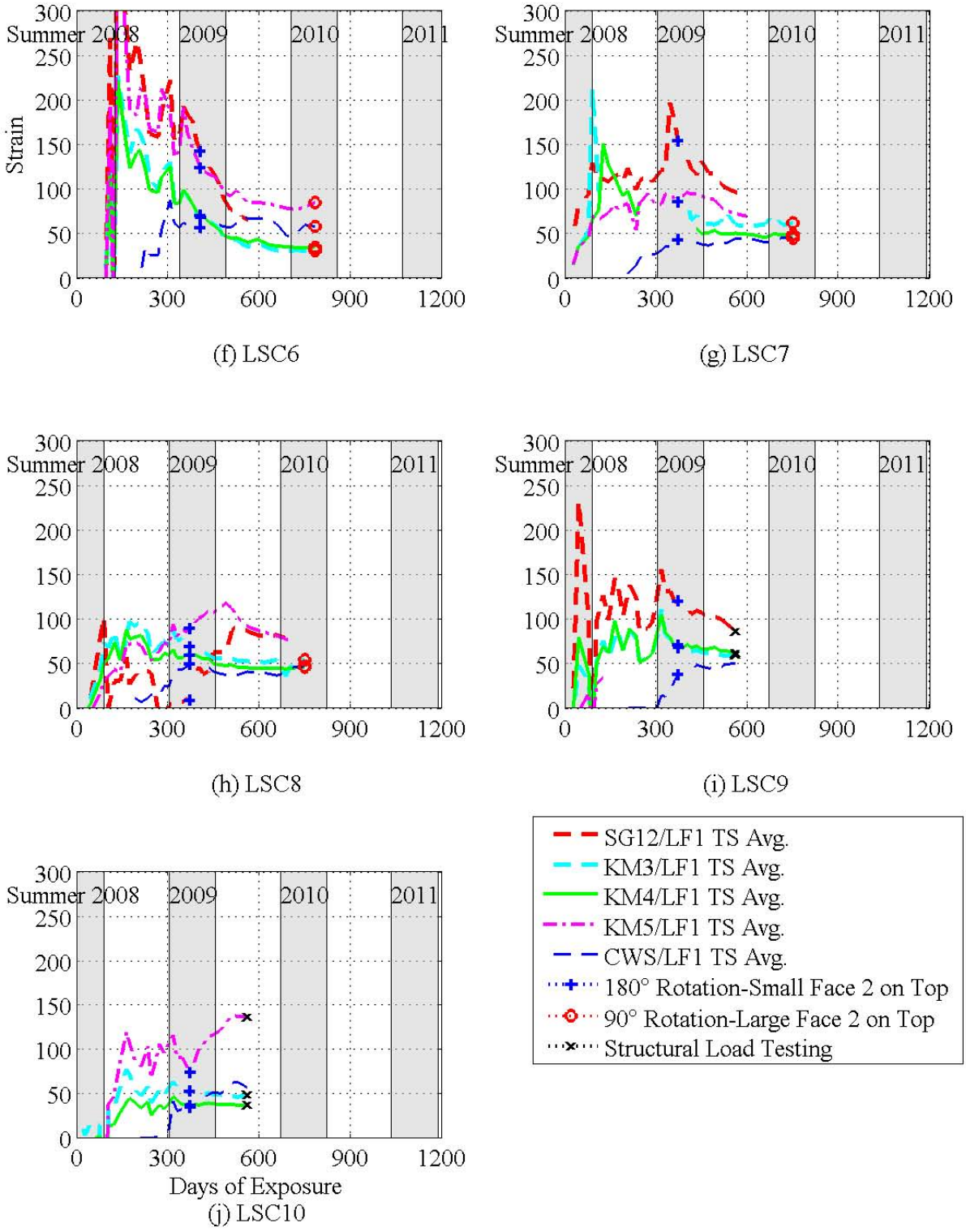

Figure 3-26. Percentages of Surface Strains on LSC Specimens' Large Face 1. (Continued)

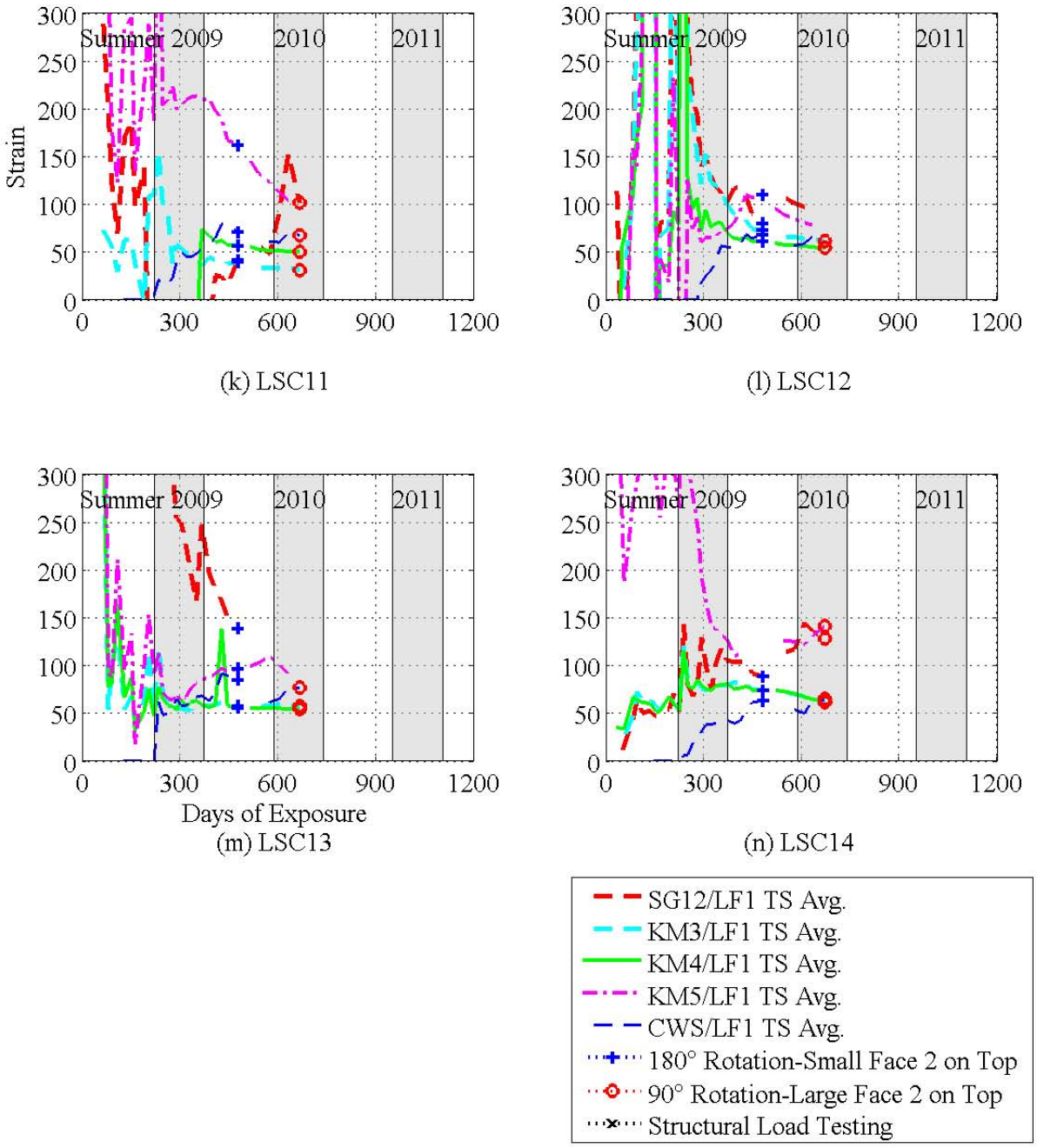

Figure 3-26. Percentages of Surface Strains on LSC Specimens' Large Face 1. (Continued)

3.4 PETROGRAPHIC ANALYSIS RESULTS

To determine if ASR and/or DEF was evident in the large-scale specimens, researchers took a series of concrete cores from the specimens following their testing; TxDOT personnel then independently performed petrographic analysis on the cores. Specifically, the identification, severity, and progression of the ASR and/or DEF damage were desired, as well as visual documentation of any distress due to ASR/DEF. To date, multiple concrete cores were taken from LSC1, LSC3, LSC5, LSC8, and LSC9, which were then tested at different damage stages of ASR/DEF deterioration. Appendix A shows three petrographic analysis reports produced from cores analyzed; the results are summarized below.

Multiple 4-inch (102 mm) diameter concrete cores of varying depths were taken from each of the five LSC specimens after they had undergone the four-point and three-point experimental load testing. Figure 3-27 shows the Hilti DD200 coring machine attached to the specimen. The cores were taken from various locations within the splice region. Figure 3-28 shows the rebar layout of the specimens as well as typical coring locations. Between three and seven cores were extracted from each beam. An attempt was made to check if ASR/DEF had different effects on different parts of the beams. Therefore, cores were drilled near or through longitudinal and transverse reinforcement, locations with severe or large cracks on the exterior, locations with mild or no cracking, and through an unknown white residue that had developed on some the beams. Figure 3-29 shows an example of a core drilled through the splice with one removed #11 bar and another that remained in the beam. Figure 3-30 displays a shorter core taken through a #5 hoop. A large surface crack, approximately 0.5 inches (12.7 mm) deep, is also shown. These locations were specifically chosen for two reasons:

- To investigate if there was any ASR/DEF along the reinforcement-concrete interface that could potentially lead to bond issues.
- To find how deep the surface cracks were embedded into the specimen, which could lead to other durability issues such as corrosion once the crack depths approached the reinforcing steel.

Figure 3-27. Coring Machine Attached to Beam.

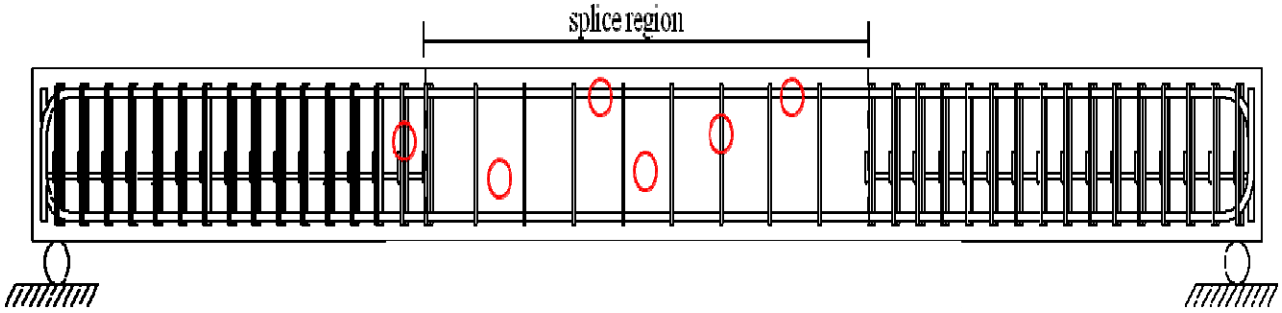

Figure 3-28. Typical Coring Locations.

Figure 3-29. Core Extracted above Splice (left) and the Hole from that Core (right).

Figure 3-30. Core Extracted above Hoop with Surface Cracking.

Table 3-4 gives details on the cores and from which specimen they were obtained. Note that specimens were selected for testing based on the extent of ASR/DEF expansion and resulting concrete cracking, and not the age of the specimen.

Table 3-4. Concrete Core Summary.

Specimen	Core Name	Date of Initial Exposure	Date of Structural Load Test	Location
LSC1	LSC1S1	5/2008	8/2010	Near #5 hoop steel
LSC1	LSC1S2	5/2008	8/2010	Concrete only
LSC1	LSC1S3	5/2008	8/2010	Near #11 longitudinal steel
LSC3	LSC3S1	5/2008	8/2010	Near #5 hoop steel
LSC3	LSC3S2	5/2008	8/2010	Concrete only
LSC3	LSC3S3	5/2008	8/2010	Near #11 longitudinal steel
LSC9	LSC9S1	7/2008	2/2010	Mild surface cracks
LSC9	LSC9S2	7/2008	2/2010	Mild surface cracks
LSC9	LSC9S3	7/2008	2/2010	Near #5 hoop steel
LSC9	LSC9S4	7/2008	2/2010	Near #11 longitudinal steel
LSC9	LSC9S5	7/2008	2/2010	Near #5 hoop steel
LSC9	LSC9S6	7/2008	2/2010	Mild surface cracks
LSC9	LSC9S7	7/2008	2/2010	Near #11 longitudinal steel
LSC5	LSC5S1	5/2008	7/2011	N/A
LSC5	LSC5S2	5/2008	7/2011	N/A
LSC5	LSC5S3	5/2008	7/2011	N/A
LSC8	LSC8S1	7/2008	7/2011	N/A
LSC8	LSC8S2	7/2008	7/2011	N/A
LSC8	LSC8S3	7/2008	7/2011	N/A

Appendix A has two Petrographic Analysis Reports: the first is for LSC9, and the second is for LSC1 and LSC3. The results from a related TxDOT project (0-5997) are also listed in the Petrographic Analysis Reports. For cores taken from LSC 1, 3 and 9, the petrographic analysis

reported that all cores analyzed displayed moderate to late stages of ASR, and that ASR was the primary cause for distress in the samples provided. Surface cracking was evident in all cores with few cracks being nearly 1-inch (25.4 mm) deep. ASR gel, distressed aggregates, and micro cracking were present in the cores. Specifically, the first report indicated a layer of ASR gel at the interface of a #11 bar (longitudinal spliced bar) imprint in one core and as well as a conduit imprint in a different core. Both reports indicate that in all cores, DEF caused minimal distress. Although the petrographic analysis found ettringite in microcracks created by ASR as well as air voids and the paste-aggregate interface, there was not enough evidence to confirm that DEF caused the distress. The ettringite around the rebar indicated possible debonding on a core from LSC3, but it is uncertain if the coring process caused the debonding.

The petrography analysis also included microscopic documentation which gave additional evidence of micro damage and distress that primarily ASR had caused. The following figures were taken from the petrographic analysis reports. Figure 3-31 shows a high-resolution close-up image of an ASR-distressed aggregate, while Figure 3-32 displays ASR gel accumulation in a void and cracking in the paste. Fluorescent imaging shown in Figure 3-33 and Figure 3-34 was used to highlight the distress in the aggregates and paste.

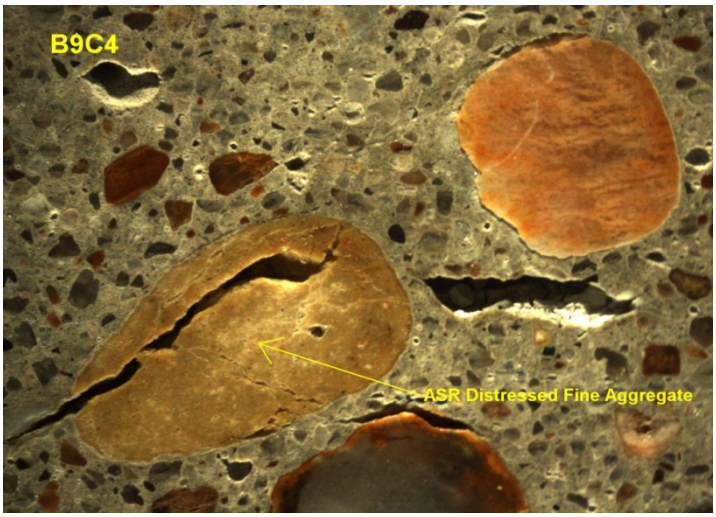

Figure 3-31. ASR Distressed Fine Aggregate.

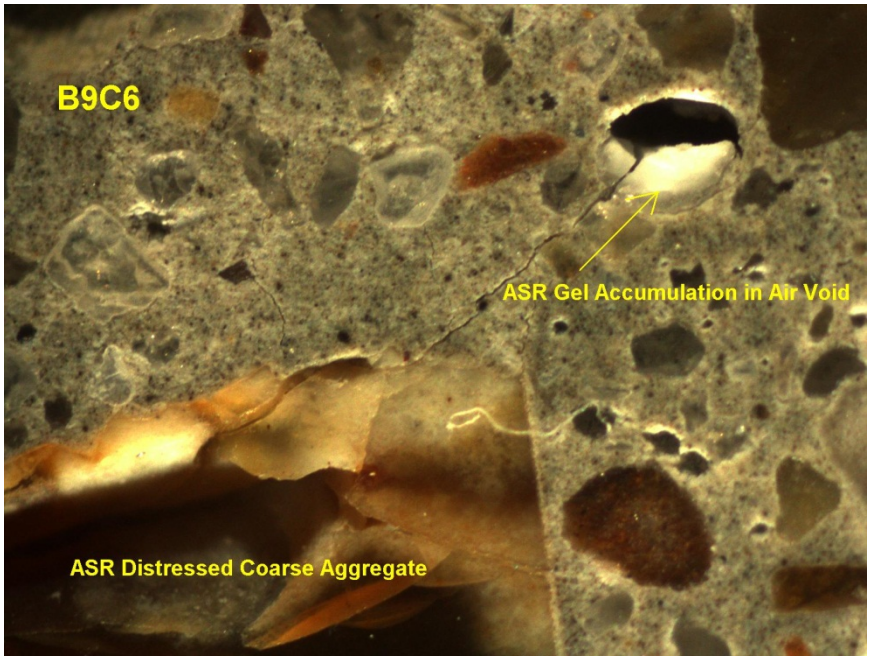

Figure 3-32. ASR Gel Accumulation and Distressed Coarse Aggregate.

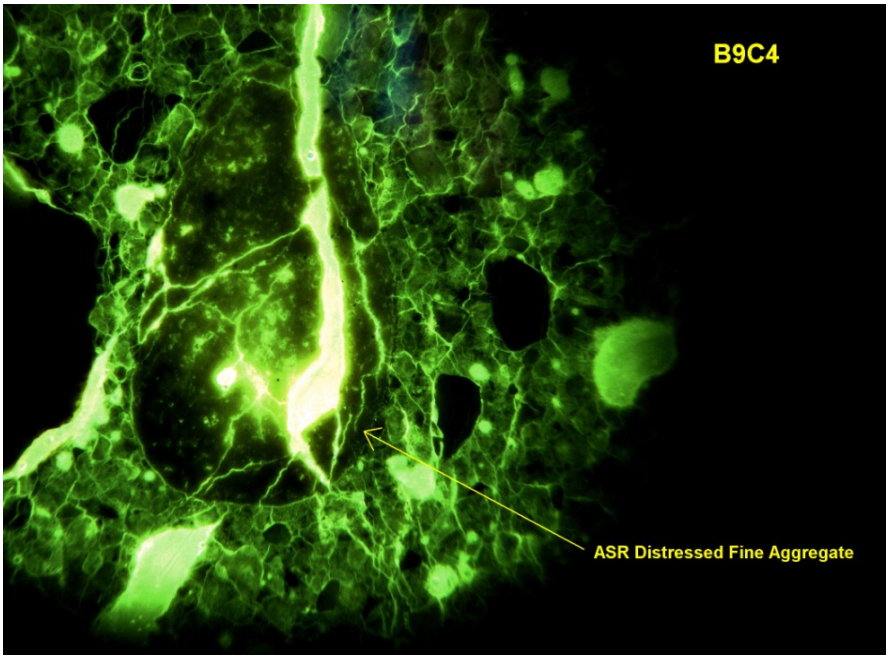

Figure 3-33. Fluorescent Imaging of ASR Distressed Fine Aggregate.

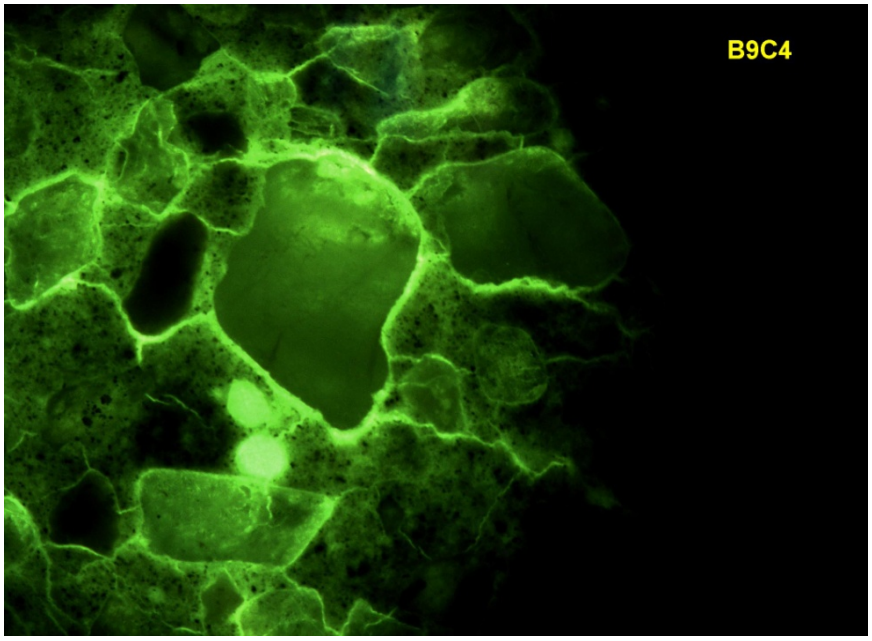

Figure 3-34. Fluorescent Imaging of Aggregate/Paste Interface.

3.5 SUMMARY AND CONCLUSIONS

In summary, 14 large-scale specimens stored at the Riverside Campus were exposed to outdoor weather conditions in Bryan, TX, and to wet-dry cycles using supplemental water to accelerate the ASR/DEF deterioration mechanisms. Internal instrumentation and external surface measurements were continually recorded for all specimens throughout the deterioration program. These measurements provided significant information about the expansion mechanism in the LSC specimens due to ASR and minimal DEF. Chapter 5 presents the structural effects of this expansion on the column splice region of the LSC specimens.

From the information provided in this chapter, it can be concluded that all specimens to date have successfully developed significant premature concrete deterioration due to ASR and minimal DEF in terms of concrete expansion and surface cracking that is representative of observations in in-service bridges. In addition, the deterioration mechanism is continuing. To develop more severe damage states, additional exposure time is required. Therefore, eight untested specimens continue to deteriorate at the Riverside Campus.

The following highlights some of the findings derived from the deterioration program to date:

- The direct sunlight on the specimens made a large impact on the expansion due to ASR and minimal DEF. The surface strain at the top of Large Face 1 (LF1 TS1) reached only 61 percent of the transverse strain on the top surface (Small Face 1), and an average of the other transverse strains on Large Face 1 (LF1 TS2, LF1 TS3, LF1 TS4, and LF1 TS5) reached only 22 percent of the transverse strain on Small Face 1 before the first rotation.

- The LSC specimens expanded at a higher strain rate during the summer months (May through September). The increase in the average strain/month on Small Face 1 was calculated to measure this. The rate of increase was different for the three groups of specimens first exposed to the high temperatures and supplemental water at different times, (May, July, and September). The strain rate on the first six specimens, which were exposed during all of the summer of 2008, was 1.7 times as large during summer 2009 than the non-summer months of 2008 and 2009. The next four LSC specimens were exposed only during half of the 2008 summer. The average strain rate of the transverse strain on the top, Small Face 1, was 2.7 times as large during the summer of 2009 than the non-summer months. The last four specimens were not exposed to the environmental conditions anytime during summer in 2008. The strain rate increase during the first summer months on these LSC specimens was 6.5 of that during the initial strain rate prior to the summer months.

- The transverse surface strains were about 10 times larger than the longitudinal surface strains due to the longitudinal restraint from the axial post-tensioning steel and longitudinal column reinforcement and the transverse tension field induced by Poisson's effect under post-tensioning.

- The average strains calculated from measuring the sum of the crack widths between DEMEC points were about 50 percent of the surface strains calculated from measuring the distance between DEMEC points.

- The measured strains were larger on the surface than inside the specimen with the strain in the cover reaching about 58 percent and the strain in the core concrete reaching about 52 percent of the surface strain. These percentages are an average of the values found on Small Face 1 and Large Face 1. The strain on the steel hoop in the middle of the splice region had very different values on the Small and Large Face with strains of 0.0036 and 0.0054 on Small Face 1 and Large Face 1, respectively. The hoop strain percentage of the surface strain was 40 percent on Small Face 1 at the time of the first rotation. The Large Face 1 hoop strain percentages of the surface strain were 83 percent and 78 percent at the first two rotations.

- Using measured internal and external concrete expansion data throughout the deterioration program, measured crack widths and lengths throughout the deterioration program, and from petrography analysis of concrete cores taken from the specimens after they were structural tested, the three groups of tested specimens were categorized as having varying levels of primarily ASR deterioration ranging from none to late stage and none/minimal levels of DEF.

CHAPTER 4:
ANALYSIS OF COLUMN SPLICE REGION

4.1 INTRODUCTION

Columns are vertical members designed to carry axial loads, shear forces, and bending moments. Events such as hurricanes can provide large flexural and shear demands to the columns that might lead to overturning or sidesway failure mechanisms. Because past research has shown that ASR may not significantly affect the compression strength, the LSC specimens are tested to evaluate the flexural capacity of the splice region, or more significantly, the tensile capacity of the spliced longitudinal reinforced section. If ASR and/or DEF deteriorate the bond strength of the splice region, the capacity of the column might be negatively impacted. Alternatively, if ASR and/or DEF do not affect the bond strength of the splice region, the capacity of the column may not be reduced.

In this work, the analytical strength of the splice region and end region is calculated using code-based development length calculations for the bars being spliced and flexure theory for reinforced concrete sections. For a cantilevered column, the lateral force distribution is triangular. The experimental testing was carried out with a four-point and three-point test setup. The four-point test setup imitates an overturning moment near the base of a column; however, it provides a conservative constant moment across the splice length instead of the triangular moment distribution. The three-point test was designed to create an unrealistic high demand on the splice region to intentionally try to promote bond failure.

4.2 ANALYTICAL – MODEL FOR CAPACITY ANALYSIS USING FLEXURE THEORY

4.2.1 Objectives

The objectives of the analytical program are:

- Develop an analytical model to estimate the strength-deformation characteristics of a column lap splice region and its effect on the overall structural capacity of the column.
- Calibrate the analytical model with test results from the four-point and three-point tests of the two undamaged control specimens and the varying degrees of damage from six deteriorated specimens with ASR/DEF deterioration.

4.2.2 Modeling Assumptions

The following assumptions were made to use an analytical methodology based on bending theory:

- Plane sections remain plane (compatibility).
- The reinforcing steel is perfectly bonded with the surrounding concrete, which means the strain in the steel is equal to the strain in the surrounding concrete (compatibility).
- Both the concrete and reinforcing steel are assumed to behave linearly in the elastic region according to Hooke's Law (constitutive law) and the stress-strain relationship of the reinforcing steel is modeled as elastic—perfectly plastic.
- The reinforcing steel develops strength proportional to the ratio of the embedment length provided to the development length required.
- The concrete is neglected in tension after it has cracked so that the load is redistributed to the reinforcement.
- Concrete crushes at a compressive strain of 0.003 (ε_{cu}) as AASHTO LRFD (2010) and ACI 318 (2008) have specified.

4.2.3 Splice Capacity Model

A capacity model for the splice region of an RC column was developed using the basic laws of mechanics with the assumptions described in Section 4.2.2 and the additional condition of equilibrium, the sum of sectional forces and moments must balance. Figure 4-1 shows the strains, stresses, and resultant forces for the three different limit states of structural flexural capacity:

- At first crack in the concrete.
- When the tensile reinforcing steel first yields.
- At ultimate when governed by crushing of the concrete in compression.

The axial load from the PT strands representative of in-service loading was accounted for in the flexural capacity, thus shifting the neutral axis down and creating a larger compression region. The scale for the figure is not consistent due to the drastic difference in values. Therefore, the strains and stresses at first cracking are illustrated twice as large as they would with the same scale used with the other two limits. The large stress from the steel is illustrated at 75 percent the scale of the concrete stress.

The height (h) and width (b) of the section and the depths to the tension reinforcement (d) and compression (d′) reinforcement are shown in the figure. The depth of the neutral axis is c, and a is the depth of Whitney's stress block. The strains in the concrete (ε_c), tension steel, (ε_s), and compression steel (ε'_s) are shown with the stresses from those strains, concrete (f_c), tension steel (f_s), and compression steel (f'_s) are also shown. The tensile stress in the concrete (f_r) is present until first cracking of the concrete. The resultant forces are found from the stresses from the concrete in compression (C_c), concrete in tension (T_c), tension steel (T_s), and compression steel (C'_s).

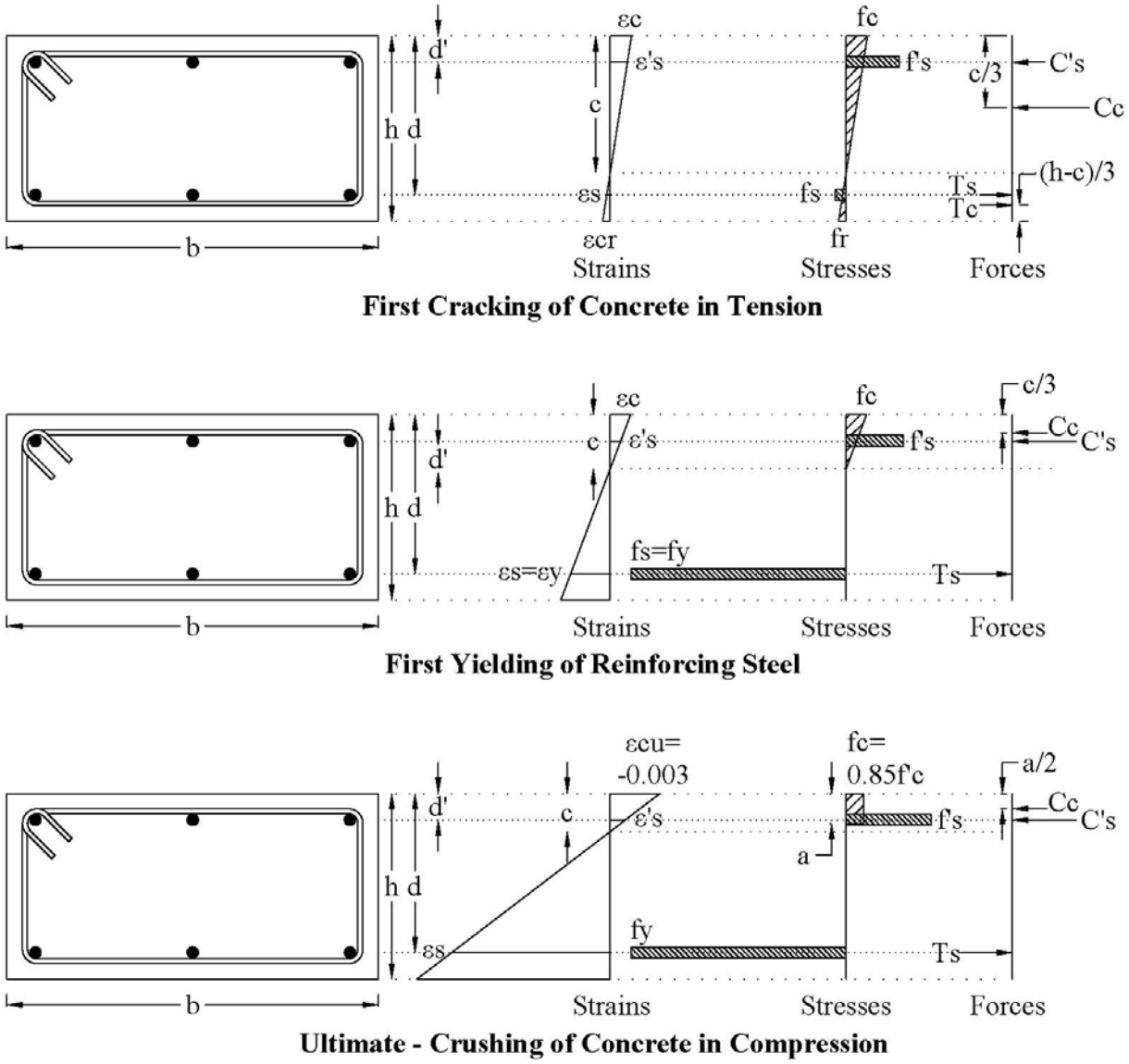

Figure 4-1. Strains, Stresses, and Resultant Forces at Three Flexural Limits.

Up to first cracking of the concrete, the entire section contributes to resisting the external load. The limiting criterion is based upon the ability of the concrete to resist tensile loads. The tensile stress in concrete or rupture modulus, f_r, is usually calculated as a function of the 28-day cylinder compressive strength, f'_c. Eq. 4-1 shows the equation for f_r at first cracking according to ACI 318 (2008). AASHTO (2010) lists 0.24 as the coefficient to account for the different units (ksi). For

a f_c' of 5000 psi, the ACI 318 gives a value of 530 psi and the ASSHTO gives a value of 537 psi. Note that these equations are only good for the units listed.

$$f_r = 7.5\sqrt{f_c'} \quad \text{(Eq. 4-1)}$$

Eq. 4-2 shows the modulus of elasticity (E_c in psi) for the normal weight concrete (ACI318-08). Once again, AASHTO gives a similar value with slight differences in the coefficient from the unit difference.

$$E_c = 57000\sqrt{f_c'} \quad \text{(Eq. 4-2)}$$

Given the concrete tensile stress and the modulus of elasticity, the tensile strain at the bottom of the concrete at first cracking can be calculated as follows:

$$\varepsilon_{cr} = \frac{f_r}{E_c} \quad \text{(Eq. 4-3)}$$

For the second limit state where the tension reinforcement first yields at the stress of f_y, the strain in the reinforcing steel is found from Hooke's Law as:

$$\varepsilon_{sy} = \frac{f_y}{E_s} \quad \text{(Eq. 4-4)}$$

At the ultimate limit state, the concrete crushes in compression when the strain is -0.003 (ε_{cu}) (ACI 318-08 and AASHTO 2010). The compression strains are negative for the sign convention used in this report.

The analytical model is developed so that it can be used at any cross section of the column specimen. First, the area of the steel reinforcement within the splice region is calculated. Since the bars are spliced, the simple multiplication of the number of bars times the area of each bar is not sufficient. The development length for the spliced bar is first calculated and used to find the effective area of the steel at each section. The number and location of the bars is first discussed, then the application of the development length.

Figure 4-2 shows an elevation view of the reinforcement in the LSC specimens. The stirrups are not shown for clarity. Figure 4-3 shows the cross section of the LSC specimens in the splice region. The splice bars, illustrated as solid circles in the cross section views, are located in the splice region and the end region. The straight bars, illustrated as open circles, are only located in the end region (Figure 4-4). Figure 4-5 illustrates where the splice and straight bars begin and end. Note that Figure 4-5 depicts that the splice and straight bars are on top of each other to clearly distinguish between bars. Figure 4-3 and Figure 4-4 properly illustrate these bars are side by side. The longitudinal bars are #11s; these bars are spliced with three more #11 bars both on the top (compression) and bottom (tension) during the four-point load test. The straight bars were placed in the specimen to enhance the specimen strength away from the splice region. However, these bars do not contribute toward the specimen's strength in the splice region. Chapter 2 provides a more thorough description of the reinforcement including the stirrups.

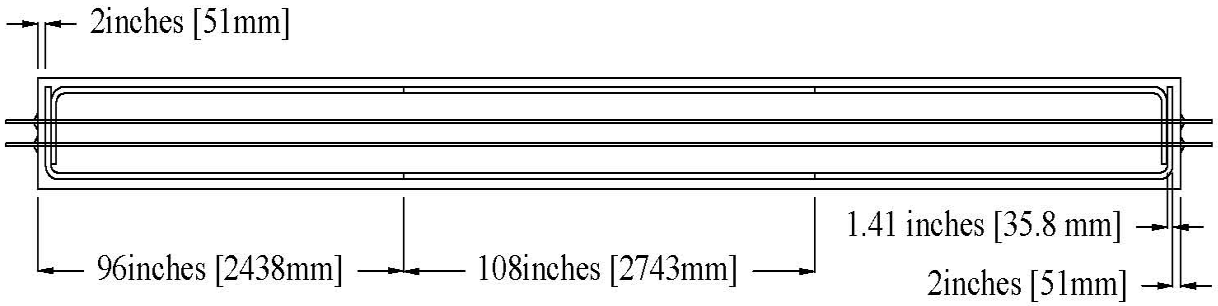

Figure 4-2. Reinforcement Elevation View.

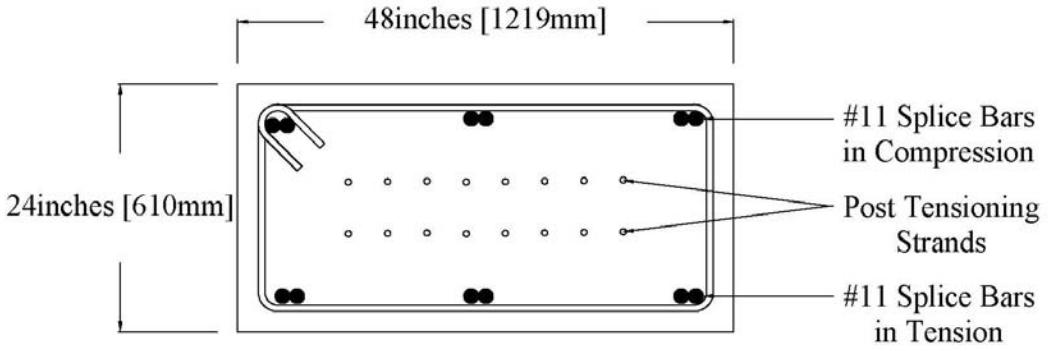

Figure 4-3. Cross Section at Splice Region.

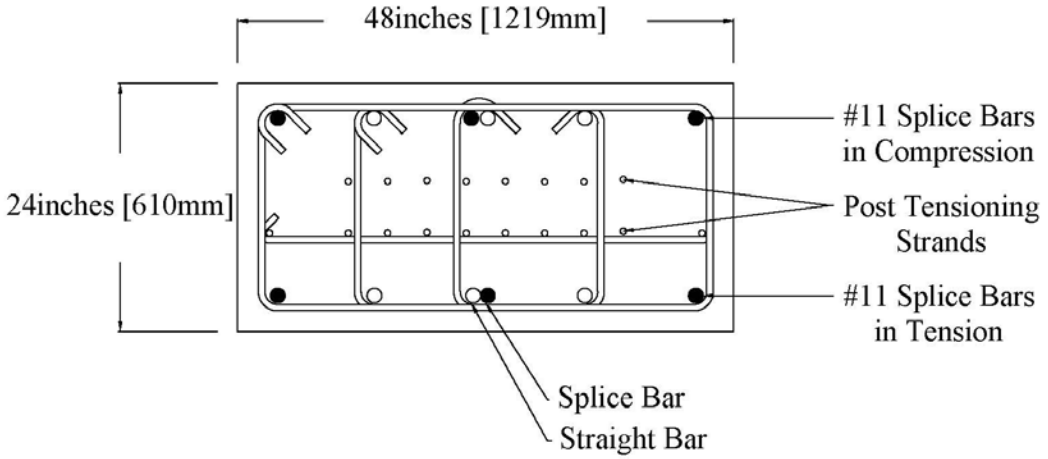

Figure 4-4. Cross Section at End Region.

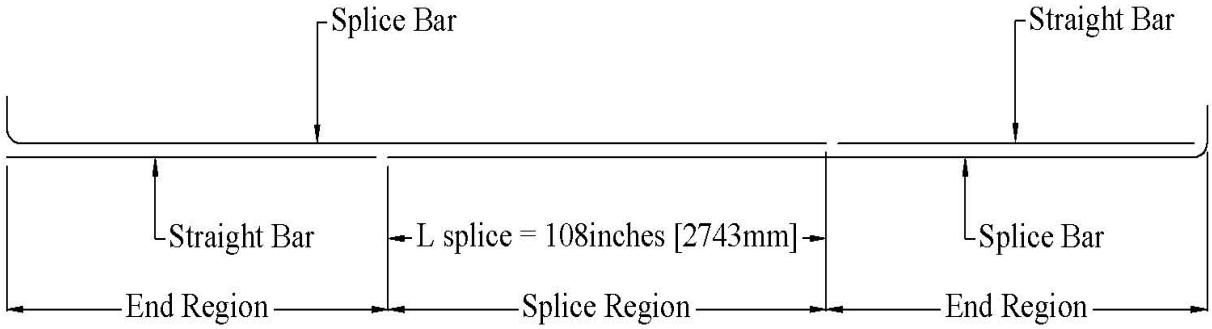

Figure 4-5. Longitudinal Section of Tension Reinforcing Steel.

AASHTO (2010) gives the development length for reinforcing steel in tension (L_d) as:

$$L_d = \frac{1.25 A_b f_y}{\sqrt{f'_c}} \text{ but not less than } 0.4 d_b f_y \quad \text{(Eq. 4-5)}$$

where A_b is the area of the steel bar (inches^2) and d_b is the diameter of the steel bar (inches).

The development length for reinforcing steel in compression (L_{dc}) is given below (AASHTO 2010) as:

$$L_{dc} \geq \frac{0.63 d_b f_y}{\sqrt{f'_c}} \text{ or } 0.3 d_b f_y \quad \text{(Eq. 4-6)}$$

AASHTO (2010) gives the development length for a hooked bar with a f_y greater than or equal to 60 ksi (414 MPa) as:

$$L_{dh} = \frac{38.0 d_b}{\sqrt{f'_c}} \frac{f_y}{60} \quad \text{(Eq. 4-7)}$$

These development length calculations were used in conjunction with the reinforcement layout to find the effective steel area at the critical sections, and thus the capacity at those sections. The effective area is found assuming the steel has no contribution at the bar end and linearly increases in contribution up to the development length of the bar, where it then has full contribution (A_b). Figure 4-6 shows the linear increase in the effective bar area at the splice region. The length of the splice, L_{splice} is 108 inches (2743) and x_{splice} the distance from the splice end to the section in question. Figure 4-7 shows the linear increase in the effective bar area at the end region. The length of the straight bar, $L_{straight\ bar}$, is 94 inches (2388 mm), which accounts for the 2-inch (50.8mm) cover and $x_{straight\ bar}$ is the distance from the end of the straight bar to a particular section. The splice bars are hooked at the end, not in the splice (see Figure 4-5). Therefore, in the splice

region, these bars are called Splice Bar 1 and Splice Bar 2; in the end region, they are referred to as the Hooked Bar.

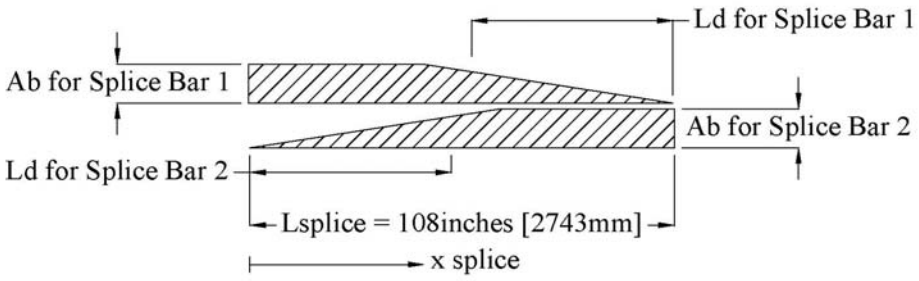

Figure 4-6. Linear Increase in Effective Area at the Splice Region.

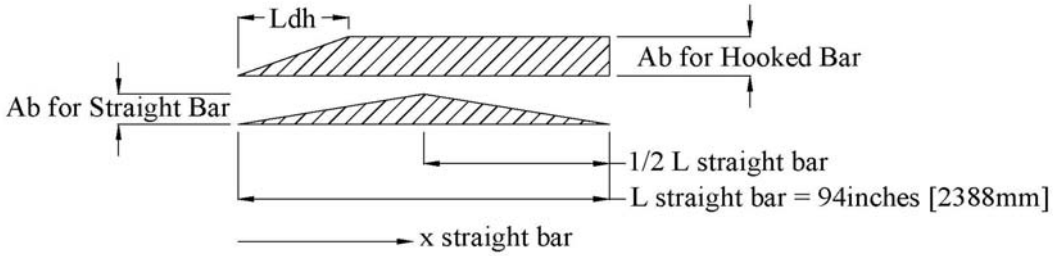

Figure 4-7. Linear Increase in Effective Area at the End Region.

The total effective reinforcement area at each section for the tension steel ($A_{s,eff}$) is then calculated by summing the contributions of each bar. Eqs. 4-8 through 4-10 calculate the effective steel area in tension Splice Bar 1 and Splice Bar 2 (A_{s1} and A_{s2}). The sum of the effective tension steel in the splice region is $A_{s,efff,splice}$. The total effective reinforcement area at the splice ends is calculated with x_{splice} = 0 inches and x_{splice} = 108 inches (2743 mm). Since there are three bars spliced with three others at each steel layer, the total effective reinforcement area is three times the area of each bar, A_b, at the splice ends and is more than $3A_b$ at every other section within the splice length.

$$A_{s1} = \begin{cases} 3A_b, & x_{splice} \le L_{splice} - L_d \\ 3A_b\left[1 - \frac{(x_{splice} - (L_{splice} - L_d))}{L_d}\right], & x_{splice} \ge L_{splice} - L_d \end{cases} \quad \text{(Eq. 4-8)}$$

$$A_{s2} = \begin{cases} \frac{3A_b(x_{splice})}{L_d}, & x_{splice} \le L_d \\ 3A_b, & x_{splice} \ge L_d \end{cases} \quad \text{(Eq. 4-9)}$$

$$A_{s,eff,splice} = A_{s1} + A_{s2} \quad \text{(Eq. 4-10)}$$

Eqs. 4-11 through 4-13 calculate the effective steel area in the compression Splice Bar 1 and Splice Bar 2 (A'_{s1} and A'_{s2}) then are summed to give the total effective area in the compression bars at the splice region $A'_{s,eff,splice}$.

$$A'_{s1} = \begin{cases} 3A_b, & x_{splice} \le L_{splice} - L_{dc} \\ 3A_b[1 - \frac{(x_{splice} - (L_{splice} - L_{dc}))}{L_{dc}}], & x_{splice} \ge L_{splice} - L_{dc} \end{cases} \quad \text{(Eq. 4-11)}$$

$$A'_{s2} = \begin{cases} \frac{3A_b(x_{splice})}{L_{dc}}, & x_{splice} \le L_{dc} \\ 3A_b, & x_{splice} \ge L_{dc} \end{cases} \quad \text{(Eq. 4-12)}$$

$$A'_{s,eff,splice} = A'_{s1} + A'_{s2} \quad \text{(Eq. 4-13)}$$

Eqs. 4-14 through 4-16 calculate the effective areas of the hooked bar ($A_{s,hooked}$) and straight bar ($A_{s,straight\ bar}$) in tension are summed to give the effective tension steel area at the end region, $A_{s,efff,end}$. Since the straight bar has a length of 94 inches (2388 mm), it is shorter than twice the development length for the tension bars. Therefore, $A_{s,straight\ bar}$ is never $3A_b$.

$$A_{s,hooked} = \begin{cases} \frac{3A_b(x_{straight\ bar})}{L_{dh}}, & x_{straight\ bar} \le L_{dh} \\ 3A_b, & x_{straight\ bar} \ge L_{dh} \end{cases} \quad \text{(Eq. 4-14)}$$

$$A_{s,straight\ bar} = \begin{cases} \frac{3A_b(x_{straight\ bar})}{L_d}, & x_{straight\ bar} \le \frac{1}{2} L_{straight\ bar} \\ \frac{3A_b}{L_d}(L_{straight\ bar} - x_{straight\ bar}), & x_{straight\ bar} \ge \frac{1}{2} L_{straight\ bar} \end{cases} \quad \text{(Eq. 4-15)}$$

$$A_{s,eff,end} = A_{s,hooked} + A_{s,straight\ bar} \quad \text{(Eq. 4-16)}$$

Eqs. 4-17 through 4-19 calculate the effective areas of the hooked bar ($A'_{s,hooked}$) and straight bar ($A'_{s,straight\ bar}$) in tension are summed to give the effective tension steel area at the end region, $A'_{s,eff,end}$. Since L_{dc} is shorter than L_d, $A'_{s,straight\ bar}$ does reach $3A_b$.

$$A'_{s,hooked} = \begin{cases} \frac{3A_b(x_{straight\ bar})}{L_{dh}}, & x_{straight\ bar} \le L_{dh} \\ 3A_b, & x_{straight\ bar} \ge L_{dh} \end{cases} \quad \text{(Eq. 4-17)}$$

$$A'_{s,straight\ bar} = \begin{cases} \frac{3A_b(x_{straight\ bar})}{L_{dc}}, & x_{straight\ bar} \le L_{dc} \\ 3A_b, & L_{dc} \le x_{straight\ bar} \le L_{straight\ bar} \\ 3A_b\left[1 - \frac{(x_{straight\ bar} - (L_{straight\ bar} - L_{dc}))}{L_{dc}}\right], & x_{straight\ bar} \ge L_{straight\ bar} - L_{dc} \end{cases} \quad \text{(Eq. 4-18)}$$

$$A'_{s,eff,end} = A'_{s,hooked} + A'_{s,straight\ bar} \quad \text{(Eq. 4-19)}$$

Figure 4-8 shows the effective steel areas at every location of the LSC specimens using the equations above. The figure shows the effective steel area is 3 A_b at the splice ends. Since the compression steel has a shorter development length, the linear increase in effective area has a larger slope. There is a change in slope at the end region where the hooked bar is fully developed and the straight bar continues to develop.

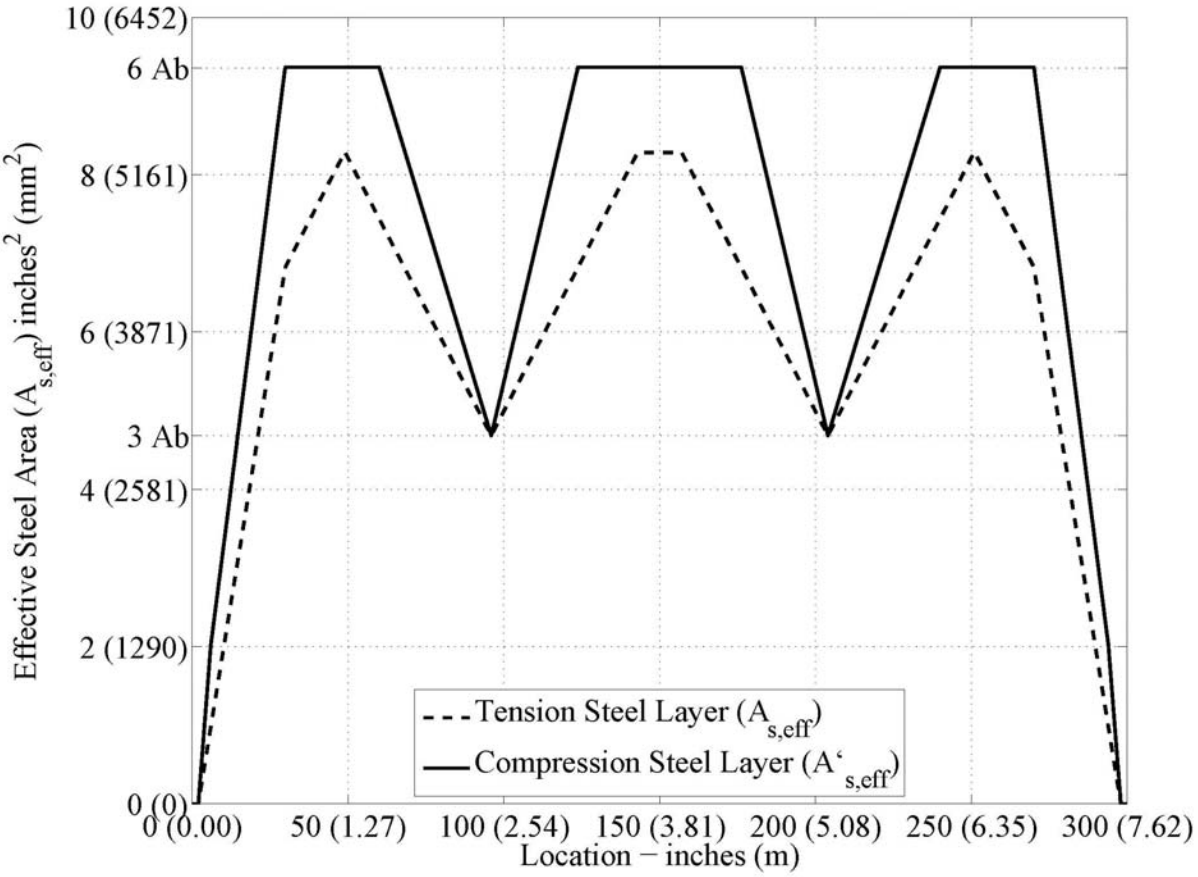

Figure 4-8. Effective Steel Areas along the Length of the LSC Specimens.

4.2.4 Iterative Analytical Model for Flexural Capacity with Constant Axial Loading

This section discusses equations used for concrete flexural capacity. The depth of the neutral axis, c, is found such that the sum of the forces in the section equals the axial load from the post-tensioning representing a column service load.

The strain at the top section of concrete, ε_c, is found from similar triangles for the cracking and yield limit states and is given as ε_{cu} for the ultimate limit state (Figure 4-1). Eq. 4-20 is used when the concrete first cracks, where ε_{cr} is given in Eq. 4-3.

$$\varepsilon_c = \frac{-\varepsilon_{cr}}{h-c} c \qquad \text{(Eq. 4-20)}$$

At first yielding of the longitudinal tension reinforcement, ε_c is found as function of the yield strain of the tension reinforcement, ε_{sy}, from Eq. 4-4.

$$\varepsilon_c = \frac{-\varepsilon_{sy}}{d-c} c \quad \text{(Eq. 4-21)}$$

The concrete stress in the compression region at the first and second limit states, first cracking of concrete and first yielding of steel, is calculated below according to Hooke's Law:

$$f_c = \varepsilon_c E_c \quad \text{(Eq. 4-22)}$$

When the concrete compression strain reaches ε_{cu}, the effective concrete stress is found using the Whitney's Stress Block approximation shown below, noting that the stress is negative in compressive.

$$f_c = -0.85\, f'_c \quad \text{(Eq. 4-23)}$$

The force from the concrete, C_c, when the stress is linearly proportional to the strain (triangular), which occurs before ε_c reaches ε_{cu}, is found below.

$$C_c = \frac{1}{2}(f_c\, c)b \quad \text{(Eq. 4-24)}$$

At ultimate, when the Whitney's Stress Block assumption is used (Wight and MacGregor 2009), the concrete compression force is found as follows:

$$C_c = 0.85 f'_c\, a\, b \quad \text{(Eq. 4-25)}$$

$$a = \beta_1 \mathbf{c} \quad \text{(Eq. 4-26)}$$

where coefficient, β_1 is found as (ACI318-08):

$$\beta_1 = 0.85 - 0.05\left(\frac{f_c' - 4000}{1000}\right) \text{ for } 4000 < f_c' < 8000 \text{ psi} \quad \text{(Eq. 4-27)}$$

Note that β_1 has a minimum value of 0.65 and a maximum value of 0.85. Therefore, β_1 is 0.65 for f_c' values greater than or equal to 8000 psi and 0.85 for f_c' values less than or equal to 4000 psi. Eq. 4-27 only works with f_c' in psi.

Prior to cracking of the concrete in tension, the concrete tension force is determined using Hooke's Law. Eq. 4-28 shows the expression for the concrete tension force at first cracking.

$$T_c = \frac{1}{2}[f_r(h - c)]b \quad \text{(Eq. 4-28)}$$

The strains in the tension reinforcing steel, ε_s, and compression reinforcing steel, ε_s', at first cracking are given in Eq. 4-29 and Eq. 4-30, respectively, from similar triangles using the assumption that plane sections remain plane.

$$\varepsilon_s = \frac{-\varepsilon_c}{c}(d - c) \quad \text{(Eq. 4-29)}$$

$$\varepsilon_s' = \frac{\varepsilon_c}{c}(c - d') \quad \text{(Eq. 4-30)}$$

Note that the negative sign in Eq. 4-29 results in a positive tensile strain.

The stresses in the tension reinforcing steel, f_s, and compression reinforcing steel, f_s', at first cracking are found from Hooke's Law and given in Eqs. 4-31 and 4-32, respectively. For the

other limit states, the reinforcing steel is modeled as elastic-perfectly plastic and the strength is limited to f_y.

$$f_s = \varepsilon_s E_s \leq f_y \quad \text{(Eq. 4-31)}$$

$$f'_s = \varepsilon'_s E_s \leq f_y \text{ and } \geq -f_y \quad \text{(Eq. 4-32)}$$

The force from the tension reinforcing steel is found from Eq. 4-33 multiplied by $A_{s,eff}$ as shown below. Since this steel is in the tension region, there is no adjustment necessary for the concrete compression force beyond cracking. The first equation in Eq. 4-33 was used for the first limit state when there is a tensile concrete force below the neutral axis. The steel force subtracts out the force in the concrete calculated at the location of the steel. The second equation was used right after cracking when the tensile concrete force equals zero. The general variable, $A_{s,efff}$, is used for both $A_{s,efff,splice}$ and $A_{s,efff,splice}$. This generalization is also used for the compression steel.

$$T_s = \begin{cases} (f_s - \varepsilon_s E_c)A_{s,eff}, & T_c < 0 \\ f_s A_{s,eff}, & T_c = 0 \end{cases} \quad \text{(Eq. 4-33)}$$

Similarly, the force from the compression reinforcing steel is found using the stress calculated in Eq. 4-32 multiplied by $A'_{s,eff}$ as shown below in Eq. 4-34. The equation subtracts the force from the concrete at the location of the steel already accounted for in the concrete force. Researchers used the first part of the equation when the stress is linearly proportional to the strain. They used the second part when the Whitney's Stress Block assumption was applied. When the top layer of steel is below a, the concrete force does not include the steel area and can be neglected in these equations.

$$C'_s = \begin{cases} (f'_s - \varepsilon_s E_c)A'_{s,eff}, & d' < a, \varepsilon_c < 0.003 \\ (f'_s - .85f'_c)A'_{s,eff}, & d' < a, \varepsilon_c \geq 0.003 \\ f'_s A'_{s,eff}, & d' \geq a \end{cases} \quad \text{(Eq. 4-34)}$$

The axial load at a given section is a sum of the compression and tension forces at that section. Eq. 4-35 is a summation of the forces in the section where the compression forces are negative and the tension forces are positive. Since the axial load is constant from the post-tensioning of the strands, the model is iterated with different values of c until P_{axial} reaches the desired value of post-tensioning force for equilibrium. The LSC specimens were initially post-tensioned to 580.5 kips (2582 kN) in compression, therefore the model was iterated until $P_{axial} = -580.5$ kips.

$$P_{axial} = C_c + T_c + C_s' + T_s \quad \text{(Eq. 4-35)}$$

The total moment capacity of the column section can next be calculated by summing the section forces about the centroidal axis of the section as shown below in Eqs. 4-36 through 4-38 for first cracking ($M_{\text{total cap}_{cr}}$), first yield ($M_{\text{total cap}_{y}}$), and ultimate limit states ($M_{\text{total cap}_{ult}}$). The moments from the compression forces and tension forces are counterclockwise about the centroid; therefore, the negative sign is used in front of the compression forces counter the negative force value from equations listed above.

$$M_{\text{total cap}_{cr}} = -C_c\left(\frac{h}{2} - \frac{c}{3}\right) + T_c\left(\frac{h}{2} - \frac{h-c}{3}\right) - C_s'\left(\frac{h}{2} - d'\right) + T_s\left(d - \frac{h}{2}\right) \quad \text{(Eq. 4-36)}$$

$$M_{\text{total cap}_{y}} = -C_c\left(\frac{h}{2} - \frac{c}{3}\right) - C_s'\left(\frac{h}{2} - d'\right) + T_s\left(d - \frac{h}{2}\right) \quad \text{(Eq. 4-37)}$$

$$M_{\text{total cap}_{ult}} = -C_c\left(\frac{h}{2} - \frac{\beta_1 c}{3}\right) - C_s'\left(\frac{h}{2} - d'\right) + T_s\left(d - \frac{h}{2}\right) \quad \text{(Eq. 4-38)}$$

The section curvature, ϕ, (or slope of the strain diagram) at each limit state is calculated from similar triangles as follows:

$$\phi = \frac{\varepsilon_c}{c} \quad \text{(Eq. 4-39)}$$

Figure 4-9 shows the calculated moment vs. curvature response of the LSS specimen section directly under actuator (or at the splice end) where the effective reinforcing steel area is $3A_b$ or 4.68 square inches (3019 mm^2), P_{axial} is −580.5 kips (−2582 kN), the design concrete compressive strength, f'_c, is 5.0 ksi (34 MPa), and the yield strength of the reinforcement, f_y, is taken as 70 ksi (483 Mpa) to account for over strength in Grade 60 steel. The three points are for the three limit states as discussed above: first cracking of the concrete, first yielding of the tension steel, and concrete crushing.

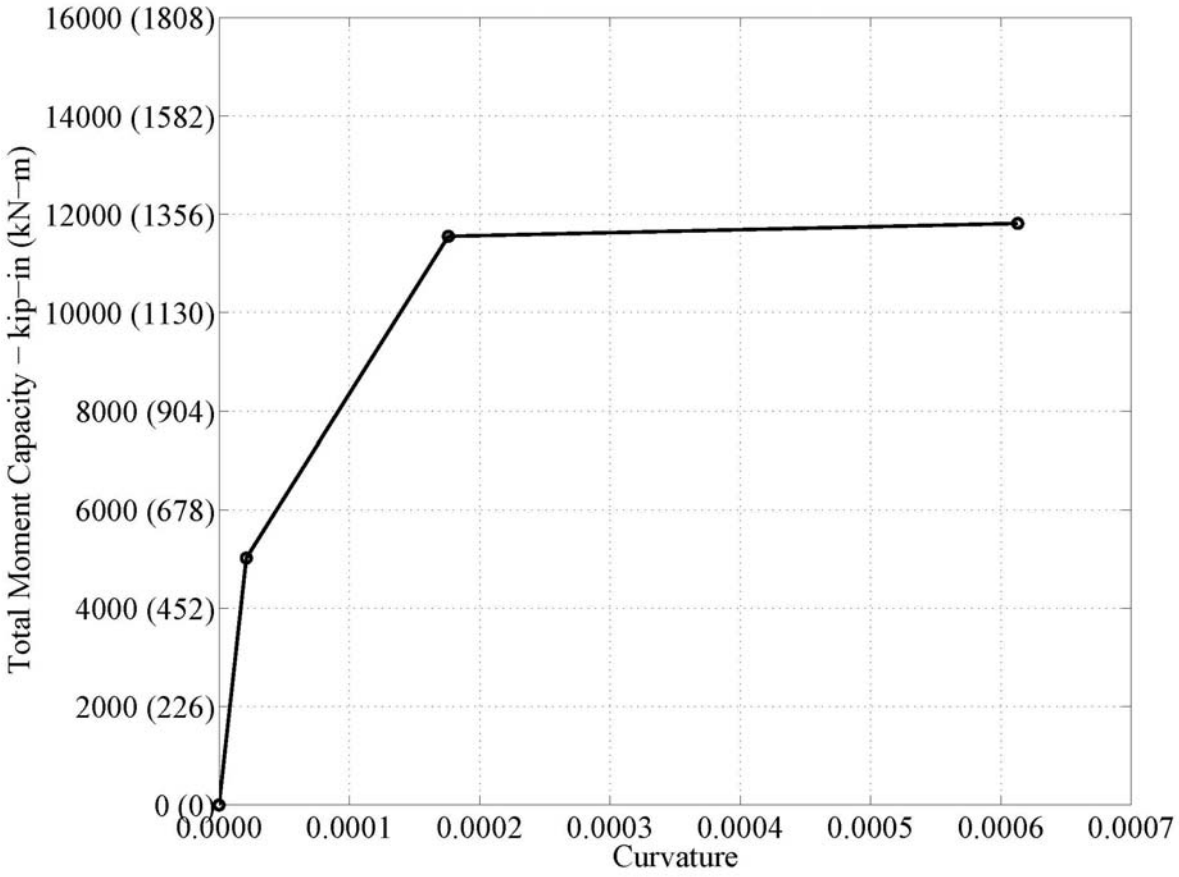

Figure 4-9. Moment vs. Curvature at the Section under the Actuator.

4.3 ANALYTICAL PREDICTIONS

4.3.1 Four-Point Test Predictions

The moment calculated from the iterative procedure listed above gives a total moment capacity for any given section. To compare the analytical capacity for the LSS specimens in the four-point load setup to the experimental demands from the actuator loading, the moment demands from the self-weight of the specimens must be considered, even though the self-weight moment is much smaller than the moment demand from actuators. Figure 4-10 shows the shear and moment diagram for the self-weight of the LSC specimens in the four-point test setup. The total length of the LSC specimen, L, is 300 inches (7620 mm). The distance from the support to the desired cross section is x_{supp} and x is the distance from the end to the cross section. These variables will be used in the deflection equations.

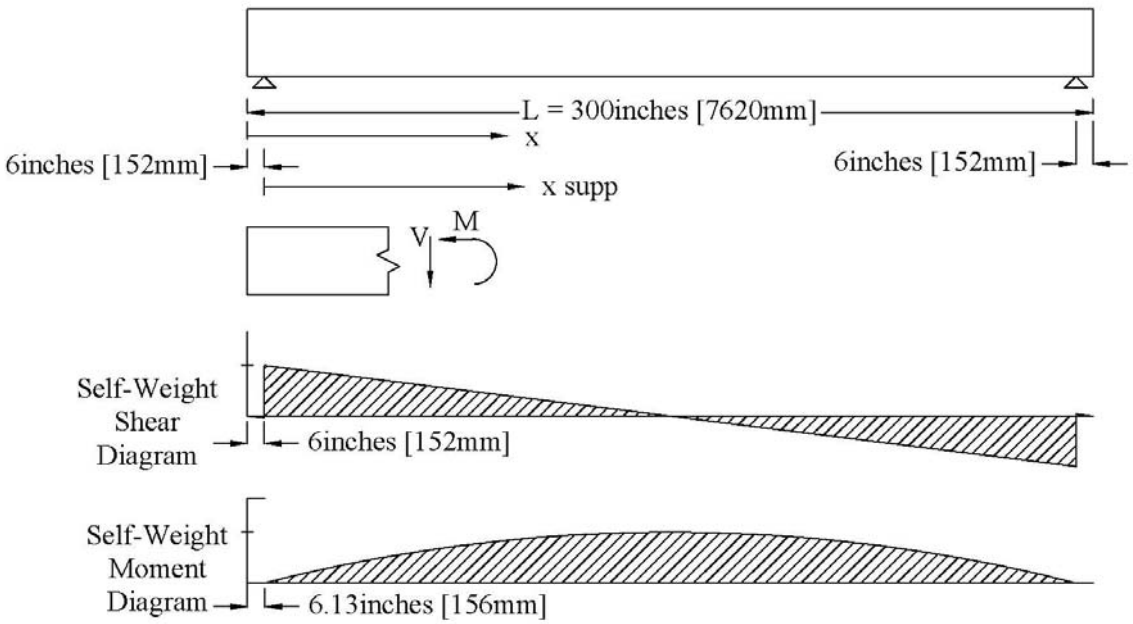

Figure 4-10. Shear and Moment Diagram for Self-Weight in the Four-Point Setup.

The moment from self-weight when the specimen is in the four-point setup ($M_{SW,4pt}$) is calculated as follows.

$$M_{SW,4pt} = \frac{w}{2}(L * x_{supp} - x^2) \quad \text{(Eq. 4-40)}$$

The values for the variables L, x_{supp}, and x are illustrated in Figure 4-10. The cross sectional weight per inch of the specimen, w, is calculated using the actual dimensions for the specimens in this research (24 inches by 48 inches) below:

$$w = \left(0.15\frac{kips}{ft^3}\right)(24 \cdot 48\ in^2)\left(\frac{ft^3}{12^3 inches^3}\right) = 0.1\frac{kips}{inch}\ \ (0.018\frac{kN}{mm}) \quad \text{(Eq. 4-41)}$$

Figure 4-11 shows the shear and moment diagrams from the actuator loading in the four-point test setup. In this test setup, the moment is constant along the splice length and is actuator load times L_{supp}, where L_{supp} is the distance between the support and actuator. The distance between each support is L_s.

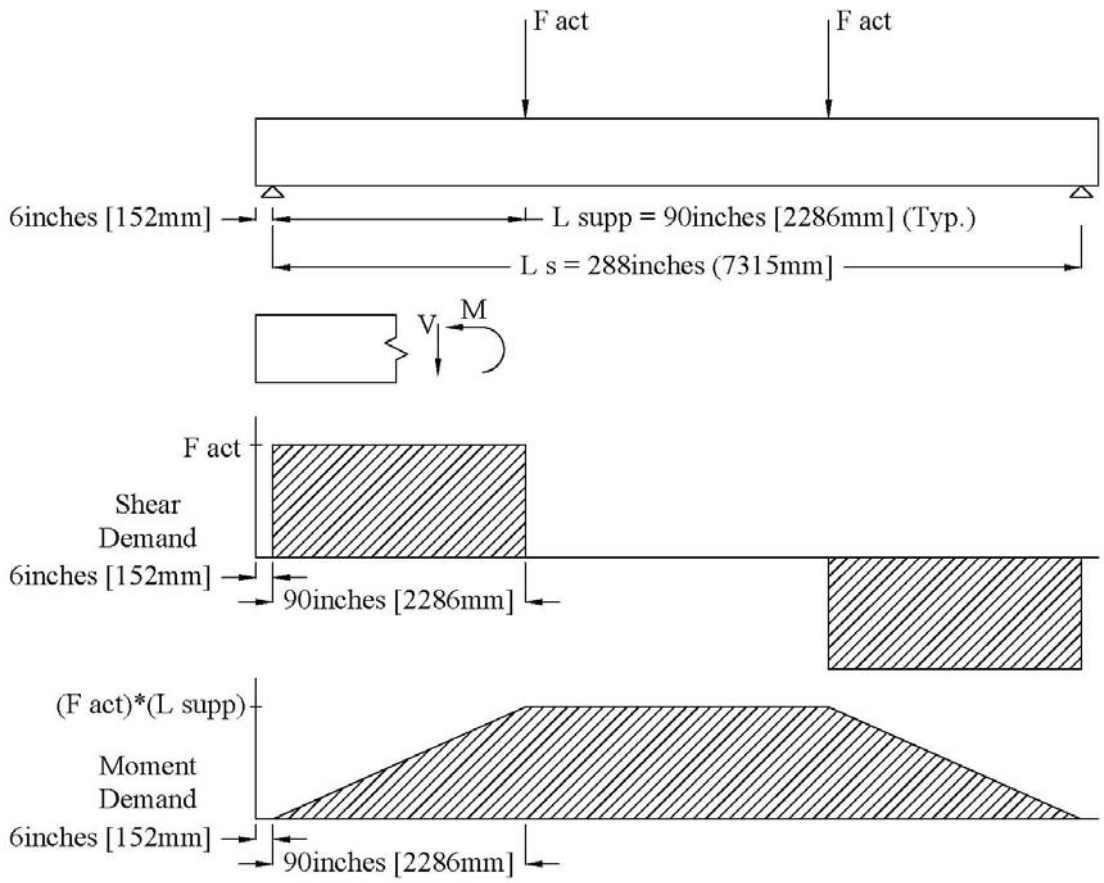

Figure 4-11. Four-Point Test Shear and Moment Diagram.

Eq. 4-42 calculates the individual actuator loads for the four-point setup, $F_{act,4pt}$, located at the critical splice end sections, are found from the total moment capacity of the section, the moment due to self-weight at that location, and the distance between the support and actuator. $M_{total\ cap}$ is used as a general variable for the total moment capacity at each limit state or between limit states.

$$F_{act,4pt} = \frac{M_{total\ cap} - M_{SW,4pt}}{L_{supp}} \quad \text{(Eq. 4-42)}$$

Figure 4-12 shows the ultimate moment capacity and demand from the actuator at each section of the LSC specimen. The moment capacity shown is the difference between the total moment capacity and the moment the specimen resists from the self-weight. The highest moment

demand the specimen can resist until failure (concrete crushing) is located at the splice end (section under actuator) and is 10926 kip-inches (1234 kN-m). The load from each actuator equals the moment divided by the moment arm. For the four-point setup, the moment arm equals the distance between the support and the actuator which is 90 inches (2286 mm). Therefore, expected actuator load at failure is 121 kips (538 kN).

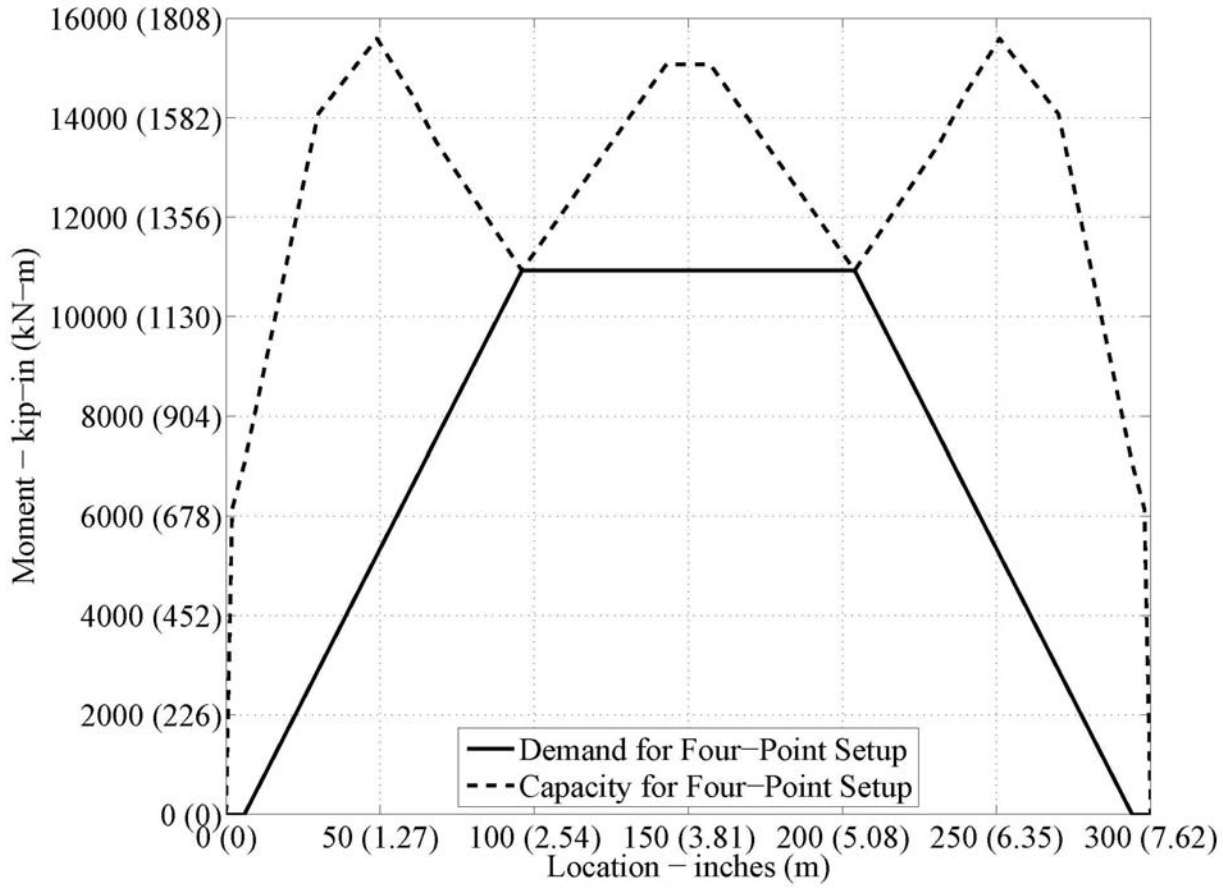

Figure 4-12. Ultimate Moment Capacity vs. Demand for Four-Point Setup.

Next the deformations in the specimens at first cracking, first yield and ultimate limit states are discussed below. Eq. 4-43 is used to find the elastic deflection of the specimen at any point between the actuator loads (Δ_{4pt}).

$$\Delta_{4pt} = \frac{F_{act,4pt}\, L_{supp}}{6\, E_c\, I}\left(3L_s x_{supp} - 3L_s x_{supp}^2 - {L_{supp}}^2\right) \qquad \text{(Eq. 4-43)}$$

The values for the variables used in Eq. 4-43 are shown in Figure 4-10 and Figure 4-11. The value of the second moment of area, I, depends on the limit state; these equations are listed next. Note that this deflection equation is only used to calculate the elastic deformations. Plastic deformations can also occur when the specimens yields and another equation is used to determine the approximated plastic deformations, which will be listed later. These plastic deformations can be added to the elastic deformations to find total deformations at any cross section.

Figure 4-13 shows the specimen cross section dimensions and depths of each steel layer needed for the second moment of area calculation.

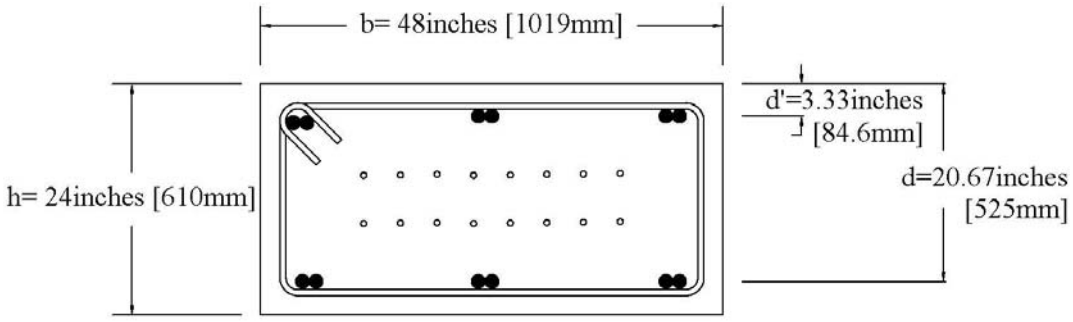

Figure 4-13. Cross Section at Splice Region with Steel Depths.

Neglecting the steel reinforcement, the second moment of area, I_g, can be found directly from the following column dimensions for the equations below:

$$I_g = \frac{1}{12} bh^3 \qquad \text{(Eq. 4-44)}$$

Considering the contribution of the steel reinforcement, the transformed second moment of area can be calculated as follows:

$$I_{gt} = \frac{1}{12} bh^3 + bh\left(\frac{h}{2} - y_t\right)^2 + A_{s,eff,tr}(d - y_t)^2 + A'_{s,eff,tr}(d' - y_t)^2 \qquad \text{(Eq. 4-45)}$$

where y_t is calculated from the equation below.

$$y_t = \frac{\frac{bh^2}{2} + A_{s,eff,tr}(h-d) + A'_{s,eff,tr}(h-d)}{bh + A_{s,eff,tr} + A'_{s,eff,tr}} \quad \text{(Eq. 4-46)}$$

The effective steel areas (Eqs. 4-8 through 4-19) are transformed to account for the different modulus of elasticity between the steel and concrete and calculated below:

$$A_{s,eff,tr} = (n-1)A_{s,eff} = (\frac{E_s}{E_c} - 1)A_{s,eff} \quad \text{(Eq. 4-47)}$$

$$A'_{s,eff,tr} = (n-1)A'_{s,eff} = \left(\frac{E_s}{E_c} - 1\right)A'_{s,eff} \quad \text{(Eq. 4-48)}$$

where n is the ratio of the modulus of elasticity of steel to concrete.

After first cracking of the concrete, the second moment of area at a critical section should not include any concrete area in tension or c, which is different than at the uncracked state. So the cracked second moment of area, I_{cr}, is calculated about c, for the cracked section instead of the centroid in Eq. 4-45.

$$I_{cr} = \frac{1}{12}bc^3 + bc\left(\frac{c}{2} - c\right)^2 + A_{s,eff,tr}(d-c)^2 + A'_{s,eff,tr}(c-d')^2 \quad \text{(Eq. 4-49)}$$

For loading beyond yielding of the reinforcing steel, linear deformations up to yielding and plastic deformations beyond yielding must be considered in determining the ultimate deflections for the specimens. For the plastic deformations, the plastic hinge rotation of a critical section is first calculated using Eq. 4-50.

$$\theta_p = (\phi_u - \phi_y)l_d \quad \text{(Eq. 4-50)}$$

The curvatures at ultimate and first yielding limit states, □$_u$ and □$_y$, are calculated using Eq. 4-39 with the corresponding values are each limit state. The plastic hinge length, l_d, is calculated using Eq. 4-51 (Mattock 1967).

$$l_d = (.5d + .05(z)) \quad \text{(Eq. 4-51)}$$

where z is the distance between the maximum moment and zero moment. For the four-point setup, z equals L_{supp} and 90 inches (2286 mm).

Assuming that the entirety of plastic deformations occur at the critical splice ends within the specimens (having the least effective steel area), the plastic deformations can be found from the plastic hinge rotations and the geometry of the test setup illustrated in Figure 4-14. Therefore, the total deflection at the ultimate limit, $\Delta_{4pt,u}$, is the sum of the elastic deflection up to first yield of the steel, $\Delta_{4pt,y}$, and the plastic deflection (see Eq. 4-52).

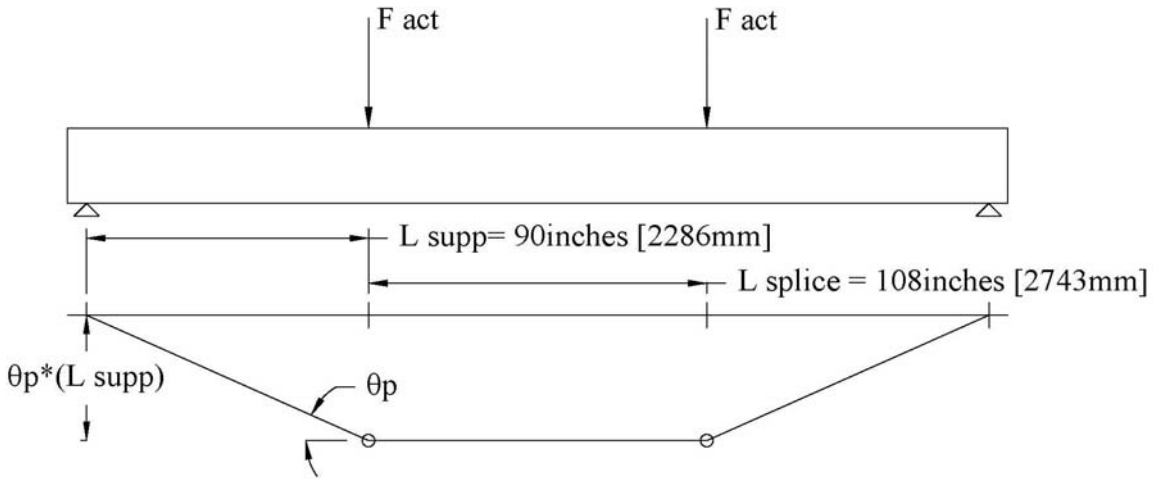

Figure 4-14. Plastic Hinge Rotation for Four-Point Setup.

$$\Delta_{4pt,u} = \theta_p L_{supp} + \Delta_{4pt,y} \quad \text{(Eq. 4-52)}$$

To calculate a complete moment vs. deformation response, different methods for computing the second moment of area beyond cracking were reviewed in the literature for computing deflections as listed above. The *PCI Design Handbook* that Naaman explains further (PCI 2004, Naaman 2004) recommends the use of I_g for the deflections up to the cracking moment. For deformations beyond cracking, up to when the tension steel yields, the cracked second moment of area, I_{cr}, is used. Figure 4-15 illustrates that difference between the load at cracking (L1) and the load beyond cracking is the load (L2) used with I_{cr} to compute the deflection between cracking and beyond cracking (Δ2). The total deflection (Δ1+ Δ2) is found by adding the deflection at cracking (Δ1) to the additional deflection (Δ2).

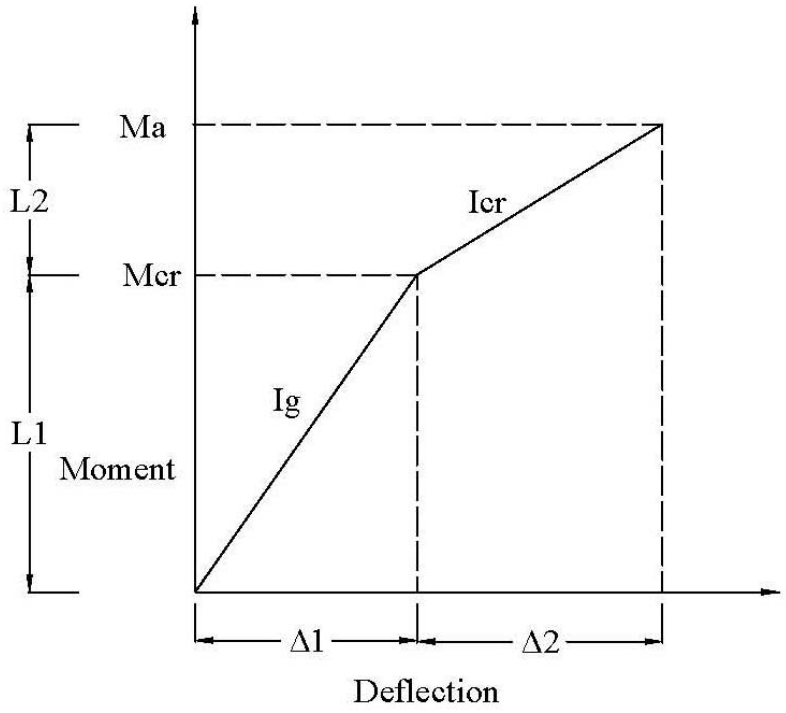

Figure 4-15. Bilinear Moment vs. Deflection Relation (Naaman 2004).

The bilinear method described from PCI and Naaman is used in conjunction with plastic analysis for the deflection at ultimate and is referred to as the Tri-Linear method for the three slopes used in the method. The linear deflection equation for the four-point test set up, Eq. 4-43, can be modified for Tri-Linear method. Eqs. 4-53 and Eq. 4-54 calculate the deflection at cracking using I_g ($\Delta_{4pt,cr,Ig}$) and at the yield limit ($\Delta_{4pt,y,Tri-Linear}$) for the Tri-Linear method. The load

from the actuator when the concrete begins to crack and when the steel yields is $F_{act,4pt_{cr}}$ and $F_{act,4pt_y}$ respectively. $F_{act,4pt_{cr}}$ and $F_{act,4pt_y}$ are calculated using Eq. 4-42 with $M_{total\ cap_{cr}}$ and $M_{total\ cap_y}$ respectively. When the steel begins to yield, the load at cracking is subtracted from the load at yielding and the deflection at cracking is added to the yield deflection to account for the deflection found in Eq. 4-53. The other variables are illustrated in Figure 4-10 and Figure 4-11.

$$\Delta_{4pt,cr,Ig} = \frac{F_{act,4pt_{cr}} L_{supp}}{6\, E_c\, I_g}(3L_s x_{supp} - 3L_s x_{supp}^2 - {L_{supp}}^2) \quad \text{(Eq. 4-53)}$$

$$\Delta_{4pt,y,Tri-Linear} = \frac{(F_{act,4pt_y} - F_{act,4pt_{cr}})L_{supp}}{6\, E_c\, I_{cr}}(3L_s x_{supp} - 3L_s x_{supp}^2 - {L_{supp}}^2) + \Delta_{cr,4pt,Ig} \quad \text{(Eq. 4-54)}$$

For finding beam deflections beyond cracking of the concrete, ACI-318 (2008) proposes an effective section moment of area, I_e, for reinforced concrete beams and states it is suitable for Class C (cracked) and Class T (transition) members as follows:

$$I_e = \left(\frac{M_{cr}}{M_a}\right)^3 I_g + [1 - \left(\frac{M_{cr}}{M_a}\right)^3] I_{cr} \quad \text{(Eq. 4-55)}$$

where M_{cr} is the total bending moment at cracking. M_{cr} is referred to as $M_{total\ cap_{cr}}$ in this report. M_a is the critical section bending moment at the step the deflection is computed which is referred to as the general $M_{total\ cap}$ in this report. Eq. 4-55 approximates the second moment of area of the section between I_g and I_{cr}. At and prior to first cracking, I_g can be used for the deflection calculation. Therefore the deflection at cracking using the I_e method from ACI 318 is the same as the Tri-Linear method described above (Eq. 4-53). However, after cracking according to ACI, the specimen deflection can be calculated as shown below:

$$\Delta_{4pt,y,Ie} = \frac{F_{act,4pt_y} L_{supp}}{6\, E_c\, I_e}(3L_s x_{supp} - 3L_s x_{supp}^2 - {L_{supp}}^2) \quad \text{(Eq. 4-56)}$$

Note that the load in Eq. 4-51 is simply $F_{act,4pt_y}$ and the load at first cracking, $F_{act.4pt_{cr}}$, does not need to be subtracted. This is a characteristic of the I_e formula. To calculate the ultimate deflection when there is plasticity in the critical section, the plastic deformations are calculated with Eq. 4-52 in the same way as explained previously.

Further calculations were done by the author to find that beams with no axial force have a constant neutral axis depth immediately after first cracking to first yielding of the tension reinforcement. This was found by computing the calculations presented in section 4.2.4 with a desired P_{axial} = 0 kips (0 kN) instead of 580.5 kips (2582 kN) in compression. In the case of no axial force, the Tri-Linear method and the I_e method provide the similar deflection approximations. The two methods have the same results at each data point for the Tri-Linear method; however for the I_e method, the points between first cracking and first yielding form a curve. Figure 4-16 compares the two methods with no axial load using the dimensions and reinforcement from the specimens in this research. Two arbitrary points between first cracking and first yielding were chosen for this illustration.

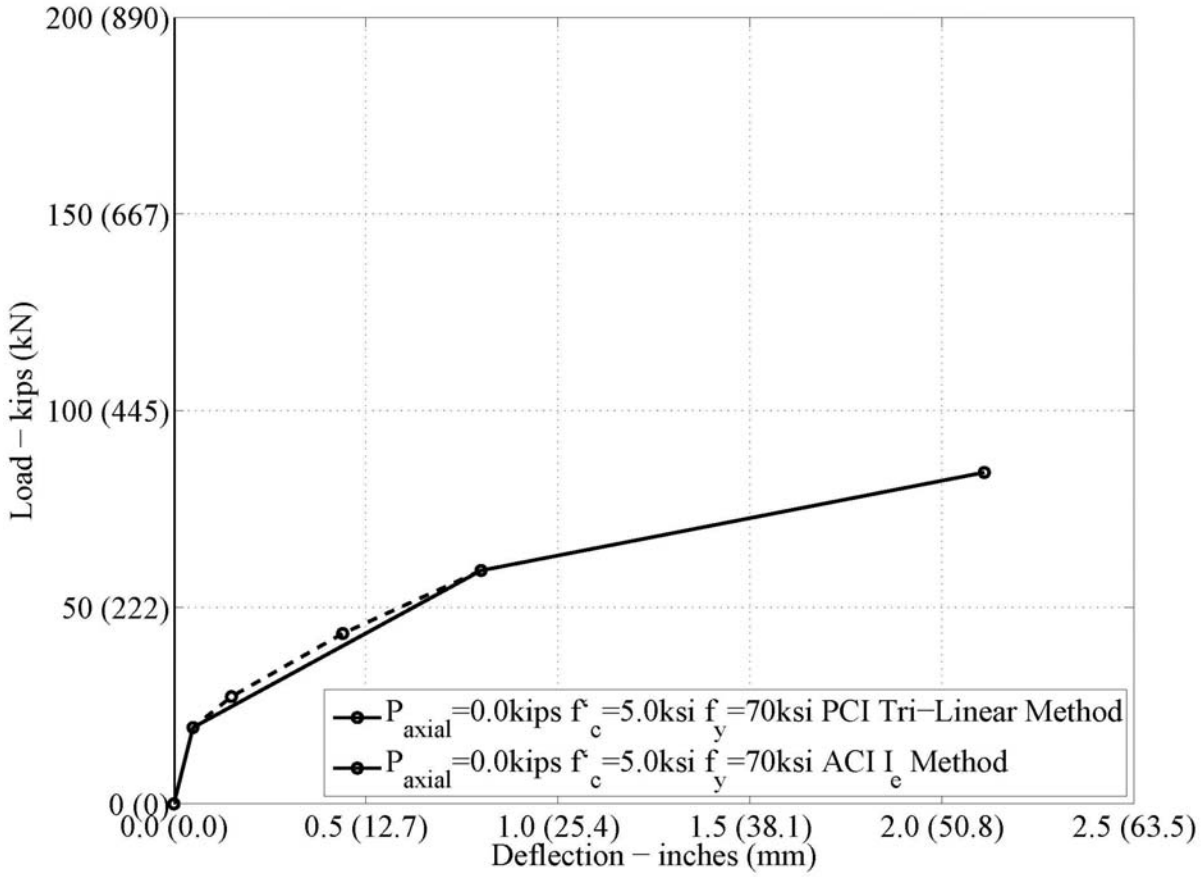

Figure 4-16. Load vs. Deflection for Tri-Linear and I_e Methods with No Axial Load.

However, in columns and beams with an axial force, the neutral axis is constantly changing between first cracking of the concrete and first yielding of the tension reinforcement. Therefore, I_{cr} is constantly changing from first cracking to first yielding of the tension reinforcement. To account for this varying stiffness between first cracking and yield in members with axial loading, the Step-by-Step I_{cr} method is proposed where I_{cr} is calculated at several different stages between first cracking and yielding. In this work, I_{cr} is calculated at three intermediate points between first cracking and yield based on the varying neutral axis depth, c, which can be calculated at each point based on bending theory and the required constant level of axial loading that was presented previously in section 4.2.4. Additional intermediate calculation points can be used; however, three points provided sufficient simplicity and accuracy for this research.

In this research, the developed analytical program first calculates the section curvatures at cracking and yielding using Eq. 4-39 and the appropriate c and strain values at each limit state.

Then the three intermediate curvatures ($\phi_{cr,y,i}$) are calculated using Eq. 4-57 where i equals the intermediate step and n equals the total number of intermediate steps desired. In our case, n=3 and there are three curvature equations for value of i: 1, 2, and 3.

$$\phi_{cr,y,i} = (\phi_y - \phi_{cr})\frac{i}{(n+1)} \quad \text{(Eq. 4-57)}$$

Since the strain at the top of the concrete section, ε_c, is not dependent on strain limits for the intermediate steps, a different equation, Eq. 4-53, was used for the three intermediate ε_c values ($\varepsilon_{c,i}$). The neutral axis depths at the intermediate steps, c_i, are iterated until the P_{axial} equaled the desired force.

$$\varepsilon_{c,i} = c_i \phi_{cr,y,i} \quad \text{(Eq. 4-58)}$$

Eq. 4-59 calculates the deflection at cracking in the Step-by-Step I_{cr} method ($\Delta_{4pt,cr,Step-by-Step\ Icr}$) using I_{gt} instead of I_g.

$$\Delta_{4pt,cr,Step-by-Step\ Icr} = \frac{F_{act,4pt_{cr}} L_{supp}}{6\, E_c\, I_{gt}}\left(3L_s x_{supp} - 3L_s x_{supp}^2 - {L_{supp}}^2\right) \quad \text{(Eq. 4-59)}$$

The deflection for the intermediate values was calculated using Eq. 4-60 where $F_{act,4pt_i}$ and I_{cr_i} are the load and second moment of area calculated at each step using Eq. 4-42 and Eq. 4-49. For the calculation of $\Delta_{cr,y,1}$, $F_{act,4pt_{cr}}$ must be used for $F_{act,4pt_{i-1}}$ since the force at cracking is the preceding force.

$$\Delta_{4pt,cr,y,i} = \frac{(F_{act,4pt_i} - F_{act,4pt_{i-1}})\, L_{supp}}{6\, E_c\, I_{cr_i}}\left(3L_s x_{supp} - 3L_s x_{supp}^2 - {L_{supp}}^2\right) \quad \text{(Eq. 4-60)}$$

The deflection at yielding is calculated using Eq. 4-61 where the preceding force that is subtracted from the load when steel yields is $F_{act,4pt_n}$ which is the last intermediate force. The second moment of area using the neutral axis at yielding, I_{cr_y}, is also used.

$$\Delta_{4pt,y,Step-by\ Step\ Icr} = \frac{(F_{act,4pt_y} - F_{act,4pt_n})\, L_{supp}}{6\, E_c\, I_{cr_y}} \left(3L_s x_{supp} - 3L_s x_{supp}^2 - {L_{supp}}^2\right) \quad \text{(Eq. 4-61)}$$

The deflection at ultimate for the Step-by-Step I_{cr} method was found using Eq. 4-47 which accounts for the plastic behavior in the critical hinge regions at the splice ends, as previously described.

Figure 4-17 shows the three methods described for calculating the force vs. deflection response for a sample specimen with constant axial loading in the four-point test configuration: Tri-Linear, I_e, and Step-by-Step I_{cr}. Since the ACI 318 I_e method can be used to find equivalent second moment of areas beyond first cracking and up to yielding of the reinforcing steel, three intermediate calculations between first cracking and yield were also computed similar to the Step-by-Step I_{cr} method and the resulting force-deflection calculations were joined linearly. In the Step-by-Step I_{cr} method, the deflection at each intermediate point and yield point depends on the force and deflection at the prior step. Therefore, the deflection at yield changes when the number of intermediate steps changes. However, with the I_e method, the deflection at yield is the same regardless of the number of intermediate steps since Eqs. 5-50 and 5-51 do not depend on the prior step, only the moment at cracking. The figure shows none of the methods calculate the same deflection at first yielding.

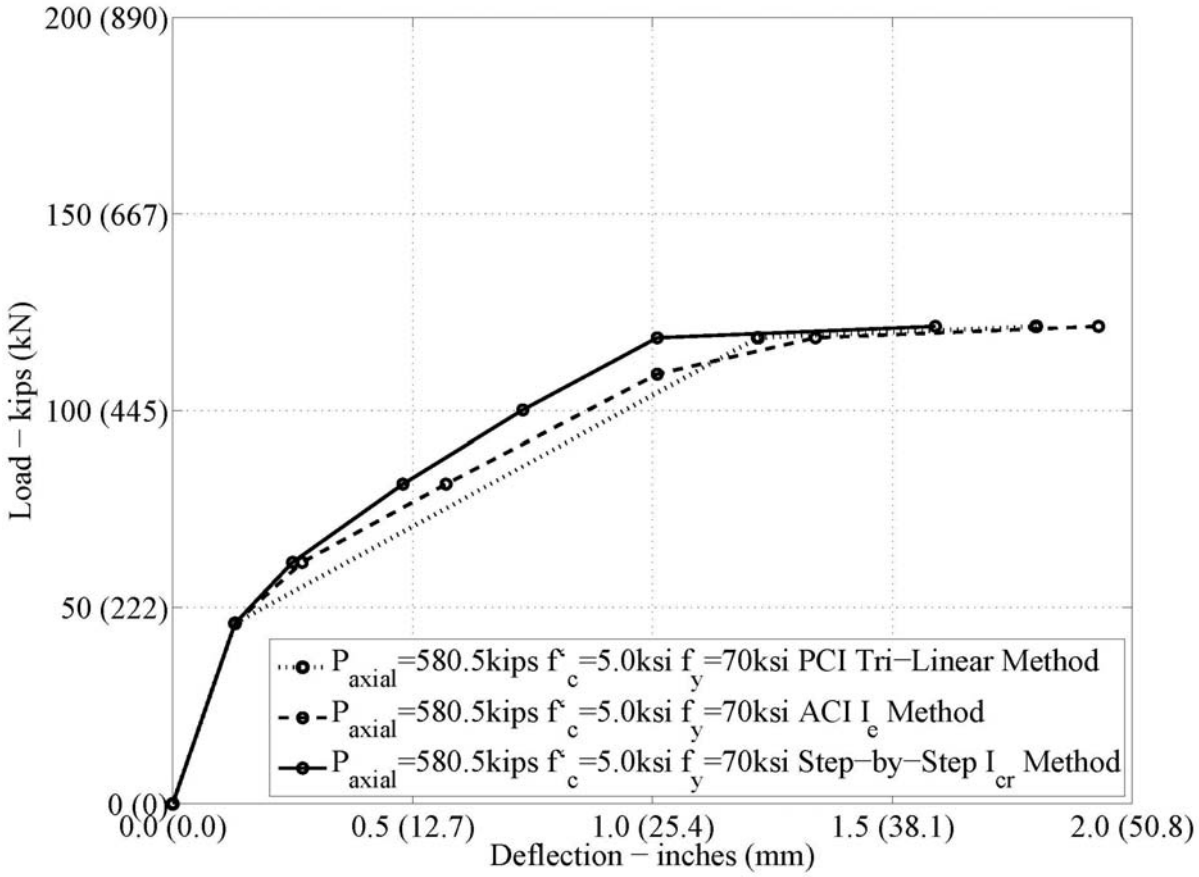

Figure 4-17. Load vs. Deflection for Tri-Linear, I_e, and Step-by-Step I_{cr} Methods for the Four-Point Test Setup.

4.3.2 Three-Point Test Predictions

Experimentally, the three-point test was executed after the four-point test. For the three-point test setup, the actuators were adjusted to their new positions, 15 ft (180 inches, 4.57 m) (L_{act}) apart. Before the test, the LSC specimen was rotated so that the tension face from the four-point test was the tension face for the three-point test and then balanced on a pin connection at the specimen's center. **Figure** 4-18 illustrates the three-point test setup and the shear and moment diagrams for this test. The figure shows that the shear force is constant between the actuators (i.e., constant along the splice length), whereas there was no shear force present in the splice region for the four-point test. The moment varies along the splice length in the three-point test, instead of a constant moment as in the four-point test. The maximum moment occurs at the center of the specimen which is also at the pinned support.

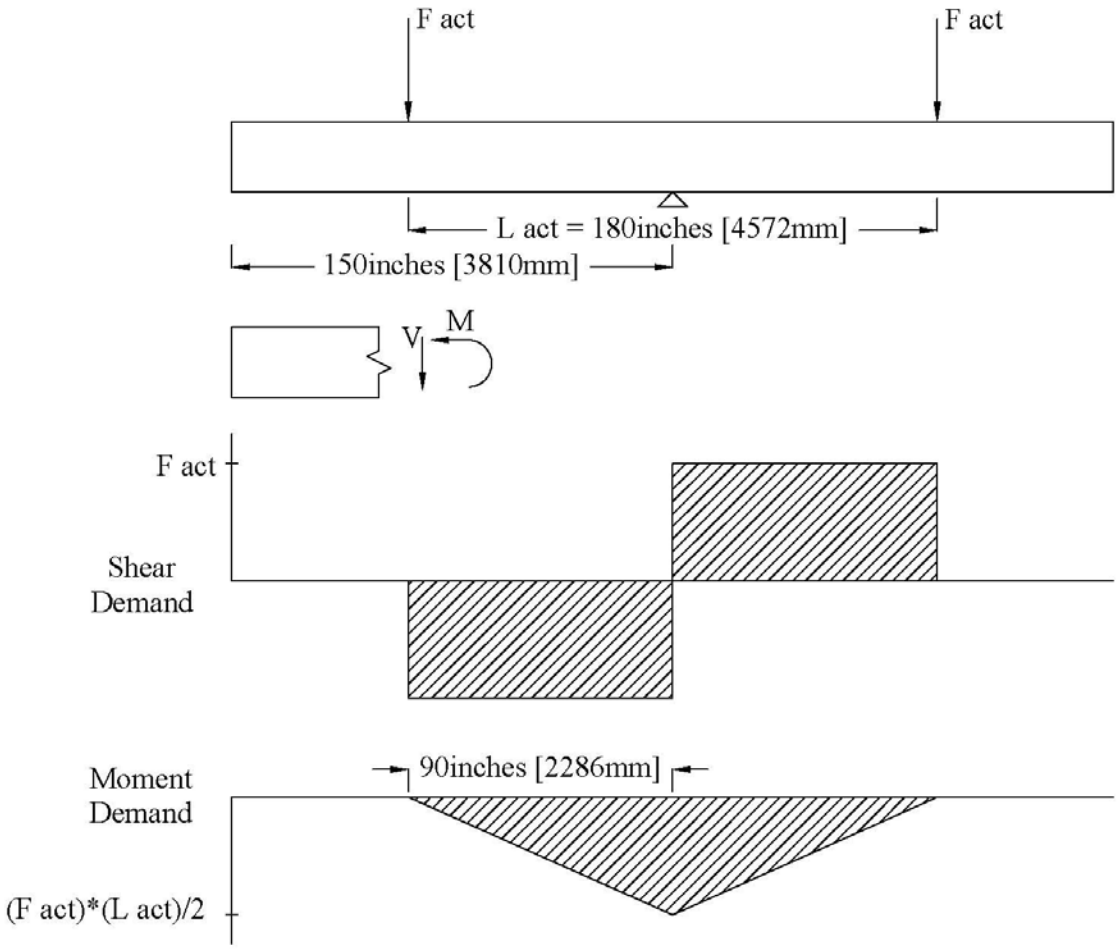

Figure 4-18. Three-Point Test Shear and Moment Diagram.

As in the four-point test, the self-weight moment was accounted for by subtracting it from the total moment capacity. Figure 4-19 shows the shear and moment diagrams from self-weight in the three-point setup. The moment from self-weight for the three-point setup ($M_{SW,3pt}$) is calculated using Eq. 4-56 for points between the end and the midpoint.

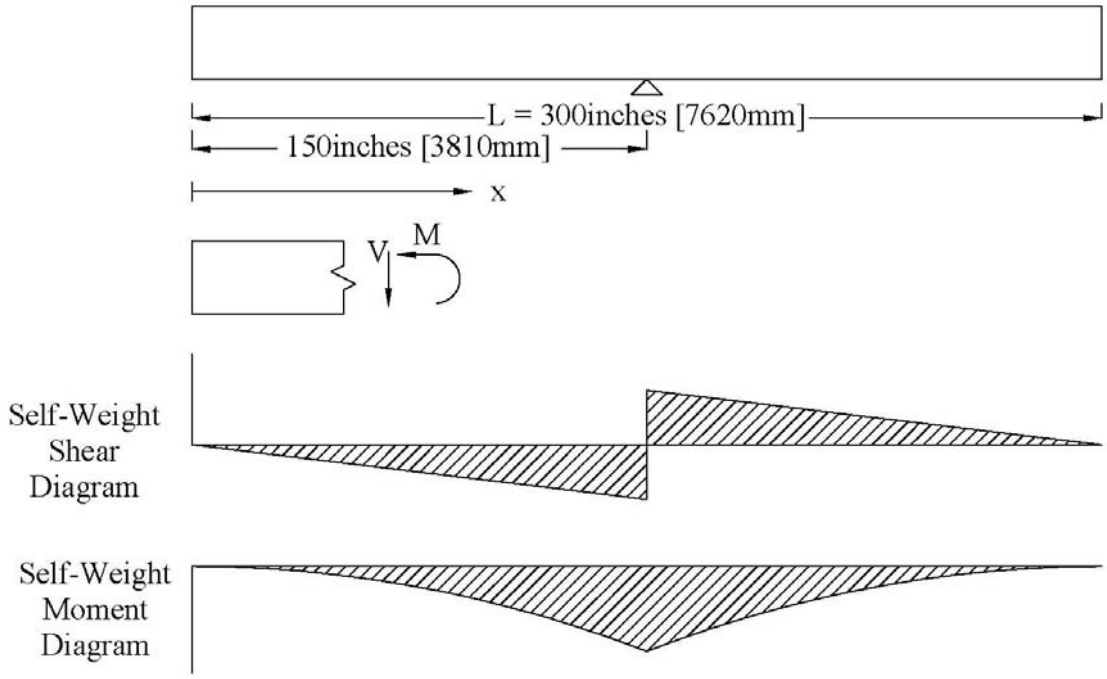

Figure 4-19. Shear and Moment Diagram for Self-Weight in the Three-Point Setup.

$$M_{SW,3pt} = \frac{w\,x^2}{2} \qquad \text{(Eq. 4-62)}$$

The distance between the end and the section the self-weight moment is being calculated is x (see Figure 4-19). The weight of the specimen was calculated in Eq. 4-41.

The force from each actuator in the three-point setup ($F_{act,3pt}$) is found with the following equation:

$$F_{act,3pt} = (M_{total\ cap} - M_{SW,3pt})\frac{2}{L_{act}} \qquad \text{(Eq. 4-63)}$$

Figure 4-20 compares the ultimate moment capacity of the LSC specimens to the moment demand from the three-point test setup. The moment capacity shown is the difference between the total moment capacity and the self-weight. The figure shows that the LSC specimens should fail from bending when the load from each actuator reaches 167 kips (743 kN). The three-point

moment capacity is the same as the four-point except for the self-weight subtracted from the total capacity. The cracks formed from the four-point test were neglected since they formed under the actuators (splice end) and the bending cracks from the three-point form at the center. Bond slip can reduced the specimen strength if the reinforcing steel is not able to yield. However, in the structural tests on the specimens performed to date, bond slip did not occur.

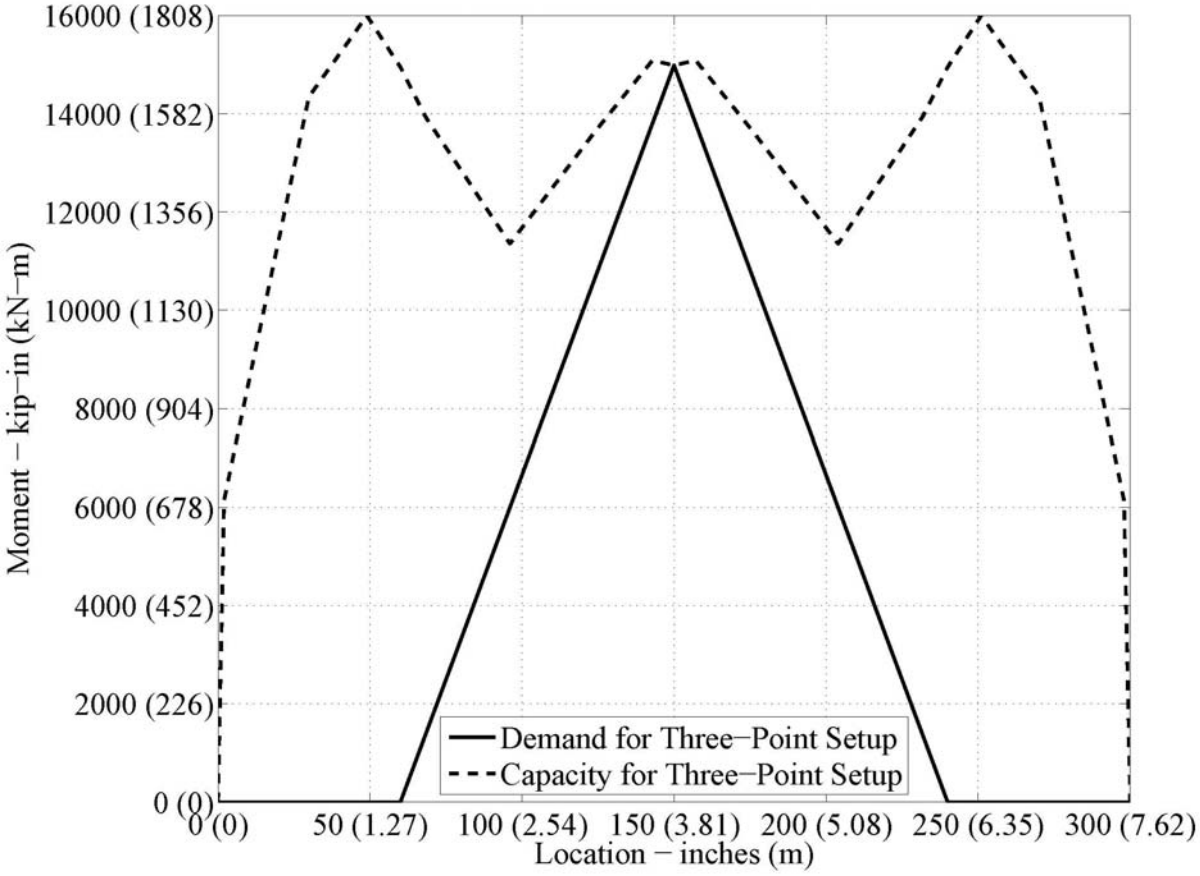

Figure 4-20. Ultimate Moment Capacity vs. Demand for the Three-Point Setup.

Shear failure has also been considered since the three-point setup provides a shear demand in the splice region. Several methods to compute the shear capacity were explored and two are presented in the following equations. The first procedure is the AASHTO Method 1, simplified procedure for non-prestressed sections. The following equations calculate the shear resistance, V_n comprised of the resistance from the concrete and transverse shear reinforcement, V_c and V_s, respectively reusing the AASHTO Method 1 (AASHTO 2010) as follows:

$$V_c = 0.0316\beta\sqrt{f'_c}b_v d_v \quad \text{(Eq. 4-64)}$$

$$V_s = \frac{A_v f_y d_v (\cot\theta)}{s} \quad \text{(Eq. 4-65)}$$

$$V_n = \text{lesser of} \begin{cases} V_c + V_s \\ 25f'_c b_v d_v \end{cases} \quad \text{(Eq. 4-66)}$$

where β equals 2.0 and θ equals 45°. The other variables are defined as: A_v is the area of shear reinforcement within spacing, s; the width of the section is b_v; and the shear depth is d_v. The units for the variables mentioned are square inches, inches and kips per square inch. This method is technically not applicable for the specimens in the research program since the specimens have axial load from post-tensioning, similar to service load conditions. However, this common procedure was included to show the difference between methods.

The second method is the AASHTO Method 3 which is the simplified procedure for prestressed and non-prestressed sections. The equations for V_s and V_n are the same as listed previously, Eqs. 4-59 and Eq. 4-61, respectively. However, the shear resistance from the concrete is the larger of the resistance when shear and moment cause cracking, V_{ci}, and the resistance when tension in the web cause cracking, $V_{cw,}$ which is given below.

$$V_c = \begin{cases} V_{ci} = 0.02\sqrt{f'_c}b_v d_v + V_d + \frac{V_i M_{cre}}{M_{max}} \geq 0.06\sqrt{f'_c}b_v d_v \\ V_{cw} = \left(0.06\sqrt{f'_c} + 0.30f_{pc}\right)b_v d_v + V_p \end{cases} \quad \text{(Eq. 4-67)}$$

The shear force from dead load and external loads is V_d and V_i, respectively. The maximum moment from the external loads is M_{max} and the moment causing cracking is M_{cre}. An equation is listed in the AASHTO code for M_{cre}. However, the flexural capacity when the concrete begins to crack was previously calculated based on bending theory and was documented earlier in this chapter. M_{cre} is calculated below from the flexural capacity results at any location along the specimen.

$$M_{cre} = M_{\text{total cap}_{cr}} - M_{SW,3pt} \quad \text{(Eq. 4-68)}$$

The stress from the post-tensioning is accounted for in the variable, f_{pc}, given below.

$$f_{pc} = \frac{P_{axial}}{bh} \quad \text{(Eq. 4-69)}$$

Chapter 2 fully describes the design of the specimens; however, the important information for calculating the shear resistance is described below. The area of transverse shear reinforcement and the spacing of this reinforcement is different in the end region and splice region. Figure 4-21 and Figure 4-22 show the transverse reinforcement in the splice region and the end region. Table 4-1 summarizes the area of the transverse shear reinforcement and the center-to-center spacing, s, between each stirrup.

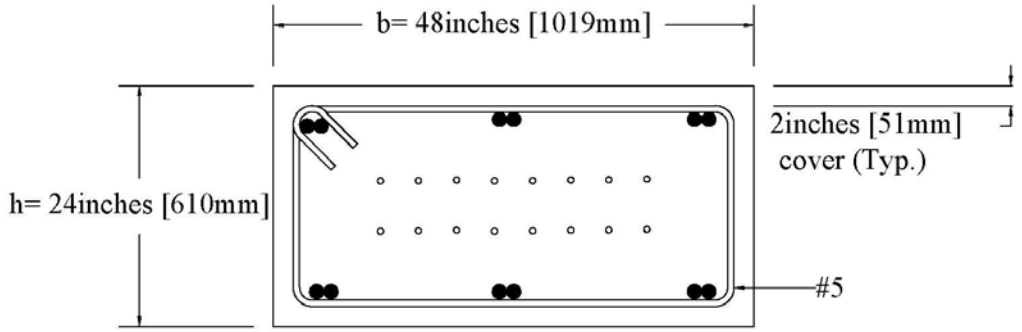

Figure 4-21. Cross Section at Splice Region with Transverse Reinforcement.

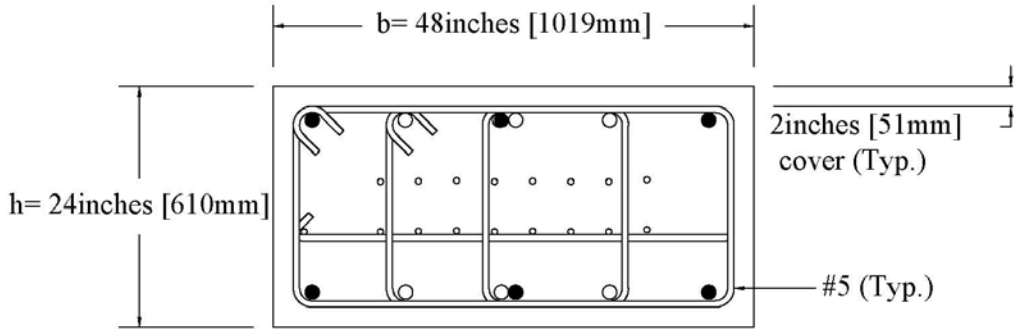

Figure 4-22. Cross Section at End Region with Transverse Reinforcement.

Table 4-1. Area and Spacing of Transverse Shear Reinforcement.

Region	A_v (inches^2)	s (inches)
Splice	0.62	12
End	1.55	6

Figure 4-23 shows the calculated shear capacity from the varying methods and the shear demand from the 3-point test setup along the LSC specimen. The shear values shown are in absolute values. The methods are constant for the given A_v and s, except at the splice end for AASHTO Method 3. At all locations, V_{ci} governed over V_{cw}. The second part of the V_{ci} equation governs for the all locations except at the splice ends where a larger value was computed for the first part. A closer look at this formula shows that in the end region, no maximum moment is present except between under the actuator and the splice end. Therefore, the fraction with M_{max} is omitted at those locations. Also, the ratio between M_{cre} and M_{max} is over twice as much at the splice end than the other locations, which gives reason for the second part of the equation to govern when the ratio is small. From the AASHTO Method 3, the specimen should fail from shear at the splice region from 201 kips (894 kN) at each actuator.

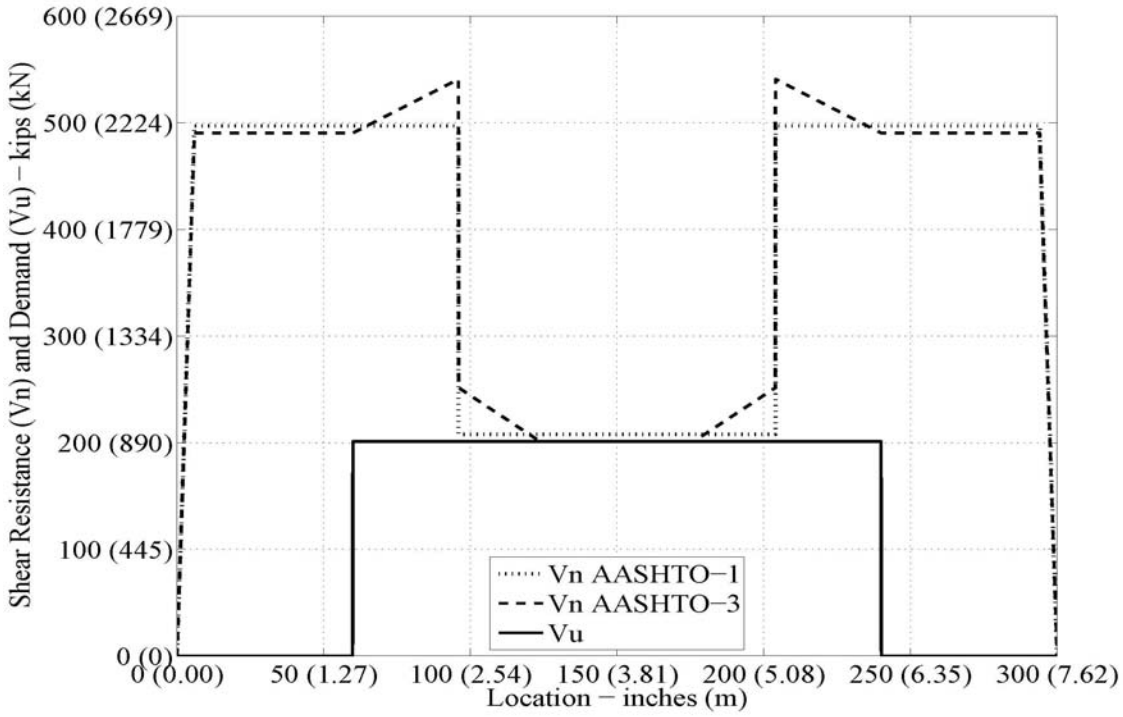

Figure 4-23. Three-Point Load Test Shear Demand and Capacity (Absolute Values).

The LSC specimens were first tested in the four-point setup, then in the three-point setup. The tension side was the same for both tests. Therefore, cracks were present prior to the three-point test. The significant cracking from the four-point test occurred under the actuators (at splice end). Since the critical section for the three-point test is at the specimen center, the previous cracking was ignored for the analysis of the three-point test and the same I_{gt} and I_{cr} values were used. The only deflection method described for the three-point setup is the Step-by-Step I_{cr} method since the differences between the methods are the same for both test setups and the Step-by-Step I_{cr} was the best one for the four-point setup.

The deflection at first concrete cracking for the three-point setup ($\Delta_{3pt,cr,Step-by-Step\ Icr}$) is calculated below:

$$\Delta_{3pt,cr,Step-by-Step\ Icr} = \frac{F_{act,3pt_{cr}}}{6\ E_c\ I_{gt}}\left(4x - 3L_{act}x^2 - {L_{act}}^2\right) \quad \text{(Eq. 4-70)}$$

The deflection at the intermediate values between first cracking and first yielding are calculated using the Step-by-Step I_{cr} method described for the four-point setup. The deflection at intermediate steps for the three-point test $\Delta_{3pt,cr,y,i}$ is calculated as follows:

$$\Delta_{3pt,cr,y,i} = \frac{(F_{act,3pt_i} - F_{act,3pt_{i-1}})}{24\, E_c\, I_{cr_i}}\left(4x - 3L_{act}x^2 - {L_{act}}^2\right) \quad \text{(Eq. 4-71)}$$

where $F_{act,3pt_i}$, and I_{cr_i} are the load and second moment of area calculated at each step using Eq. 4-63 and Eq. 4-49. For the calculation of $\Delta_{cr,3pt,y,1}$, $F_{act,3pt_{cr}}$ must be used for $F_{act,3pt_{i-1}}$ since the force at cracking is the preceding force.

The deflection at first yielding is calculated as follows where the preceding force that is subtracted from the load when steel yields is F_{act_n}, which is the last intermediate force. The second moment of area using the neutral axis at yielding, I_{cr_y}, is also used.

$$\Delta_{3pt,y,Step-by\ Step\ Icr} = \frac{(F_{act_y} - F_{act_n})\, L_{supp}}{6\, E_c\, I_{cr_y}}\left(3L_s x_{supp} - 3L_s x_{supp}^2 - {L_{supp}}^2\right) \quad \text{(Eq. 4-72)}$$

The deflection at ultimate must consider the plastic deformations that occur after the reinforcing steel yields similarly to the four-point setup. The plastic hinge rotation is the same for each test setup. The plastic hinge length is also the same. This is caused by the same depth of the bottom layer of the reinforcing steel, 20.67 inches (525 mm), and the same distance between the maximum moment and no moment, 90 inches (2286 mm).

Assuming that the entirety of plastic deformations occurs at the center support, the plastic deformations can be found from the plastic hinge rotations and the geometry of the test setup illustrated in Figure 4-24. The elastic deflection at first yielding for the three-point setup, $\Delta_{3pt,y}$, was added to the plastic deflection to calculate the total deflection at the ultimate limit, $\Delta_{3pt,u}$, in Eq. 4-73.

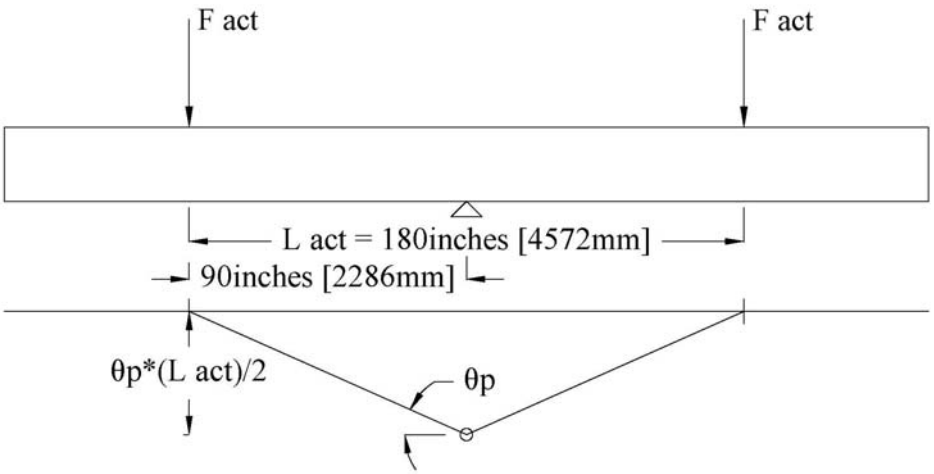

Figure 4-24. Plastic Hinge Rotation for the Three-Point Setup.

$$\Delta_{3pt,u} = \theta_p \frac{L_{act}}{2} + \Delta_{3pt,y} \qquad \text{(Eq. 4-73)}$$

Figure 4-25 shows the calculated load vs. deflection for the three-point setup. The deflection calculated for the three-point setup is under the actuator which is 60 inches (1524mm) from the end of the specimen. Shear deflection was neglected in the deflection calculations for simplicity and a check on whether the response is governed by bending. The deflections from the three-point setup were smaller than the four-point setup. At the same load from each actuator in both setups, the deflection for the four-point test under the actuator (90 inches [2286 mm] from end) is 2.8 times the deflection for the three point test under the actuator (60 inches [1524mm] from end). The specimen can resist the calculated shear failure until each actuator is loaded with 201 kips (894 kN). However, the specimen will fail from flexural bending at 167 kips (743 kN). Therefore, the moment capacity and demand controls the failure for both the three-point and four-point test setups.

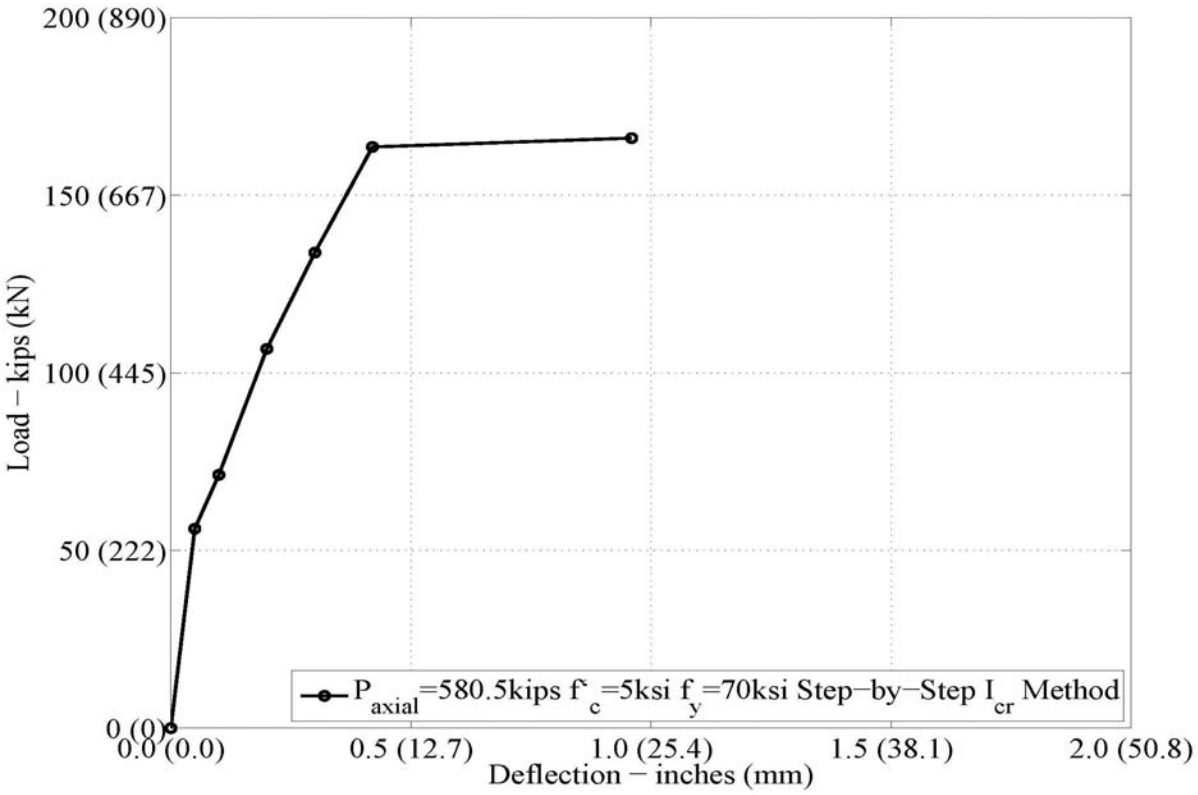

Figure 4-25. Load vs. Deflection for Step-by-Step I_{cr} Method under Actuator for the Three-Point Test Setup.

4.4 SUMMARY

Analytical models were developed based on flexure theory to characterize the force-deformation behavior of the LSC specimens in both the four-point and three-point load test setups. Both in the critical splice region and in the specimen end regions, the longitudinal reinforcing steel was assumed to develop tensile resistance linearly from zero resistance at the end of the bar to the yield strength at the code calculated development length of the bar. Based on this equivalent steel area for all sections of the specimen, the force-deformation characteristics were calculated for the LSC specimens for both the four-point and three-point test setups based on flexure theory. This analysis of the specimens will be compared with the experimental response of undamaged LSC specimens and also those with varying levels of premature concrete deterioration due to ASR and DEF in the next chapter.

CHAPTER 5:
EXPERIMENTAL TESTING PROGRAM

5.1 INTRODUCTION

This chapter discusses the experimental test setups, specimen instrumentation, and specimen behavior during structural load testing. LSC specimens 1, 3, 5, 8, 9, 10, 15, and 16 were tested with varying degrees of ASR/DEF deterioration at the time of testing. The LSC specimens are numbered chronologically with the casting date. This chapter also reports the concrete compression strength results from cylinders stored in a curing room and in the field conditions at the Riverside Campus. The control specimens, LSC15 and LSC16, were stored inside the Structure and Materials Testing Laboratory with no exposure to the environmental weather conditions or supplemental water, thus eliminating ASR and DEF from forming. In a similar project with the same concrete composition, a TxDOT petrography report confirmed from cores taken from specimens kept in the lab that no ASR or DEF distress had formed.

Table 5-1 shows the dates of the specimen casting, initial environmental exposure, structural load testing, and the degree of deterioration from ASR and DEF. The degree of ASR and DEF deterioration was established from knowledge gained from the internal and external strains measured (Chapter 3) and the petrography analysis report summarized in Chapter 3. Table 5-2 shows the last average transverse surface strains of all faces before the LSC specimen was tested and the maximum crack width measured on each face. LSC1, LSC3, LSC9, and LSC10 were tested before the 90° rotations are described in Chapter 3; therefore data readings on Large Face 2 had not begun. Of the specimens exposed to the ASR and minimal DEF deterioration conditions, LSC9 and LSC10 had the smallest amount of surface expansion and the least amount of surface cracking on all sides prior to testing. A moderate amount of surface expansion and cracking occurred in LSC 1 and LSC3. LSC5 and LSC8 had the most expansion and surface cracking prior to structural testing of all specimens tested to date. These surface expansions and maximum crack width amounts are summarized in the tables as one way of trying to characterize the degree of deterioration.

Table 5-1. Specimen Age and Degree of Deterioration.

LSC Specimen #	Date of Casting	Date of Initial Exposure	Date of Structural Load Test	Degree ASR	Degree DEF
1	1/2008	5/2008	8/2010	M/L	N/E
3	2/2008	5/2008	8/2010	M/L	N/E
5	4/2008	5/2008	7/2011	M/L	N/E
8	5/2008	7/2008	7/2011	M/L	N/E
9	6/2008	7/2008	2/2010	M/L	N/E
10	6/2008	7/2008	2/2010	M/L	N/E
15	8/2008	N/A	2/2009	N	N
16	8/2008	N/A	2/2009	N	N

N/A – Specimen was not exposed to the environmental deterioration conditions.
N – None; E – Early stage; M – Middle stage; L – Late stage. Note that these stages were established based on the petrography analysis of concrete cores taken from specimens after structural testing, and also from the surface and internal expansion measurements and cracking throughout the specimen prior to testing.

Table 5-2. Specimen Surface Expansions.

LSC #	Average Transverse Surface Strain at Time of Load Test (strain)				Maximum Crack Width at Time of Load Test inches (mm)			
	Small Face 1	Small Face 2	Large Face 1	Large Face 2	Small Face 1	Small Face 2	Large Face 1	Large Face 2
1	0.0064	0.0024	0.0070	N/A	0.03 (0.8)	0.04 (1.0)	0.04 (1.0)	N/A
3	0.0067	0.0026	0.0054	N/A	0.04 (0.9)	0.03 (0.6)	0.03 (0.6)	N/A
5	0.0080	0.0087	0.0090	0.0123	0.03 (0.6)	0.03 (0.6)	0.03 (0.6)	0.04 (1.0)
8	0.0082	0.0092	0.0088	0.0112	0.01 (0.3)	0.03 (0.8)	0.03 (0.8)	0.03 (0.6)
9	0.0051	0.0009	0.0026	N/A	0.01 (0.2)	0.01 (0.2)	0.01 (0.2)	N/A
10	0.0052	0.0013	0.0038	N/A	0.01 (0.2)	0.02 (0.4)	0.02 (0.4)	N/A
15	N/A	N/A	N/A	N/A	N/A	N/A	N/A	N/A
16	N/A	N/A	N/A	N/A	N/A	N/A	N/A	N/A

N/A – Data not taken, but presumed to be minimal.

The LSC specimens were structurally tested in two different test setup arrangements to evaluate the performance of the column lap splice region under varying levels of premature concrete

deterioration due to ASR and minimal amounts of DEF. The test setups, structural performance and comparison of results will be reported in the remainder of the chapter.

5.2 FOUR-POINT FLEXURAL LOAD SETUP

The design of the LSC specimens was based on the four-point load test setup, which applies a constant moment demand and no shear demand across the entire splice region. The objective of this testing is to identify the structural behavior and ultimate capacity of the splice region due to flexure demands and determine the mode of failure in the cases of varying levels of ASR and minimal amounts of DEF deteriorations. If the bars in the splice are sufficiently anchored, then the failure mechanism should develop at the splice ends, which would mean that the provided splice length was sufficient to satisfy ultimate demand loading. However, if the longitudinal reinforcing bars undergo bond slip and are not developed sufficiently to attain its yield strength during ultimate demand loading, then the provided splice length is not adequate. The structural load testing of specimens with varying levels of premature concrete deterioration will help determine the capability of column splice regions in TxDOT field structures with similar ASR/DEF deterioration and structural detailing in resisting ultimate demand loads to ensure safety design requirements.

5.2.1 Experimental Design and Specimen Layout

Figure 5-1 shows a typical LSC specimen positioned on two "pinned" supports 6 inches (152.4 mm) from either end of the specimen. This distance was chosen to prevent the concrete cover from crushing. The "pinned" supports were attached to the strong floor of the Structures and Materials Testing Laboratory, and a thin layer of neoprene was placed between the bottom of the LSC specimens and the upper plate of the support (see Figure 5-2). The supports at 6 inches (152.4 mm) from the ends provided space for the neoprene helped prevent a concentration of stresses in the concrete due to imperfections on the concrete surface. However, the neoprene also easily compressed and resulted in slight vertical deflections during loading, which was taken into account by proper placement of the instrumentation. Similar supports were positioned under the load actuators at 8 ft (2.4 m) from each end of the LSC specimens (at the splice end). To

ascertain a stable system, the top plates of the supports were supported on each side by three bars of 2-inch (51 mm) round stock to make the support a "fixed" support at the actuator end (see Figure 5-3) and the actuator was braced in the out-of-plane direction to ensure that it only moved vertically during testing. Neoprene pads were also placed between the concrete and the support to create a better interface for the transfer of forces.

Figure 5-1 shows the shear and moment demand from the four-point load setup. The max shear force is the force from each actuator, F_{act}, which is constant between the support and the load. There is no shear force in the splice region, which is between the two actuator loads. The maximum moment is the F_{act} times the distance between the supports, L_{supp}.

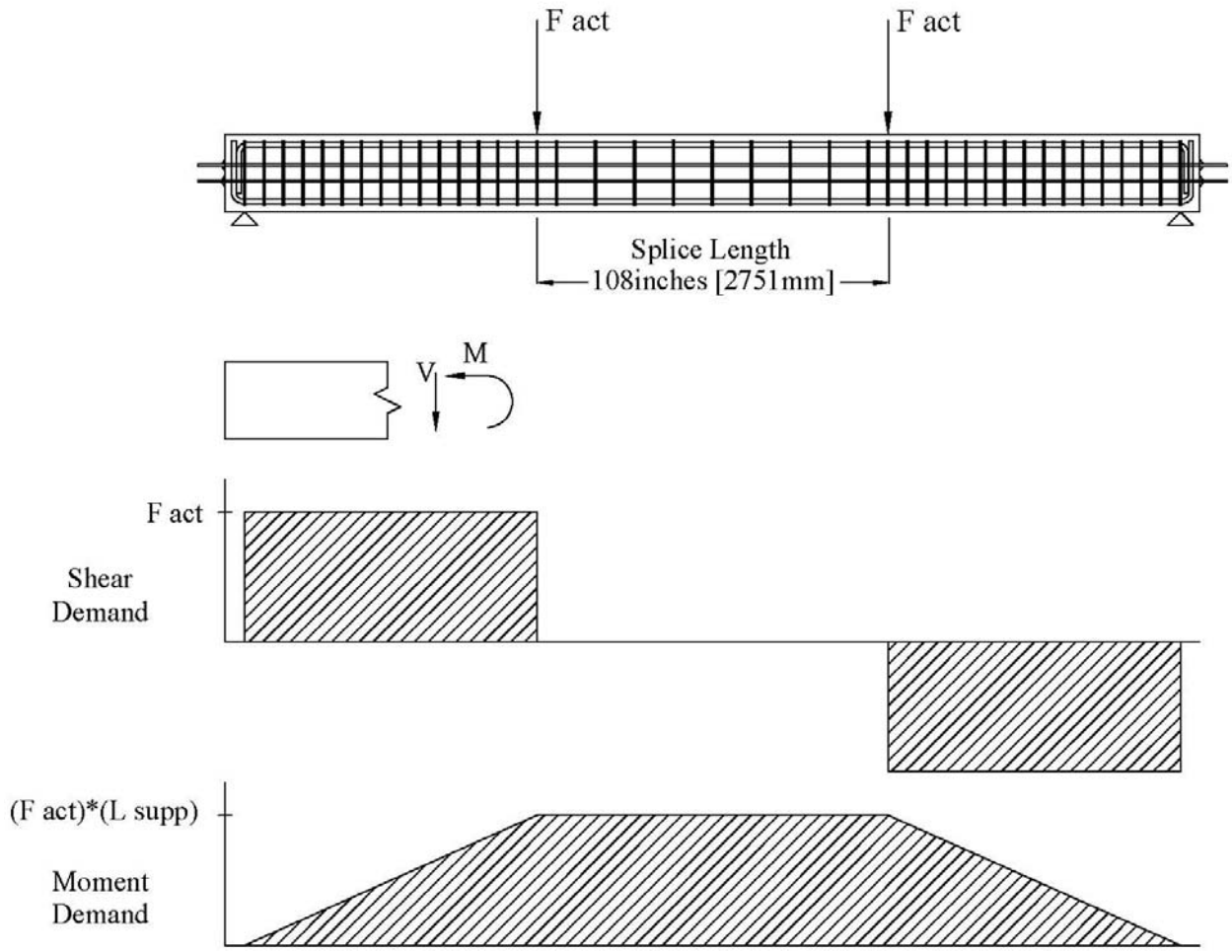

Figure 5-1. Four-Point Load Test Setup and Demand Loading.

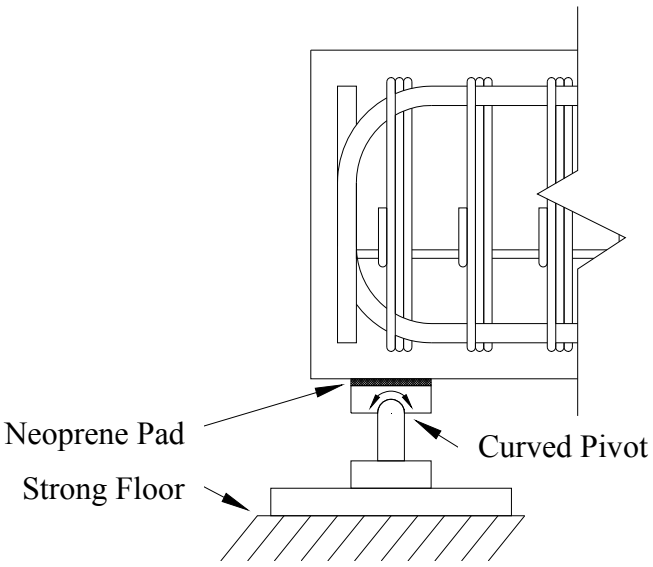

Figure 5-2. "Pinned" Support Setup.

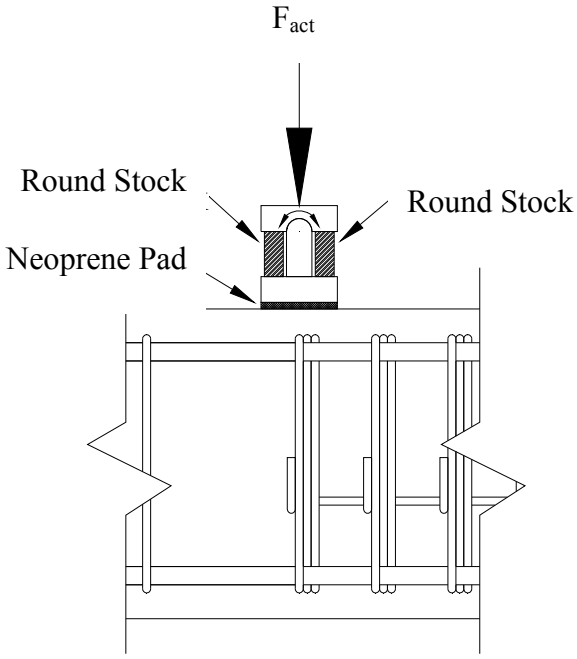

Figure 5-3. "Fixed" Support Setup.

Two 220 kips (979 kN) actuators attached to an overhead steel frame were used to load the specimen in displacement control loading. The steel frame was anchored to the strong floor in the Structure and Materials Testing Laboratory. Figure 5-4 shows the actuators positioned over one of the LSC specimens.

Figure 5-4. Specimen in the Four-Point Test Setup.

5.2.2 Instrumentation

In addition to the internal instrumentation installed during construction (see Section 2.4), external instrumentation was attached to the LSC specimens to measure the deflections and external surface strains during the structural load testing. String potentiometers (STR) with a 4-inch (102 mm) stroke were used to measured the specimen deflections at various points. Figure 5-5 shows a typical STR connected to the bottom of the LSC specimen to measure vertical deformations. Figure 5-6 shows the position of the STRs on the LSC specimen to measure critical deformations during testing.

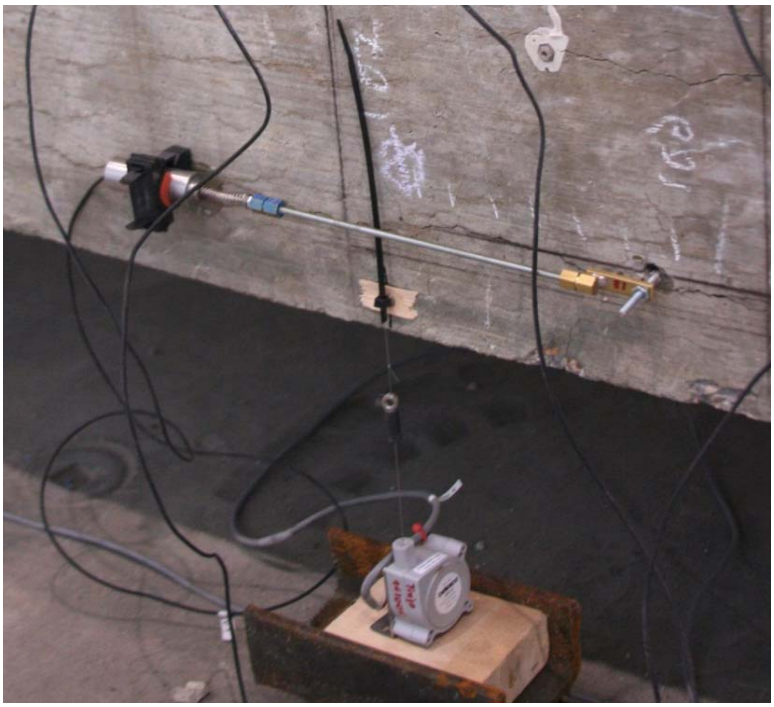

Figure 5-5. STR Installation Prior to Testing.

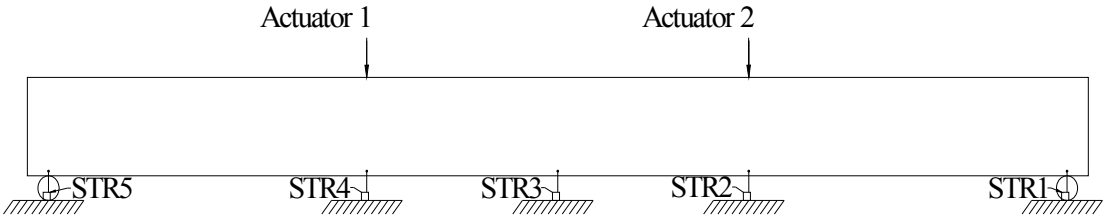

Figure 5-6. STR Locations for the Four-Point Test.

The relative specimen deflections under Actuator 1 and Actuator 2 were calculated using STR readings. The initial readings from the STRs were zeroed to account for the flexibility in the test setup and neoprene support conditions. The deflection under Actuator 1 and Actuator 2 ($\Delta_{\text{act 1,4pt}}$ and $\Delta_{\text{act 2,4pt}}$) was calculated by subtracting the deflection at the ends (Δ_{STR5} and Δ_{STR1}), which accounted for the flexibility in the test setup and neoprene support conditions from the original deflection under the actuators (Δ_{STR4} and Δ_{STR2}).

$$\Delta_{\text{act 1,4pt}} = \Delta_{\text{STR4}} - \Delta_{\text{STR5}} \quad \text{(Eq. 5-1)}$$

$$\Delta_{\text{act 2,4pt}} = \Delta_{\text{STR2}} - \Delta_{\text{STR1}} \quad \text{(Eq. 5-2)}$$

Linear variable differential transformers (LVDT) and concrete embedment gages (type KM) were also used to measure the tension and compression strains of the specimen in various locations during the load testing. LVDTs were securely attached to the concrete specimen separated by a gage length of 4 inches (102mm) or 12 inches (305 mm). Holes (1/4 inch) were drilled into the specimen face and ¼ inch stainless steel threaded couplers were hammered into the holes and secured using adhesive epoxy. These couplers provided an anchor to screw the threaded rods into the specimen. The threaded rods were then attached to the LVDT using metal and plastic brackets. Figure 5-5 and Figure 5-7 show sample LVDTs on the LSC specimens. The final positioning of the LVDTs on the specimens and the LVDT gage lengths are discussed in the forthcoming paragraphs.

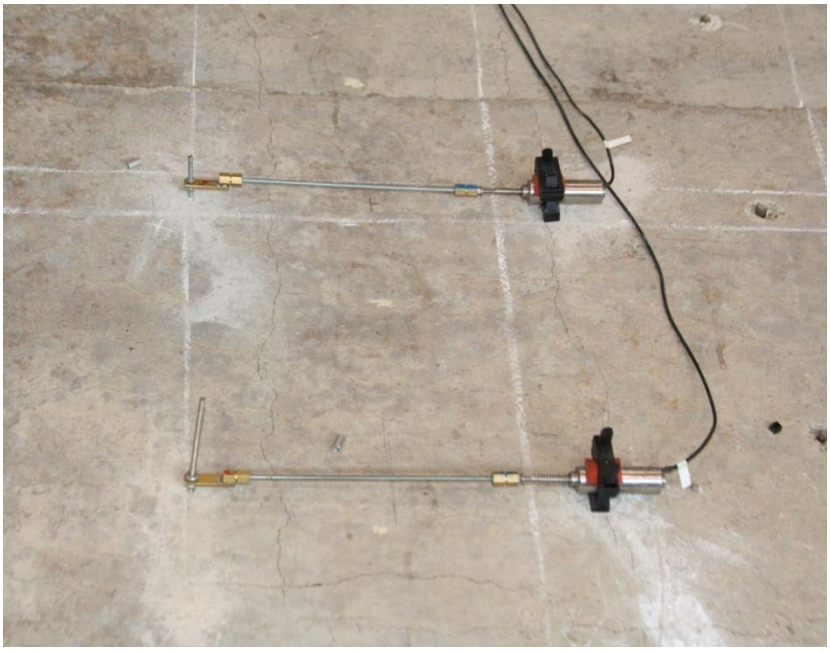

Figure 5-7. LVDT Installation prior to Testing.

KM gages were attached to the surface of the LSC specimens using adhesive epoxy. First, the surface was smoothed by sanding across the entire footprint of the KM base plates. A spacing bar was placed between the KM base plates to keep the base plates a proper distance apart (4 inches [100 mm] gage length). Before testing, the base plates were epoxied to the concrete surface, the

spacing bars were then removed, and the KM gages were attached to the base plates. Figure 5-8 shows a KM gage attached to the LSC specimen.

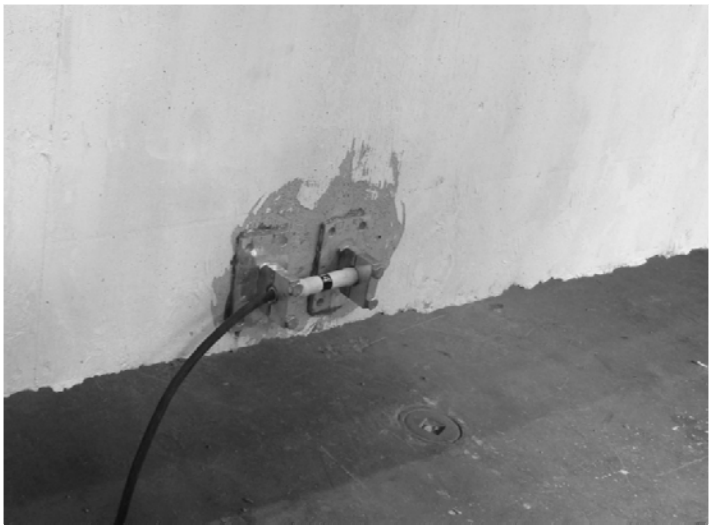

Figure 5-8. KM Gage Installation prior to Testing.

For the four-point test on LSC16, which was the first specimen that was tested in this research program, the placement of the KM gages and LVDTs were mirrored across the longitudinal axis of the specimen. This was done to compare the accuracy of the KM gages and the LVDTs for compression and tension strain measurements. Figure 5-9 shows the locations of the external sensors on each face of the LSC specimens. The letters "A" and "B" are used to label each end of the specimen. The LVDTs are labeled with "LV" followed by a number.

LV1, LV2, and LV3 were placed 3 inches (76.2 mm) from the bottom, at the specimen mid-height, and 3 inches (76.2 mm) from the top, respectively, to measure the section strains at the splice end, which was the calculated critical section during loading. On the opposite side, KM6, KM7, and KM8 were placed in the same positions as LV1, LV2, and LV3, respectively. These gages compared the accuracy of the LVDTs and KM gages at the tension steel.

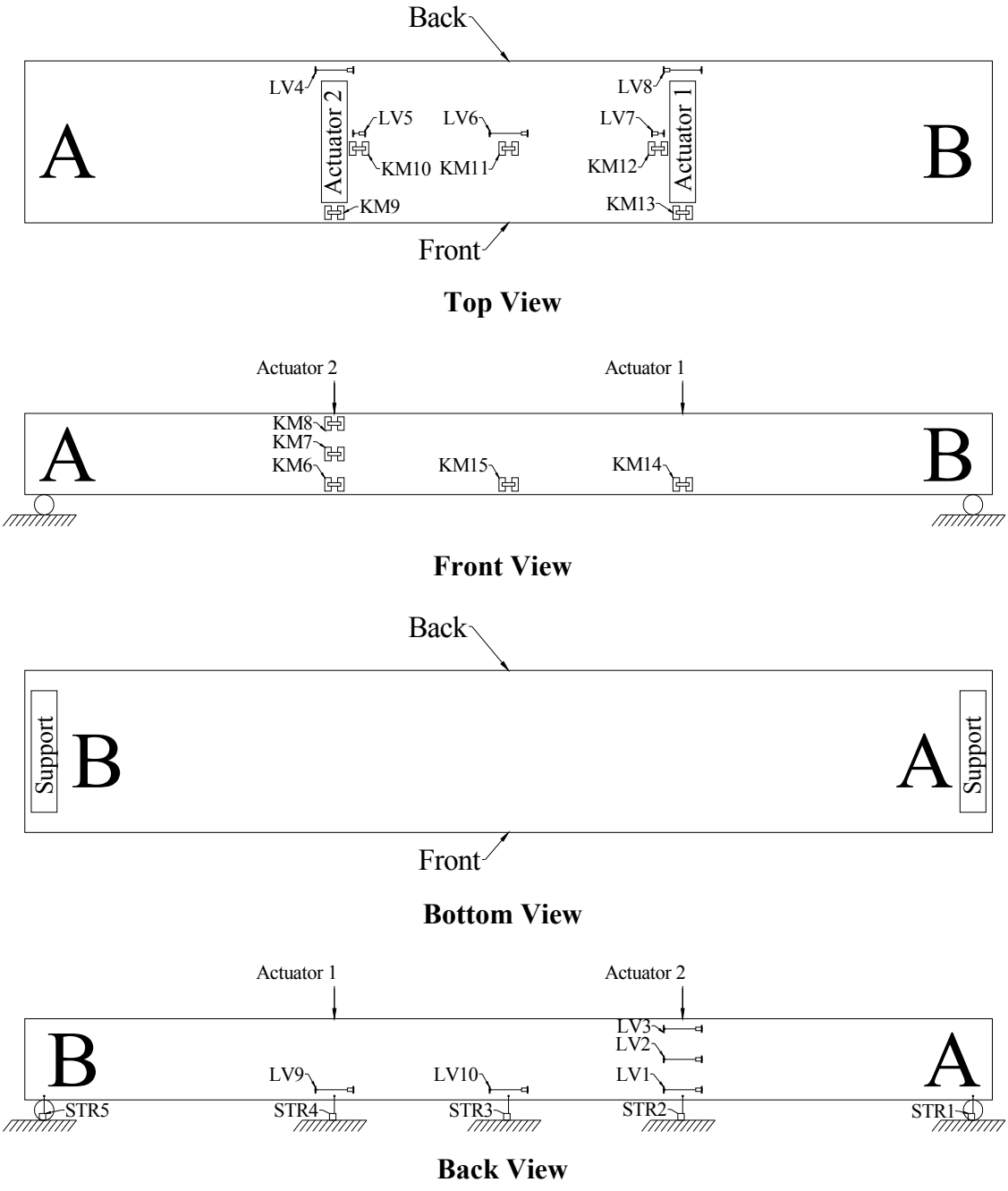

Figure 5-9. External Instrumentation Layout for the Four-Point Test of LSC16.

Figure 5-9a shows the mirrored layout of LV4 through LV8 and KM9 through KM13 respectively. LV4, LV8, KM9, and KM13 were positioned next to the actuators to measure the compression strain in the outermost fibers of the critical region. Likewise, LV6 and KM11 were used to measure the compression strains across the splice length of LSC16. LV5 and LV7 (KM10 and KM12) were used to check for different compression strains in the middle of the critical region compared to the gages on the side. To center the LVDT and KM gages at this location, a gage length of 4 inches (102 mm) was used for LV5 and LV7 instead of the 12-inch (305 mm) gage length used elsewhere. The remaining gages were placed in the tension region at the other critical section and the mid-section of the LSC specimens to measure strains at each structurally significant location. LV9 and KM14 were placed on the opposite splice end as LV1 and KM6. LV10 and KM15 were placed 3 inches (76 mm) from the bottom at the midsection.

However, this instrumentation layout was used only for LSC16. The instrumentation layout for the other specimens changed to improve the quality of the gathered measured data from the knowledge gained during testing of the first specimen. From the first test, it was found that some cracks in the tension region progressed through the mounting plate of the KM Gages or was not within the small gage length for the gage, which influences the true strain reading (see Figure 5-10). However, the KM gages provided representative and reliable data when applied to the compression regions of the LSC. Therefore, the KM gages were used for the compression regions in the following tests and the LVDTs, which measured the larger tension strains much better, were solely used for tension strain monitoring.

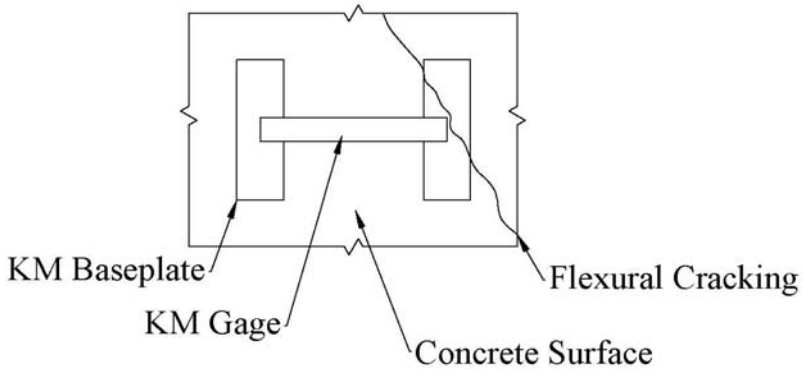

Figure 5-10. KM Gage Detail.

Figure 5-11 shows the instrumentation layout for the remainder of the LSC specimens in this research program. Only nine out the 10 external KM gages were used on the compression face, KM15 was used on the side to measure the compression strain in the strain diagram. KM6, KM7, KM13, and KM14 were positioned at the splice end to measure the strains in this critical section. According to the analytical model presented in Chapter 4, crushing of the concrete will occur at this location, which indicates ultimate failure of the LSC specimens. KM8, KM9, KM11, and KM12 were positioned in the center of the LSC specimens on the compression side (the top) and located above the internal strain gages in the specimen (Chapter 2) and KM10 was placed in the center of the mid-section of the LSC specimens to monitor compression strains in the middle of the splice. KM8 through KM12 were used to validate the strains from the internal SGs as well as provide a longitudinal strain profile across the length of the splice in the compression region.

Likewise, LV1 through LV7 were spaced along the tension region every 18 inches (457 mm) to monitor the longitudinal strains along the length of the splice. Again, the purpose of this was twofold: to validate the strain measurements from the internal SGs, and to create a strain profile for the splice from one end to the other. Additionally, LV8 and KM15 were used in conjunction with LV7 to produce a strain distribution across the critical region of the splice end as in the first test. Finally, LV9 and LV10 were placed on the bottom in the critical region to measure the strain in the outermost fiber of the tension region. All LVs had a 12-inch (305 mm) gage length except for the two on specimen LSC16. The locations of the STRs were the same for LSC16 and the other specimens tested.

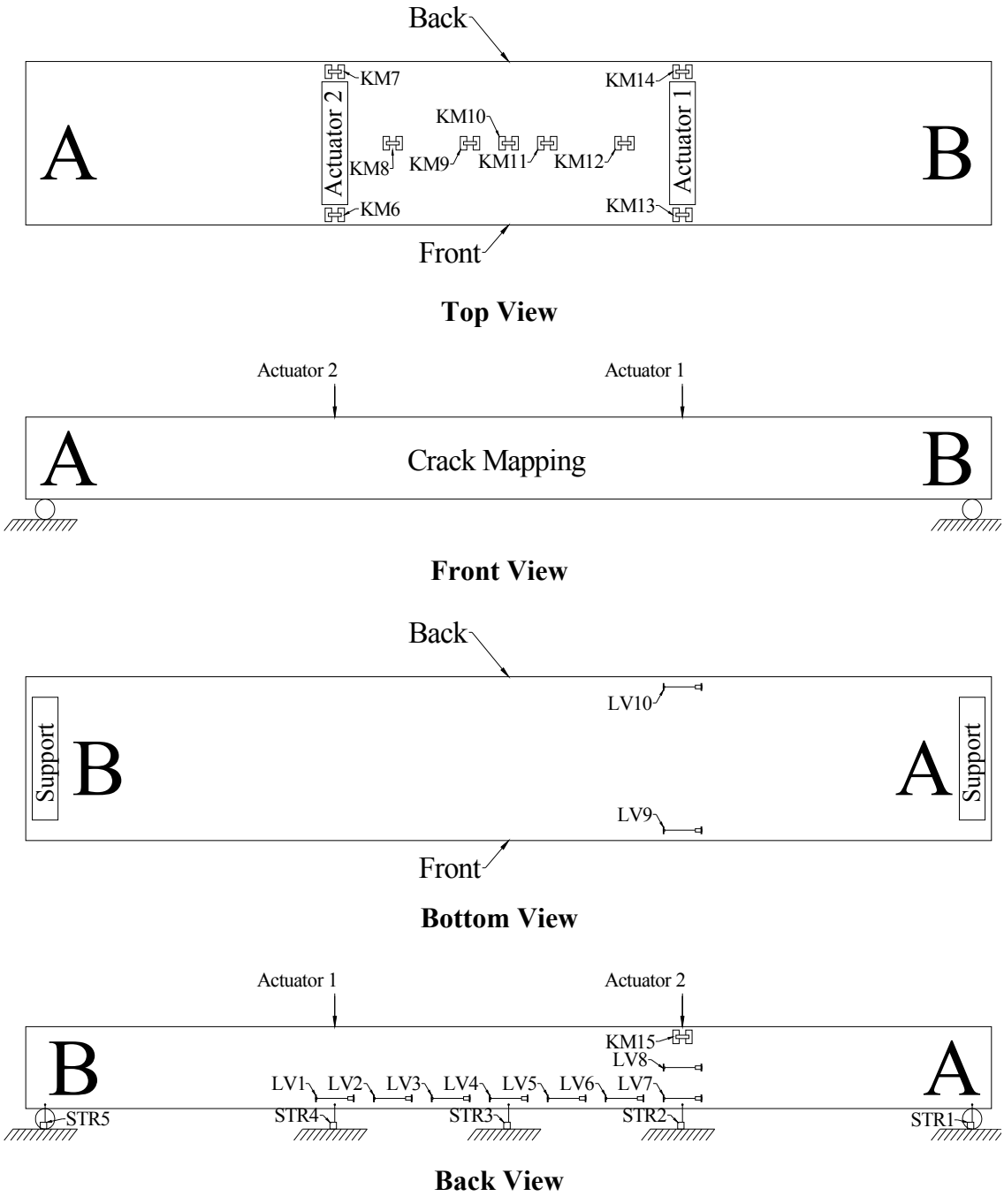

Figure 5-11. External Instrumentation Layout for the Four-Point Tests except for LSC16.

5.2.3 Test Procedures

The internal gages discussed in Chapter 2 were connected to a data acquisition system (DAQ) in the Structures and Materials Testing Laboratory and recorded data readings once every second (sampling rate). However, the internal KM gages were not installed in the control specimens (LSC15 and LSC16) since the control specimens would intentionally not expand due to ASR/DEF, so no data was taken for those channels of the DAQ.

Prior to beginning the test, the actuators were set onto the loading supports, then placed in displacement control at 0.001 inch/sec (25 μm/sec) until cracks initiated in the concrete. The research team then increased the rate to 0.002 inch/sec (50 μm/sec) until near failure of the specimen. In addition, the actuators were stopped and held periodically to map cracks and take pictures of the LSC specimens. During the loading, the instrumentation was carefully monitored to identify possible failure conditions such as crushing of the concrete and bond slip. Displacement control loading allowed for small differences in the actuator loads exerted on the LSC specimens, but provided increased control over the specimen response beyond the post-cracking behavior region up to specimen failure. The load testing in the four-point setup lasted about 30 to 45 minutes.

5.3 THREE-POINT FLEXURAL LOAD SETUP

After the four-point test was completed for a given LSC specimen, researchers performed a three-point flexural load test on the same specimen. Figure 5-12 shows the loading demand of the test setup. The shear demand is equal to the force from one actuator between the two actuators and zero elsewhere. The moment varies from zero at the location of the actuator to maximum at the support, which is the actuator force multiplied by the distance between the actuator and the support. The objective of this test was to evaluate the column splice performance by introducing large flexural moment demands that are not constant throughout the splice region, but more critical at the very middle section of the splice, which might have a more demanding influence on the bond behavior of the longitudinal reinforcing steel. Due to the nature of three-point loading, constant shear forces were also present in the splice region. It

should be emphasized that this test setup is not representative of any expected loading in the column splice region of the TxDOT bridge inventory. The test was only conducted as a way to evaluate the performance of the column splice region under a varying bending moment, shear, and possibly more demanding bond conditions under the presence of varying ASR/DEF deterioration effects.

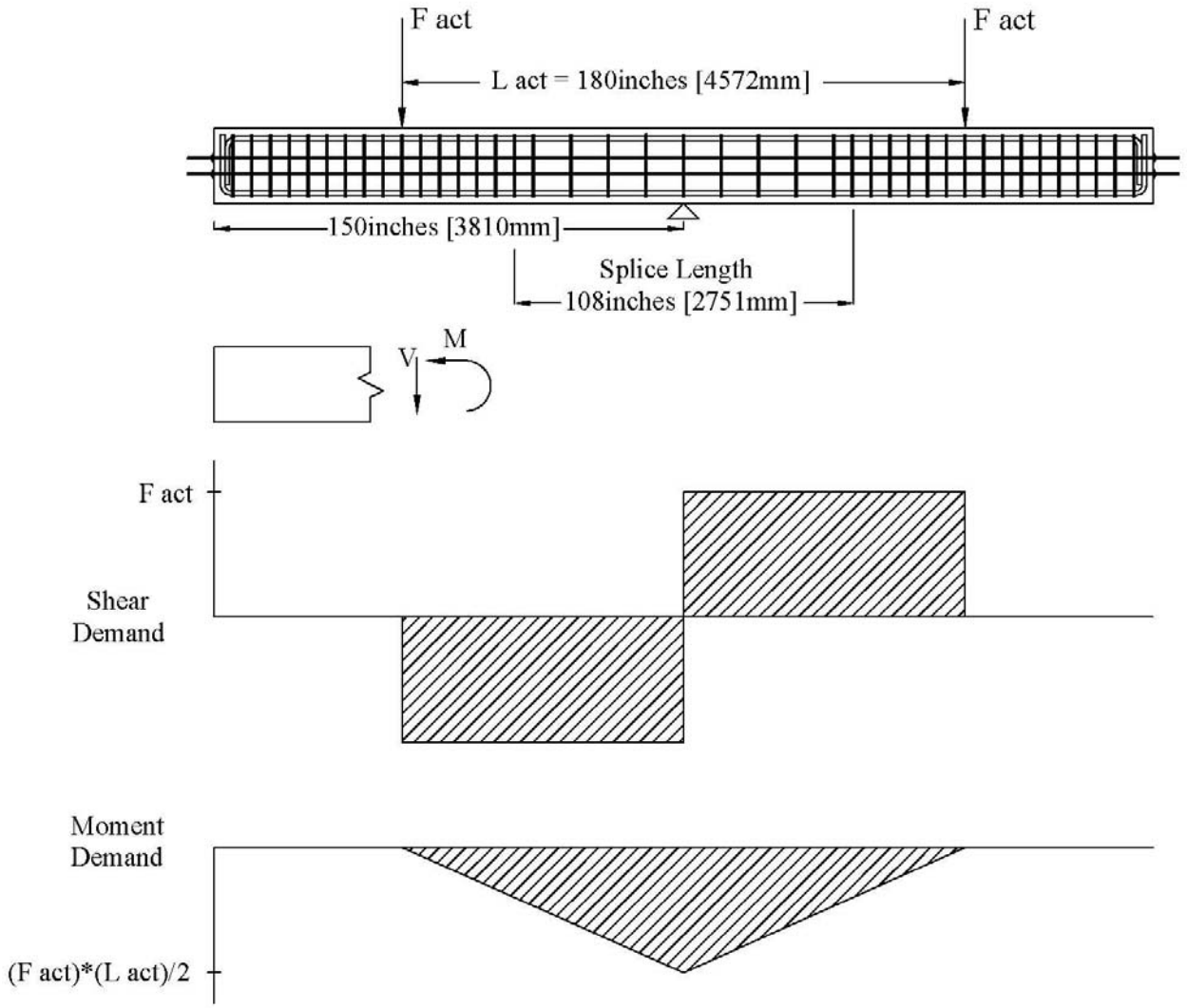

Figure 5-12. Three-Point Load Test Setup and Demand Loading.

5.3.1 Experimental Design and Specimen Layout

To be able to generate sufficient actuator force and to keep the instrumented side of the specimen in the tension region, the specimen was rolled 180° about its longitudinal axis for the three-point test. In the four-point test, the tension region was on the bottom of the LSC; rolling the LSC specimen put the same side in tension for the three-point test. After the LSC specimen was rolled, the supports were moved and a "pinned" support (see Figure 5-2) was placed at the midsection of the specimen. The specimen was then balanced on the support and safety supports were placed under the ends until the actuators were in position. The actuators were placed 15 ft (4.57 m) apart, which created the same moment demand under the same load at the support as the four-point test, but linearly decreased to the location of the actuator. However, the load applied increased in the three-point test. "Fixed" supports (see Figure 5-3) were again placed on the specimen below the actuators and neoprene padding was installed between the support and the concrete, as shown on the four-point test.

5.3.2 Instrumentation

All gages were attached to the LSC specimens in the same manner as the four-point tests, and the instrumentation layout for the three-point tests was very similar to the instrumentation layout for the four-point test, except for the first test of LSC16. The KM gages were used for compression measurements and the LVDTs were used for tension strain measurements. Figure 5-13 shows the layout of the KM gages, LVDTs, and the STRs. The LVDTs were placed along the side of the LSC specimens in the tension region to measure the longitudinal strain profile of the splice region at an interval of 18 inches (457 mm). Additionally, LV9 and LV10 were installed on the top side of the LSC specimens at the quarter point and center of the midsection, respectively, to measure the tension strain at the outermost fibers in the section with the largest moment. LV5 was placed at the centroid of the midsection of the LSC specimens to be used with LV4 and KM8 (placed at the bottom for compression strain measurements) in the measurement of the strain distribution of the critical section in this test setup. Lastly, KM6 and KM7 were placed next to the support on the bottom side of the LSC specimens to measure the compression strains in the concrete in the critical section.

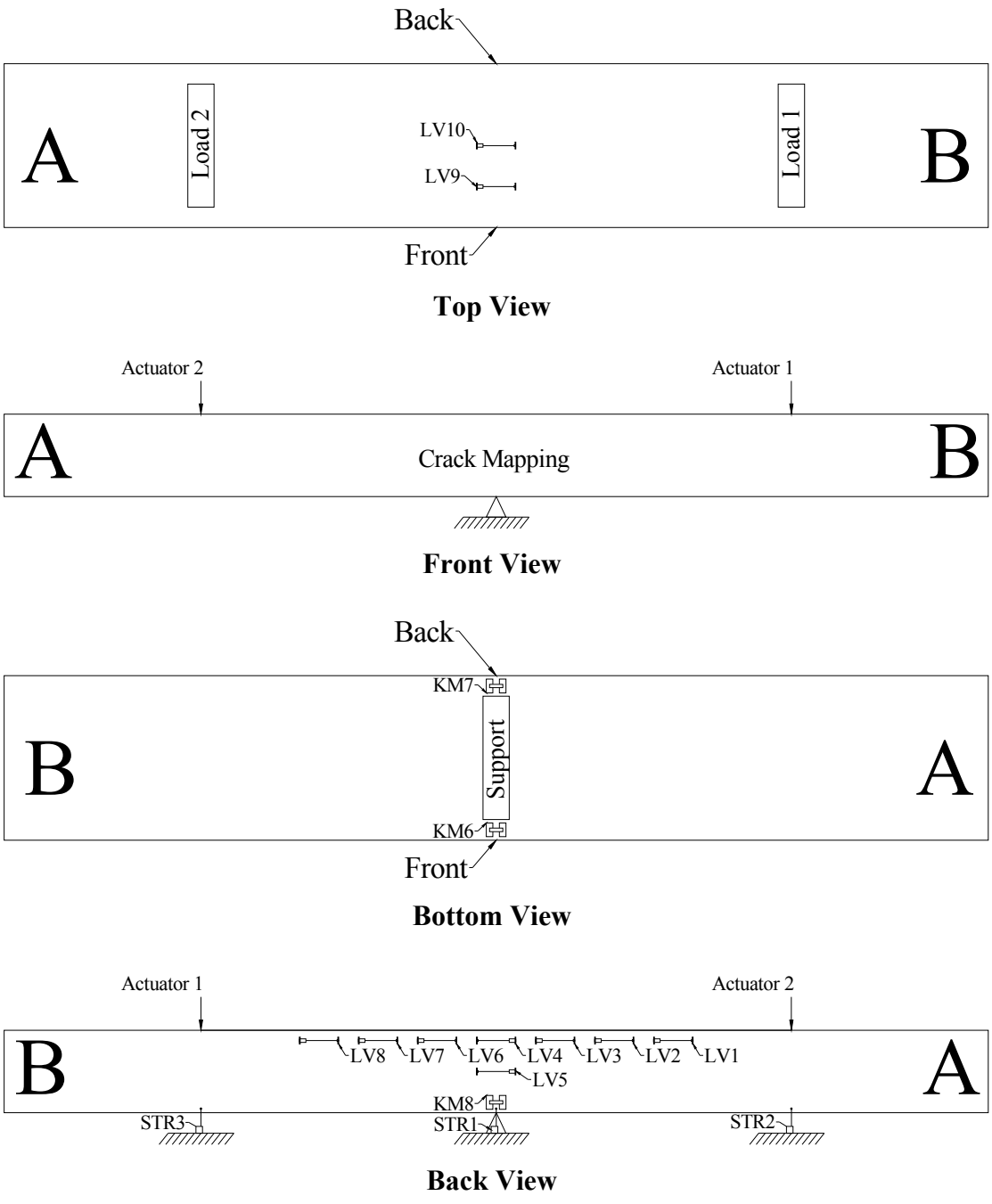

Figure 5-13. External Instrument Layout for the Three-Point Tests.

Three string potentiometers measured the specimen deflections at the support and under each actuator during the three-point test. The following equations were used to calculate the relative specimen deflection at each actuator loading point. The deflections under the support,

Actuator 1, and Actuator 2 are Δ_{STR1}, Δ_{STR3}, and Δ_{STR2}. The relative deflection under Actuator 1 and Actuator 2 are $\Delta_{act\ 1,3pt}$ and $\Delta_{act\ 2,3pt}$. The locations of the actuators and string potentiometers (STR) are pictured in Figure 5-13.

$$\Delta_{act\ 1,3pt} = \Delta_{STR3} - \Delta_{STR1} \quad \text{(Eq. 5-3)}$$

$$\Delta_{act\ 2,3pt} = \Delta_{STR2} - \Delta_{STR1} \quad \text{(Eq. 5-4)}$$

5.3.3 Test Procedures

The test procedures for the three-point test were similar to the four-point test previously described in Section 5.2.3. The only difference from the four-point test was that a load rate of 0.002 inch/sec (50.8 μm/sec) was used throughout the three-point loading test since the specimens were already cracked from the previous four-point tests. Additionally, when the actuators were lowered into place, the safety supports were removed from the ends of the LSC specimens prior to loading, which was not necessary for the four-point tests.

5.4 EXPERIMENTAL RESPONSE

During all tests, the DAQ logged data for both the internal and external sensors installed in the LSC specimens at a rate of one sample per second. As a point of clarification in the upcoming presentation, a hydraulic valve on one of the actuators malfunctioned during the LSC15 and LSC16 four-point tests and the LSC16 first three-point test, which caused the actuator loadings to slightly oscillate. The effects of the oscillations were minor but noticeable, and will be noted in the following measured response plots. This oscillation did not affect the outcome of the performance of the column splice specimen during the load testing.

5.4.1 Material Strength Test Results

During the casting of the large-scale specimens, 12 4 inch × 8 inch (101 mm × 203 mm) cylinders were cast according to ASTM C39-01 (2001). Half of the cylinders were stored in a curing room at 73.4°F (23°C) and 100 percent relative humidity (RH) as AASHTO T126 (2001) specified. The other half of the cylinders were kept with the LSC specimens where they were exposed to accelerated atmospheric conditions at the Texas A&M University Riverside Campus and supplemental watering. Three cylinders from both the field as well as the curing room were tested for 28-day strength as ASTM C39-01 (2001) specified. To determine the material strength at the time of LSC specimen testing, cylinders from the field and curing room were also tested around the same time as the LSC structural tests.

Table 5-3 displays the individual and average compressive strength of three cylinders for all cases as well as the cylinder test date. Note that the "field" cylinders for LSC15 and LSC16 were not exposed to the same environmental conditions as the others since these were the control specimens. The specimens were all cast separately, therefore with different mixes, even though the same mix design was used throughout. The concrete mix was designed for a compressive strength of 5000 psi (34 MPa); however, few cylinder tests resulted with this strength. Only 2 percent of the cylinders had a compressive strength above the 5000 psi (34 MPa) design at 28 days and 56 percent of cylinders reached this strength at the time of the structural load test. The control specimens' compressive strength averaged 1000 psi (7 MPa) lower than that of the non-control specimens, which is probably due to excess water during batching from aggregate moisture. The non-control specimens increased an average of 900 psi (6 MPa) from the 28-day strength test and the time of the structural load test, which shows the concrete continued to gain strength after 28 days as usual. The strength at the time of the structural load test for control specimens was 200 psi (1 MPa) lower than at the 28-day strength, which may be due to the small sample size.

Table 5-3. Concrete Cylinder Compressive Strengths.

	28-Day Strength, psi (Mpa)					Strength at Time of Structural Testing, psi (Mpa)				
	Test Date	Cured		Field		Test Date	Cured		Field	
		Sample	Avg.	Sample	Avg.		Sample	Avg.	Sample	Avg.
LSC1	02/2008	4592	4554	4543	4549	09/2010	4281	5533	5276	5300
		4479	(31)	4682	(31)		6135	(38)	5005	(37)
		4592		4423			6183		5618	
LSC3	03/2008	4740	4813	4626	4449	09/2010	6223	5684	5077	5196
		4854	(33)	4288	(31)		5364	(39)	6613	(36)
		4846		4432			5467		3899	
LSC5	04/2008	4652	4602	4280	4293	08/2011	5913	5637	6101	6046
		4602	(32)	4293	(30)		5432	(39)	6208	(42)
		4551		4307			5566		5828	
LSC8	06/2008	3990	3937	3963	3891	08/2011	5286	5339	5254	5246
		3817	(27)	3767	(27)		5304	(37)	5448	(36)
		4004		3944			5427		5035	
LSC9	07/2008	4679	4869	3789	4111	03/2010	4639	4244	5371	4966
		5016	(34)	4231	(28)		4361	(29)	4082	(34)
		4911		4314			3732		5443	
LSC10	07/2008	4589	4609	4492	4418	03/2010	4647	4886	5053	5024
		4584	(32)	4414	(30)		4735	(34)	5690	(35)
		4655		4349			5276		4329	
LSC15	09/2008	3784	3891	3776	3874	02/2009	3398	3528	3987	3942
		4014	(27)	3802	(27)		3844	(24)	3740	(27)
		3875		4044			3342		4098	
LSC16	09/2008	4017	3964	3899	3744	02/2009	3676	3862	3175	3462
		3919	(27)	3536	(26)		3899	(27)	3509	(24)
		3956		3797			4011		3700	

Figure 5-14 shows a cylinder from LSC1 that was kept in the curing room since the time it was casted. The figure shows that very few and very small surface cracks developed throughout the duration of the cylinder storage in the curing room. The largest crack width measured on the cured cylinders was 0.009 inch (0.23 mm). The figure also shows a white residue that has

leached from a crack. This residue was found on numerous cylinders stored in the curing room and was also present in some locations on the LSC specimens.

Figure 5-14. Cracking of a Cylinder Stored in the Curing Room.

For comparison purposes, Figure 5-15 shows a cylinder exposed to the same environmental conditions as the LSC specimens at the Riverside campus during the specimen deterioration phase (exterior weather conditions and supplemental watering four times a day). In general, these cylinders had more numerous and larger surface cracking than the cylinders taken from the curing room. The largest crack widths were nearly 0.02 inches (0.50 mm) measured with a crack comparator and up to 0.125 inch (3.2 mm) deep. The researchers determined crack depth by inserting a very thin wire into the largest cracks and determining how far in the wire could go. However, most cracks were very small and the depth could not be measured. Figure 5-16 shows the cylinders with the LSC specimens at the Riverside Campus. The photos were taken approximately after the cylinders had been exposed to the environmental conditions for 43 months. The cylinders located in the field at the Riverside Campus exhibited more cracking than the cylinders stored in the curing room. However, the difference between strengths at 28 days and at the time of the structural load test only differed by an average of 100 psi (1 MPa).

Figure 5-15. Cracking of a Cylinder Stored at the Riverside Campus.

Figure 5-16. Cylinders at the Riverside Campus.

To estimate the stress-strain behavior of the concrete, the research team used an analytical model that applied Todeschini's concrete stress function (Todeschini et al. 1964):

$$f_c'' = 0.9f_c' \quad \text{(Eq. 5-5)}$$

$$\varepsilon_0 = 1.71\frac{f_c'}{E_c} \quad \text{(Eq. 5-6)}$$

$$f_c = \frac{2f_c''\frac{\varepsilon}{\varepsilon_0}}{1+\left(\frac{\varepsilon}{\varepsilon_0}\right)^2} \quad \text{(Eq. 5-7)}$$

where f_c and ε are the varying stress and strain, respectively. The specified concrete strength, f'_c , is shown in Table 5.3 for the different specimens and E_c was calculated from the f'_c per ACI. An additional computation for E_c can be found in Gardoni et al. (2007). The cylinders for LSC15 and LSC16 were instrumented with two LVDT's, one on each side of the cylinder. These LVDTs were used to measure the axial strain during the compression tests. The average displacements from each LVDT were divided by the gage length of the LVDTs to calculate the strain as follows.

$$\varepsilon_{LVDT} = \frac{(\Delta_{LVDT\,1}+\Delta_{LVDT\,2})/2}{L_{LVDT}} \quad \text{(Eq. 5-8)}$$

The concrete stress was calculated by dividing the applied force by the cross sectional area of the cylinder. Figure 5-17 shows the stress vs. strain from the cylinder compression tests on LSC15 and LSC16 cylinders. The cylinders stored in the field are about 75 percent less stiff than the cylinders stored in the curing room. The analytical model with an f'c of 4 ksi (28 MPa) is a good match for average cylinders.

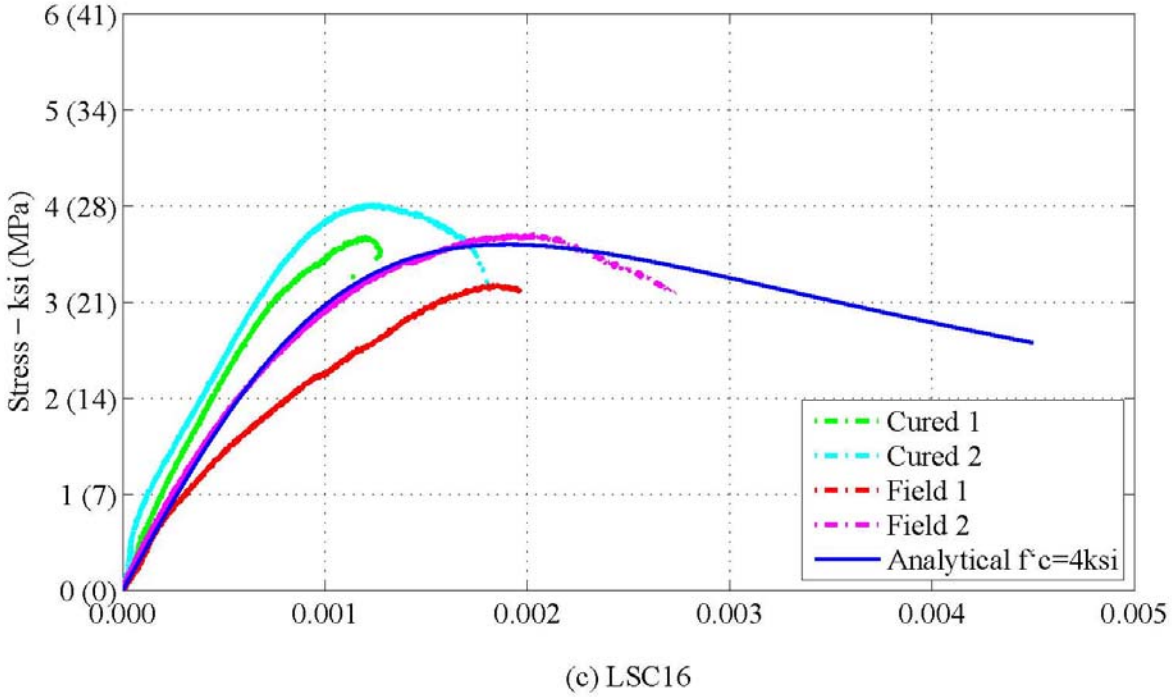

(c) LSC16

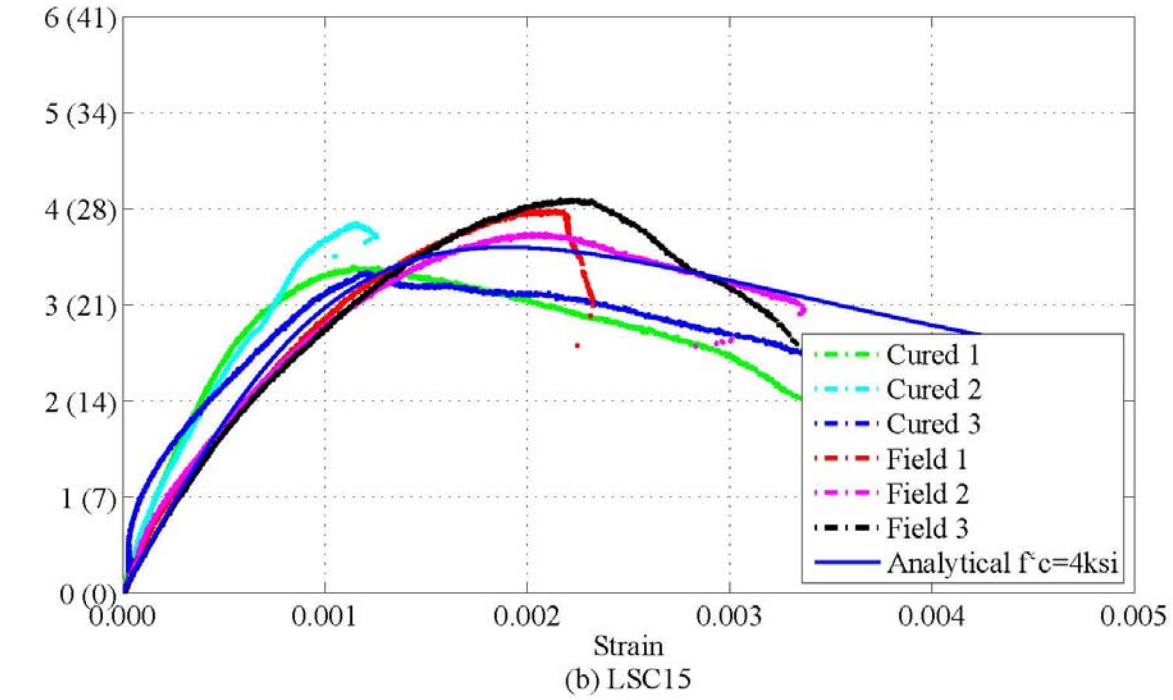

(b) LSC15

Figure 5-17. Compression Stress vs. Strain for LSC15 and LSC16 Cylinders.

In addition to the cylinder compression tests, the research team took one 4-inch diameter core from LSC1 and LSC3 after they tested these structurally. The cores were tested and instrumented in the same manner as the cylinders from LSC15 and LSC16. Figure 5-18 shows the compressive stress-strain plots for the two cores. The strength of the core from LSC1 was about 1 ksi (7 MPa) lower than both the cured and field cylinder strengths for LSC1 at the time of structural testing. The LSC3 core had about the same strength as the field cylinder and was around 0.5 ksi (3 MPa) lower than the cured cylinder average at time of structural testing. The loss in strength could be due to material deterioration, but is most likely due to imperfections in the cores as a result of the coring process. In addition, it seems that the analytical axial stress-strain stiffness is somewhat larger than the experimentally measured stiffness, possibly due to the effects of premature concrete deterioration.

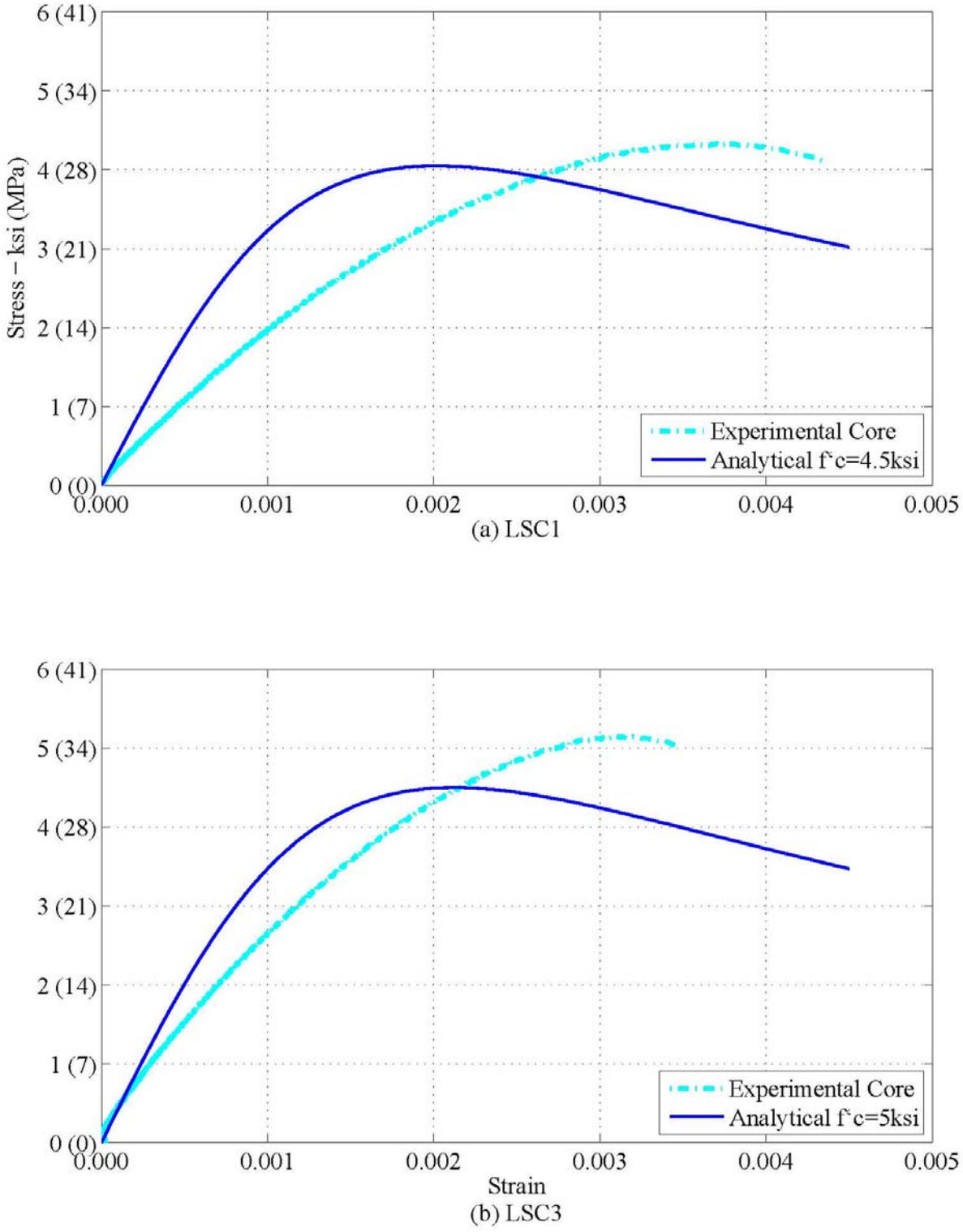

Figure 5-18. Compression Stress-Strain Response for LSC1 and LSC3 Cores.

5.4.2 Four-Point Flexural Test Results and Comparison with Analytical Model

The four-point test results from LSC specimens 1, 3, 5, 8, 9, 10, 15, and 16 are presented in this section. Some things to note prior to further discussion is that LSC15 and LSC16 were the control specimens and were kept in the climate-controlled Structure and Materials Testing Laboratory for six months before testing without supplemental water and no developed premature concrete deterioration. Figure 5-19 compares the experimentally measured force-deformation response from all specimens tested to date. There are two lines for each specimen, one for each actuator. The actuator load is plotted vs. the deflection measured under the respective actuator using the string pot data and Eqs. 5-1 and 5-2. For specimens LSC15 and LSC16, the hydraulic valve in one of the actuators caused minor oscillations in the structural response during testing. The loading was stopped a few times during the tests to view the cracking and assess the condition of the specimen. Therefore, the results show a slight drop in load at a view strains when the loaded halted for a short time. All of the specimens had about the same stiffness (force-deflection slope) until first cracking. The deteriorated specimens were about 25–35 percent stiffer and had a slight (5–15 percent) increase in yield strength than the two control specimens (LSC15 and LSC16) between first cracking and first yielding of the reinforcing steel. The results from each specimen will be shown separately in figures later in this chapter.

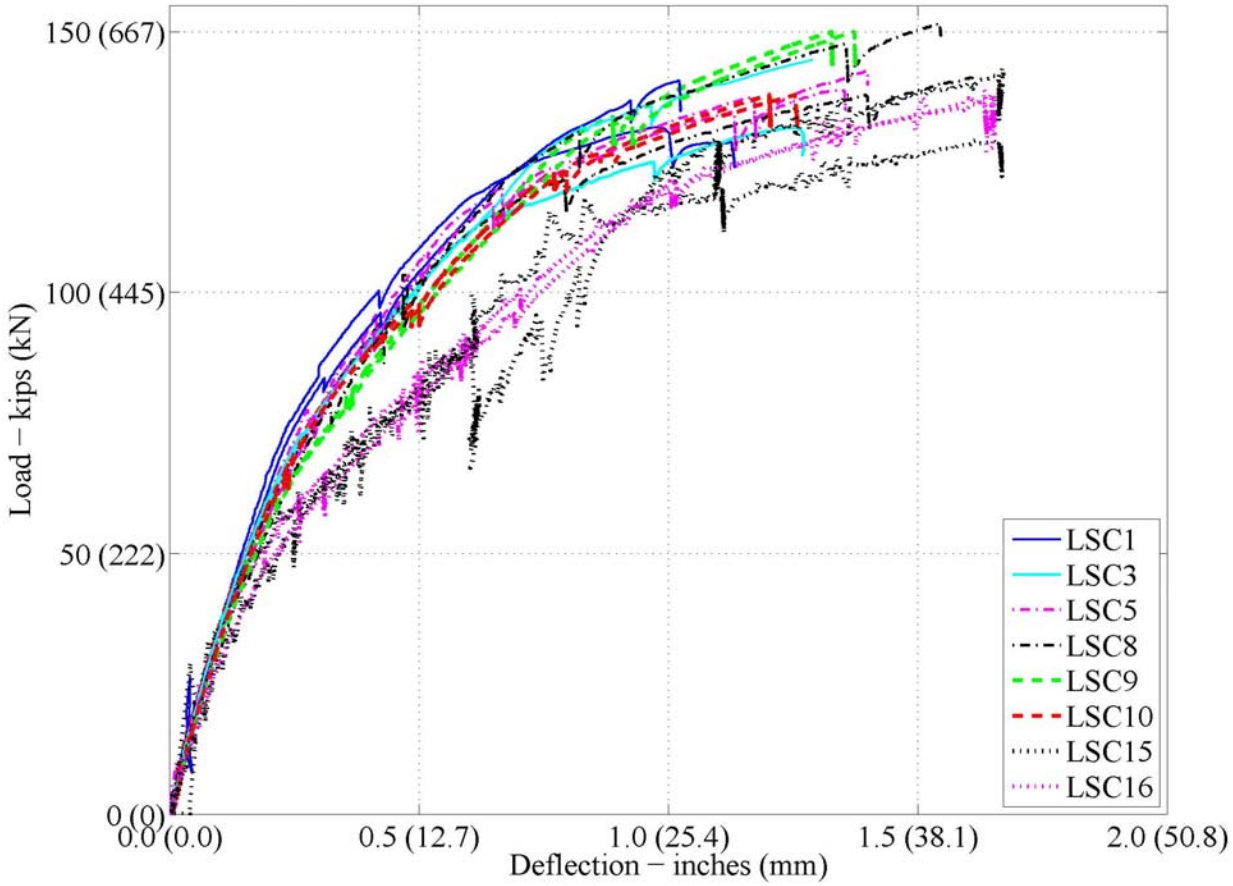

Figure 5-19. Experimental Load vs. Deflection during Four-Point Test: All Tested Specimens at the Actuator Load Point (Splice End).

Figure 5-20 compares the experimental data from LSC15 and LSC16 with the three analytical models described in Chapter 4. The figure clearly shows that the analytical Step-by-Step I_{cr} method best correlated with the experimental test behavior up to the yield point. Beyond the yield point, the results from all analytical models did not fit the post-yield stiffness of the experimental data well since confinement of the concrete and strain hardening of the reinforcement were intentionally not accounted for. In addition, the four-point structural load tests were not meant to find the ultimate specimen strength and deformation, and were not done so experimentally in the four-point test setup. Because of this, the LSC specimens were able to be further tested in the three-point test setup.

The analytical models described in Chapter 4 assumed f_y, was 70 ksi (483 MPa) and f'_c, was 5 ksi (34 Mpa). For the forthcoming comparison of the analytical model with the experimental behavior, the yield strength of the reinforcement, ASTM Grade 60 steel, was also taken to be 70 ksi (483 MPa) for all specimens since it seemed to give the best fit for the data and probably is on the higher end of actual material yield strength produced. Although the degree of concrete deterioration of the test cylinders differed significantly from that of the LSC specimens, the concrete compression strength of the cylinders were mostly unaffected by the deterioration due to ASR/DEF and was consistent for all LSC specimens (see Table 5-3). Therefore, the concrete compression strength used in the analytical model was taken as an average of the data from cylinders that were stored at the Riverside Campus and tested at the time of the specimen's structural load test. The data from the cylinder tests of LSC specimens 1, 3, 5, 8, 9, and 10 were averaged to obtain the analytical f'_c value of 5.3 ksi (37 MPa) that was used for all non-control LSC specimens. The two control specimens, LSC15 and LSC16, had lower f'_c values from the cylinders tested at the time of the load test (see Table 5-3). Therefore, the f'_c used in the analytical model for the control specimens was 3.9 ksi (26MPa).

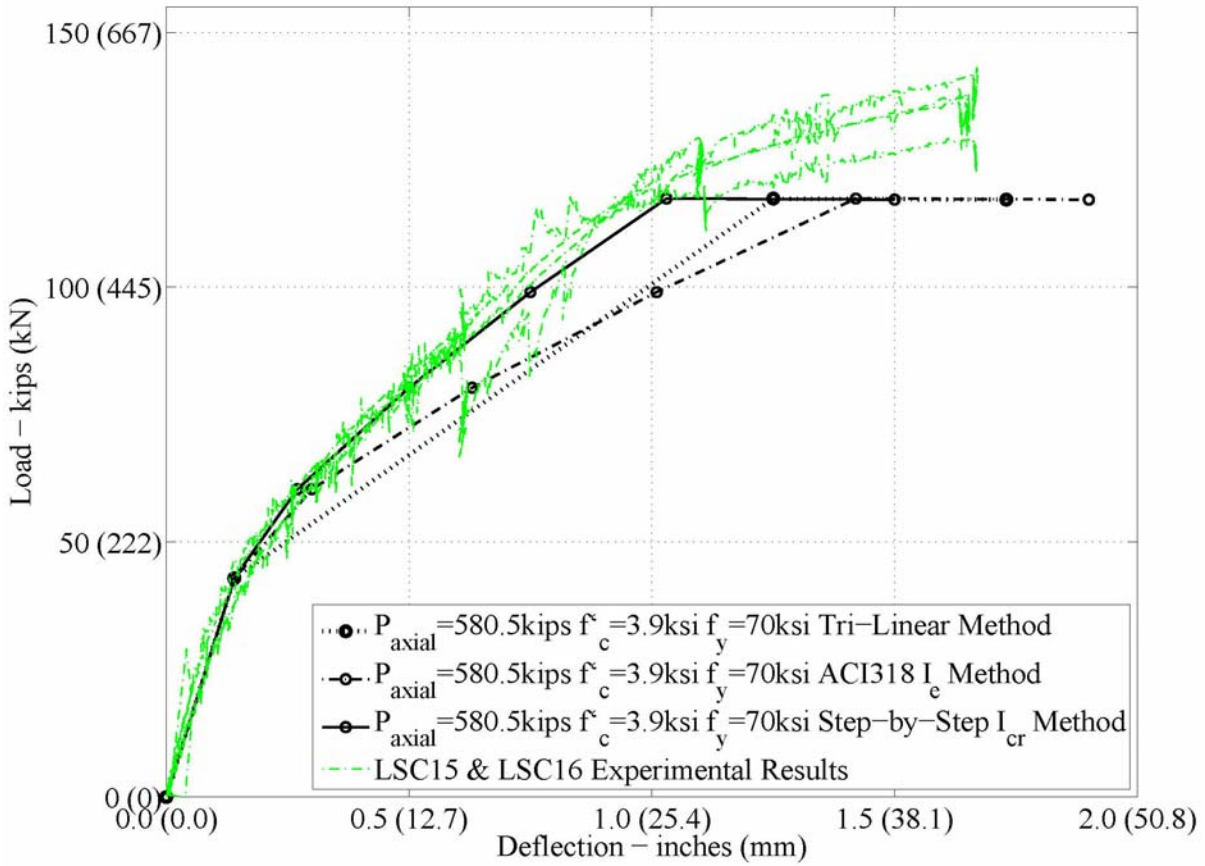

Figure 5-20. Experimental and Analytical Load vs. Deflection of Control Specimens for the Four-Point Test at the Actuator Load Point (Splice End).

Since the column specimens had a presumed constant axial loading from post-tensioning strands of 580.5 kips (2582 kN), the analytical model used this value for computing the first predicted analytical response for the control specimens. The axial loading on the specimen from the strands and column longitudinal reinforcement presumably increased since the other specimens in the deterioration program expanded longitudinally due to ASR and minimal DEF effects (measured from surface mounted instrumentation and internal instrumentation as shown in Chapter 3). Although the post-tensioning strands were not strain gaged to measure the actual strain at testing, Table 5-4 shows the average longitudinal surface strain expansions on all four faces for the deteriorated specimens at the time of structural testing. These measurements show that the specimens expanded in the longitudinal direction, thus indicating the potential for higher levels of axial loading from the post-tensioning strands and longitudinal reinforcement.

Table 5-4. Longitudinal Strains in Tested LSC Specimens.

LSC Specimen #	Date of Casting	Date of Initial Exposure	Date of Structural Load Test	Average Longitudinal Surface Strain at Time of Load Test (strain)			
				Small Face 1	Small Face 2	Large Face 1	Large Face 2
1	1/2008	5/2008	8/2010	0.0006	0.0003	0.0010	N/A
3	2/2008	5/2008	8/2010	0.0005	0.0003	0.0010	N/A
5	4/2008	5/2008	7/2011	0.0004	0.0007	0.0010	0.0014
8	5/2008	7/2008	7/2011	0.0004	0.0007	0.0009	0.0011
9	6/2008	7/2008	2/2010	0.0003	0.0002	0.0006	N/A
10	6/2008	7/2008	2/2010	0.0004	0.0004	0.0008	N/A
15	8/2008	N/A	2/2009	N/A	N/A	N/A	N/A
16	8/2008	N/A	2/2009	N/A	N/A	N/A	N/A

Since the Step-by-Step method best fits the test data for controls specimens, it is the only method used for comparing the analytical model to the experimental test data for the remainder of the specimens. The deteriorated specimens have aged and have induced longitudinal expansions; therefore, Figure 5-21 compares the Step-by-Step I_{cr} analytical model using different values of the column axial loading, F_{act}, and the concrete compression strength, f'_c , to the test results from LSC specimens 1, 3, 5, 8, 9, and 10. Comparing the black dashed lines with the dotted lines, the change in concrete compression strength did not significantly influence the analytical model behavior. However, the increase in the column axial loading (determined based on a best fit of the experimental data) significantly affected the post-cracking stiffness and the yield strength of the analytical response and is shown to fit the experimental response data very well. Therefore, in the analytical model for the non-control specimens, an increased axial force on the specimen was determined to best fit the measured structural response. Table 5-5 shows the final values used for the analytical model, where the LSC specimens were grouped by control and non-control specimens.

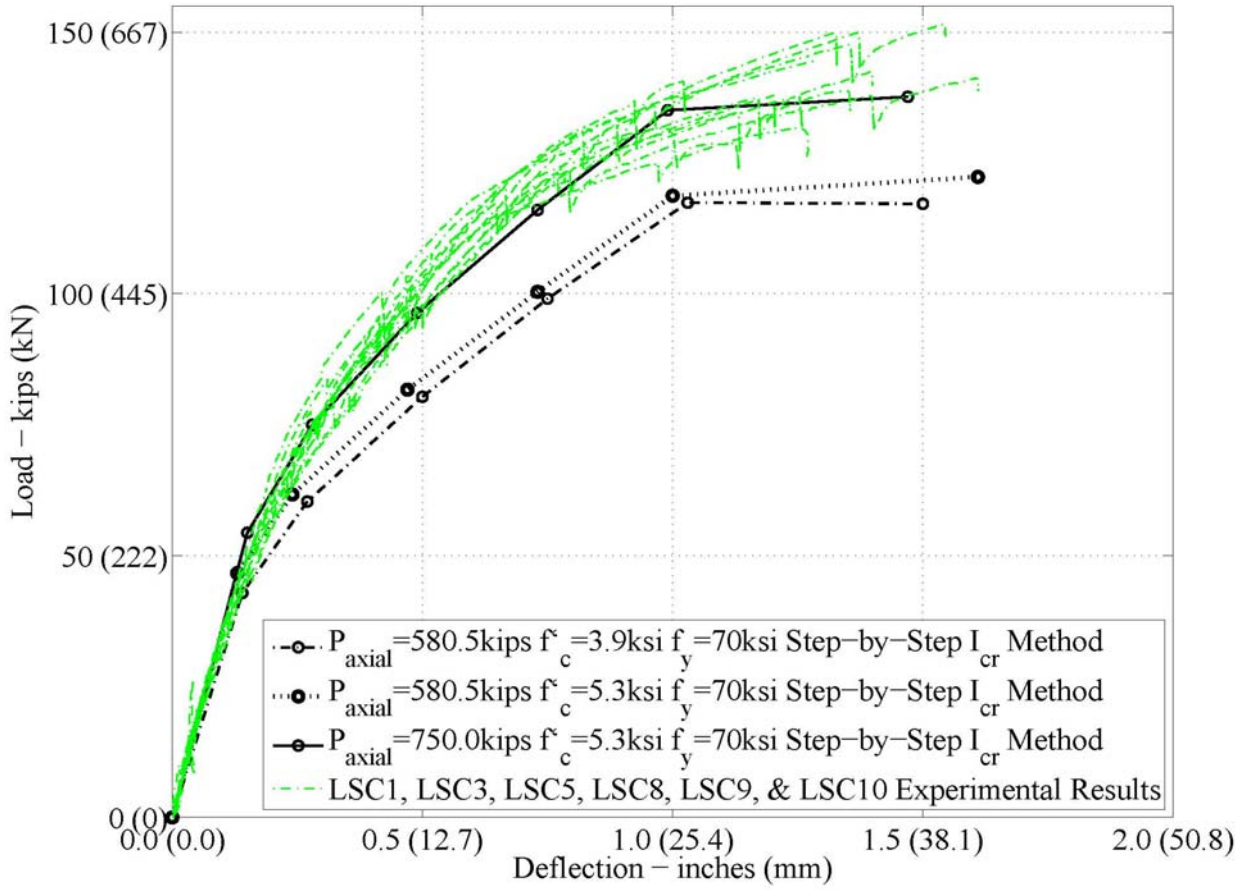

Figure 5-21. Experimental and Analytical Load vs. Deflection of Non-Control Specimens for the Four-Point Test at the Actuator Load Point (Splice End).

Table 5-5. Variables Used for Analytical Model.

	f'_c		f_y		P_{axial}	
	ksi	(Mpa)	ksi	(Mpa)	kips	(kN)
Non-Control LSC Specimens: 1, 3, 5, 8, 9, and 10	5.3	37	70	483	750	3336
Control LSC Specimens: 15 and 16	3.9	27	70	483	580.5	2582

Figure 5-22 compares the experimental and analytical actuator load vs. deflection results for the control specimens and non-control specimens. Note that the figure shows the results for each group of two specimens that were tested at various stages of ASR and minimal DEF

deterioration. LSC16 and LSC15 are shown first since they were the control specimens with no ASR/DEF deterioration and tested first. The results from LSC 9 and 10, LSC 1 and 3, and then LSC 5 and 8 are subsequently shown according to their increasing exposure time and deterioration. The variables from Table 5-5 used for the Step-by-Step I_{cr} analytical model almost accurately predict the structural response up to the yield point for all specimens. However, beyond yielding, the analytical model does not fit the post-yield stiffness of the experimental behavior well because the model does not account for concrete core confinement and strain hardening of the reinforcing steel, which was not the focus of the research.

The figure also highlights the difference in the load vs. deflection response at the sections under each actuator near the yielding point of the specimen response. Experimentally, the actuators were placed in displacement control loading with the exact same displacement targets and displacement rates (implying that they displace the same amount at any given time). However, the measured actuator loading shows slightly different values starting near yielding, most likely due to the uneven accumulation of damage in the specimen at the critical section under each actuator during testing. This slight difference in actuator loadings had no impact on the overall findings of the experimental structural behavior.

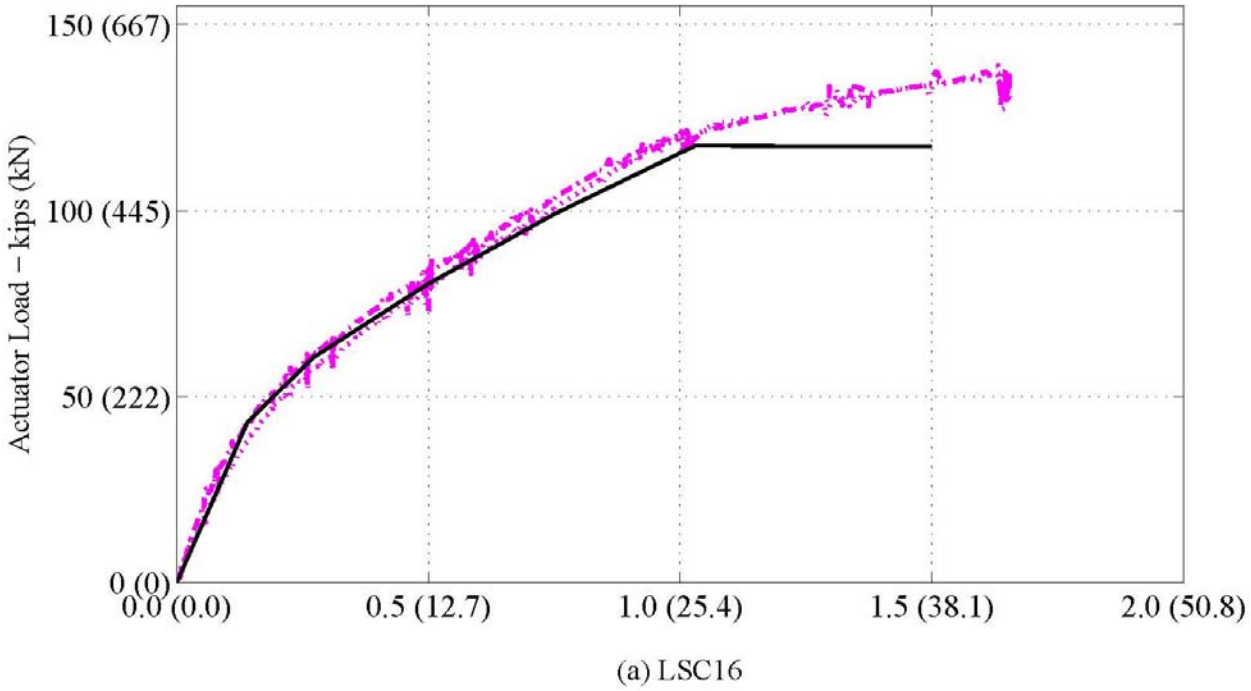

(a) LSC16

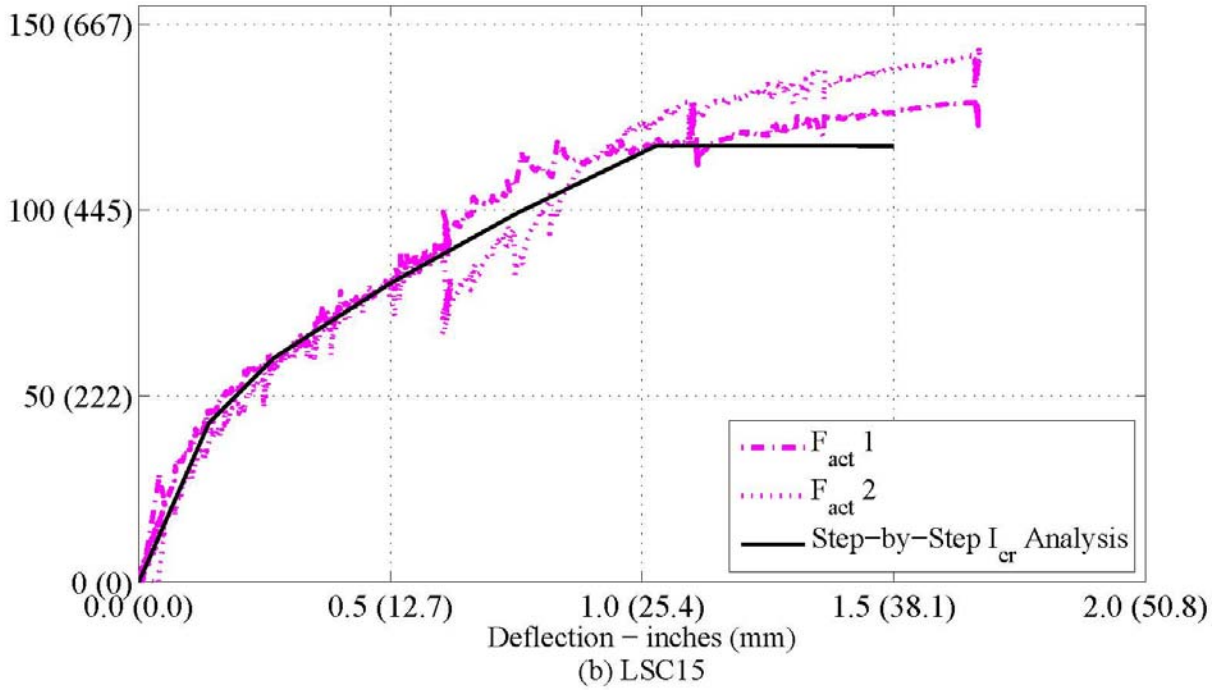

(b) LSC15

Figure 5-22. Experimental and Analytical Load vs. Deflection during the Four-Point Test: At the Actuator Load Point (Splice End).

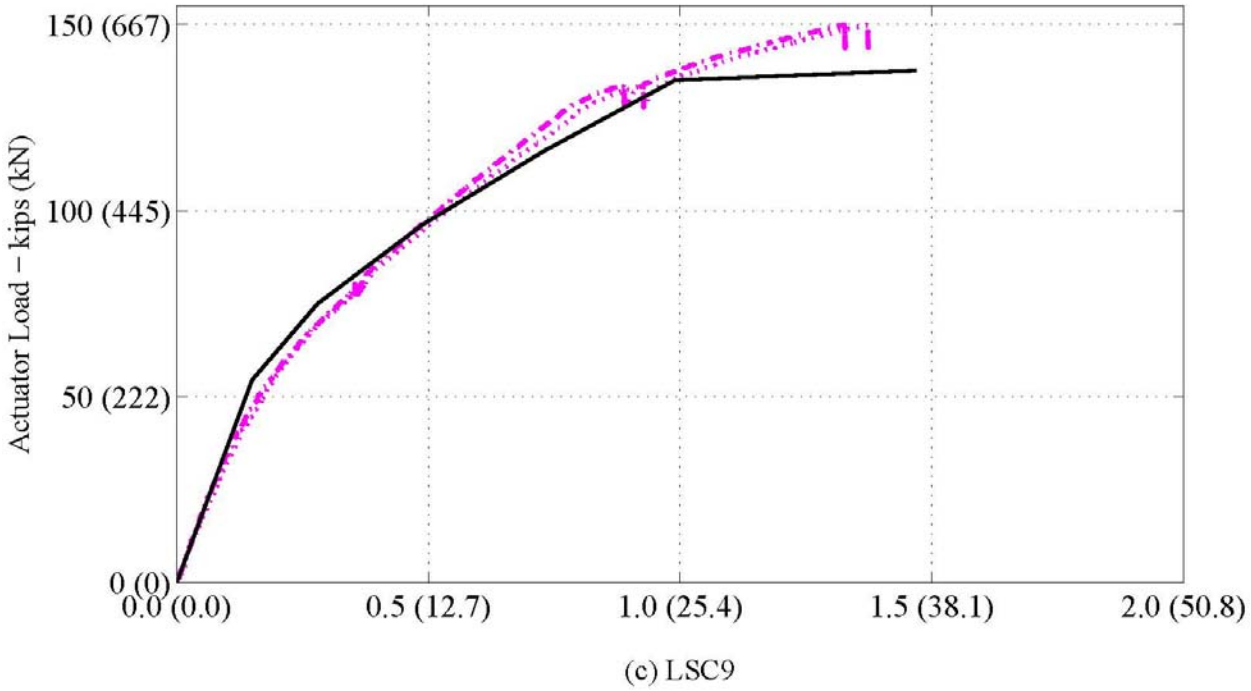

(c) LSC9

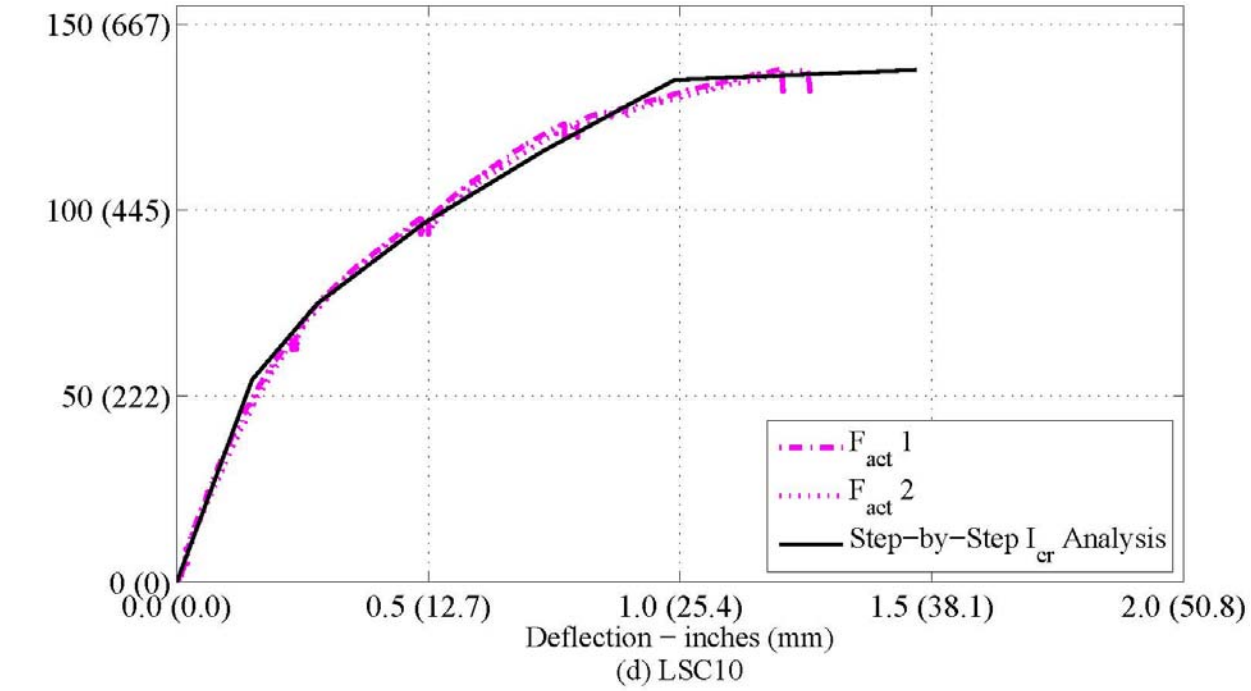

(d) LSC10

Figure 5-22. Experimental and Analytical Load vs. Deflection during the Four-Point Test: At the Actuator Load Point (Splice End). (Continued)

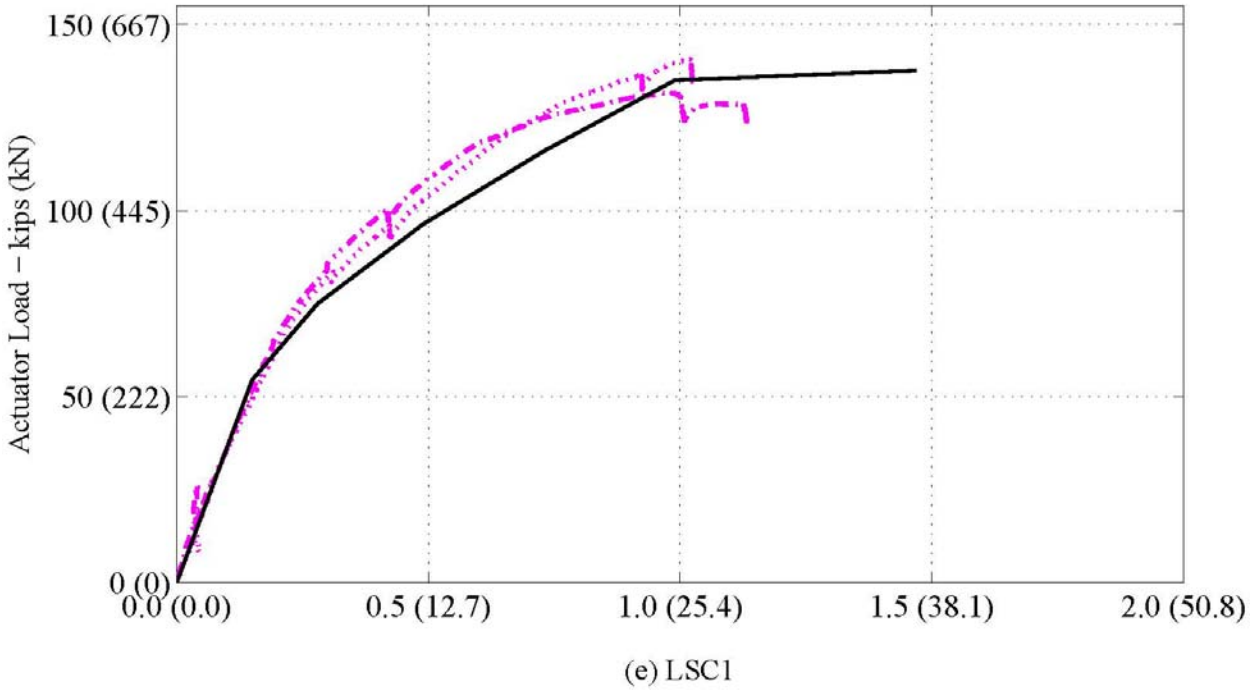

(e) LSC1

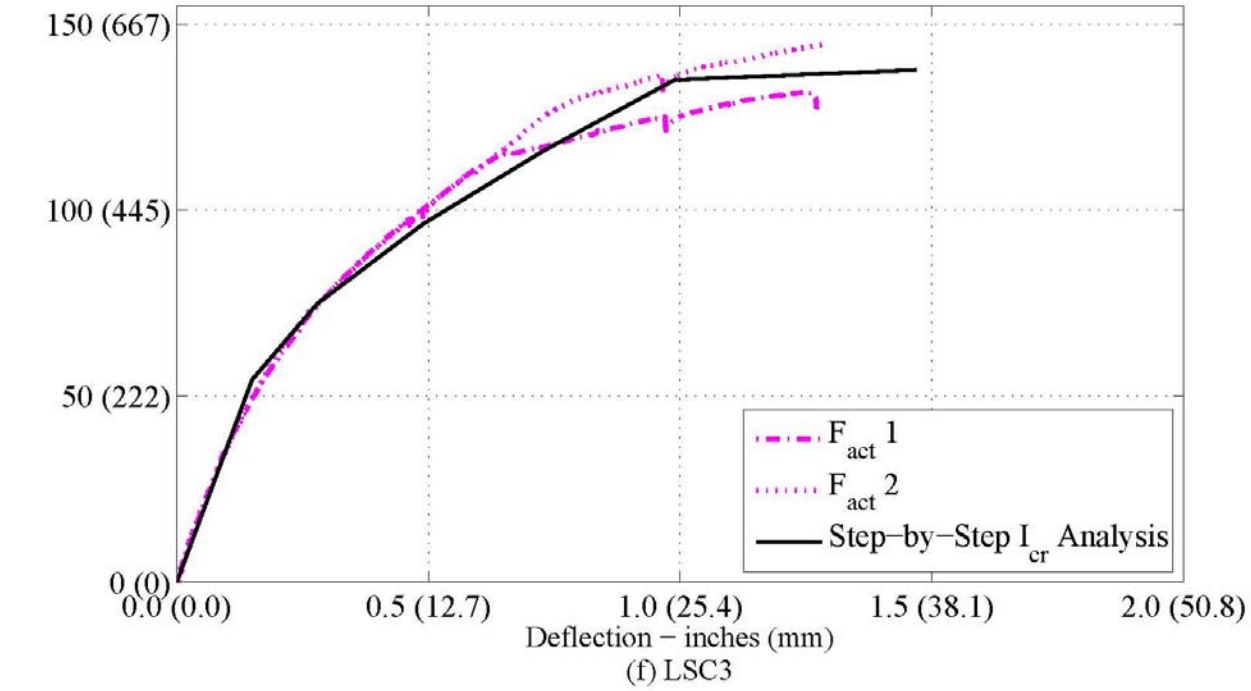

(f) LSC3

Figure 5-22. Experimental and Analytical Load vs. Deflection during the Four-Point Test: At the Actuator Load Point (Splice End). (Continued)

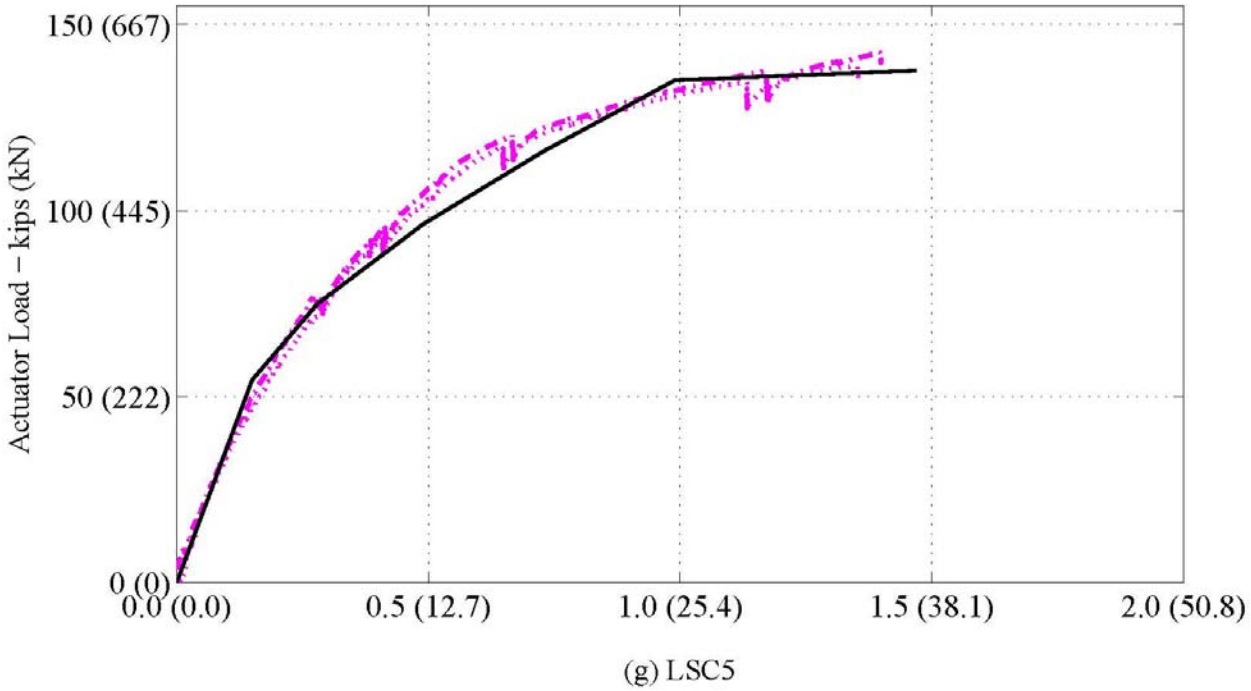

(g) LSC5

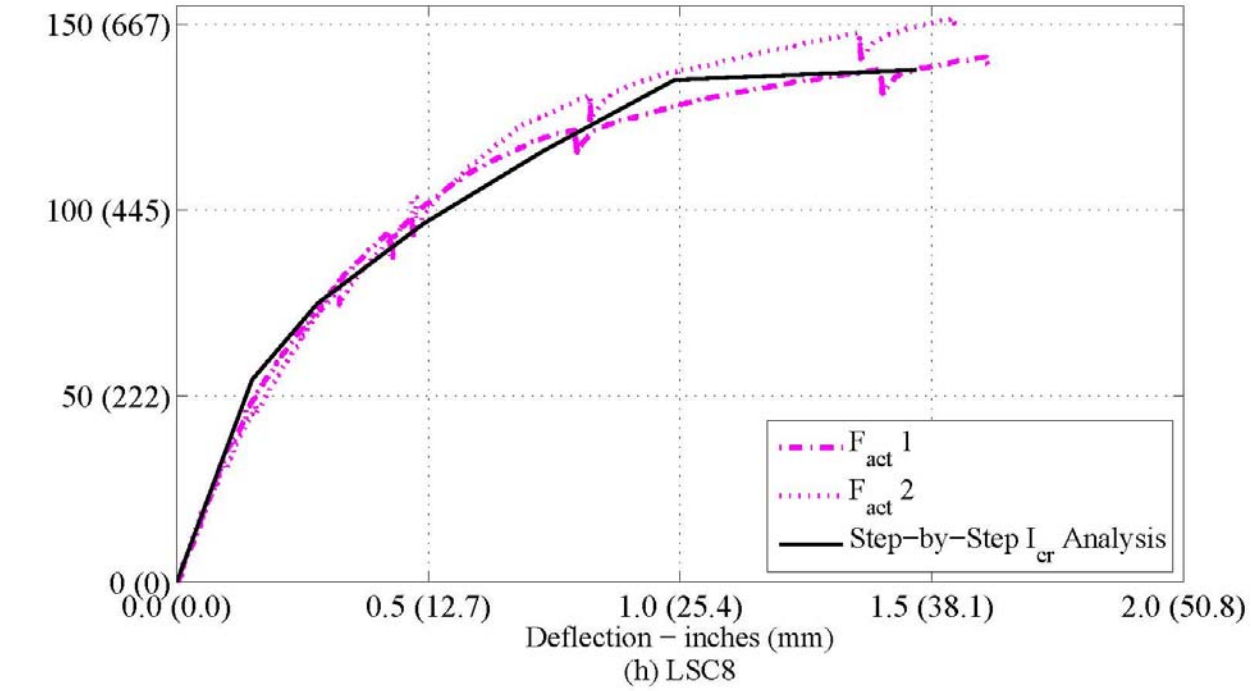

(h) LSC8

Figure 5-22. Experimental and Analytical Load vs. Deflection during the Four-Point Test: At the Actuator Load Point (Splice End). (Continued)

The internal and external strains were measured with the instrumentation presented in Chapter 2 (internal) and section 5.2.2 (external). The results from these measurements are presented to show the behavior of the specimen in the compression and tension regions during structural load testing. If the capacity of the lap splice was not adequate, an assessment of the strains can show the location of the lap splice failure and also the load at which it occurred. The reinforcing steel within the splice region was instrumented internally with strain gages (SGs) as discussed in Chapter 2. Four gages (SG1–SG4) were located on the bottom (tension side during loading) edge reinforcing steel; four gages (SG5–SG8) were located on the bottom center steel; and two gages (SG9–SG10) were located on the top (compression side during loading) center splice bars. Figure 5-23 shows a cross section in the splice region with the locations of the strain gages identified. Figure 5-24 illustrates the longitudinal location of the strain gages. Note that the three groups of strain gages were located on the same splice bar, and SG4 and SG8 were located near the end of the bar with little available anchorage.

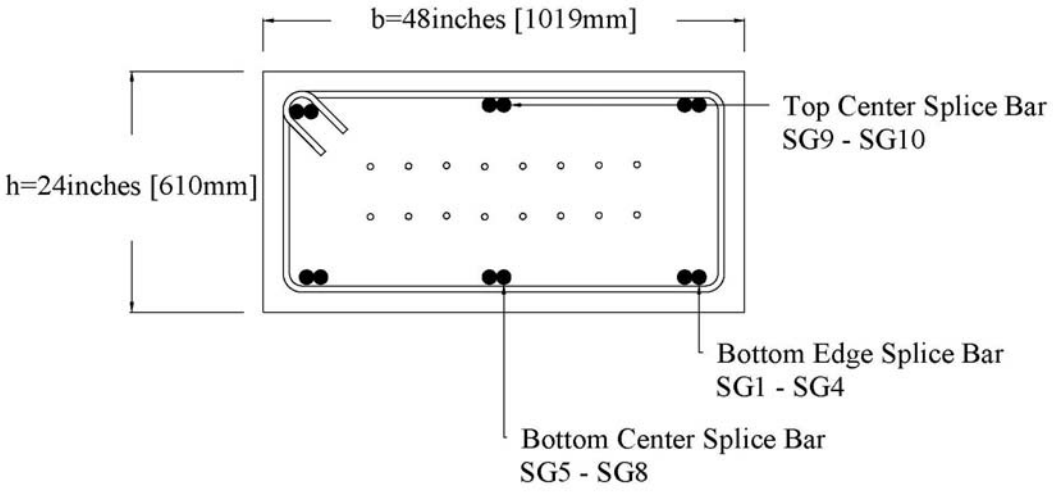

Figure 5-23. Cross Section at Splice Region with SG Locations.

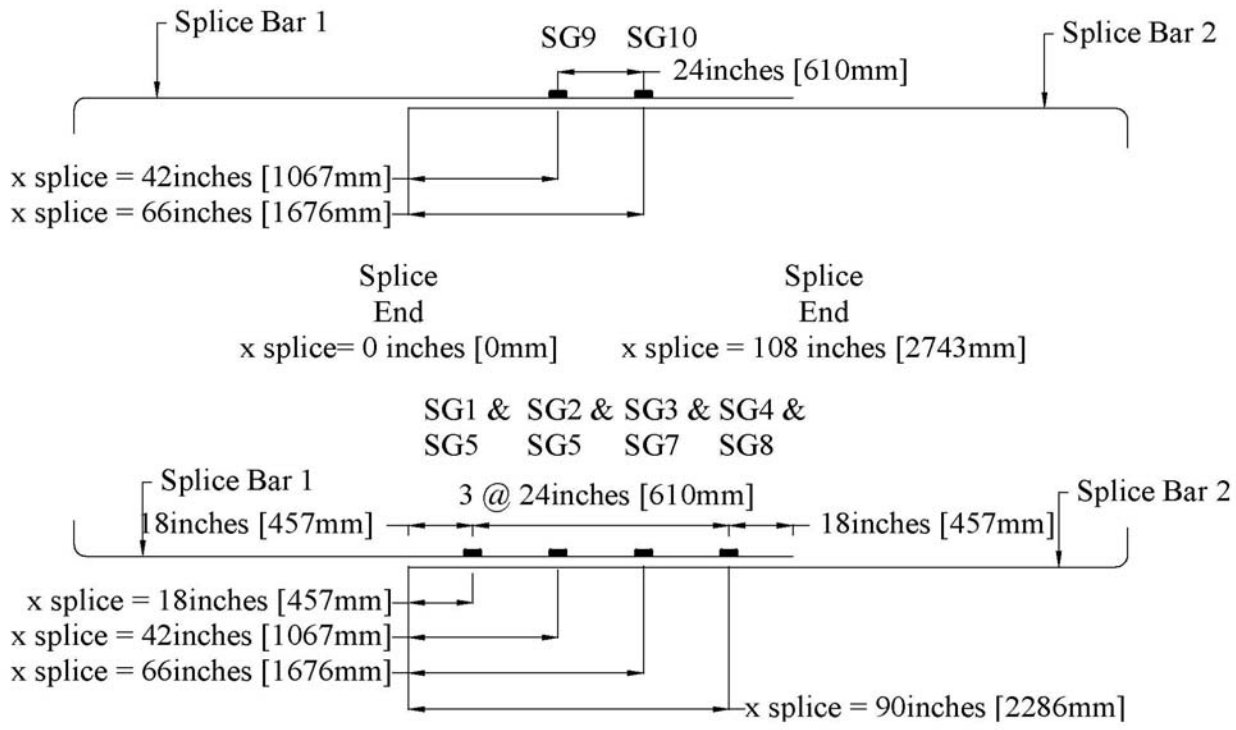

Figure 5-24. SG Locations on Steel in Compression and in Tension.

Figure 5-25 shows the average actuator force plotted versus the internal strains measured by the SG1–SG4. The values from the gages were set to zero at the beginning of the test; therefore, the strains from deterioration are not shown. Figure 3-20, Figure 3-21, and Figure 3-22 showed the strains in SG1–SG10 during the deterioration process and also showed that some of these SG readings had significantly scattered behavior. However, as shown in Figure 5-26, it seems these gages were still able to work during the experimental load testing. In general, Figure 5-26 shows the strain measured with SG1 is usually the largest, and SG4, the smallest. This is the result of the locations of the SGs with respect to the splice bar development. In Chapter 4, the effective area of the reinforcing steel is calculated based on a linear increase up to full participation at the development length of the bar. Since SG4 is located near the bar end and has very little anchorage, the contributing area is very small compared to the full area contributing on the bar where SG1 is located. The analytical model used the sum of the effective areas from Splice Bar 1 and Splice Bar 2 to calculate the strain at the tension steel. To compare the experimental strain gage readings on Splice Bar 1 to the analytical model, an SG factor was proposed to modify the

calculated strain values at a given section so that individual bars strains could be approximated as shown below:

$$\text{SG Factor} = \frac{A_{s1}}{A_{s,eff,splice}} \quad \text{(Eq. 5-9)}$$

A_{s1} is the area from Splice Bar 1 and $A_{s,eff,splice}$ is the area from both splice bars depending on the location with respect to the development length of each bar. The formulas for these variables are in Chapter 4. The SG distances from the bar ends are shown in Figure 5-24.

Figure 5-26 shows the strains on the bottom reinforcing steel measured with SG5–SG8. These strains are assumed to be the same as SG1–SG4 since the only difference is SG1–SG4 are located on an edge bar and SG5–SG8 are located on a center bar. Therefore, the analytical predictions for SG5–SG8 are the same as SG1–SG4.

The four SG analytical values in Figure 5-25 and Figure 5-26 are different since the distance from the end of Splice Bar 1 (development of splice bar) is different for each gage. The analysis assumed the steel and concrete remained bonded (plane sections remain plane). However, when the research team mounted the SGs to the steel bars, they placed a sleeve around each SG to protect the gage. This presumably did not allow for a perfect bond between the concrete and the steel at the location of the SGs. The figure shows the steel within the splice region is within the yield strain of the reinforcement (around 0.002) with very few exceptions (SG1 in LSC15, SF5 in LSC8, and SG8 in LSC10); therefore, the sections between the spliced ends have not yielded. When comparing the analytical and experimental response, the differences are evident; however, general trends of the response are similar. The SG application that removed the bond between the reinforcing steel and concrete at the location of the gage possibly caused the experimental results to be five times larger than the analytical model at the first cracking limit state.

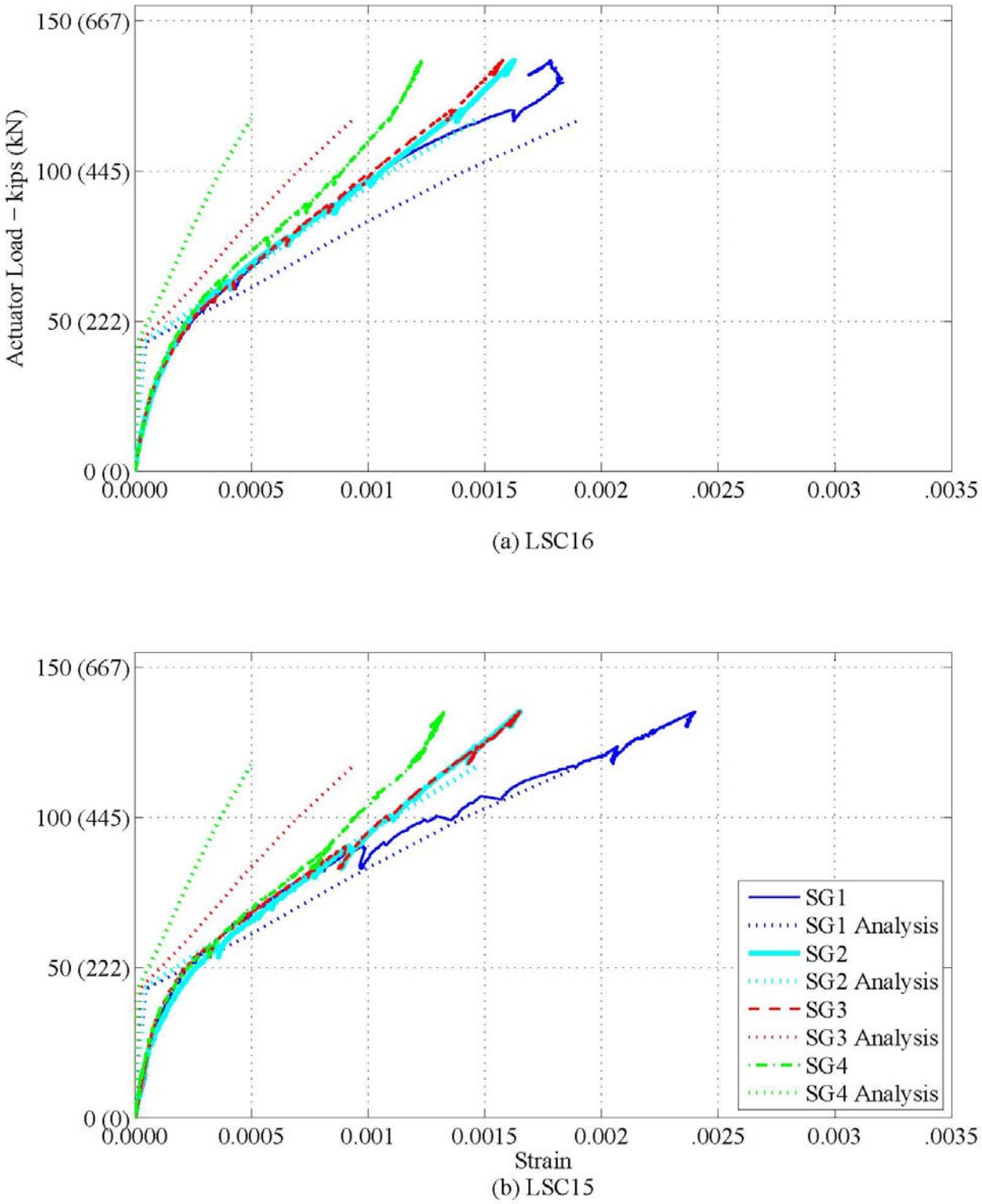

Figure 5-25. Experimental and Analytical Load vs. Strain during the Four-Point Test: Internal Strain Gages (SG1–SG4) along the Tension Steel of the Splice Region.

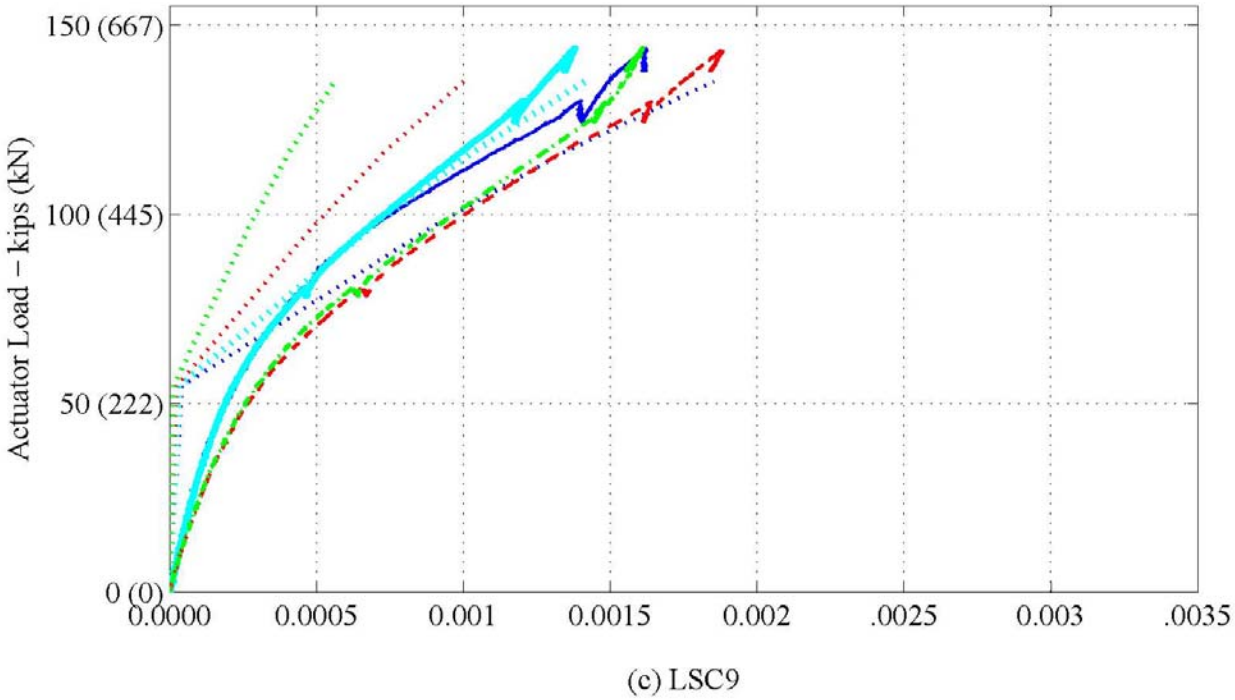

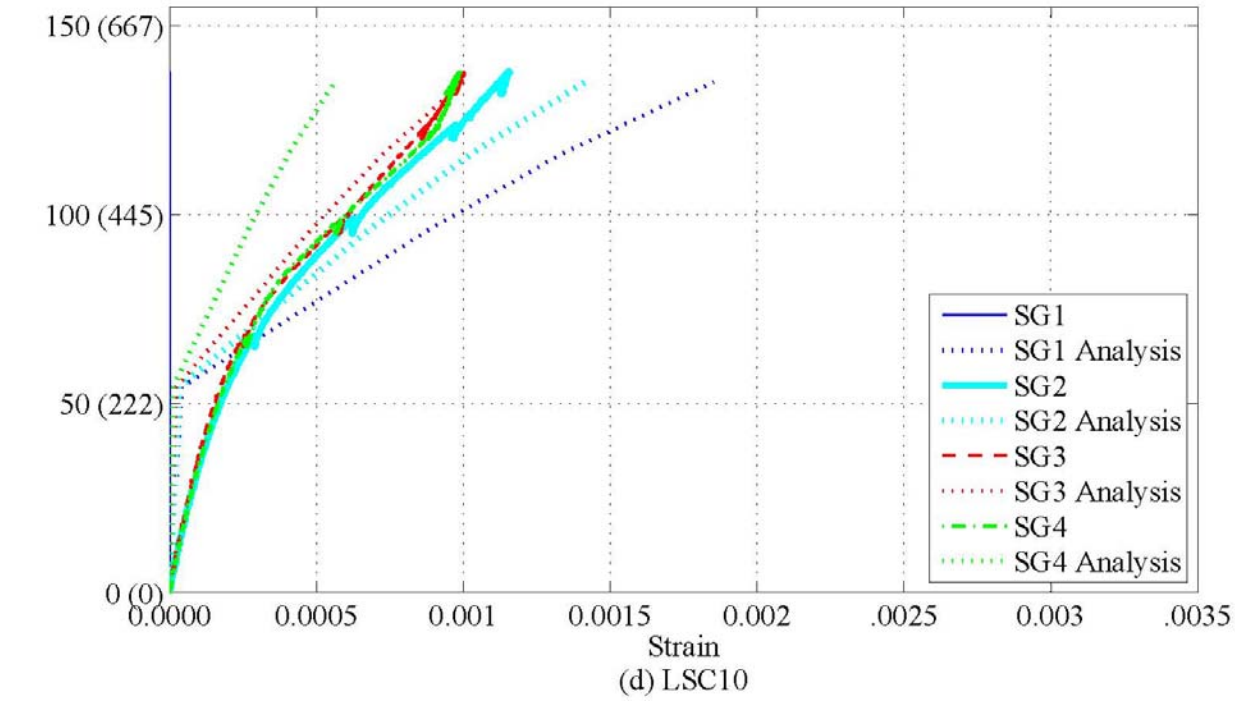

Figure 5-25. Experimental and Analytical Load vs. Strain during the Four-Point Test: Internal Strain Gages (SG1–SG4) along the Tension Steel of the Splice Region. (Continued)

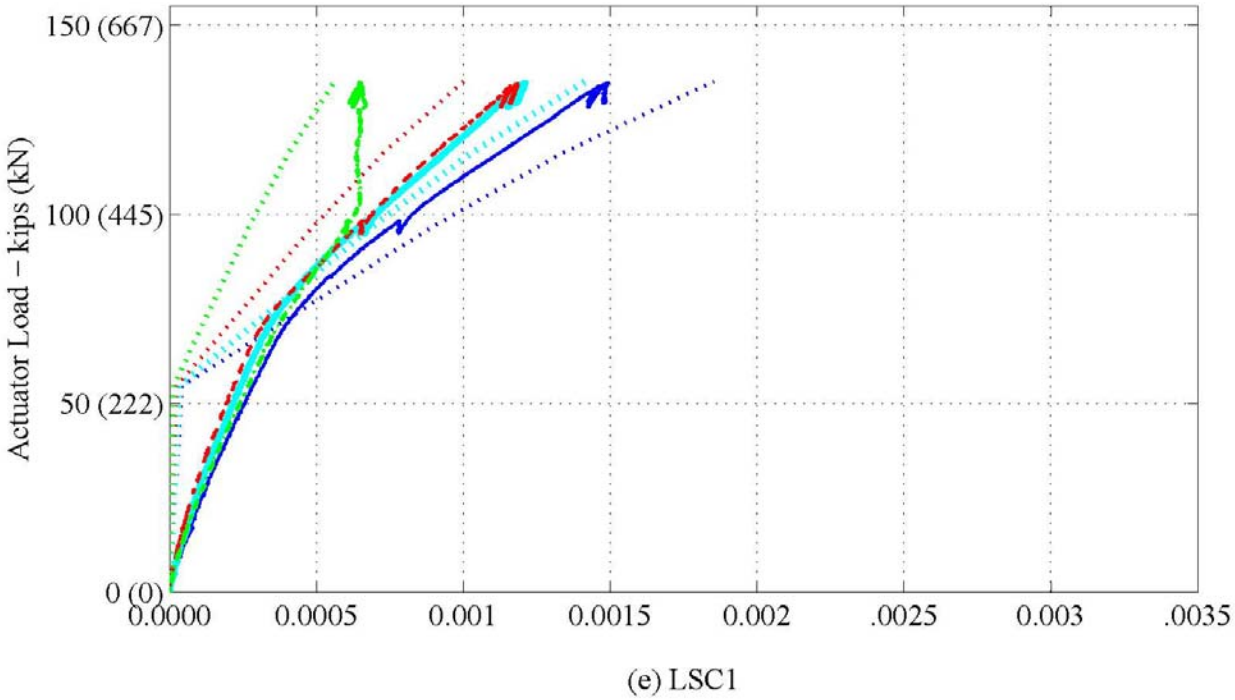

(e) LSC1

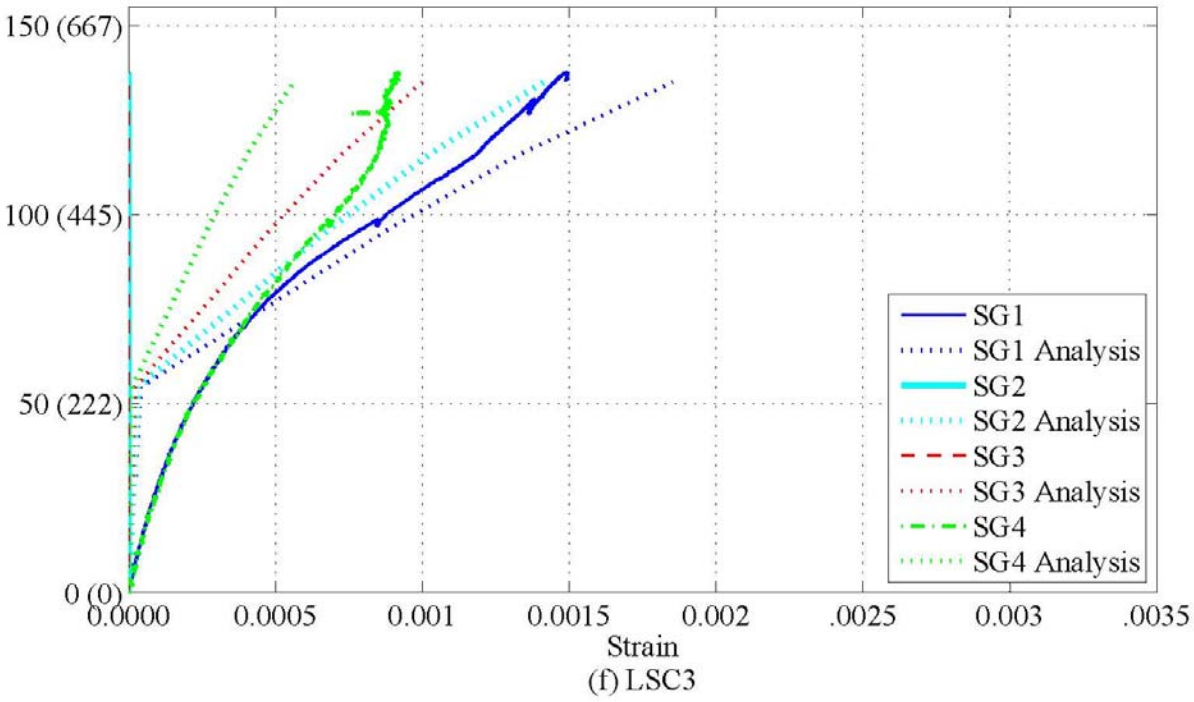

(f) LSC3

Figure 5-25. Experimental and Analytical Load vs. Strain during the Four-Point Test: Internal Strain Gages (SG1–SG4) along the Tension Steel of the Splice Region. (Continued)

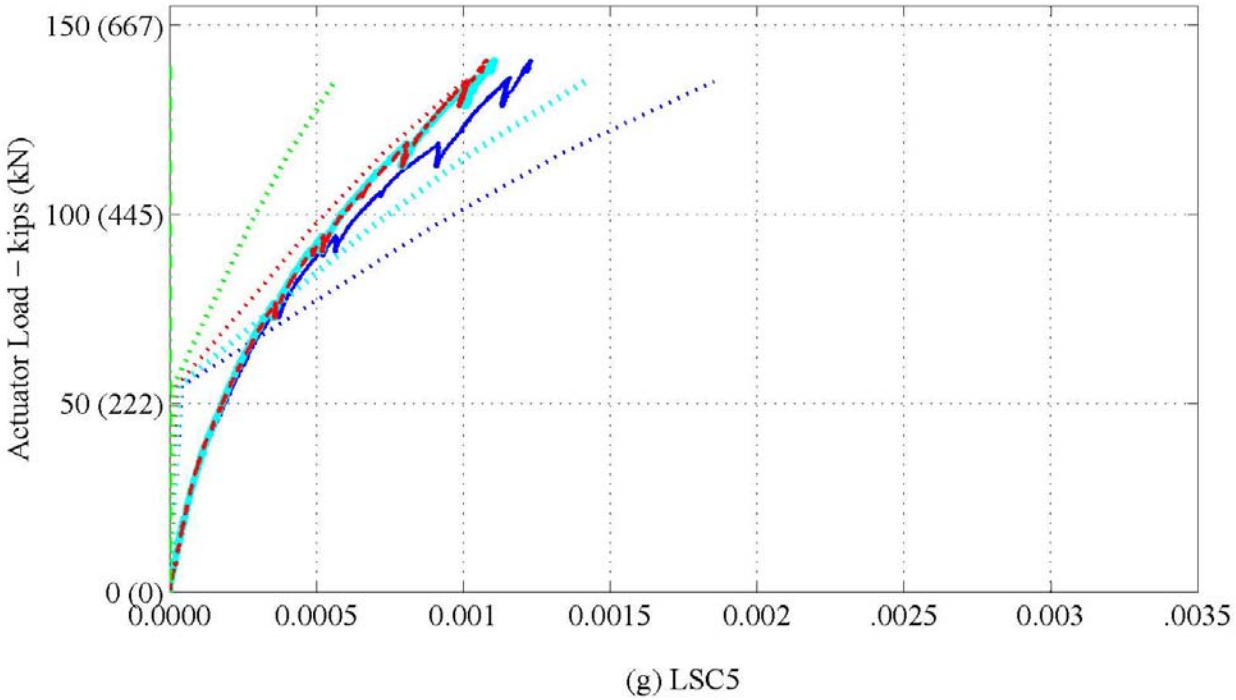

(g) LSC5

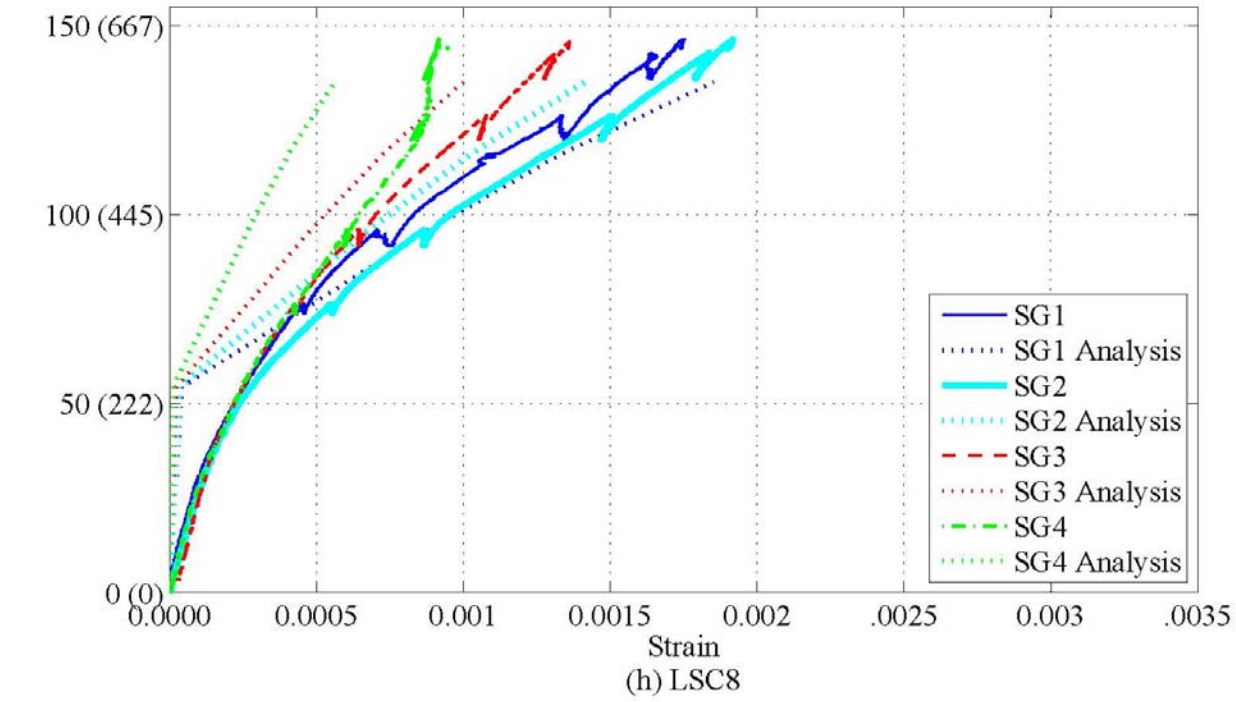

(h) LSC8

Figure 5-25. Experimental and Analytical Load vs. Strain during the Four-Point Test: Internal Strain Gages (SG1–SG4) along the Tension Steel of the Splice Region. (Continued)

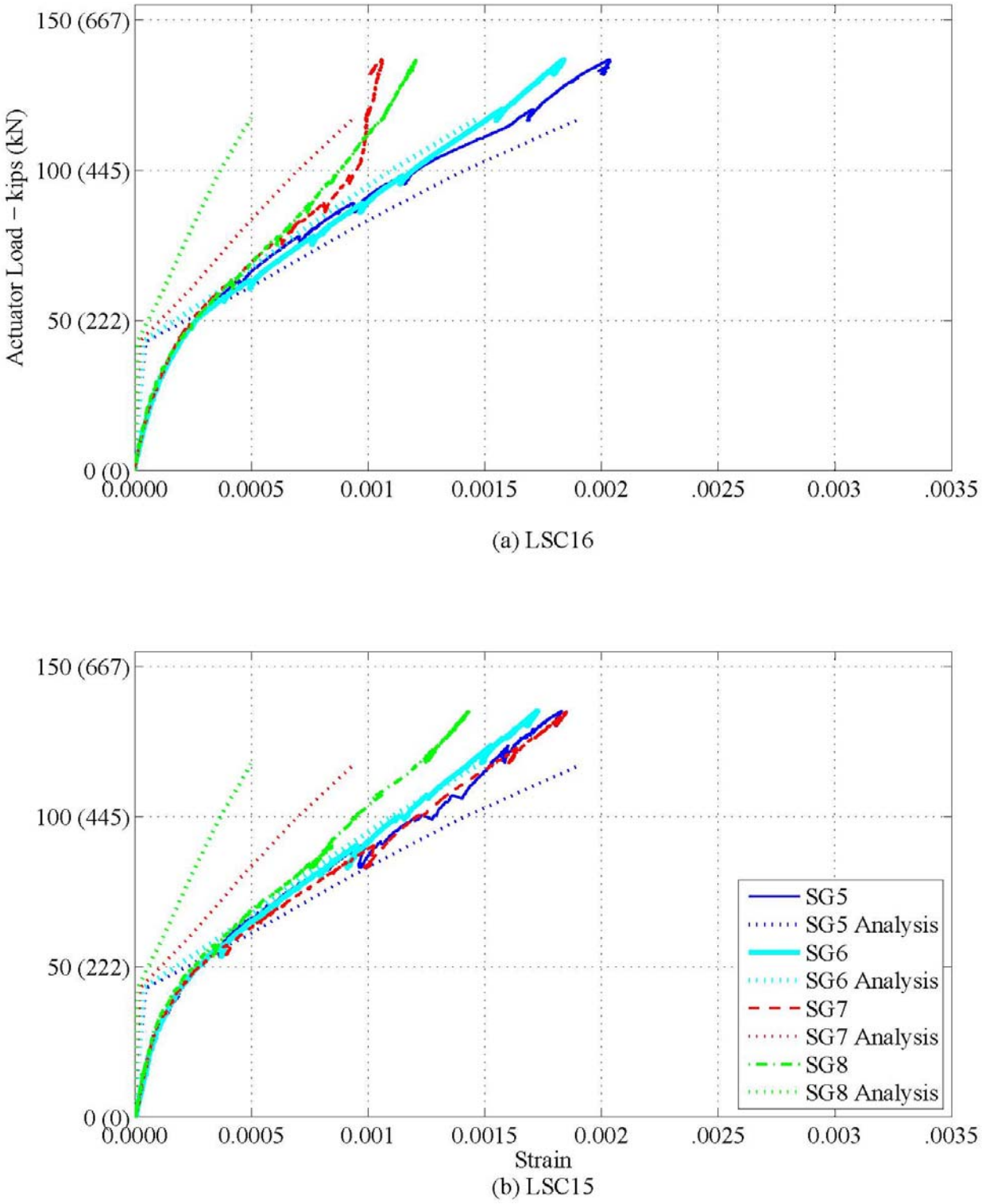

Figure 5-26. Experimental and Analytical Load vs. Strain during the Four-Point Test: Internal Strain Gages (SG5–SG8) along Tension Steel of the Splice Region.

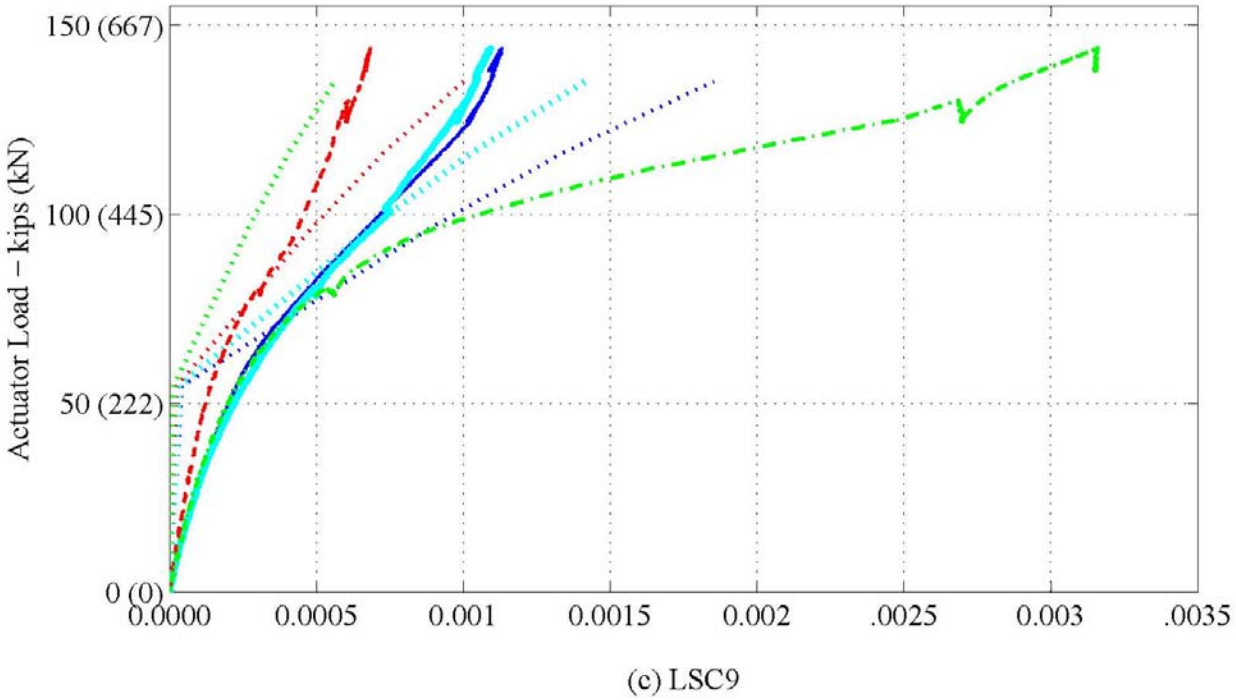

(c) LSC9

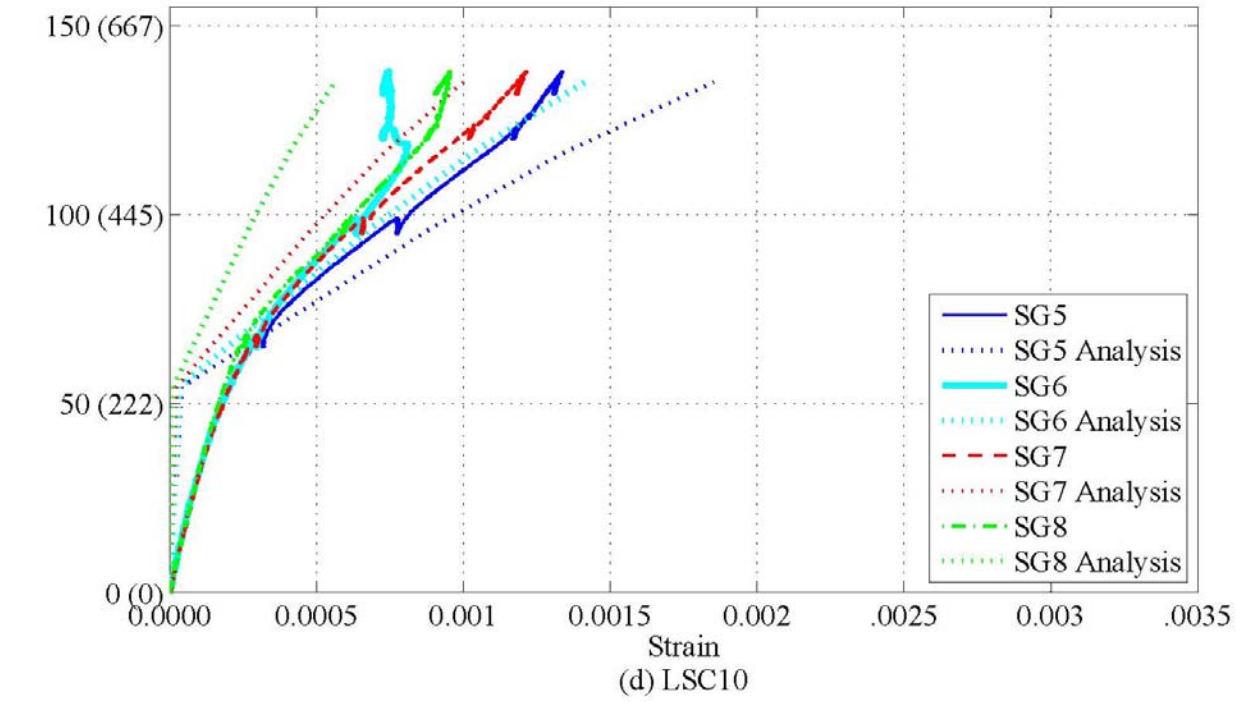

(d) LSC10

Figure 5-26. Experimental and Analytical Load vs. Strain during the Four-Point Test: Internal Strain Gages (SG5–SG8) along Tension Steel of the Splice Region. (Continued)

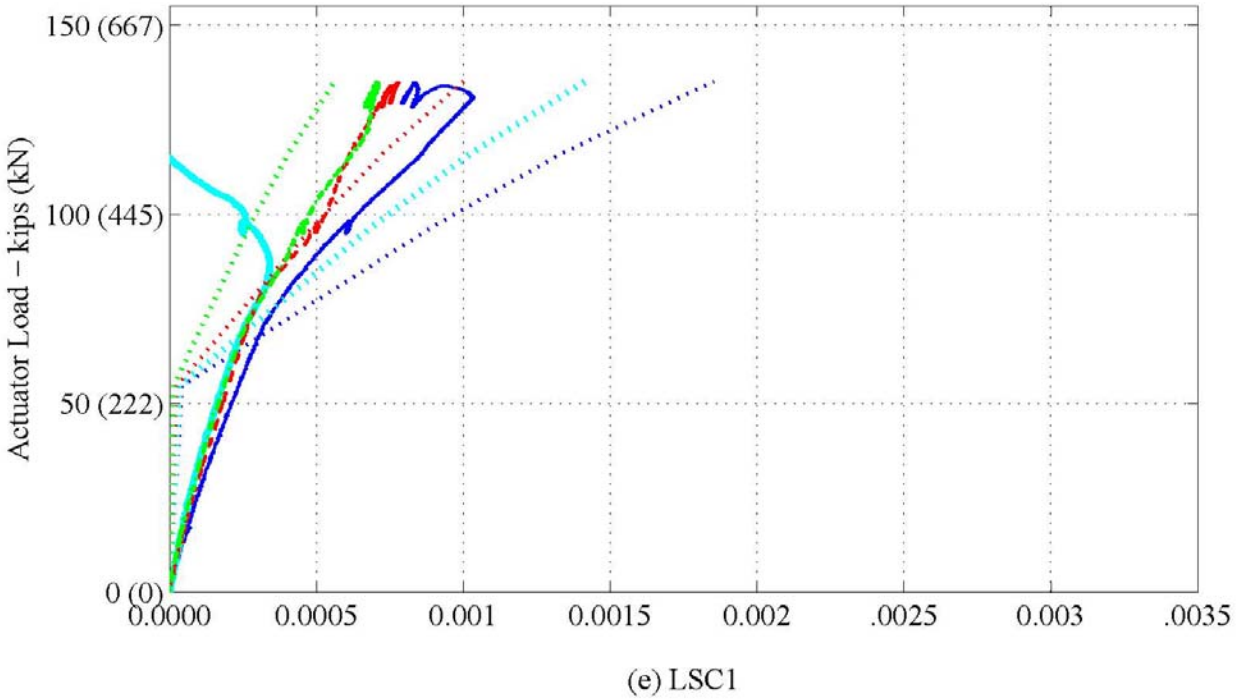

(e) LSC1

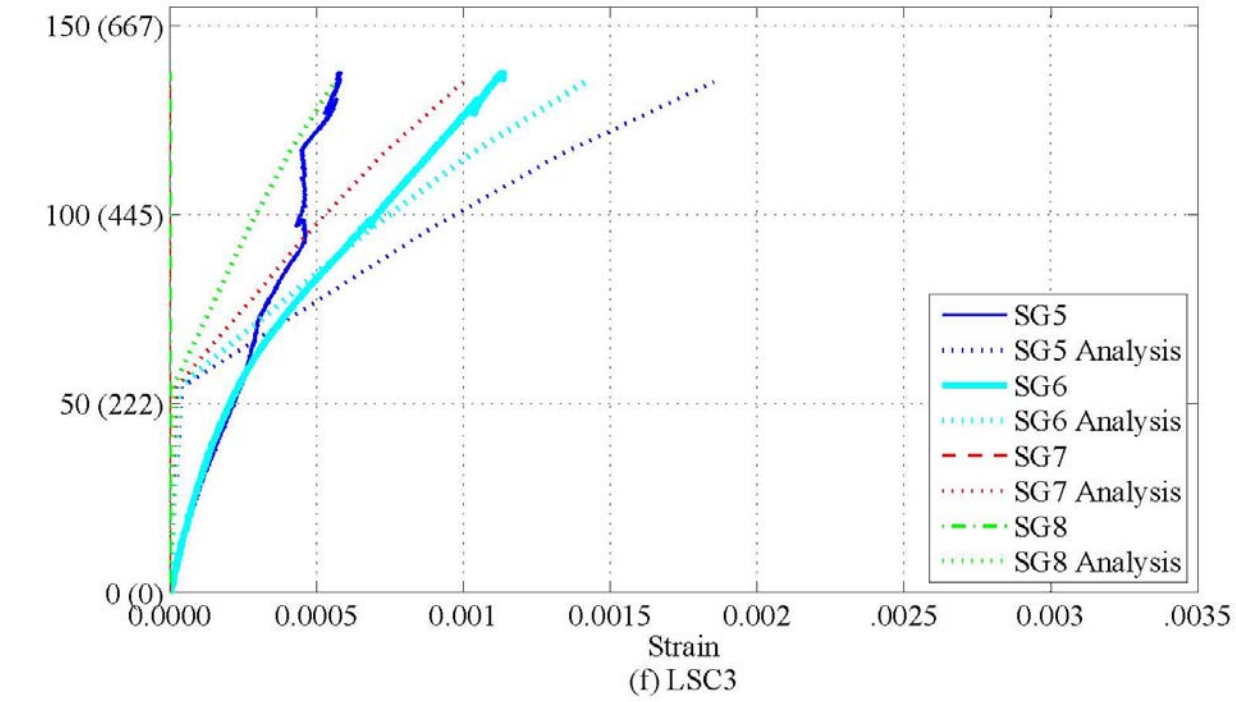

(f) LSC3

Figure 5-26. Experimental and Analytical Load vs. Strain during the Four-Point Test: Internal Strain Gages (SG5–SG8) along Tension Steel of the Splice Region. (Continued)

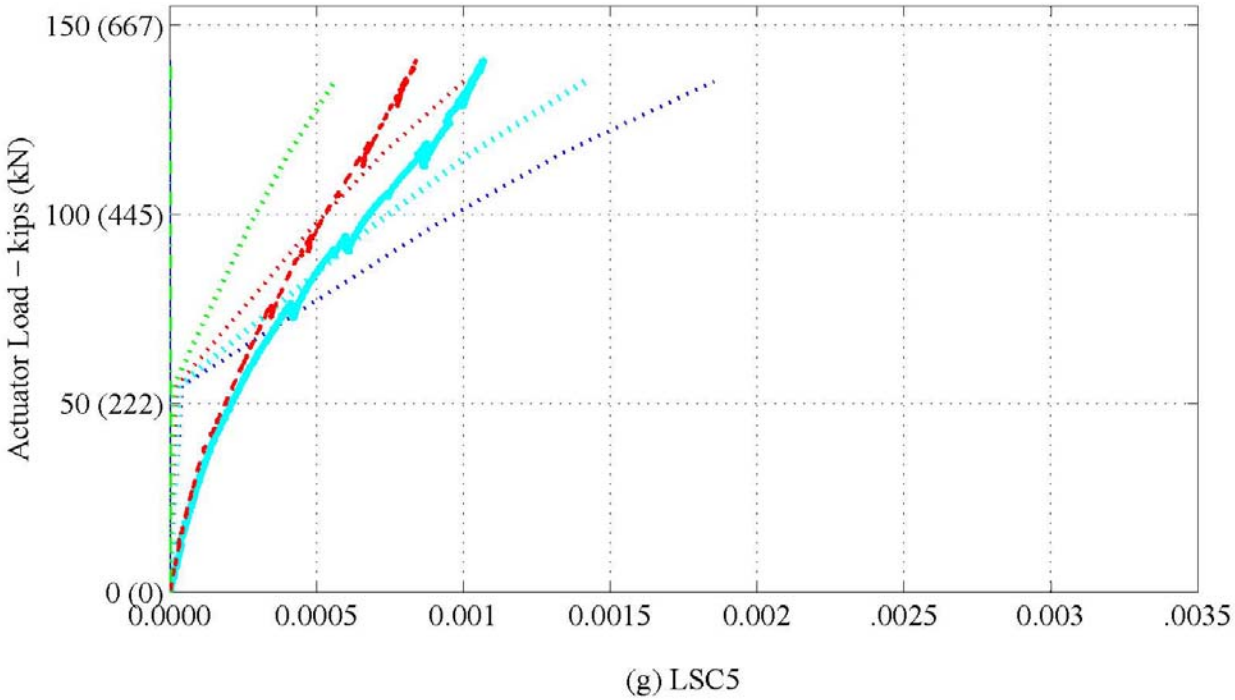

(g) LSC5

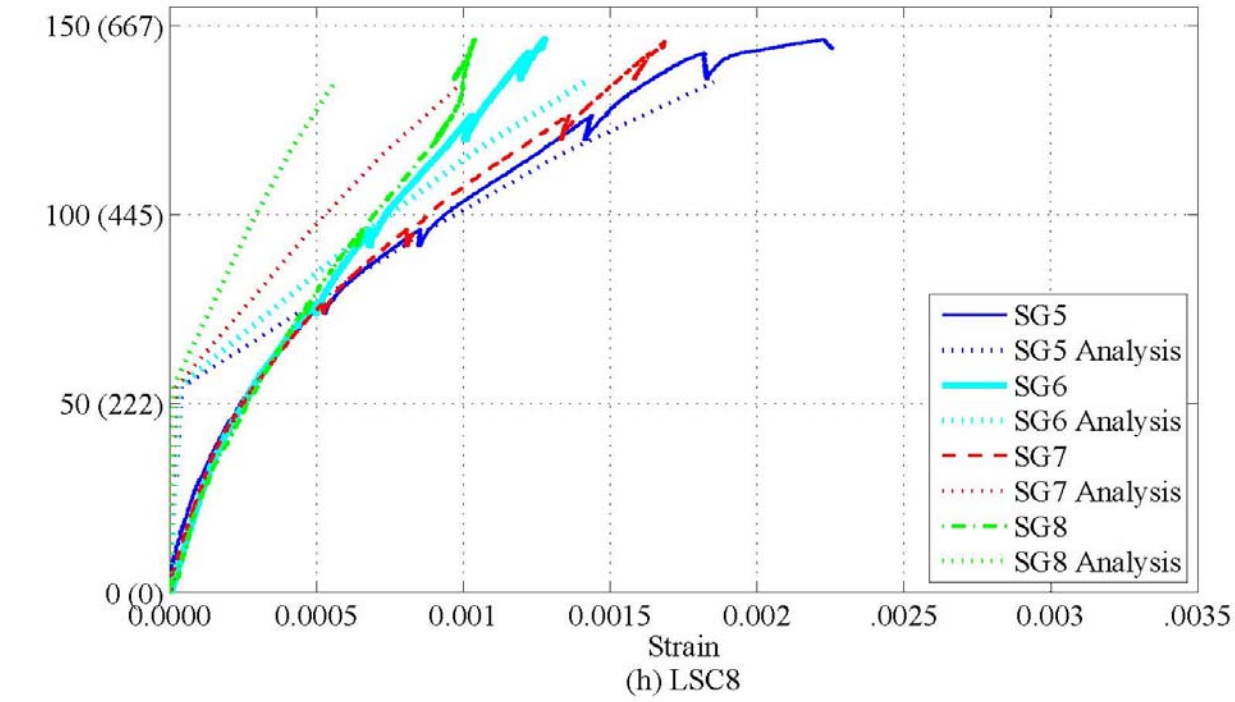

(h) LSC8

Figure 5-26. Experimental and Analytical Load vs. Strain during the Four-Point Test: Internal Strain Gages (SG5–SG8) along Tension Steel of the Splice Region. (Continued)

Figure 5-27 shows the strains in the top reinforcing steel measured with SG9 and SG10. These strains are compressive strains and therefore have negative strains. An SG Factor was used on the top steel in the same manner as the bottom steel previously described. The development length for compression steel is smaller than tension steel and smaller than the distance from the splice end to SG10. Therefore, at the location of SG9 and SG10, both Splice Bar 1 and Splice Bar 2 were fully developed. This gave an SG Factor of 0.5 for both gages, predicting the same strain measured in each gage. LSC10, LSC3, LSC5, and LSC8 have one or two gages that measured no variation in strains during the test. Therefore, these gages were considered not reliable. The figure shows the experimental compression strains are about 80 percent of the analytical model at first cracking and have similar differences after first cracking. This is a much closer match than the analytical and experimental comparison for the tension splice bar strains.

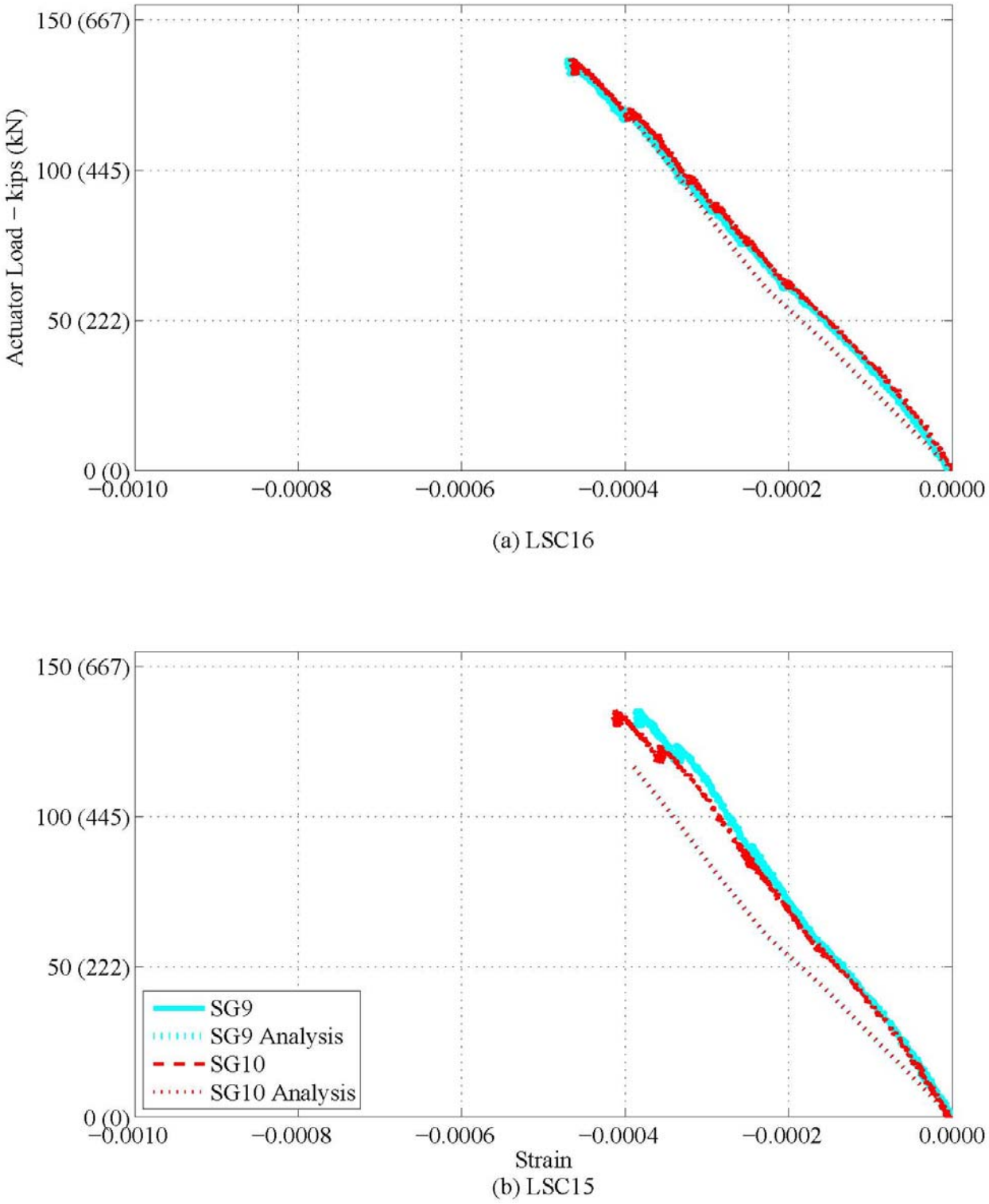

Figure 5-27. Experimental and Analytical Load vs. Strain during the Four-Point Test: Internal Strain Gages (SG9–SG10) along the Compression Steel of the Splice Region.

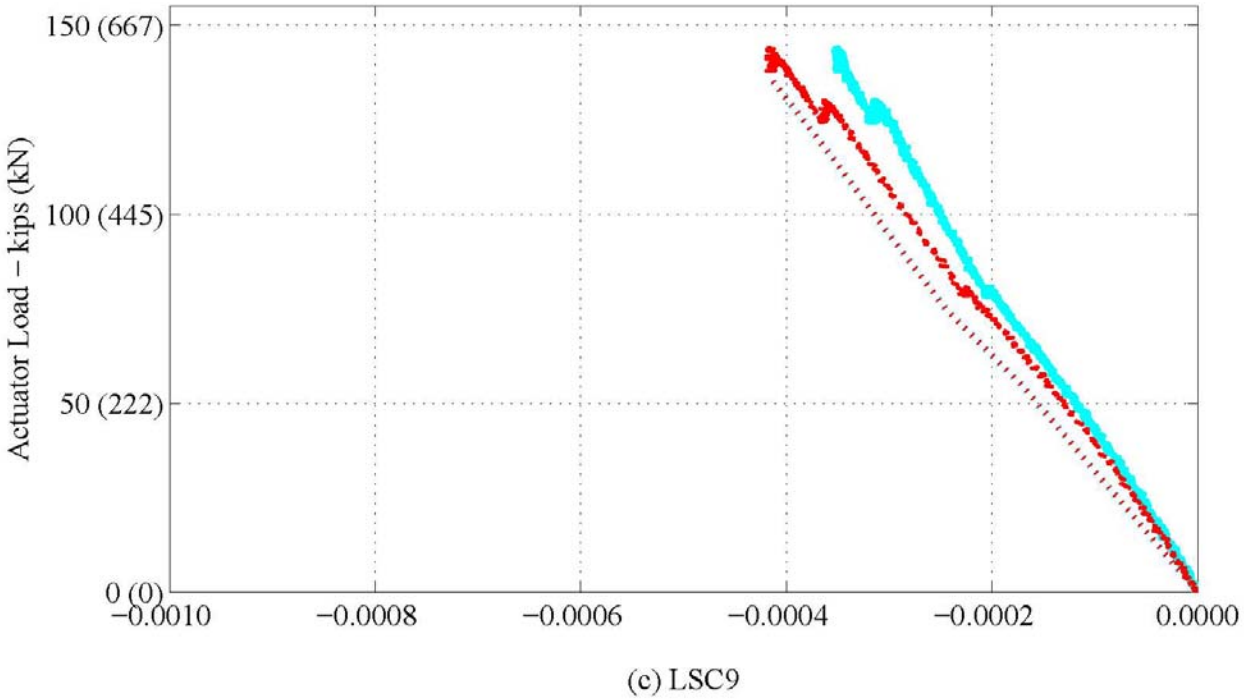

(c) LSC9

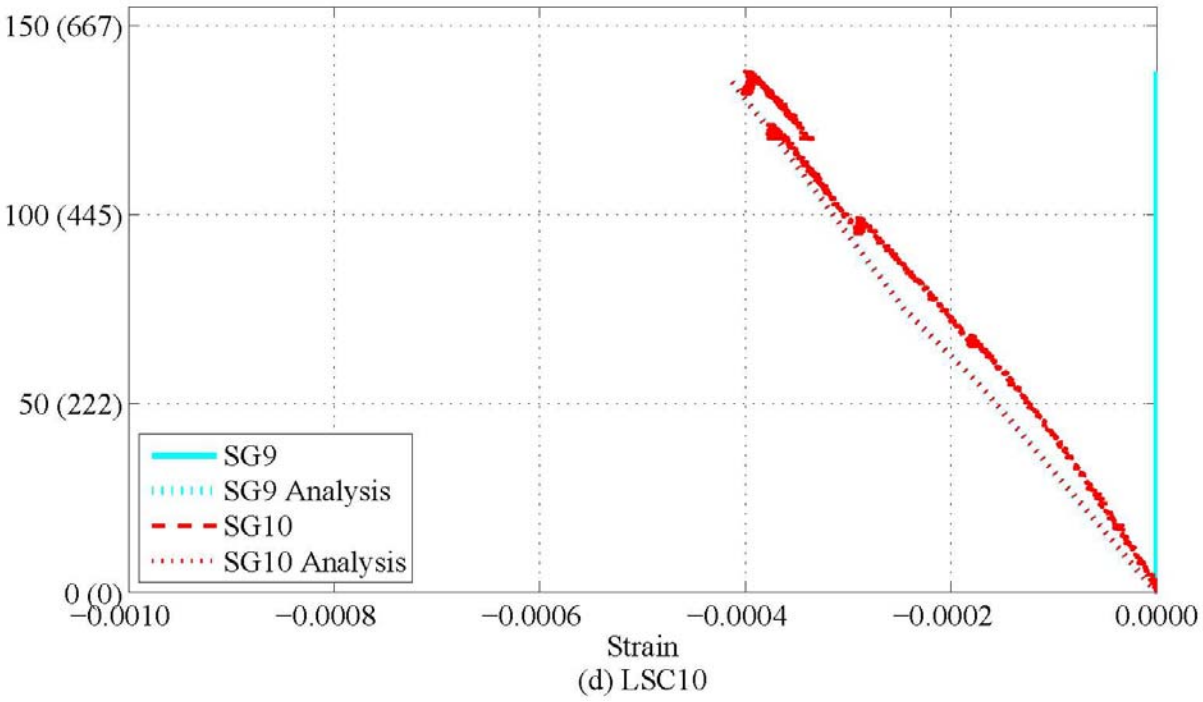

(d) LSC10

Figure 5-27. Experimental and Analytical Load vs. Strain during the Four-Point Test: Internal Strain Gages (SG9–SG10) along the Compression Steel of the Splice Region. (Continued)

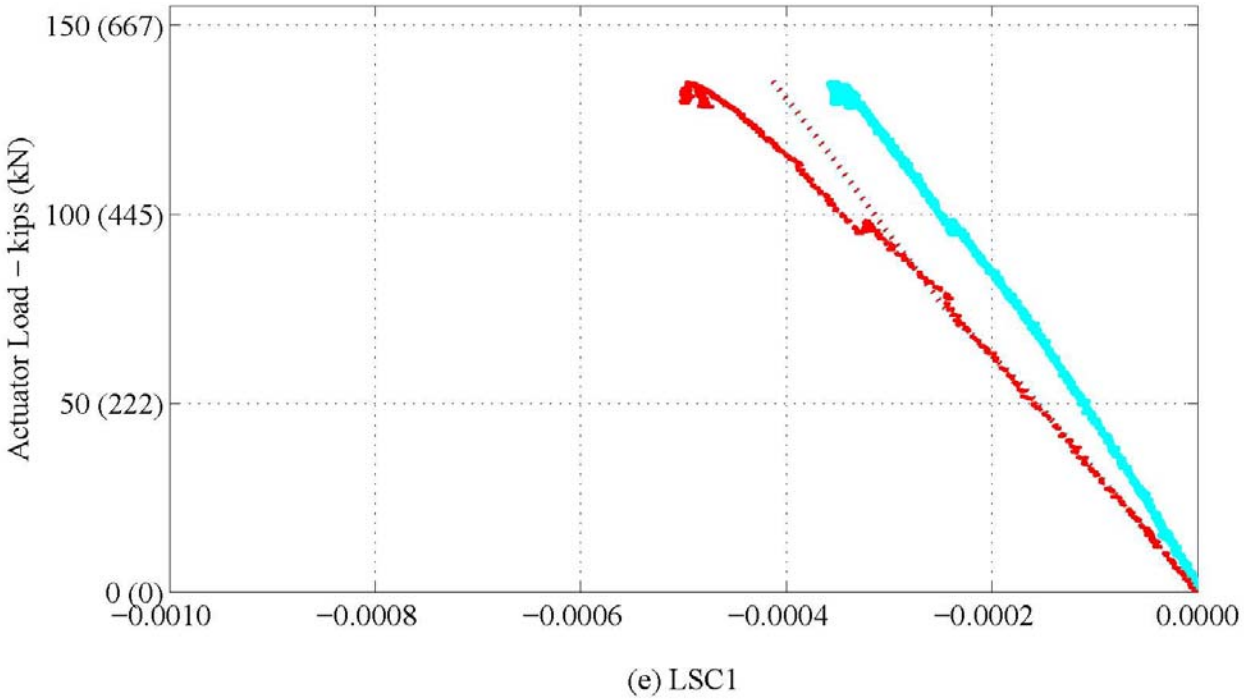

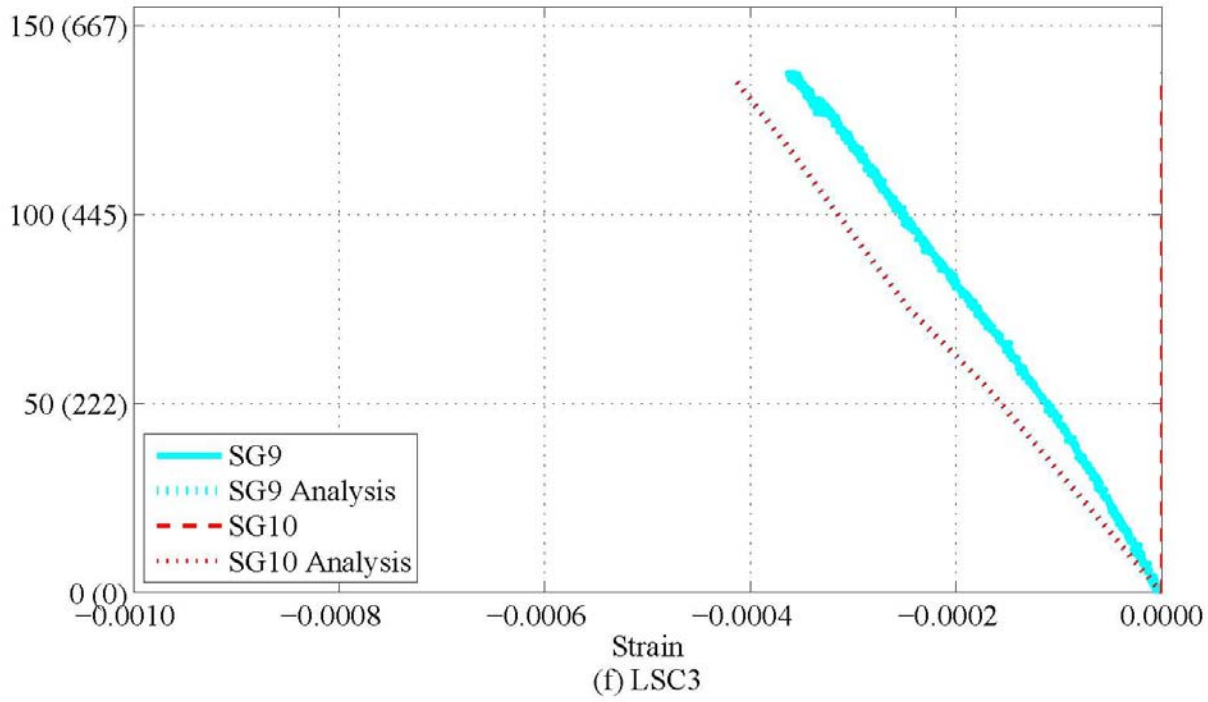

Figure 5-27. Experimental and Analytical Load vs. Strain during the Four-Point Test: Internal Strain Gages (SG9–SG10) along the Compression Steel of the Splice Region. (Continued)

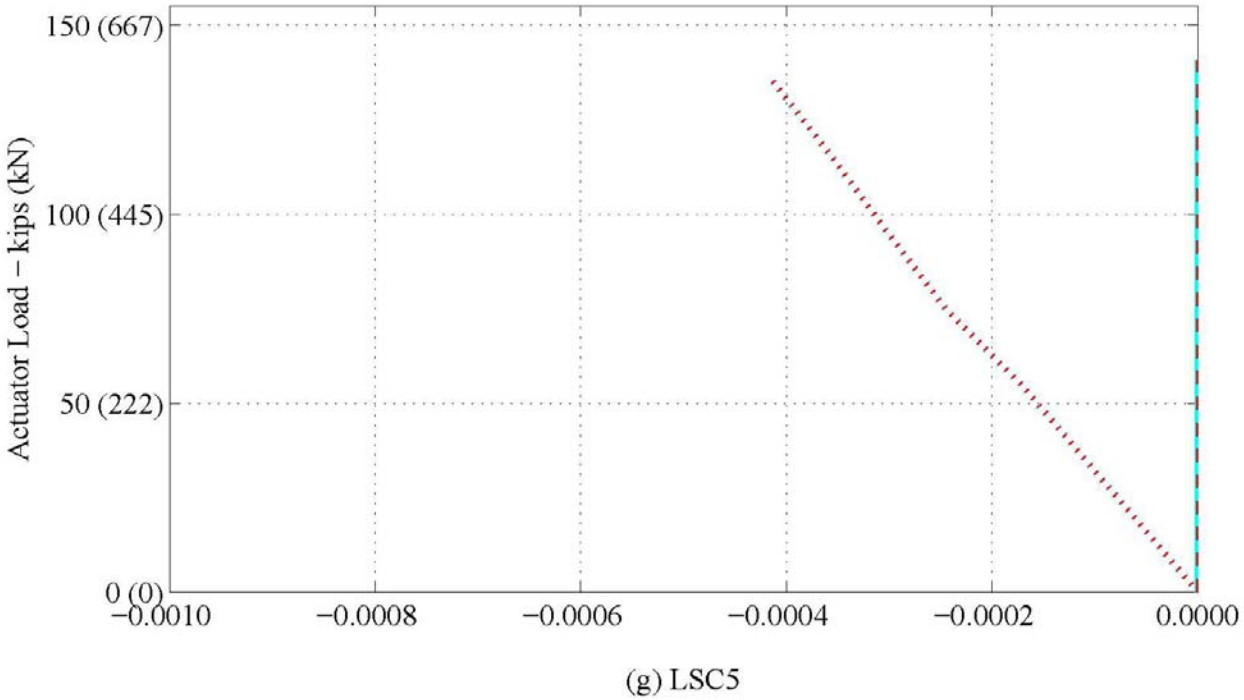

(g) LSC5

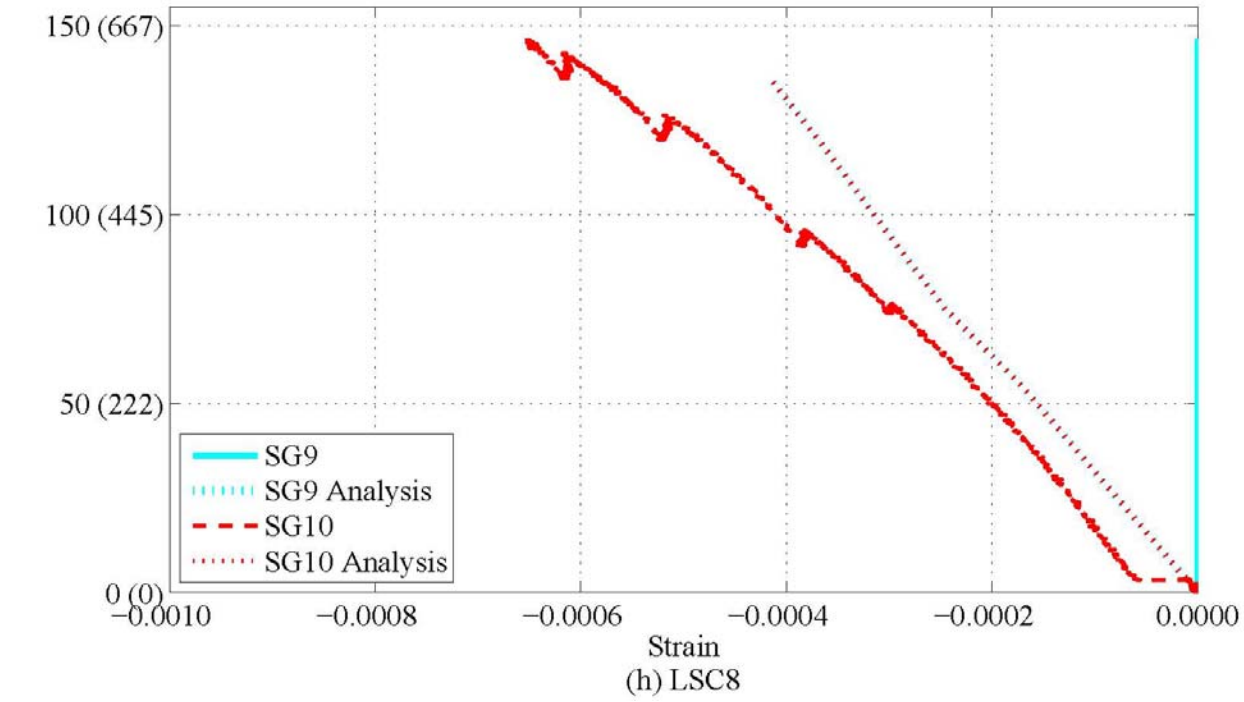

(h) LSC8

Figure 5-27. Experimental and Analytical Load vs. Strain during the Four-Point Test: Internal Strain Gages (SG9–SG10) along the Compression Steel of the Splice Region. (Continued)

Figure 5-28 shows the measured external surface strains across the splice region at the same depth as the tension reinforcing steel as shown in Figure 5-11. LSC16 (Figure 5-28[a]) was instrumented with KM and LV gages on the tension regions of the specimen as shown in Figure 5-9. Figure 5-28(a) shows compression values recorded by KM14 and KM6 in the tension region of LSC16. The KM gages were not reliable in the tension region because the KM gages had a small gage length of 4 inches (102 mm), and some developing cracking did not form within the gage length of the instrument, but rather between gages. Since the LVDTs had a 12-inch (305mm) gage length, they were better able to capture the cracking within the specimen. The rest of the specimens were instrumented as shown in Figure 5-11. Note that LV1 and LV7 measured the strains at the sections directly under actuator 1 and actuator 2, respectively, and the others were within the splice region. The strains from the LVDTs were calculated using Eq. 5-10.

$$LV_{strain} = \frac{\Delta L_{LVDT}}{L_{LVDT}} \qquad \text{(Eq. 5-10)}$$

The LVDTs were positioned with 12 inches (305mm) between the couplers attached to the concrete. The increase in length, ΔL_{LVDT}, was recorded and divided by the length between the couplers, L_{LVDT}.

As shown previously, most of the plastic bending rotations within the specimen occurred only in the sections directly under each actuator. Figure 5-28(b)–(h) shows that the LV1 and LV7 measured surface strains were nonlinear and much larger than any other LV measurement within the splice region. Thus, this further confirmed that only the sections under the actuators were deforming plastically, and those sections within the spliced region of the specimen remained within the elastic limits. Also, the significant nonlinear response from the LV1 and LV7 gages started at a strain of about 0.002 for most specimens. The LV1 and LV7 gages on LSC9, LSC10, and LSC5 did not show yielding until a strain of about 0.0025 to 0.0030. This shows that it was reasonable to assume the rebar had yield strength of 70 ksi (783 MPa), instead of the specified 60 ksi (414 MPa), resulting in a theoretical yield strain of 0.0024. Also, this indicates that the

plane-sections-remain-plane-modeling assumption is completely valid for the specimens tested in the four-point test setup.

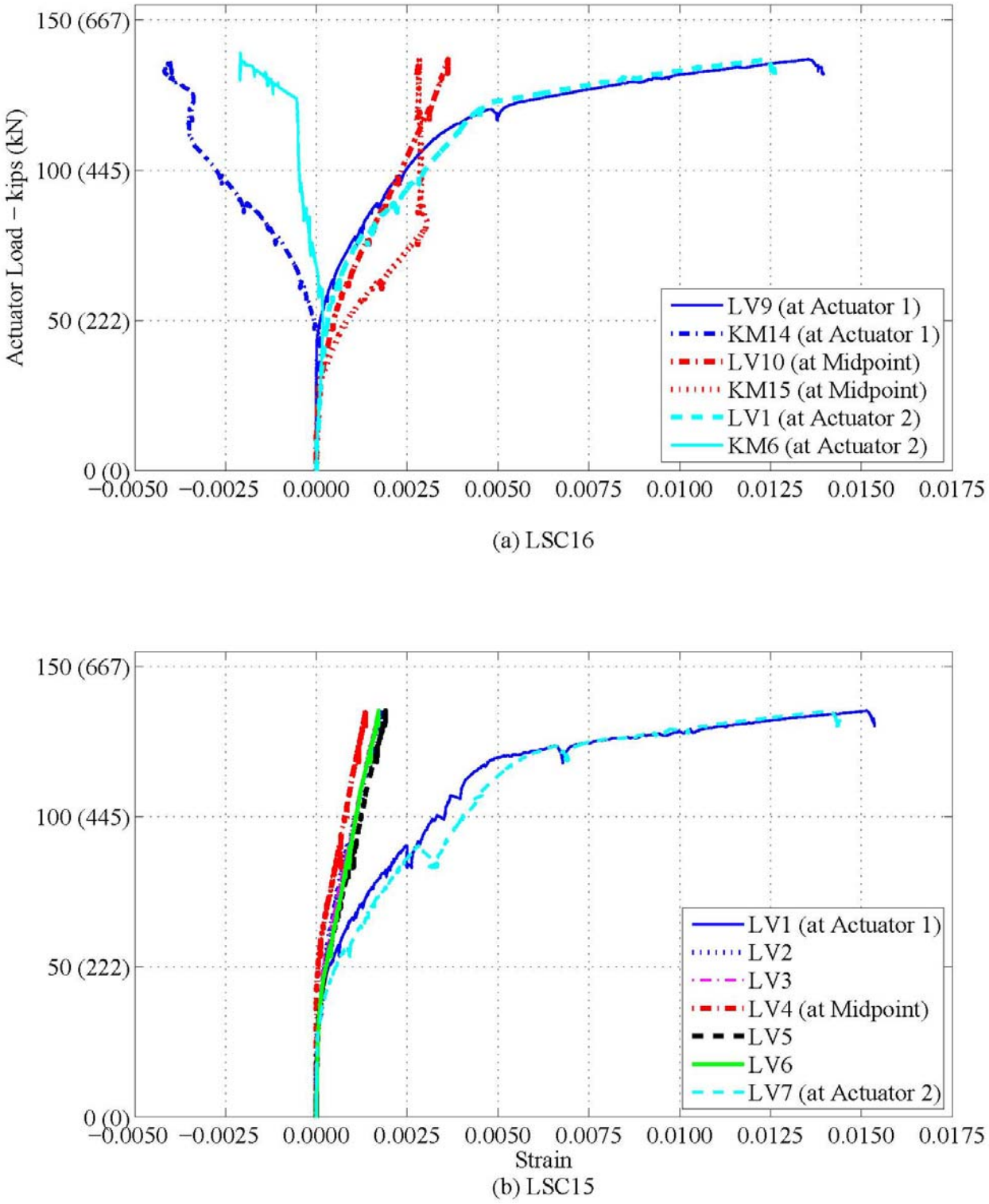

Figure 5-28. Experimental Load vs. Strain during the Four-Point Test: LVDTs across the Splice Length in the Tension Region.

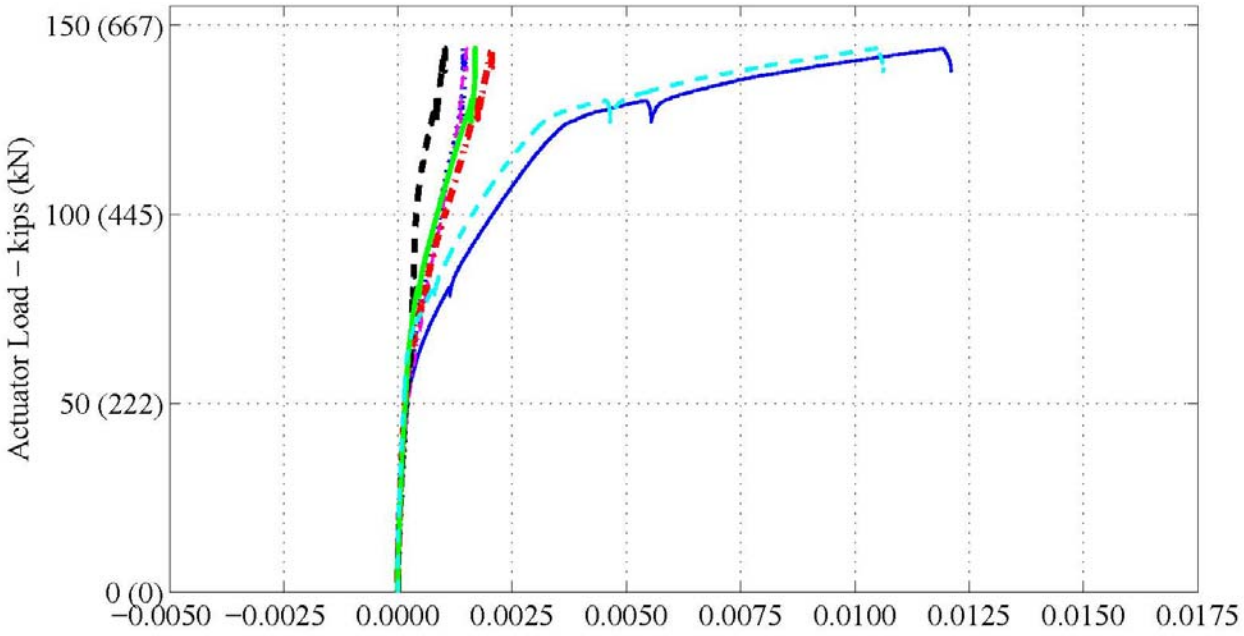

(c) LSC9

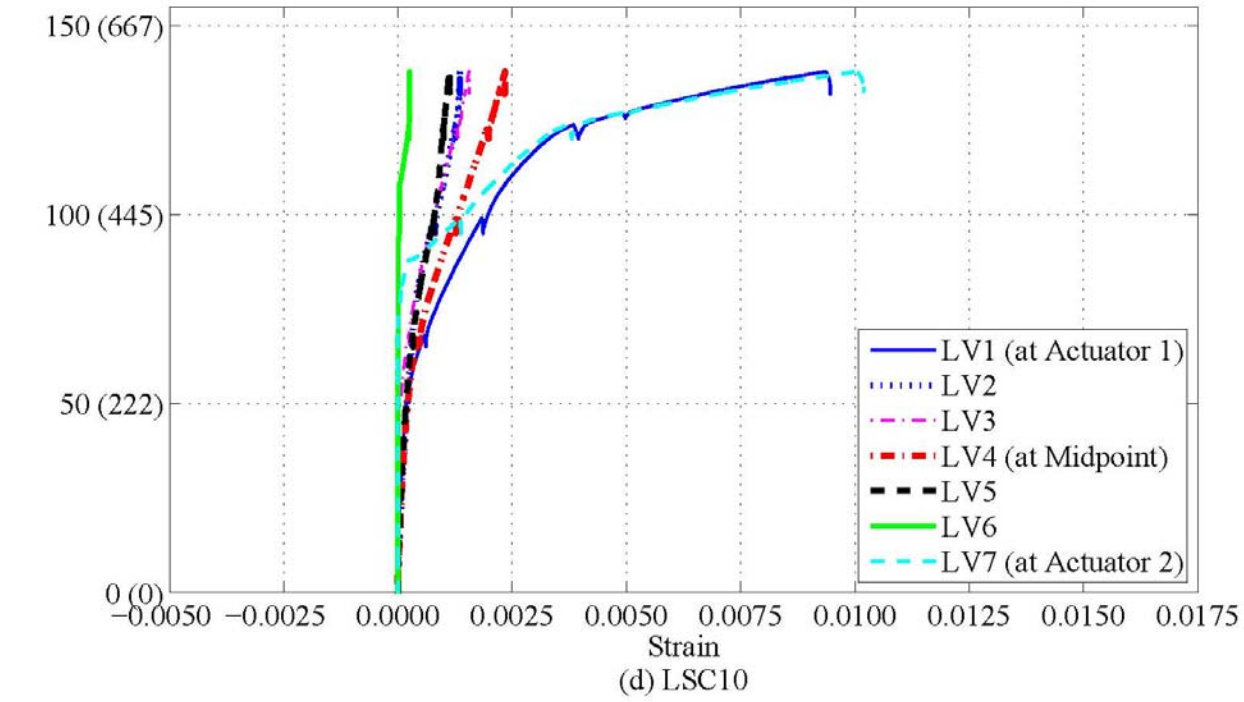

(d) LSC10

Figure 5-28. Experimental Load vs. Strain during the Four-Point Test: LVDTs across the Splice Length in the Tension Region. (Continued)

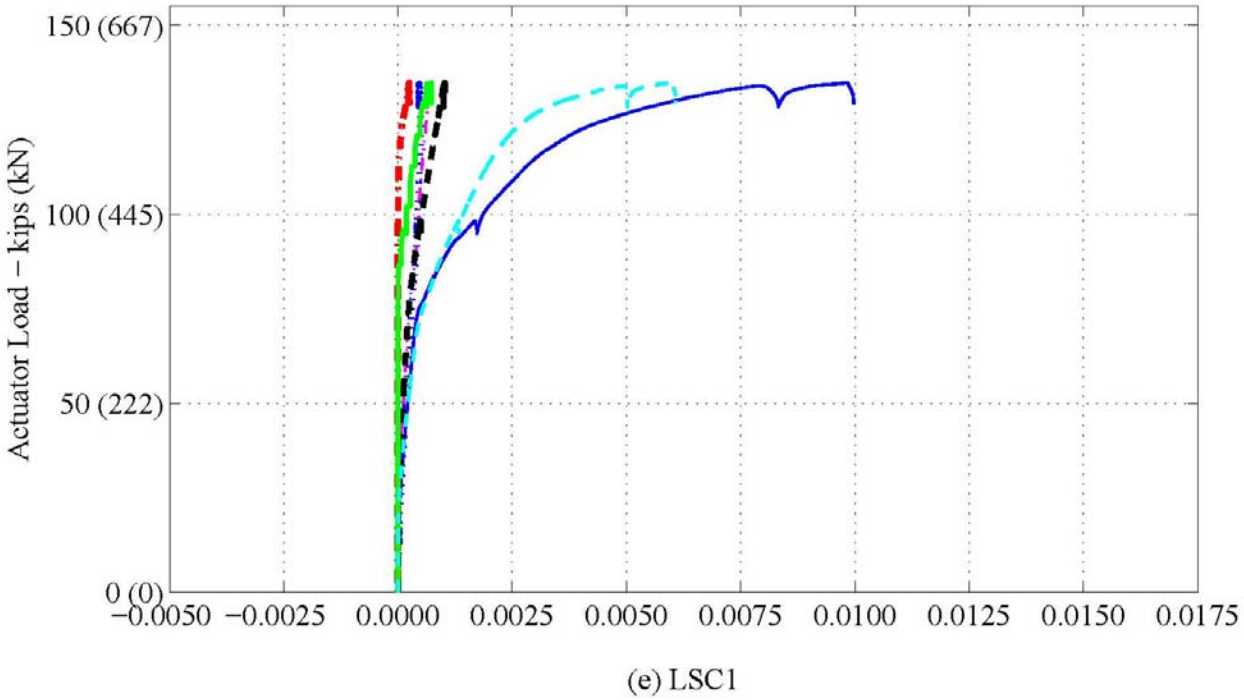

(e) LSC1

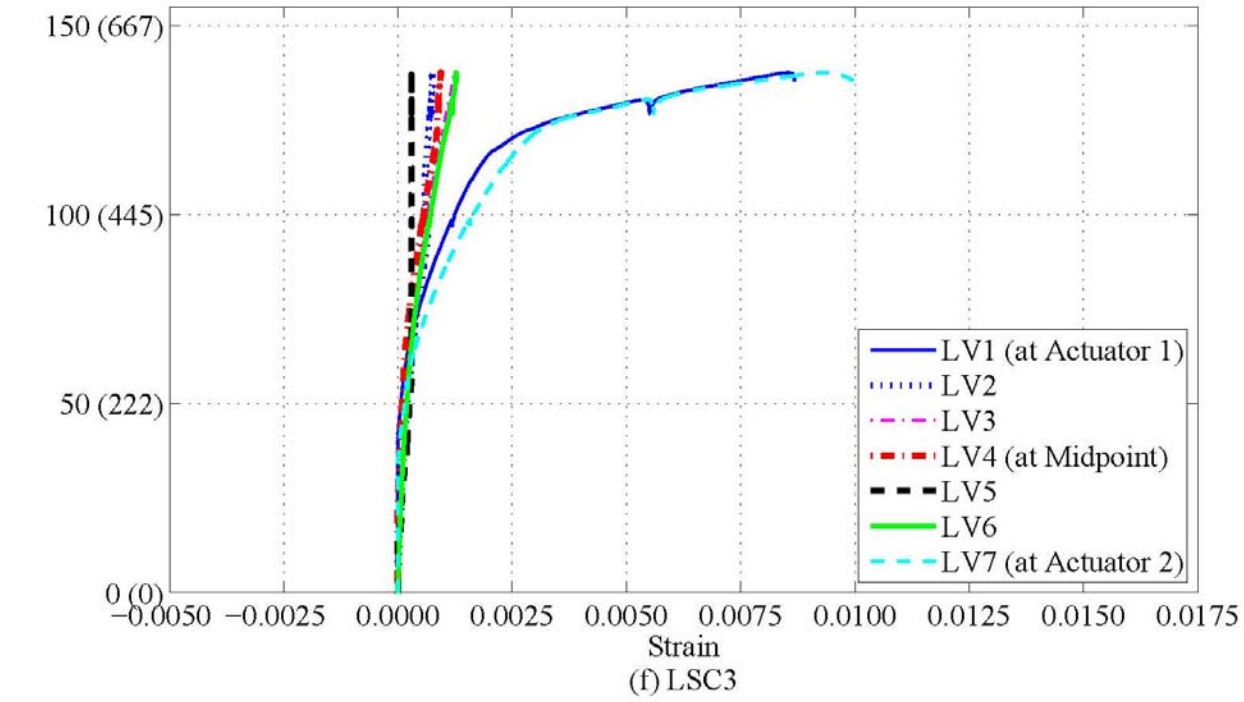

(f) LSC3

Figure 5-28. Experimental Load vs. Strain during the Four-Point Test: LVDTs across the Splice Length in the Tension Region. (Continued)

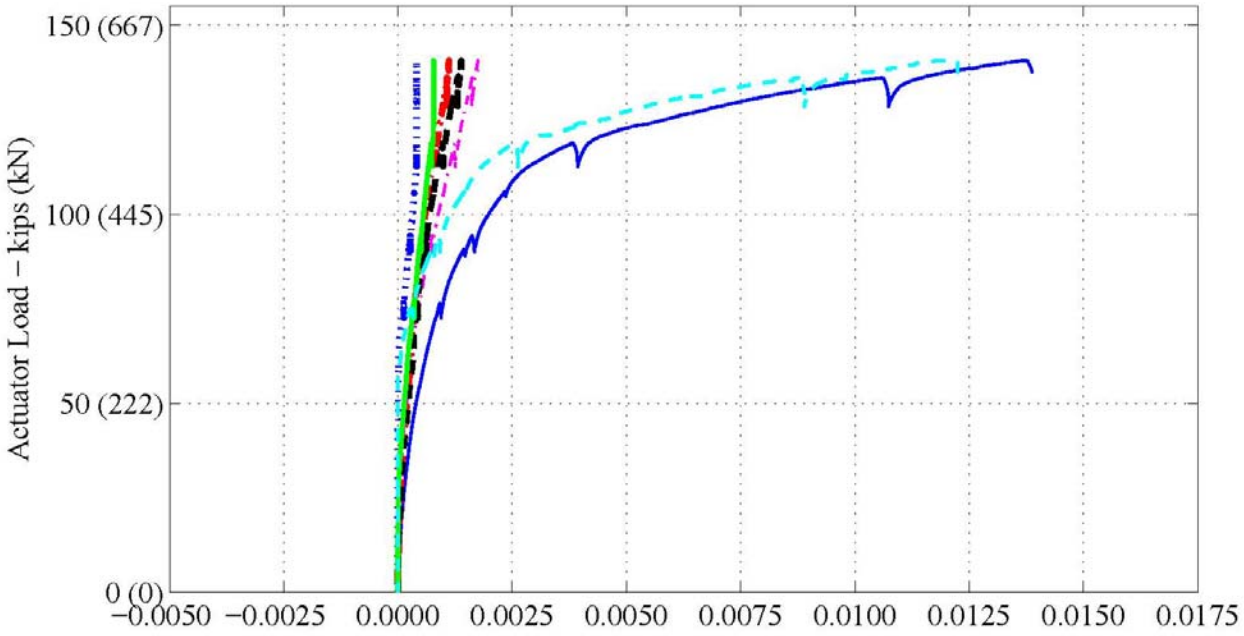

(g) LSC5

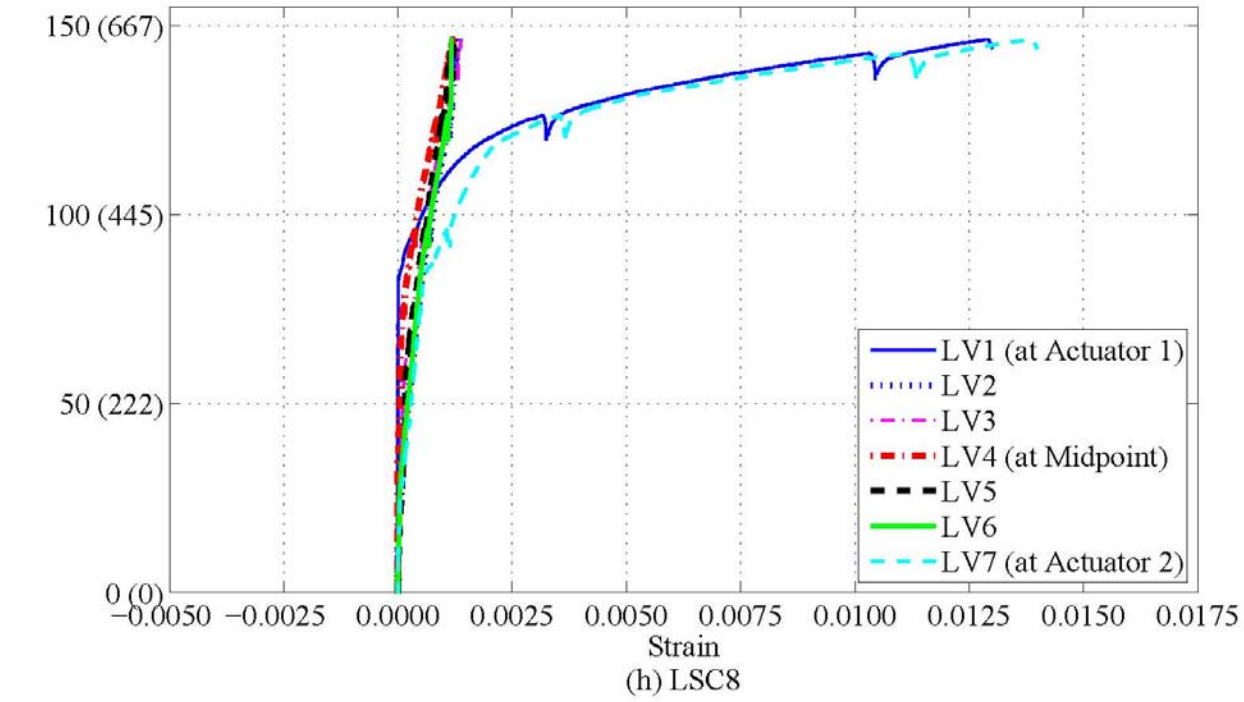

(h) LSC8

Figure 5-28. Experimental Load vs. Strain during the Four-Point Test: LVDTs across the Splice Length in the Tension Region. (Continued)

Figure 5-29 compares the internal strains to the external strains across the splice length. LV1 and LV7 were removed from this figure since no internal gages were located at the splice ends. The closest SGs to the splice end were 18 inches (457mm) away. This figure better depicts the differences between LV2 through LV6 since the range of strains shown is smaller than Figure 5-28. Also, this figure clearly shows that the response within the splice region remained in the elastic region, and there was no sign of degradation within the splice region. In addition, the figure shows that the internal strain measurement and external surface strain measures were comparable; again, validating the plane-sections-remain-plane-modeling assumption.

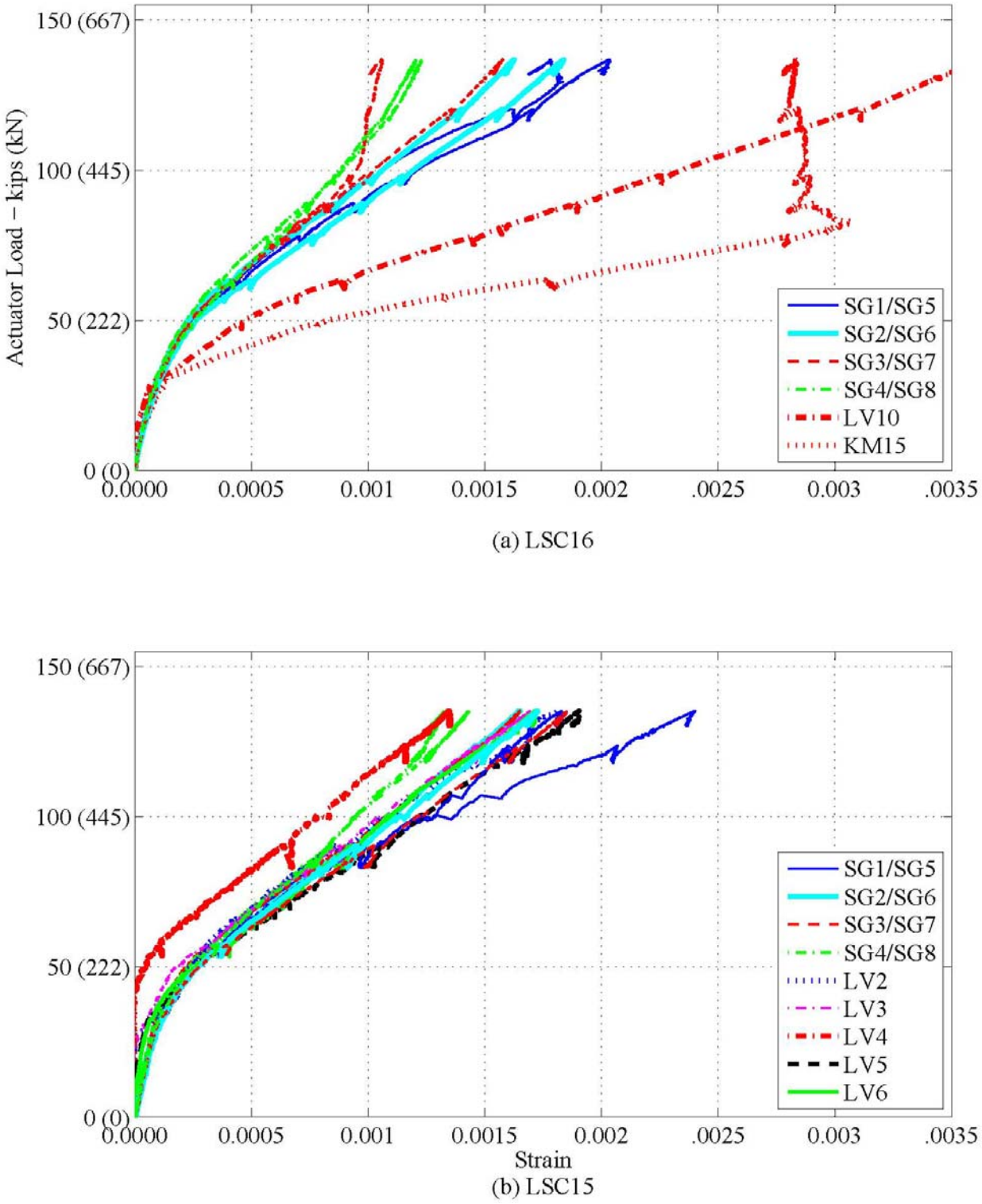

Figure 5-29. Experimental Load vs. Strain during the Four-Point Test: Internal and External Strain Comparison across Splice Length.

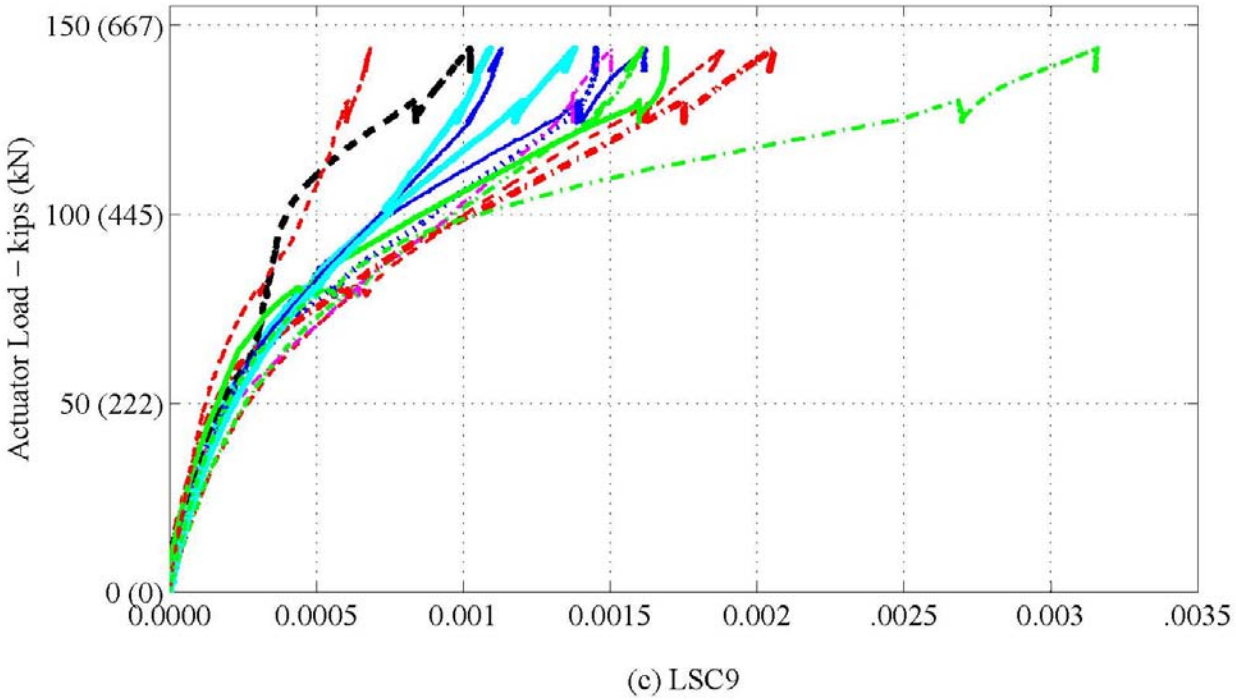

(c) LSC9

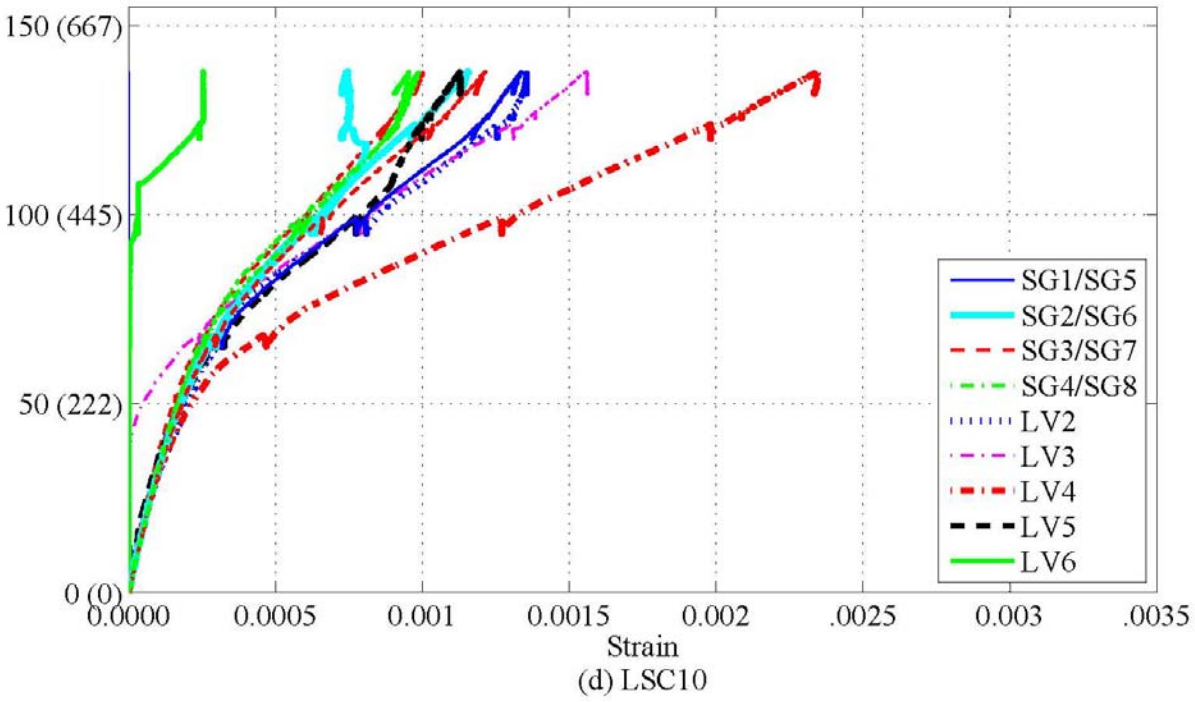

(d) LSC10

Figure 5-29. Experimental Load vs. Strain during the Four-Point Test:
Internal and External Strain Comparison across Splice Length. (Continued)

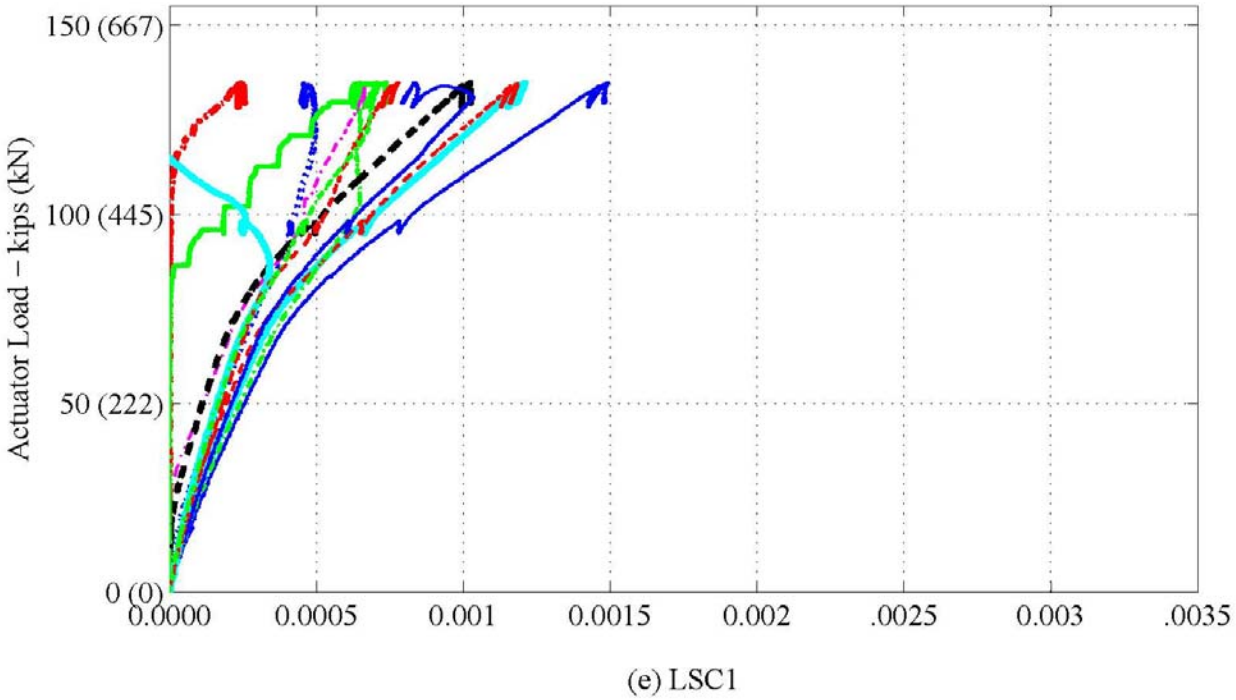

(e) LSC1

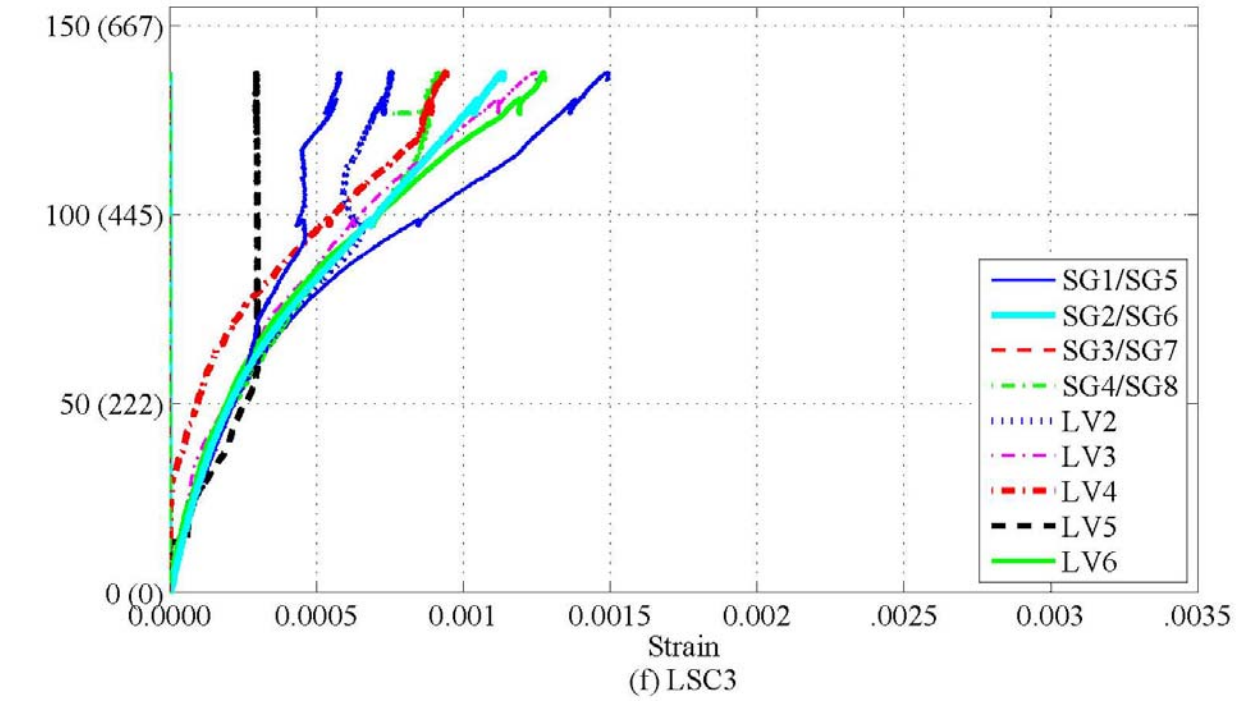

(f) LSC3

Figure 5-29. Experimental Load vs. Strain during the Four-Point Test: Internal and External Strain Comparison across Splice Length. (Continued)

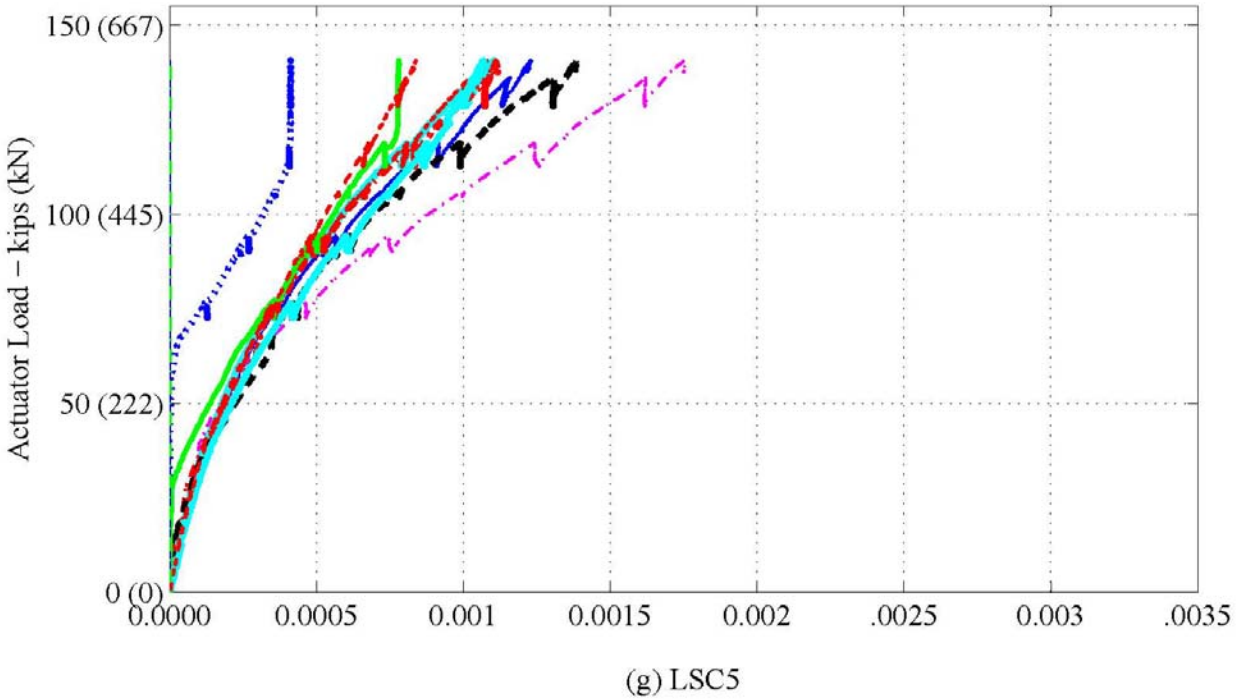

(g) LSC5

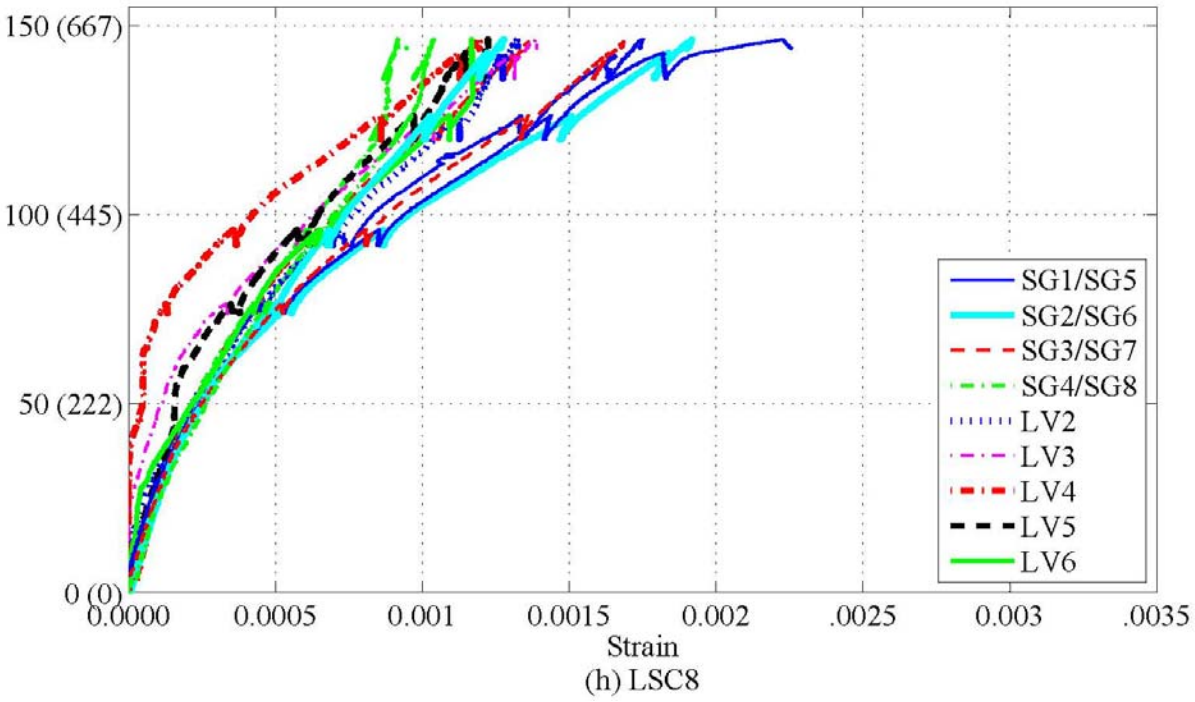

(h) LSC8

Figure 5-29. Experimental Load vs. Strain during the Four-Point Test: Internal and External Strain Comparison across Splice Length. (Continued)

Figure 5-30 shows the actuator force vs. the measured strains at varying depths in the section directly below actuator 2. Figure 5-30(a) shows the strains in LSC16 using KM gages at the top of the section and LVDTs elsewhere (Figure 5-9). As discussed previously, the LVDTs and KM gages gathered better data in the tension and compression regions, respectively. Therefore, external location of the compression steel was instrumented with a KM gages for the rest of the specimens (Figure 5-11). No LVDT gages were placed on the bottom of LSC16 to measure the bottom strain, but two LVDTs were placed for the remaining specimens. Figure 5-30 also shows the actuator force vs. corresponding strains calculated from the analysis. The figure shows that the analytical response is comparable to the experimentally measured response up to yielding of the reinforcement, and misses the post-yield stiffness due to reasons explained earlier. Also, it is noticeable that the load at which the strains reached plasticity is almost constant throughout the section.

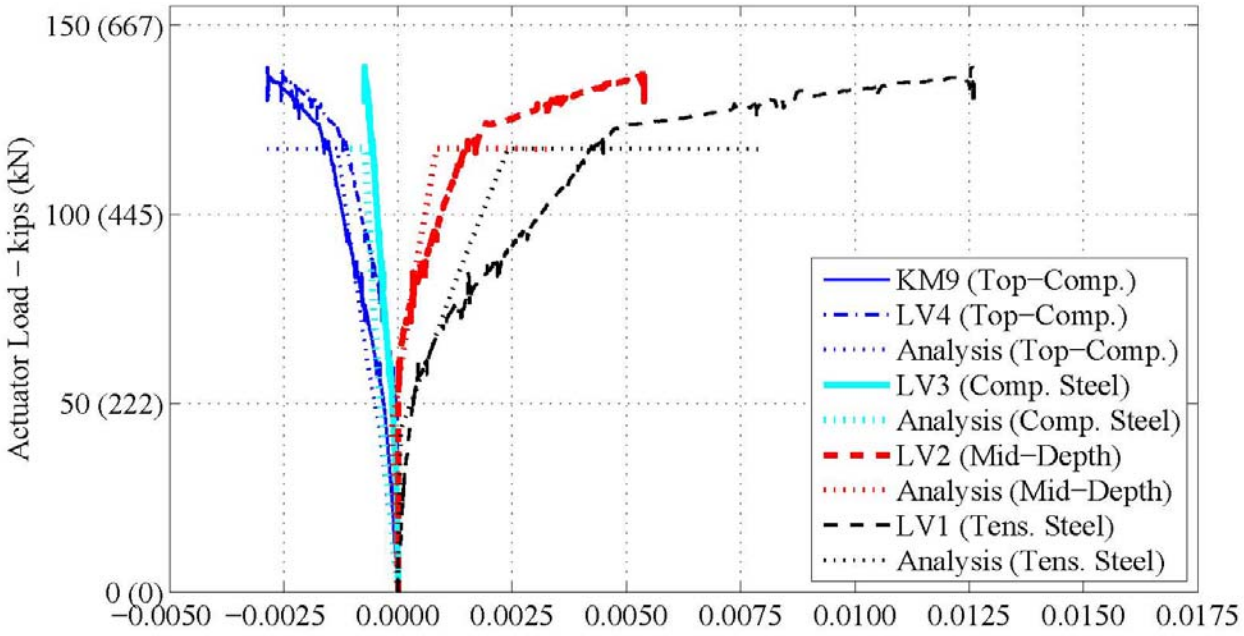

(a) LSC16

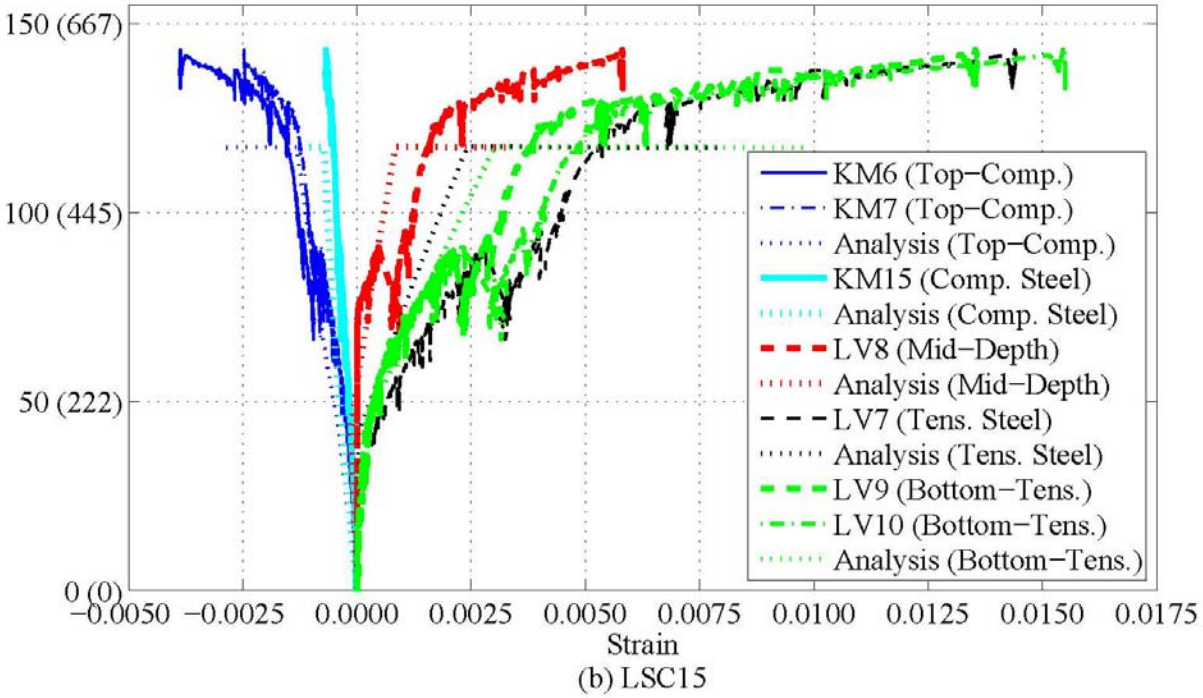

(b) LSC15

Figure 5-30. Experimental and Analytical Load vs. Strain during the Four-Point Test: External Strain Gages across the Depth of the Splice End.

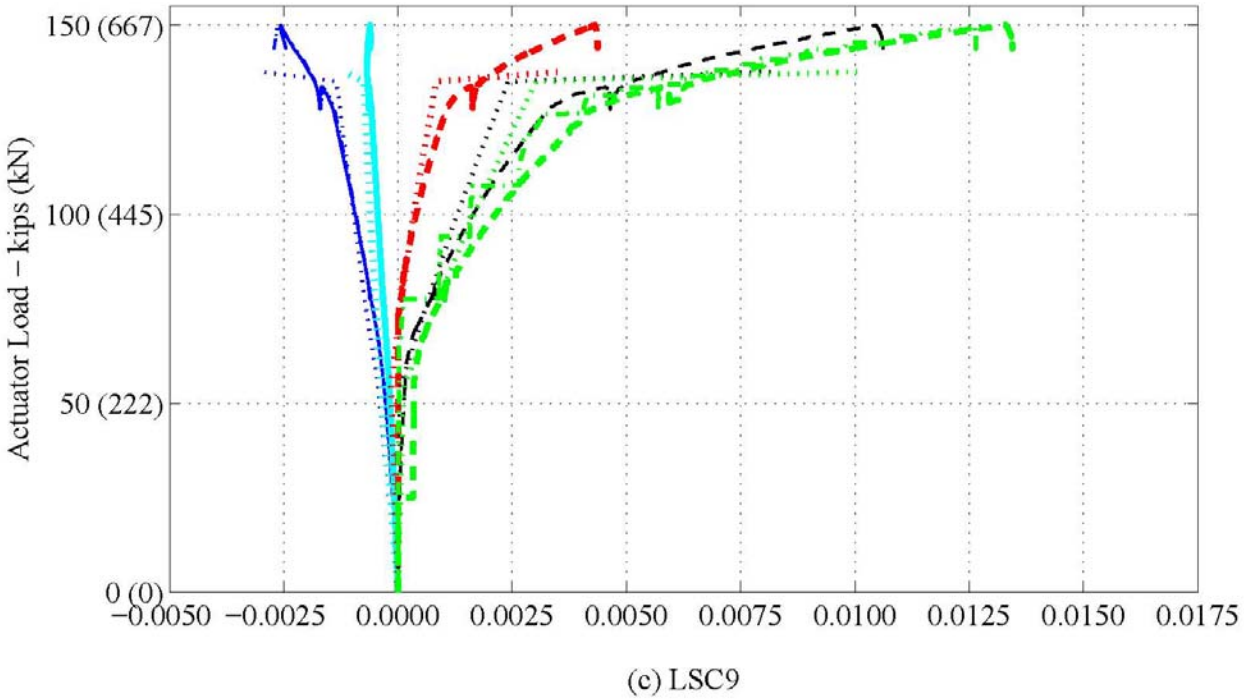

(c) LSC9

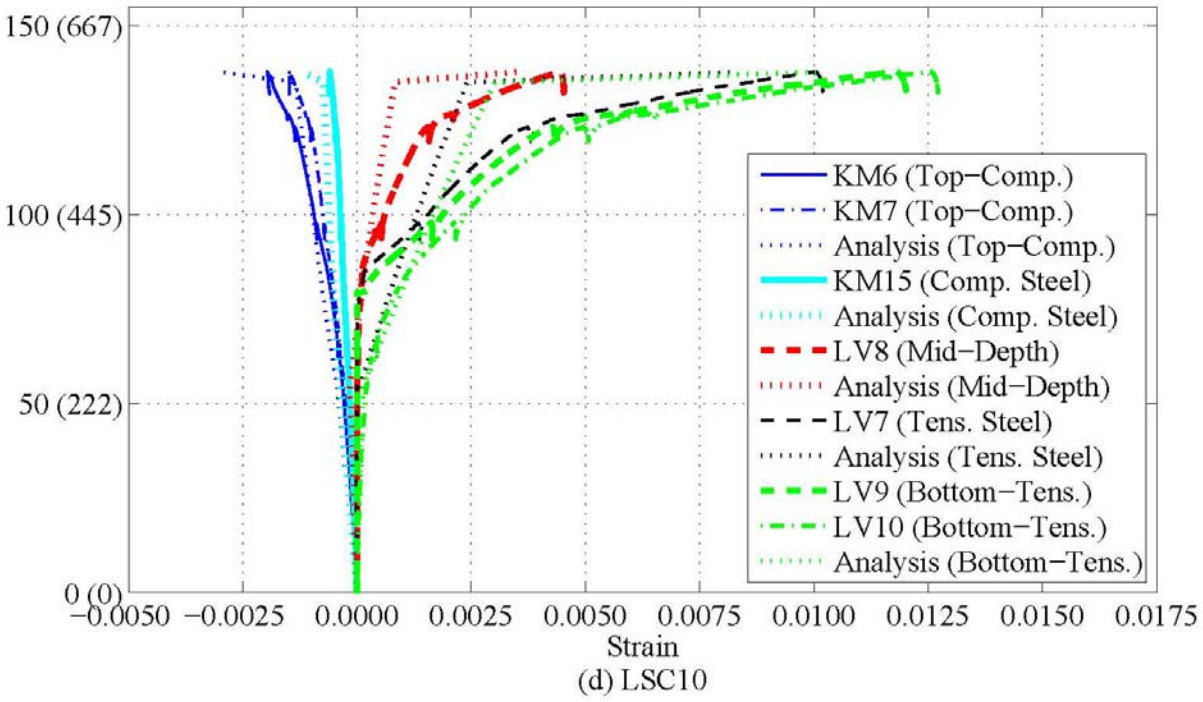

(d) LSC10

Figure 5-30. Experimental and Analytical Load vs. Strain during the Four-Point Test: External Strain Gages across the Depth of **the Splice End. (Continued)**

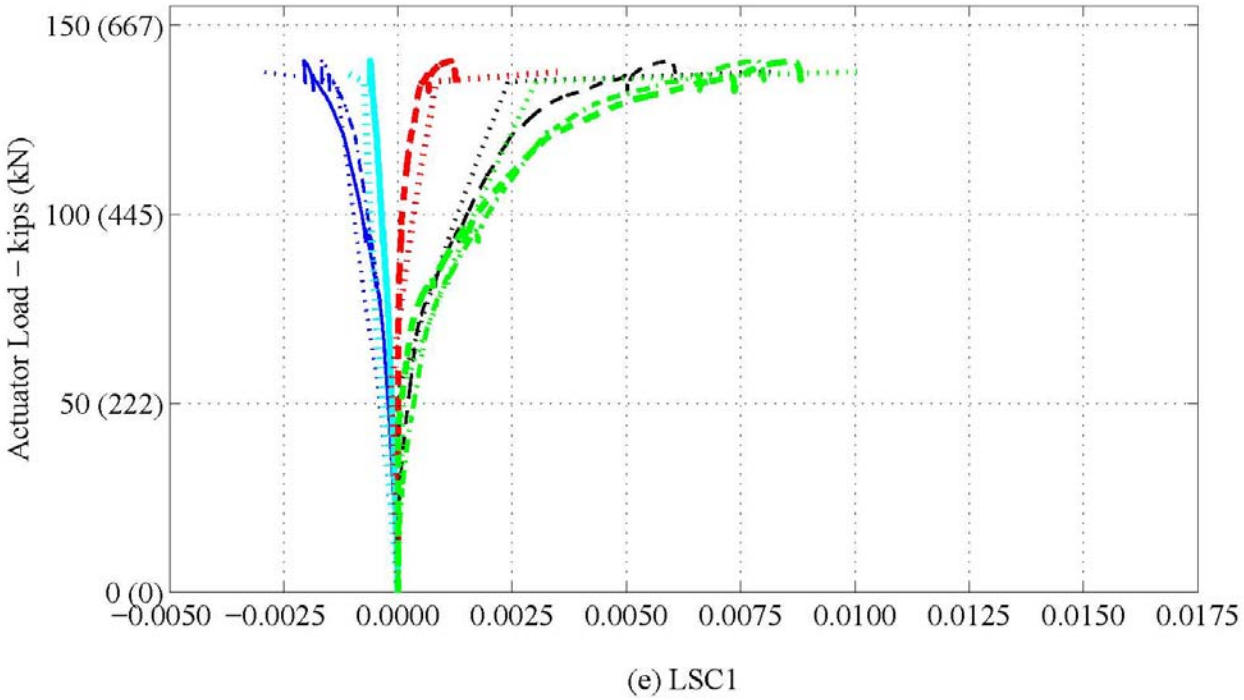

(e) LSC1

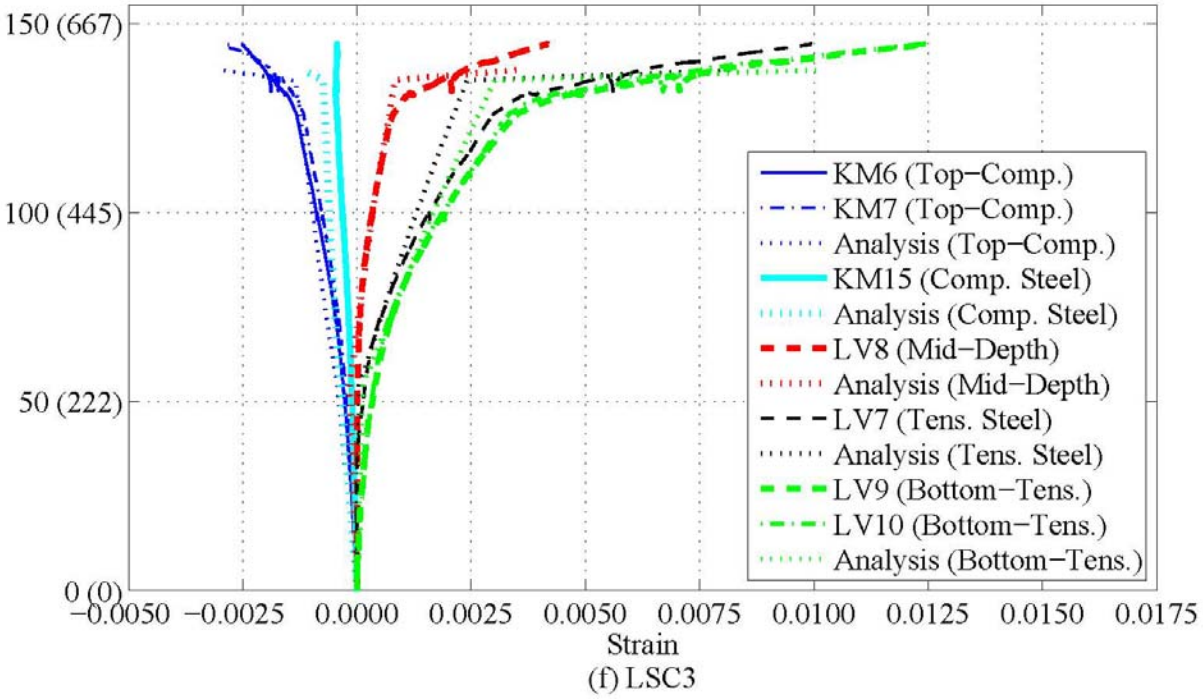

(f) LSC3

Figure 5-30. Experimental and Analytical Load vs. Strain during the Four-Point Test: External Strain Gages across the Depth of the Splice End. (Continued)

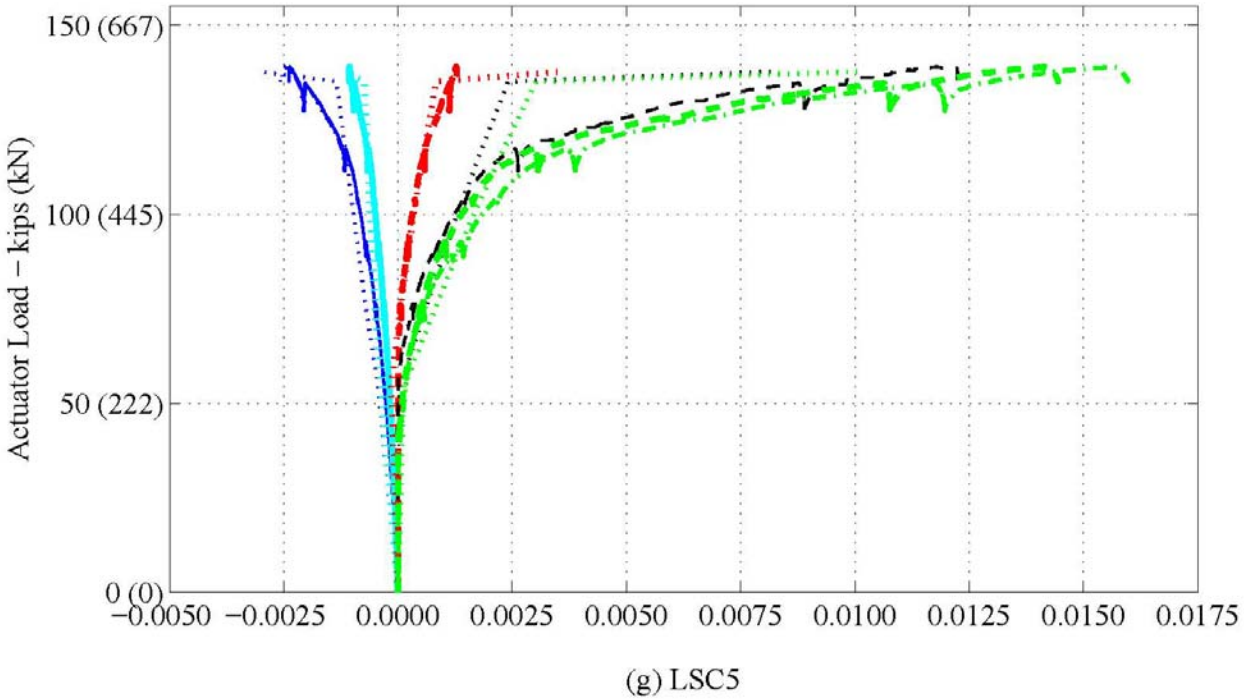

(g) LSC5

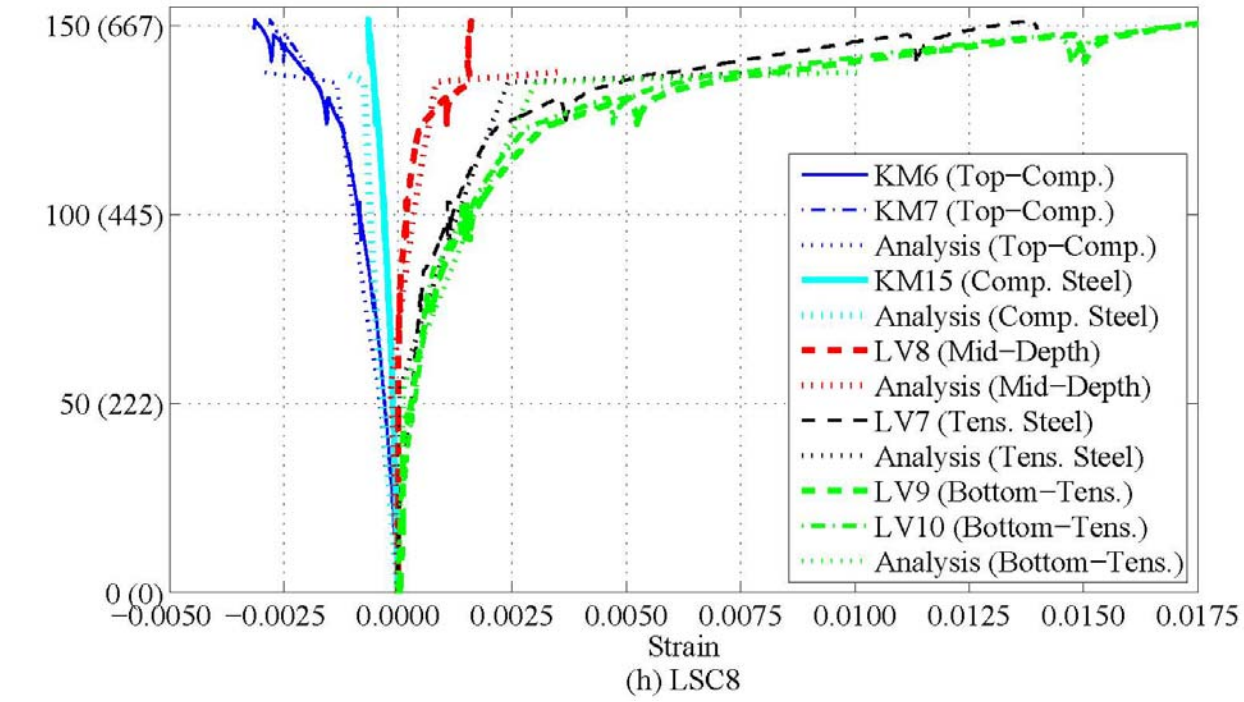

(h) LSC8

Figure 5-30. Experimental and Analytical Load vs. Strain during the Four-Point Test: External Strain Gages across the Depth of the Splice End. (Continued)

As another illustration of the behavior under the actuator, Figure 5-31 shows a large flexure crack (vertical crack in the figure) from the section directly under actuator 1 during the four-point test for LSC5 at the maximum load, 140 kips (623 kN). The crack width is approximately 0.25 inches (6.4 mm) at the bottom of the section and is within the gage length of LV1. Although this picture was taken under Actuator 1, the cracking is very similar to the cracking under actuator 2 with data presented in Figure 5-30. Figure 5-31 also shows several cracks from premature concrete deterioration orthogonal to the bending crack from the load testing.

Figure 5-31. Flexural Crack under Actuator 1 during the Four-Point Test for LSC5.

To compare the compression strains near the two actuators, Figure 5-32 shows the actuator force vs. strains from KM9, LV4, KM13, and LV8 for LSC16 and KM6, KM7, KM13, and KM14 for the other specimens. Figure 5-9 shows the KM locations on LSC16 and Figure 5-11 shows the KM locations for the other LSC specimens. About half of the specimens were loaded until the compression strain reached 0.003 (theoretical ultimate crushing limit). The figure shows that the

experimental strains are smaller than the analytical strains similar to the internal compressive strains on the splice bar (Figure 5-27). The average load at yielding is the same for the analytical model and the control specimens (LSC15 and LSC16). However, the analytical yielding load is higher than the experimental results for the non-control specimens varying up to about 20 kips (89 kN) larger than the experimental results.

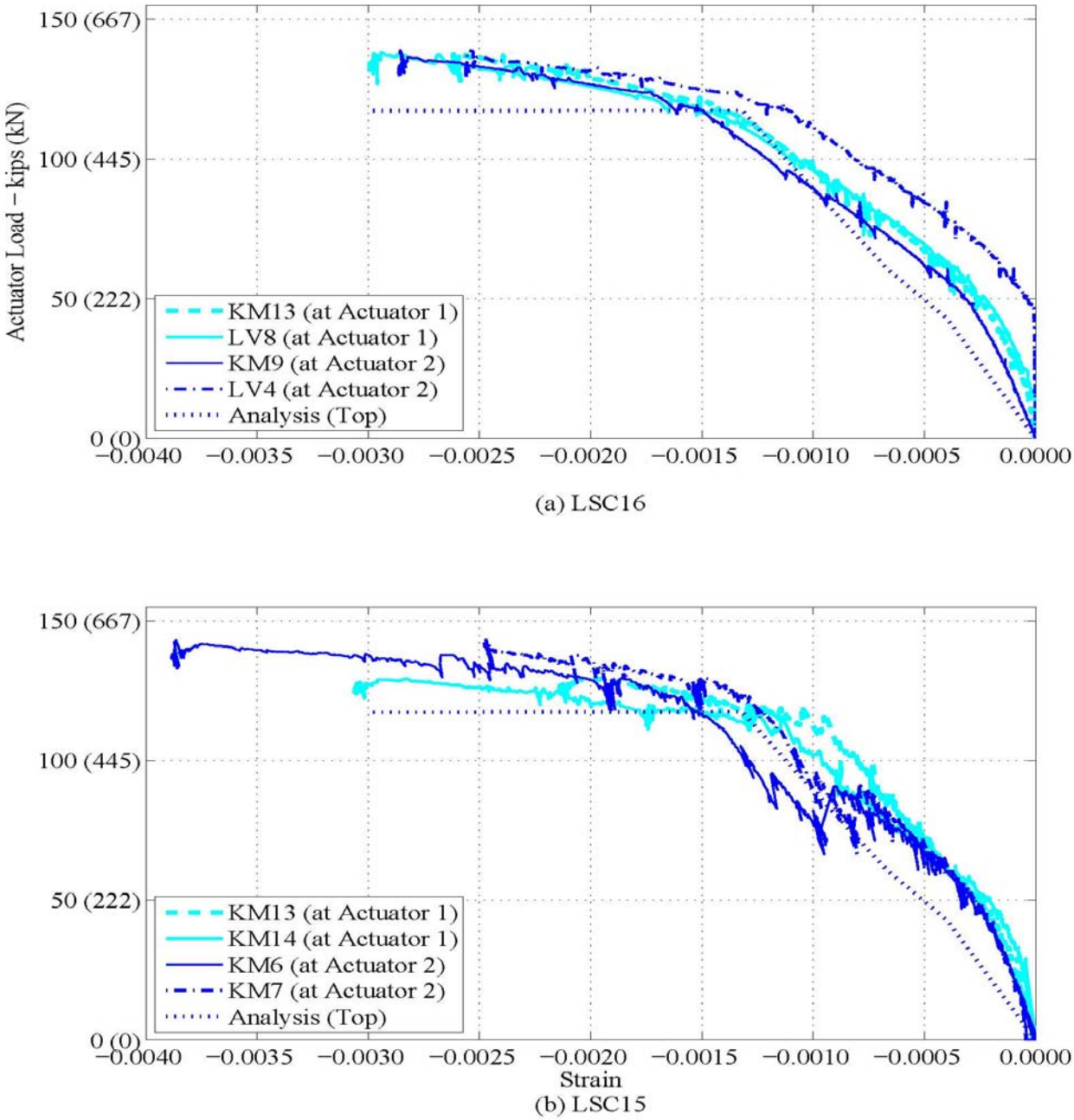

Figure 5-32. Experimental Load vs. Strain during the Four-Point Test: KM Gages at the Splice End in the Compression Region.

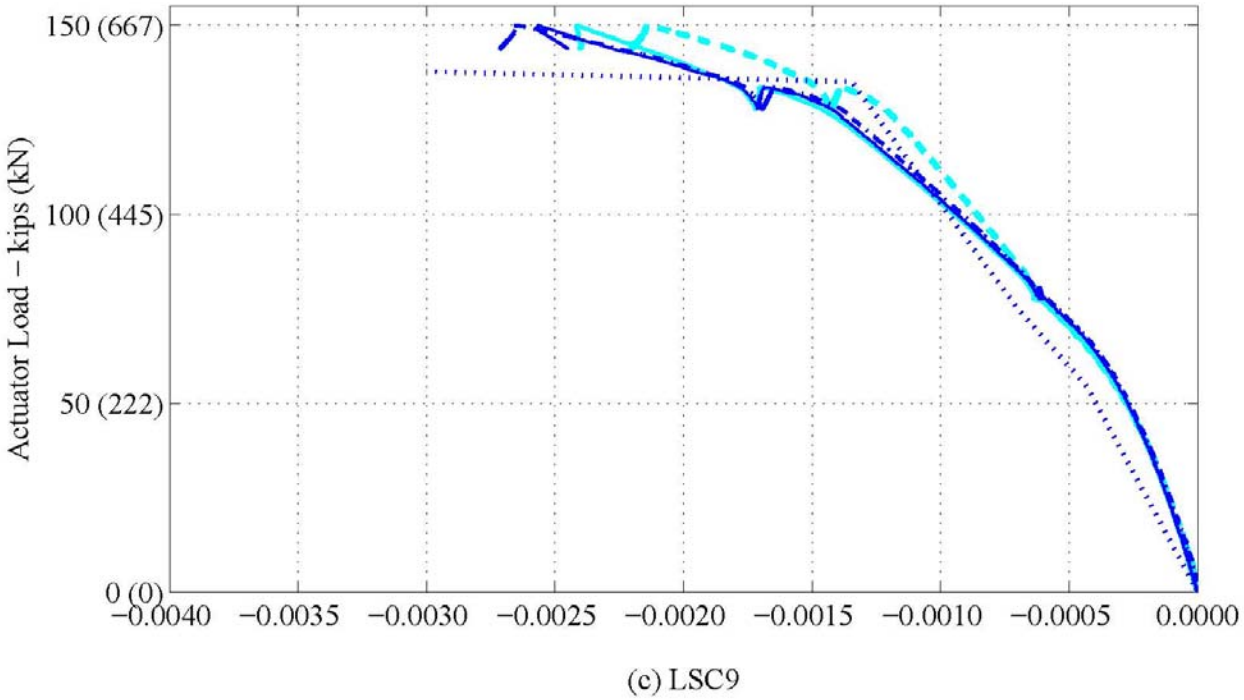

(c) LSC9

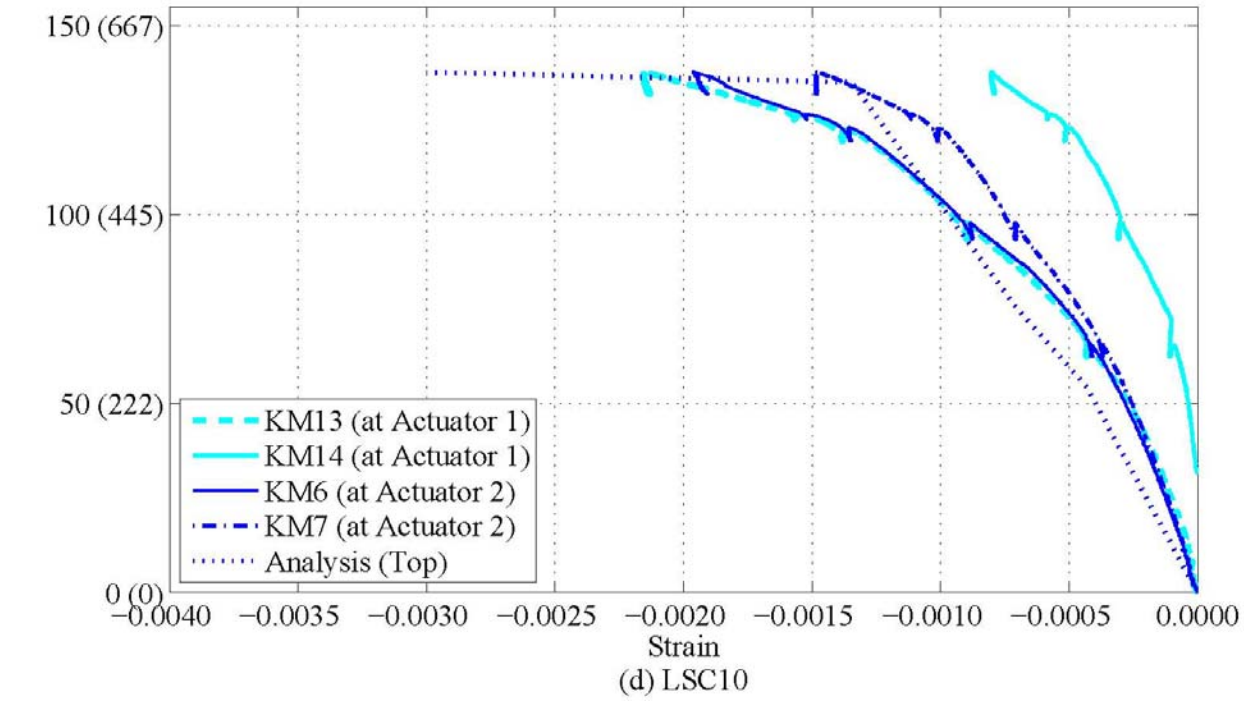

(d) LSC10

Figure 5-32. Experimental Load vs. Strain during the Four-Point Test: KM Gages at the Splice End in the Compression Region. (Continued)

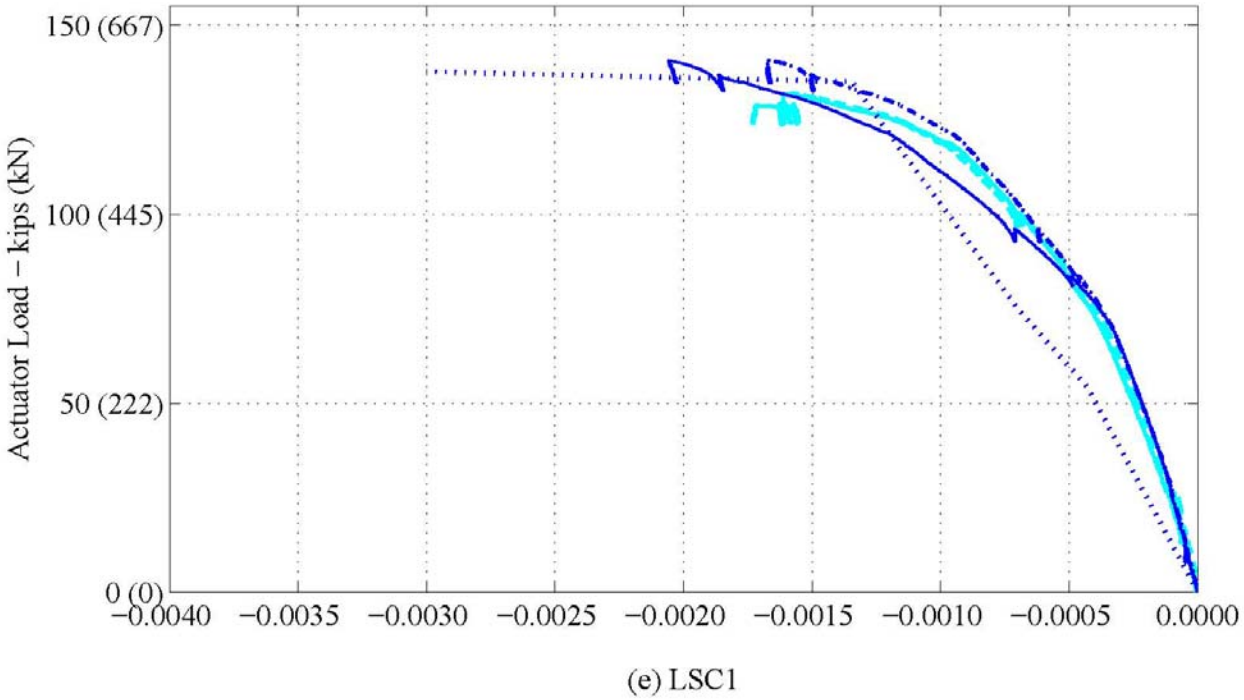

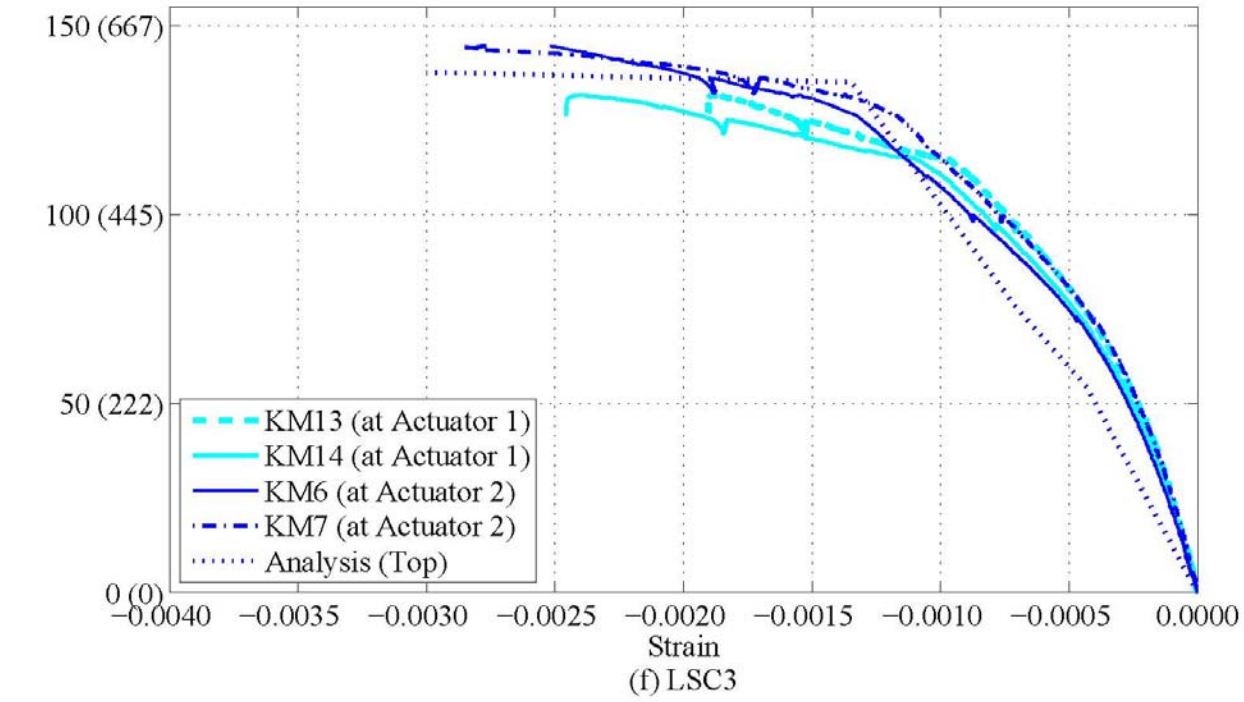

Figure 5-32. Experimental Load vs. Strain during the Four-Point Test: KM Gages at the Splice End in the Compression Region. (Continued)

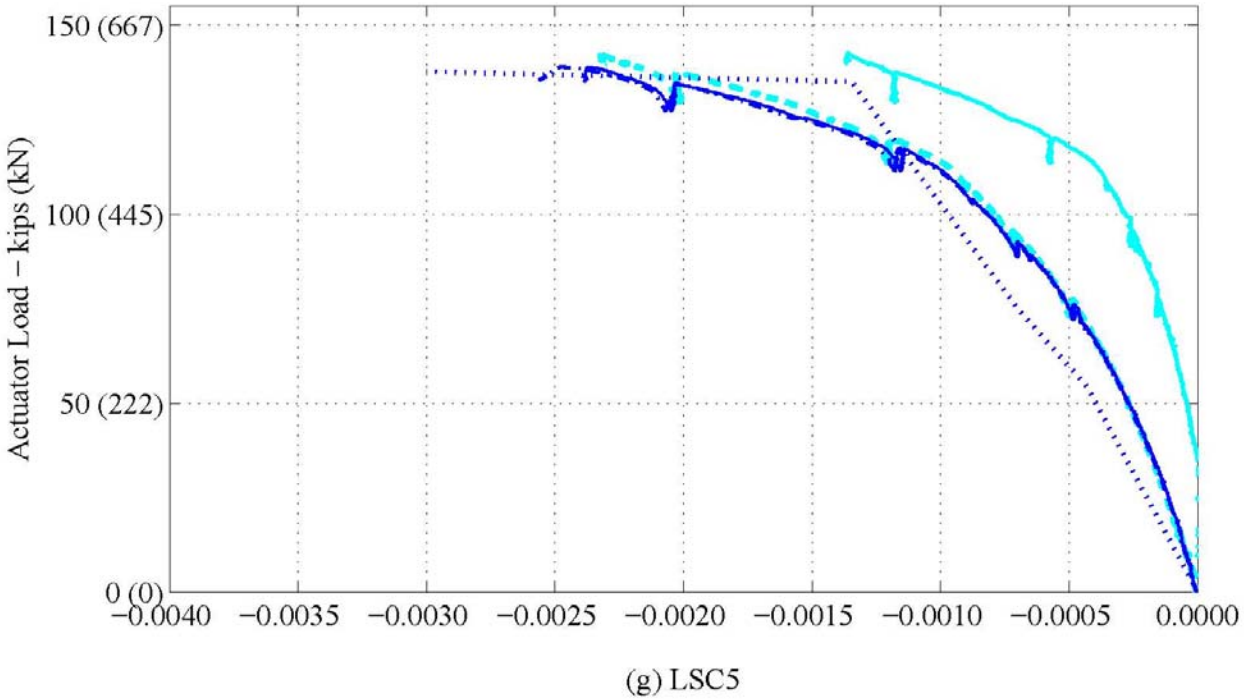

(g) LSC5

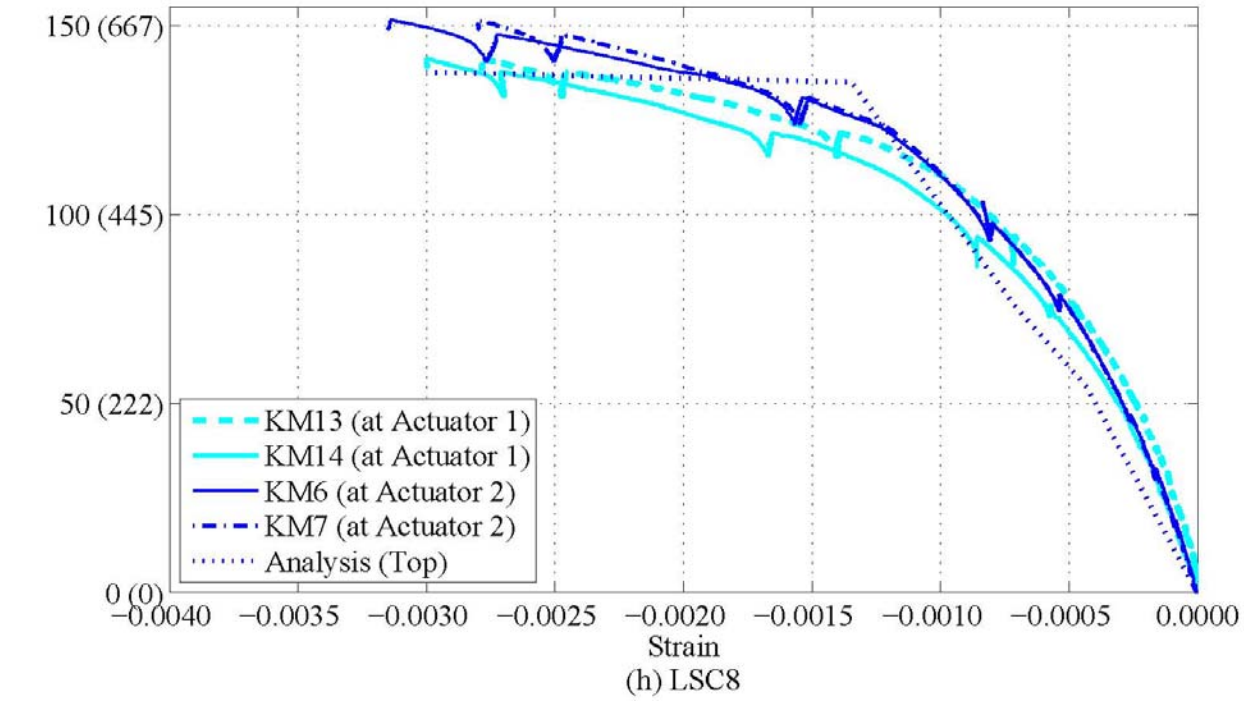

(h) LSC8

Figure 5-32. Experimental Load vs. Strain during the Four-Point Test: KM Gages at the Splice End in the Compression Region. (Continued)

Figure 5-33 shows the compression surface strains across the splice length. Figure 5-33(a) compares the KM and LVDT gages in the compression region. This figure shows the compression strains at each actuator were very similar. KM gages were chosen to instrument the remaining specimens shown in Figure 5-33(b) – (h). The compression strains across the splice length were smaller and did not reach plasticity, unlike the compression strains at the actuator load point (Figure 5-32). This has the same finding as the tension region, where the strains at the splice ends (actuator load points) deformed plastically and the splice region remained primarily elastic.

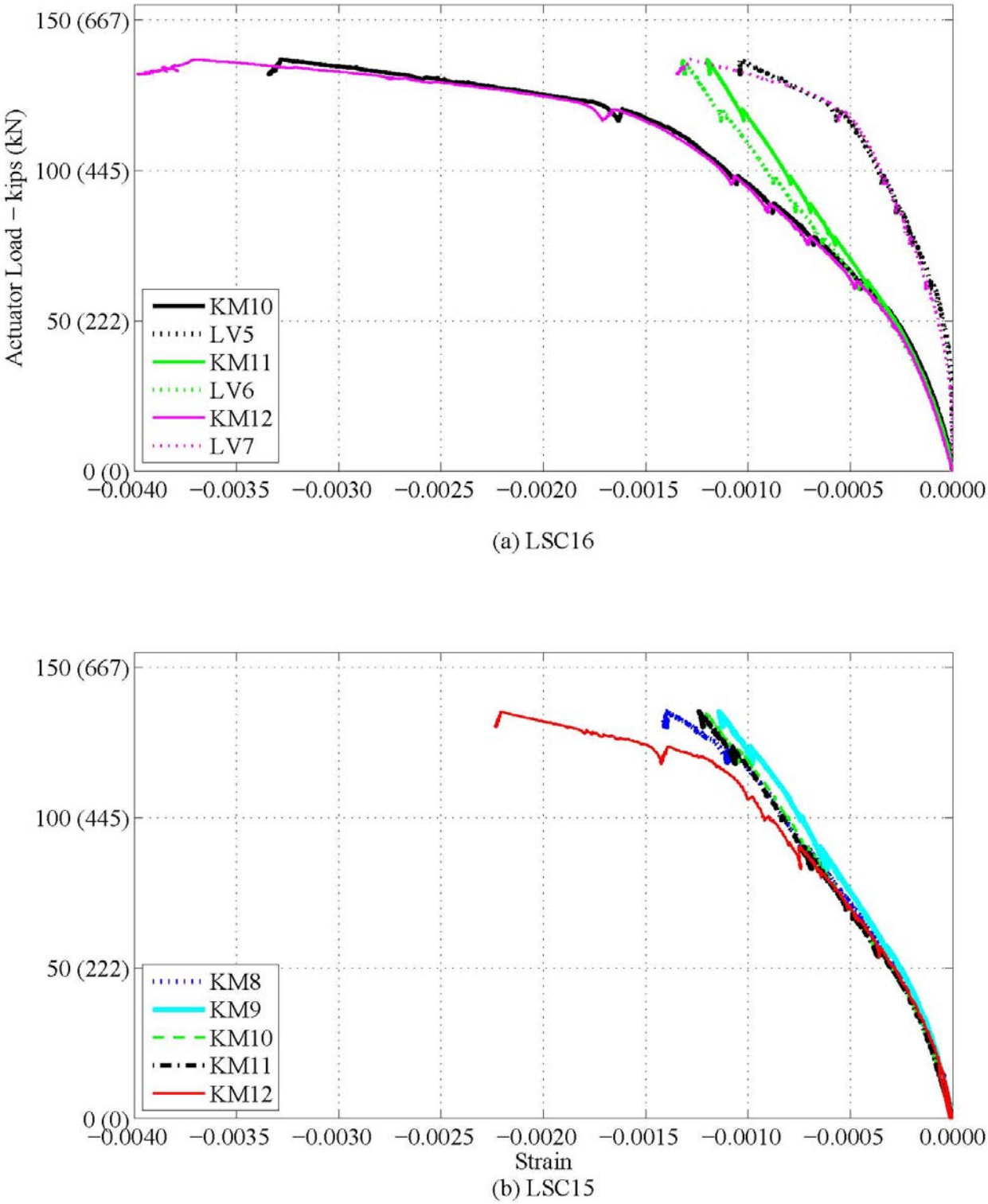

Figure 5-33. Experimental Load vs. Strain during the Four-Point Test: KM Gages across the Splice Length in the Compression Region.

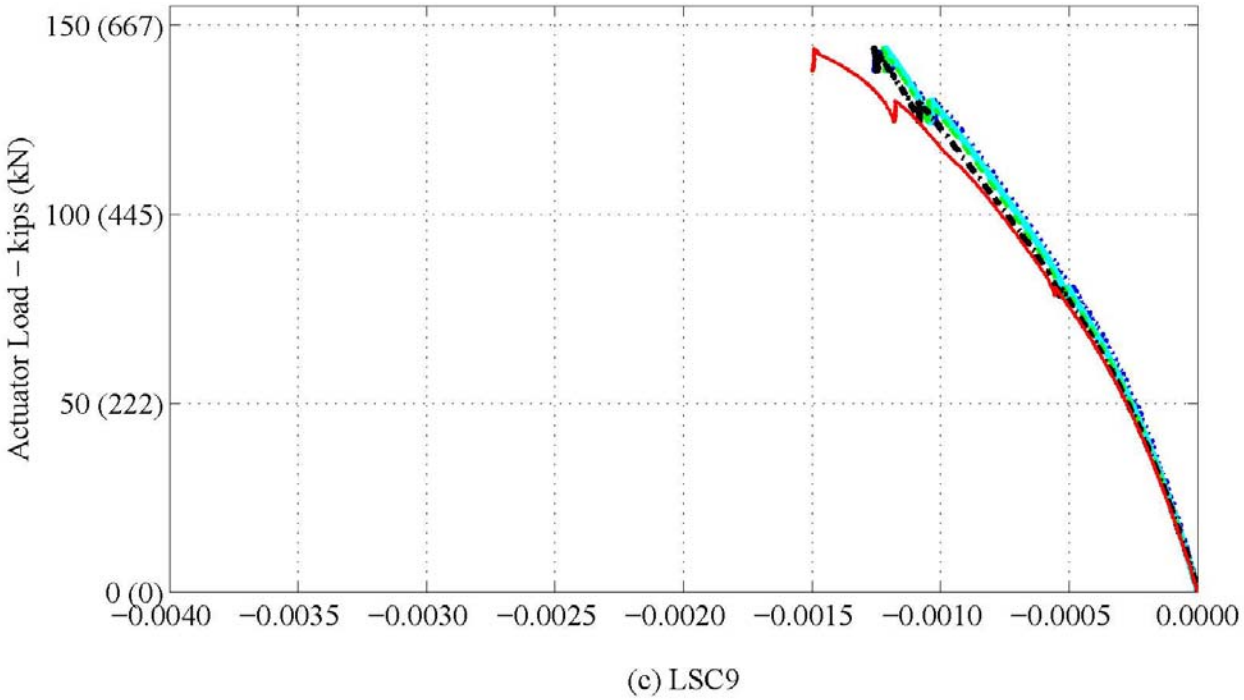

(c) LSC9

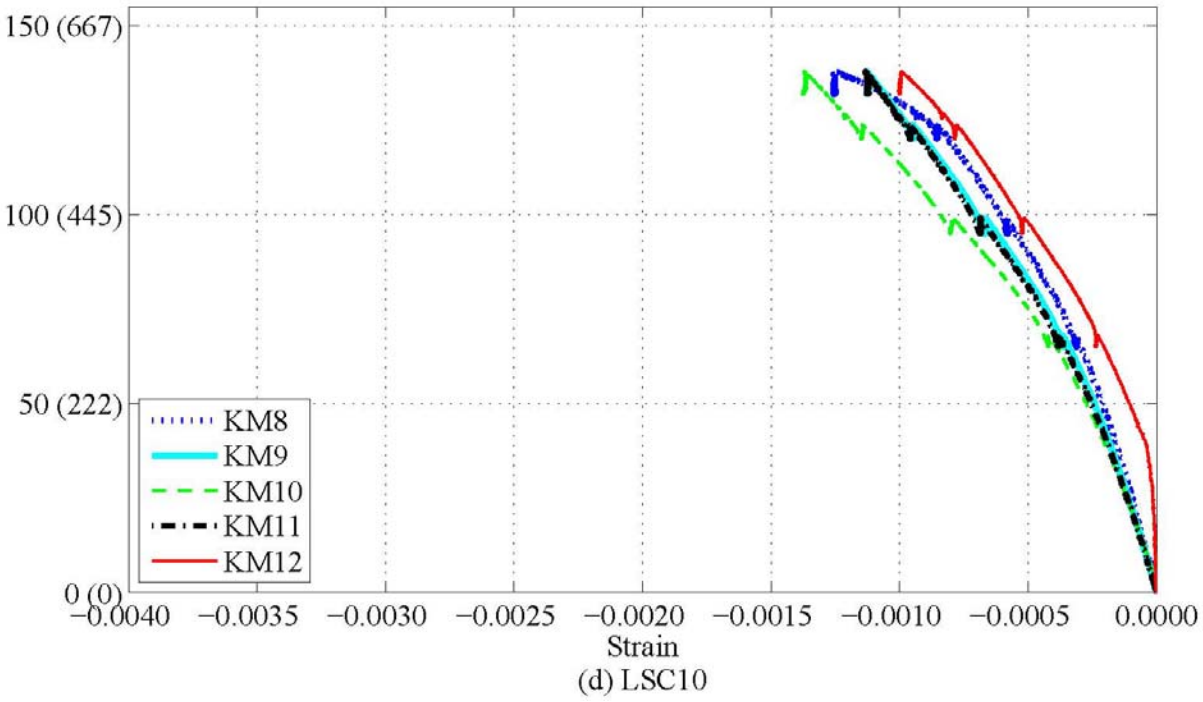

(d) LSC10

Figure 5-33. Experimental Load vs. Strain during the Four-Point Test: KM Gages across the Splice Length in the Compression Region. (Continued)

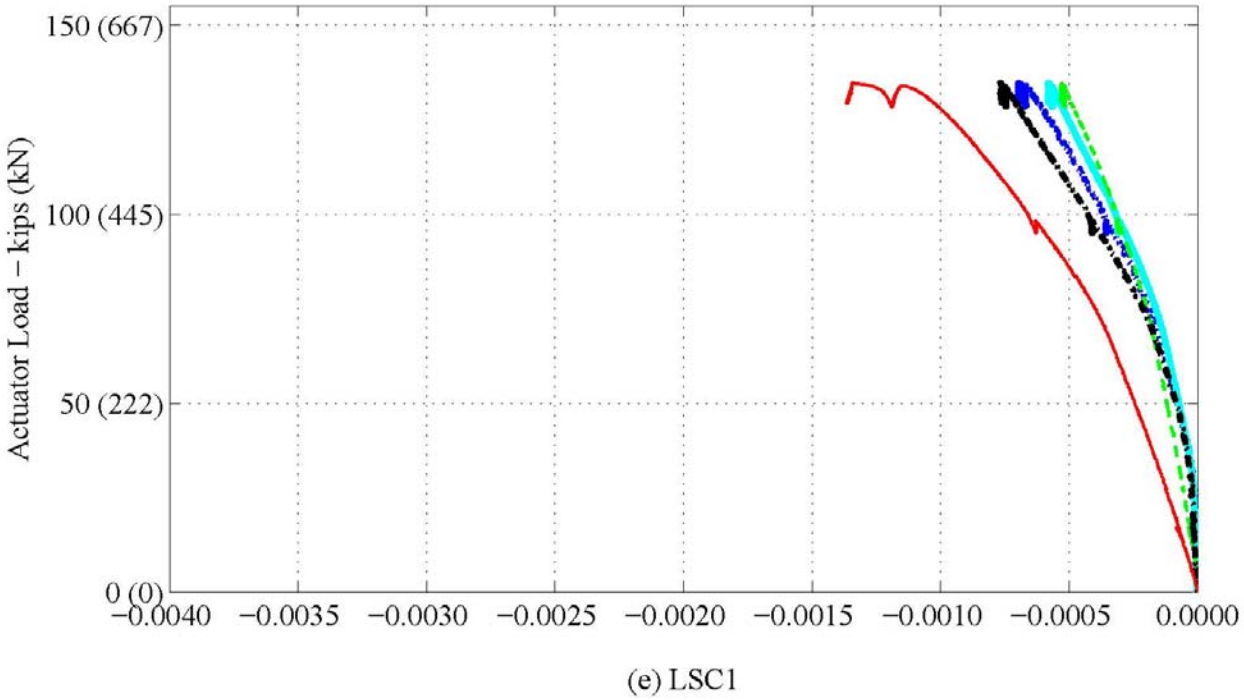

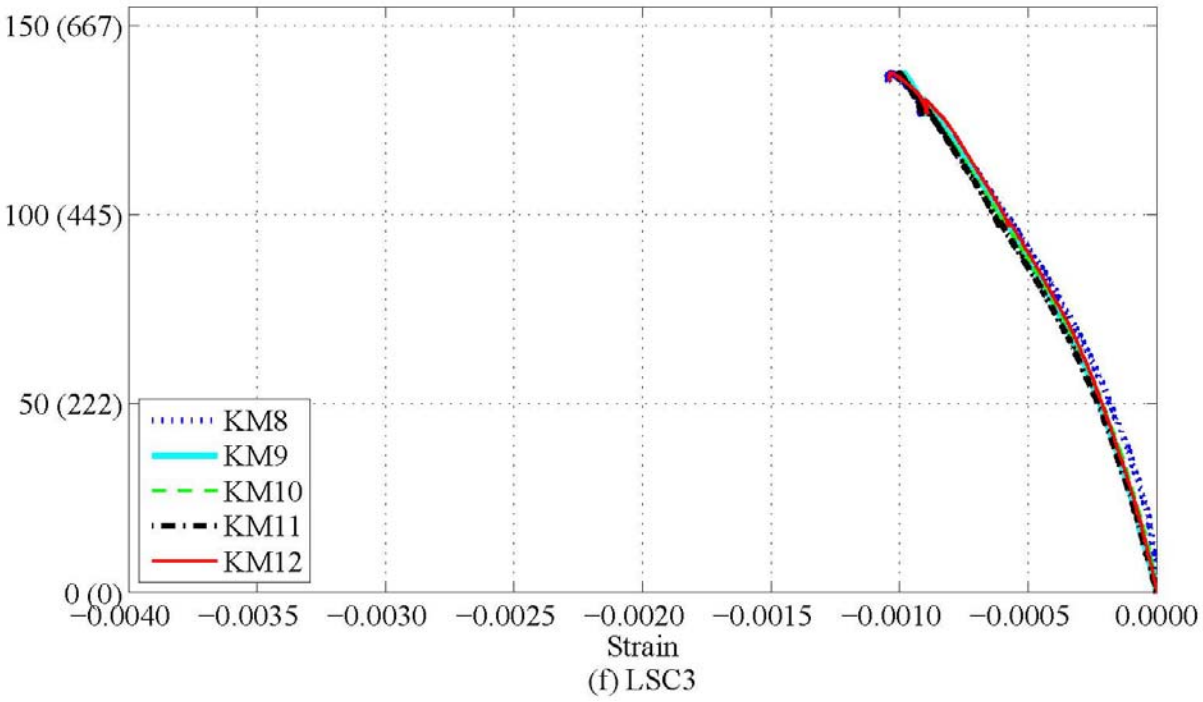

Figure 5-33. Experimental Load vs. Strain during the Four-Point Test: KM Gages across the Splice Length in the Compression Region. (Continued)

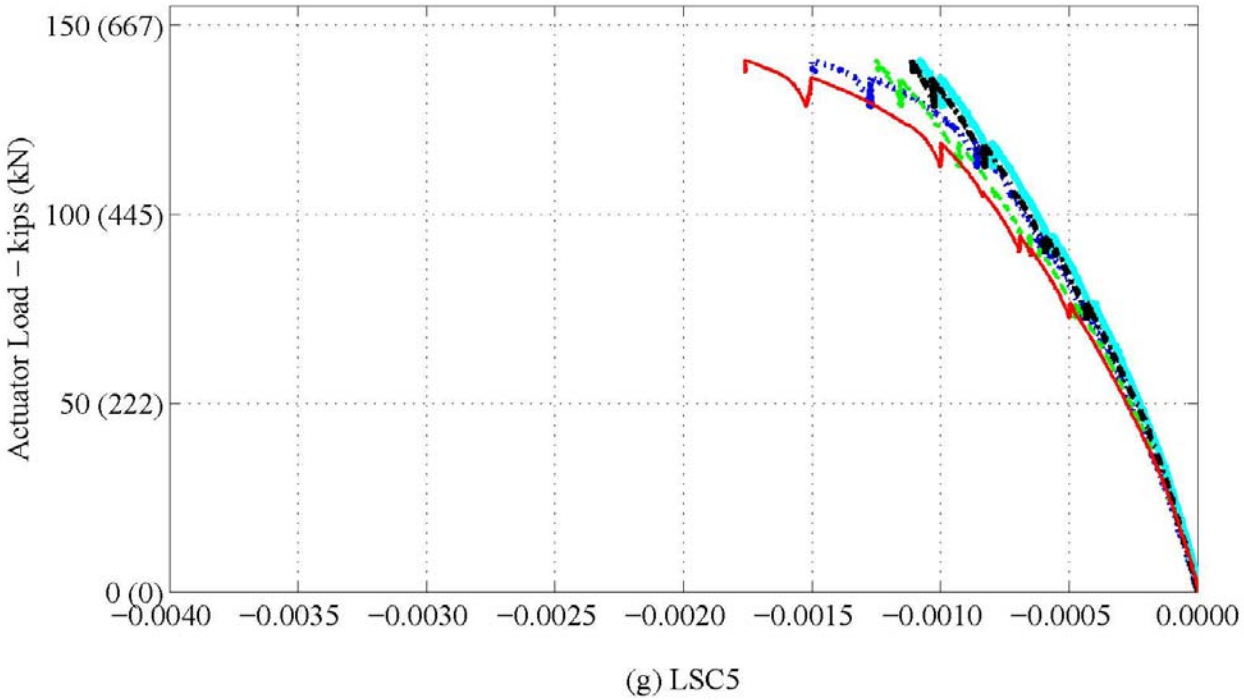

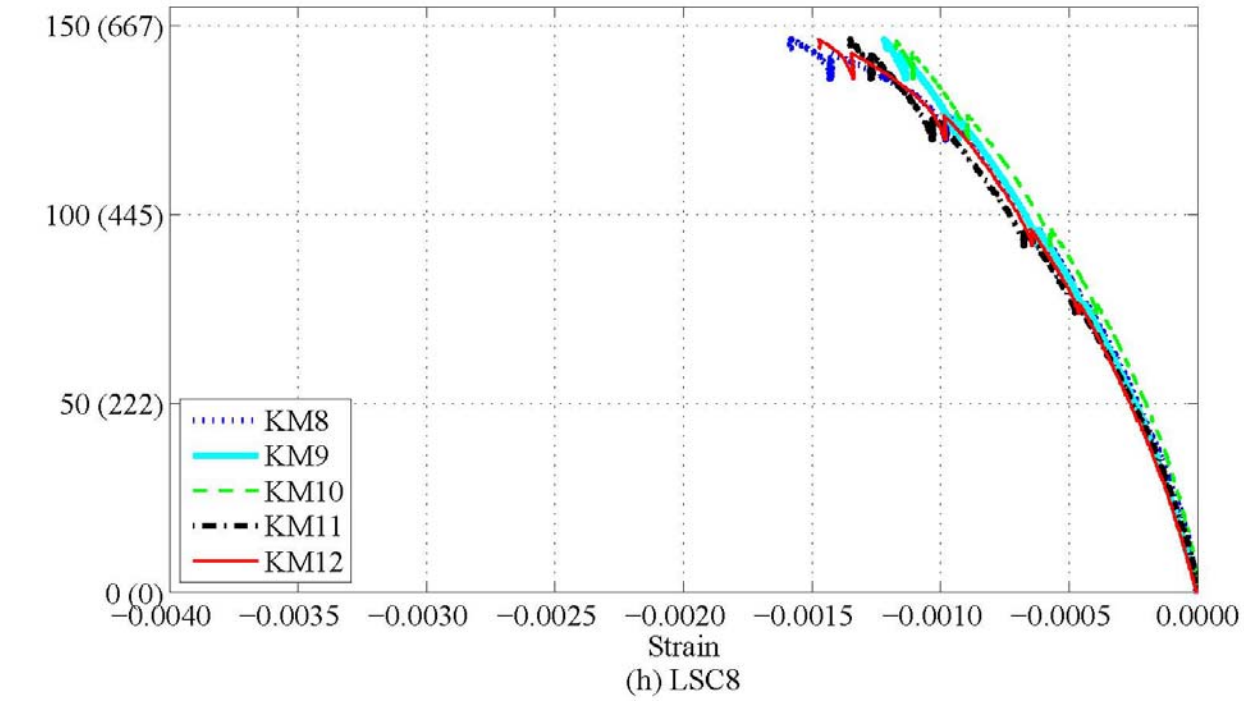

Figure 5-33. Experimental Load vs. Strain during the Four-Point Test: KM Gages across the Splice Length in the Compression Region. (Continued)

Figure 5-34 shows the transverse hoop strains from SG11, and comparable concrete cover and core from KM1, and KM2 near Small Face 1. These strains were measured during the deterioration process (Chapter 3) and set to zero before the four-point test. Figure 5-35 shows the transverse hoop strains from SG12 and the comparable concrete cover and core strains KM3, KM4, and KM5 near Large Face 1, which were also set to zero before the four-point test. The figures show some of the measured data had completely malfunctioned, and others gave inconsistent strain measurements. This most likely means that these measurements were not completely reliable following the large resulting strains during the deterioration program.

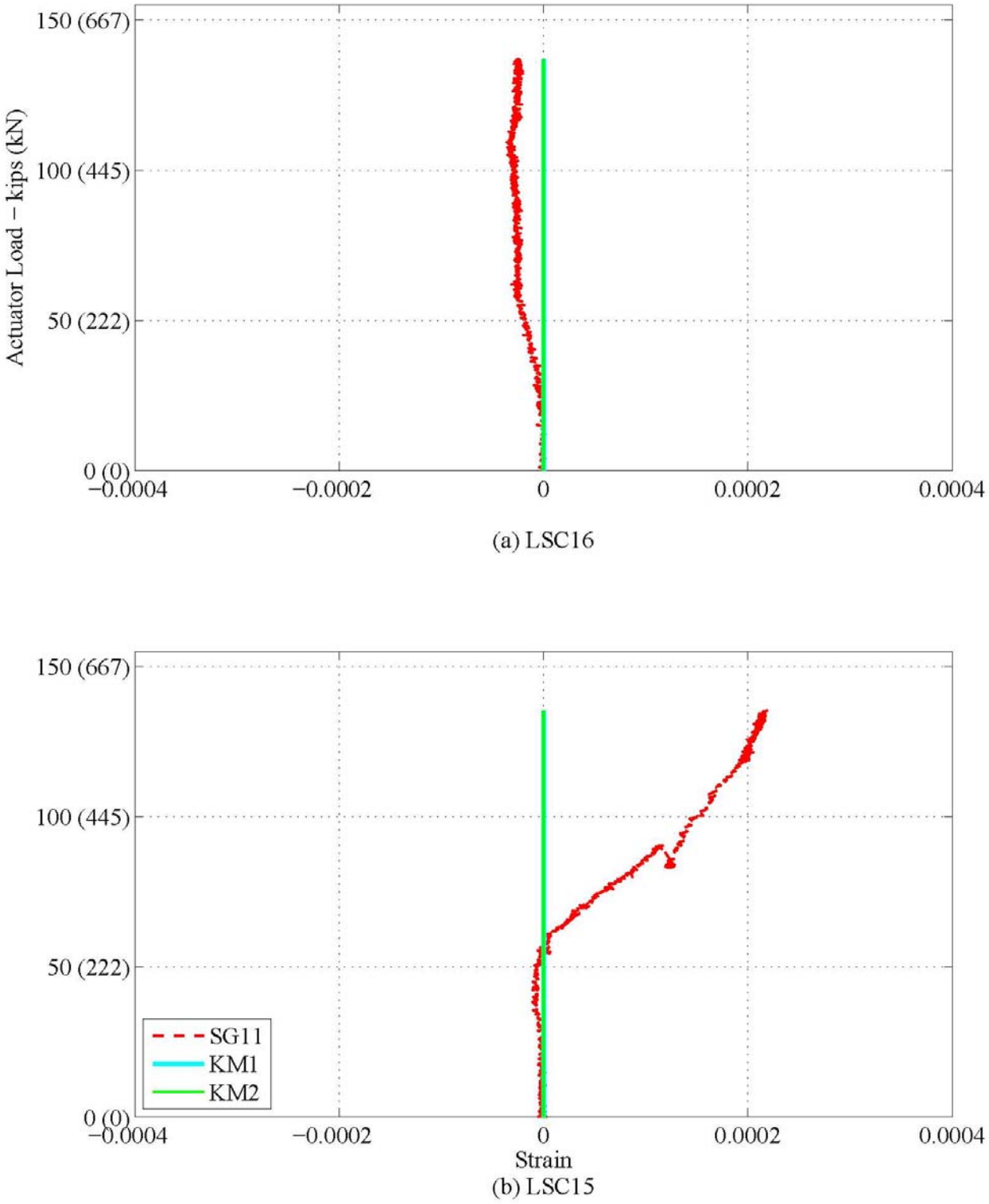

Figure 5-34. Experimental Load vs. Strain during the Four-Point Test: Internal Gages: SG11, KM1–KM2 by Small Face 1.

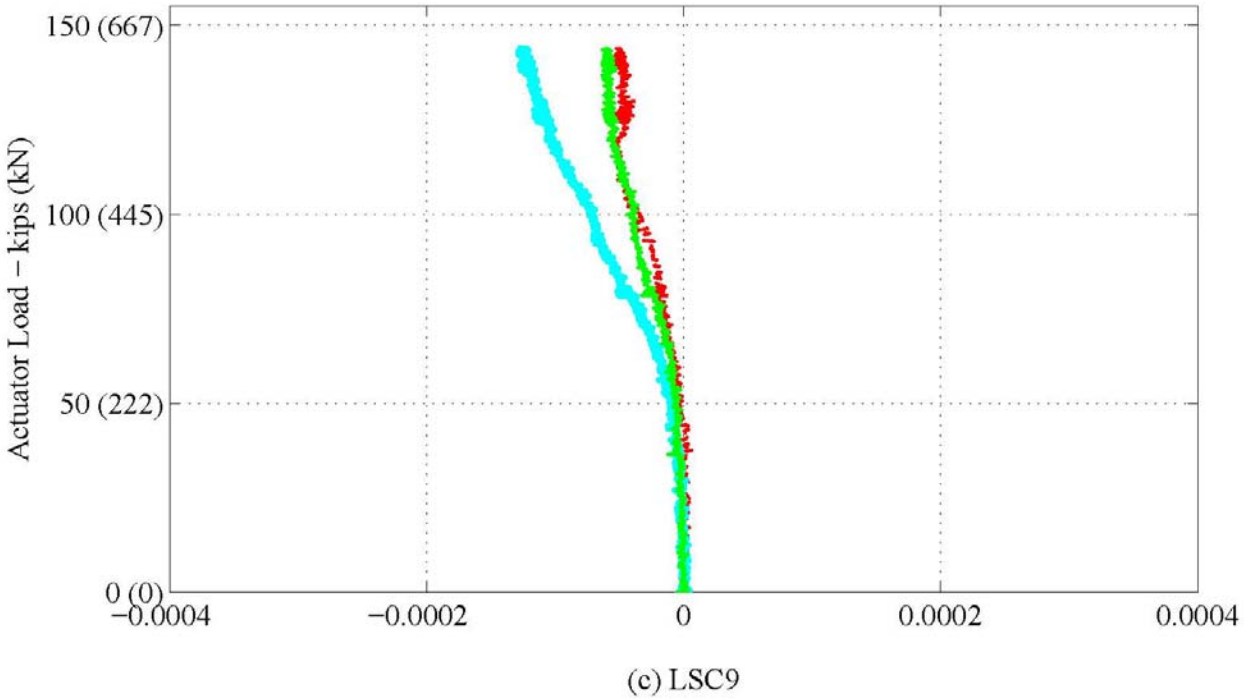

(c) LSC9

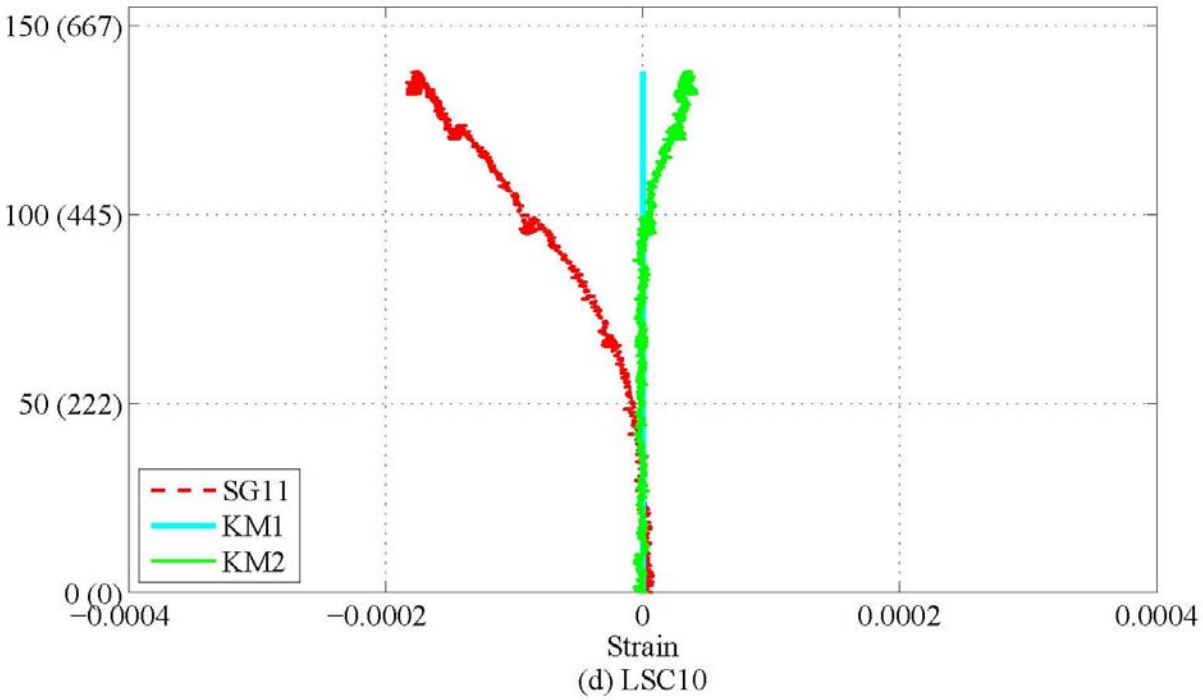

(d) LSC10

Figure 5-34. Experimental Load vs. Strain during the Four-Point Test: Internal Gages: SG11, KM1–KM2 by Small Face 1. (Continued)

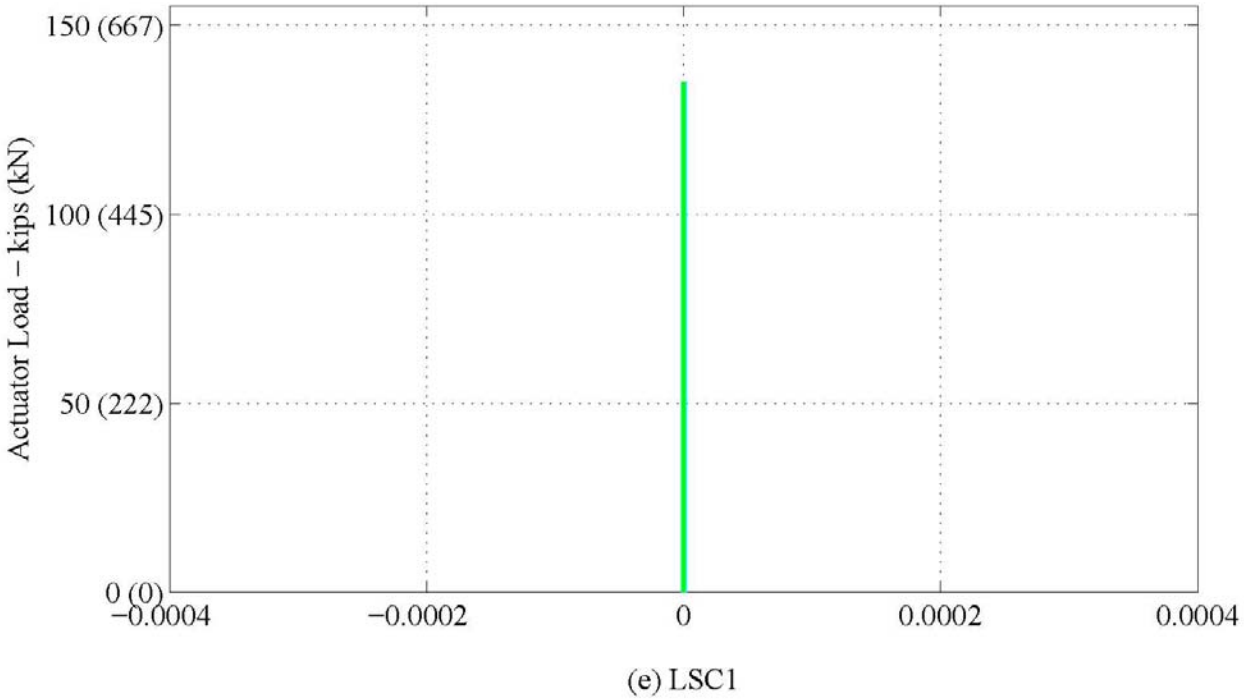

(e) LSC1

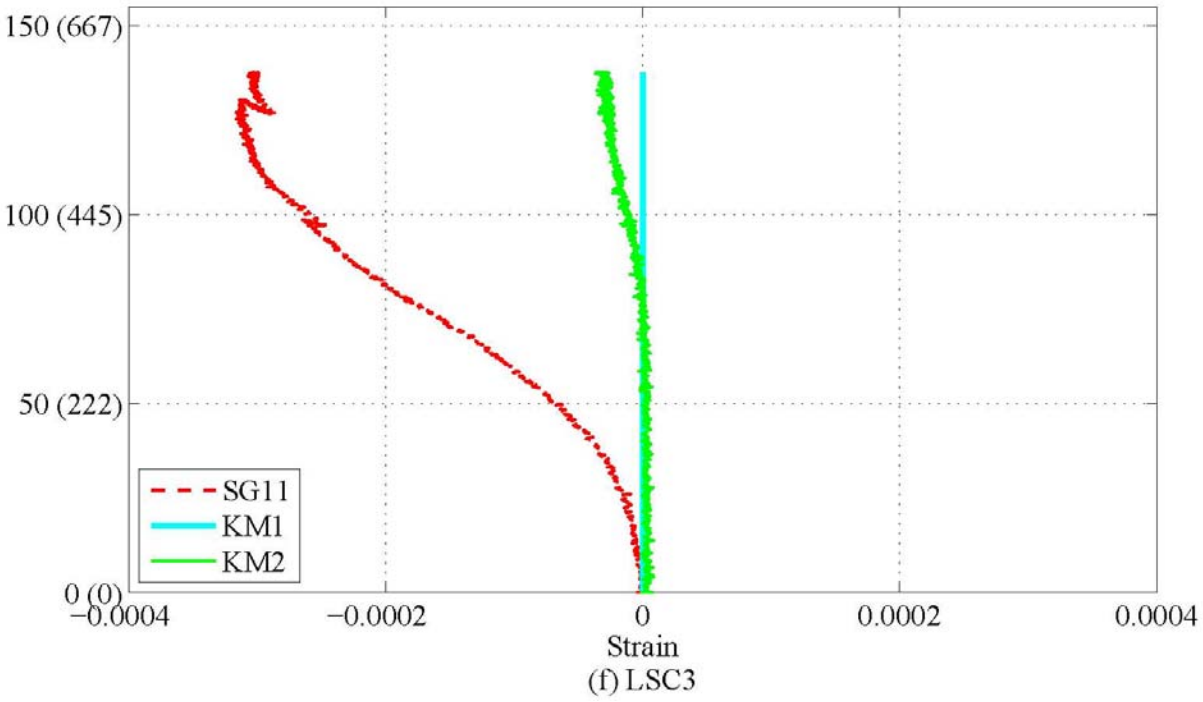

(f) LSC3

Figure 5-34. Experimental Load vs. Strain during the Four-Point Test: Internal Gages: SG11, KM1–KM2 by Small Face 1. (Continued)

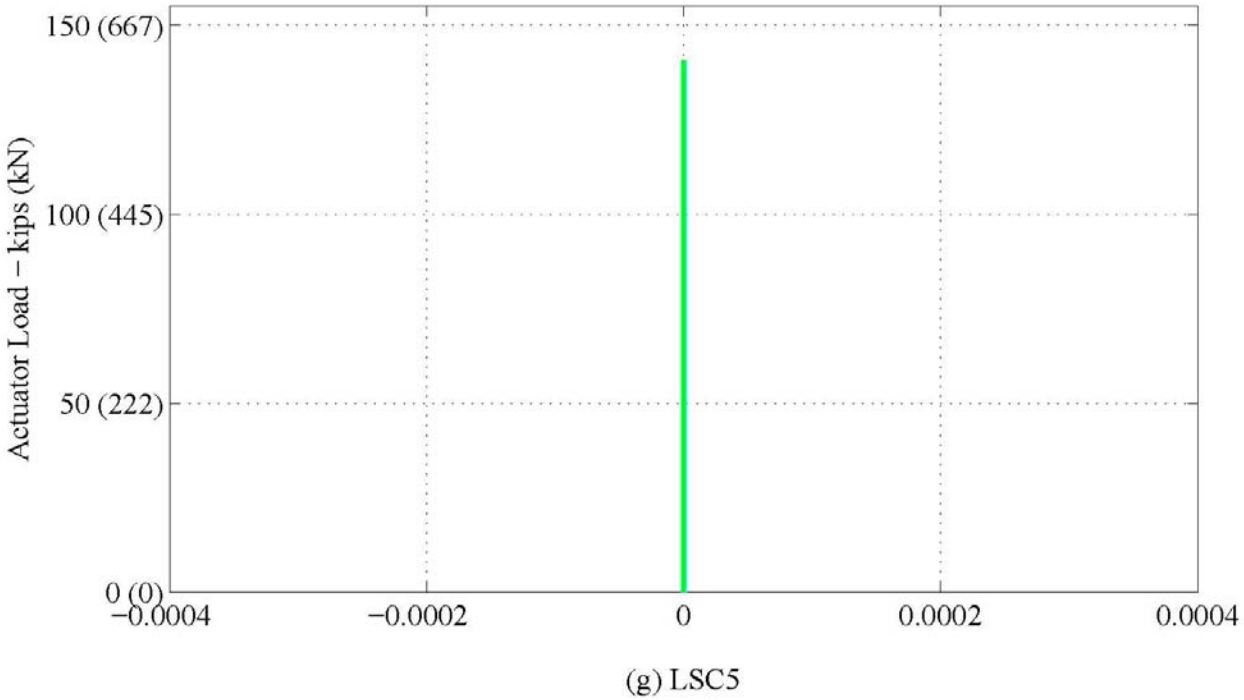

(g) LSC5

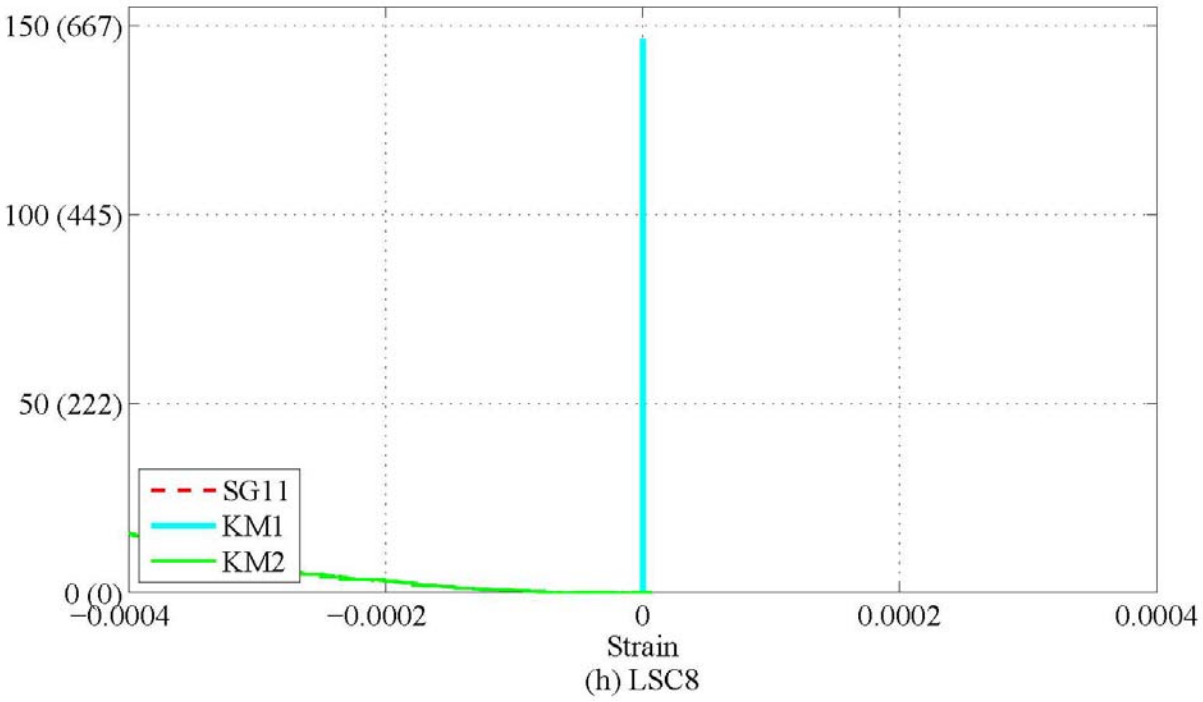

(h) LSC8

Figure 5-34. Experimental Load vs. Strain during the Four-Point Test: Internal Gages: SG11, KM1–KM2 by Small Face 1. (Continued)

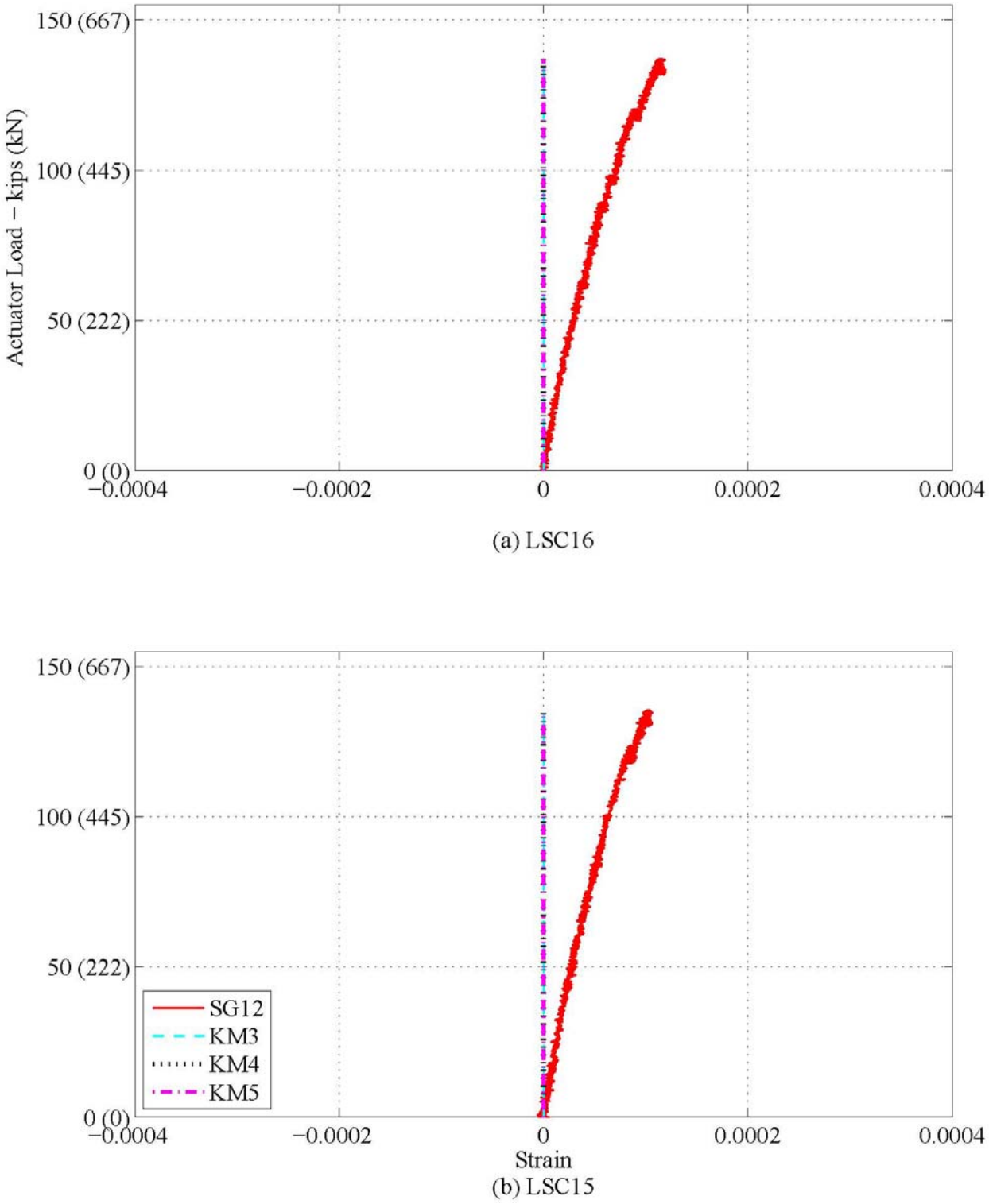

Figure 5-35. Experimental Load vs. Strain during the Four-Point Test: Internal Gages: SG12, KM3–KM5 by Large Face 1.

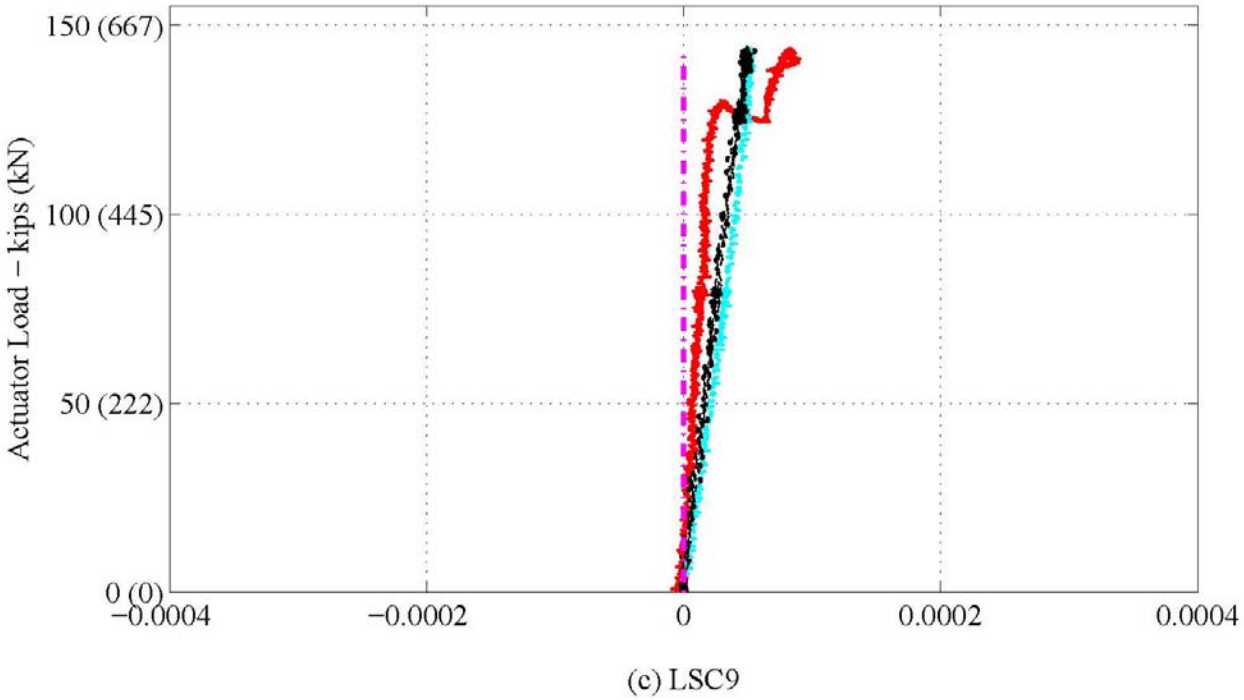

(c) LSC9

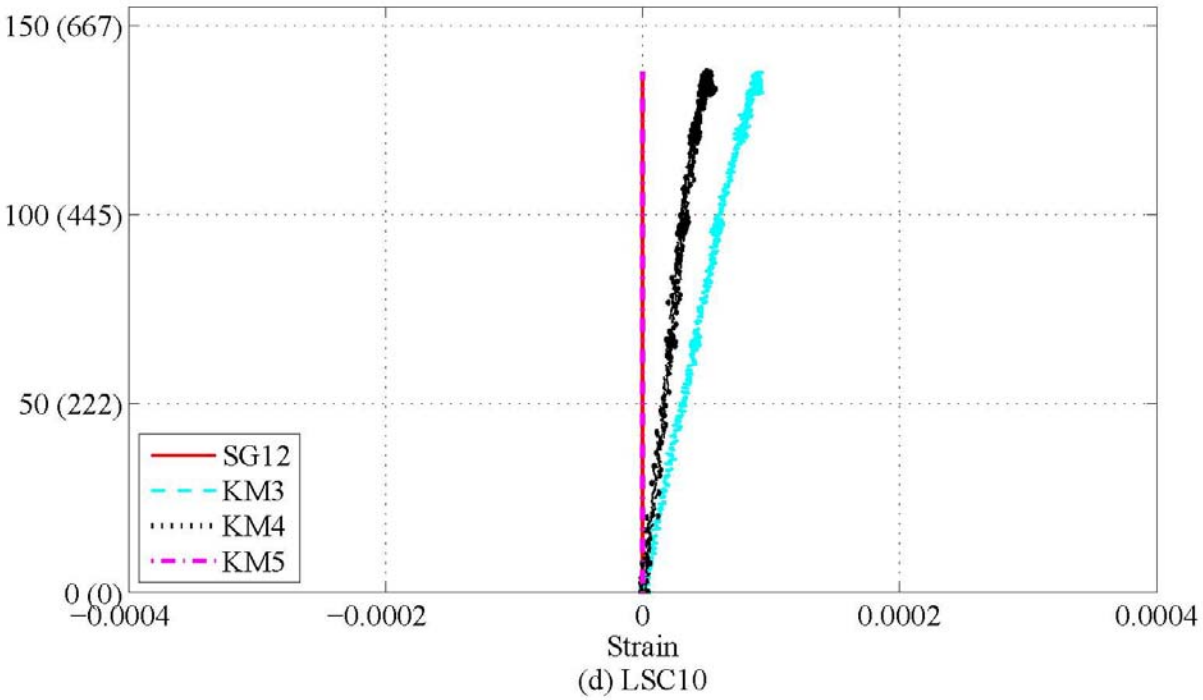

(d) LSC10

Figure 5-35. Experimental Load vs. Strain during the Four-Point Test: Internal Gages: SG12, KM3–KM5 by Large Face 1. (Continued)

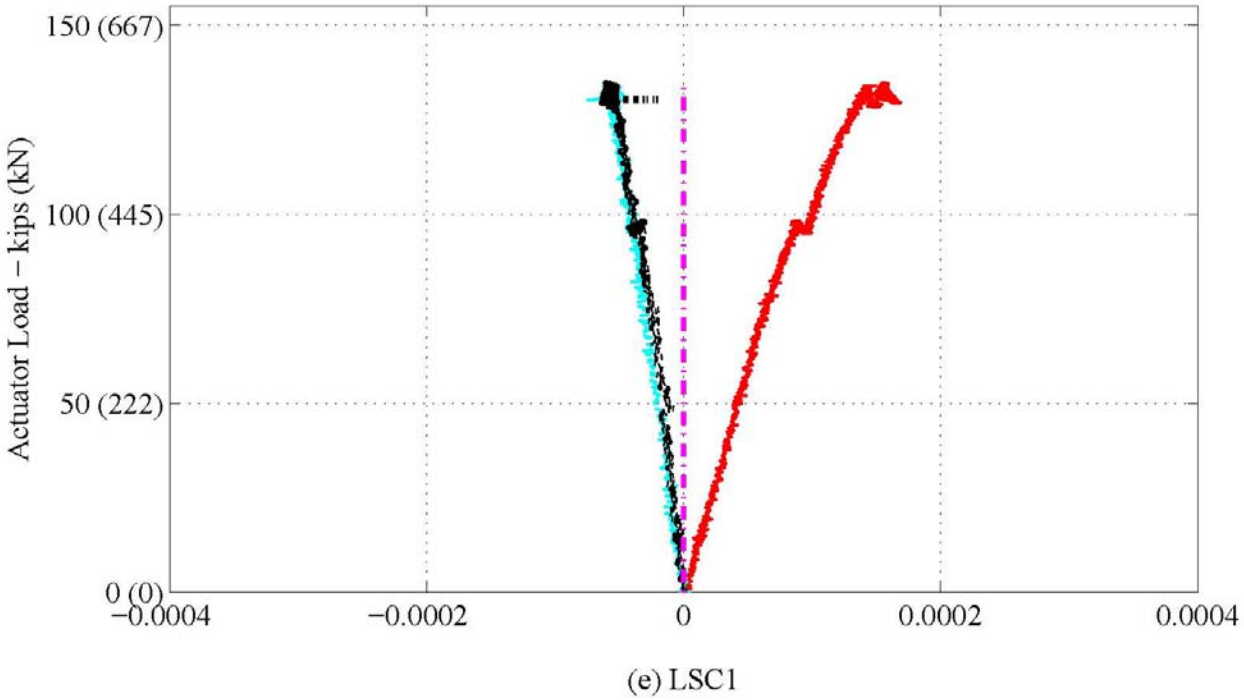

(e) LSC1

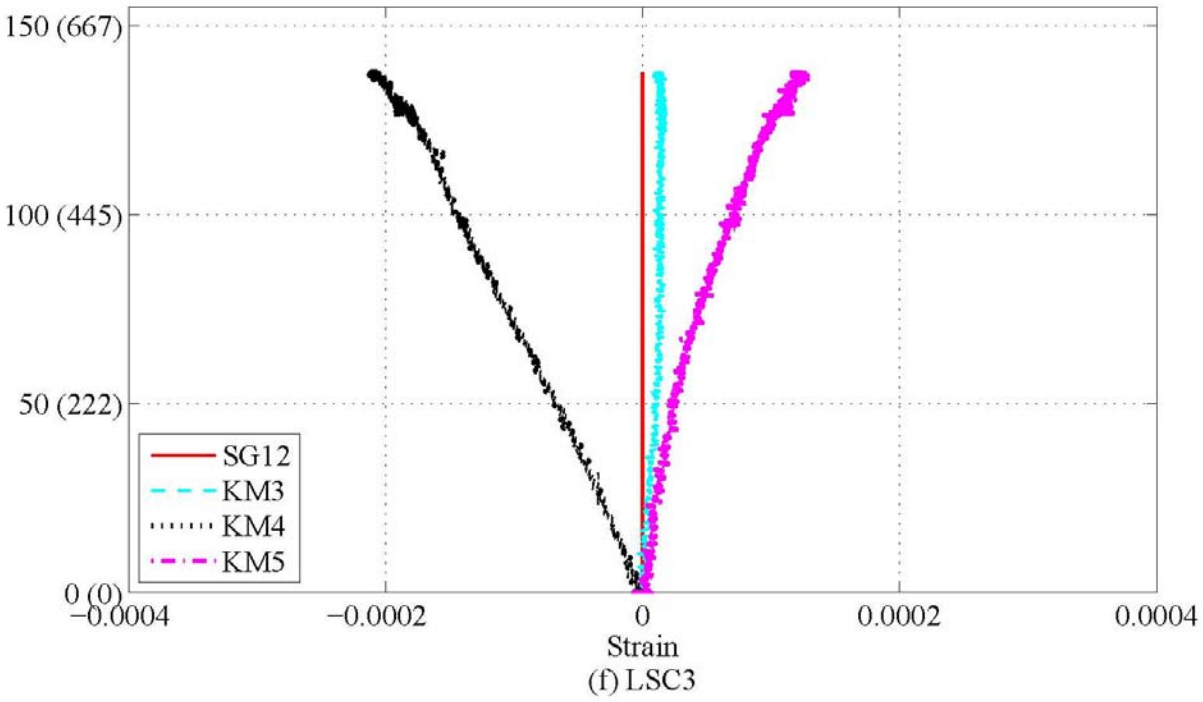

(f) LSC3

Figure 5-35. Experimental Load vs. Strain during the Four-Point Test: Internal Gages: SG12, KM3–KM5 by Large Face 1. (Continued)

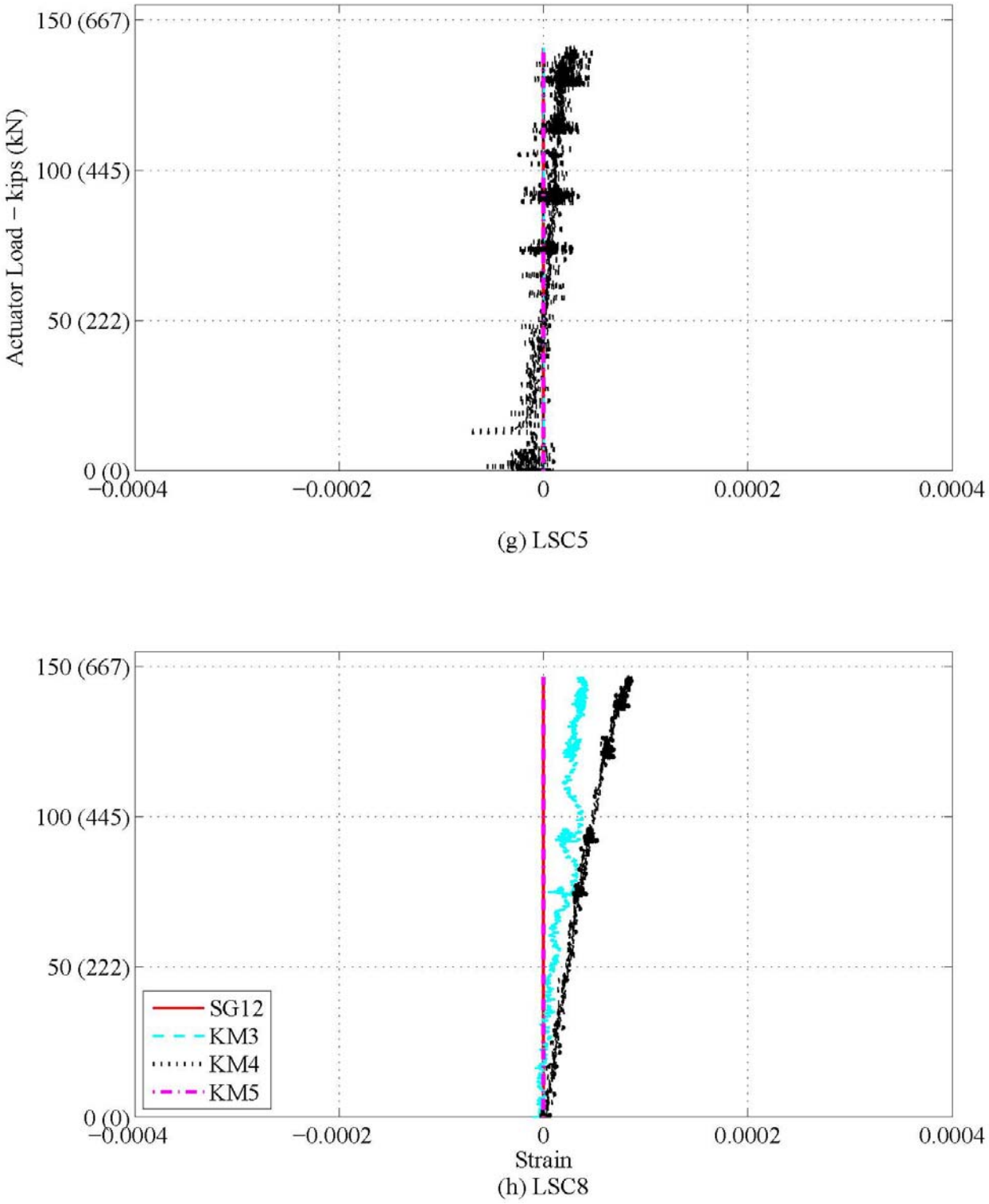

Figure 5-35. Experimental Load vs. Strain during the Four-Point Test: Internal Gages: SG12, KM3–KM5 by Large Face 1. (Continued)

5.4.3 Three-Point Flexural/Shear Test Results

The specimen behavior from the three-point tests is presented below. As explained previously, the specimen was rotated such that the tension side on the four-point test was also the tension side on the three-point test. Figure 5-12 illustrates the three-point setup as well as the shear and moment diagrams for this test. The resulting damage from the four-point test that primarily developed at the splice ends had minimal impact on the performance of the specimen in the three point setup since the critical section for flexure is now at the center of the splice length region at the support reaction. The same internal gages as the four-point test were monitored during the test; however, some of these gages proved to be unreliable from the previous deterioration program and four-point load testing. The internal gages were set to zero prior to the three-point test. External instruments, LVDTs, KM, and STR were reinstalled to measure the strains and deflections during the three point test as illustrated in Figure 5-13.

Figure 5-36 compares the actuator load vs. deflection response at the loading point from all tested specimens during the three-point test. Higher actuator loads were achieved during this test as compared to the previous four-point load test due to the different demand from the test setups and because these specimens were loaded to near failure since no further testing was planned. Note that LSC8 had the smallest measured load during the three-point test since severe cracking resulted and the test was terminated due to safety concerns. Similar to the four-point test, there are a few strain values that show a drop in load due to the halt in the loading to view cracks during the tests. Figure 5-36 shows that during the three-point test, the non-control specimens had about 5–15 percent higher yield strengths and were about 25–35 percent stiffer (similar to the four-point test) from post-cracking until yield than the control specimens (LSC15 and LSC16) for the same reasons as explained for the four-point test.

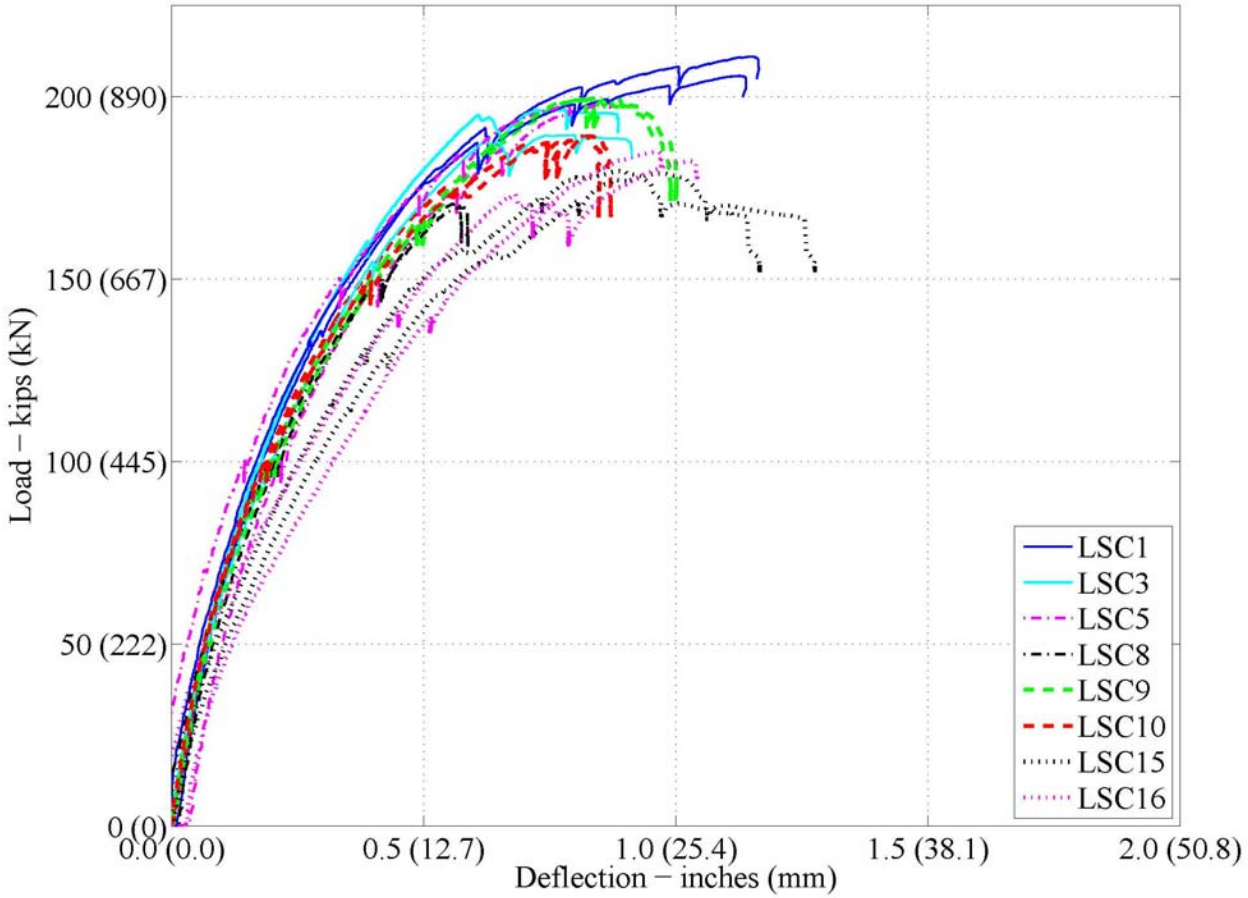

Figure 5-36. Experimental Load vs. Deflection during the Three-Point Test: All Tested Specimens at the Actuator Load Point.

Figure 5-37 shows the experimental and analytical load versus deflection response for each specimen separately during the three point test. The analytical model also shows higher actuator loads during the three-point test than in the four-point test. The figure shows that the analytical model for the three-point test is fairly representative of the experimental data; however, the analytical results are about 15 percent stiffer. This deviation can be explained because the analytical model did not account for the previous cracking in the specimen from the four-point load test and the modeling assumption that all plasticity only occurred in the section at the support. In addition, shear deformations were not accounted for in the analytical model and may be more prevalent in the three-point test setup since there are shear demands between the actuators in the three-point test setup.

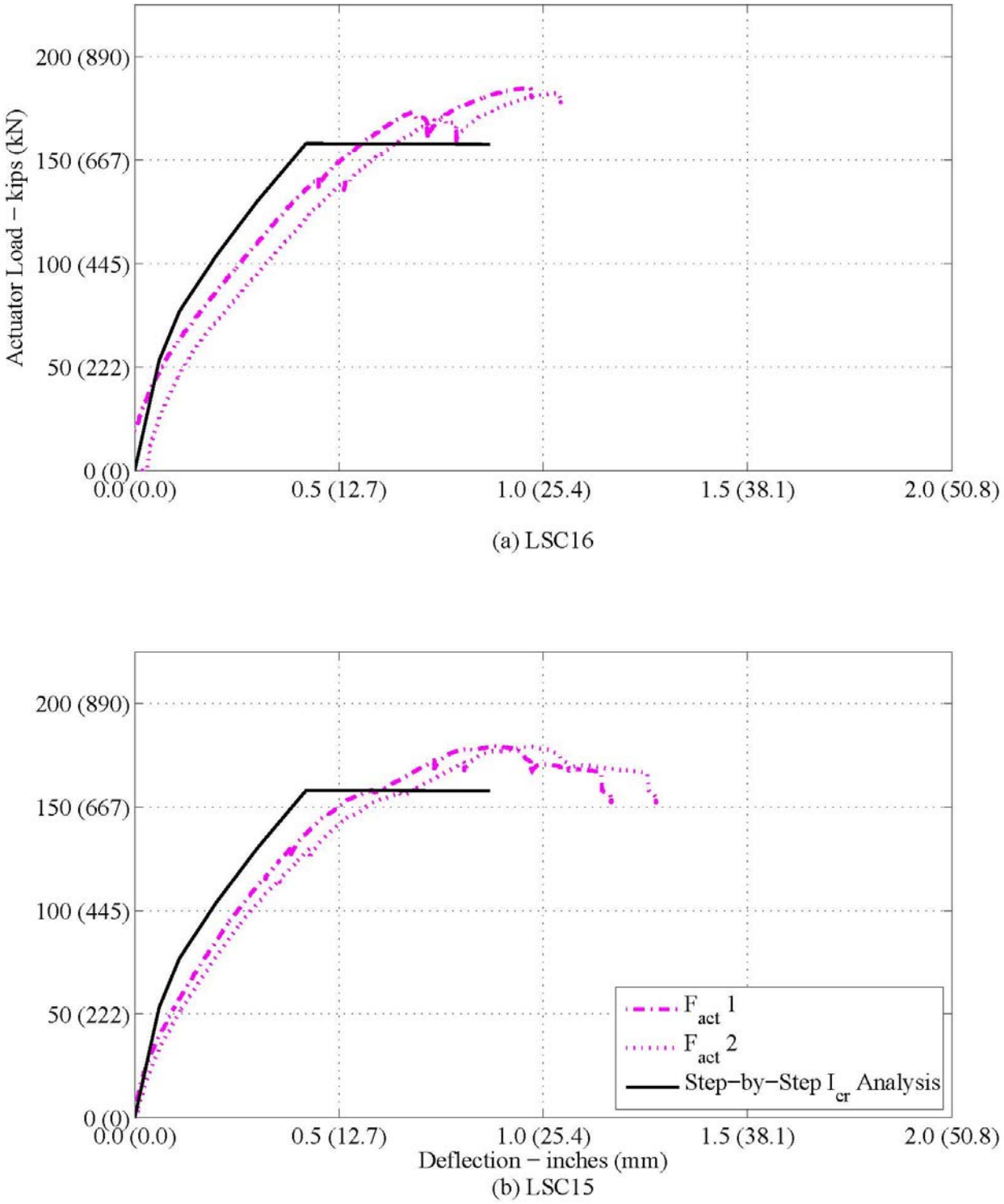

Figure 5-37. Experimental and Analytical Load vs. Deflection during the Three-Point Test: at the Actuator Load Point.

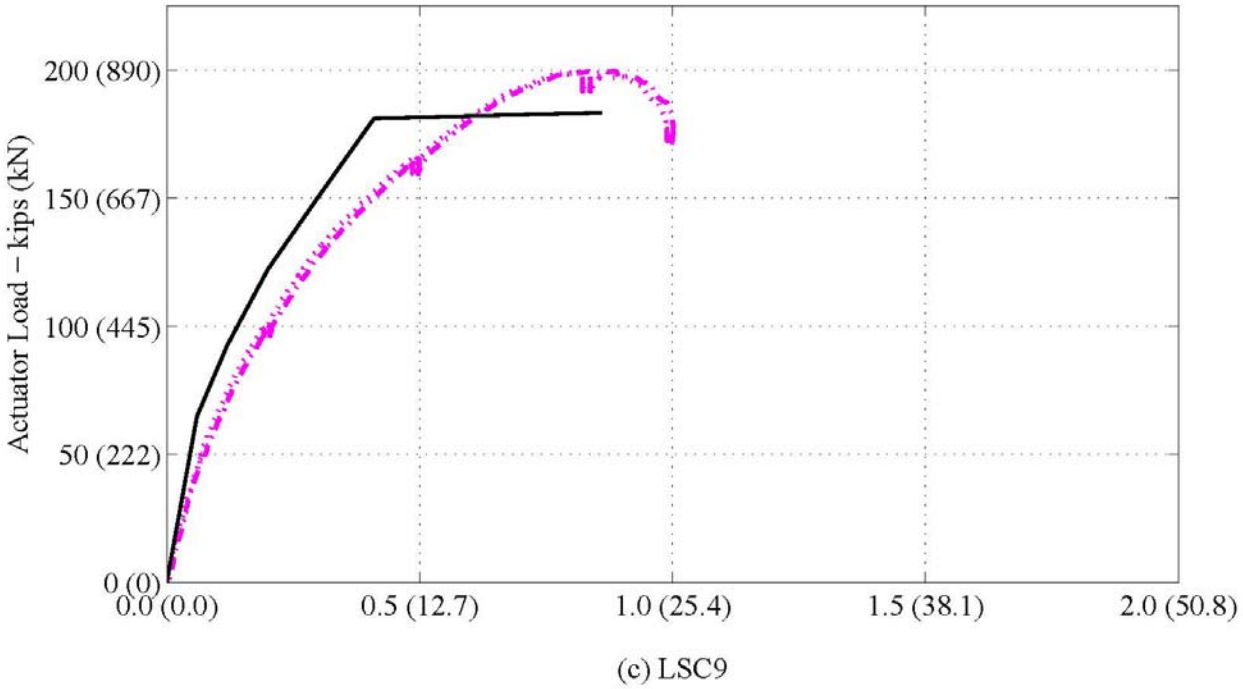

(c) LSC9

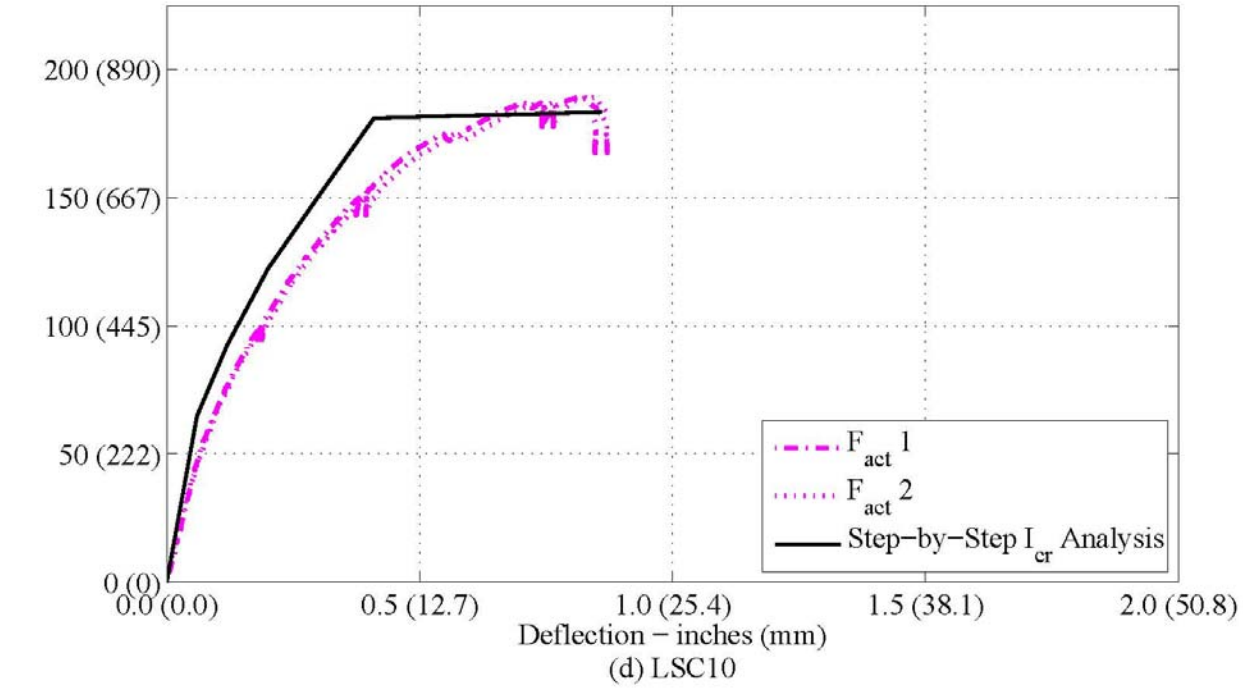

(d) LSC10

Figure 5-37. Experimental and Analytical Load vs. Deflection during the Three-Point Test: at the Actuator Load Point (Continued)

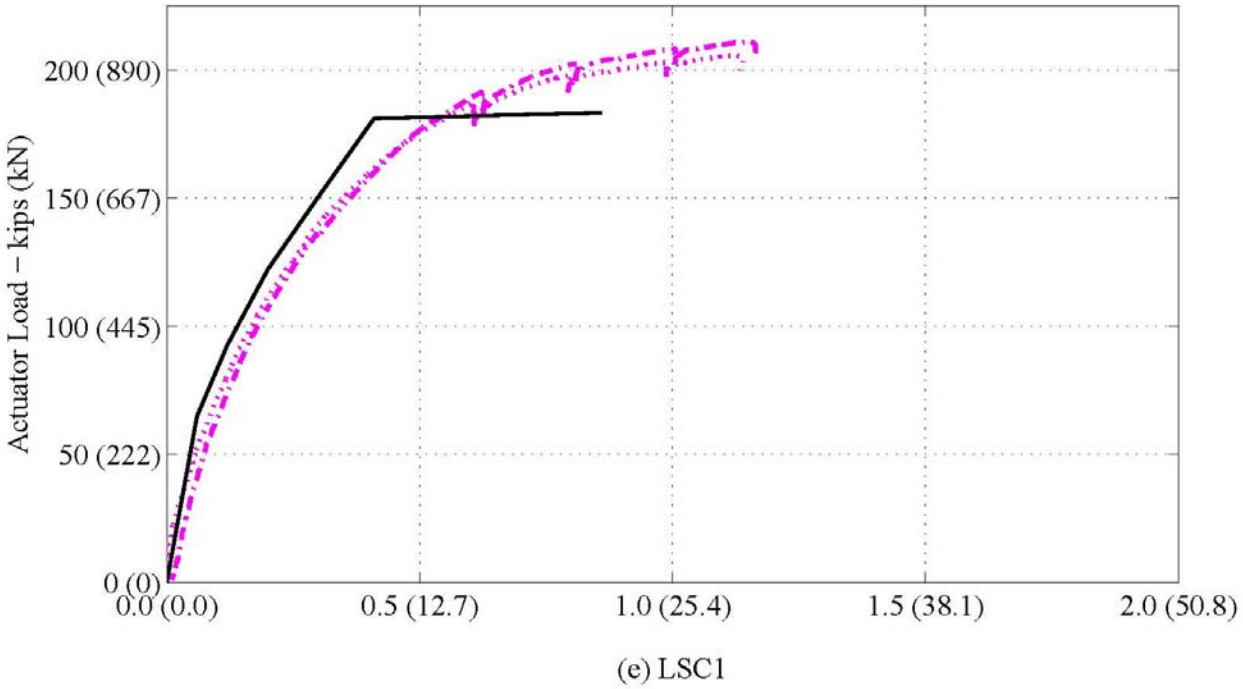

(e) LSC1

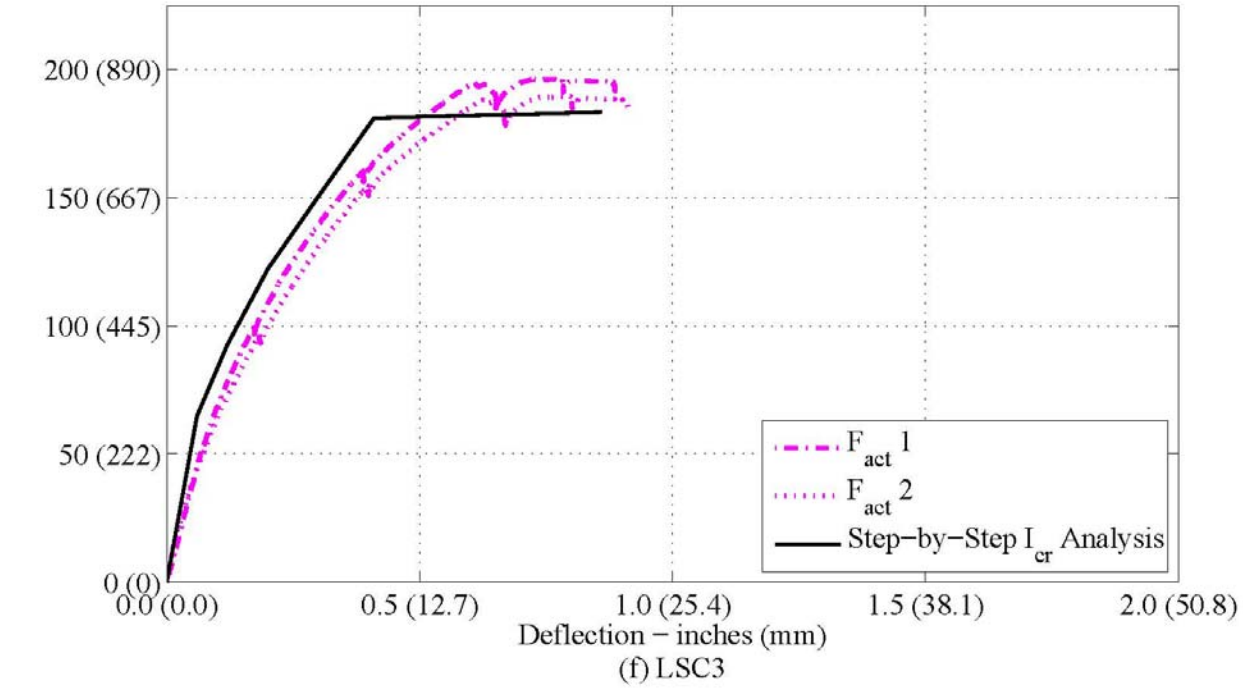

(f) LSC3

Figure 5-37. Experimental and Analytical Load vs. Deflection during the Three-Point Test: at the Actuator Load Point (Continued)

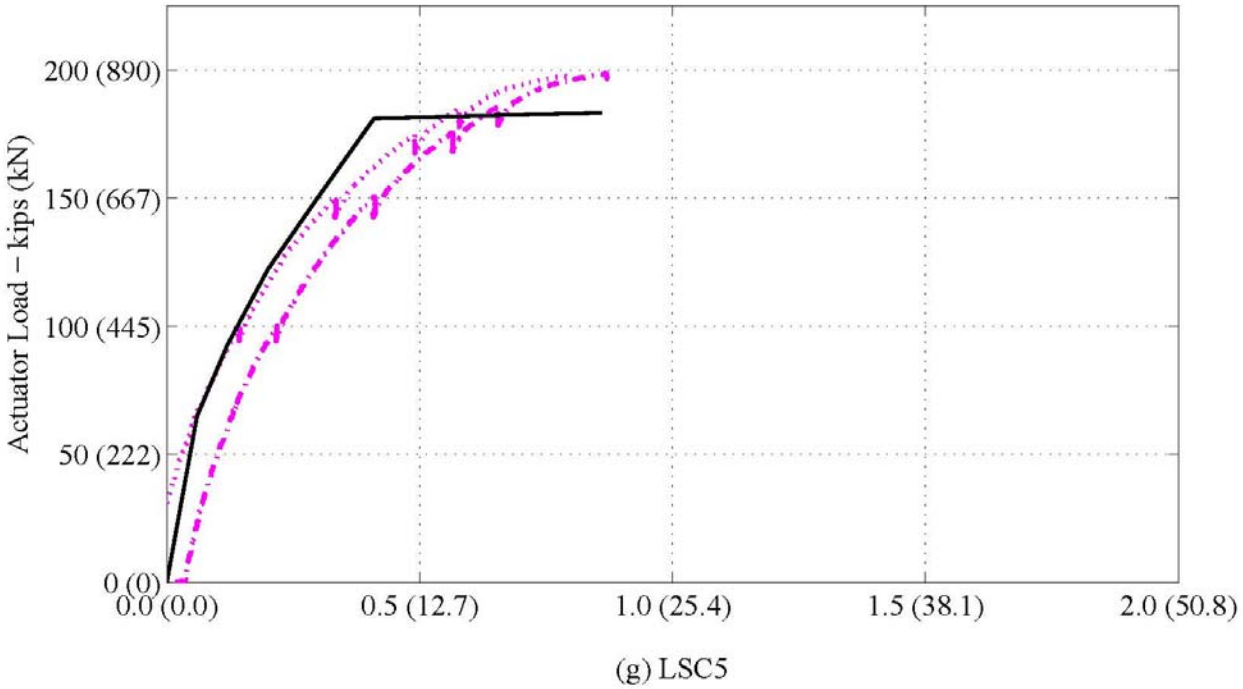

(g) LSC5

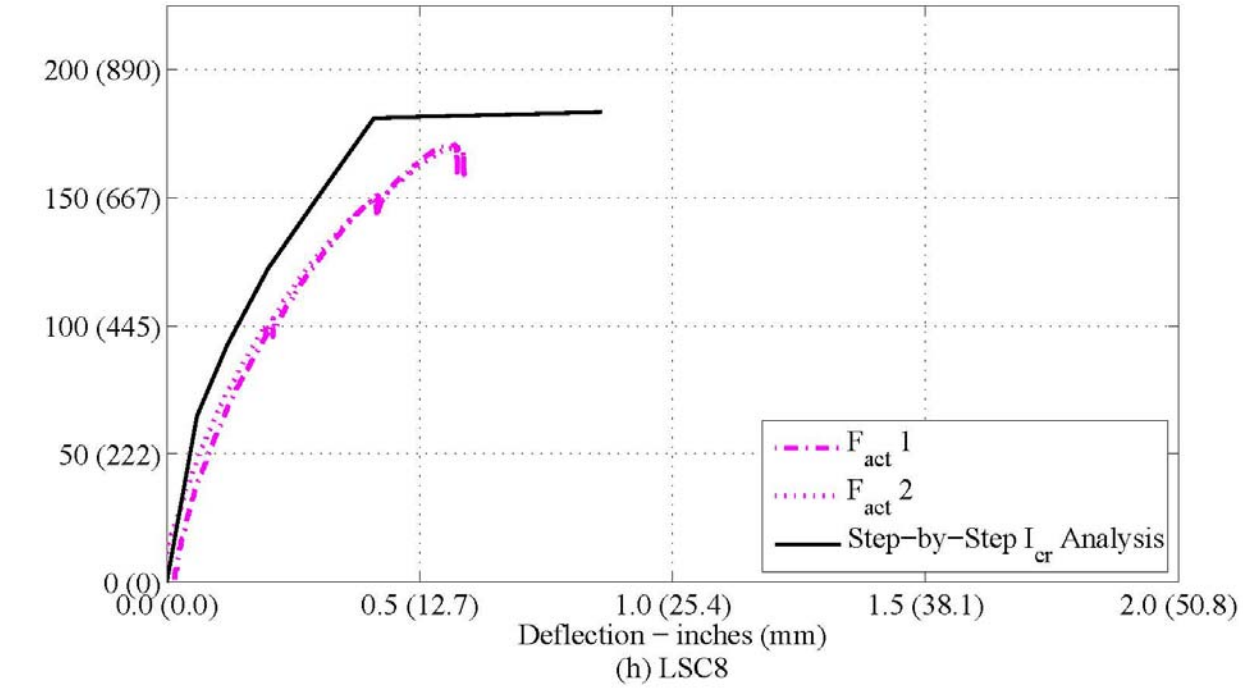

(h) LSC8

Figure 5-37. Experimental and Analytical Load vs. Deflection during the Three-Point Test: at the Actuator Load Point (Continued)

Figure 5-38 and Figure 5-39 show the total actuator load (sum of the two actuators) versus the internal strains in the reinforcing steel along the tension bars in the splice region. The total actuator load was used since this test is an inverted simply supported beam with one center point load. The strains on the splice bars reach yielding (0.002) about ¾ of the time and are close when yielding is not reached. However, SG4 and SG8, which are located at the end of the splice bars (little anchorage), only reached yielding on two specimens.

Figure 5-40 shows the same force versus the internal strains in the compression reinforcing steel. Internal compression gages on LSC16, LSC1, and LSC9 showed non-linear responses as early as first cracking in the concrete and proved to be unreliable in this test setup especially beyond the yield strains of steel of 0.002 inches/inches (mm/mm). LSC3, LSC5, LSC8, and LSC10 had SGs not functioning properly and recorded no strain during the three-point test.

Figure 5-41 and Figure 5-42 show the strain in the transverse reinforcing steel and surrounding cover and core concrete on Small Face 1 and Large Face 1 above the center support. Small Face 1 is on the side of the specimen and Large Face 1 is on the bottom, in compression during the three-point test.

Overall, the figures show that the longitudinal tension reinforcement throughout the splice region has yielded and that the analytical model reasonably correlates with the experimental behavior. However, several internal gages showed non-linear responses as early as first cracking in the concrete and proved to be unreliable in this test setup especially beyond the yield strains of steel of 0.002 inch/inch (mm/mm). Also, several gages recorded no strain which shows these gages were not working properly. They are shown here for completeness.

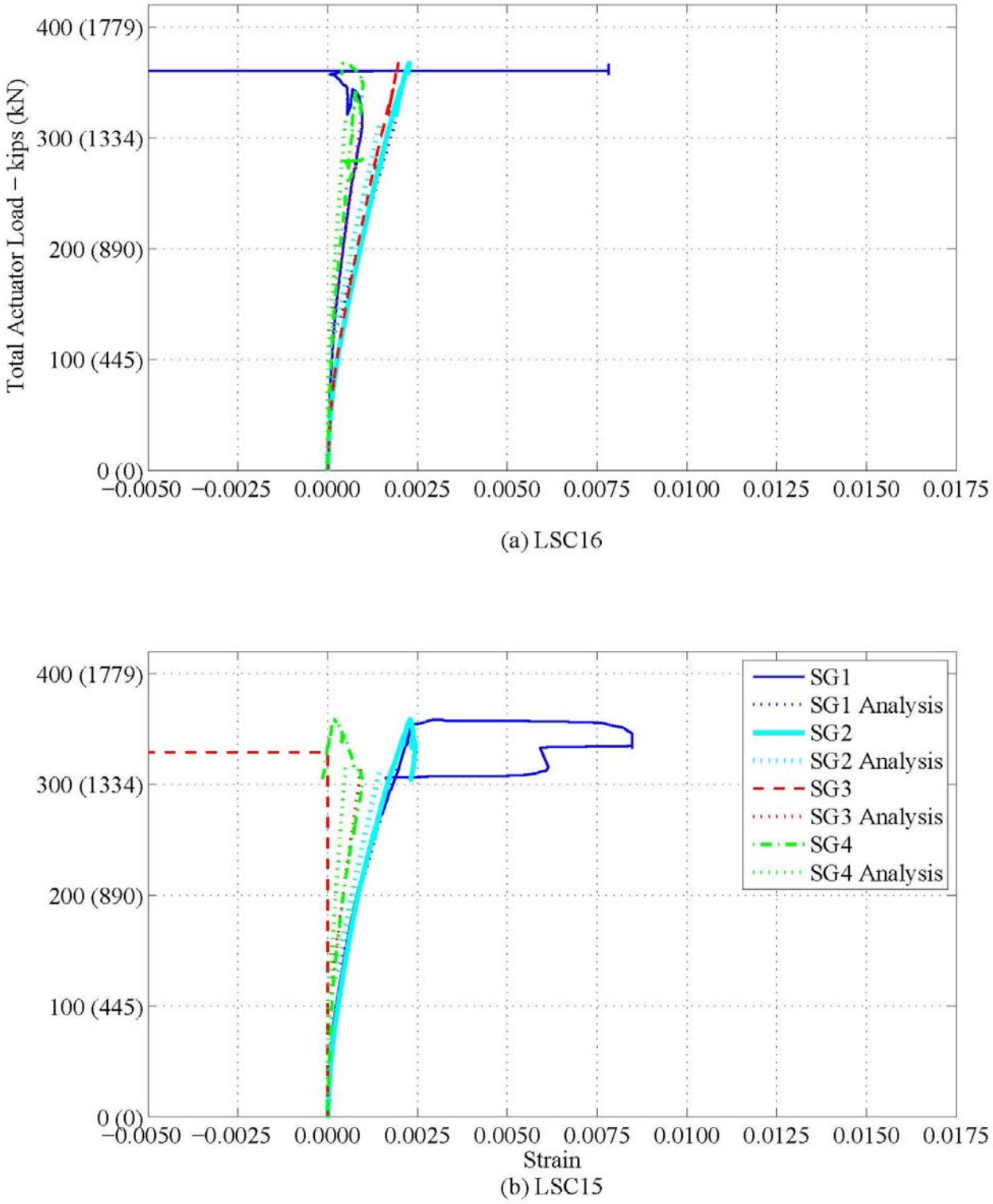

Figure 5-38. Experimental and Analytical Load vs. Strain during the Three-Point Test: Internal Strain Gages (SG1–SG4) along the Tension Steel of the Splice Region.

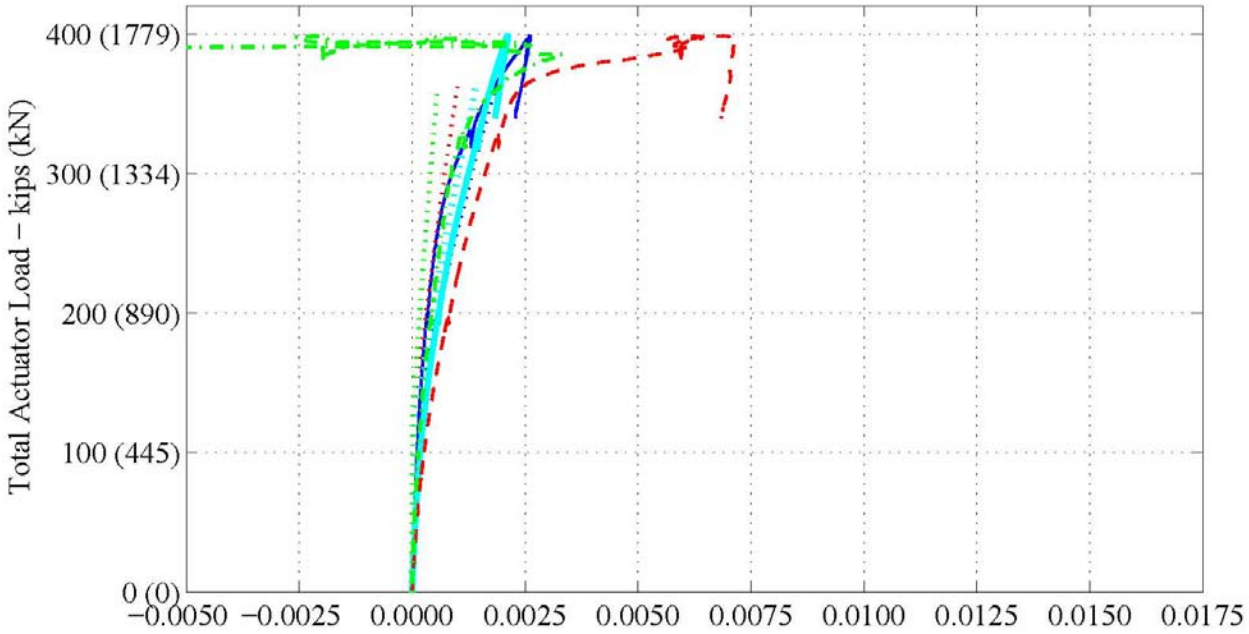

(c) LSC9

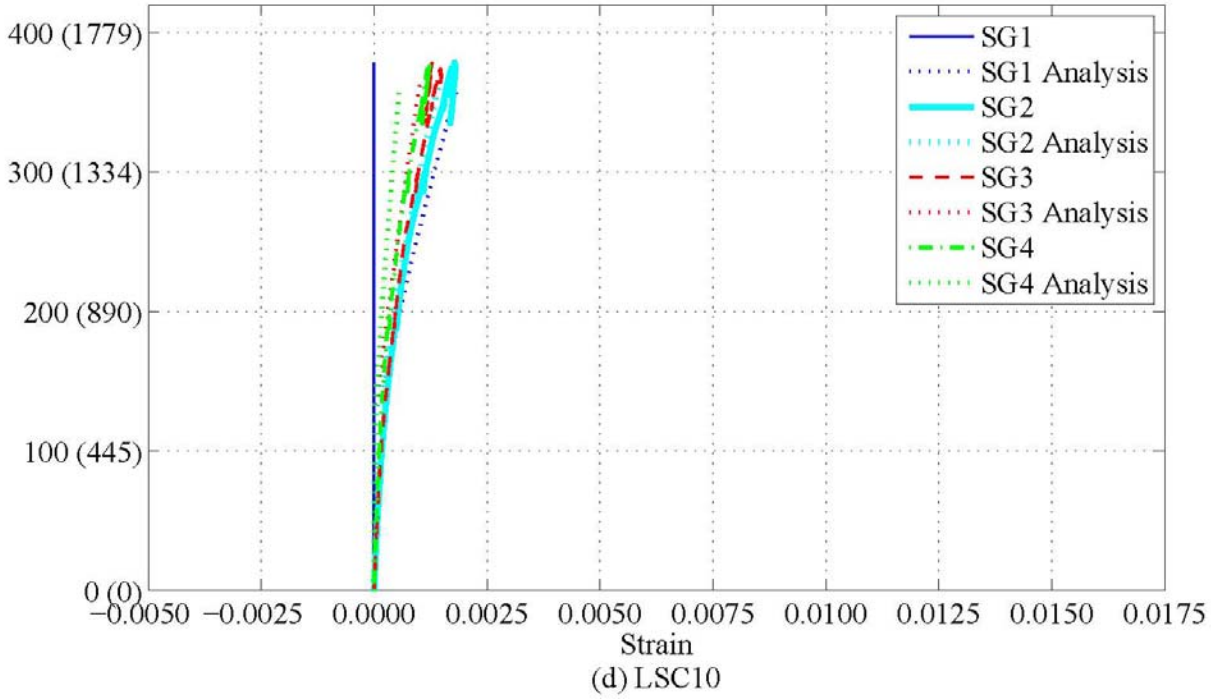

(d) LSC10

Figure 5-38. Experimental and Analytical Load vs. Strain during the Three-Point Test: Internal Strain Gages (SG1–SG4) along the Tension Steel of the Splice Region. (Continued)

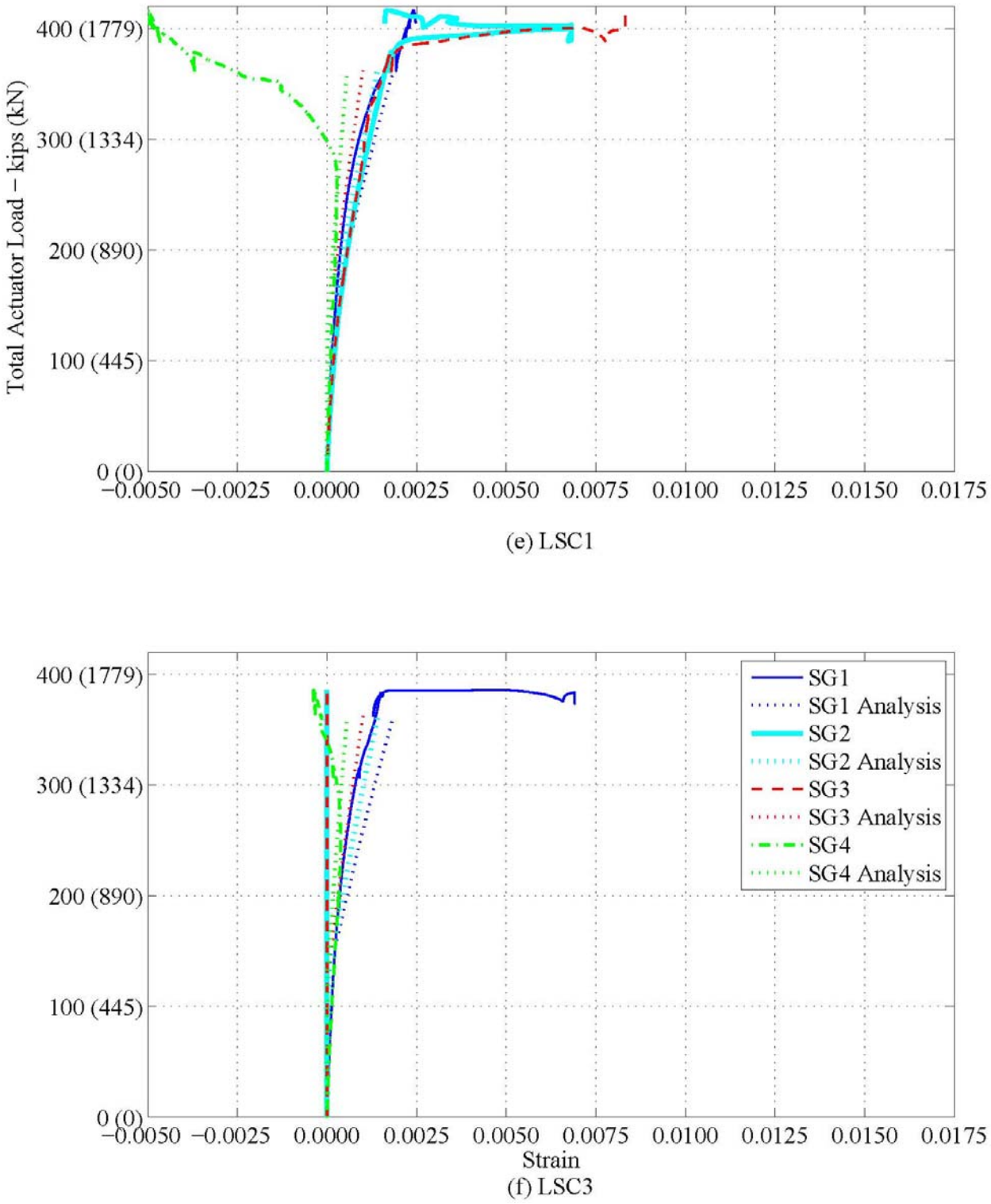

Figure 5-38. Experimental and Analytical Load vs. Strain during the Three-Point Test: Internal Strain Gages (SG1–SG4) along the Tension Steel of the Splice Region. (Continued)

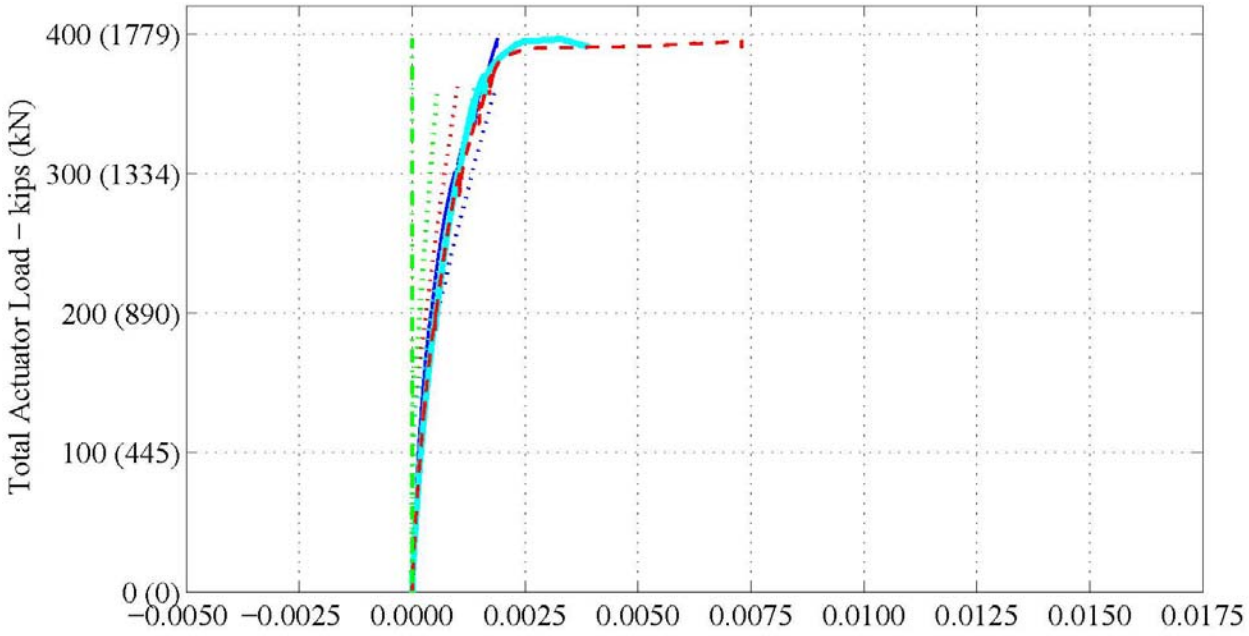

(g) LSC5

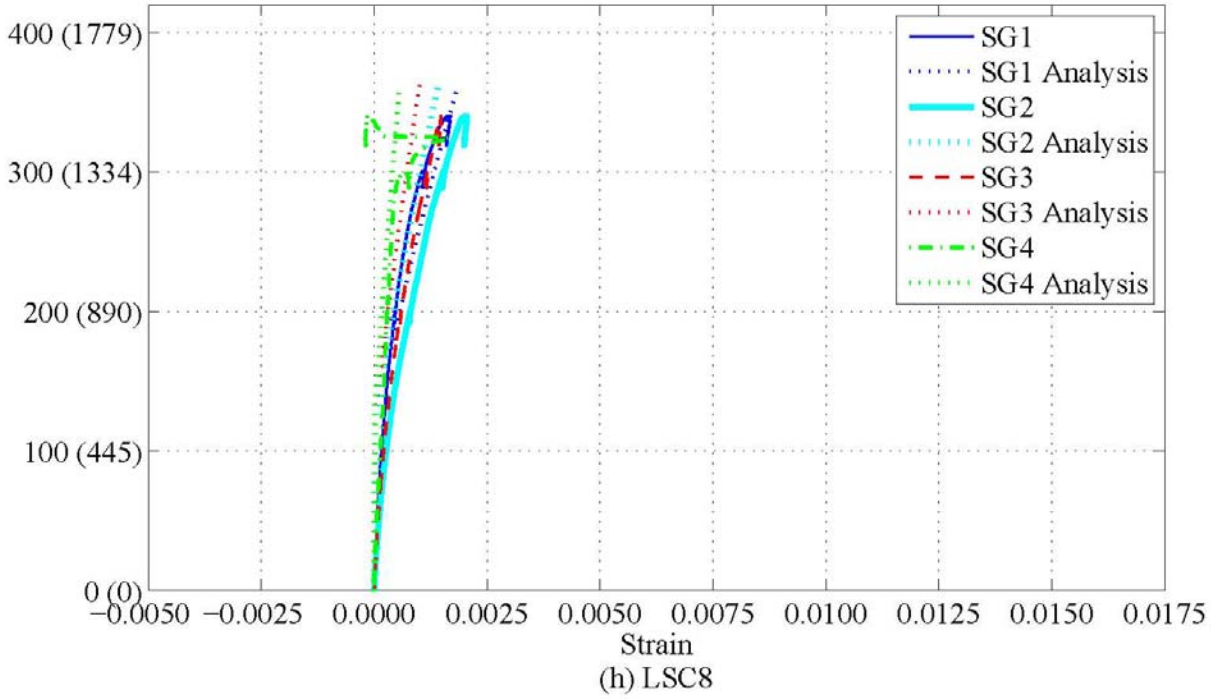

(h) LSC8

Figure 5-38. Experimental and Analytical Load vs. Strain during the Three-Point Test: Internal Strain Gages (SG1–SG4) along the Tension Steel of the Splice Region. (Continued)

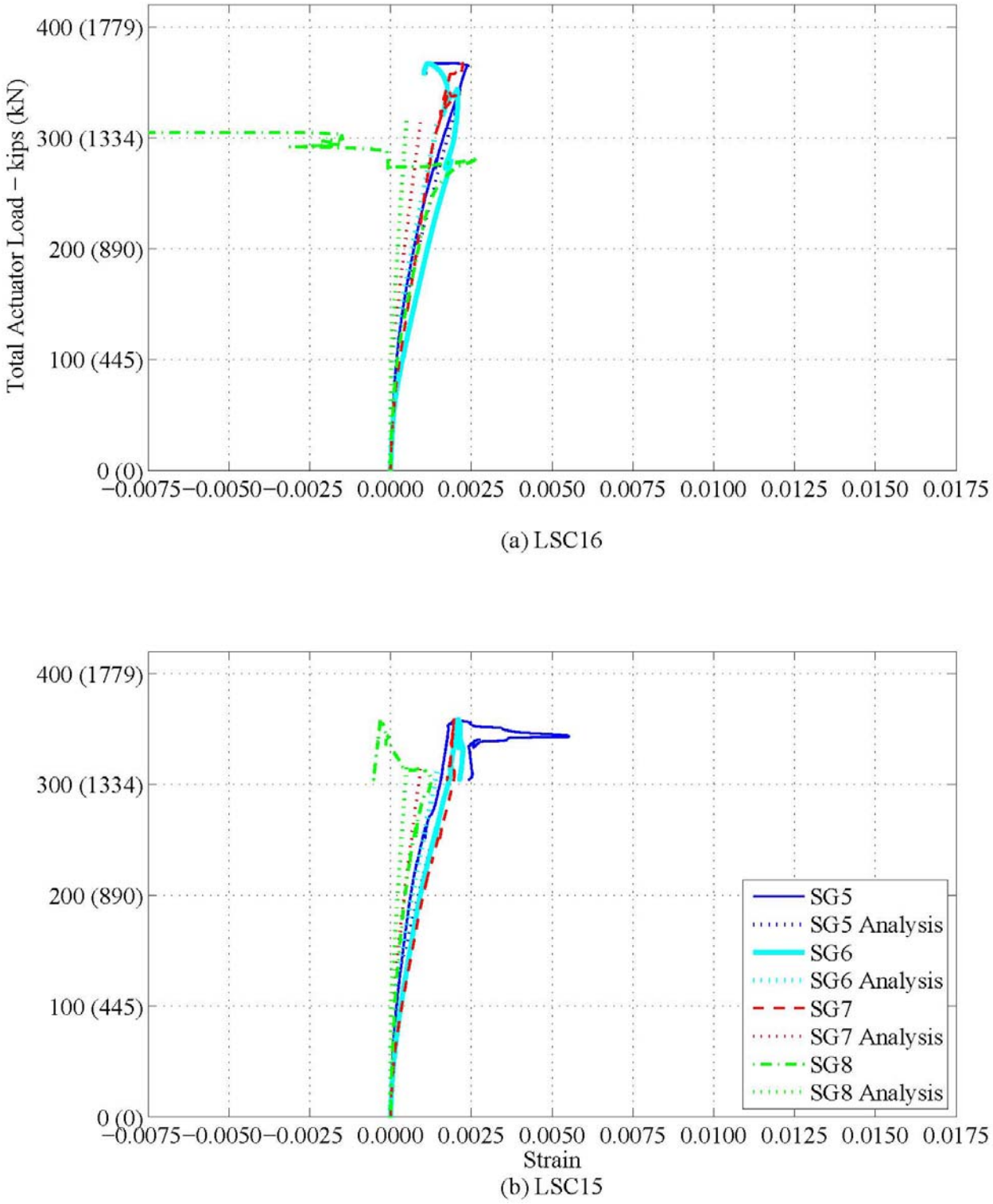

Figure 5-39. Experimental and Analytical Load vs. Strain during the Three-Point Test: Internal Strain Gages (SG5–SG8) along the Tension Steel of the Splice Region.

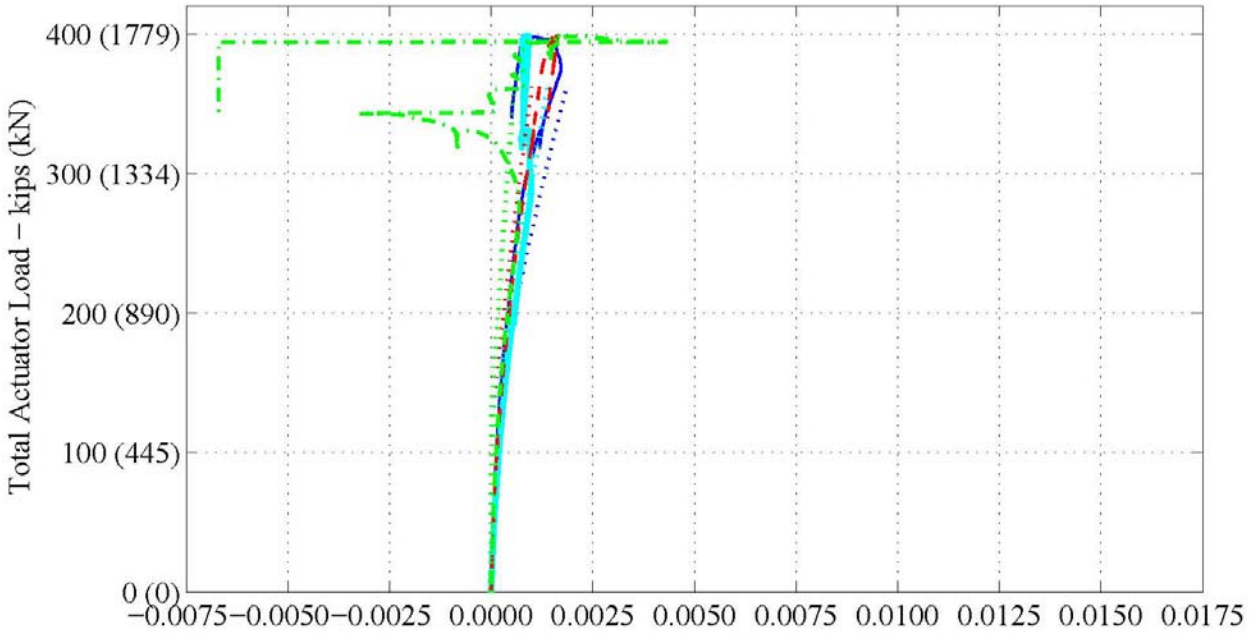

(c) LSC9

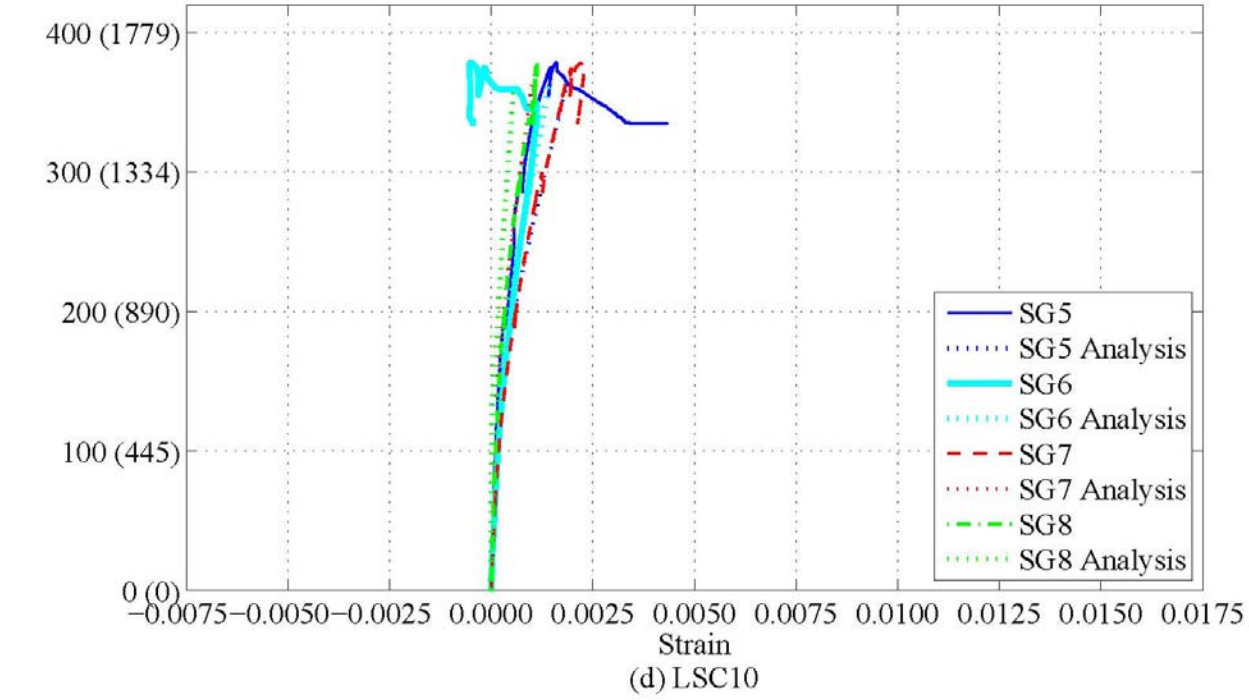

(d) LSC10

Figure 5-39. Experimental and Analytical Load vs. Strain during the Three-Point Test: Internal Strain Gages (SG5–SG8) along the Tension Steel of the Splice Region. (Continued)

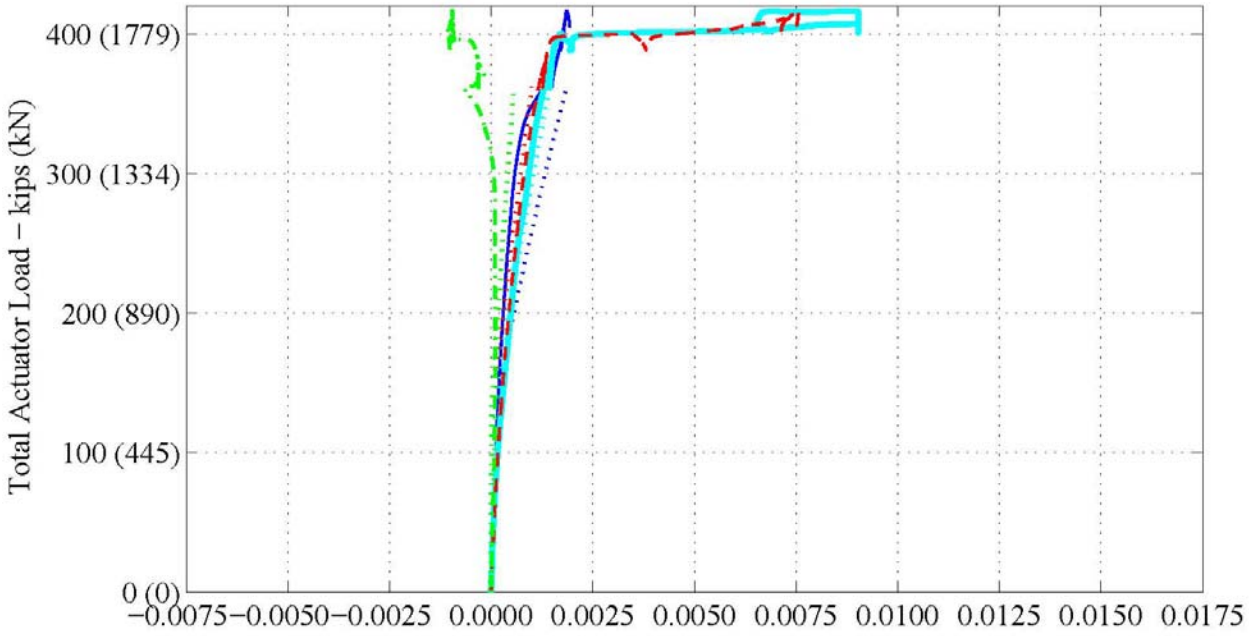

(e) LSC1

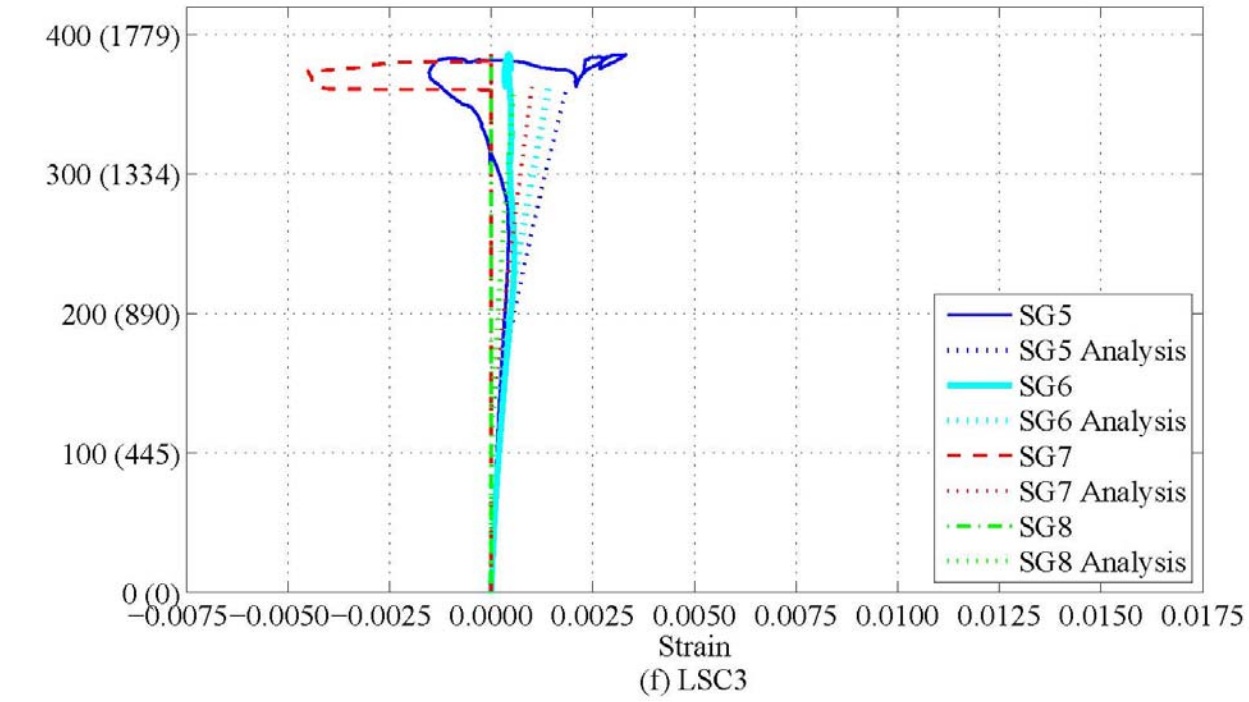

(f) LSC3

Figure 5-39. Experimental and Analytical Load vs. Strain during the Three-Point Test: Internal Strain Gages (SG5–SG8) along the Tension Steel of the Splice Region. (Continued)

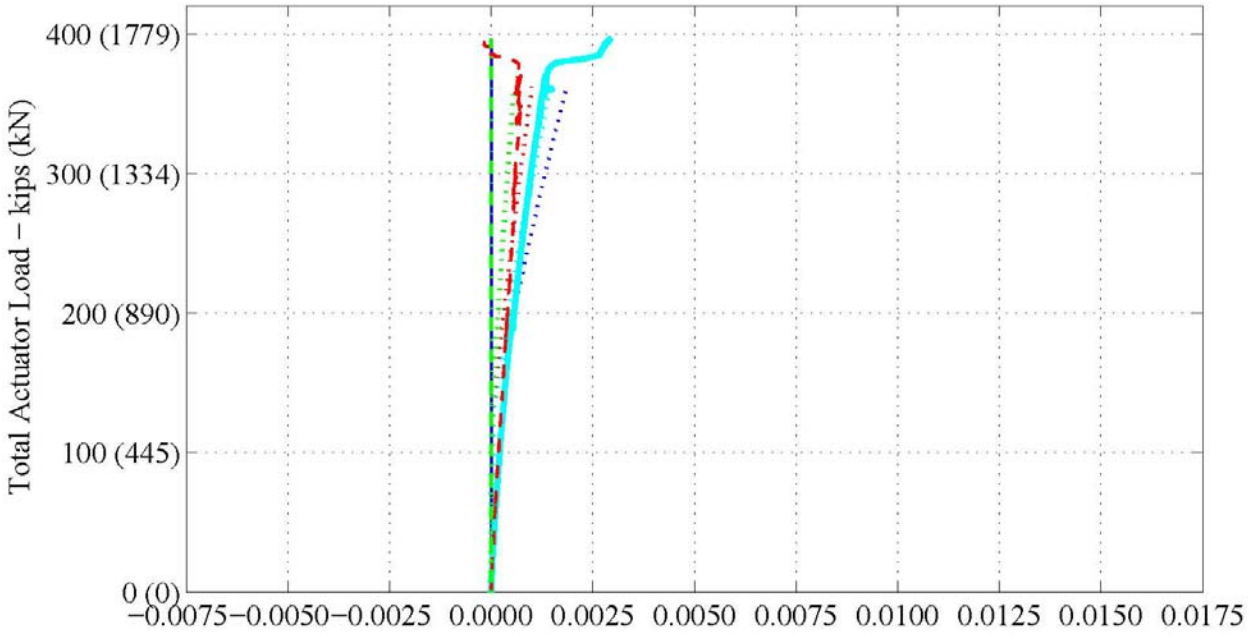

(g) LSC5

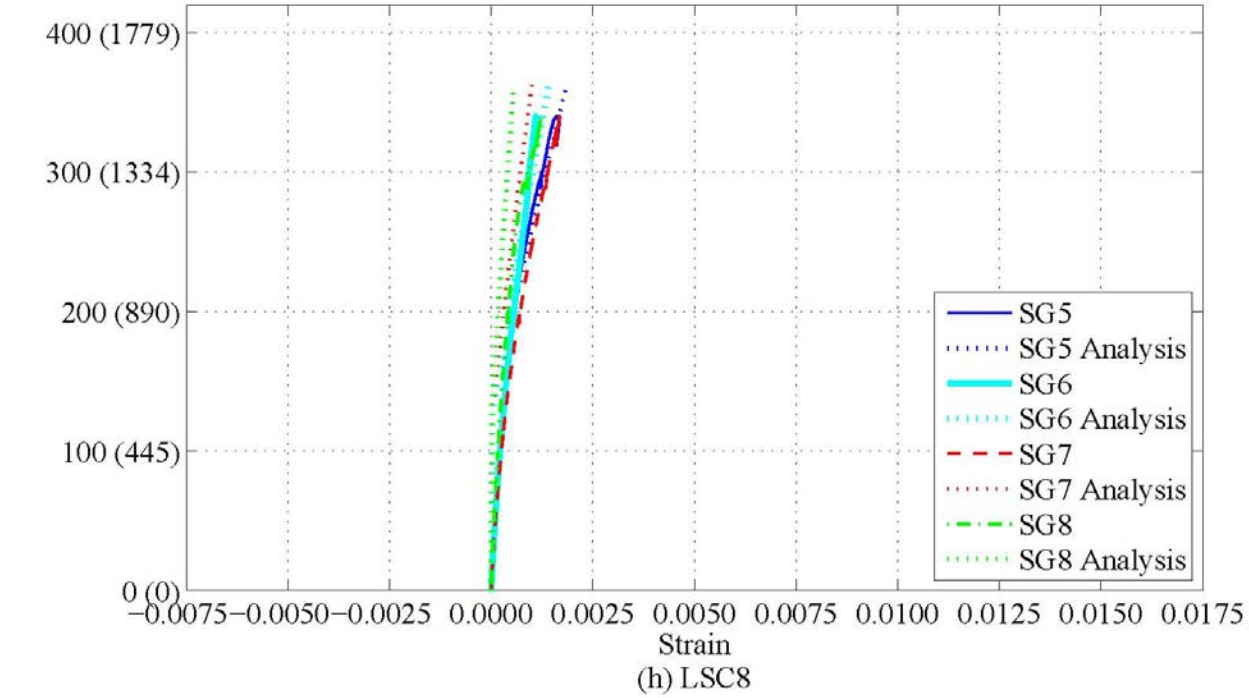

(h) LSC8

Figure 5-39. Experimental and Analytical Load vs. Strain during the Three-Point Test: Internal Strain Gages (SG5–SG8) along the Tension Steel of the Splice Region. (Continued)

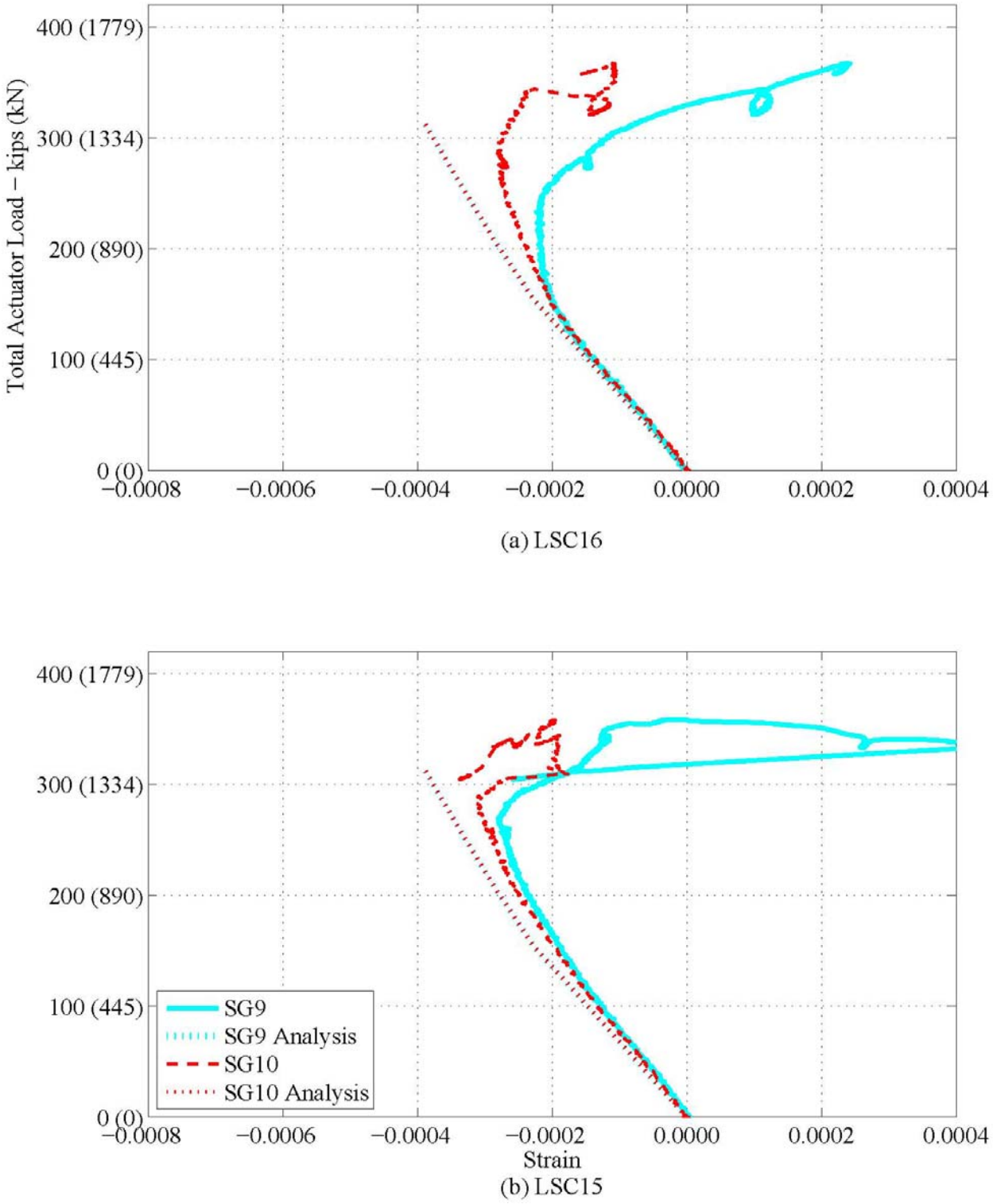

Figure 5-40. Experimental and Analytical Load. vs. Strain during the Three-Point Test: Internal Strain Gages (SG9–SG10) along the Compression Steel of the Splice Region.

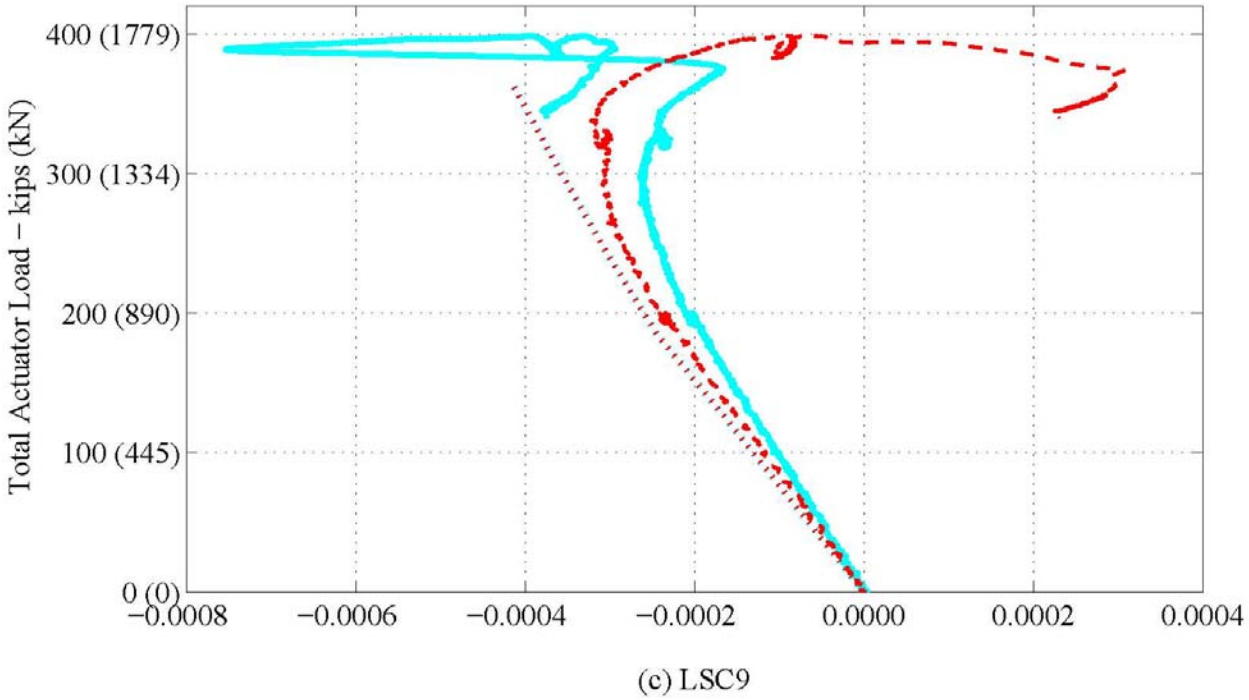

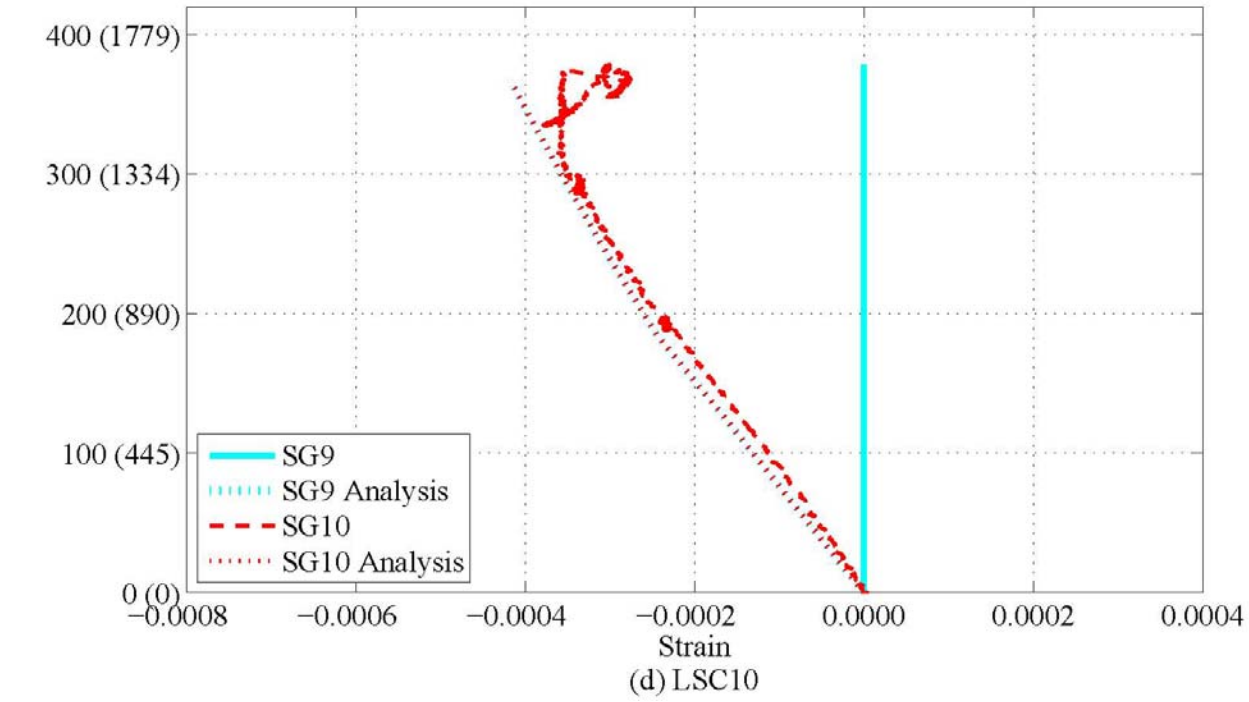

Figure 5-40. Experimental and Analytical Load. vs. Strain during the Three-Point Test: Internal Strain Gages (SG9–SG10) along the Compression Steel of the Splice Region. (Continued)

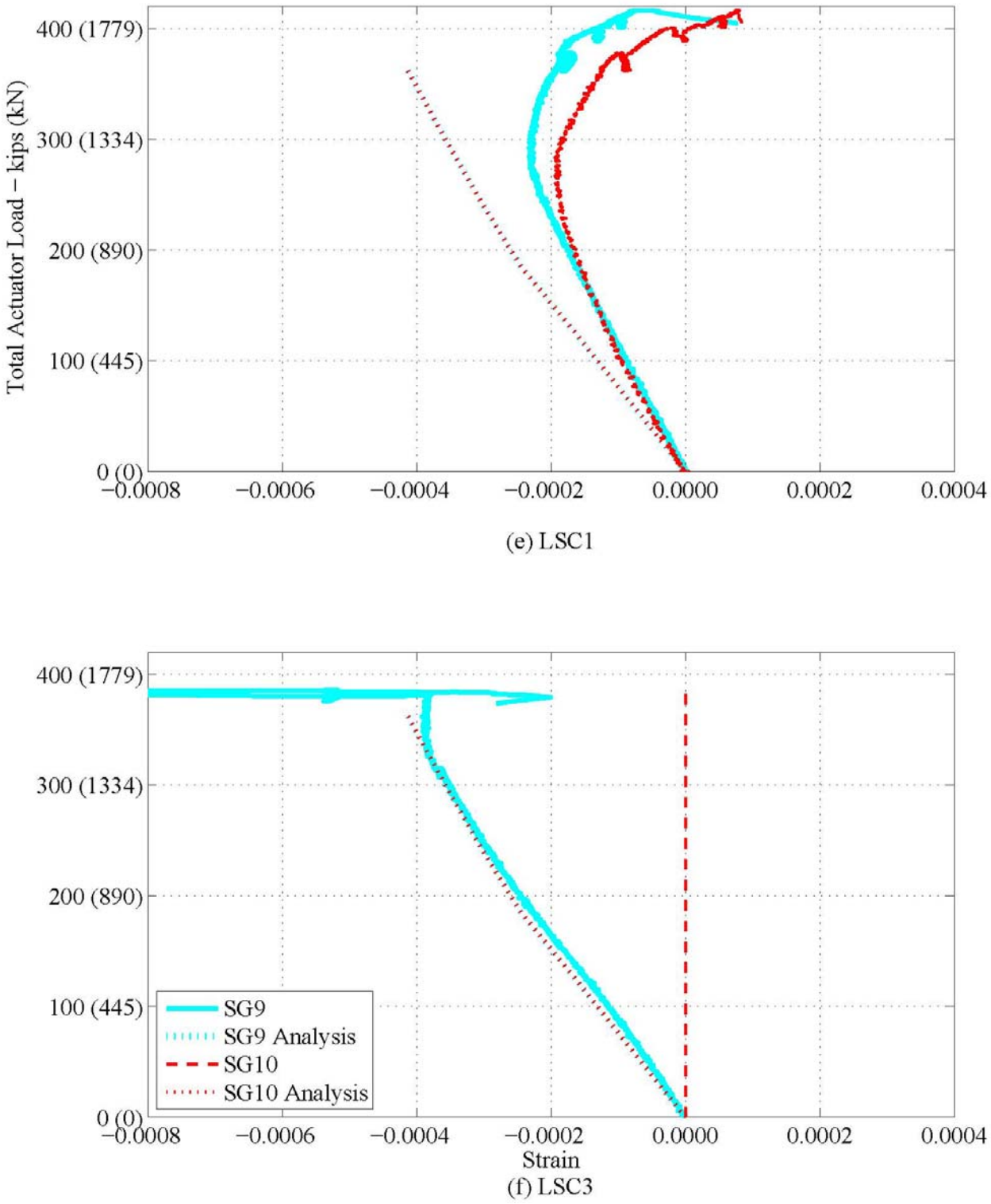

Figure 5-40. Experimental and Analytical Load. vs. Strain during the Three-Point Test: Internal Strain Gages (SG9–SG10) along the Compression Steel of the Splice Region. (Continued)

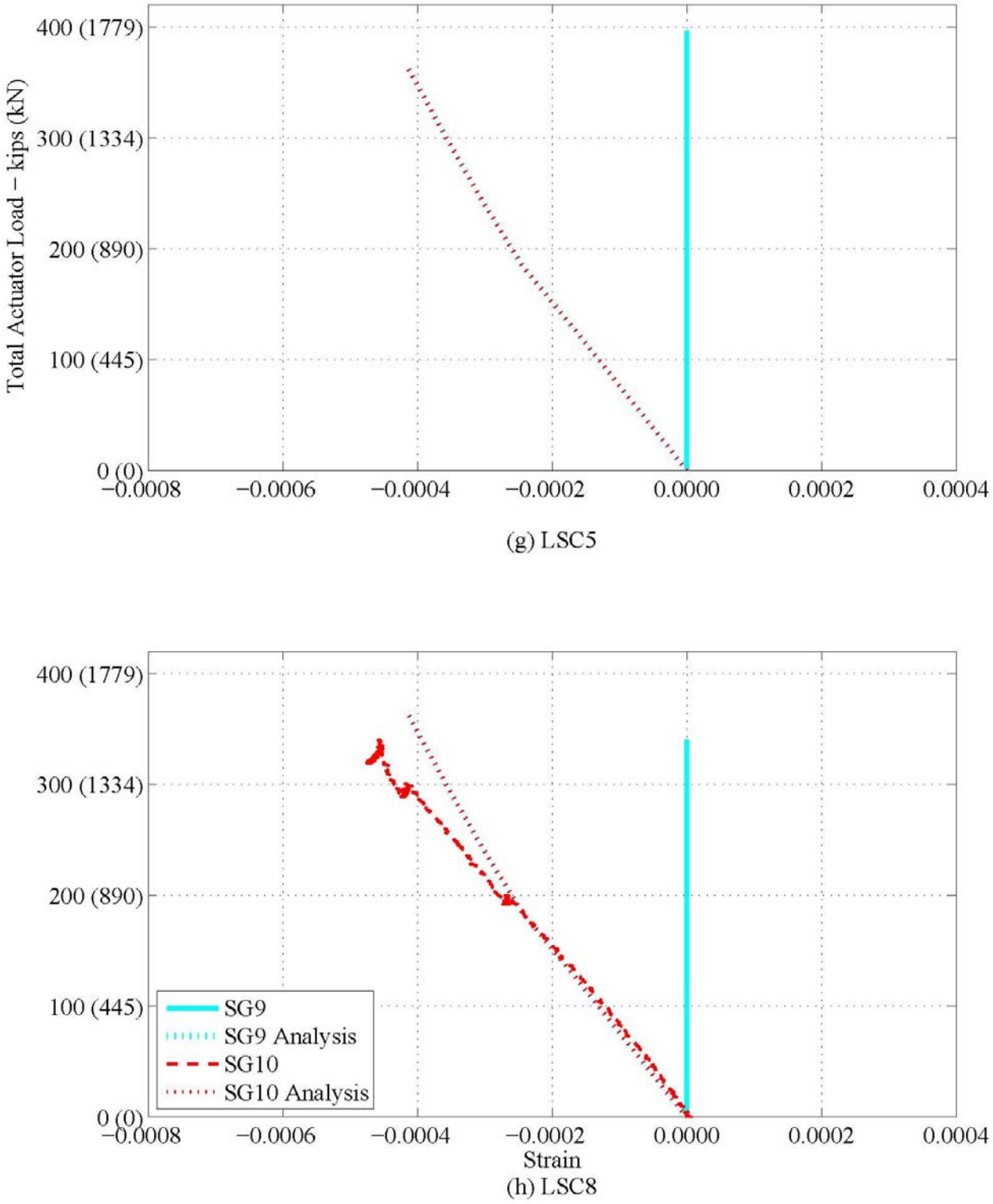

Figure 5-40. Experimental and Analytical Load. vs. Strain during the Three-Point Test: Internal Strain Gages (SG9–SG10) along the Compression Steel of the Splice Region. (Continued)

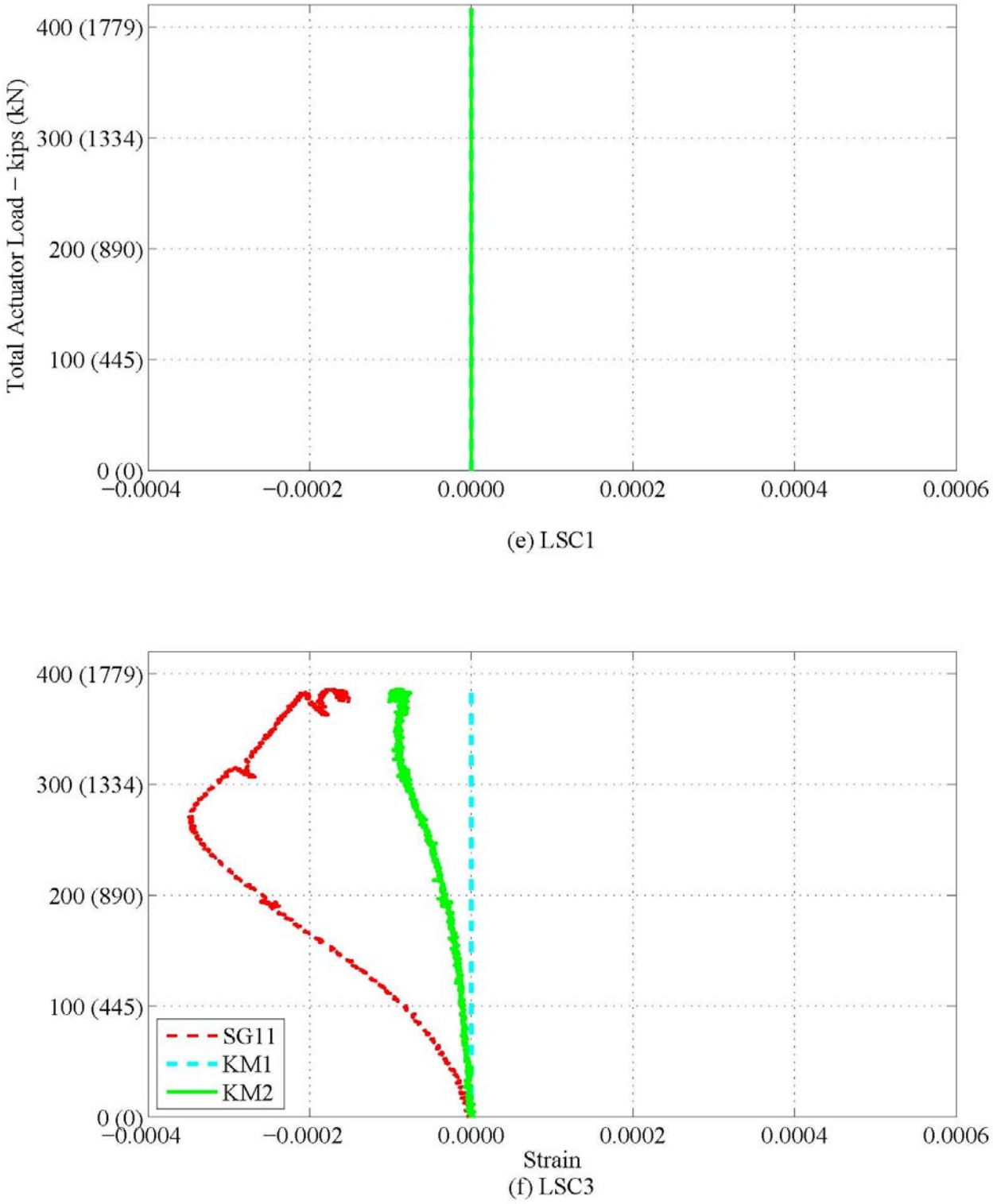

Figure 5-41. Experimental Load vs. Strain during the Three-Point Test: Internal Strain Gages (SG11, KM1–KM2) on Small Face 1 above the Center Support.

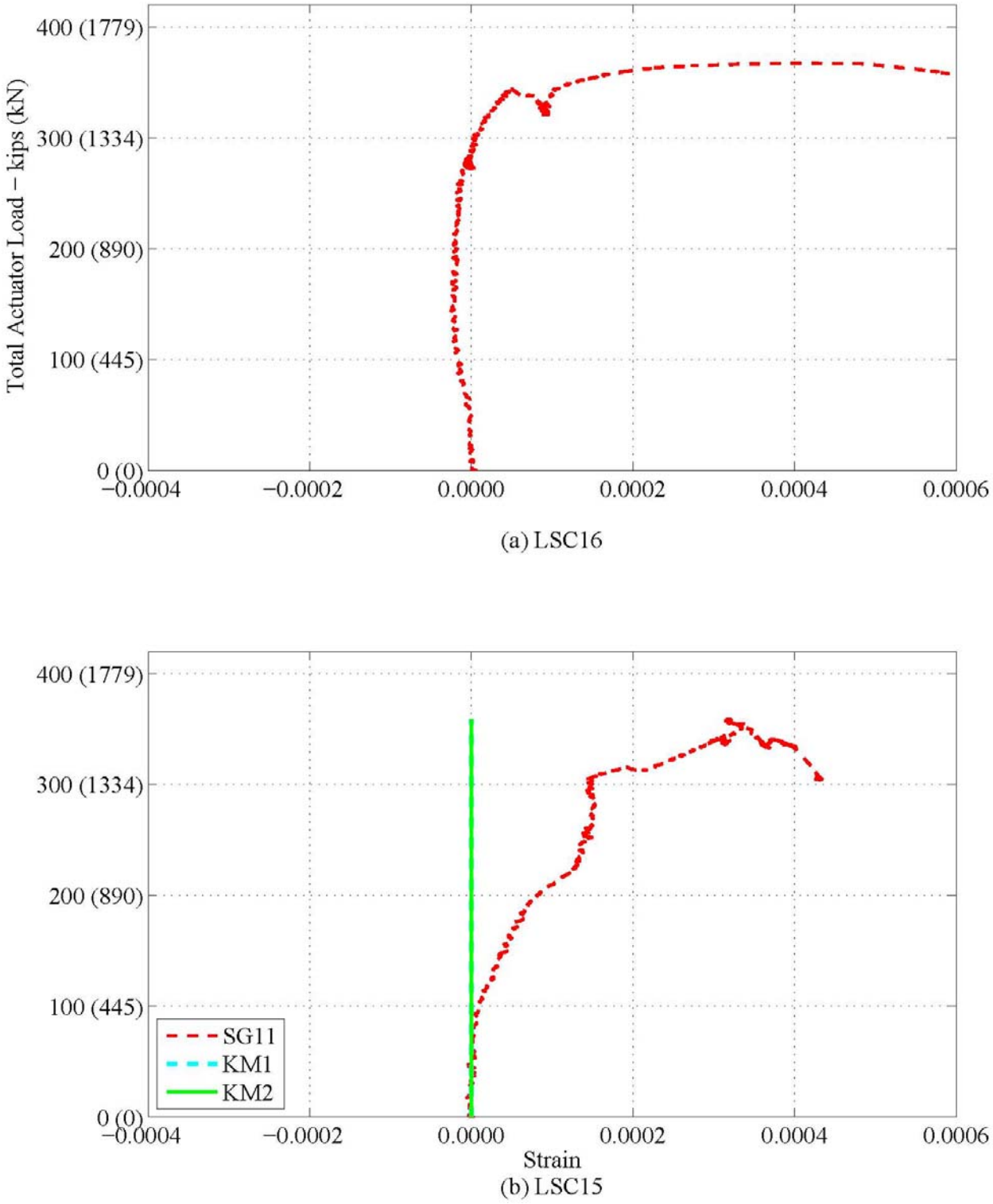

Figure 5-41. Experimental Load vs. Strain during the Three-Point Test: Internal Strain Gages (SG11, KM1–KM2) on Small Face 1 above the Center Support. (Continued)

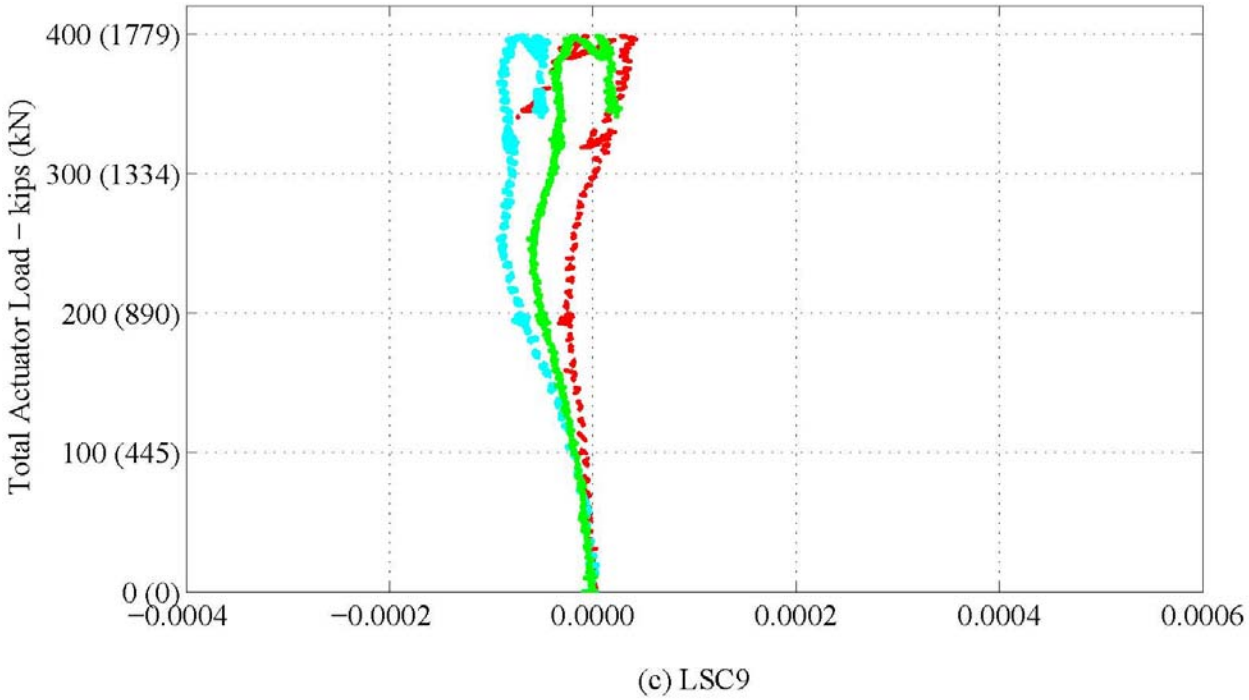

(c) LSC9

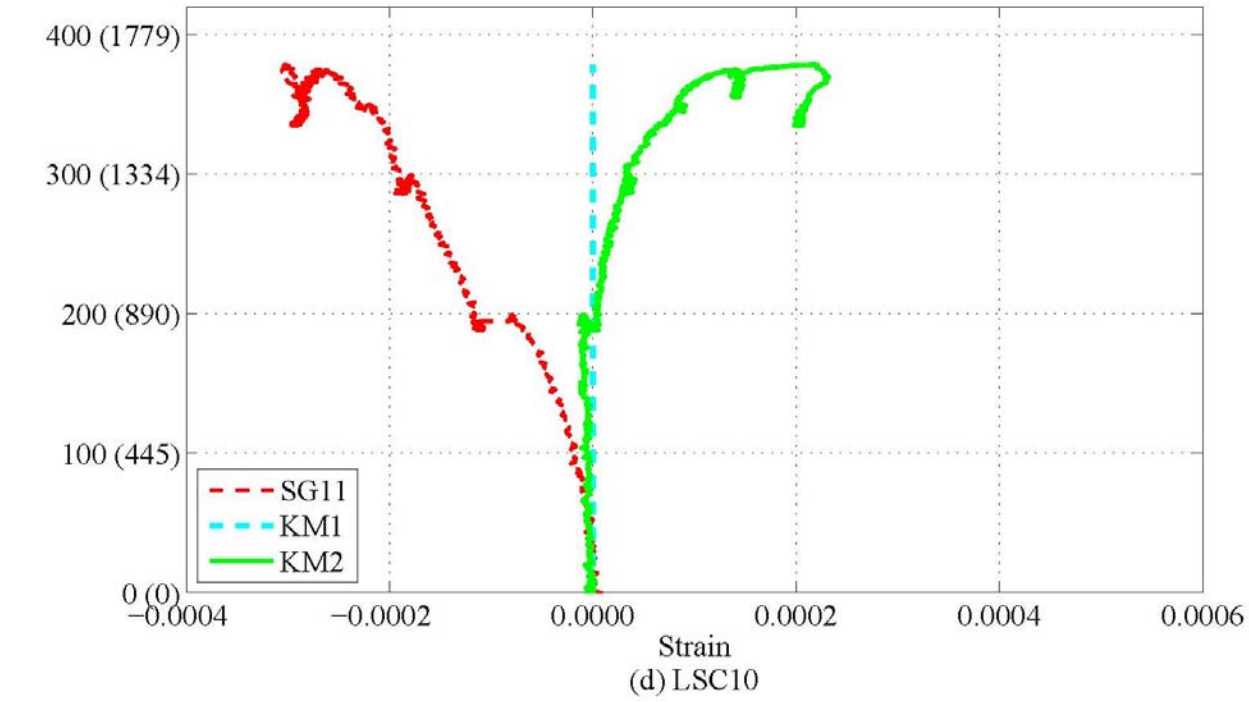

(d) LSC10

Figure 5-41. Experimental Load vs. Strain during the Three-Point Test: Internal Strain Gages (SG11, KM1–KM2) on Small Face 1 above the Center Support. (Continued)

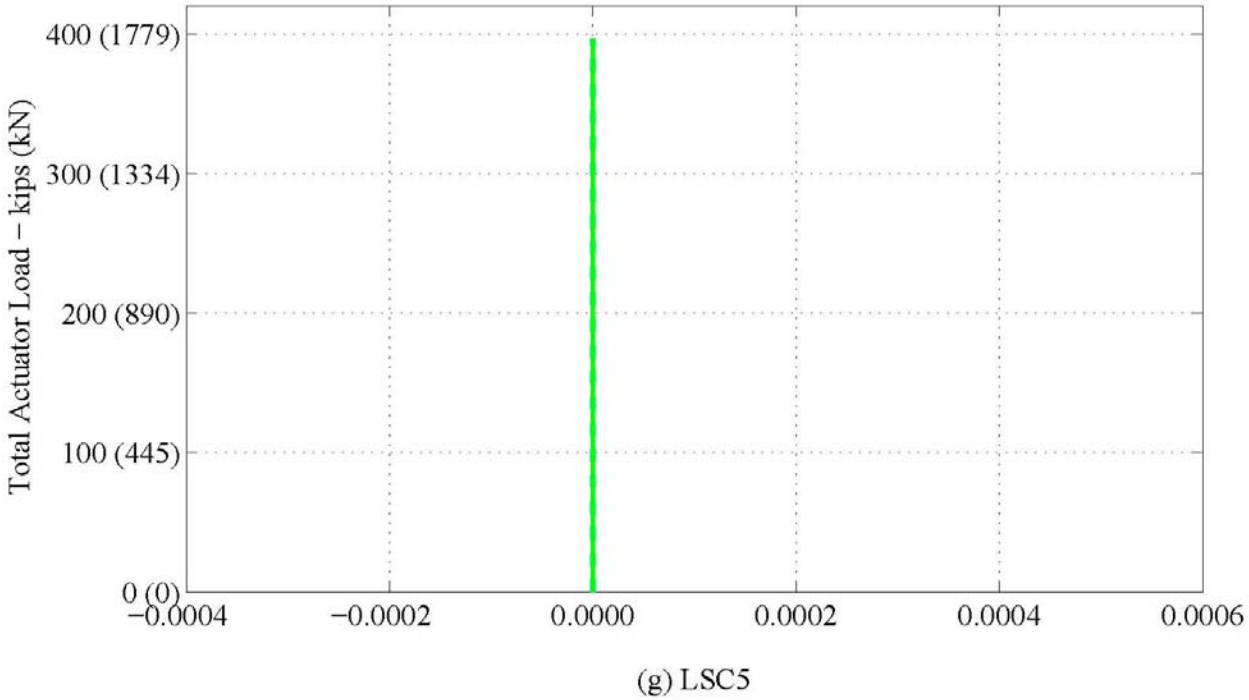

(g) LSC5

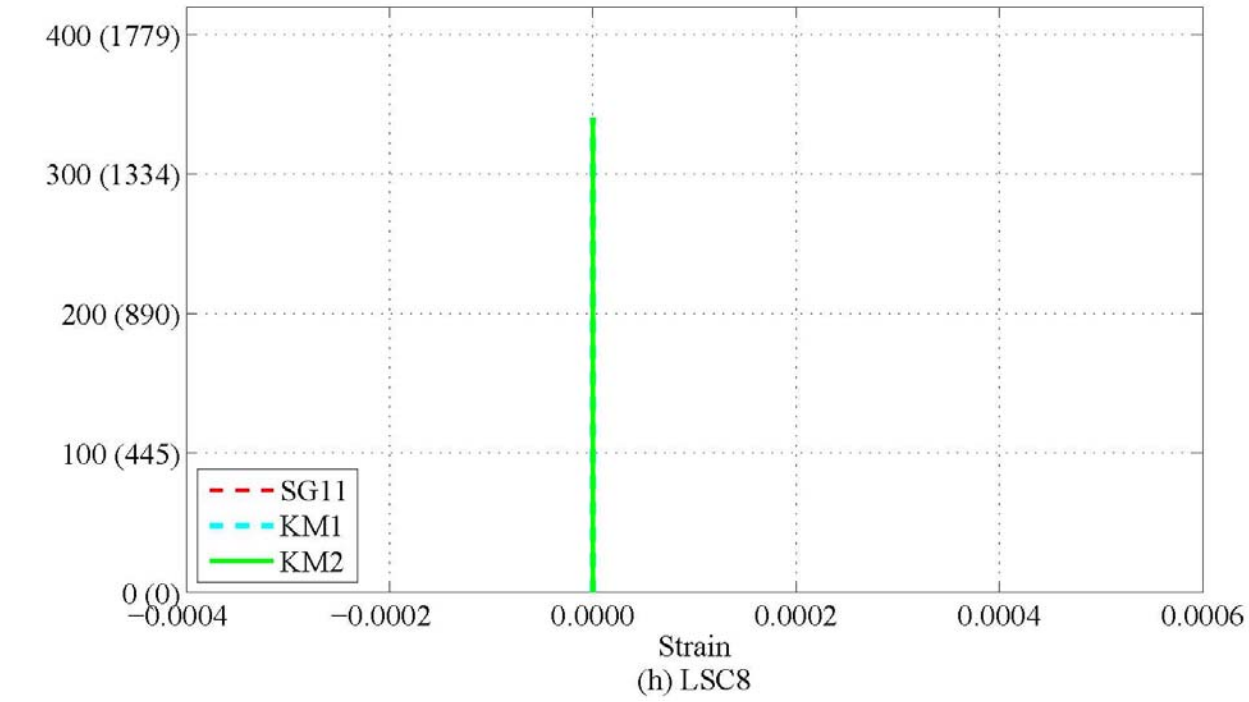

(h) LSC8

Figure 5-41. Experimental Load vs. Strain during the Three-Point Test: Internal Strain Gages (SG11, KM1–KM2) on Small Face 1 above the Center Support. (Continued)

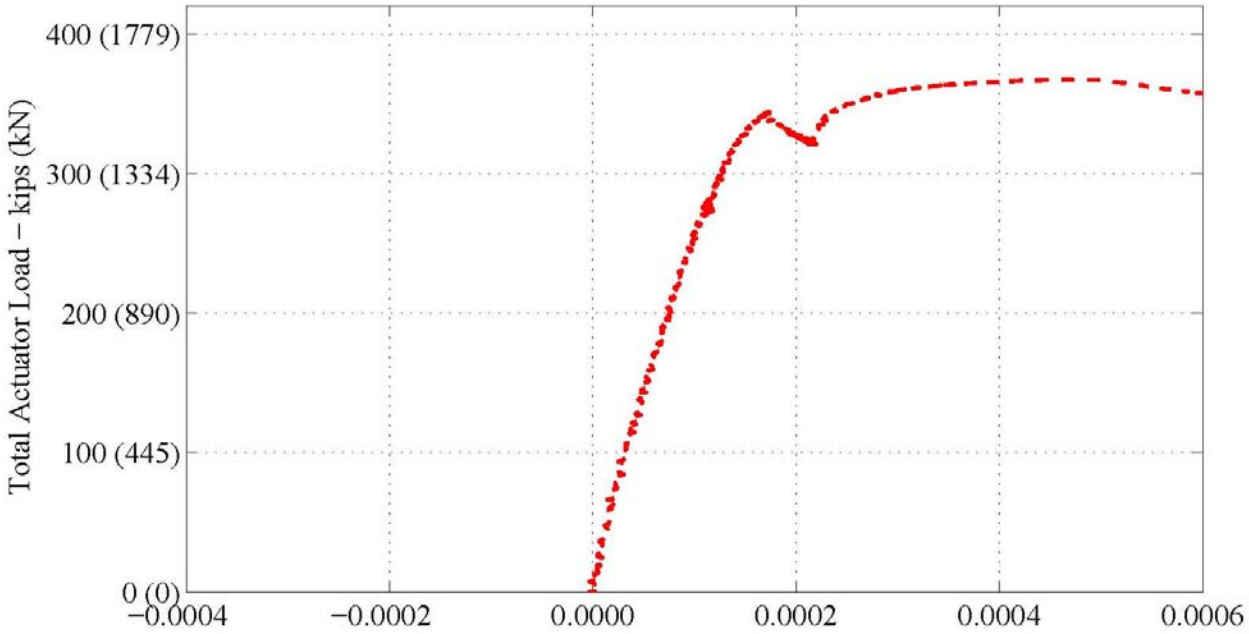

(a) LSC16

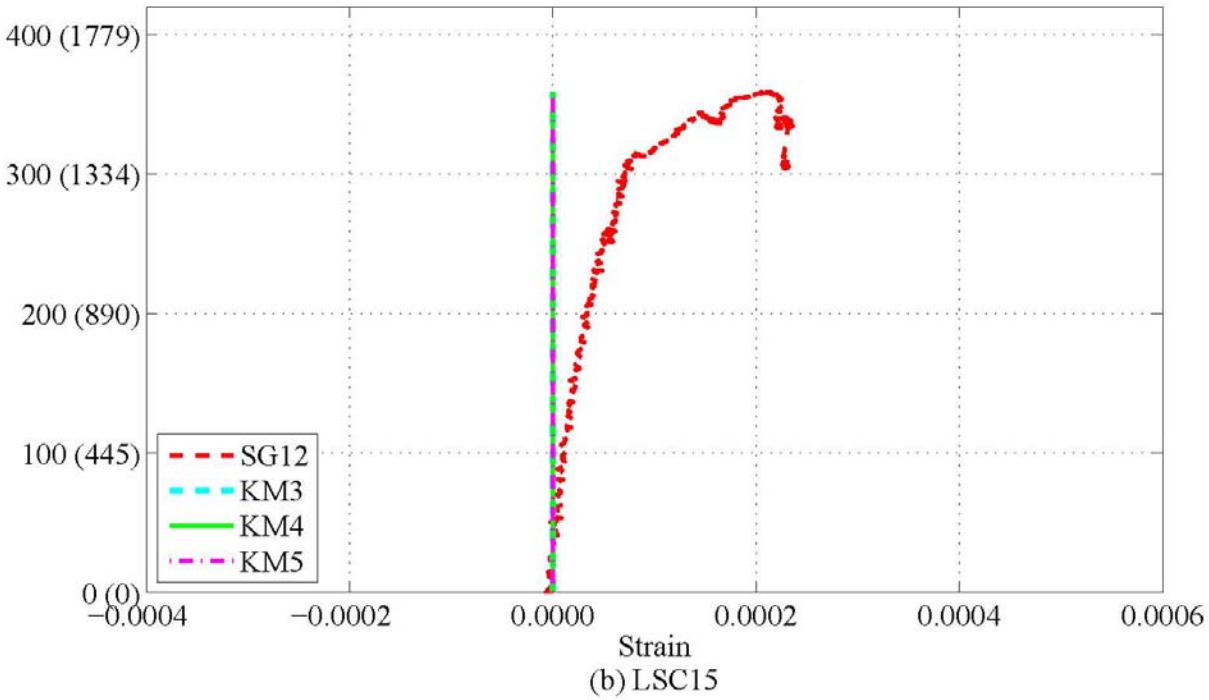

(b) LSC15

Figure 5-42. Experimental Load vs. Strain during the Three-Point Test: Internal Strain Gages (SG12, KM3–KM5) on Large Face 1 above the Center Support.

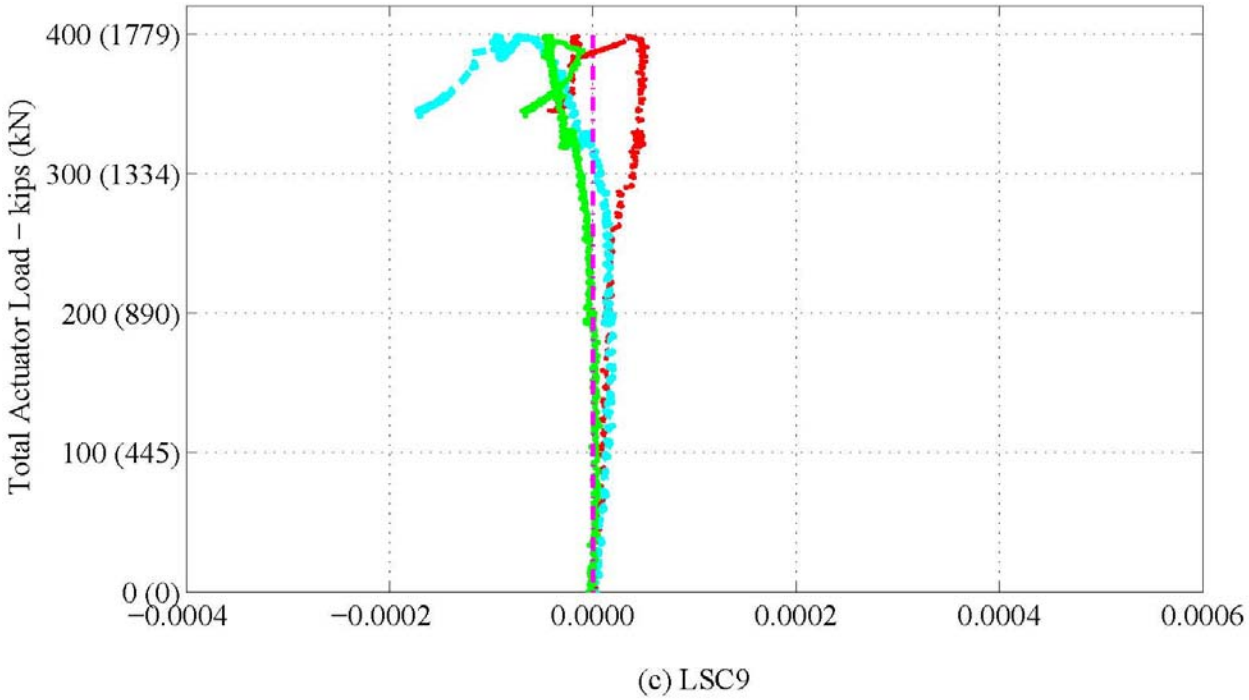

(c) LSC9

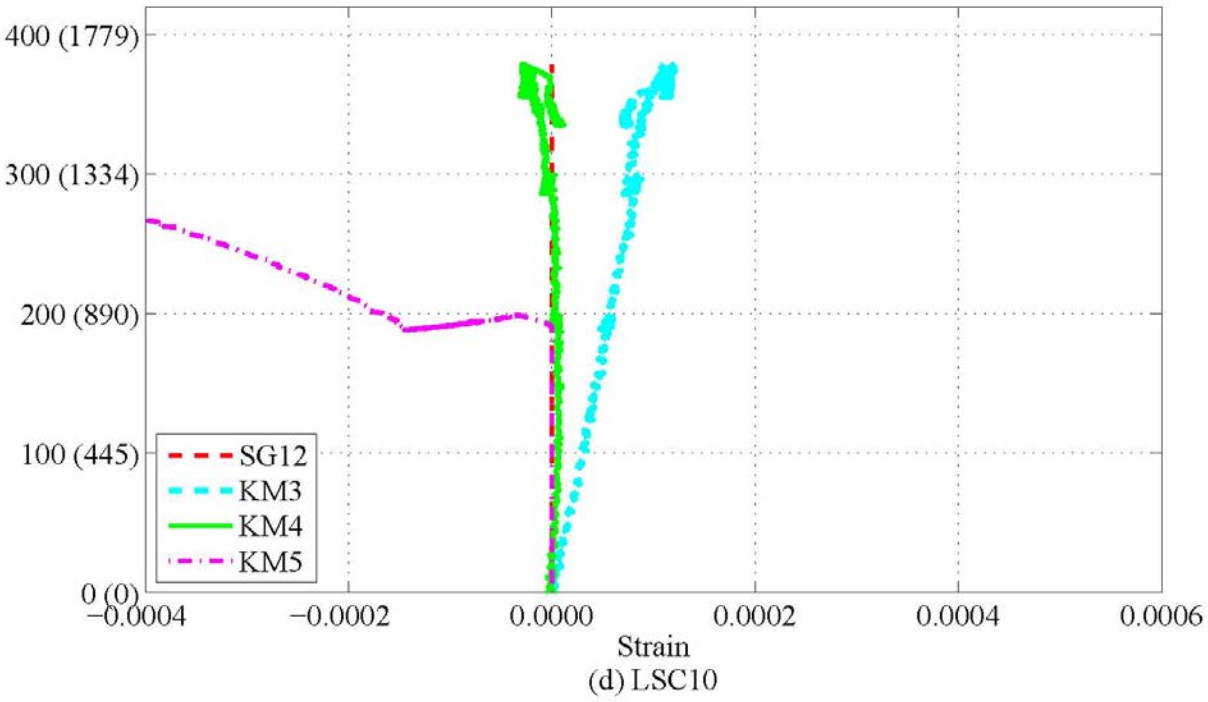

(d) LSC10

Figure 5-42. Experimental Load vs. Strain during the Three-Point Test: Internal Strain Gages (SG12, KM3–KM5) on Large Face 1 above the Center Support. (Continued)

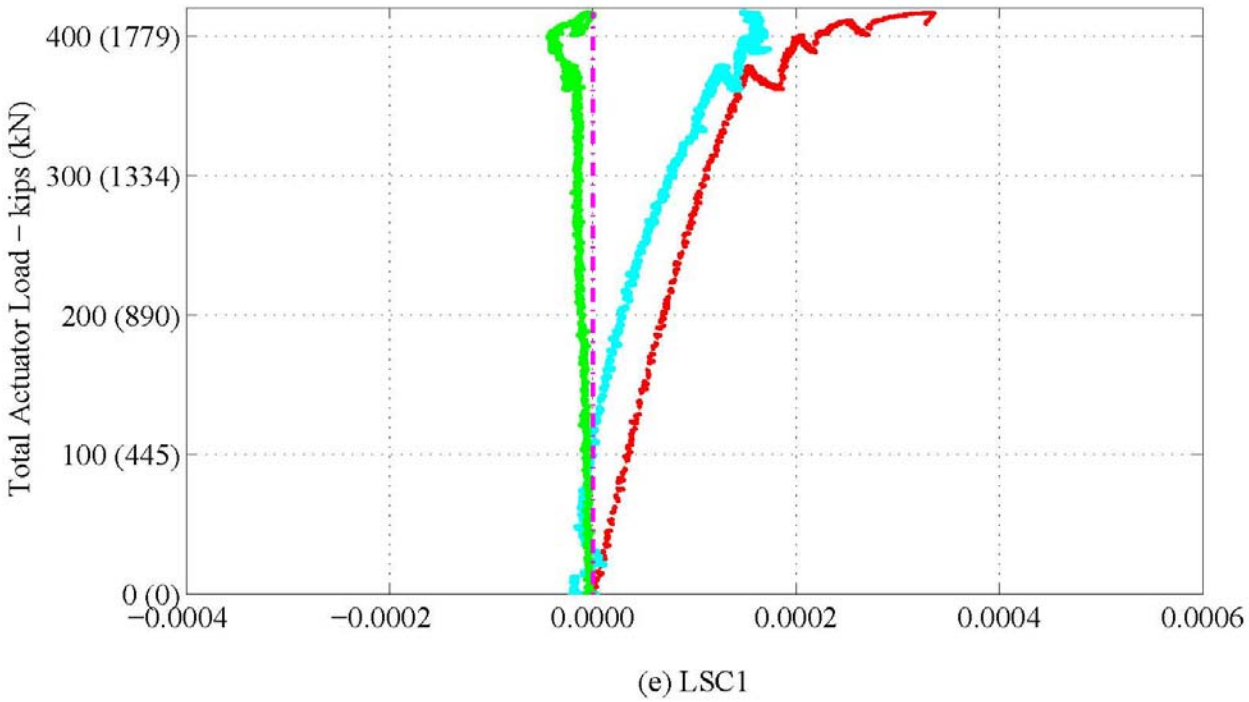

(e) LSC1

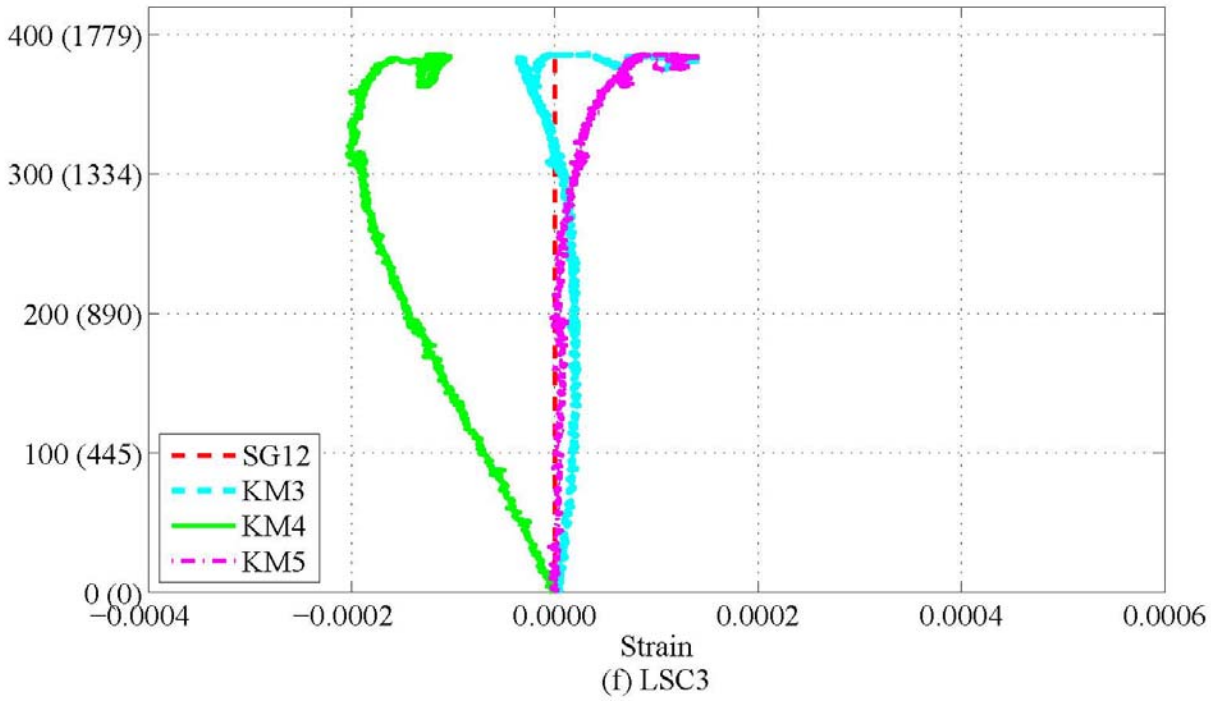

(f) LSC3

Figure 5-42. Experimental Load vs. Strain during the Three-Point Test: Internal Strain Gages (SG12, KM3–KM5) on Large Face 1 above the Center Support. (Continued)

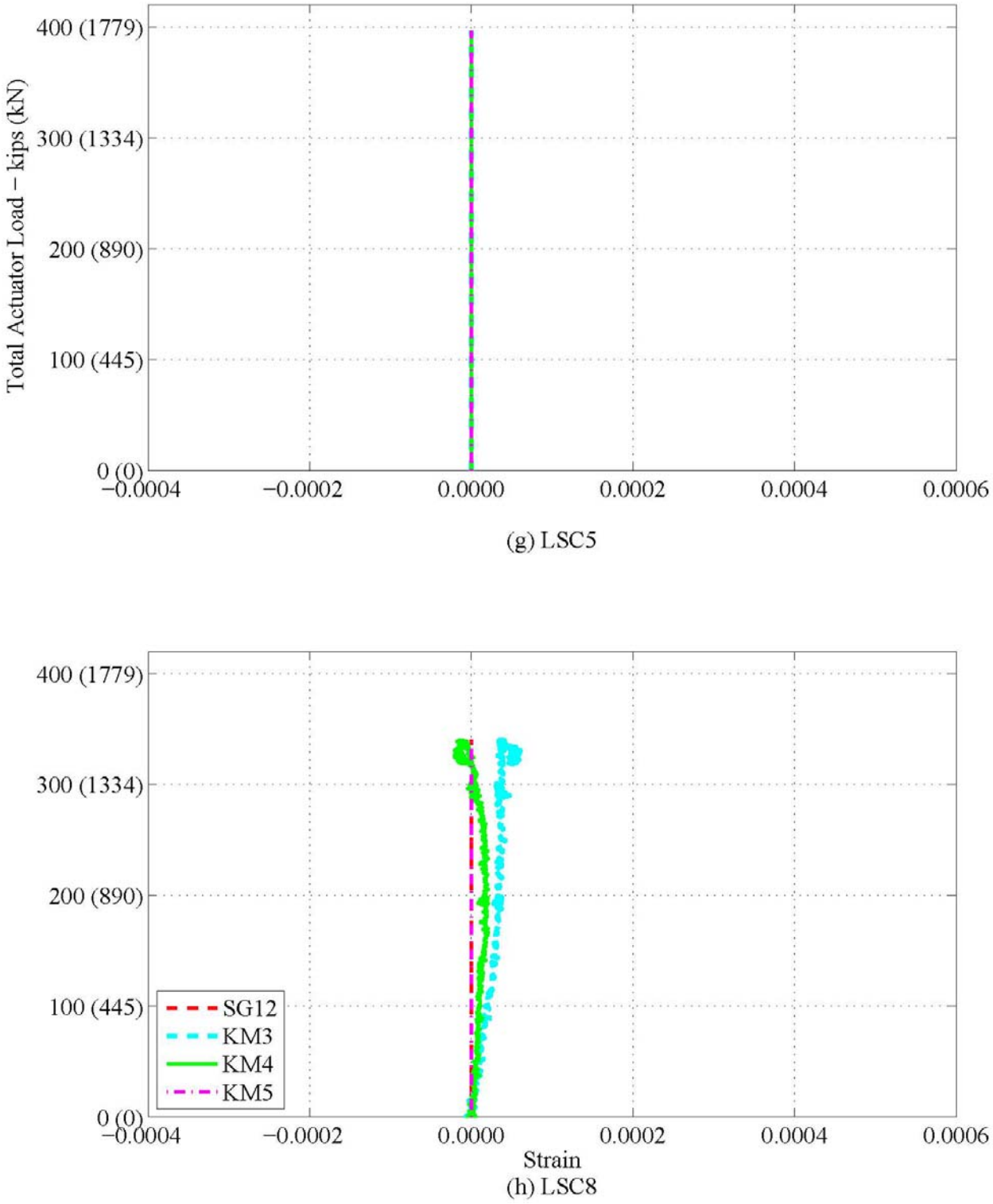

Figure 5-42. Experimental Load vs. Strain during the Three-Point Test: Internal Strain Gages (SG12, KM3–KM5) on Large Face 1 above the Center Support. (Continued)

Figure 5-43 shows a crack and LV4 above the support during the three-point test on LSC8. The flexural crack width at the maximum actuator load of 195 kips (867 kN) was approximately 0.05 inch (1.27 mm). This crack is one-fifth the width of the crack pictured in Figure 5-31 during the four-point test at near-peak loading.

Figure 5-43. Flexural Crack above the Center Support from Three-Point Test (LSC5).

Figure 5-44 shows the external strain measurements in the splice region using the LVDTs. Note that LV1 and LV8 were closest to the actuators and not under the actuator as was the case for the four-point test. Therefore, the strains from LV1 and LV8 in the three-point test were not as large as the strains from LV1 and LV7 in the four-point test. LV4 measured the critical surface strains primarily from flexural deformations directly above the support. Either, LV1 or LV8 has the largest strain or begins plastic deformation first in all specimens. It is important to note that the LV above the support that resists the maximum moment does not have the largest strains.

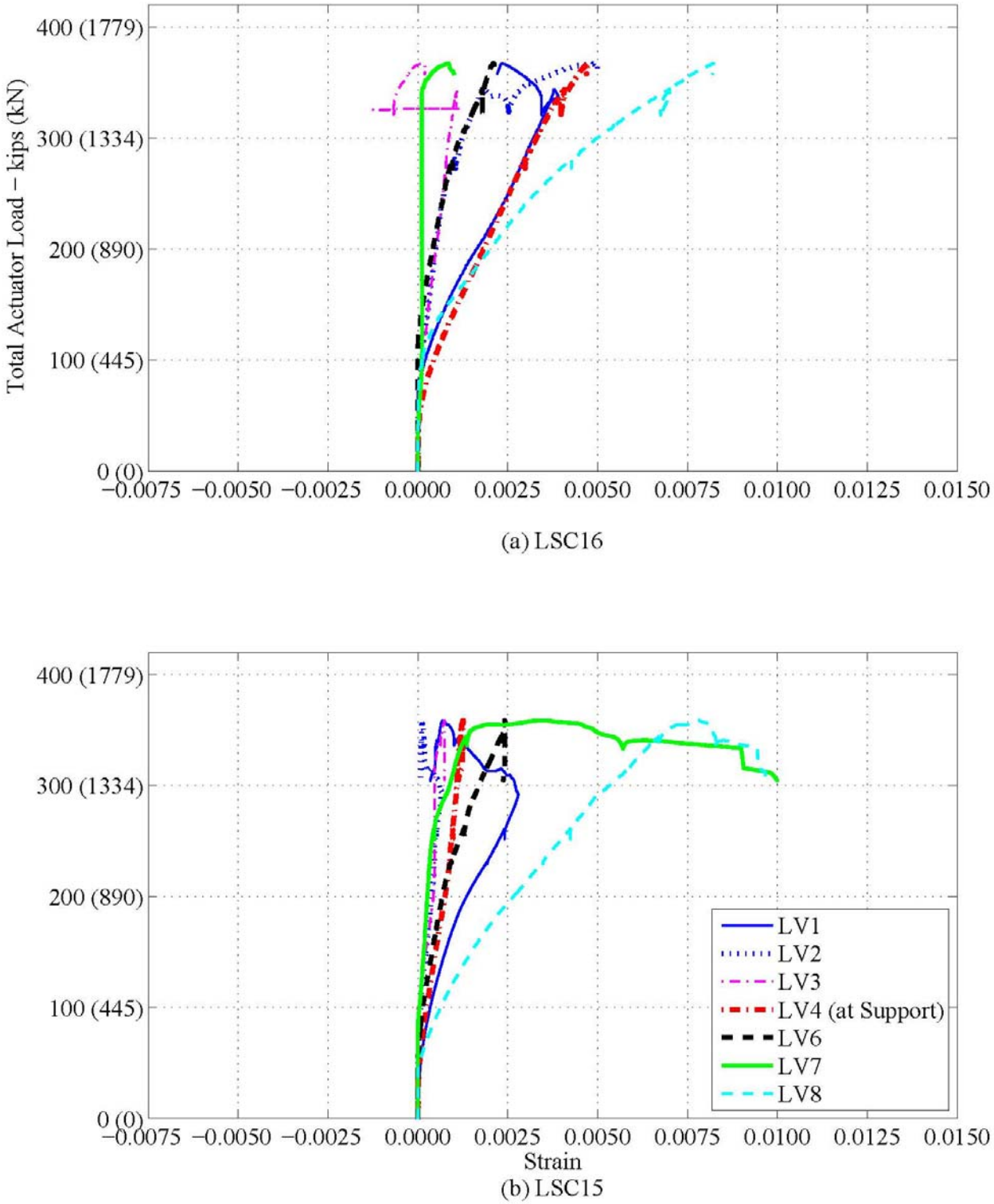

Figure 5-44. Experimental Load vs. Strain during the Three-Point Test: LVDTs along the Splice Region.

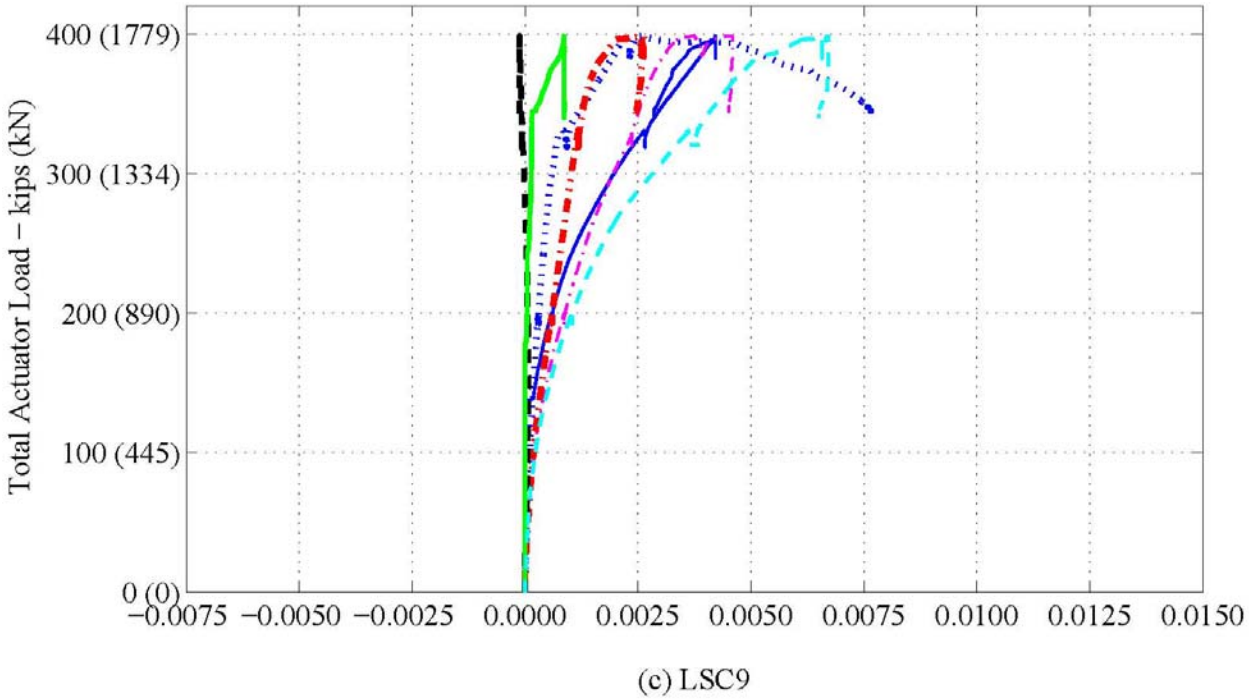

(c) LSC9

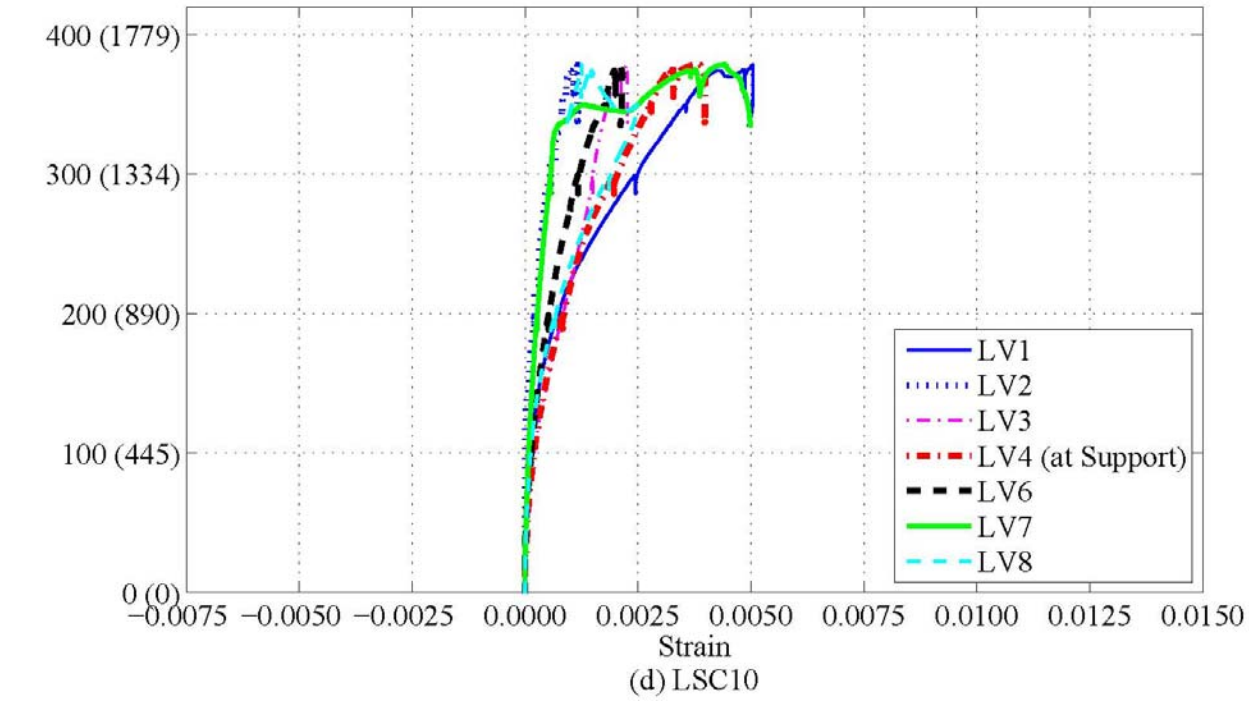

(d) LSC10

Figure 5-44. Experimental Load vs. Strain during the Three-Point Test: LVDTs along the Splice Region. (Continued)

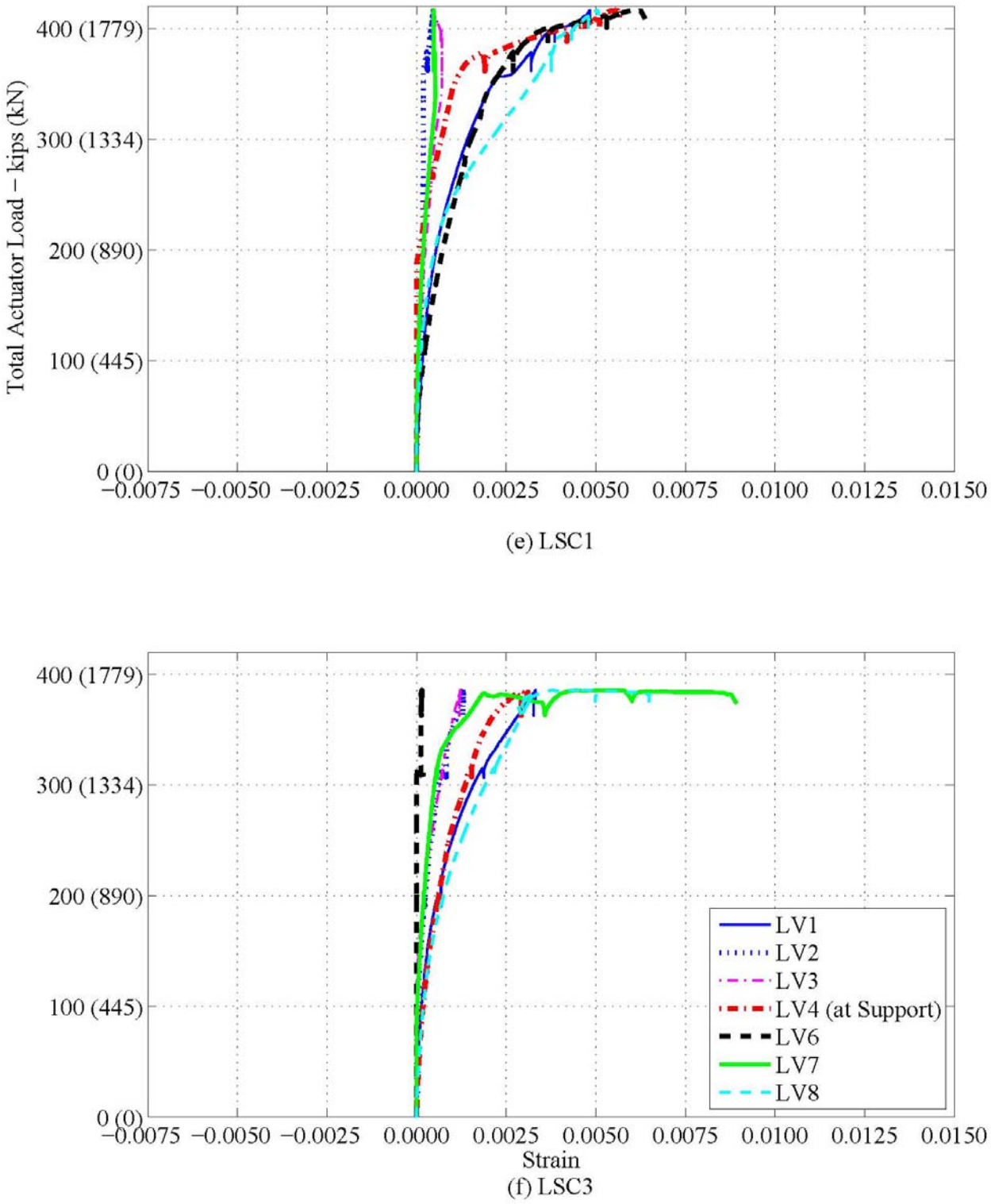

Figure 5-44. Experimental Load vs. Strain during the Three-Point Test: LVDTs along the Splice Region. (Continued)

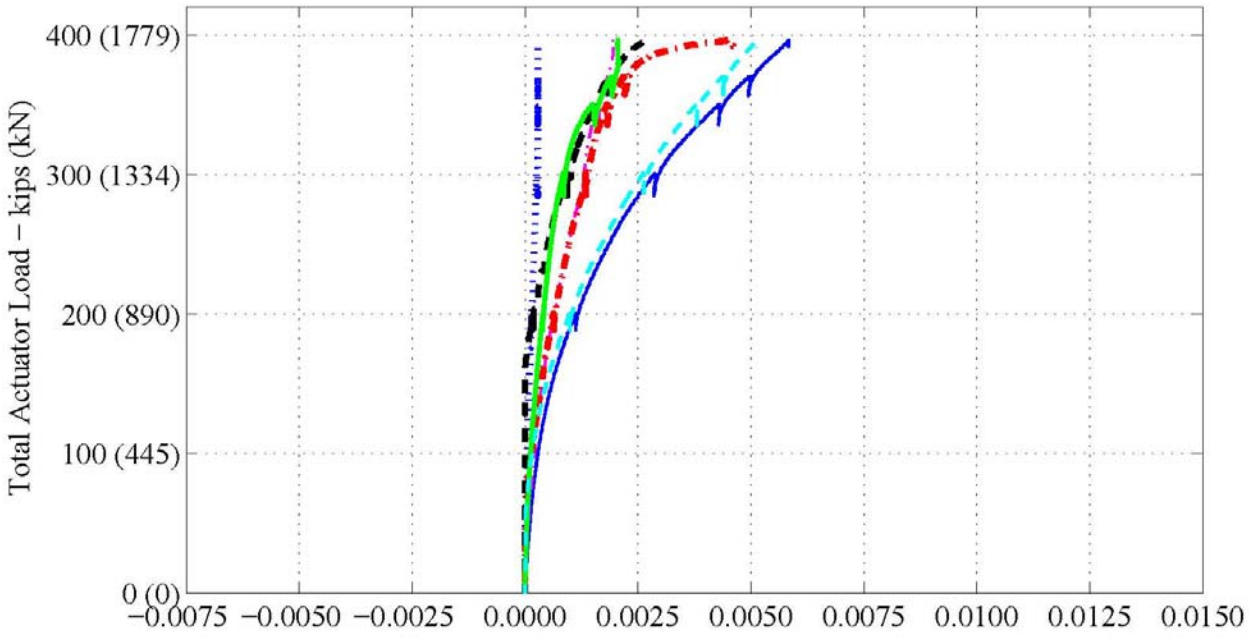

(g) LSC5

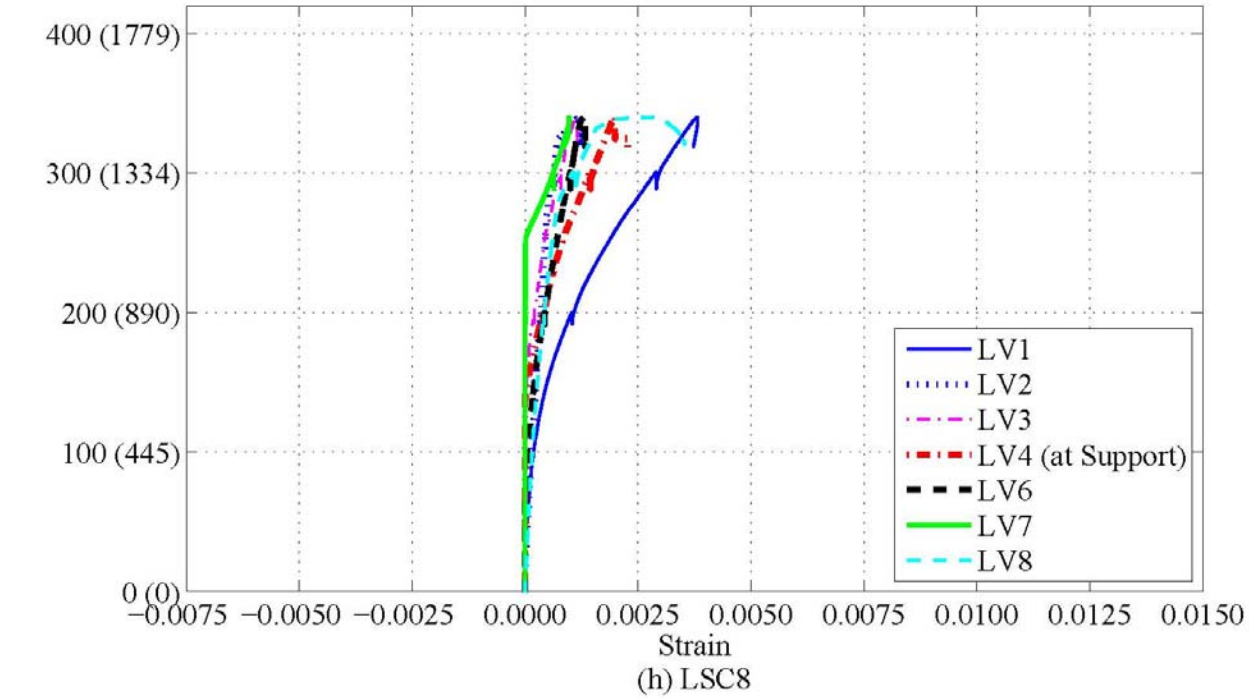

(h) LSC8

Figure 5-44. Experimental Load vs. Strain during the Three-Point Test: LVDTs along the Splice Region. (Continued)

Figure 5-45 shows the total actuator loading versus the internal and external surface strains in the splice region using the SG and LV data. This comparison is similar to the same comparison for the four-point test. The figure shows that the internal and external surface strains are comparable, implying a plane stress.

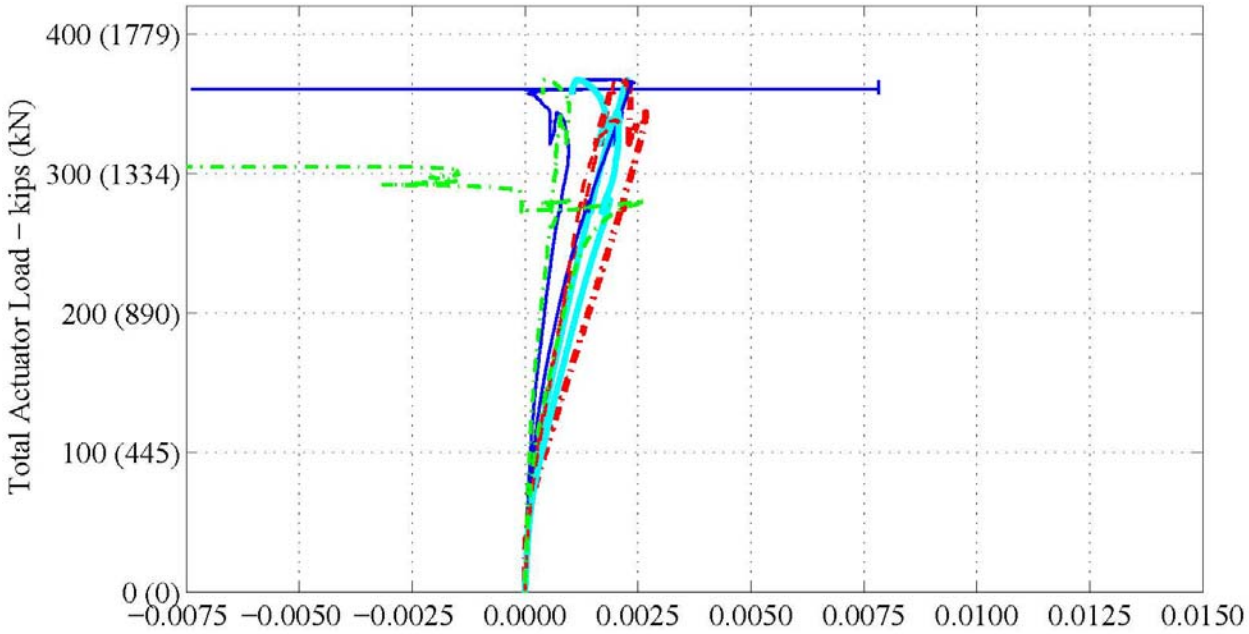

(a) LSC16

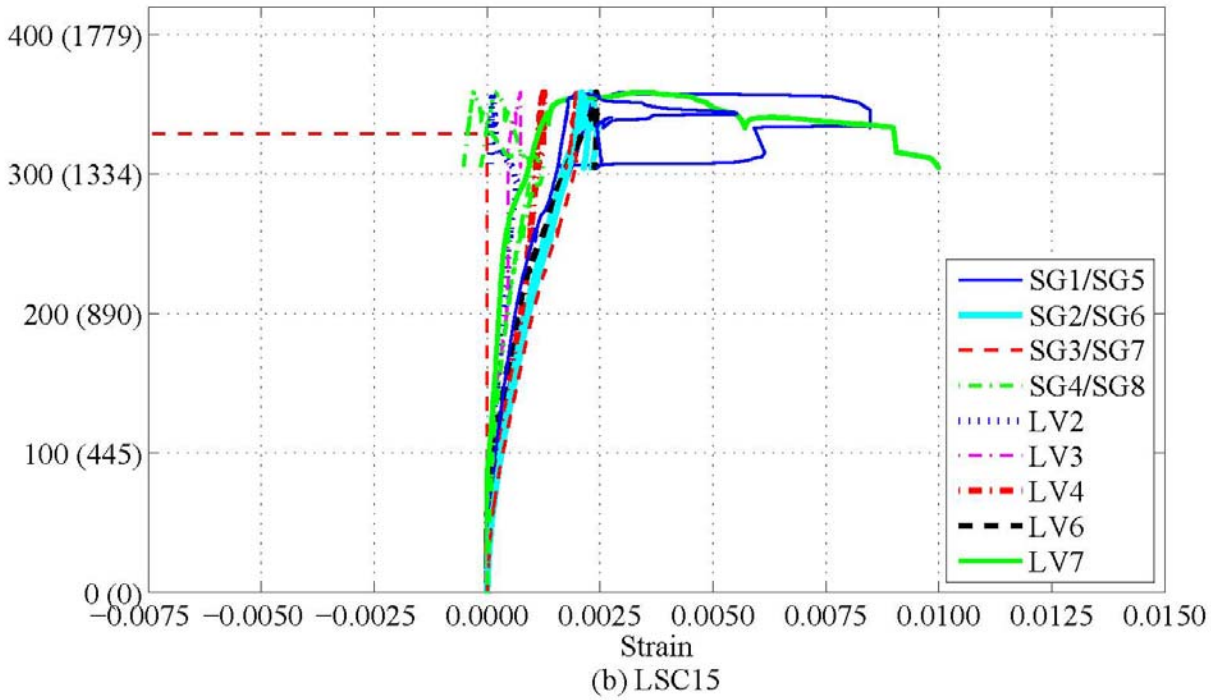

(b) LSC15

Figure 5-45. Experimental Load vs. Strain during the Three-Point Test: Comparison of Internal and External Strains across Tension Region.

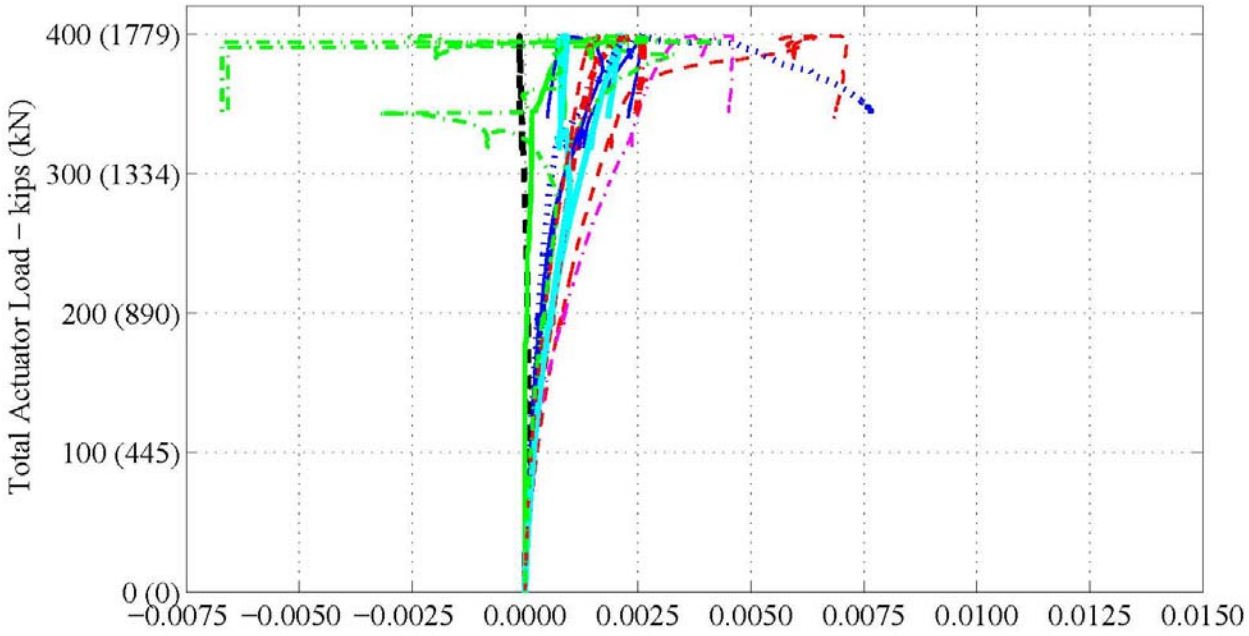

(c) LSC9

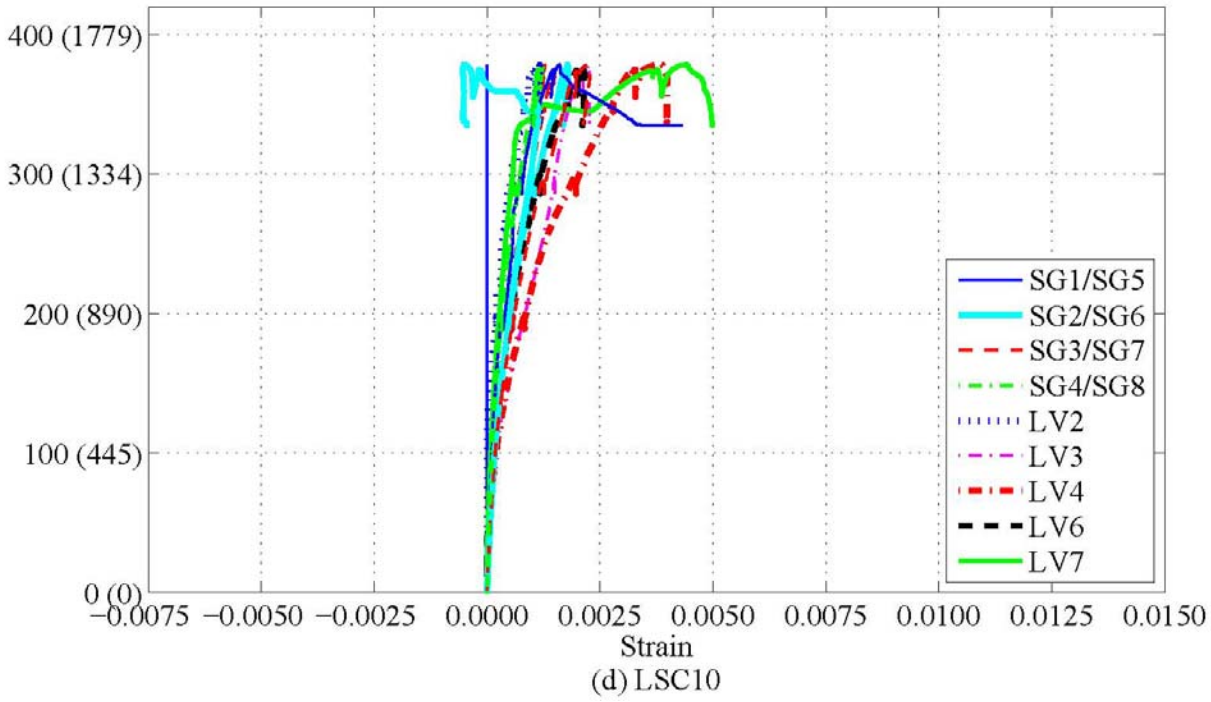

(d) LSC10

Figure 5-45. Experimental Load vs. Strain during the Three-Point Test: Comparison of Internal and External Strains across Tension Region. (Continued)

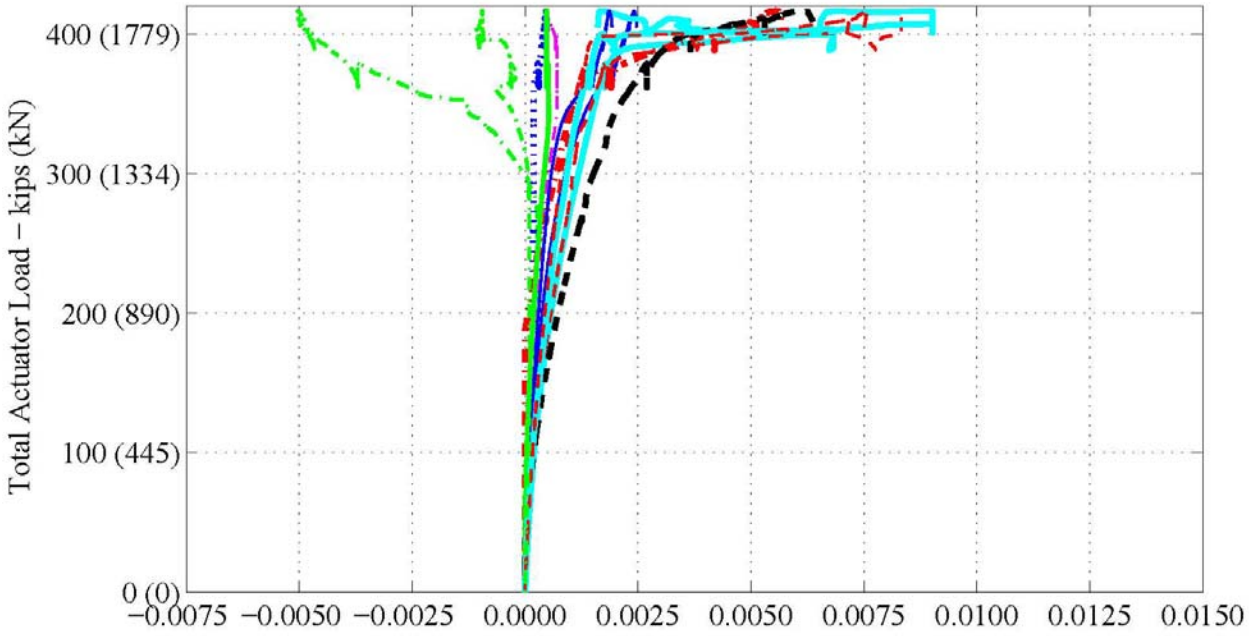

(e) LSC1

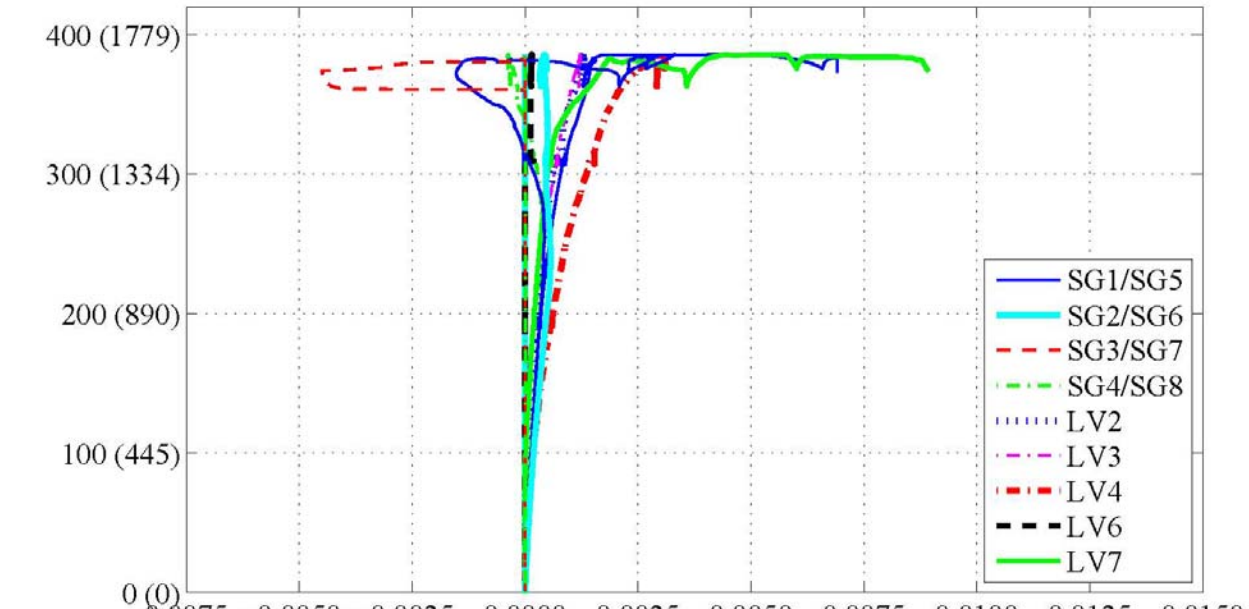

(f) LSC3

Figure 5-45. Experimental Load vs. Strain during the Three-Point Test: Comparison of Internal and External Strains across Tension Region. (Continued)

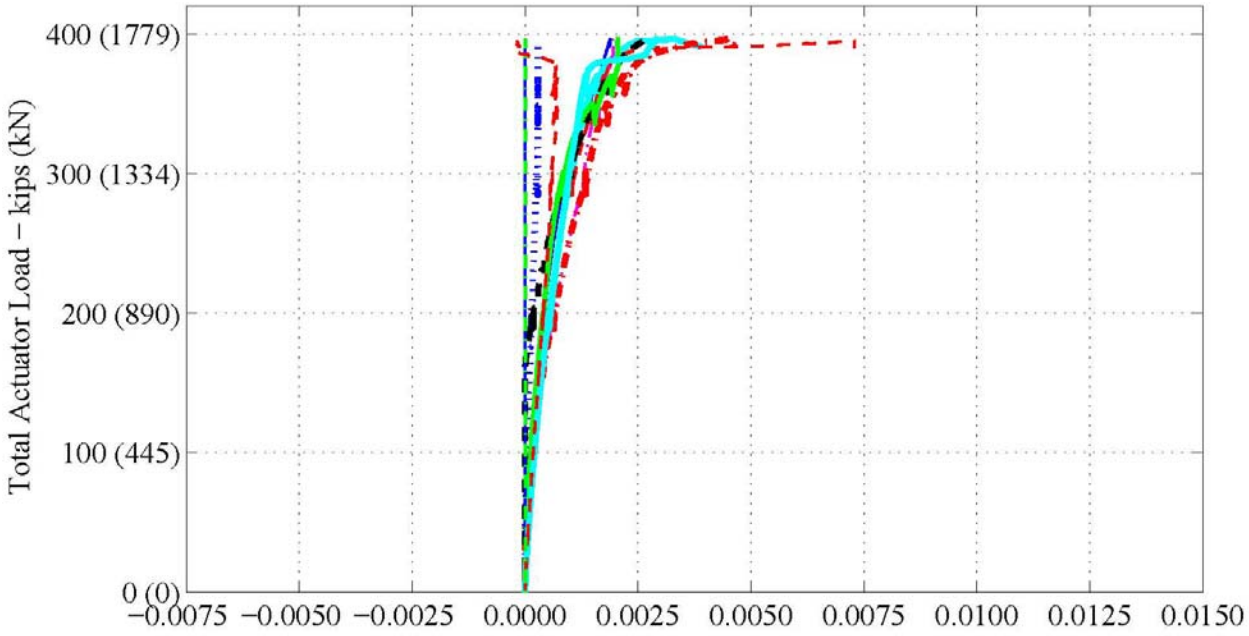

(g) LSC5

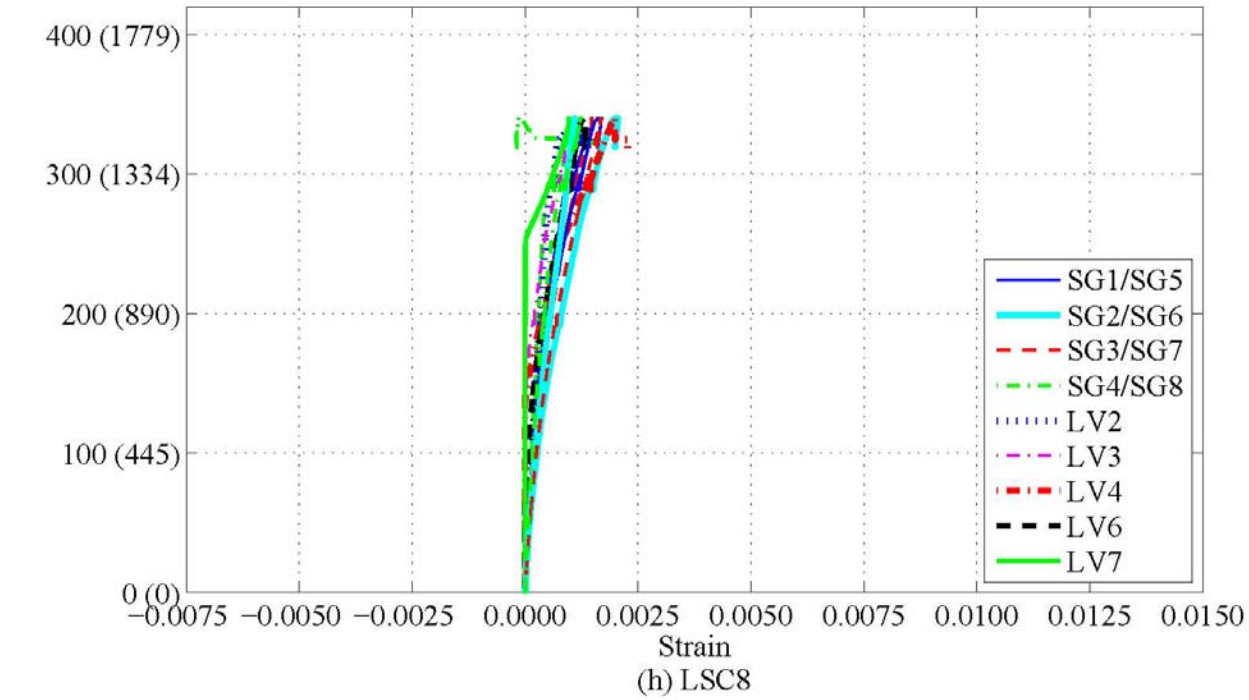

(h) LSC8

Figure 5-45. Experimental Load vs. Strain during the Three-Point Test: Comparison of Internal and External Strains across Tension Region. (Continued)

Figure 5-46 shows the total actuator loading versus the strains across the depth of the section directly above the support, which is the location of the largest moment demand. The strains follow the theoretical variation of large tension strains on top, very small strains in the midsection, and large compression strains on the bottom. The tension on top and compression on bottom is opposite from the four-point test, because of the specimen orientation in the test setup. The analytical model closely predicted the strains in this section. However, the experimental tension strain on the top is often greater than the analytical model and the maximum load is not accurately predicted as explained previously.

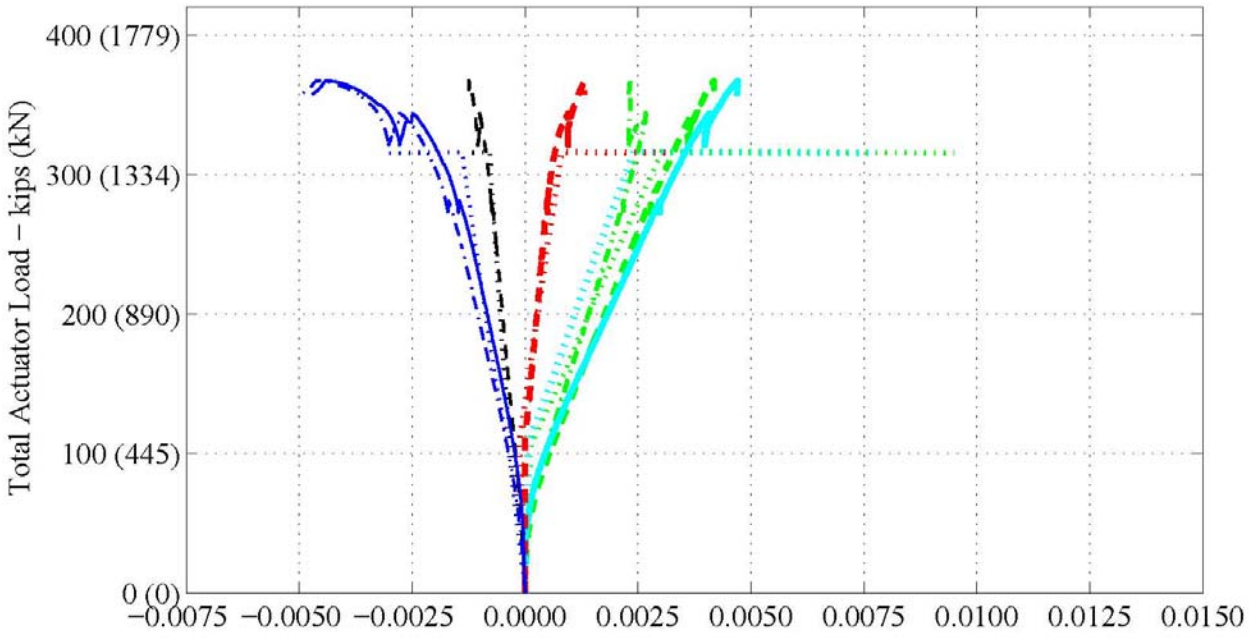

(a) LSC16

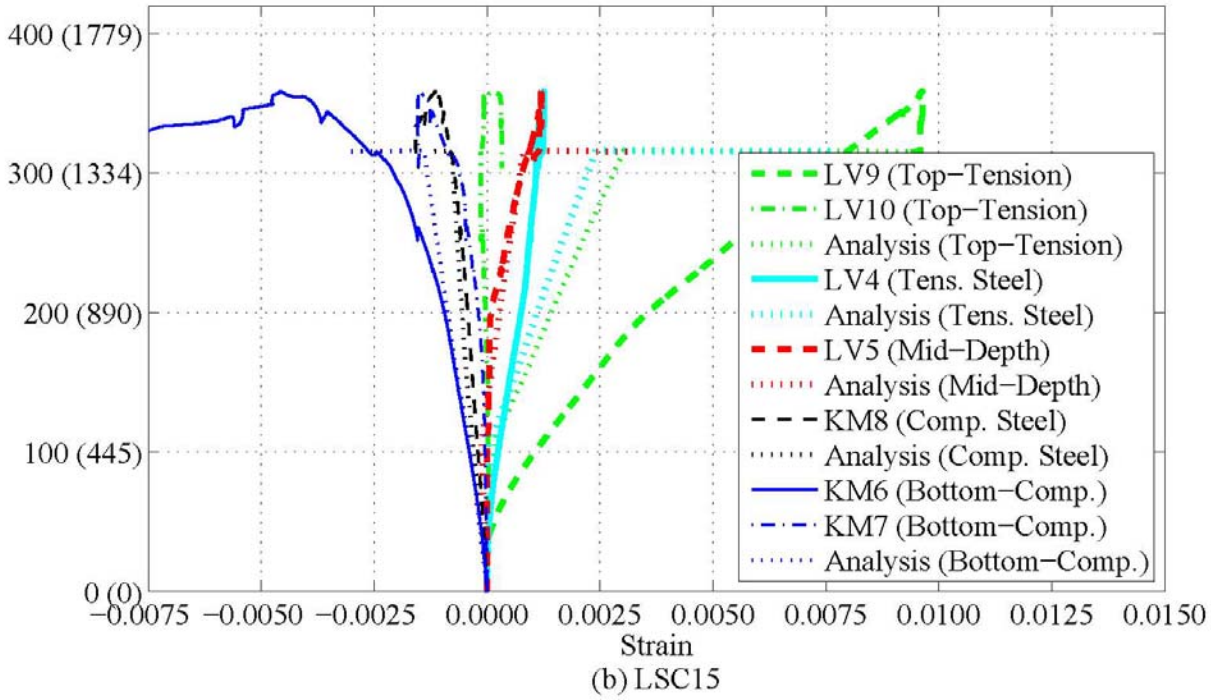

(b) LSC15

Figure 5-46. Experimental and Analytical Load vs. Strain during the Three-Point Test: External Strain Gages across the Depth of the Specimen above the Center Support.

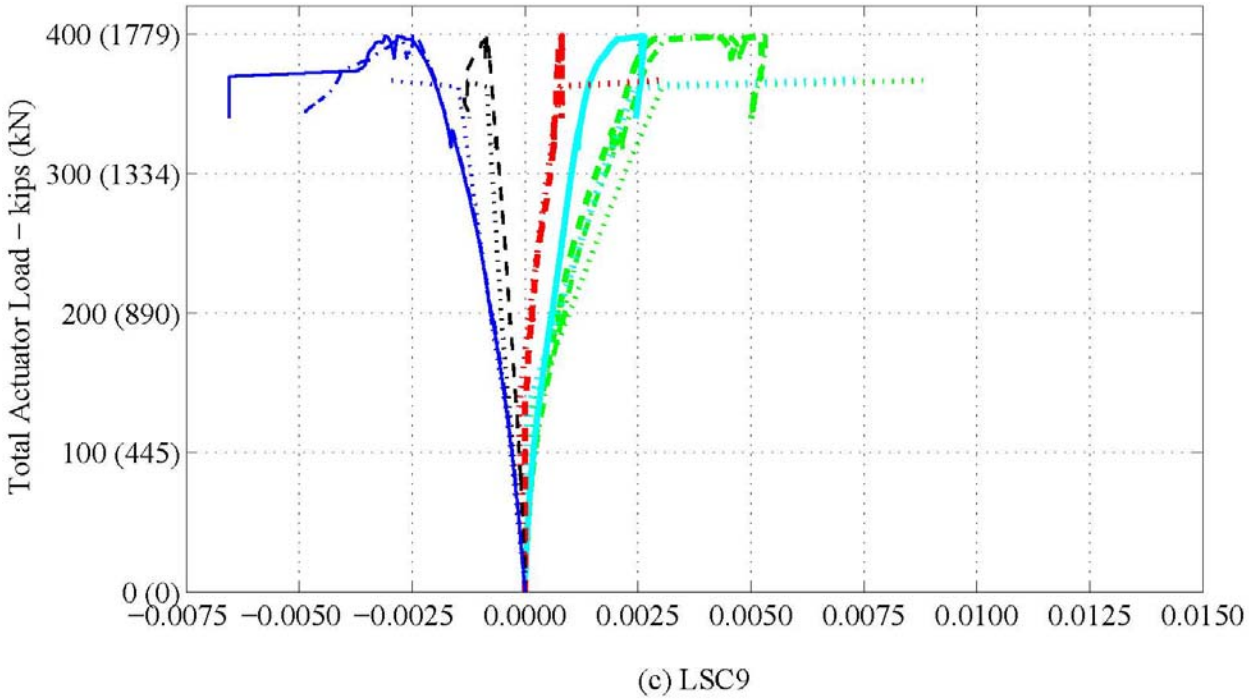

(c) LSC9

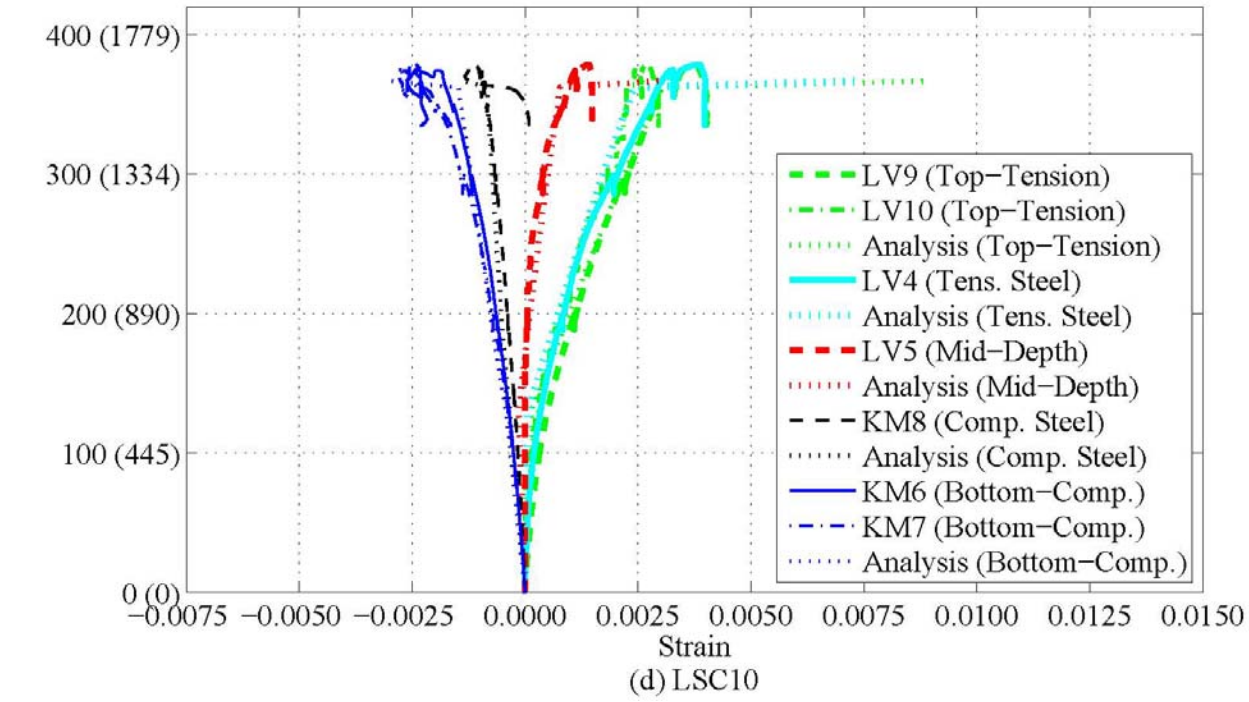

(d) LSC10

Figure 5-46. Experimental and Analytical Load vs. Strain during the Three-Point Test: External Strain Gages across the Depth of the Specimen above the Center Support. (Continued)

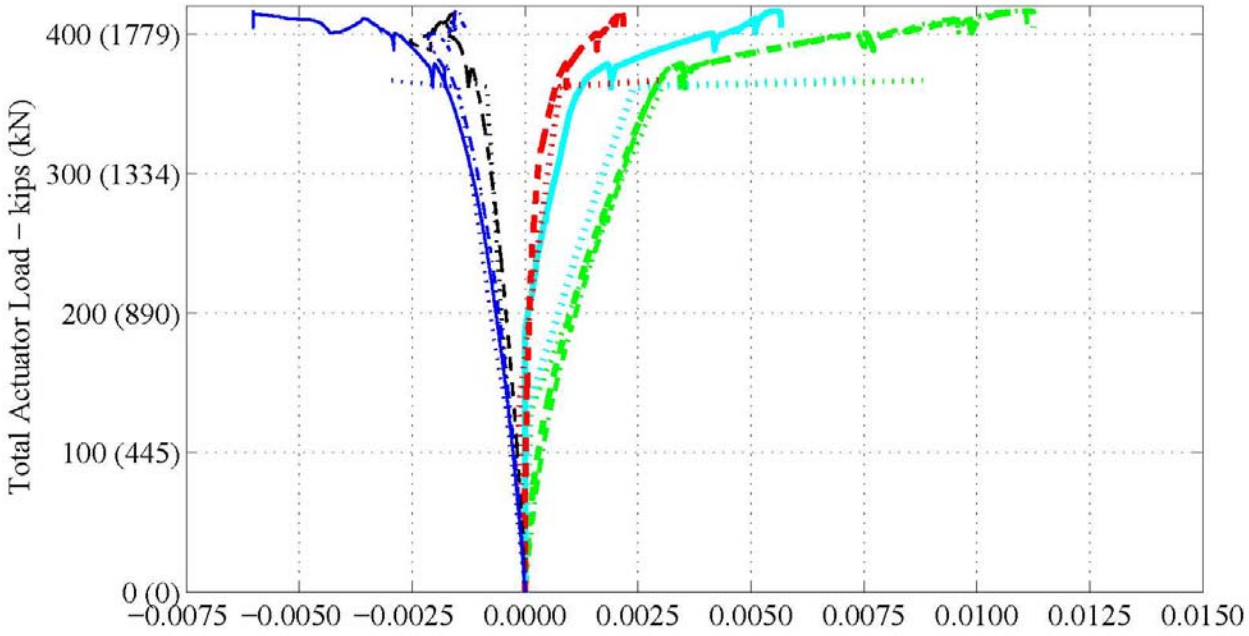

(e) LSC1

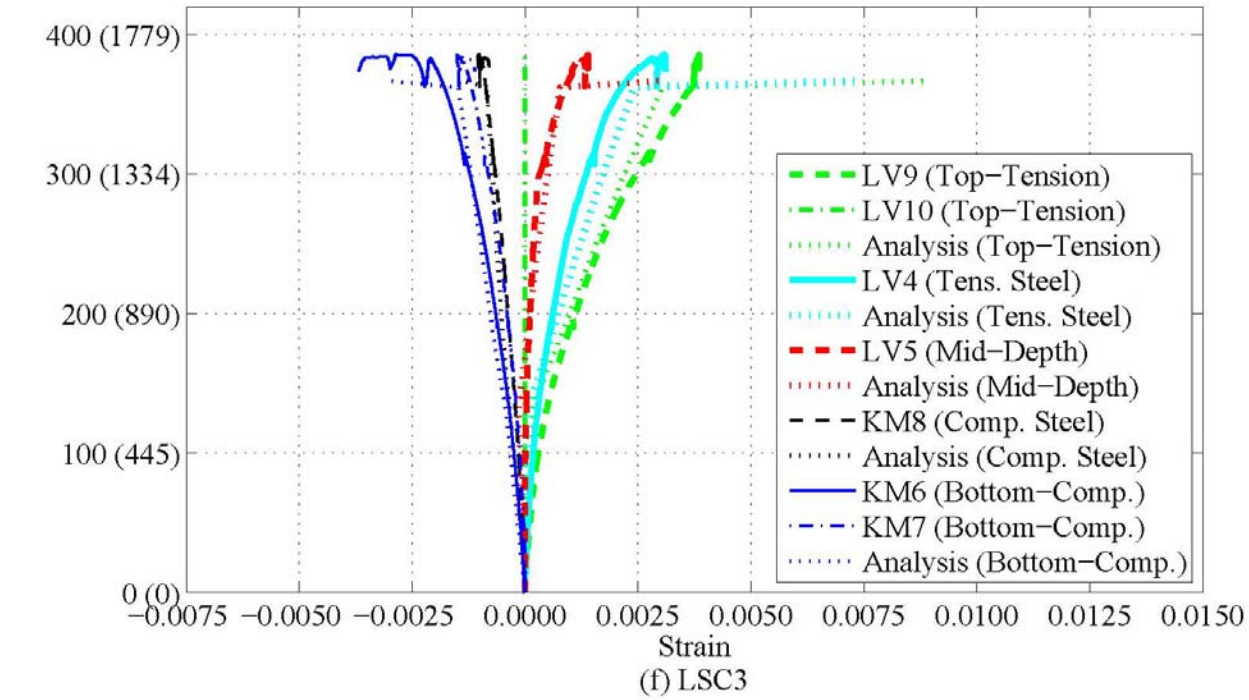

(f) LSC3

Figure 5-46. Experimental and Analytical Load vs. Strain during the Three-Point Test: External Strain Gages across the Depth of the Specimen above the Center Support. (Continued)

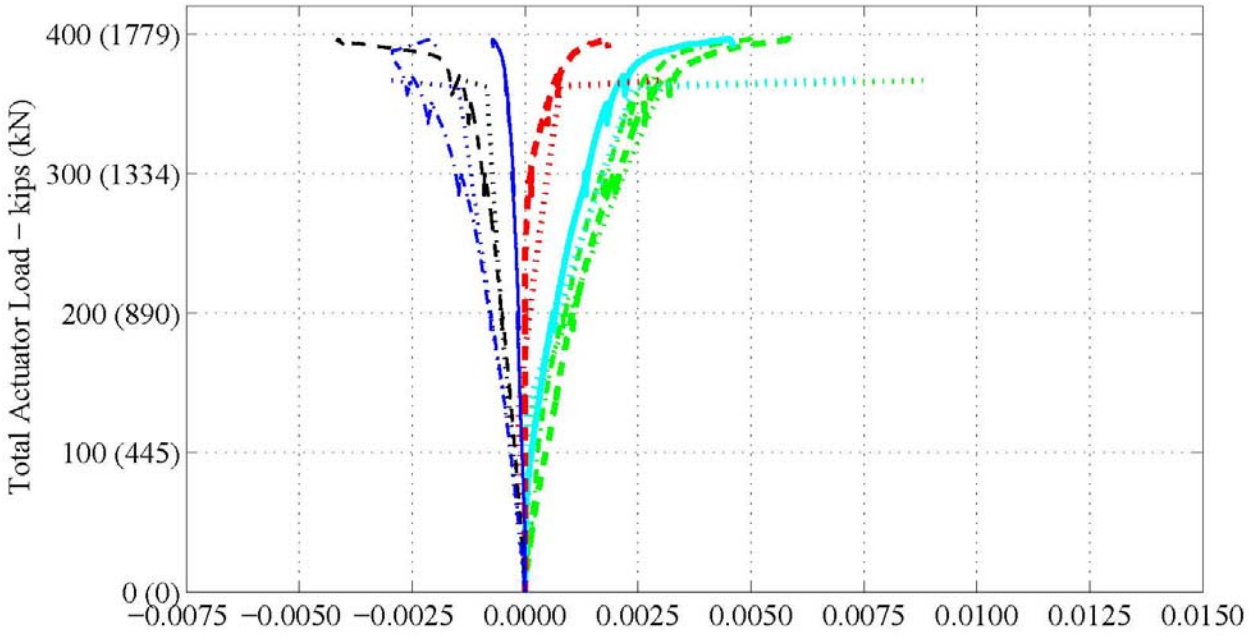

(g) LSC5

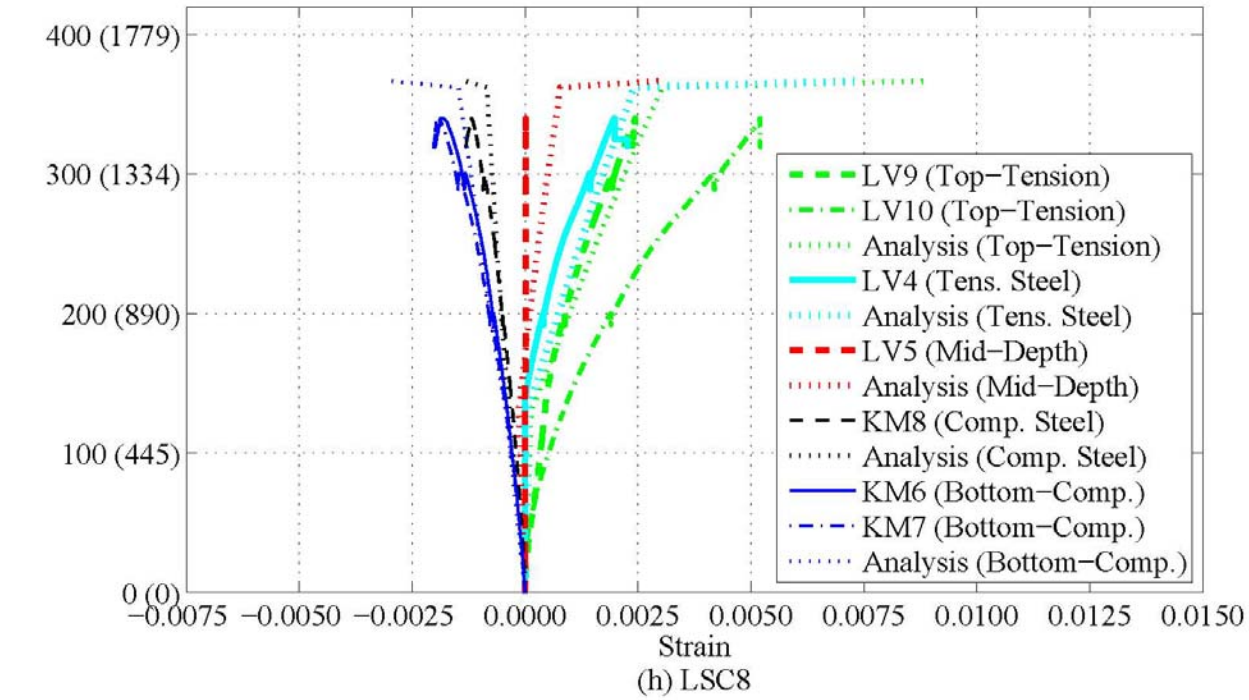

(h) LSC8

Figure 5-46. Experimental and Analytical Load vs. Strain during the Three-Point Test: External Strain Gages across the Depth of the Specimen above the Center Support. (Continued)

5.5 SUMMARY AND KEY FINDINGS

The experimental testing program in this research consisted of the design, construction, curing, deterioration, and structural load testing of 16 large-scale column specimens with a critical lap splice region under varying degrees of premature concrete deterioration due to ASR/DEF. Of these specimens, two control specimens without any ASR/DEF deterioration and three groups of two specimens with varying levels of ASR and minimal DEF were structurally load tested in both the four-point and three-point load test setups to date. The remaining eight specimens are still deteriorating under the environmental conditions and supplemental watering at the Texas A&M Riverside Campus with the hope of developing more severe damage from DEF, and will be structurally load tested at a later date.

The key findings from the experimentally measured structural force-deformation response, internal strain measurements, and developing failure mechanisms on the specimens tested to date are the following:

- Comparing the structural behavior of specimens with the varying degrees of ASR and minimal DEF deterioration to the control specimens with no ASR/DEF deterioration, researchers found that these have similar initial stiffness and behavior up to first cracking, about a 25–35 percent increase in post-cracking stiffness up to yielding, 5–15 percent increase in yield strength, and showed no overall detrimental effects on the structural response. The increase in stiffness and strength can be explained by the resulting volumetric expansion of the concrete due to ASR/DEF that engaged the longitudinal and transverse reinforcement for better confinement of the core concrete. In addition, the expansion further engaged the supplemental post-tensioning reinforcement and the longitudinal reinforcement to generate additional axial compression load.

- The step-by-step analytical modeling approach of the control and non-control specimens closely replicated the experimentally measured force-deformation behavior as well as internal strain measurements, in the two different test setups. However, the analytical load versus deformation for the three-point test was about 15 percent stiffer than the

experimental due to previous testing, some modeling assumptions, and intentionally neglected shear deformations. For the non-control specimens, the analytical model better fit the experimental behavior when the level of axial loading was increased as explained above.

- Although the structural performance of column splice regions with varying levels of ASR and minimal DEF showed no detrimental effects, the vulnerability of column splices with increased levels of DEF deterioration could not be evaluated to date. In spite of the research team's best efforts and the unprecedented rates of concrete expansion that were achieved, more time is needed to allow the remaining large-scale column splice specimens to further deteriorate in order to determine the performance of splice regions under severe DEF deterioration. The experimental testing of these specimens will be reported later.

CHAPTER 6:
SUMMARY, CONCLUSIONS, AND FUTURE WORK

6.1 SUMMARY

Over the past 25 years or so, the Texas Department of Transportation (TxDOT) has had an aggressive construction program in place to accommodate the expanding population growth within Texas. However, there is a significant amount of the reinforced concrete construction that has developed early cracking, termed premature concrete deterioration. Most of this deterioration has been identified or at least suspected to be from alkali silica reaction (ASR) and/or delay ettringite formation (DEF). Both deterioration mechanisms lead to volumetric expansion of the concrete due to ASR gel and/or the reformation of ettringite within the concrete, respectively. As such, the initial development of cracking from these mechanisms typically occurs in the tension field of the concrete member due to gravity loading during service conditions. An area of concern for TxDOT is the performance of column splice regions when varying levels of premature concrete deterioration (due to ASR and/or DEF) adversely affect it.

Therefore, the major objectives of this research program were to:

- Evaluate the experimental behavior of critical column lap splice regions using large-scale specimens under varying levels of premature concrete deterioration due to ASR and/or DEF.
- Develop an analytical model that can evaluate the behavior of a splice region under varying levels of concrete deterioration based on calibration with the experimental behavior.

In summary, the experimental testing program in this research consisted of the design, construction, curing, deterioration, and structural load testing of 16 large-scale column specimens with a critical lap splice region under varying degrees of premature concrete deterioration due to ASR/DEF. Two of these specimens were constructed, preloaded to simulate gravity load conditions, and stored in the climate-controlled structural laboratory without

supplemental water, which basically eliminated the premature concrete deterioration. The experimental behaviors of these two specimens were considered as the undamaged control behavior. The other 14 large-scale specimens were constructed, preloaded to simulate gravity load conditions, and then stored in an open field at the Texas A&M University Riverside Campus where they were exposed to wet-dry cycles and experienced ASR and minimal DEF deterioration. Data was recorded for surface expansions measurements in all specimens throughout the deterioration program. All specimens have successfully developed ASR/DEF deterioration (described as late-stage ASR and minimal DEF from the measured instrumentation, crack width data, and petrography analysis) in terms of internal concrete and reinforcing steel expansion, external surface expansion, and surface cracking that is representative of observations in in-service bridges.

Of the 16 specimens, two control specimens without any ASR/DEF deterioration and three groups of two specimens with varying levels of ASR and minimal DEF were structurally load tested in both the four-point and three-point load test setups to date. The remaining specimens are still deteriorating under the environmental conditions and supplemental watering at the Texas A&M Riverside Campus with the objective of developing more severe damage from DEF. These specimens will be structurally load tested at a later date.

To complement the experimental program, analytical models were developed based on flexure theory to characterize the force-deformation behavior and internal strains of the LSC specimens in both the four-point and three-point load test setups. In both the critical splice region and the specimen end regions, the longitudinal reinforcing steel was assumed to develop tensile resistance linearly from zero resistance at the end of the bar to the yield strength at the code calculated development length of the bar. The research team compared results from these models with the experimental response of undamaged LSC specimens, and then adjusted these for the increased axial load due to the longitudinal expansion from ASR and minimal DEF.

6.2 CONCLUSIONS

The conclusions and key findings from each phase of the research program are presented in this section.

6.2.1 Deterioration Program

In summary, the 14 large-scale specimens stored at the Riverside Campus were exposed to the outdoor weather conditions of Bryan, TX, and to wet-dry cycles using supplemental water to accelerate the ASR and minimal DEF deterioration mechanisms. Internal instrumentation and external surface measurements were continually recorded for all specimens throughout the deterioration program. It can be concluded that all specimens have successfully developed significant premature concrete deterioration due to ASR and/or DEF in terms of concrete expansion and surface cracking that is representative of observations in in-service bridges. In addition, the deterioration mechanism is continuing. To develop more severe damage states, additional exposure time is required. Therefore, eight untested specimens continue to deteriorate at the Riverside Campus.

The following highlights some of the findings derived from the deterioration program to date:

- The direct sunlight on the specimens made a large impact on the expansion due to ASR and minimal DEF. The transverse surface strain on the side of the specimen were as larger as 61 percent of the transverse surface strain on the top surface with direct sunlight and some were less than 20 percent the top surface strain.

- The LSC specimens expanded at a higher strain rate during the summer months (May through September); therefore, the high temperatures accelerate and increase the deterioration. The increase in the average strain/month on the top surface was calculated to measure this. The rate of increase was different for the three groups of specimens first exposed to the high temperatures and supplemental water at different times: May, July, and September. The strain rate on the first six specimens, which were exposed during all of the summer of 2008, was1.7 times higher during the summer of 2009 than during the non-

summer months of 2008 and 2009. The next four LSC specimens were exposed only during half of the 2008 summer. The average strain rate of the transverse strain on the top was 2.7 times as higher during the summer of 2009 than the non-summer months. The last four specimens were not exposed to the environmental conditions during any time in the summer of 2008. The strain rate increase during the first summer months on these LSC specimens was 6.5 times higher than the initial strain rate prior to the summer months.

- The transverse surface strains were about 10 times larger than the longitudinal surface strains due to the longitudinal restraint from the axial post-tensioning steel and longitudinal column reinforcement and the transverse tension field induced by Poisson's effect under post-tensioning.

- The average strains calculated from measuring the sum of the crack widths between DEMEC points were about 50 percent of the surface strains calculated from measuring the distance between DEMEC points.

- The measured strains were larger on the surface than inside the specimen with the strain in the cover reaching about 58 percent and the strain in the core concrete reaching about 52 percent of the surface strain. The strain on the steel hoop in the middle of the splice region ranged from 0.0036 and 0.0054. The hoop strain percentage of the surface strain was 40 percent on Small Face 1 at the time of the first rotation. The Large Face 1 hoop strain percentages of the surface strain were 83 percent and 78 percent at the first two rotations.

- The researchers used the measured internal and external concrete expansion data throughout the deterioration program, measured crack widths and lengths throughout the deterioration program, and petrography analysis of concrete cores taken from the specimens after they were structural tested. They then categorized the three groups of tested specimens as having varying levels of primarily ASR deterioration ranging from none to late stage and none/minimal levels of DEF.

6.2.2 Experimental Testing Program

The research group compared the structural behavior of specimens with the varying degrees of ASR and minimal DEF deterioration to that of control specimens without ASR/DEF deterioration. They found that these specimens have similar initial stiffness and behavior up to the first cracking, about a 25–35 percent increase in post-cracking stiffness up to yielding, 5–15 percent increase in yield strength, and showed no overall detrimental effects on the structural response. The increase in stiffness and strength can be explained by the resulting volumetric expansion of the concrete due to ASR/DEF that engaged the longitudinal and transverse reinforcement for better confinement of the core concrete. Moreover, ASR/DEF further engaged the supplemental post-tensioning reinforcement and the longitudinal reinforcement to generate additional axial compression load.

6.2.3 Analytical Modeling

The step-by-step I_{cr} analytical modeling approach for the column splice region in the control and non-control specimens in the two different test setups close to accurately replicated the experimentally measured force-deformation behavior, as well as internal strain measurements. For the non-control specimens, the analytical model better correlated with the experimental behavior when the level of axial loading was increased to account for the engagement of the reinforcement and additional post-tensioning load due to the volumetric expansion of the concrete as a result of ASR and minimal DEF. Based on these findings, no modification factors are currently necessary for the analytical modeling to account for deterioration of the column splice regions. However, if future testing results in bond-slip issues of the spliced longitudinal reinforcement and warrants such modifications of the analytical modeling, a simple procedure will be implemented such that the longitudinal reinforcing steel develops at the reduced development length of the bar compared to the code calculated development length of the bar.

6.3 FUTURE WORK

In spite of the research team's best efforts and the unprecedented rates of concrete expansion due to ASR/DEF that were achieved, more time is needed to allow the remaining large-scale column splice specimens to further deteriorate to determine the performance of splice regions under severe DEF deterioration. Currently, eight specimens remain at the Texas A&M University Riverside Campus and exposed to supplemental water from a sprinkler system four times a day and for 15 minutes each watering. The measured concrete expansions and surface cracking during the further deterioration program and the subsequent experimental testing of these specimens will be reported later.

In TxDOT Project 0-6491, a finite element model (FEM) was built to model the behavior of the specimens at the microscopic level instead of the macroscopic level in this project. A bond-slip model is explicitly used to model the interface of the concrete and reinforcing bar. The bond-slip model is then calibrated using the experimental data obtained from the four-point and three-point tests in this research. The research team is planning to apply the calibrated bond models to FEMs with different configurations (different geometries and material properties) of bridge columns. Based on the data generated from FEMs, probabilistic capacity and demand models for reinforced concrete bridge columns will be developed to account for the effects of de-bonding in the splice region. The probabilistic models will be used to assess the reliability of reinforced concrete bridges subject to de-bonding in the lap-splice region and to compute a reliability-based minimum development length (Huang et al. 2012).

In addition, nondestructive testing (NDT) procedures took place prior to the structural load tests of LSC5 and LSC8. Pulse-echo techniques such as impact-echo and ultrasonic guided waves were employed to determine the state of bond. These techniques monitor the characteristics of impact-generated and harmonically excited stress waves as they propagate throughout the structure. These procedures can also be used in the field. Small-scale testing is being used to assess the limitations of these techniques for detecting deliberate alterations to the steel concrete interface such as fabricated voids to correlate the results with the LSC5, LSC8 and others in the

future. Other techniques will also be investigated for their use in the detection of bond damage and other potential modes of failure such as hoop fracture (Pagnotta et al. 2012).

REFERENCES

AASHTO, "LRFD Bridge Design Specifications," American Association of State Highway and Transportation Officials, Washington D.C., 2007.

ACI Committee 318, "Building Code Requirements for Structural Concrete (ACI 318-08) and Commentary," American Concrete Institute, Farmington Hills, MI, 2008.

ACI Committee 318, "Building Code Requirements for Structural Concrete (ACI 318-89) and Commentary," American Concrete Institute, Farmington Hills, MI, 1989.

ACI Committee 318, "Building Code Requirements for Structural Concrete (ACI 318-63) and Commentary," American Concrete Institute, Farmington Hills, MI, 1963.

ACI Committee 318, "Building Code Requirements for Structural Concrete (ACI 318-71) and Commentary," American Concrete Institute, Farmington Hills, MI, 1971.

ACI Committee 318, "Building Code Requirements for Structural Concrete (ACI 318-95) and Commentary," American Concrete Institute, Farmington Hills, MI, 1995.

ACI Committee 408, "Bond and Development of Straight Reinforcing Bars in Tension," ACI 408R-03, *ACI Manual of Concrete Practice*, American Concrete Institute, Farmington Hills, MI, 2005.

Ahmed, T., E. Burley, and S. Rigden. "Effect of Alkali-Silica Reaction on Tensile Bond Strength of Reinforcement in Concrete Tested under Static and Fatigue Loading," *ACI Structural Journal*, Vol. 96, No. 4, July–August 1999a, pp. 419–428.

Ahmed, T., E. Burley, and S. Rigden. "Effect of Alkali-Silica Reaction on Bearing Capacity of Plain and Reinforced Concrete," *ACI Structural Journal*, Vol. 96, No. 4, July–August 1999, pp. 557–570.

Ahmed, T., E. Burley, and S. Rigden. "The Static and Fatigue Strength of Reinforced Concrete Beams Affected by Alkali-Silica Reaction," *ACI Structural Journal*, Vol. 95, No. 4, July–August 1998, pp. 376–388.

American Society for Testing and Materials. ASTM C 1293: Standard Test Method for Determination of Length Change of Concrete Due to Alkali-Silica Reaction, Annual Book of ASTM Standards: Volume 04.02, Concrete and Aggregates. West Conshohocken, PA, 2008.

American Society for Testing and Materials. ASTM C143-00 Standard Practice for Slump of Hydraulic-Cement Paste Concrete: Volume 04.02, Concrete and Aggregates. West Conshohocken, PA, 2000.

American Society for Testing and Materials. ASTM C39-01 Standard Test Method for Compressive Strength of Cylindrical Concrete Specimens, Annual Book of ASTM Standards: Volume 04.02, Concrete and Aggregates. West Conshohocken, PA, 2001.

American Society for Testing and Materials. ASTM C78-07 Standard Test Method for Flexural Strength of Concrete (Using Simple Beam with Third-Point Loading): Volume 04.02, Concrete and Aggregates. West Conshohocken, PA, 2007.

Bae, S., O. Bayrak, J.O. Jirsa, and R.E. Klingner. "Anchor Bolt Behavior in ASR/DEF-Damaged Drilled Shafts," Technical Report IAC 88-5DDIA004, The University of Texas at Austin, TX, 2007.

Bauer, S., B. Cornell, D. Figurski, T. Ley, J. Miralles, and K. Folliard. "Alkali-Silica Reaction and Delayed Ettringite Formation in Concrete: A Literature Review," Report No. FHWA/TX-06/0-4085-1. Center for Transportation Research, The University of Texas at Austin, TX, 2006.

Berube, M.-A., D. Chouinard, M. Pigeon, J. Frenette, L. Boisvert, and M. Rivest. "Effectiveness of Sealers in Counteracting Alkali-Silica Reaction in Plain and Air-Entrained Laboratory Concrete Exposed to Wetting and Drying, Freezing and Thawing, and Salt Water," *Canadian Journal of Civil Engineering*, 29, pp. 289–300, 2002.

Burgher, B., Thibonnier, A., Folliard, K.J., Ley, T., and Thomas, M. "Investigation of the Internal Stresses Caused by Delayed Ettringite Formation in Concrete," Technical Report No. FHWA/TX-09/0-5218-1, The University of Texas at Austin, Center for Transportation Research, 2008.

Carse, A., and Dux, P. F. "Measurement of Concrete Expansive Strains due to Alkali-Silica Reaction in Australian Concrete Structures," *Cement and Concrete Research,* 20(3), pp. 376–384, 1990.

CEB-FIP model code 1990 design code, T. Telford Services, Ltd., London, 1993.

Chana, P.S. "Bond Strength of Reinforcement in Concrete Affected by Alkali-Silica Reaction: Phase 1," Contractor Report CR141, Transport and Road Research Laboratory, 1989.

Chana, P.S., and Korobokis, G.A. "Structural Performance of Reinforced Concrete Affected by Alkali Silica Reaction," Contractor Report 267, Transport and Road Research Laboratory, 1991.

Folliard, K.J., R. Barborak, T. Drimalas, L. Du, S. Garber, J. Ideker, T. Ley, S. Williams, M. Juenger, M. Thomas, and B. Fournier., "Preventing ASR/DEF in New Concrete : Final Report," Technical Report No. 0-4085-5, The University of Texas at Austin, Center for Transportation Research, 2006.

Darwin D., J. Zuo, M.L. Tholen, and E.K. Idun. "Development Length Criteria for Conventional and High Relative Rib Area Reinforcing Bars," *ACI Structural Journal*, Vol. 93, No. 3, May–June, 1996, pp. 347–359.

Darwin, D., S.L. McCabe, E.K. Idun, and S.P. Schoenekase. "Development Length Criteria: Bars Not Confined by Transverse Reinforcement," *ACI Structural Journal*, Vol. 89, No. 6, November–December, 1992, pp. 709–720.

Fan, S., and J.M. Hanson. "Length Expansion and Cracking of Plain and Reinforced Concrete Prisms due to Alkali-Silica Reaction," *ACI Materials Journal*, Vol. 95, No. 4, July–August, pp. 480–487, 1998a.

Fan, S. and J.M. Hanson. "Effect of Alkali Silica Reaction Expansion and Cracking on Structural Behavior of Reinforced Concrete Beams," *ACI Structural Journal*, Vol. 95, No. 5, September–October, pp. 498-505, 1998b.

Gardoni, P., K.M. Nemati, and T. Noguchi. "Bayesian Statistical Framework to Construct Probabilistic Models for the Elastic Modulus of Concrete," *Journal of Materials in Civil Engineering*, 19(10), pp. 898–905, 2007.

Grattan-Bellew, P. E., J.J. Beaudoin, and V.G. Vallee. "Effect of Aggregate Particle Size and Composition on Expansion of Mortar Bars due to Delayed Ettringite Formation," *Cement and Concrete Research*, 28(8), pp. 1147–1156. 1998.

Huang, Q., P. Gardoni, A. Pagnotta, and D. Trejo (2012). "Effect of ASR on Steel-Concrete Bond Behavior in the Lap-Splice Region of Bridge Column," 6th International Conference on Bridge Maintenance, Safety and Management, Villa Erba, Lake Como, Italy, July 8–12, 2012 (in preparation).

Jensen, V., "Elgeseter Bridge in Trondheim Damaged by Alkali Silica Reaction: Microscopy, Expansion and Relative Humidity Measurements, Treatment with Mono-silanes and Repair," 9th Euroseminar on Microscopy Applied to Building Materials, September 9–12, 2003, Trondheim, Norway.

Kelham, S. "Effect of Cement Composition and Fineness on Expansion Associated with Delayed Ettringite Formation," *Cement & Concrete Composites*, 18(3), pp. 171–179, 1996.

Liu, S.-H. "Structural Assessment of 'D' Region Affected by Premature Concrete Deterioration," Doctoral Dissertation, Texas A&M University, College Station, TX, 2012 (in preparation).

MacGregor, J. G., and J. K. Wight. *Reinforced Concrete Mechanics and Design*, Fifth Edition, Prentice-Hall Inc., Upper Saddle River, NJ, 2009.

"Monthly Weather for Bryan, TX." The Weather Channel. Web. May 9, 2011. http://www.weather.com/outlook/homeandgarden/home/wxclimatology/monthly/graph/77801

Mander, J.B., J.M. Bracci, S. Hurlebaus, Z. Grasley, M.M. Karthik, R.M. Scott, and S.-H. Liu. "Structural Assessment of 'D' Regions Affected by Premature Concrete Deterioration," Report 0-5997, Texas Transportation Institute, Texas A&M University, October 2011.

Mattock, Alan H. "Rotational Capacity of Hinging Regions in Reinforced Concrete Beams by W.G. Corley, Discussion by A.H. Mattock," *Journal of the Structural Division*, ASCE, Vol. 93, No. ST2, April, pp. 519–522, 1967.

Monette, L.J., N.J. Gardner, and P.E. Grattan-Bellew. "Residual Strength of Reinforced Concrete Beams Damaged by Alkali-Silica Reaction- Examination of Damage Rating Index Method," *ACI Materials Journal*, Vol. 99, No. 1, January-February, pp. 42-50, 2002.

Naaman, A. *Prestressed Concrete Analysis and Design,* Second Edition, Techno Press, Ann Arbor, MI, 2004.

Odler, I. and Y. Chen. "On the Delayed Expansion of Heat-Cured Portland Cement Pastes and Concrete," *Cement and Concrete Composites*, Vol. 18, pp. 181–185, 1996.

Orangun, C.O., J.O. Jirsa, and J.E. Breen. "Reevaluation of Test Data on Development Length and Splices," *ACI Journal*, Proceedings, Vol. 74, No. 3, March-April, pp. 114–122, 1977.

Orangun, C.O., Jirsa, J.O., and Breen, J.E., "The Strength of Anchored Bars: A Reevaluation of Test Data on Development Length and Splices," Research Report No. 154-3F, Center for Highway Research, The University of Texas at Austin, TX, January, 1975.

Pagnotta, A., D. Trejo, P. Gardoni, and Q. Huang. "Assessing Impact-Echo Test Variables for Detecting Loss of Bond in RC Bridge Columns," 6th International Conference on Bridge Maintenance, Safety and Management, Villa Erba, Lake Como, Italy, July 8–12, 2012 (in preparation).

PCI, *PCI Design Handbook Precast and Prestressed Concrete*, Precast/Prestressed Concrete Institute, Chicago, IL, 2004.

Petrov, N., M. Thibault, and A. Tagnit-Hamou. "Expansion Due to DEF in Normally Cured Concrete Heated by Cement Hydration," ACI Special Publication 234-16, American Concrete Institute, Farmington Hills, MI, pp. 239-250, 2006.

Poole, A. B. "Introduction to Alkali-Aggregate Reaction in Concrete," *The Alkali-Silica Reaction on Concrete*, Blackie, Glasgow, Scotland, and London, Van Nostrand Reinhold, NY, 1992.

Scrivener, K. and M. Lewis. "A Microstructural and Microanalytical Study of Heat Cured Mortars and Delayed Ettringite Formation," Proceedings of the 10th International Congress on the Chemistry of Cement, Gothenburg, Sweden, 1997.

Standard Method of Test for Making and Curing Concrete Test Specimens in the Laboratory. Publication no. AASHTO T126. N.p.: American Association of State Highway and Transportation Officials, Washington D.C., 2001.

Standard Specifications for Construction and Maintenance of Highways, Streets, and Bridges. Publication. N.p.: Texas Department of Transportation, 2004.

Swamy, R. N. "Testing for Alkali-Silica Reaction," *The Alkali-Silica Reaction on Concrete*, Blackie, Glasgow, Scotland, and London, Van Nostrand Reinhold, NY, 1992.

Swamy, R. N., and M.M. Al-Asali. "Effect of Alkali-Silica Reaction on the Structural Behavior of Reinforced Concrete Beams," *ACI Structural Journal*, Vol. 86, No. 4, July–August, pp. 451-459, 1989.

Y. Fu, "Delayed Ettringite Formation in Portland Cement Paste Products. Ottawa: Department of Civil Engineering, University of Ottawa, Ph.D. Thesis, p. 199, 1996.

Zhang, Z., J. Olek, and S. Diamond. “Studies on Delayed Ettringite Formation in Early-Age, Heat-Cured Mortars I. Expansion Measurements, Changes in Dynamic Modulus of Elasticity, and Weight Gains,” *Cement and Concrete Research*, Vol. 30 pp. 1729–1736, 2002.

Zuo, J. and D. Darwin. “Splice Strength of Conventional and High Relative Rib Area Bars in Normal and High Strength Concrete,” *ACI Structural Journal*, V. 97, No. 4, July–August, pp. 630–641, 2000.

Zuo, J., and D. Darwin. “Bond Strength of High Relative Rib Area Reinforcing Bars,” SM Report No. 46, University of Kansas, Center for Research, Lawrence, Kansas, 350 pages, 1998.

BIBLIOGRAPHY

Park R. and Paulay, T. *Reinforced Concrete Structures*. New York: John Wiley & Sons, Inc., 1975 Print.

APPENDIX A

PETROGRAPHIC ANALYSIS REPORT 1

Petrographic Analysis

06/29/2010

Report:	TTI ASR DEF
Date Received:	04/12/2010
Structure Type:	Unknown
Sample Type:	Cores
Location:	Unknown
Coarse Aggregate Producer:	NA
Coarse Aggregate Type:	Siliceous Gravel
Fine Aggregate Producer:	NA
Fine Aggregate Type:	Siliceous Sand
Cement Producer:	NA
Cement Type:	NA

Comments:
This petrographic analysis was performed in response to a request from Dr. Joseph Bracci to assist the Texas A&M University in an ASR/DEF investigation of nine submitted cores. The following objectives were specified by Texas A&M:

- General observations on concrete quality. (Comments on placement, mixture proportions, water-cement ratio).
- Visual documentation of ASR and/or DEF micro structural damage. (Images depicting gel/ettringite locations, cracking and gapping of paste/aggregate interfaces).
- Qualitative study of damage severity in each sample. (Comparison of micro structural damage between all samples).
- Qualitative study of damage progression through the length of the sample. (Comparison of micro structural damage in surface and core concretes of each sample).

General observations on concrete quality (comments on placement, mixture proportions, water-cement ratio)

General Appearance: Eleven cores were submitted for analysis and were designated as: B9S1, B9S2, ASRIIBeam1Core1, ASRIIBeam1Core2, ASRIIBeam1Core3, ASRIIBeam1Core4, B9C3, B9C4, B9C5, B9C6 and B9C7. The submitted cores were 3-3/4 inch in diameter and ranged from 2.0 to 6-1/8 inches in length. Cores B9S1, B9S2, B9C3, B9C4, B9C5, B9C6 and B9C7 had obvious distress cracks on the surface of the core. The four remaining cores, ASRII Beam1 designation had no surface cracking.

Water/Cement Ratio: None of the cores had abnormal or elevated w-c ratio. Based on appearance of the paste (color, ferrite distribution and granularity of the hydrates) estimates of w-c ratio for the eleven cores were consistent with the mix design.

Proportioning and types of aggregate: Based on point count data the paste volume indicate a high sack mix, low coarse aggregate factor and gap grading was noted in all the cores. Coarse aggregate consist of a siliceous gravel comprised of chert, agate and granite. Fine aggregate consist of quartz, agate, feldspar and chert. The following table summarizes the point count data:

Core ID	Paste Volume	FA Volume	CA Volume	% Entrapped Air	% Entrained Air
ASRIIBeam1Core2	27.06	39.24	30.50	0.49	2.58
ASRIIBeam1Core4	29.49	44.52	22.5	0.68	2.81
B9C6	34.88	32.66	28.01	1.38	2.96

Paste content and appearance: Paste content is indicative of a high sack mix and appearance is normal except for the numerous fine micro cracking observed in the all the cores except for the ASRII Beam 1 cores. No fly ash or other mineral admixtures were present in the mix.

Air Content: Non-Air Entrained.

Degree of Hydration: Normal.

Carbonation: Carbonation was noted at the exterior surface of all the cores. The following chart represents the depth of carbonation for each core:

Core ID	Carbonation Depth From Exterior Surface of Core	Carbonation Depth Observed Along Surface Crack
B9S1	2.2mm	NA
B9S2	3mm	NA
ASRIIBeam1Core1	None	NA
ASRIIBeam1Core2	None	NA
ASRIIBeam1Core3	None	NA
ASRIIBeam1Core4	None	NA
B9C3	2.2mm	3mm
B9C4	2mm	NA
B9C5	2mm	3mm
B9C6	2mm	3mm
B9C7	2mm	NA

Deleterious Reaction Mechanism: All the B9 cores are experiencing moderate to late stage ASR distress. ASRII beam 1 cores are producing some isolated sites of gel with very limited signs of distress. The primary ASR aggregate type in both the fine and coarse aggregate is a microcrystalline chert. Numerous

sites (air voids, exudation and within distressed aggregates) of ASR gel and distress aggregate were observed in the B9 cores. Copious amounts of gel were observed at the interface of the #11 bar in core B9C7. A layer of gel was also observed at the interface of the PVC conduit in core B9S1. ASR gel was also noted in the ASR II cores; however, the amount was sparse. Gel in the ASR II cores was observed at the paste aggregate interfaces and oozing of small droplets from some of the aggregates. The gel consistency was extremely viscous and did not exhibit normal shrinkage cracking when dried indicating that the gel had not absorbed much water. Ettringite was observed filling most of the micro cracks generated by ASR distress. Ettringite was also noted in many of the air voids and in some discrete nests within the paste. Some ettringite was noted at the interface of the # 11 rebar of core B9C7. The occurrence of gapping around aggregates due to paste expansion (DEF) was limited. Complete gapping of the aggregates was only observed in a minor amount of the particles

Microscopic documentation of ASR and/or DEF micro structural damage.
(Images depicting ASR gel/ettringite formation, cracking and gapping at paste/aggregate interfaces)

ASR Related Evidence

Digital image representing ASR distressed aggregate

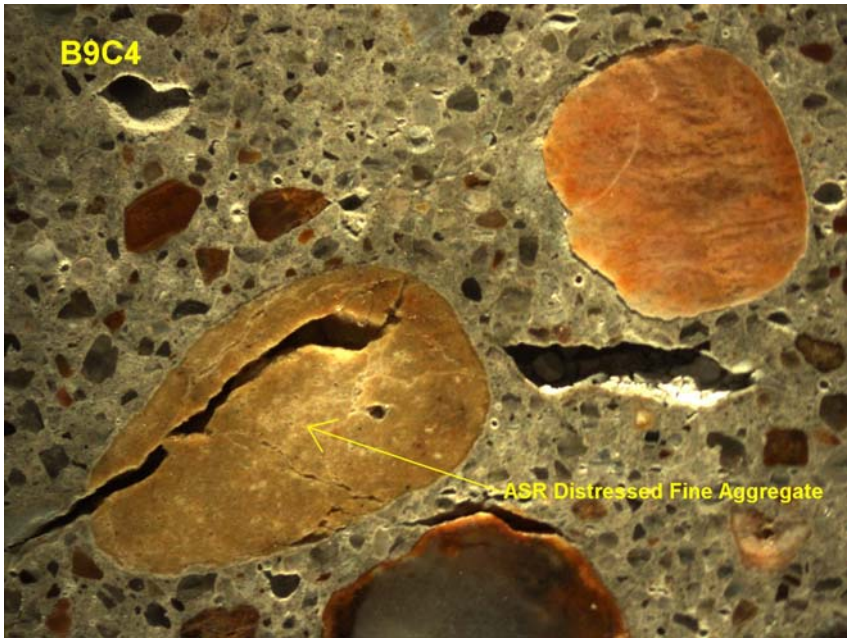

Dissolution and distress in coarse aggregate associated with ASR

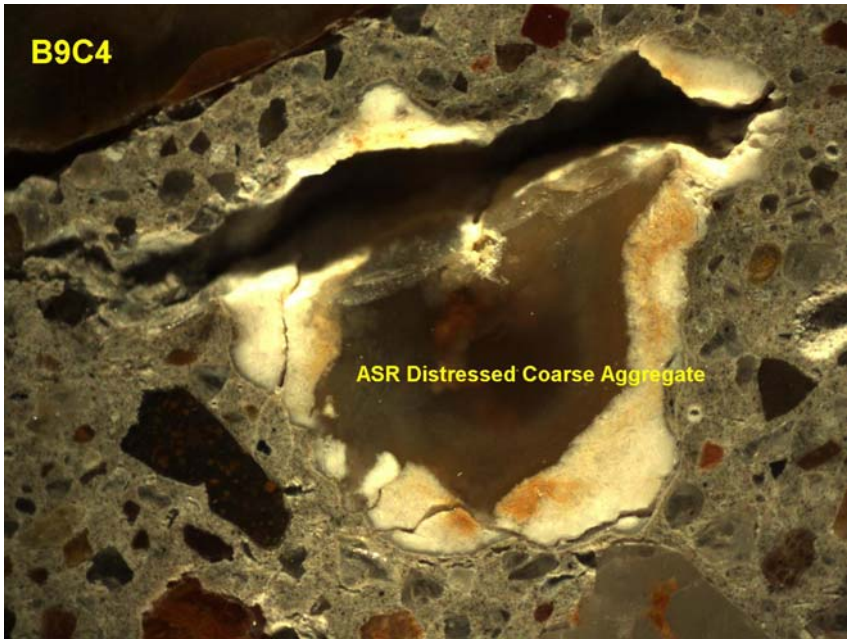

Two intermediate size aggregate showing signs of ASR distress

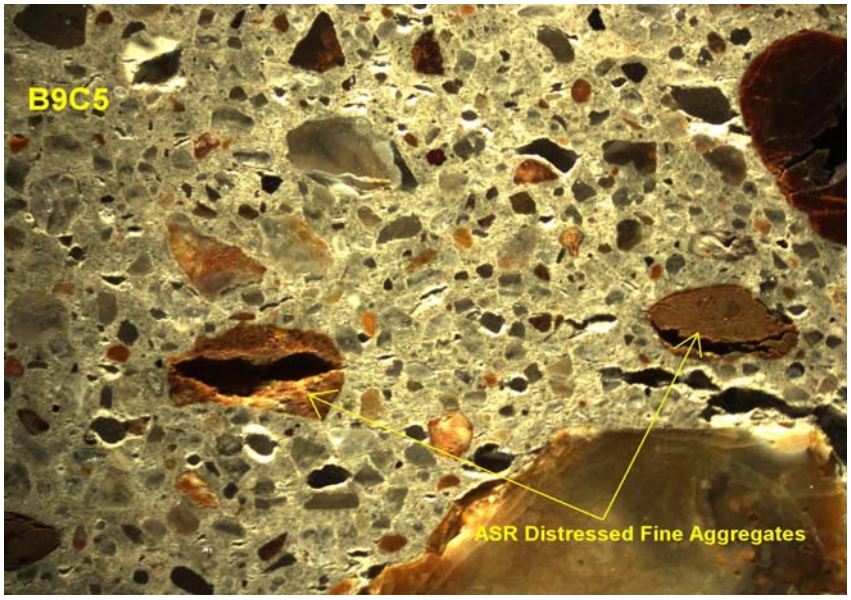

ASR gel rim observed around fine aggregate

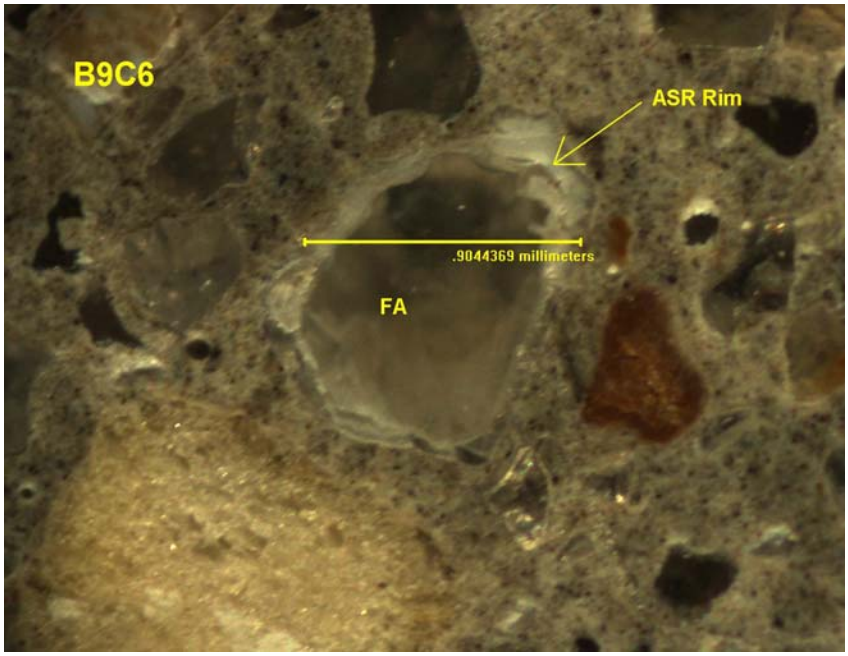

Distress observed in fine aggregate associated with ASR

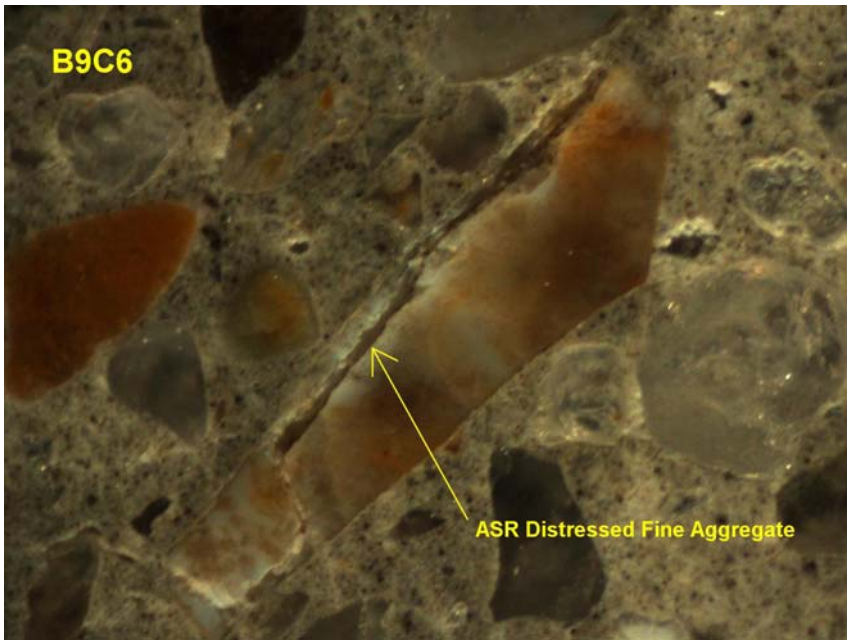

Distress and gel accumulation observed from chert coarse aggregate

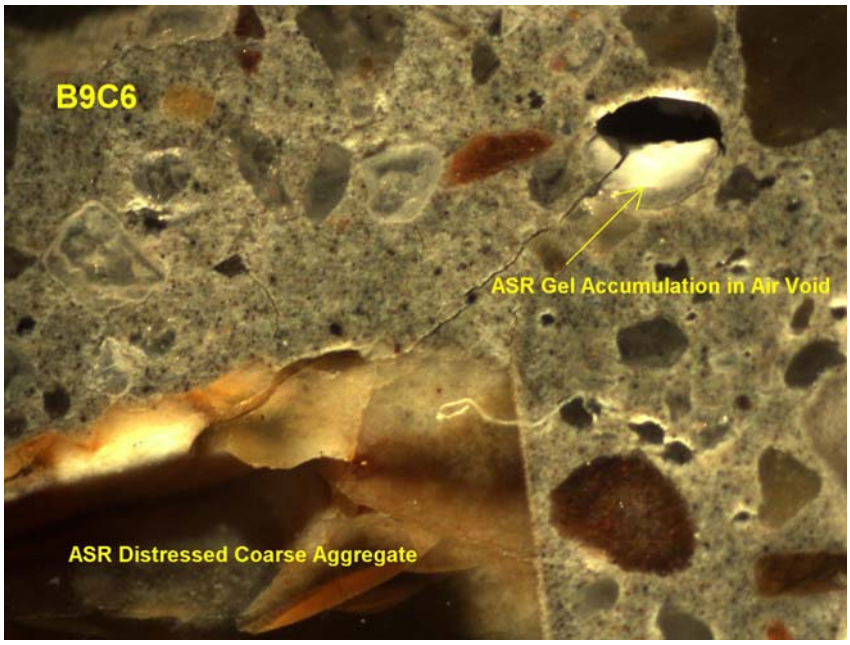

Small accumulation of ASR gel near paste/aggregate interface

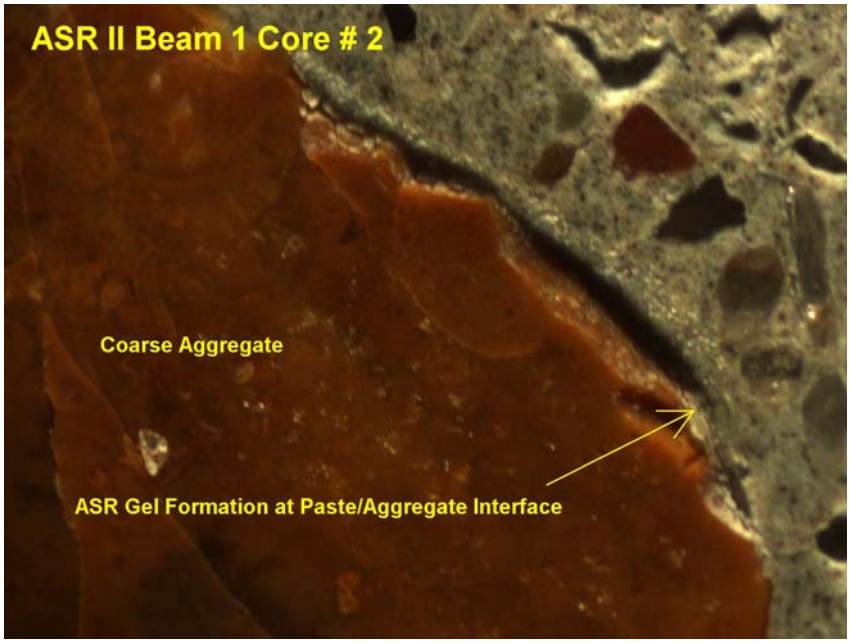

Small droplet of ASR gel which oozed out of aggregate after cutting and polishing

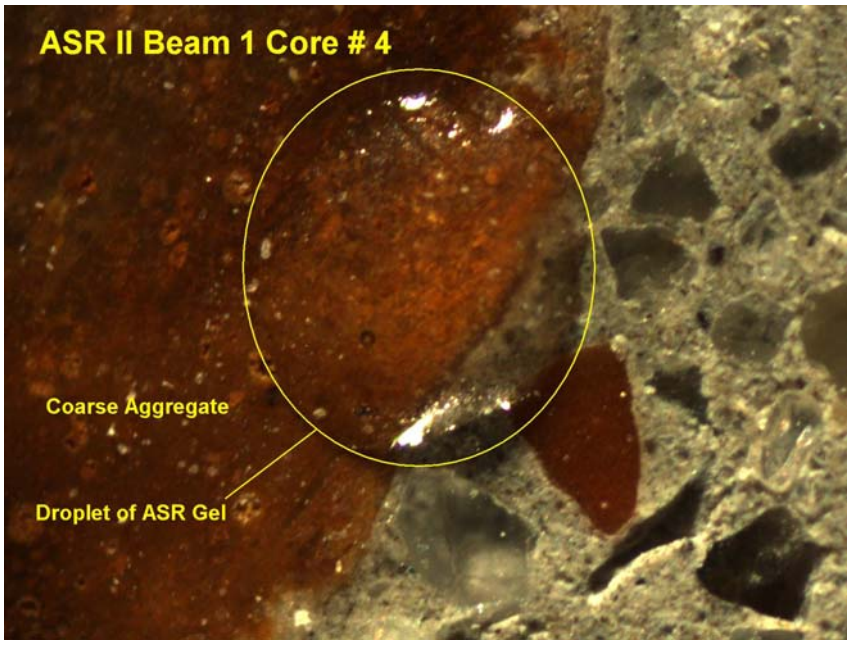

Small droplet of ASR gel which oozed out of fine aggregate

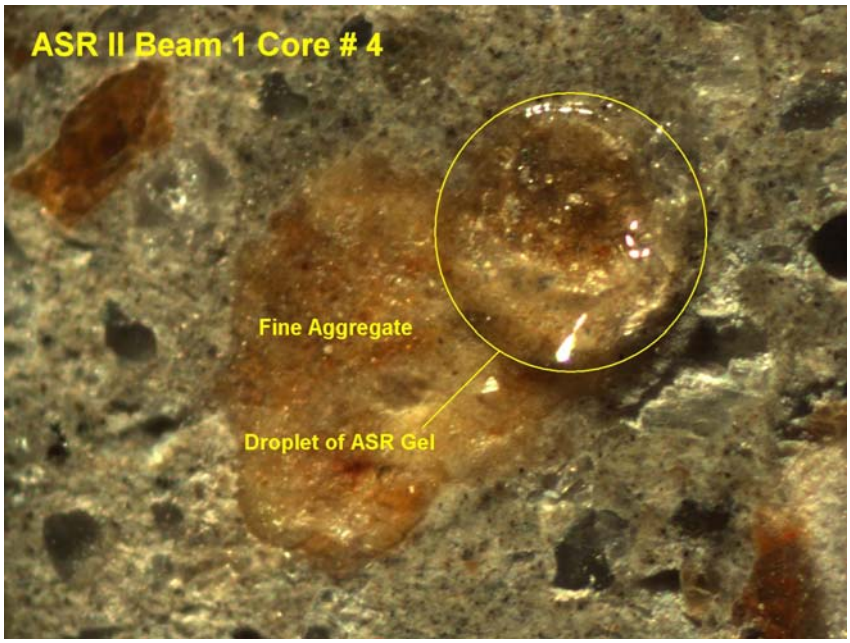

Fluorescence Microscopy Documentation

Fluorescent imaging is very useful tool in highlighting the fine micro cracking associated with PCD mechanism. The following images illustrate the level of distress associated with the reaction:

Fluorescent image illustrating numerous ASR distress cracking

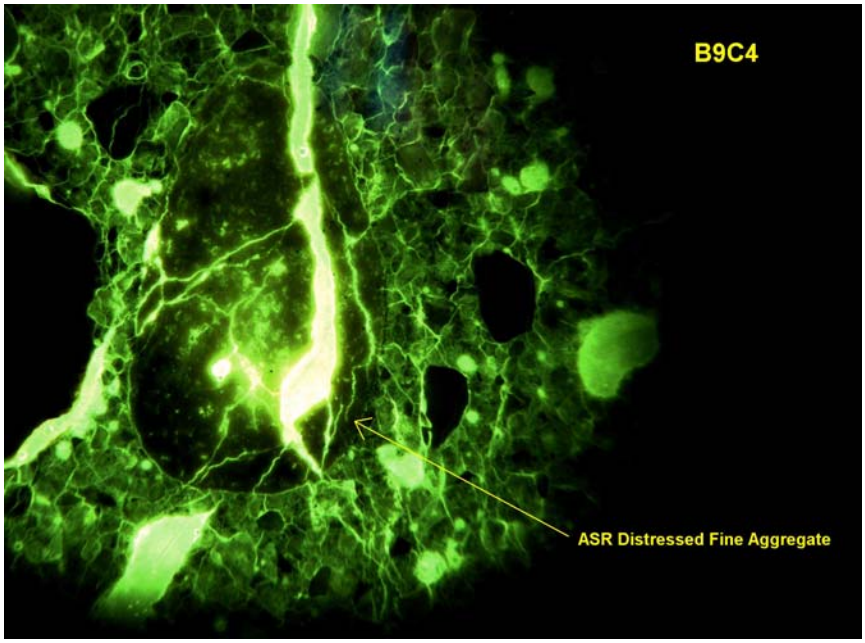

Fluorescent image illustrating radial cracking associated with ASR reactive fine aggregate

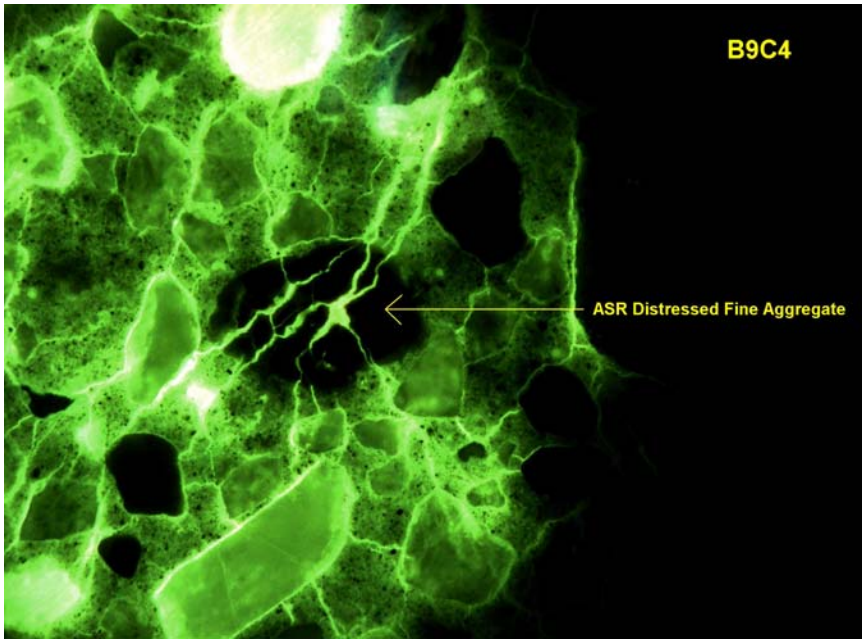

Image illustrating ASR generation of numerous fine micro cracks

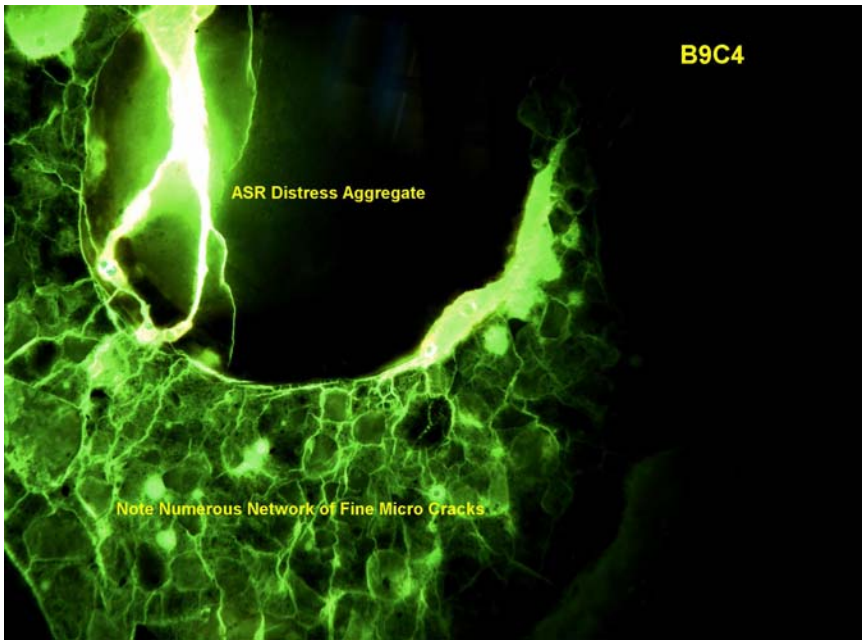

Fluorescent image illustrating distress associated with ASR reactive fine aggregate

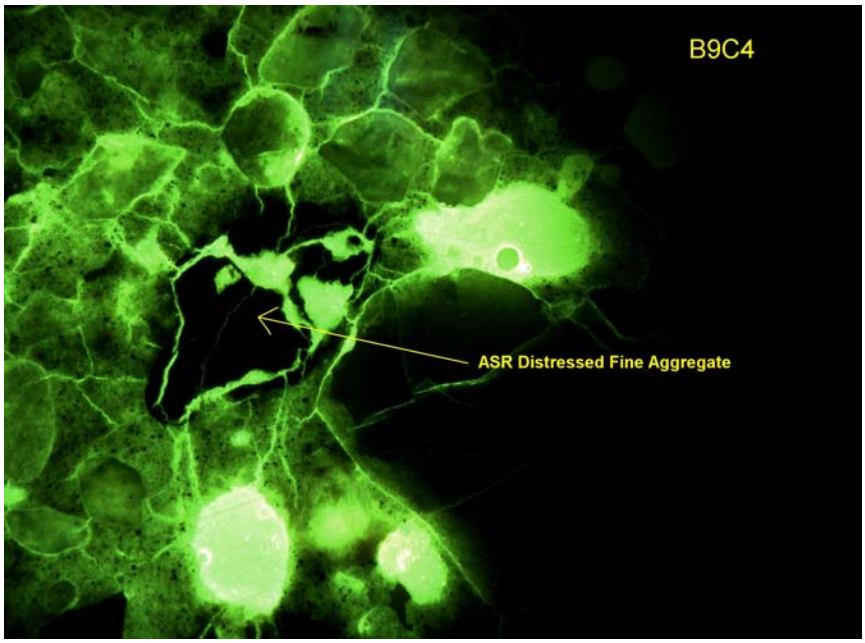

ASR Distress fine aggregate

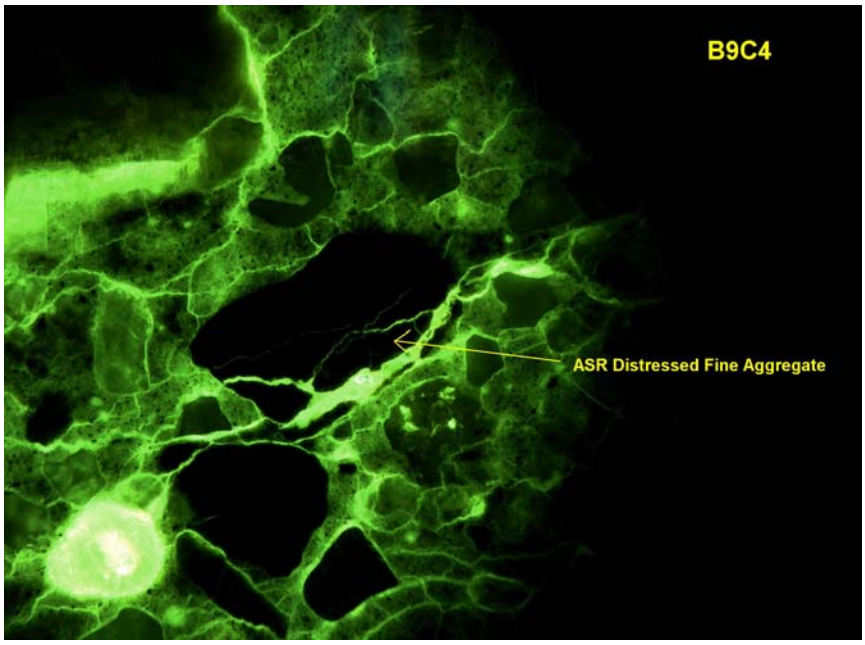

ASR Distress fine aggregate

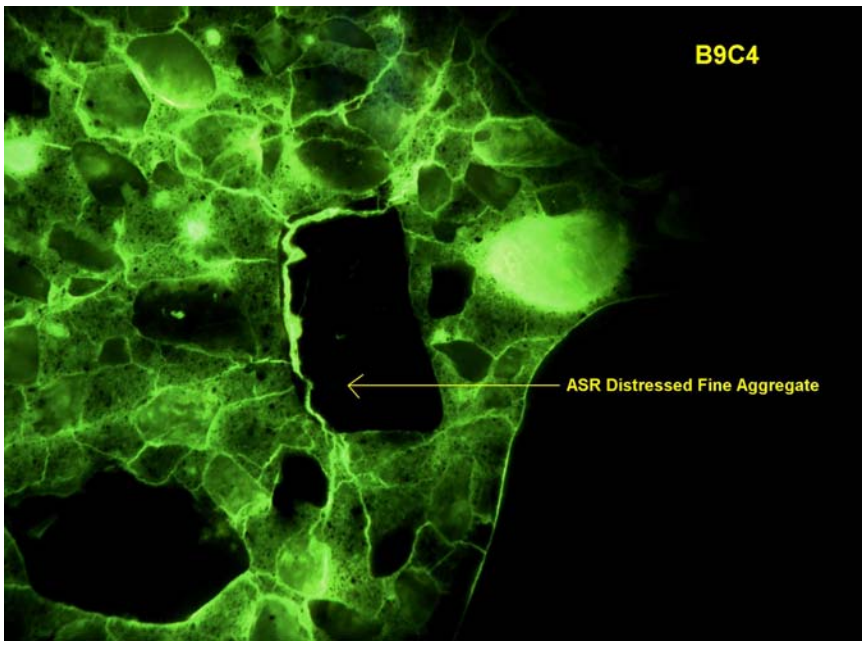

Image illustrating migration of fine ASR crack (note intersection and wrapping around fine)

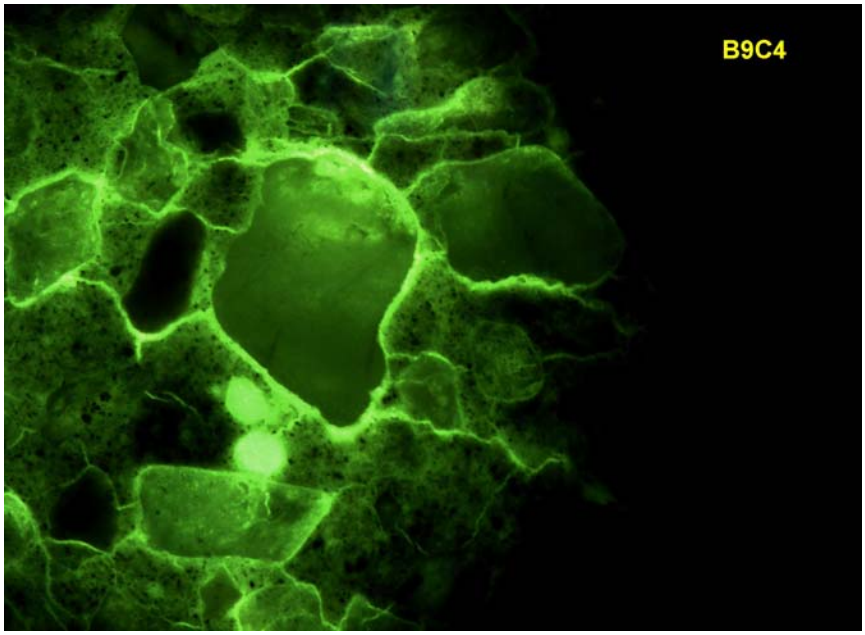

Scanning Electron Microscope (SEM) Documentation

The SEM analysis was performed on a Hitachi brand 3200N variable pressure microscope with an Oxford EDS system. This tool was used to document and confirm the type of PCD responsible for the distressed concrete. EDS spectral analysis was used to verify reaction site chemistry and relationship to other phases in the mix (paste, aggregate). EDS elemental dot mapping was performed to document the location of reaction product within the mix. The following images document numerous ASR distressed aggregates and ettringite formation sites:

B9S1 SEM Documentation

ASR Gel accumulation in air void adjacent to reactive coarse aggregate

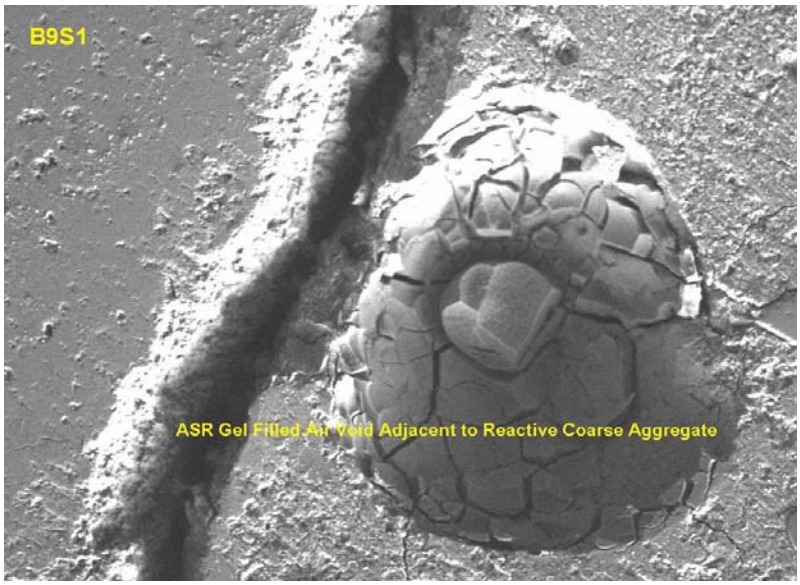

SEM/EDS spectra illustrating typical gel chemistry of air void gel

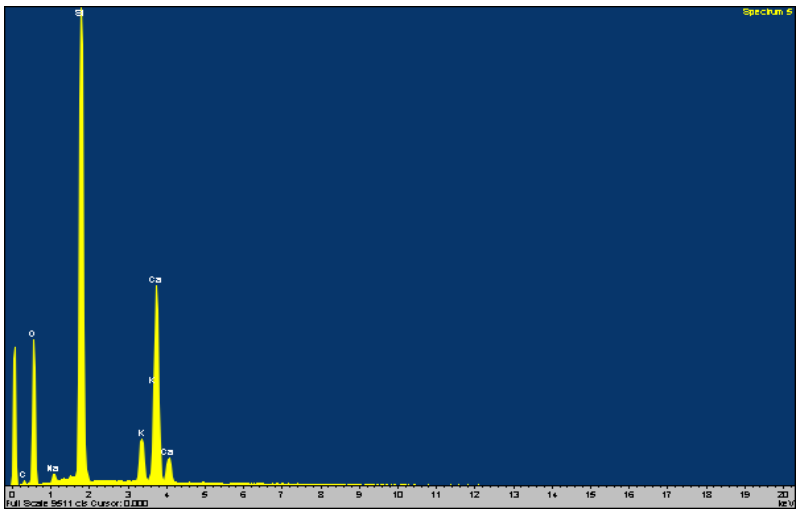

Illustration of ASR gel exudation from fine aggregate

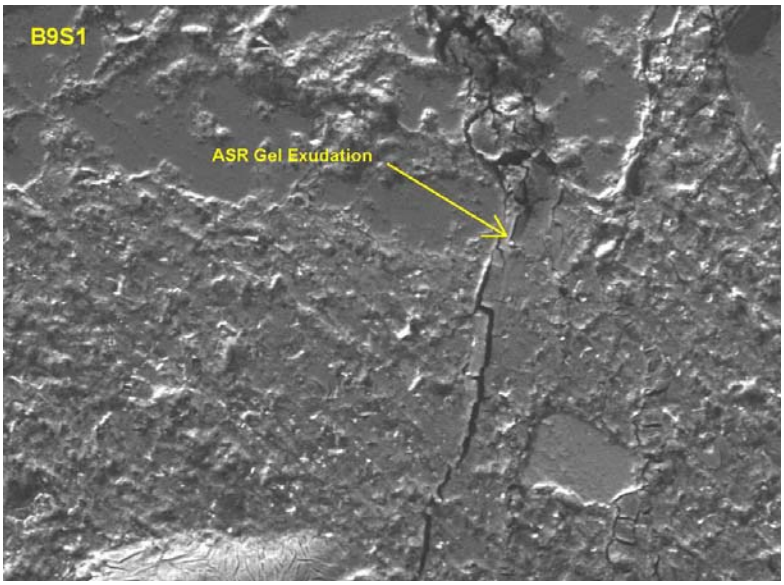

SEM/EDS spectra of ASR gel exudation

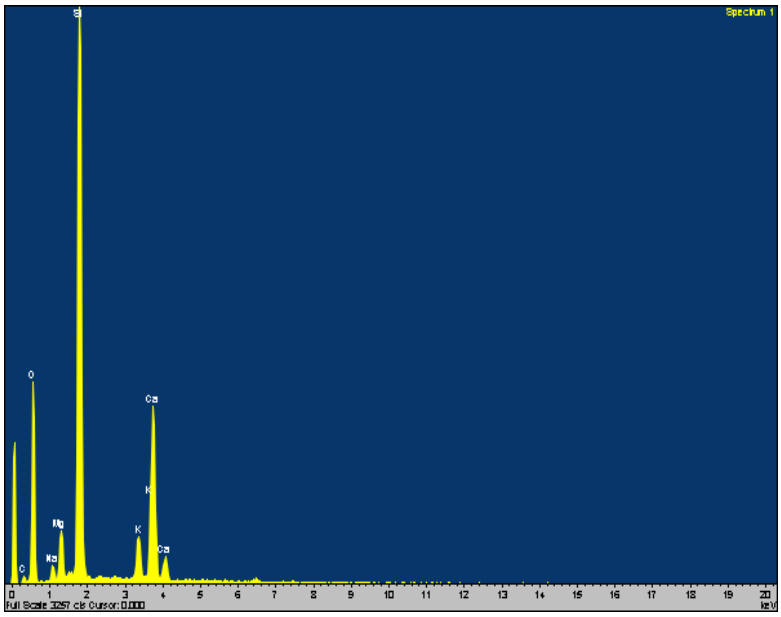

Copious amount of gel exudation from coarse aggregate

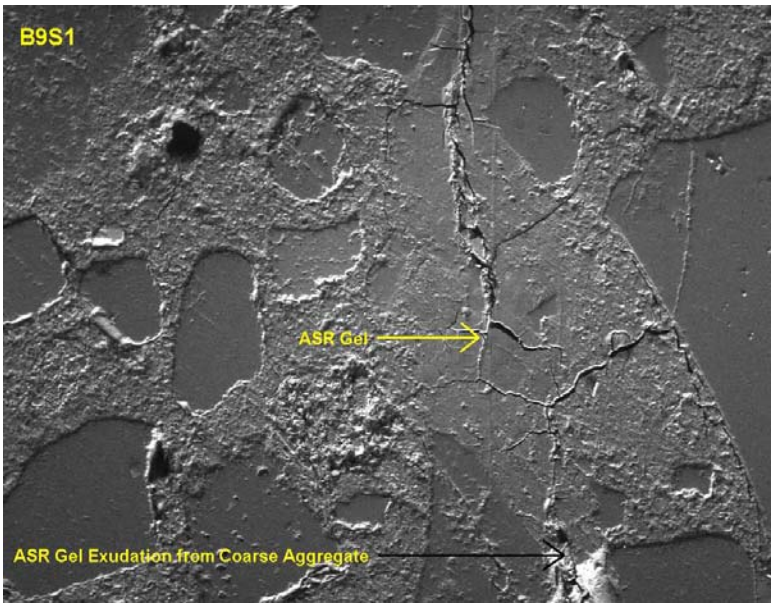

Potassium dot map of gel exudation from previous BSE image

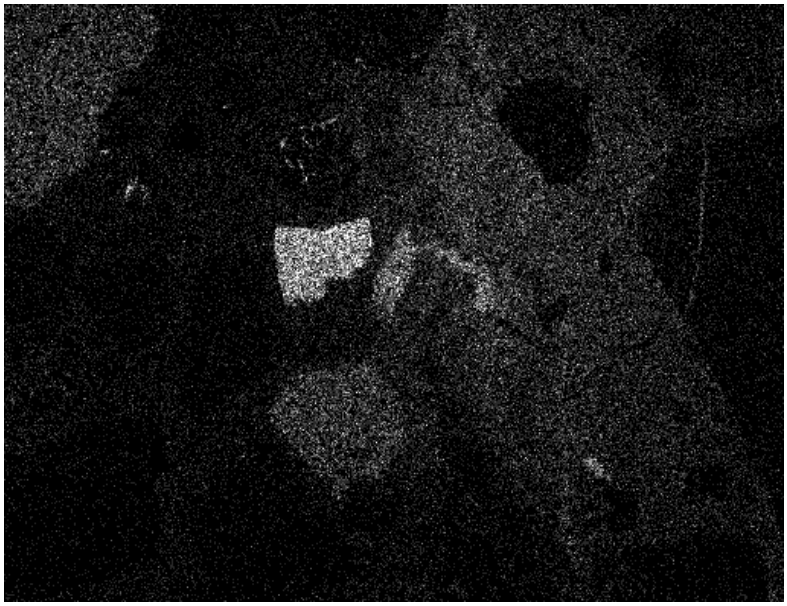

Silica dot map from previous BSE image

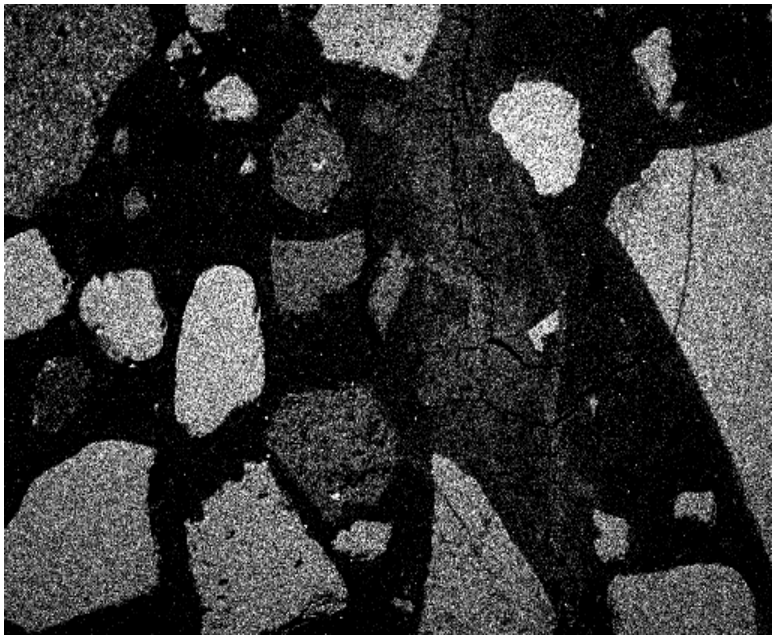

Coating of ASR gel at interface between PVC conduit and paste

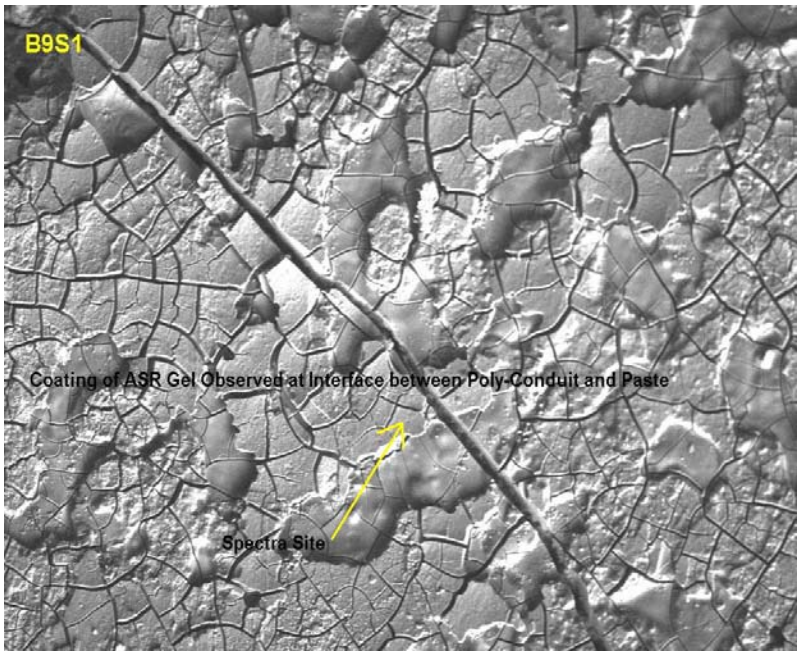

SEM/BSE spectra of gel chemistry from previous BSE image

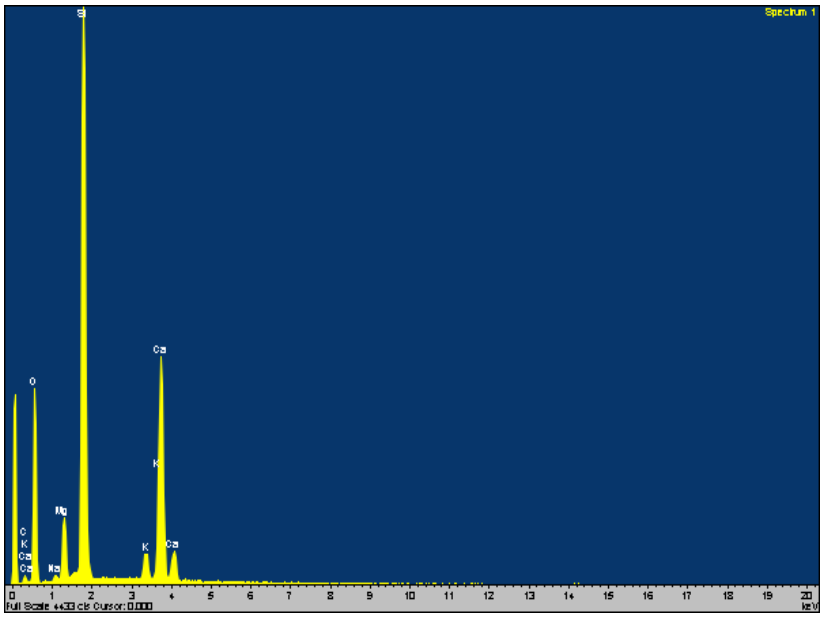

B9C5 SEM Documentation

Image illustrating ASR gel exudation

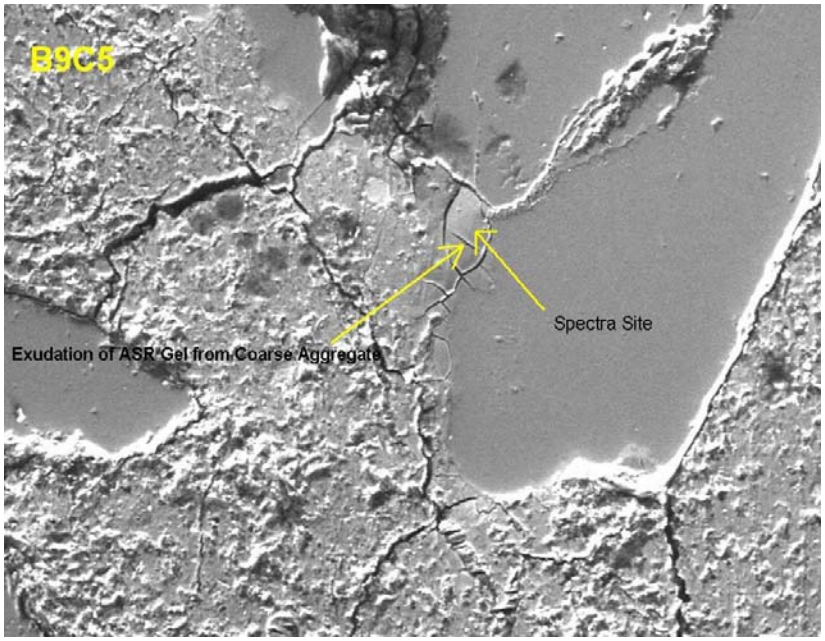

SEM/EDS spectra of gel exudation product

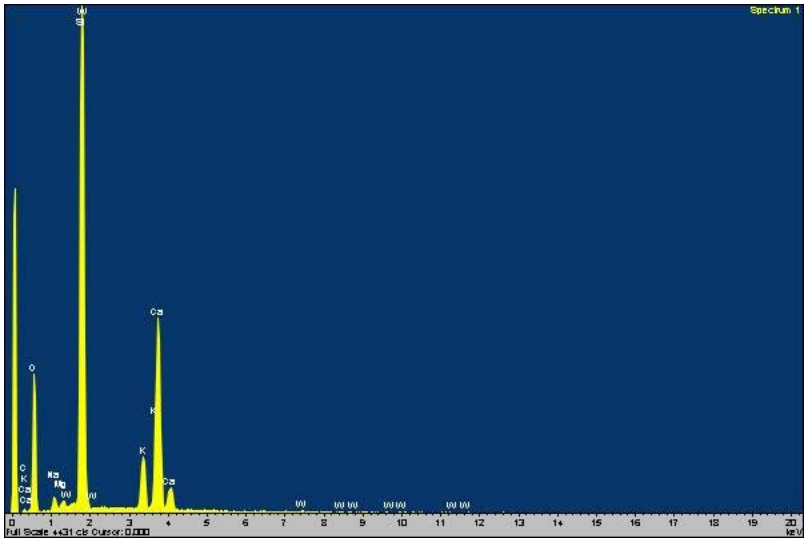

BSE image illustrating highly distress aggregate

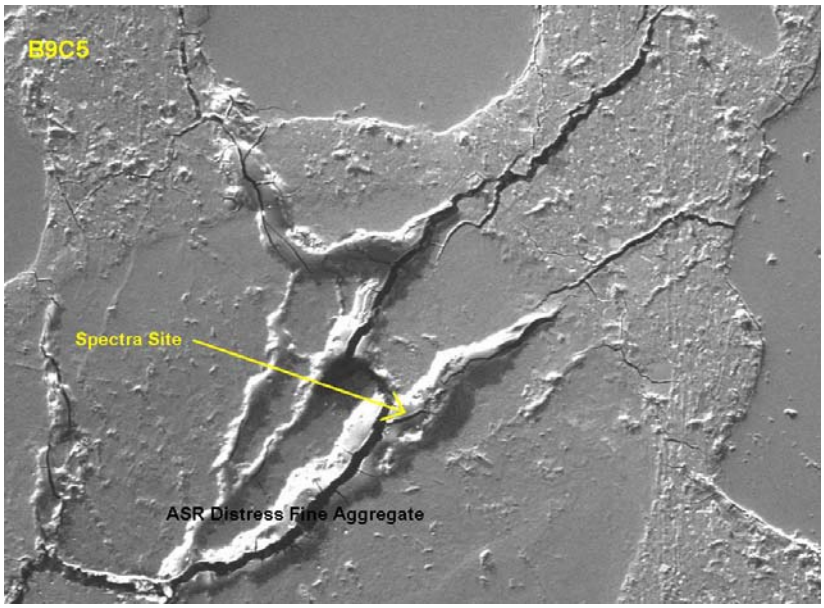

SEM/EDS spectra of from previous BSE image

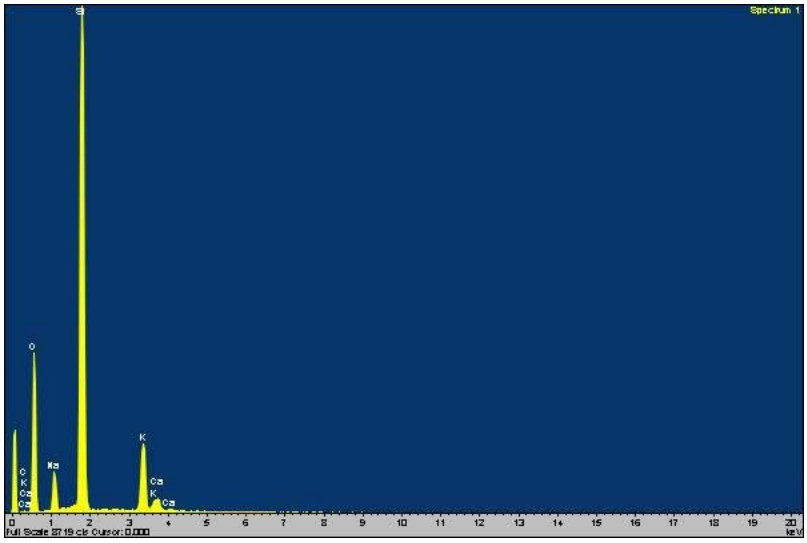

ASR distressed fine aggregate illustrating level of distress

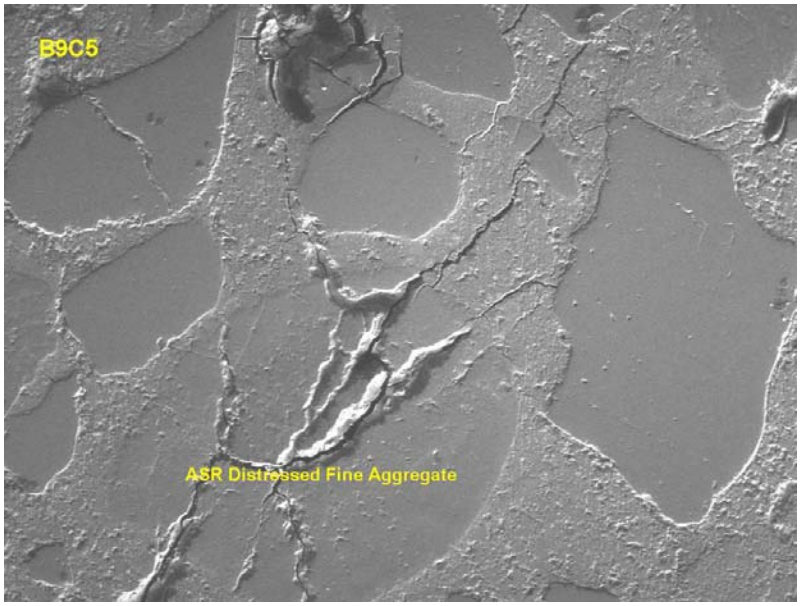

Left image is potassium dot map and right image is silica dot map

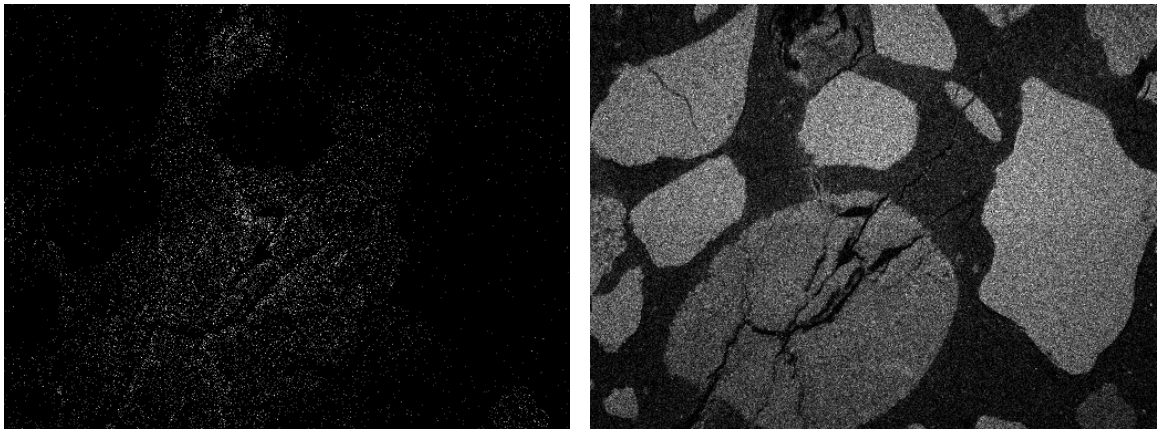

B9C6 SEM Documentation

BSE image illustrating ASR reaction rim and gel formation

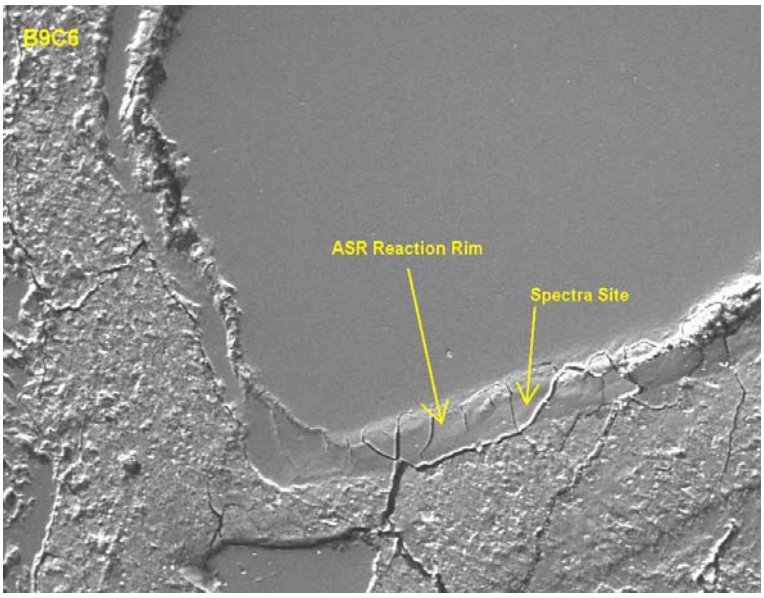

EDS spectra illustrating ASR gel chemistry from previous BSE image

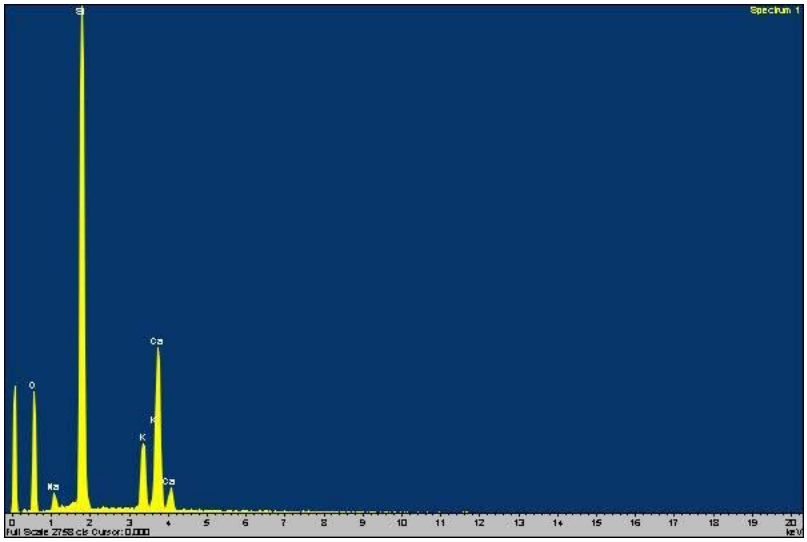

Illustration of ASR reaction rim

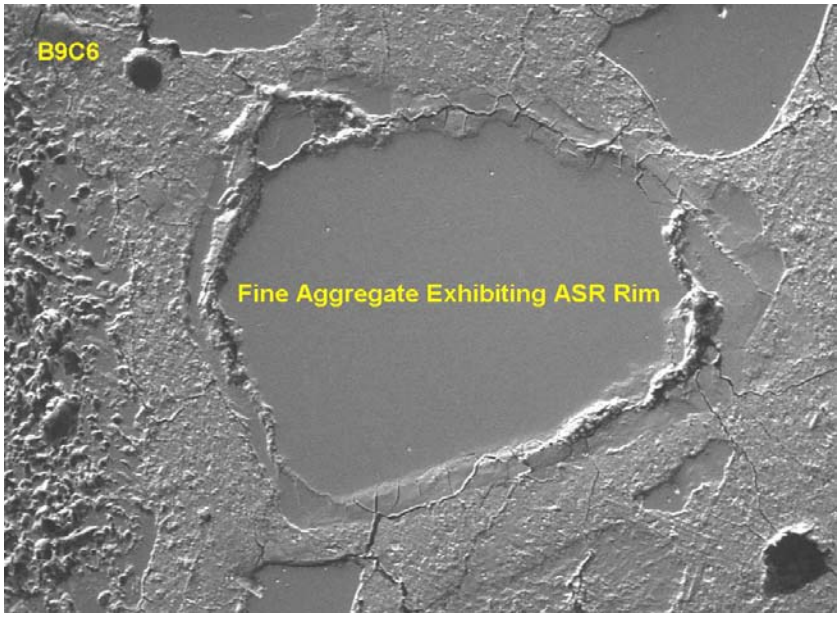

SEM/EDS dot maps illustrating concentration of gel with respect to reactivity of previous BSE image

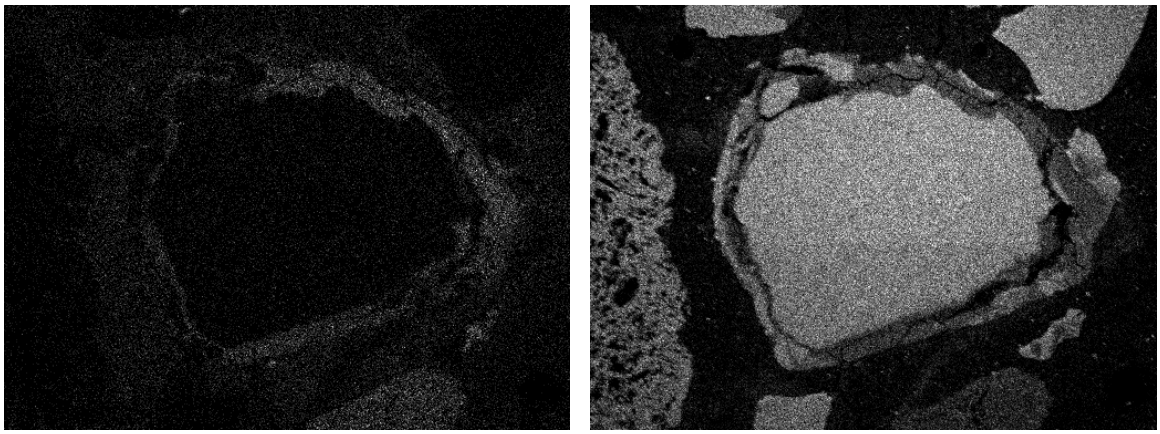

ASRII Beam 1 SEM Documentation

Image illustrating droplet of gel that oozed out of aggregate

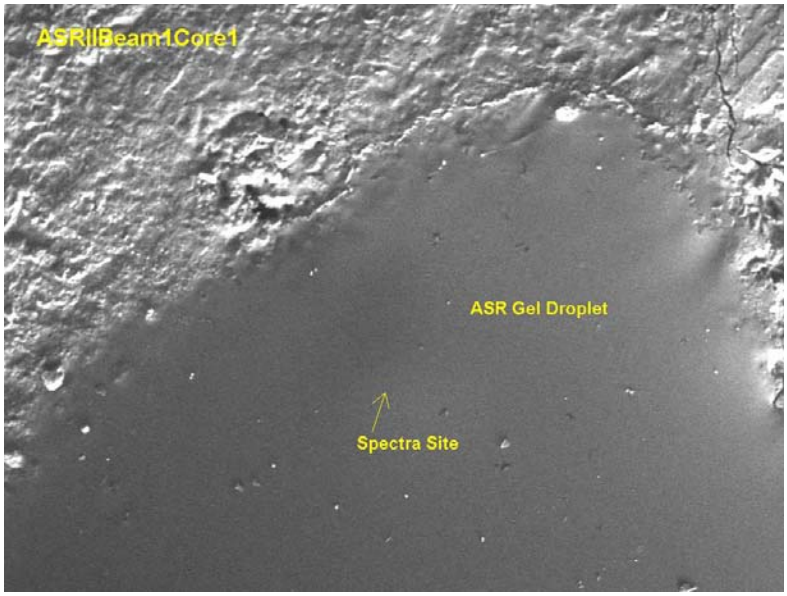

Spectra taken from previous BSE image illustrating gel chemistry

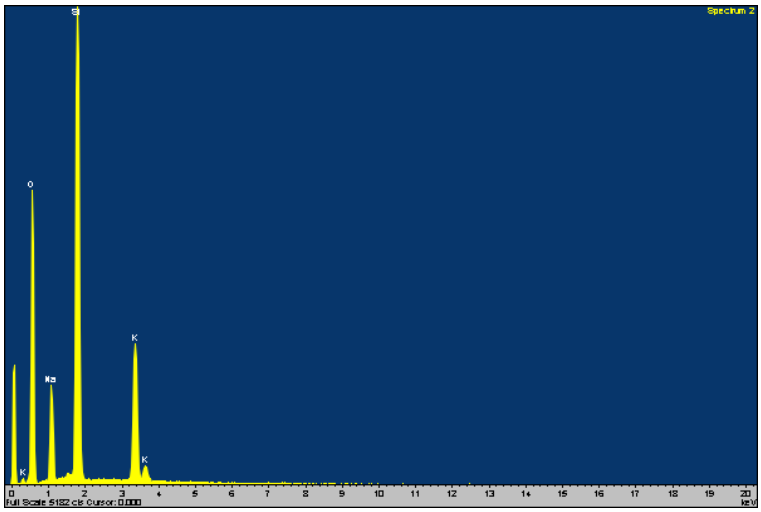

ASR gel accumulation in elongated air void

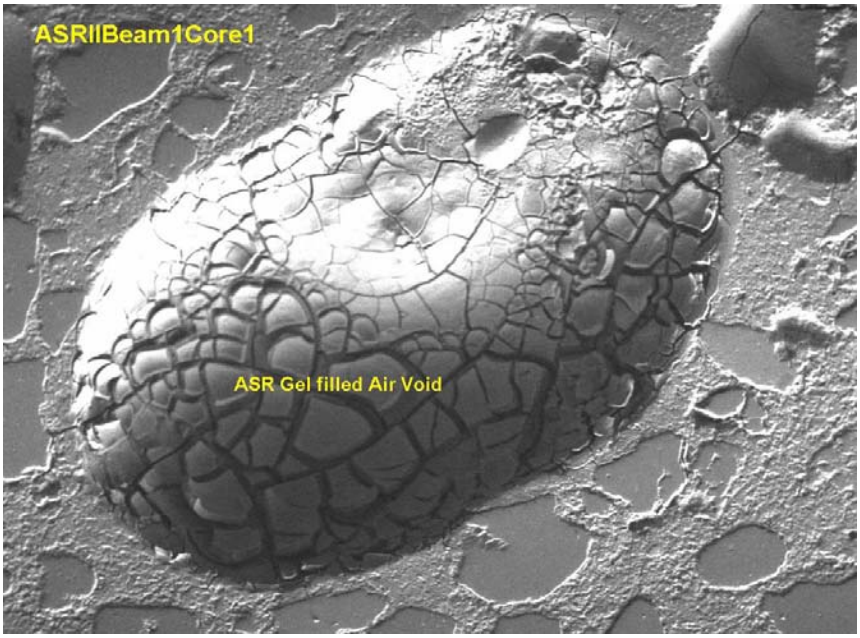

Qualitative study of damage severity in each sample and damage progression through the length of the sample. (Comparison of micro structural damage between all samples).

Core ID (length)	Level of ASR Distress	Level of DEF Distress	Distress Characteristics and Crack Orientation
B9S1(6-1/8″)	Medium to late stage ASR	Very low to Negligible	One vertical macro crack from surface to 2-inch depth. Significant amount of cracking associated with reactive particles, some oriented in radial fashion. Approximately 2 inches from surface is a network of fine micro cracks filled with ettringite-oriented parallel to sub parallel to the surface.
B9S2(2-5/8″)	Medium to late stage ASR	Very low to Negligible	One vertical macro crack from surface to 1/2-inch depth. Significant amount of cracking associated with reactive particles, some oriented in radial fashion. Approximately 2 inches from surface is a network of fine micro cracks filled with ettringite-oriented parallel to sub parallel to the surface.
ASRIIBeam1Core1 (3-5/8″)	Very early stage ASR	No Evidence	Very fine micro cracks at surface of core. Did not observe ASR distress crack on polished sections.
ASRIIBeam1Core2 (3-5/8″)	Very early stage ASR	No Evidence	Very fine micro cracks at surface of core. Did not observe ASR distress crack on polished sections.
ASRIIBeam1Core3 (3-5/8″)	Very early stage ASR	No Evidence	Very fine micro cracks at surface of core. Did not observe ASR distress crack on polished sections.
ASRIIBeam1Core4 (3-5/8″)	Very early stage ASR	No Evidence	Very fine micro cracks at surface of core. Did not observe ASR distress crack on polished sections.

B9C3(2″)	Late stage ASR	Very low to Negligible	Macro cracks observed at surface of core. At approximately 1-1/2″ from surface, a network of fine ettringite filled micro crack-oriented parallel to sub parallel to the surface was observed.
B9C4(3″)	Late stage ASR	Very low to Negligible	Macro cracks observed at surface of core. At approximately 1-1/2″ from surface, a network of fine ettringite filled micro crack-oriented parallel to sub parallel to the surface was observed.
B9C5(2″)	Late stage ASR	Very low to Negligible	Macro cracks observed at surface of core. At approximately 1-1/2″ from surface, a network of fine ettringite filled micro crack-oriented parallel to sub parallel to the surface was observed.
B9C6(5-1/2″)	Late stage ASR	Very low to Negligible	Macro cracks observed at surface of core. At approximately 1-1/2″ from surface, a network of fine ettringite filled micro crack-oriented parallel to sub parallel to the surface was observed.
B9C7(4-3/4″)	Late stage ASR	Very low to Negligible	Macro cracks observed at surface of core. At approximately 1-1/2″ from surface, a network of fine ettringite filled micro crack-oriented parallel to sub parallel to the surface was observed.

The following schematic is a representation of the cracking and orientation observed in these specimens.

Representation of Micro

Structural Damage

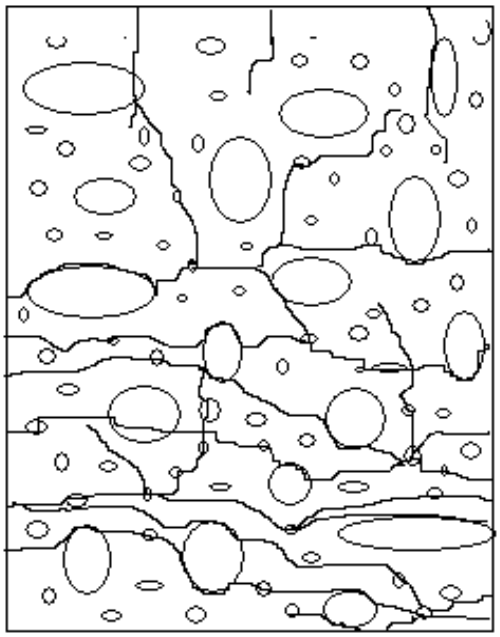

Conclusion: Based on this analysis ASR is the primary PCD mechanism responsible for the distressed concrete in the B9 cores. Although gel formation was observed in very sparse amount, the ASRII beam 1 cores showed very little evidence of distress from ASR. Microcrystalline chert in both the fine and coarse aggregates is the principle lithologic mineral associated with the reaction. Micro structural damage from the ASR resulted in an extensive network of fine micro cracks (see above images) observed throughout these cores. The expansive reactions resulting in development of larger vertical surface crack observed in all of the cores except the ASR II cores. With the aid of our stereomicroscope very fine surface cracks were observed in the ASR II cores.

It is inconclusive whether DEF played a role in the distressed concrete. Due to the limited occurrence of true gapping (resulting from bulk expansion of the paste), DEF does not appear to have played a significant role in the distress. Most of the sites that appear to be gapping were created as a result of ASR generated micro cracks intersecting the aggregate and then partially wrapping around them (fluorescent and SEM demonstrates this occurrence) with subsequent precipitation of ettringite. Bifurcation of the intersecting cracks can sometimes create a situation that appears to look like gapping has occurred. It is unclear whether the ettringite precipitation and potential imbibing of moisture could generate enough stress to potentially widen these cracks at the paste aggregate interfaces. Some ettringite was noted as small discrete nests within the paste and in air voids. A coating of both ettringite and ASR gel (primarily gel) was also noted on the rebar imprint where the rebar had debonded (on imprint of rebar) during the coring process in Core B9C7. Gel accumulation was noted at the interface between the PVC conduit and the paste as well in core B9S1. This indicates that either a separation occurred (debonding)

between the rebar and paste forming a gap large enough for ettringite and gel to form or possibly settlement gaps or thermal cracks had occurred.

PETROGRAPHIC ANALYSIS REPORT 2

Petrographic Analysis

02/09/2011

Report:	TTI ASR DEF
Date Received:	12/01/2010
Structure Type:	Unknown
Sample Type:	Cores
Location:	Unknown
Coarse Aggregate Producer:	NA
Coarse Aggregate Type:	Siliceous Gravel
Fine Aggregate Producer:	NA
Fine Aggregate Type:	Siliceous Sand
Cement Producer:	NA
Cement Type:	NA

Comments:

This petrographic analysis was performed in response to a request from Dr. Joseph Bracci to assist the Texas A&M University in an ASR/DEF investigation of nine submitted cores. The following objectives were specified by Texas A&M:

- General observations on concrete quality. (Comments on placement, mixture proportions, water-cement ratio).
- Visual documentation of ASR and/or DEF micro structural damage. (Images depicting gel/ettringite locations, cracking and gapping of paste/aggregate interfaces).
- Qualitative study of damage severity in each sample. (Comparison of micro structural damage between all samples).
- Qualitative study of damage progression through the length of the sample. (Comparison of micro structural damage in surface and core concretes of each sample).

General observations on concrete quality (comments on placement, mixture proportions, water-cement ratio)

General Appearance: Fourteen cores were submitted for analysis and were designated as: ASR IIS2C1, ASRIIS2C2, ASRIIS2C3, ASRIIS2C4, ASRIIS2C5, ASRIIS2C6, ASRIIB2C7, ASRIIB2C8, Trans Bar B1, Trans Bar B3, Conc. Only B1, Conc. Only B3, Long Bar B1 and Long Bar B3. The majority of the submitted cores were 3-3/4 inches in diameter and ranged from 1-3/4 to 9-1/2 inches in length except for ASR II Specimen 2 Cores 1, 3, and 4 which were 6 inches in diameter. Most of the cores had obvious distress cracks on the surface of the core.

Water/Cement Ratio: None of the cores had abnormal or elevated w-c ratio. Based on appearance of the paste (color, ferrite distribution and granularity of the hydrates), estimates of w-c ratio for the 14 cores were consistent with the mix design.

Proportioning and types of aggregate: Based on microscopic observations, the paste volume indicates a high sack mix, low coarse aggregate factor and gap grading was noted in all the cores. Coarse aggregate consist of siliceous gravel comprised of chert, agate, and granite. Fine aggregate consist of quartz, agate, feldspar, and chert. The following table summarizes the point count data:

Paste content and appearance: Paste content is indicative of a high sack mix and appearance is normal, except for the numerous fine micro cracking and reaction products. The reaction products consist of ASR gel and ettringite. No fly ash or other mineral admixtures were present in the mix.

Air Content: Non-Air Entrained.

Degree of Hydration: Normal.

Carbonation: Carbonation was noted at the exterior surface of all the cores. The following chart represents the depth of carbonation for each core:

Core ID	Carbonation Depth from Exterior Surface of Core
ASR II Specimen 2 Core 1	2 mm
ASR II Specimen 2 Core 2	Minimal
ASR II Specimen 2 Core 3	Minimal
ASR II Specimen 2 Core 4	2.3 mm
ASR II Specimen 2 Core 5	3 mm
ASR II Specimen 2 Core 6	4 mm
ASR II Beam 2 Core 7	2 mm
ASR II Beam 2 Core 8	2 mm
Trans Bar Beam 1	3 mm
Trans Bar Beam 3	3 mm
Conc. Only Beam 1	2 mm
Conc. Only Beam 3	2 mm
Long Bar Beam 1	2 mm
Long Bar Beam 3	2 mm

Deleterious Reaction Mechanism: The primary distress mechanism in all the cores is attributed to ASR. Although ettringite was noted in various amounts within some of the samples, it is not believed to have

contributed much to the overall distress of the specimens. The following table describes the various levels of distress observed in the cores:

Sample #	Surface Distress	Level of ASR Distress	Reactive Aggregate count/cross-sectional length	Evidence of DEF
ASR II Specimen 2 Core 1	Mod–High (surface cracks to 14 mm deep from the surface)	Mod. to High (reactive particles noted near surface of core)	52 reactive particles counted in top 3-3/4 inches of core	Ettringite was noted within voids, cracks and at paste aggregate interfaces and as semi continuous coating on re bar imprint
ASR II Specimen 2 Core 2	High (Surface cracks up to 11 mm deep)	Mod to High with reactive particles noted near top of core.	27 reactive particles counted in top 1-3/4 inches of the core	Ettringite was noted within voids, cracks and at paste aggregate interfaces
ASR II Specimen 2 Core 3	Moderate (surface cracks tighter than previous cores, to 10 mm)	High	56 reactive particles counted in top 3-5/8 inches from the surface	Ettringite noted within voids, cracks and at paste aggregate interfaces
ASR II Specimen 2 Core 4	High (surface crack traced from surface to re bar at 2-1/2 inches deep)	High	70 reactive particles counted in top 3-3/4 inches from the surface	Ettringite noted within voids, cracks, at paste aggregate interfaces and as semi-continuous coating at re bar imprint
ASR II Specimen 2 Core 5	Low to Moderate (surface crack to 1-1/4 inch intersecting rebar)	Moderate	38 reactive particles counted in top 3-1/2 inches from the surface	Minor accumulations of ettringite
ASR II Specimen 2 Core 6	Low	Low to Moderate (more reactive particles near the bottom of this section)	Eight reactive particles counted in top 2 inches from the surface	Negligible accumulations
ASR II Beam 2 Core 7	Low to moderate	Moderate	34 reactive particles counted in top 3-7/8 inches from the surface	Negligible accumulations

ASR II Beam 2 Core 8	Low	Low (reactive particles were deeper in section)	Seven reactive particles counted in top 3-3/4 inches from the surface	Negligible accumulations
Trans Bar Beam 1	Low to Moderate	Moderate (horizontal crack at re bar)	32 reactive particles counted in top 3-3/4 inches from the surface	Negligible accumulations
Trans Bar Beam 3	Moderate	Moderate (vertical crack intersected re bar)	52reactive particles counted in top 4 inches from the surface	Negligible accumulations (re bar has good bond with paste)
Conc. Only Beam 1	Moderate (surface cracks 20 mm)	Moderate (ASR particles more abundant the farther from the surface)	33 reactive particles counted in top 3-3/4 inches from the surface	Negligible accumulations
Conc. Only Beam 3	Low (11 mm surface cracks)	Low to Moderate (ASR particles more abundant the farther from the surface)	17 reactive particles counted in top 3-3/4 inches from the surface	Negligible accumulations
Long Bar Beam 1	High (surface cracks to 7/8 inch)	High	57 reactive particles counted in top 3-3/4 inches from the surface	Negligible accumulations
Long Bar Beam 3	Moderate to High	High	40 reactive particles counted in top 2-3/4 inches from the surface	Ettringite noted in voids, cracks, paste aggregate interfaces and on the rebar imprints

Microscopic documentation of ASR and/or DEF micro structural damage.
(Images depicting ASR gel/ettringite formation, cracking and gapping at paste/aggregate interfaces)

ASR Related Evidence

ASR Filled Air Voids Adjacent To Reactive Particle

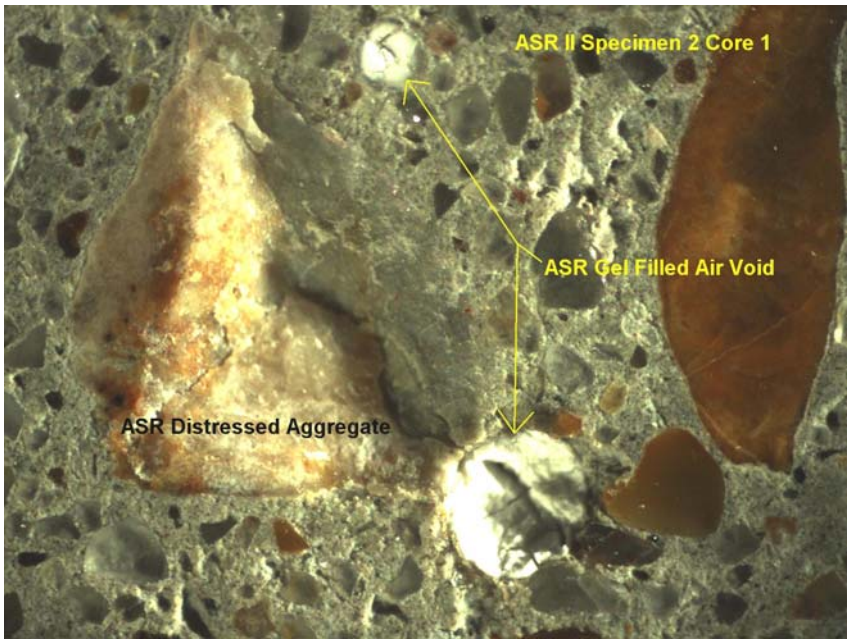

Partial Coating of Ettringite within Aggregate Socket

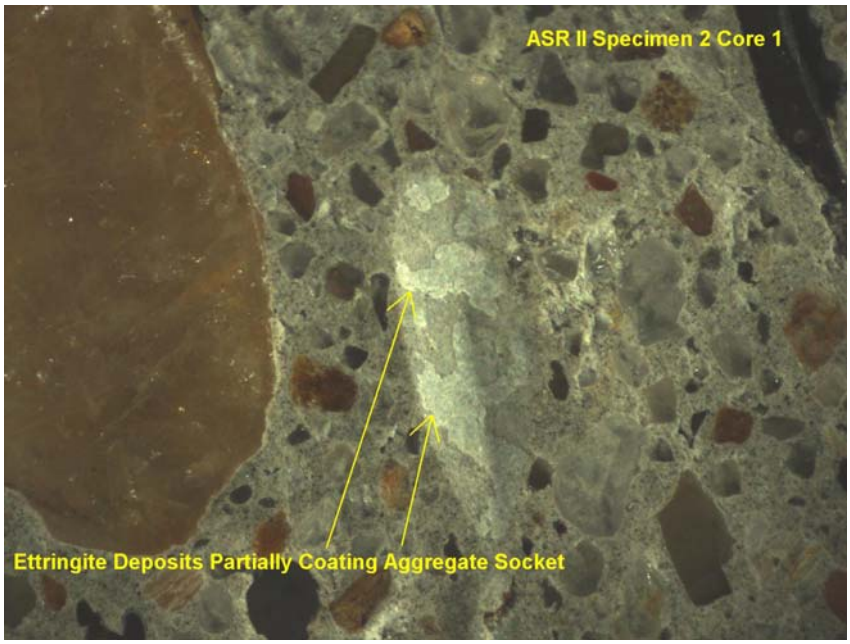

ASR Gel Exudation Noted from Reactive Aggregate Particle

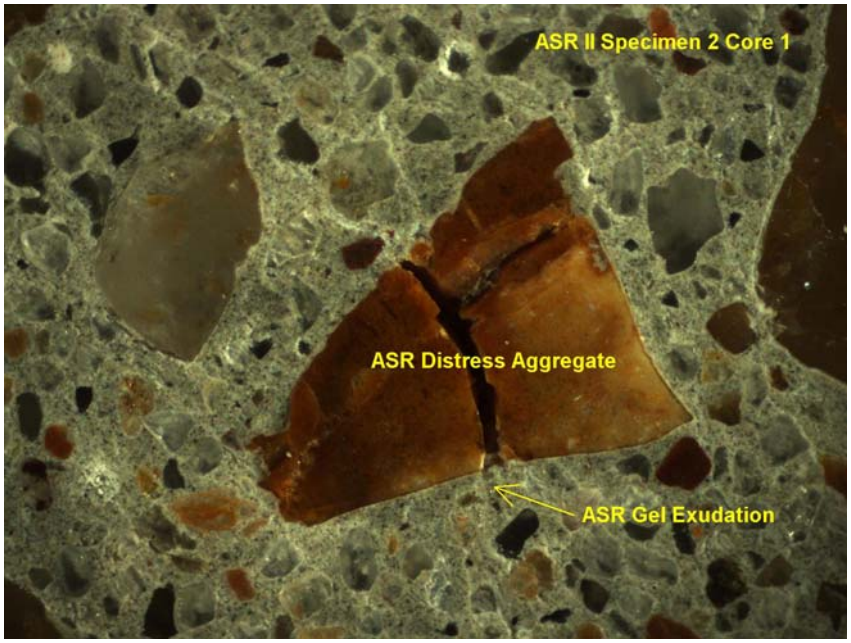

Accumulation of Ettringite in Air Void

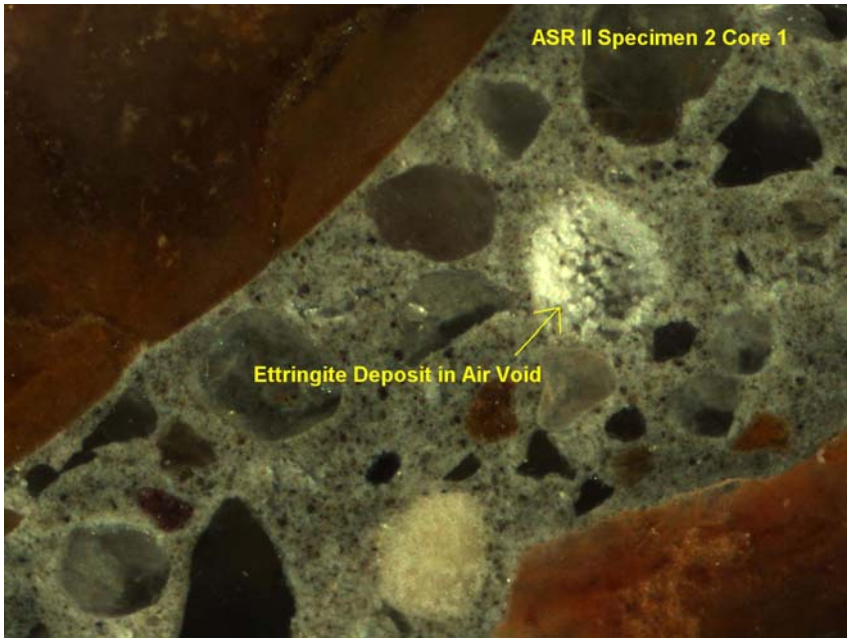

Image on Left Illustrates Coating of Ettringite and Possible Calcium Hydroxide on Imprint of Rebar; Right Image Illustrates Normal Rebar Imprint without Coating

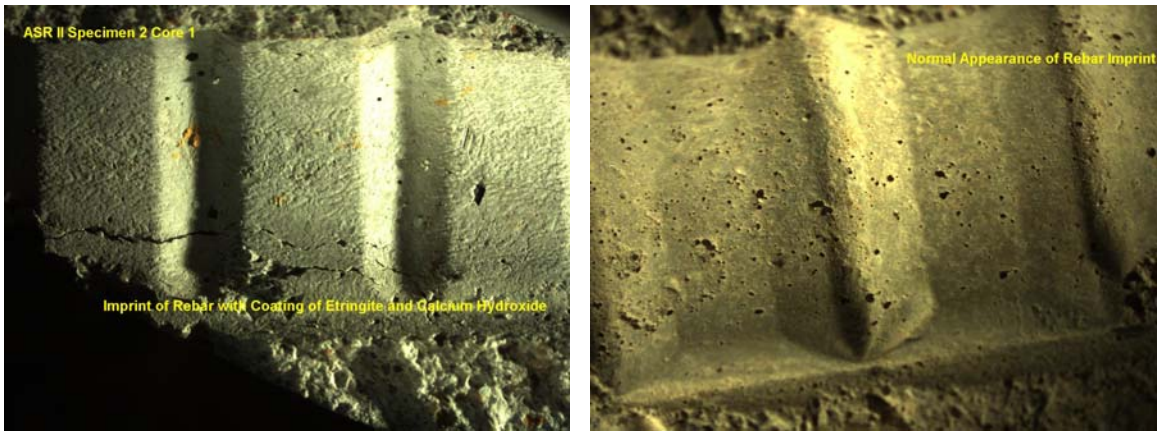

Image Illustrating Carbonation Zone at Top of Core and Accumulation of ASR Gel within Air Void

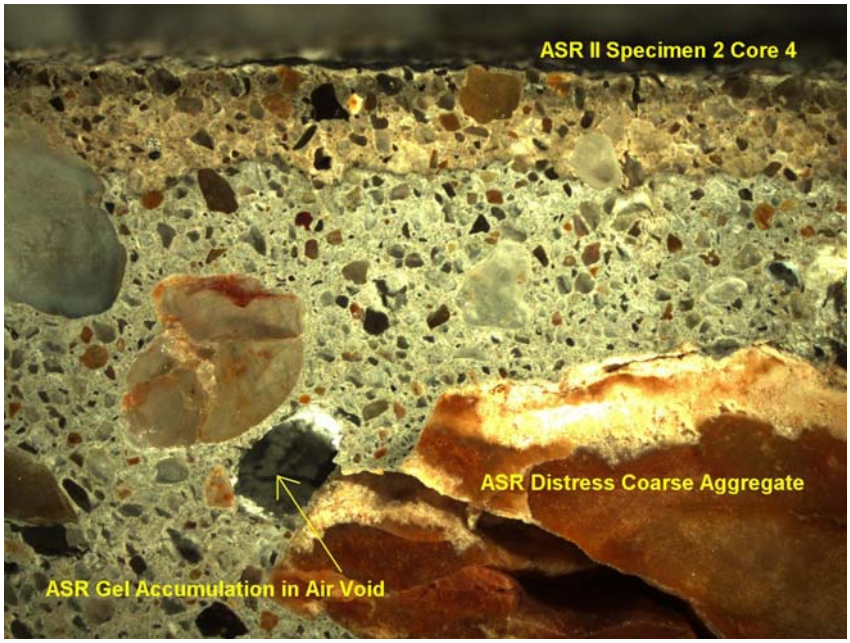

ASR Gel Filled Air Voids Adjacent to Reactive Particles

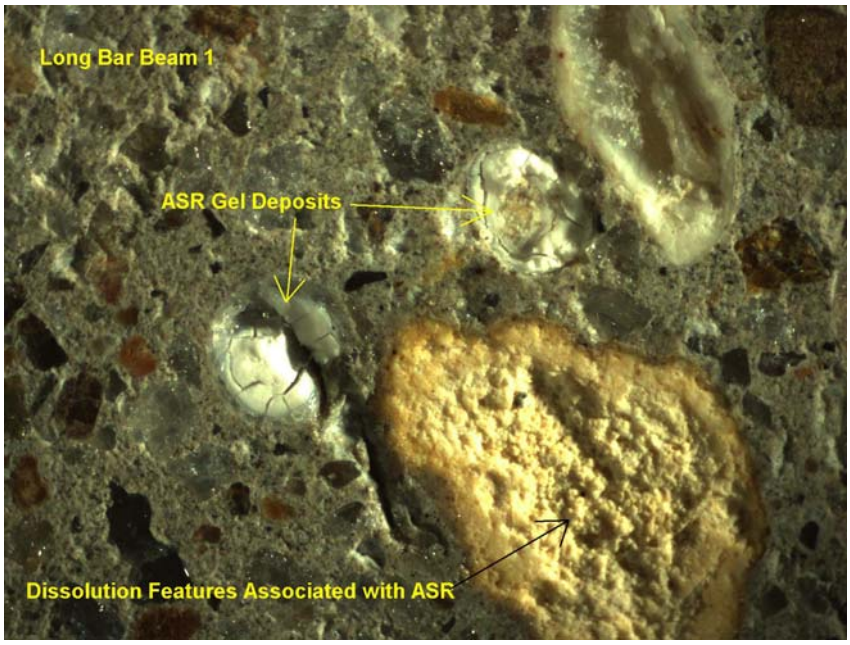

ASR Gel Filled Air Void Adjacent to Reactive Coarse Aggregate

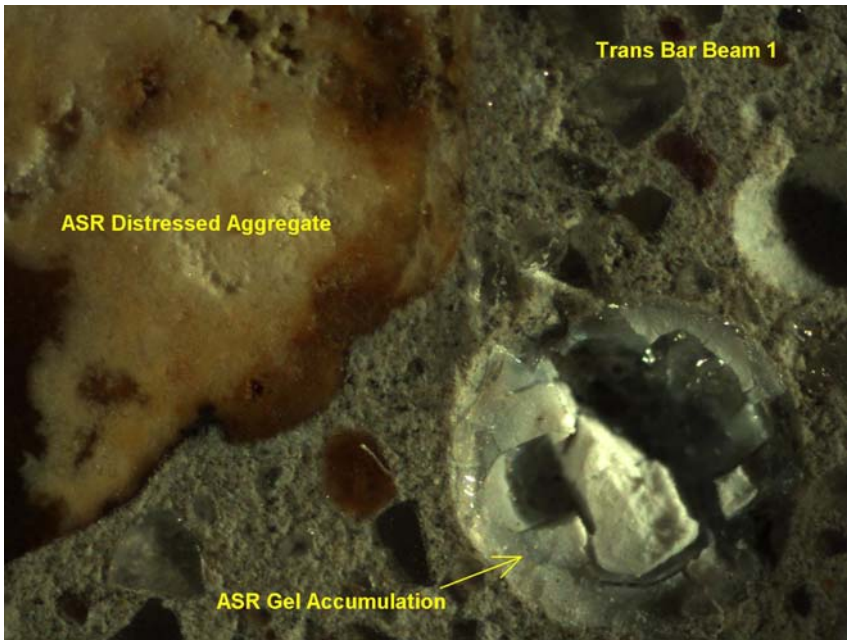

Concluding Comments: Based on this analysis the primary cause for the distress concrete is related to ASR. As indicated by the above table, the degree of ASR distress varies from low to high degrees of reactivity. Although Ettringite is noted in numerous locations within some of the cores, it is not consistent with features (Ettringite filled gapped around aggregate, nest of ettringite in paste) associated with DEF; however, the Ettringite formation within some of the cores may have played a minor role in the distress. The ettringite deposits as coating on many of the rebar imprints does indicate that debonding had occurred.

PETROGRAPHIC ANALYSIS REPORT 3

Petrographic Analysis

12/08/2011

Report:	TTI ASR DEF
Date Received:	10/01/2011
Structure Type:	Unknown
Sample Type:	Cores
Location:	Unknown
Coarse Aggregate Producer:	NA
Coarse Aggregate Type:	Siliceous Gravel
Fine Aggregate Producer:	NA
Fine Aggregate Type:	Siliceous Sand
Cement Producer:	NA
Cement Type:	NA

Comments:

This petrographic analysis was performed in response to a request from Dr. Joseph Bracci to assist the Texas A&M University in an ASR/DEF investigation of six submitted cores. The following objectives were specified by Texas A&M:

- General observations on concrete quality. (Comments on placement, mixture proportions, water-cement ratio).
- Visual documentation of ASR and/or DEF micro structural damage. (Images depicting gel/ettringite locations, cracking and gapping of paste/aggregate interfaces).
- Qualitative study of damage severity in each sample. (Comparison of micro structural damage between all samples).
- Qualitative study of damage progression through the length of the sample. (Comparison of micro structural damage in surface and core concretes of each sample).

General observations on concrete quality (comments on placement, mixture proportions, water-cement ratio)

General Appearance: Six cores were submitted for analysis and were designated as: 5-1, 5-2, 5-3, 8-1, 8-2 and 8-3. The submitted cores were 3-3/4 inch in diameter and ranged from 2-1/2 to 5.0″ inches in length. All of the cores had obvious distress cracks on the surface of the core. Reaction product was noted in voids and a coating on detached re-bar surfaces.

Water/Cement Ratio: None of the cores had abnormal or elevated w-c ratio. Based on appearance of the paste (color, ferrite distribution, and granularity of the hydrates) estimates of w-c ratio for the six cores were consistent with the mix design.

Proportioning and types of aggregate: Based on microscopic observation, the paste volume indicate a high sack mix, low coarse aggregate factor, and gap grading was noted in all the cores. Coarse aggregate consist of siliceous gravel comprised of chert, agate, granite and spares amounts of lightweight aggregate. Fine aggregate consist of quartz, chert, agate, and feldspar.

Paste content and appearance: Paste content is indicative of a high sack mix and appearance is normal except for the numerous fine micro cracking and reaction products. The reaction products consist of ASR gel and ettringite. No fly ash or other mineral admixtures were present in the mix.

Air Content: Non-Air Entrained.

Degree of Hydration: Normal.

Carbonation: Carbonation was noted at the exterior surface of all the cores. The following chart represents the depth of carbonation for each core:

Core ID	Carbonation Depth from Exterior Surface of Core
5-1	3.5 mm
5-2	2 mm
5-3	2 mm
8-1	2 mm
8-2	2 mm
8-3	3 mm

Deleterious Reaction Mechanism: The primary distress mechanism in all the cores is attributed to ASR. ASR gel was observed in air voids, within distress aggregate, and as exudation from reactive particles. Although ettringite was noted in various amounts within some of the samples it is not believed to have contributed much to the overall distress of the specimens. The ettringite was noted in air voids, within micro cracks, and as partial coating on surface of detached rebar. The following table describes the various levels of distress observed in the cores:

Sample #	Surface Distress	Level of ASR Distress	Reactive Aggregate count/cross-sectional length	Evidence of DEF
5-1	High (multiple surface cracks to 1 inch deep from the surface)	High with reactive particles noted throughout the core	123 reactive particles counted in top 3-1/2 inches of core	Ettringite was noted within voids, cracks and at paste aggregate interfaces
5-2	Moderate (Surface cracks up to ½ inch deep)	Moderate with reactive particles noted throughout the core	76 reactive particles counted in top 3-1/2 inches of the core	Ettringite was noted within voids, cracks, and at paste aggregate interfaces
5-3	Low to Moderate (Surface cracks up to 5/8-inch deep)	Moderate with reactive particles noted throughout the core	66 reactive particles counted in top 3-3/4 inches from the surface	Ettringite noted within voids, cracks, and at paste aggregate interfaces, and as semi-continuous coating at rebar imprint
8-1	Low to Moderate (surface cracks to 5/8 inches deep)	Moderate with reactive particles noted throughout the core. ASR gel was also observed as coating on rebar imprint.	64 reactive particles counted in top 3-1/2 inches from the surface	Ettringite noted within voids, cracks, at paste aggregate interfaces, and as semi-continuous coating at rebar imprint
8-2	Low to Moderate (surface cracks to 1/4 inch)	Moderate with reactive particles noted throughout the core (surface cracks to ¼ inch from surface).	62 reactive particles counted in top 3-1/2 inches from the surface	Ettringite was noted within voids, cracks, and at paste aggregate interfaces
8-3	Low to Moderate (surface cracks to ¾ inch deep)	Moderate with reactive particles noted throughout the core. ASR gel was also observed as coating on rebar imprint (surface cracks to ¾ inch from surface).	52 reactive particles counted in top 2-1/2 inches from the surface	Ettringite noted within voids, cracks, at paste aggregate interfaces, and as semi continuous coating at rebar imprint

The following Stereoscopic and SEM images illustrate distress features associated with the ASR degradation:

Image illustrating ASR distress features in core 5-2

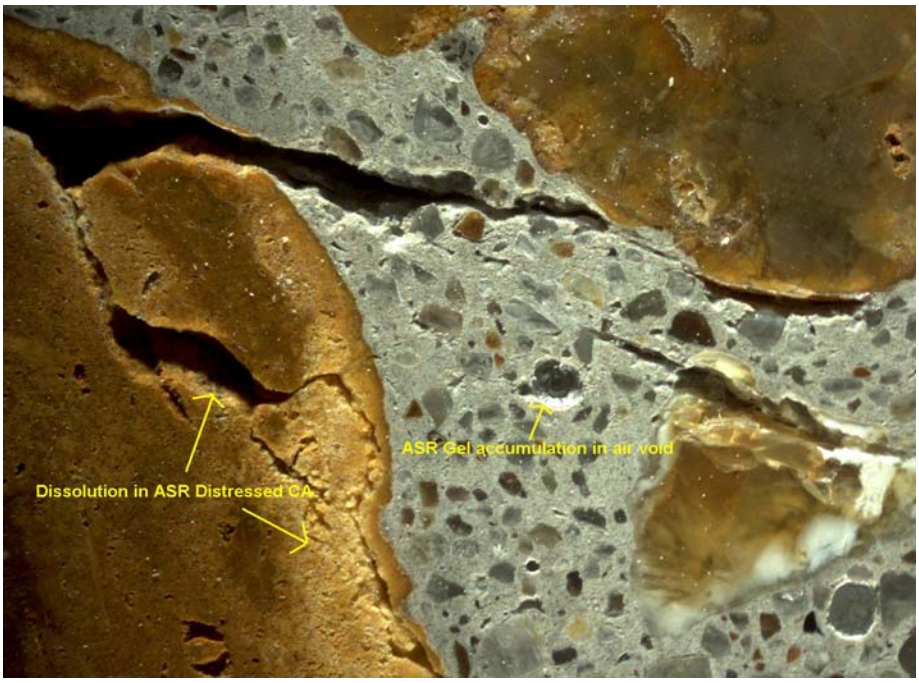

Image illustrating ASR distress in intermediate size aggregate

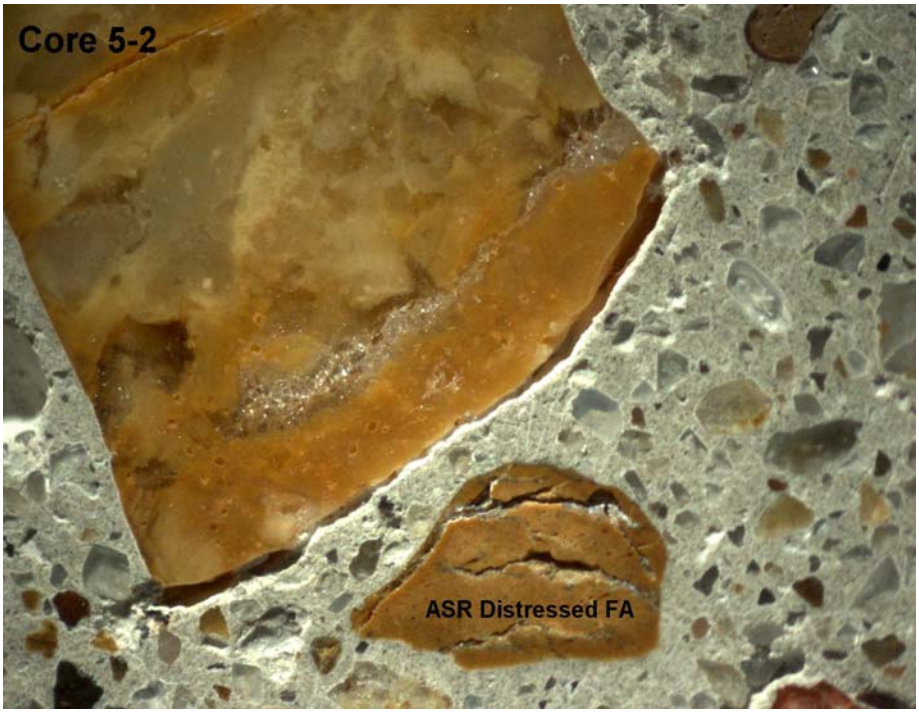

Image illustrating ASR Distress

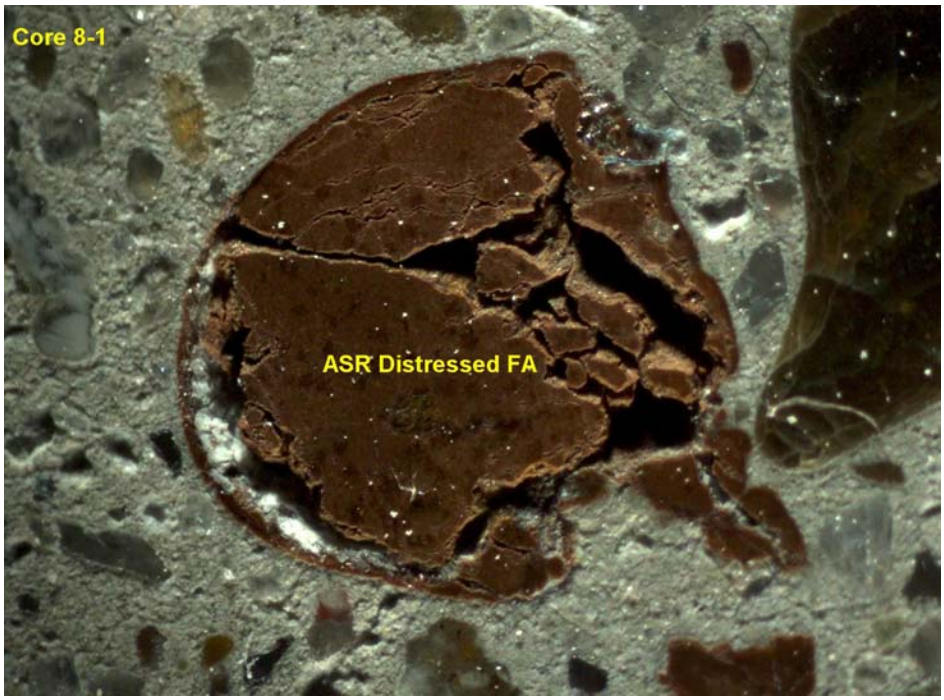

Image illustrating ASR gel accumulation in air void adjacent to reactive particle

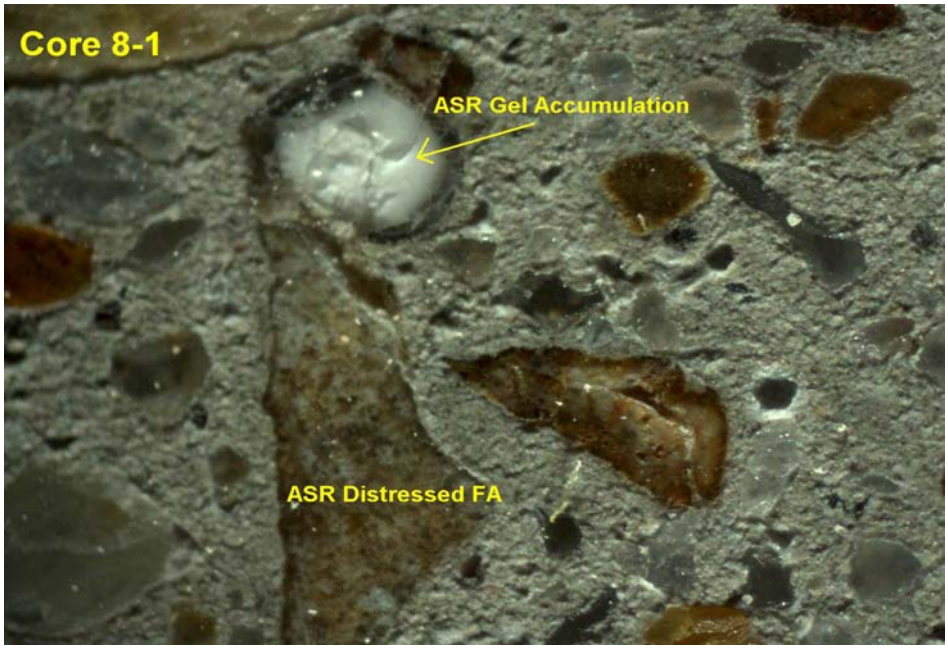

Image illustrating ASR distress aggregate

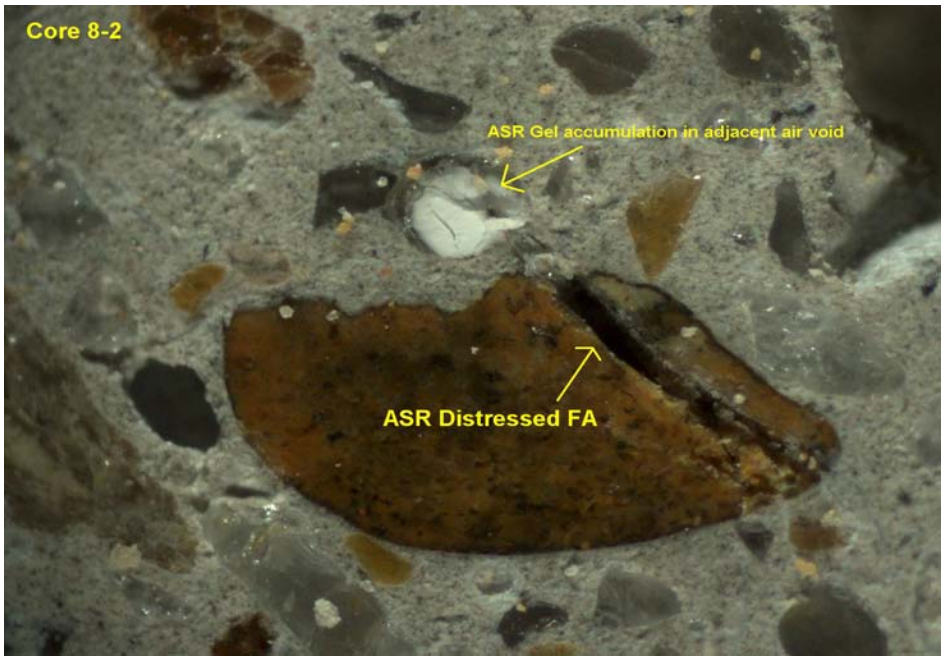

Image illustrating fine network of ettringite-filled micro cracks

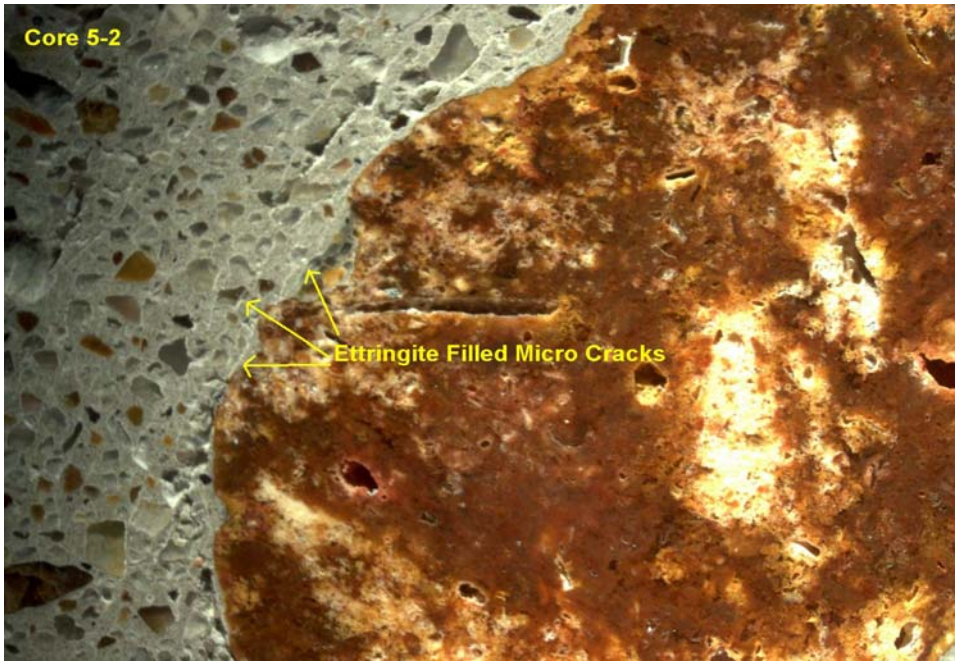

SEM BS image illustrating ASR gel formation on outer rim of distress aggregate

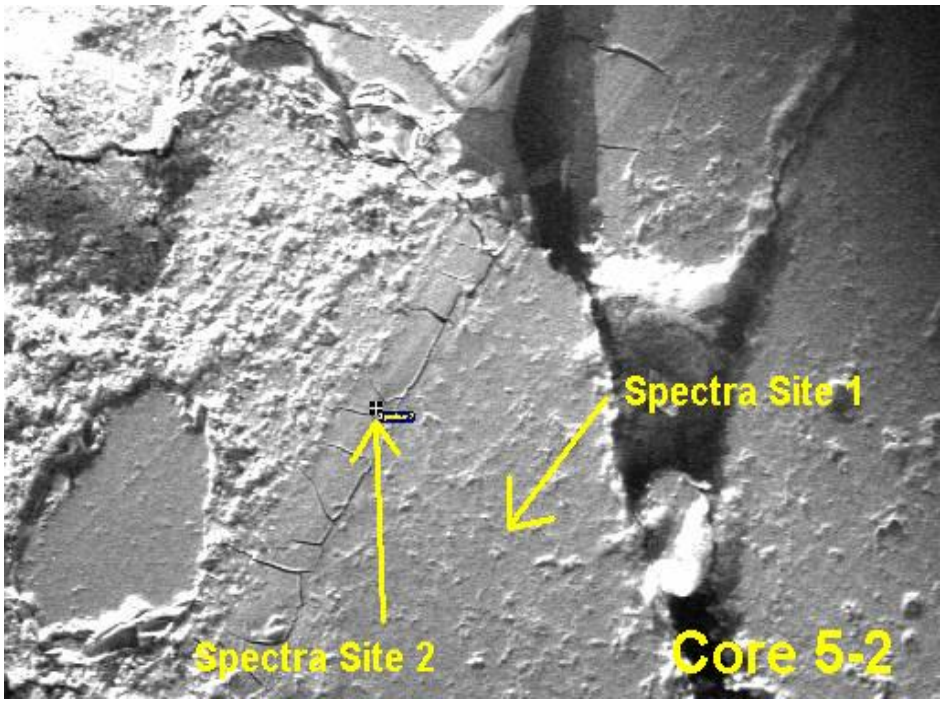

Spectra 1 from previous BS image illustrating SiO2 Chemistry of siliceous aggregate

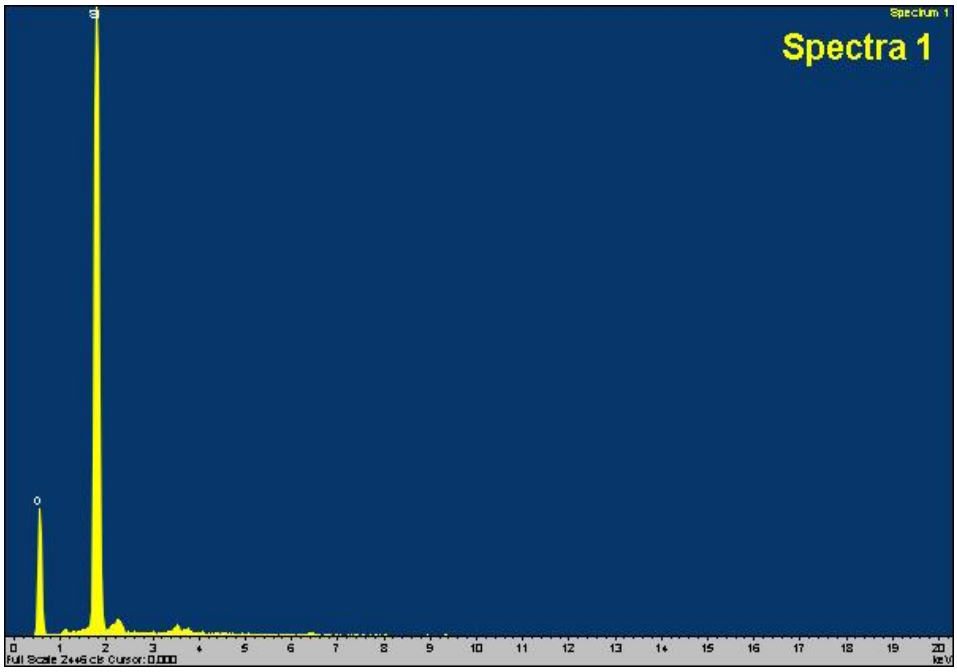

Spectra 2 from previous BS image illustrating chemistry of ASR gel

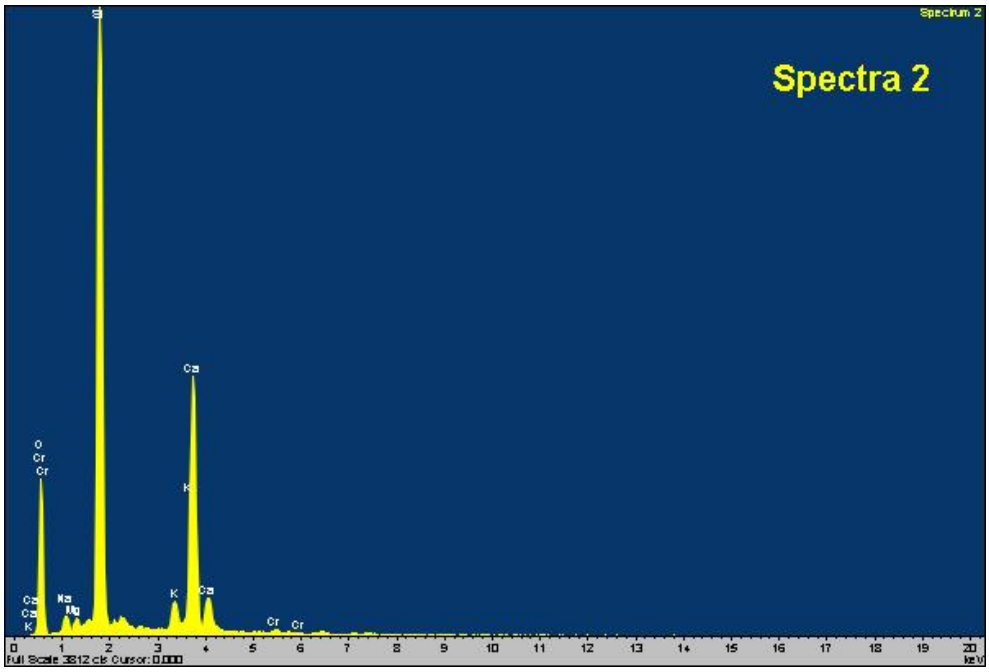

SEM/BS image illustrating ASR gel formation adjacent to distress aggregate

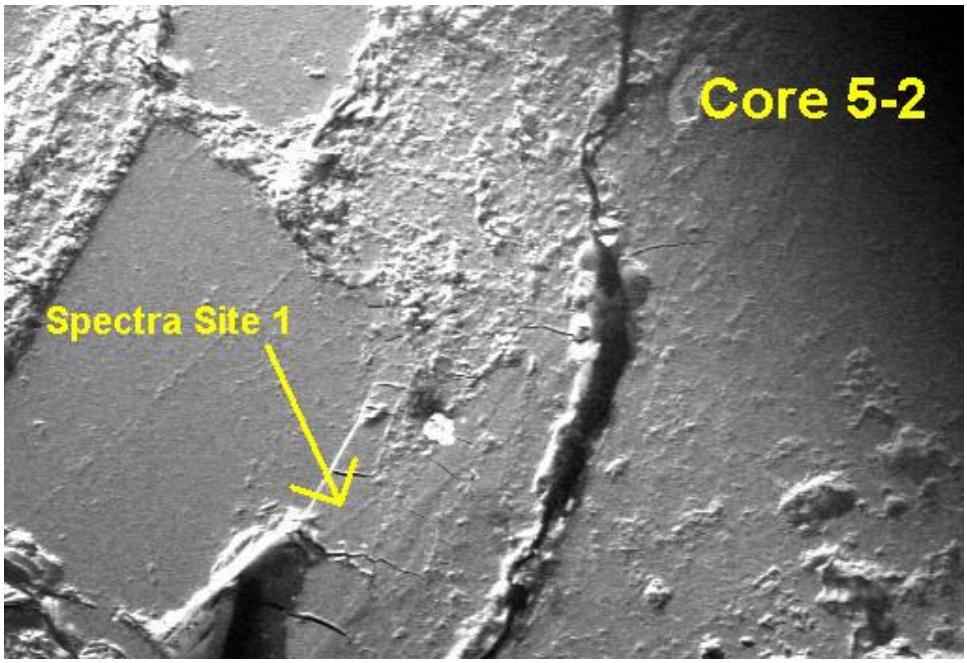

Spectra from previous BS image illustrating ASR gel chemistry

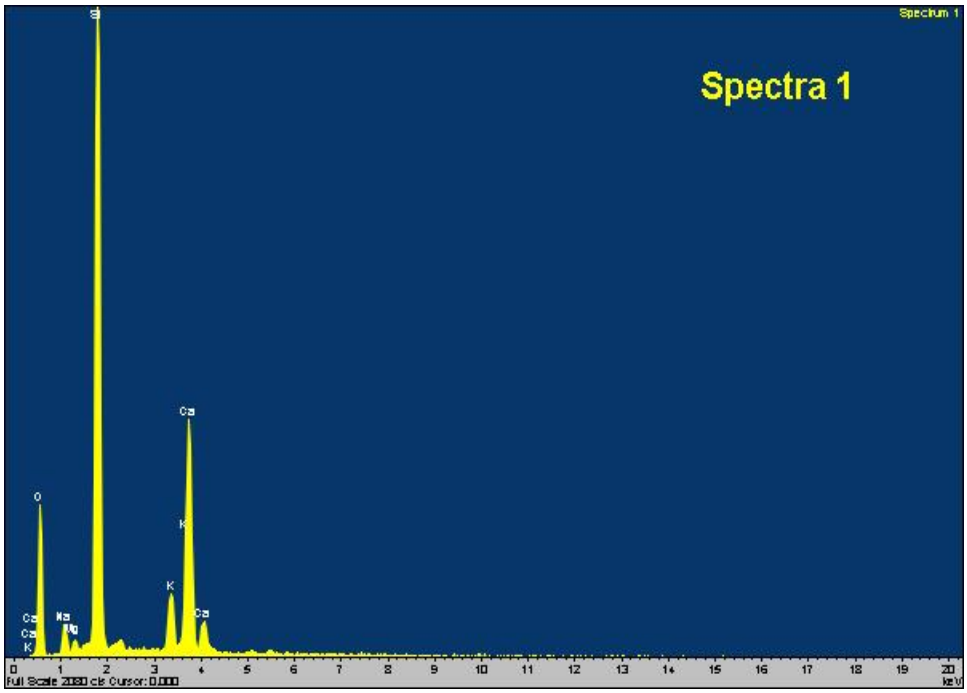

SEM/BS image illustrating site of ASR gel exudation propagating into paste from reactive aggregate

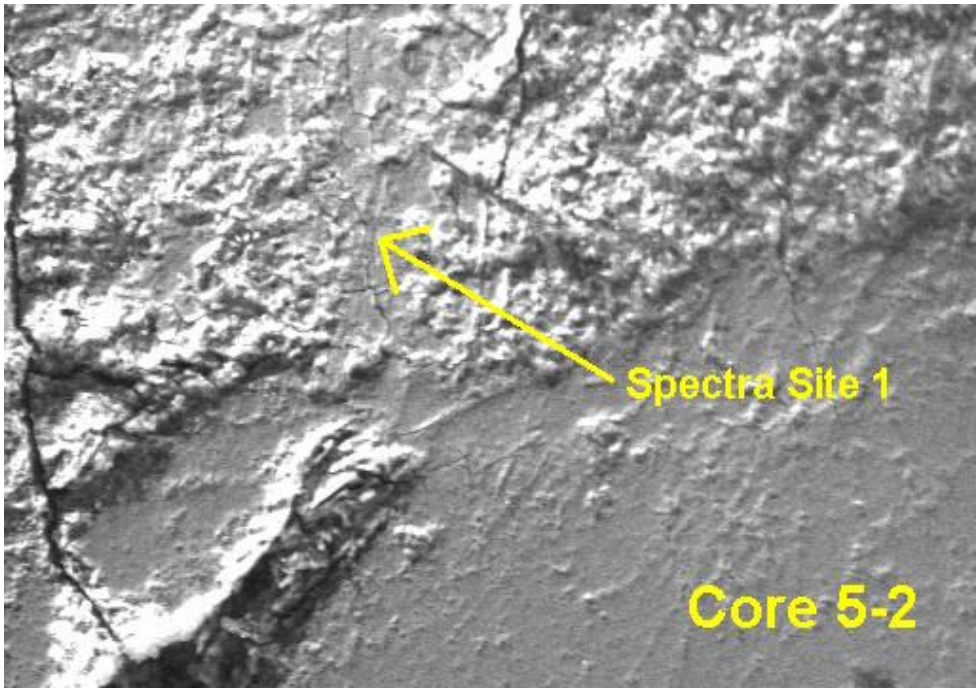

Spectra from previous BS image illustrating chemistry of ASR gel

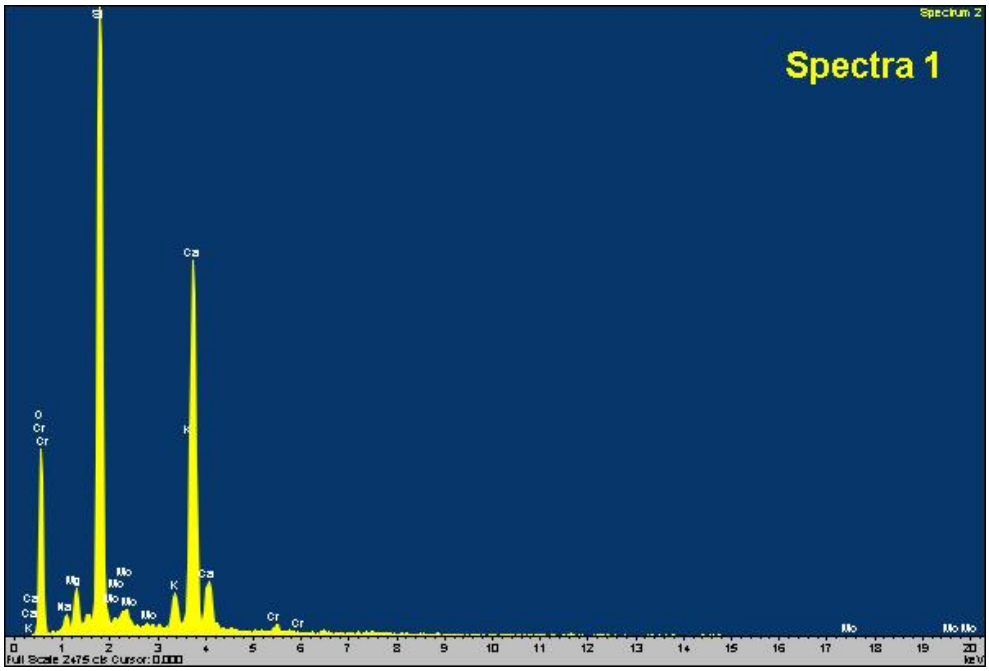

SEM/BS image illustrating accumulation of ASR gel in an air void

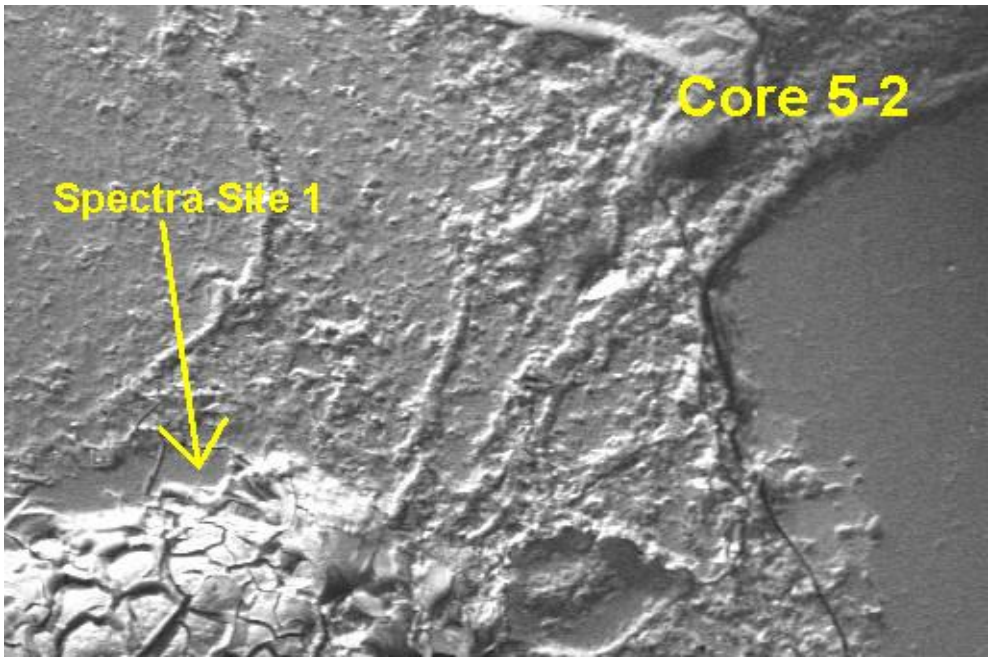

Spectra from previous BS image illustrating chemistry of ASR gel

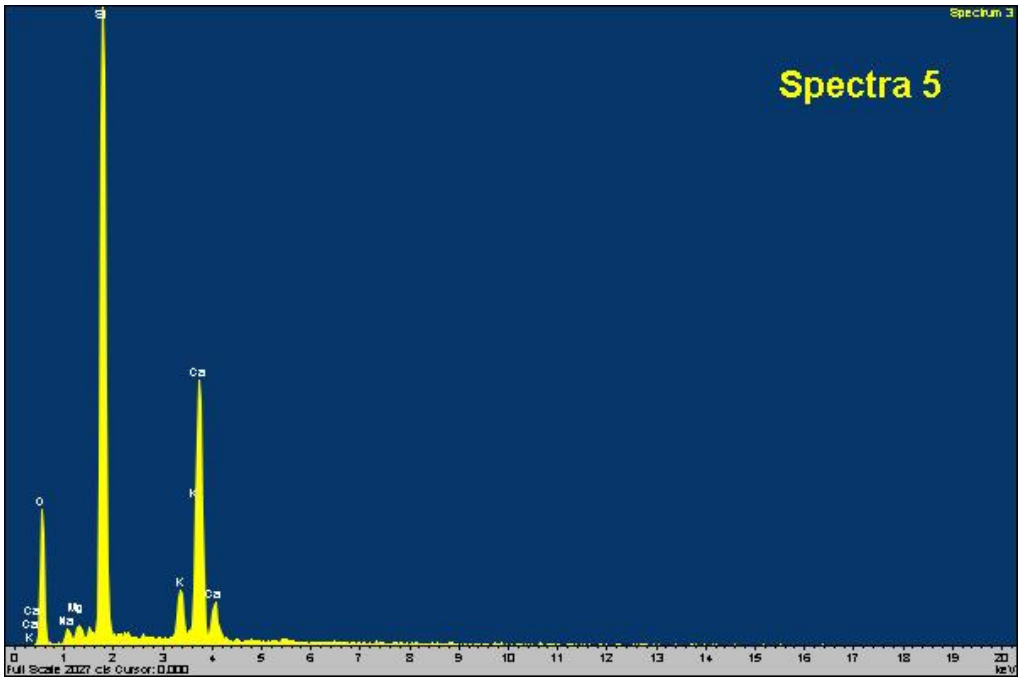

Concluding Comments: Based on this analysis, all six cores are exhibiting moderate to high levels of ASR degradation. Both the fine and coarse aggregates are experiencing ASR attack. Although ettringite is apparent and observed in many air voids, fine network of micro cracking, partial coating of detached rebar, and partial accumulation at paste aggregate interfaces, the distribution is not consistent with delayed ettringite formation.